europhysics
conference
abstracts

13 th European Conference on

Controlled Fusion and Plasma Heating

Schliersee/14–18 April 1986

Contributed Papers, Part I
Editors: G. Briffod, M. Kaufmann

Published by: European Physical Society

Series Editor: Prof. S. Methfessel, Bochum

Managing Editor: G. Thomas, Geneva

Volume
10 C
Part I

13 th European Conference on

Controlled Fusion and Plasma Heating

Schliersee/14–18 April 1986

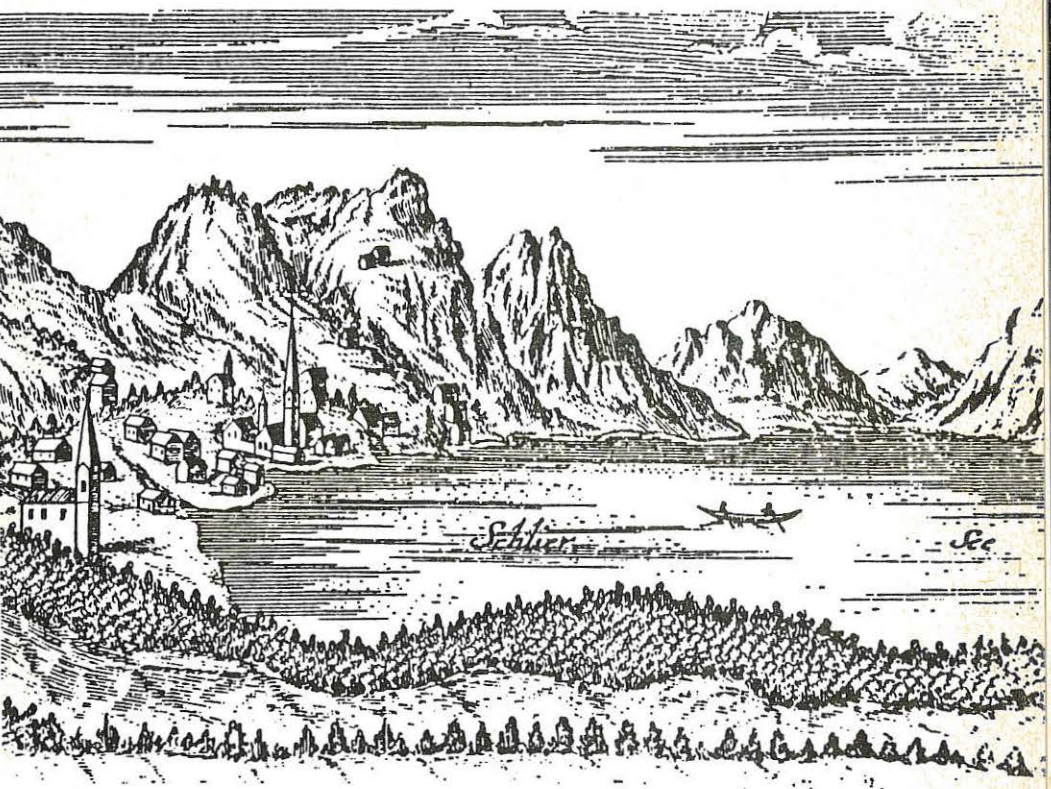

Michael Weening: Schliersee

Contributed Papers, Part I
Editors: G. Briffod, M. Kaufmann

ECA 10 C

EUROPHYSICS CONFERENCE ABSTRACTS is published by the
European Physical Society, 1986

The 13th European Conference on Controlled Fusion and Plasma Heating was held at Schliersee, Fed. Rep. of Germany from 14 to 18 April 1986. It was organized by Max-Planck-Institut für Plasmaphysik, Garching, Fed. Rep. of Germany on behalf of the Plasma Physics Division of the European Physical Society (EPS).

According to the new EPS arrangement the conference was held in spring and, because this is an even-numbered year, it concentrated on controlled fusion and plasma heating. The main topics therefore were

Plasma Confinement
Plasma Heating

with the following subtopics:

A Tokamaks
B Stellarators
C Alternative Confinement Schemes
D Plasma Edge Physics
E Alfvén and Ion Cyclotron Heating
F Electron Cyclotron Heating
G Neutral Injection Heating
H Lower Hybrid Heating and Current Drive

The Conference Programme included 18 invited lectures, 27 orally contributed papers and more than 200 papers presented in poster sessions.

The contributed papers of this 2-volume publication are photographically reduced in size from the originals provided by the authors.

Programme Committee/Paper Selection Committee

G. Briffod (Chairman), CEN, Grenoble, France
M. Kaufmann (Vice-Chairman), IPP, Garching, Fed. Rep. of Germany
T. Consoli, CEC, Brussels, Belgium
A. Gibson, JET, Abingdon, United Kingdom
C. Gormezano, CEN, Grenoble, France
G. Grieger, IPP, Garching, Fed. Rep.of Germany
H. DeKluiver, FOM, Nieuwegein, The Netherlands
F. Santini, ENEA, Frascati, Italy
V. Shafranov, Kurchatov Institute, Moscow, USSR
E. Sindoni, University of Milan, Milan, Italy

The invited papers and two post deadline orally contributed papers will be published by Pergamon Press in the journal "Plasma Physics and Controlled Fusion" Vol. 28 No. 9a and sent free of charge to each registered participant.

CONTENT OF VOLUME I

VOLUME I

A. TOKAMAKS

Oral Presentations

Poster Presentations

Poster Presentations

Poster Presentations

Poster Presentations

B. STELLARATORS

Oral Presentations

Poster Presentations

Poster Presentations

C. ALTERNATIVE CONFINEMENT SCHEMES

Oral Presentations

Poster Presentations

Poster Presentations

D. PLASMA EDGE PHYSICS

Poster Presentations

E. ALFVEN AND ION CYCLOTRON HEATING

Oral Presentations

Poster Presentations

Poster Presentations

Poster Presentations

F. ELECTRON CYCLOTRON HEATING

Oral Presentations

Poster Presentations

Poster Presentations

G. NEUTRAL INJECTION HEATING

Oral Presentations

Poster Presentation

(see next page)

VOLUME II

Poster Presentations

H. LOWER HYBRID HEATING AND CURRENT DRIVE

Oral Presentations

Poster Presentations

VOLUME II

Poster Presentations

VOLUME II

Poster Presentations

Tokamaks

SAWTOOTH ACTIVITY DURING ADDITIONAL HEATING IN JET

R D Gill, D V Bartlett, G Bracco[+], D J Campbell, S Corti, A E Costley, A W Edwards, W Engelhardt, H-U Fahrbach[o], D J Gambier[*], C W Gowers, R Granetz, A Hubbard[X], S E Kissel, N Lopes-Cardozo[Y], G Magyar, J O'Rourke, E Oord, R Prentice, S Tsuji[Z], B J D Tubbing[Y], A Weller[o], J A Wesson, V Zanza[+] and D Zasche[o]

JET Joint Undertaking, Abingdon, Oxon, OX14 3EA, UK. [+] EURATOM-ENEA Association, Frascati. [o] EURATOM-IPP Association, Garching. [*] EURATOM- CEA Association, Fontenay-aux-Roses. [X] Imperial College of Science and Technology, London. [Y] EURATOM-FOM Association. [Z]JAERI, Japan

ABSTRACT Sawtooth oscillations have been studied with a wide variety of diagnostics in JET in additionally heated discharges. Multichordal measurements, combined with tomographical reconstructions, have allowed a detailed experimental study of the sawtooth collapse with high time resolution. It is shown that the initial part of the collapse has m=1 topology.

1. INTRODUCTION Sawtooth activity has been studied in JET during both ohmically and additionally heated discharges using a large number of diagnostics, including two X-ray diode array cameras, a 12 channel ECE grating polychromator, four channel Fabry-Perot and Michelson ECE systems, a microwave transmission interferometer, a microwave reflectometer, bolometry and a multi-chord far infrared interferometer. Sawteeth have also been observed by the neutron diagnostics and on the particle fluxes and ion temperatures determined by a set of four neutral particle analysers.

2. SAWTEETH DURING ADDITIONAL HEATING During both neutral injection and radio-frequency heating the sawtooth oscillation increases in amplitude and its period becomes longer (Figure 1). The observation of partial sawteeth is common and the sawteeth are accompanied by a wide range of mhd activity in the plasma central region, generally with m=1.
In particular, we often observe: (i) strong successor oscillations following the sawtooth collapse; (ii) strong mhd activity accompanying the partial sawteeth; (iii) a large saturated m=1 mode which is sometimes seen before the sawtooth collapse during RF heating and (iv) a large amplitude m=1 mode seen during beam heating. The main sawtooth collapse generally occurs without mhd precursors. During ohmic heating typical mhd frequencies of ~ 1 kHz are seen and with ICRH this decreases, sometimes to 250 Hz. With 4.5 MW of tangential beam heating the frequency increases to ~ 5 kHz, corresponding to plasma rotation with $v = 10^5\ ms^{-1}$. The radial location and poloidal mode number of the mhd activity in the central region has been studied with both the soft X-ray cameras and the ECE systems. For a particular discharge, the maximum amplitude of the mode occurs at approximately the same minor radius slightly inside the sawtooth inversion radius, regardless of its phase within the sawtooth

cycle. These modes are thought to occur on rational q surfaces and their relation to the q=1 surface is under investigation.

3. THE SAWTOOTH COLLAPSE A detailed study has been made on JET of the rapid (~ 100 μsec) part of the sawtooth collapse with the X-ray and the ECE systems. The two X-ray cameras view the plasma from vertical and horizontal ports at the same toroidal location with 38 and 62 detectors respectively. The detectors are shielded with 140 μm of Be to enhance their sensitivity to radiation from the central region of the plasma from which the emission is due mainly to He-like Nickel for RF heated discharges and recombination for beam heated discharges.

Further information on the sawtooth collapse comes from the ECE diagnostics. In particular the electron temperature at a fixed radius is measured with very high time (10 μsec) and temperature resolution (30 eV) using a Fabry-Perot instrument and the sawtooth development in both time and radius along a fixed chord is measured with a 12 channel polychromator system with similar resolution.

A typical sawtooth collapse, with successor oscillations, taken during an RF heated discharge, is shown in Figure 2. The letters A-F indicate the times used for Figure 4. A contour plot showing the X-ray signal intensities from the vertical camera as a function of detector number and time, taken at 200 kHz sampling frequency (Figure 3a), shows that the collapse occurs in ≈ 100 μs and in this case with a rapid outward movement of the hot central plasma core. A similar plot for a different sawtooth collapse taken with the ECE polychromator with a digitization frequency of 20 kHz (Figure 3b) shows that the plasma temperature behaves in a similar way to that of the X-ray emission but in this case with an inward movement. These measurements indicate that the initial part of the sawtooth collapse is due to bulk motion of the hot centre of the plasma off axis to r/a ≈ 0.3.

The detailed nature of the collapse and its successors have been studied by tomographic analysis [1] of the data from both X-ray cameras. By fitting the experimental data with radial Zernicke polynamials ℓ=8 and angular harmonics m=2 (but excluding sin 2θ), the line integrated data observed by each X-ray detector is reduced to a two dimensional function of X-ray emissivity as a function of plasma major radius and height. The tomographic reconstructions were carried out at 5 μs intervals throughout the sawtooth collapse. Some of these reconstructions are shown in Figure 4 in the form of contour plots and illustrate the main features of the collapse. On each plot the relative times are shown and the maximum radiated power, P_m. Initially the hot central core moves rapidly away from the centre with a maximum velocity of 2×10^3 ms^{-1} until it reaches r/a ~ 0.3 where the outward motion stops. The hot region then collapses on a time scale of 100 μs while at the same time the emissivity in the remainder of the central region increases. This implies a mixing of hot and cold plasma regions or rapid conduction of heat during this phase of the collapse. The final emissivity profile is not completely poloidally symmetric and it is the subsequent rotation of this distribution which is responsible for the observations of successor oscillations as can be

seen from Figure 4. In other sawtooth collapses, without successor oscillations, the final state is completely poloidally symmetric.

The tomographic analysis clearly determines the m=1 character of the initial phase of the collapse and the strong n=1 mode seen by the magnetic coils at the plasma edge [2] to accompany the sawtooth collapse then determine the sawtooth collapse as an m=n=1 mode. The initial fast plasma motion occurs at different poloidal angles as expected for m = 1.

Our observations do not generally seem in good agreement with existing theoretical models and in particular are in disagreement with models which require growing or static magnetic islands before the sawtooth collapse

However, a very recent theoretical model[3], in which the plasma motion occurs on a rapid time-scale due to an ideal m=1 mode would account for many of the features of our observations, particularly the observed initial plasma motion.

REFERENCES 1. R S Granetz and J F Camacho, Nuclear Fusion 25, 727 (1985). 2. P A Dupperex, R Keller, M Malacarne and A Pochelon, 12th European Conference on Controlled Fusion and Plasma Physics 1, 126 (1985). 3. J A Wesson, Plasma Physics and Controlled Fusion, 28, 243 (1986)

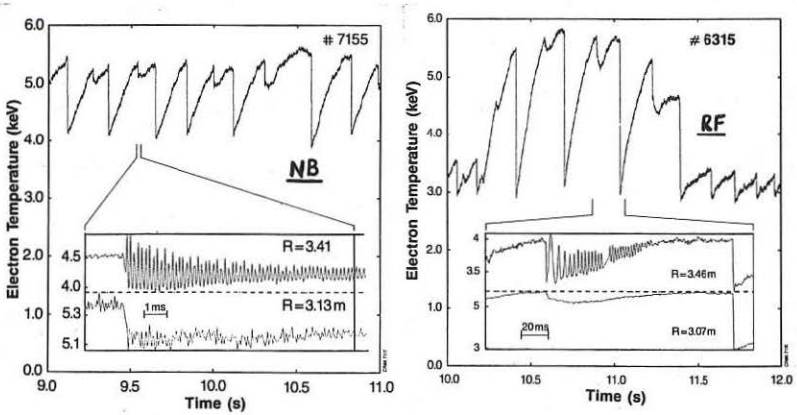

Figure 1 Sawteeth during additional heating. Note the much higher frequency mhd activity during the neutral beam heating.

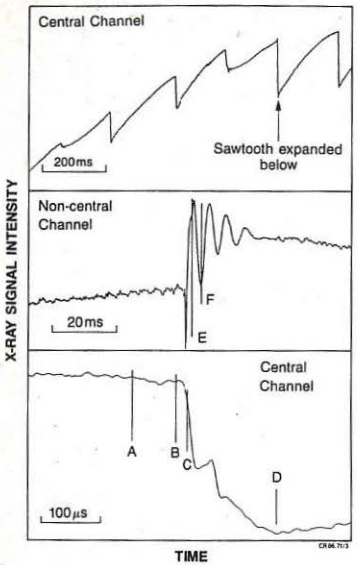

Fig. 2. X-ray signal on different timescales.

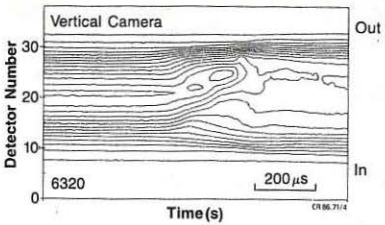

Fig. 3.(a). X-ray contour plot of line integrated intensity during sawtooth collapse

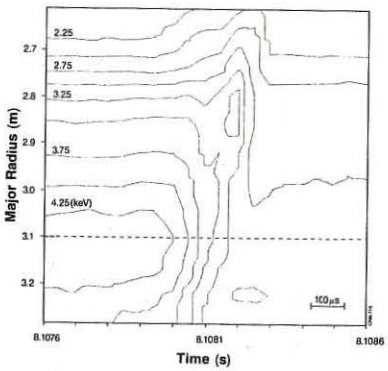

Fig. 3.(b). ECE electron temperature contour plot.

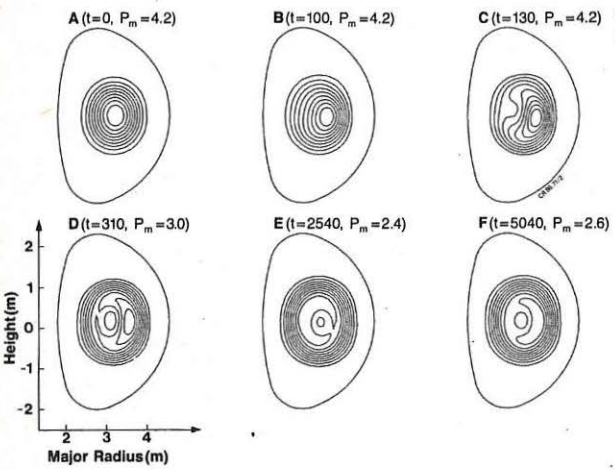

Fig. 4. Contour plots of X-ray intensity versus plasma height and major radius.

COMPARISON OF EXPERIMENTALLY-INFERRED ION THERMAL DIFFUSIVITIES WITH NEOCLASSICAL THEORY FOR NEUTRAL BEAM-HEATED DISCHARGES IN THE DOUBLET III TOKAMAK*

R.J. Groebner for the Doublet III Group
GA Technologies Inc., P.O. Box 85608, San Diego, CA 92138, USA

The study of ion transport in neutral beam-heated discharges in tokamaks is necessary to determine if neoclassical theory can reliably be used to predict the performance of future machines. Previous studies of ion transport have generally been difficult due to the lack of information regarding the ion temperature profile. The standard procedure used to study ion transport has been to model the T_i profile with the assumption that the ion thermal diffusivity profile $\chi_i(r)$ was equal to a multiplier times $\chi_i^{neo}(r)$, the ion thermal diffusivity calculated from neoclassical theory. The multiplier was varied until the calculated T_i profile agreed with the available ion temperature data, usually $T_i(0)$ or the measured neutron rate. Values of the multiplier in the range of 1 to 10 have generally been obtained with few estimates of the uncertainties in these values. Furthermore, there have been few, if any, attempts to calculate χ_i by modeling the ion temperature profiles in other ways. As a result, the issue as to whether or not the ion transport in tokamaks is in agreement with neoclassical theory has not been definitively answered.

Recently developed techniques for obtaining ion temperatures, based on measuring the Doppler-broadening of emission lines excited during charge transfer processes between high energy atoms in a hydrogen neutral beam and low-Z impurities in the plasma, can be exploited to provide improved $T_i(r)$ information.[1,2] For example, a multichordal spectrometer system has been used on the Doublet III tokamak to obtain high quality, temporally-resolved ion temperature profiles on a single shot basis.[3] Experimental values of the ion thermal diffusivity have been obtained for discharges for which measured T_i profiles were available in addition to measured T_e, n_e, and Z_{eff} profiles. For the beam heated discharges which have been examined, χ_i is larger than χ_i^{neo}, as calculated from the formulation of Chang and Hinton,[4] χ_i does not have the same spatial dependence as χ_i^{neo}, and χ_i is greater than or approximately equal to χ_e over most of the plasma profile.

The transport results presented were calculated with the $1\frac{1}{2}$D code ONETWO.[5] The plasma has been modeled as a medium in which heating input power from neutral beams and ohmic dissipation was balanced by losses primarily due to thermal conduction and convection with account also taken of losses due to line radiation, charge exchange and ionization of neutrals. The ohmic heating input power was approximately an order of magnitude smaller than the auxiliary heating power. Sawtooth transport has not been modeled due to the fact that the period of the sawteeth was sufficiently long that the plasma came to a near steady state condition before each sawtooth crash. Furthermore, the results pertain primarily to the region outside the q=1 surface.

*This is a report of work sponsored by the Department of Energy under Contract No. DE-AC03-84ER51044.

One of the data sets analyzed was a series of neutral beam-heated discharges operated in the expanded boundary divertor configuration which covered the following range of parameters: $B_T = 2.53$ T, $I_p = 0.35$ to 0.89 MA, vertical elongation = 1.4 to 1.9, $R_o = 1.43$ m, $a = 0.40$ m, $\bar{n}_e = 3.7$ to 7.9×10^{13} cm^{-3}, $P_T = 3.5$ to 6.6 MW, and $\nu_{i*} = 0.03$ to 0.22 for $r/a = 0.2$ to 0.7.[6] The plasmas were not near beta limits: $\beta_T a B_T/I_p \leq 2.2$ (%, m, T, MA). Detailed error analysis was performed on four representative discharges from this set. For the error analysis, measured parameters which were inputs to the transport analysis were varied individually to the extremes of their error bars and the transport code was rerun for each variation. The net error in a transport quantity was obtained from the quadrature sum of the errors from the individual variations.

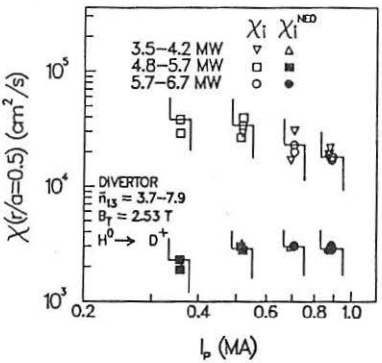

FIG. 1. Comparison of experimental and neoclassical ion thermal diffusivities at $r/a = 0.5$ for a range of plasma current and beam heating power. Error bars, due to uncertainties in measured quantities, are shown for representative discharges. $\bar{n}_{13}$ is line-averaged electron density in units of 10^{13} cm^{-3}.

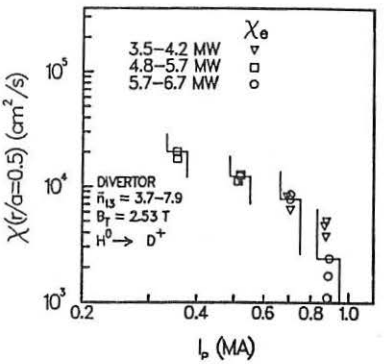

FIG. 2. Experimental electron thermal diffusivities at $r/a = 0.5$ for the set of discharges illustrated in Fig. 1.

The basic results are summarized in Fig. 1 which shows a comparison of the experimentally inferred values of χ_i at $r=a/2$ and the corresponding values of χ_i^{neo}. For all cases, χ_i is greater than χ_i^{neo}, and the error bars on the theoretical and experimental values for χ_i do not overlap. Figure 2 shows the experimentally-inferred values of χ_e for the data set of Fig. 1. For all discharges studied, χ_e was less than or equal to χ_i. For these discharges, the neutral beam heating power delivered to the ion channel was comparable to that delivered to the electron channel. Because the electron and ion

temperature profiles were very similar, the power transferred between the ions and electrons was small. The radial power balance shows that conduction was the dominant loss channel for both the ions and electrons over the inner two thirds of the plasma, and the heat loss from the plasma due to ion thermal conduction was greater than or equal to the loss from electron thermal conduction. For all discharges, χ_i was at the neoclassical level near the plasma center but was larger than expected from neoclassical theory for $r/a \gtrsim 0.2$. Furthermore, over the entire plasma, χ_e was less than or equal to χ_i. Figure 3 shows the ratio of χ_i to χ_i^{neo} and the associated error band due to uncertainties in the measurements versus minor radius for a typical discharge. For $r/a > 0.2$, the ratio is not consistent with neoclassical theory. In addition, there is no fixed value for χ_i/χ_i^{neo} which describes the data well, indicating that χ_i was not equal to a fixed multiple of χ_i^{neo}.

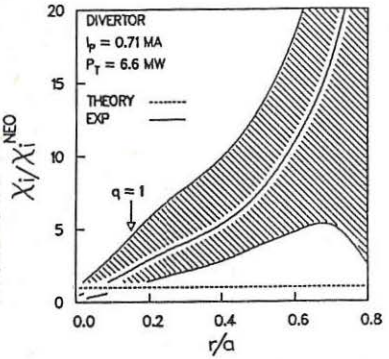

FIG. 3. The experimentally-inferred and theoretical values of χ_i/χ_i^{neo} are shown vs. r/a for a typical discharge. The error band for the experimental data is illustrated as is the location of the q=1 surface.

Table I
REGRESSION FITS
FOR χ_i*

Plasma Parameter	Exponent Theory	Exponent Experiment	χ^2
n_i	1	-0.3 ± 0.2	62
B_p	-2	-1.1 ± 0.2	103
T_i	-0.5	-1.2 ± 0.2	64
ϵ_{CH}	0.5	2.0 ± 0.2	56

*χ_i has been assumed to have the form: $\chi_i = n_i^a\, B_p^b\, T_i^c\, \epsilon_{CH}^d$ where $\epsilon_{CH} = \epsilon[1 + 2.85\, \epsilon^{0.5} - 2.33\, \epsilon]^2$.

Transport analysis has also been done for another set of discharges for which measured ion temperature profiles were available.[7] These discharges had rather different characteristics than those discussed above: they were limited on the inner wall rather than formed in the divertor configuration, they were of circular rather than elongated cross section, deuterium rather than hydrogen was used in the heating beams, and the toroidal field was 1.5 T rather than 2.5 T. The data are from a power scan up to the disruptive beta limit with $\beta_T a B_T / I_p = 3.8$. Although detailed error analysis was not performed for these discharges, it is reasonable to assume that the uncertainties in the values of χ_i are ±50% in light of the error analysis performed for the other set of discharges. The results are in agreement with those obtained for the divertor discharges: χ_i is substantially in excess of χ_i^{neo}, the ratio χ_i/χ_i^{neo} increases with minor radius, and χ_e is less than or equal to χ_i over the plasma cross section.

Regression fits for 80 experimental values of χ_i have been made to functions of the form $n_i^a\ B_p^b\ T_i^c\ [\epsilon\ (1 + 2.85\,\epsilon^{0.5} - 2.33\,\epsilon)^2]^d$. Neoclassical theory predicts that in the banana regime, a=1, b=−2, c=−0.5, and d=0.5. Due to correlation between the plasma parameters, only one exponent at a time was varied in the fitting procedure, and the other exponents were fixed to their neoclassical values. The results, displayed in Table I, show that χ_i does not have the parametric dependence expected from neoclassical theory and that the dependence of χ_i on poloidal field or aspect ratio may be less favorable than expected from neoclassical theory. These results should only be used as guides for further work; if χ_i is not neoclassical, there is no guarantee that it has the functional form used here.

Ion gradient-driven modes have been proposed as candidates for causing enhanced ion thermal diffusivity.[8] Most theories indicate that values of $\eta_i (\eta_i = d \ln T_i/d \ln n_i)$ of greater than one are needed to turn on the ion gradient modes. For the discharges examined, the uncertainty in the density gradient is sufficiently large that no useful bounds can be put on the experimental values of η_i in the inner half of the plasma. However, for typical discharges, $\eta_i \sim 0.5 - 1.3$ at $r/a = 0.6$ and $\eta_i \sim 0.3 - 1.0$ for $r/a = 0.65 - 0.80$.

For the discharges examined, if $T_i(r)$ is modeled with the assumption that $\chi_i(r)$ = multiplier × $\chi_i^{neo}(r)$ and if the multiplier is adjusted so that the calculated $T_i(0)$ is equal to the measured central ion temperature, the predicted T_i profile is considerably broader than the measured profile. As a result, the exchange term due to $T_e - T_i$ is underestimated and χ_e is forced to rise to compensate. The resulting χ_e profile generally rises with r/a and is larger than χ_i throughout much of the plasma. χ_i is forced to decrease with r/a because χ_i^{neo} invariably does so. The use of measured T_i profiles produces a rather different picture of confinement. χ_i is flat or rising with r/a and χ_e is less than or equal to χ_i throughout the plasma. For these discharges, ion confinement evidently is as important as, if not more important than, electron confinement.

References

1. Fonck, R.J., Darrow, D.S., Jaehnig, K.P., Phys. Rev. A **29**, (1984) 3288.
2. Groebner, R.J., Brooks, N.H., Burrell, K.H., Rottler, L., Appl. Phys. Lett. **43**, (1983) 920.
3. Seraydarian, R.P., Burrell, K.H., Brooks, N.H., Groebner, R.J., and Kahn, C., Rev. Sci. Instrum. **57**, (1986) 155.
4. Chang, C.J. and Hinton, F.L., Phys. Fluids **25**, (1982) 1493.
5. Pfeiffer, W., Davidson, R.H., Miller, R.L., Waltz, R.E., GA Technologies Report GA-A16178 (1980).
6. Groebner, R.J., Pfeiffer, W., Blau, F.P., Burrell, K.H., Fairbanks, E.S., Seraydarian, R.P., St. John, H., and Stockdale, R.E., GA Technologies Report GA-A17935, to be published in Nuclear Fusion.
7. Ohkawa, T., Stambuagh, R.D., and the Doublet III Physics Group, GA Technologies Report GA-A18189, to be published in Plasma Physics and Controlled Fusion.
8. Coppi, B., Rosenbluth, M.N., Sagdeev, R.Z., Phys. Fluids **10**, (1967) 582.

ENERGY TRANSPORT IN JET WITH OHMIC AND AUXILIARY HEATING

K Thomsen+, D V Bartlett, V Bhatnagar, R J Bickerton, M Brusati, M Bures, D J Campbell, J P Christiansen, J G Cordey, S Corti, A E Costley, G A Cottrell, G Duesing, A Edwards, S Ejima*, J Fessey, M Gadeberg+, A Gibson, R D Gill, N Gottardi, A Gondhalekar, C W Gowers, F Hendricks, J Jacquinot, O N Jarvis, E Kallne, J Kallne, S Kissel, L de Kock, P Lallia, E Lazzaro, P J Lomas, P D Morgan, P Nielsen, R Prentice, R T Ross, J O'Rourke, G Sadler, F C Schüller, A Stäbler#, M F Stamp, P E Stott, D R Summers, A Tanga, A Taroni, P R Thomas, E Thompson, F Tibone, G Tonetti**, B J Tubbing, M L Watkins

JET Joint Undertaking, Abingdon, Oxfordshire, OX14 3EA
On attachment from *GA Technologies, USA; +Riso National Laboratory Denmark; #IPP, Garching, FRG; **CRPP, Lausanne, Switzerland

JET has now been operated with ohmic, ion cyclotron resonance and neutral beam injection heating. A wide range of plasma conditions have been studied with ohmic and ion cyclotron resonance heating while neutral beam injection heating has just recently been applied.

1. OHMIC HEATING

During 1984 and 1985 an extensive series of experiments with ohmic heating have been carried out in both Hydrogen and Deuterium discharges [1].

The ranges of variation in the main plasma parameters covered are: Toroidal magnetic field $1.7 < B_T < 3.4$ T; plasma current $1 < I_p < 4$ MA; line average density $0.5 \times 10^{19} < n < 3.6 \times 10^{19}$ m^{-3}; elongation $1 < K$ (= b/a) < 1.7; minor radius $0.8 < a < 1.23$ m; major radius $2.5 < R < 3.4$ m; cylindrical safety factor $1.7 < q < 12$; effective charge $2 < Z_{eff} < 8$; peak electron temperature $1.5 < T_e < 5$ keV; peak ion temperature $1 < T_i < 3$ keV.

The plasma geometry has been varied from fully elliptical to small circular plasmas limited on the inside wall or on the limiter. The discharges had long flat tops in current, density and temperature, 4 - 12 secs, which was sufficient in all but the 3.5 and 4 MA discharges for the magnetic field diffusion to have been completed before the end of the flat top. Values up to 0.8 s have been achieved for the energy confinement time defined by $\tau_E = W/(P_{tot} - \dot{W})$, where $W = 3/2 \int (n_e T_e + n_i T_i)\, dv$.

The scaling of τ_E with density for a few characteristic conditions is shown in Fig. 1. The general pattern is that at low densities the confinement time increases roughly linearly with density and then saturates at higher densities ($n \geq 3 \times 10^{19}$ m^{-3}). The precise reason for the saturation is not clear, both the impurity radiation and transport losses increase as the limiting τ_E is reached. Due to the large errors in separating the ion and electron losses at high densities, it is not possible to determine which is the dominant loss channel.

The scaling of τ_E with the plasma parameters has been investigated, Fig. 1 shows that the neo-Alcator scaling, $\tau_E \propto nqR^2a$, is a reasonable fit. A marginally better fit can be obtained by a regression analysis in the form $\tau_E \propto B_T^{\alpha} q^{\beta}$ etc. The result from such an analysis is (A is the atomic mass and $\varepsilon = a/R$ the inverse aspect ratio)

$$\tau_E = 0.013\ n^{0.38}\ q^{0.33}\ B_T^{0.57}\ K^{0.21}\ R^{3.2}\ \varepsilon^{1.7}\ A^{0.56} \qquad (1)$$

The range of variation of R and ε in the JET data set is very small so the uncertainty on their indices are rather large. The JET data set has been combined with the DIII data set to get a better estimate of the scaling with dimensions. The scaling law obtained from a regression analysis on this combined data set can in terms of q (cylindrical) be written as:

$$\tau_{Ee} \propto n^{0.6}\ q^{0.5}\ B_T^{0.1}\ K^{0.3}\ R^{3.4}\ \varepsilon^{0.9} \qquad (2)$$

From analysis of the local transport properties with interpretative and predictive codes three distinct regions have been clearly identified; an inner region dominated by sawtooth activity, an intermediate region dominated by electron and ion thermal transport and an edge region dominated by impurity radiation and other atomic processes. The main loss channel at low and moderate densities in the second region is found to be via the electrons. The ion thermal conductivity is between 1 and 8 times neoclassical with the higher values of this anomaly factor occuring at lower densities. The electron thermal conductivity can be approximated by $\chi_e \sim 2.5.10^{19}/n$ at low densities, while for the highest JET densities it does not decrease with n. No clear dependence of χ_e on toroidal magnetic field or plasma current has been observed so far.

2. ION CYCLOTRON RESONANCE HEATING

Ion cyclotron resonance heating has been used in JET since the beginning of 1985. The heating system and characteristics of the different antennas are described elsewhere [2]. Various minority heating experiments have been performed in deuterium discharges with either H or ^{3}He as the minority gas.

It has been possible to couple up to 6 MW of RF power, P_{RF}, to the plasma. The increase of the total plasma energy during ICRH is partly due to a density increase. However, both the ion and electron temperatures have also been increased significantly.

In the first experiments the power scaling of W and τ_E was unclear [3]. Recent results seem to support a linear scaling of W with power in the form

$$W = W(o) + \tau_{inc}\ P_{tot} \qquad (3)$$

Fig. 2 shows W versus P_{tot} for different plasma currents obtained in D (^{3}He) limiter discharges with B_T = 3.4 T, K = 1.45 and a = 1.2 m using a frequency of 33 MHz for central power deposition. The results of fitting eq. (3) to the RF-points only are shown by dotted lines. The incremental confinement time τ_{inc}, obtained this way, ranges from 128 ms - 192 ms with no obvious current dependence.

At present no strong dependencies of τ_{inc} with respect to P_{RF}, B_T, I_P and n_e have been observed, however, comparing with results from other tokamaks there must clearly be a strong dependence on the plasma size [4]. The degradation of the total τ_E during ICRH is clearly seen in Fig. 3.

From Eq. (3) we may express the confinement of both ohmic and additional

heated plasmas in the form

$$\tau_E = \tau_E^{OH} \frac{P_\Omega(0)}{P_{tot}} + \tau_{inc} \left(1 - \frac{P_\Omega(0)}{P_{tot}}\right) \qquad (4)$$

where τ_E^{OH} and $P_\Omega(0)$ are the ohmic heating confinement time and power, respectively, in the absence of auxiliary heating. The present τ_{inc} is typically one third of τ_E^{OH}, which means we need to couple more than 10 times the ohmic power in order to confirm the saturation of τ_E.

By performing an exponential fit of the form $W(t) = W_o + \Delta W\ (1-\exp(-t/\tau))$ to the time evolution of W from the time of a change in RF-power level, we can estimate the fraction $f = (\Delta W - \tau\Delta P_\Omega)/\tau\Delta P_{RF}$ of RF-power which contributes to the increase in stored energy. This fraction f was typically ~ 70% in the experiments shown in Figs. 2, 3.

3. NEUTRAL BEAM INJECTION HEATING

Neutral beam injection heating (45 - 65 keV H into D plasma) has now been successfully applied to JET discharges [5]. Identical target plasmas have been used for NBI and ICRH making it possible to compare the two methods. Fig. 4 shows W versus P_{tot} for NBI heating, i.e. the equivalent of Fig. 2. Again a linear dependence of W with P_{tot} (eq. (3)) fits the data. In addition τ_{inc} shows an apparent current dependence which is present in all the estimates of the total plasma energy as is shown in Fig. 5.

In conclusion all NBI and ICRH experiments so far have produced values of τ_{inc} in the range 100 - 300 ms. Future heating experiments with more input power are needed to determine the dependence of τ_{inc} with power.

REFERENCES

[1] Cordey, J. G. et al., EPS Conference, Budapest (1985).

[2] Jacquinot, J. et al., Plasma Physics and Controlled Fusion 28, 1 (1986)

[3] Ejima, S. et al., APS Conference, San Diego, Paper 6p53 (1985)

[4] Jacquinot, J. et al., Royal Society Meeting, London (1986)

[5] Duesing, G. et al., Royal Society Meeting, London (1986)

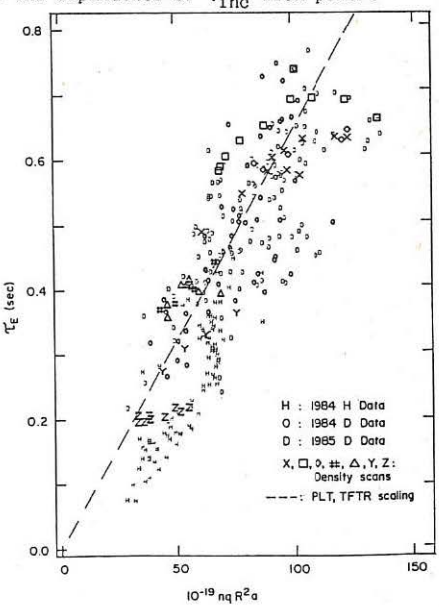

Figure 1 : Energy confinement time versus the neo-Alcator scaling. Ohmic data only.

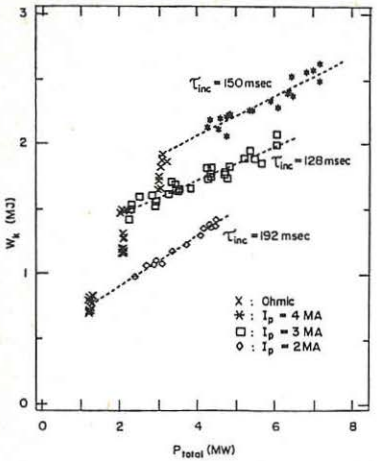

Figure 2 : Total kinetic plasma energy versus total input power from ICRH heating experiment.

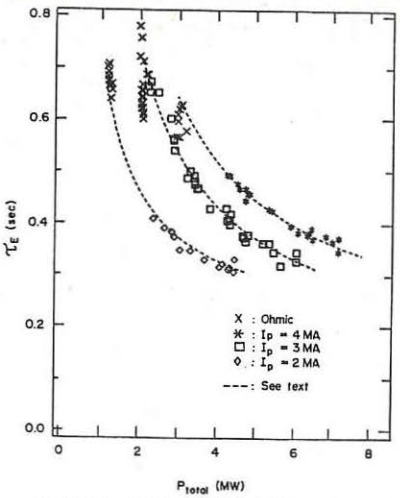

Figure 3 : Energy confinement time versus total input power from ICRH heating experiment. The dotted lines correspond to the fit lines in Fig. 2.

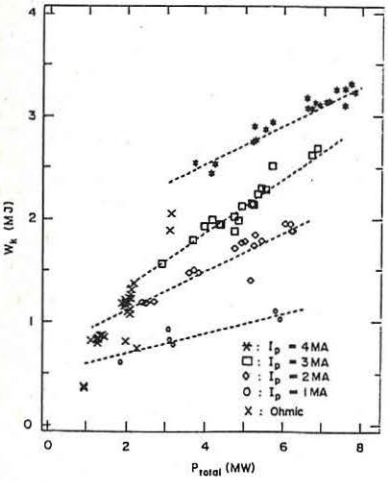

Figure 4 : Total kinetic plasma energy versus total input power from NBI heating experiment. The results of fitting the data to Eq. (3) are shown by dotted lines.

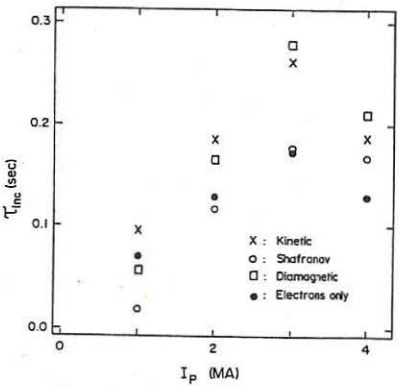

Figure 5 : The incremental confinement time, determined from the different estimates of plasma energy, shown versus plasma current, for the NBI heating experiment.

THE INFLUENCE OF THE CURRENT DISTRIBUTION ON THE ACHIEVABLE ß-VALUES IN ASDEX

G. v. Gierke and G. Becker, H. S. Bosch, H. Brocken, K. Büchl, A. Eberhagen, D. Eckhartt, G. Fussmann, O. Gehre, J. Gernhardt, E. Glock, O. Gruber, G. Haas, J. Hofmann, A. Izvozchikov[1], G. Janeschitz, F. Karger, M. Kaufmann, M. Keilhacker[2], O. Klüber, M. Kornherr, K. Lackner, R.S. Lang, M. Lenoci, F. Leuterer, G. Lisitano, F. Mast, H. M. Mayer, K. McCormick, D. Meisel, V. Mertens, E. R. Müller[2], H. Murmann, H. Niedermeyer, J.-M. Noterdaeme, A. Pietrzyk[3], W. Poschenrieder, H. Rapp, H. Riedler, H. Röhr, J. Roth, F. Ryter[4], W. Sandmann, F.Schneider, C. Setzensack, G.Siller, P.Smeulders[2], F.X. Söldner, E. Speth, K.Steinmetz, K.-H. Steuer, F. Wagner, F. Wesner, G. Vlases[3], O. Vollmer, D. Zasche

Max-Planck-Institut für Plasmaphysik
EURATOM Association, D-8046 Garching

Introduction:

In the divertor tokamak ASDEX we get in the H-regime a clear ß-limit /1/ at

$$ß_{cr} = 2.8 \frac{I}{a\ B} \ \% \ [MA,m,T] \qquad (1)$$

if we use for the volume averaged ß the ß-value measured by the diamagnetic loop. Below the ß-limit the highest ß-value during a shot, $ß_{max}$, is proportional to the normalized power

$$P_N = \frac{P}{0.33 \cdot b \cdot R \cdot B} \qquad (2)$$

where P[MW] is the total heating power, 2b the vertical diameter and B the magnetic field on axis. The confinement time at $ß_{max}$ is proportional to the plasma current I. The proportionality factor depends mainly on the isotope composition and slightly on current, impurity and other parameters not yet unraveled. The confinement time at $ß_{max}$ is $I_p/4 > \tau_E > I_p/7$, where the limits are for deuterium and hydrogen respectively. After $ß_{max}$ ß always decays to values about or even below 0.7 - 0.8 $ß_{cr}$. At this level nearly time independent ß-values could be observed. The ß-decay is usually the faster, the closer $ß_{max}$ is to $ß_{cr}$. There is no qualitative difference in any signal between discharges with $ß_{max} = ß_{cr}$ or $ß_{max} < ß_{cr}$.

After excluding all trivial reasons, like wall contact, radiation due to impurity accumulation etc, the only thinkable parameter which could change with time and would cause the observed ß decay is the current distribution. But only the longest observed decay times are in agreement with resistive current diffusion (calculated with classical resistivity throughout this paper). We hesitated for a long time to assume faster current redistributions then those.

In the numerical calculations, which result in a similar ß-limit as observed experimentally the limit seems to be caused by a combination of ballooning modes and surface kinks /2/. In a divertor tokamak the behaviour of surface kinks are unclear due to the unknown influence of the strong shear near the separatrix. In ASDEX the influence of the separatrix is very concentrated and therefore the influence should be restricted to higher n-modes. As we

---

[1]Academy of Sciences, Leningrad, USSR; [2]Present address: JET Joint Undertaking, England; [3]Univ. of Washington, Seattle, USA; [4]CEN Grenoble, France

observe no pronounced changes with varying q-values we assume tentatively that the ballooning mode is responsible mainly for the observed limit.

The influence of the current distribution

We therefore have calculated the influence of the current distribution on the ballooning mode stability limit using the inner inductivity l_i as a measure. We used the ballooning mode criterium

$$\frac{dp}{dr} = -\frac{B^2}{2\,R\,q^2} \cdot \alpha(s) \qquad s = \left(\frac{r}{q}\right)\frac{dq}{dr}$$

and the approximation $\alpha(s) = s/1.67$ /3/, but we neglected the usual condition $q_o = 1$. We assume that the ballooning mode criterium is marginal all over the cross-section.

Figure 1 shows the resulting dependence of $\beta/\varepsilon\ q^2$ on l_i for several families of current distributions as shown by the inserts ($\varepsilon = a/R$). We see the expected strong dependence of β on l_i, but the surprising result is that β depends nearly completely on the global l_i value and only marginally on the actual shape of the current distribution. We conclude that l_i is a very sensitive parameter for the description of the volume averaged β resp. the global confinement time.

The dependence found in fig. 1 can be described by the approximation:

$$\frac{\beta}{\varepsilon} = \frac{1}{q^2}\,(19\ l_i^{\,2} + 44.5\ l_i - 27). \qquad (3)$$

Comparing this formula with experimental l_i-values, evaluated as described later, we find that the general behaviour of the β-decay can be described, but that the calculated β-values are larger by 20 - 100 % depending on the q-value. Inserting the empirical law (1), found experimentally and numerically, for the β limit, transformed to $\beta_{cr}/\varepsilon = 14/q$ one finds that unreasonably small l_i-values belong to this β-limit especially at higher q-values. This is not surprising, because all the theoretical calculations have been done in the cylindrical large aspect ratio approximation. We therefore assume as a correction that the q in eq. (3) is not the cylindrical q but q_ψ . Figure 2 shows now the β/ε dependence on l_i with different q_ψ as parameter. The β-limit $\beta/\varepsilon = 14/q$ and q_{cyl}-curves are also shown. They have been calculated assuming a purely thermal β_p in the calculation of q_ψ, neglecting contributions by the beam or rotation.

By the measured $\beta(\beta_p^{dia})$ and the measured q_ψ a point in fig. 2 is defined and with it the corresponding l_i. q_ψ is evaluated from β_p^{equ} by

$$q = q_c\,[1 + \varepsilon^2(1 + 0.5\ (\beta_p^{equ})^2] \text{ with } q_c = \frac{5a \cdot b \cdot B}{R \cdot I}$$

taking into account the empirically found dependence of a on β_p^{equ}: $a = 0.375\ (1 + 0.07\ \beta_p^{equ})$ but limited to $a \leq 0.44$ m, due to our vessel dimensions, which was found roughly in agreement with equilibrium calculations, (quoted q_c values are always with a = 0.4 m).

In fig. 2 data points are shown measured in the described way of a power scan at 379 kA and $q_c = 2.79$, H^o injection (1.8-3.5 MW), where the crosses are values at β_{max} and the points intermediate β values during the β decay or the β values on the end of the heating pulses. Supplemented is this scan by shots at 311 kA, at q-values of 2.805, 2.71, and 2.85. The slightly stronger bent of the experimental curves compared with the calculated q_c = const. curves is due to the nonthermal contributions of the beam and the rotation to β_p^{equ} and by it to q_ψ and by the increasing diameter. As we shall see later the resulting l_i values agree quite well with l_i values evaluated

in quite another way beside the lowest point shown, an L-shot, where we, however, do not expect that the ballooning criterium is fulfilled all over the radius.
In fig. 3 we show q-scans at otherwise constant parameters (311 kA, 3.5 MW H_o-injection). The achieved l_i values (and consequently the ß values) are limited to values <1.5. With D_o injection (4.05 MW) otherwise the same parameters very high l_i values result and the ß-limit can be reached also at larger q_c values.

To compare the found l_i values we evaluate l_i out of the difference signal

$$ß_p^{equ} - ß_p^{dia} = \frac{l_i}{2} + \frac{ß}{2} \text{ „nontherm.}$$

neglecting $ß_{\text{„nonth.}}$. $ß_{\text{„nonth.}}$ is estimated from the injected beam, the slowing down time and an expression for the rotation, which is proportional to the energy confinement time. The absolute value of $ß_{\text{„nonth.}}$ is adjusted so that for long lasting shots where the difference signals approach a constant value, the so evaluated l_i value approaches the l_i value calculated out of the electron temperature profile. Time dependence of l_i, evaluated in this manner are shown in fig. 4. The crosses are the l_i values according to our modified ballooning criterum. The agreement is nearly in all cases satisfying in spite of the many inaccuracies involved and the difficulty of the absolute calibration. With deuterium injection the agreement can't be reached with constant proportionality factors in every case as the nonthermal contributions (probably the rotation) seems to depend nonlinearily on the beam parameters and the confinement. But the very large l_i-values and their decay are found.

Summary and discussion

We conclude that in the H-regime the ballooning mode is limiting the energy content of the discharge at $ß_{max}$ and afterwards always and already at very low ß-values. The ß-limit $ß/\varepsilon = 14/q$ can only be reached by favorable combinations of l_i and q_ψ. At large q values l_i must be larger than in the ohmic cases, which can only be reached transiently by inductive currents, for which we have some experimental hints. These currents are due to the injected beam, the plasma rotation and the $ß_p$-changes. The ß-decay after $ß_{max}$ is due to the disappearance of these inductive currents and the approach to the stationary current profile defined by the conductivity profile. As a change of $ß_p$ and the rotation induce changes of the confinement by altering the ballooning limitation, an increase as well as a decrease has a self-inforcing effect. Therefore high ß values decay faster and to values well below limits achieved with smaller power.

The ß-limit itself, but also the ballooning limited profiles below of it, are influenced by rational q_ψ-values (fig.5). This coupling of the ballooning mode with surface kinks seems to favour the current redistribution. But much finer scans are necessary to prove this convincingly as higher rational values are involved, too, and the self-inforcing effect mask the rationals.

References:

/1/ M. Keilhacker, et al., in Plasma Phys. Contr. Fusion (Spec. Issue: Proc. 12th Eur.Conf.Contr.Fus.and Plasma Phys., Budapest, 1985), 28 (1986) 29. G. v. Gierke, Europhys. Conf. Abstr., 12th Europ. Conf. on Contr. Fusion and Plasma Phys., Budapest, 1985, 9F, Part I, 331.
/2/ F. Troyon, Workshop on "The Basic Physical Processes of Toroidal Fusion Plasmas", Varenna (1985).
/3/ J.A. Wesson, A. Sykes, Nucl. Fus., 25, 85 (1985).

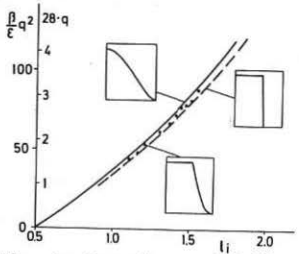

Fig. 1: Dependence of ballooning mode limited $<\beta_T>$ on the internal inductance li for different current distributions. The second scale gives the $q_o>1$ limit for different q.

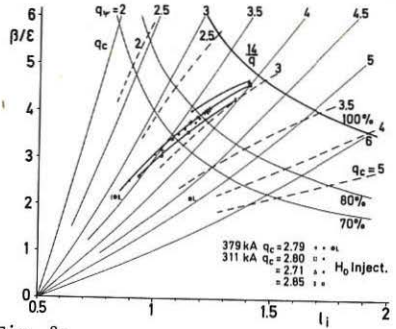

Fig. 2:
β_T dependence on li, if q_ψ instead of q_c is the important parameter in the formula derived in Fig. 1. Shown are experimental points of a power scan (q_c = const) and shots with neighbouring q_c ($+\beta_{max}$, $\cdot\beta$ at the end of the heating pulse).

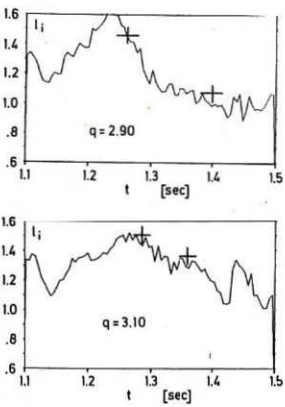

Figs. 4: Time dependence of li evaluated from the difference of $\beta_p^{equ} - \beta_p^{dia}$ and an estimated beam contribution. The crosses are li-values calculated with the modified ballooning criterion.

Fig. 3: The same as Fig. 2 but q_c-scans at constant current.

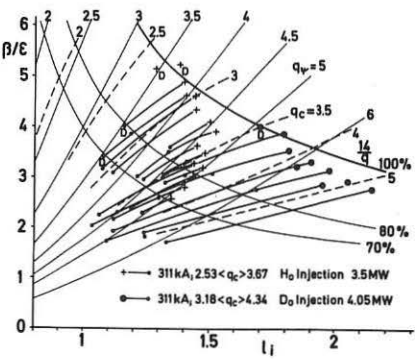

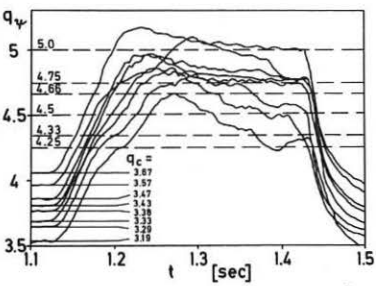

Fig. 5:
q_ψ-values calculated with β_p^{equ} showing the influence of rational q_ψ-values.

ENERGY CONFINEMENT IN TOKAMAKS

P R Thomas
JET Joint Undertaking, Abingdon, OX14 3EA, UK

1. INTRODUCTION

The presentation of the results of Ohmic and additional heating experiments on tokamaks has relied to a substantial degree on the parametric scaling of the total energy confinement time. Since the correct theory for transport in high temperature plasmas has not yet been identified, the range of validity of the resulting scaling laws is completely unknown. Also, it is not clear that the total energy confinement time is the appropriate quantity to represent the data and its use in scaling laws might even obscure the underlying physics. Tokamaks exhibit several confinement regimes with different scaling behaviour. It is proposed in this paper that tokamak plasmas can be viewed as have several phases separated by sharp transitions.

The use of the phraseology of phase transitions in thermodynamic systems is meant to suggest a framework for the representation of tokamak data. The applicability of the modern theory of phase transitions to driven systems which might not even posses a thermodynamic limit is the subject of an extensive literature [1]. In addition to discontinuous behaviour of observable quantities or their derivatives in an independent parameter, an important qualification for the theory to be useful is that the system possess a large scale order parameter. In some models of plasma turbulence [2], long wavelength pump modes appear to act as order parameters and the resulting transport exhibit the characteristics of second order phase transitions. However, the question as to whether or not tokamak plasmas undergo phase transitions will be left open here.

2. THE CONFINEMENT PHASES

There are two distinct, observable phases in tokamks. The growth of the energy density in the central region between sawtooth crashes indicates that a third (neoclassical?) phase exists within the q=1 surface. As given by Goldston [3], the low density Ohmic heating phase can be described by the neo-Alcator scaling

$$\tau_{E,OH} = 0.01\ n_e(10^{19}m^{-3})\ R^{2.04}(m)\ a^{1.04}(m)\ q^{0.5} \qquad (1)$$

whilst the high density ohmic and auxiliary heating phases are represented by

$$\tau_{E,aux} = \text{Const.}\ I_p(A)\ P_{tot}{}^{-0.5}(W)\ R^{1.75}(m)\ b^{0.5}(m)\ a^{-0.37}(m) \qquad (2)$$

The constant is in the range $3.7\text{-}7.4\times10^{-5}$ depending on the regime being represented. The variation in the constant is indicative of the neglect of a significant parameter from the description of a common transport mechanism.

In the neo-Alcator scaling, equation 1, is consistent with the Connor, Taylor constraints [4] for collisional high or low beta and collisionless

high beta models. This freedom of choice is perhaps the reason why so many explanations for neo-Alcator scaling have appeared!

The auxiliary heating scaling, equation 2, is consistent with collisional high beta and resistive MHD. The scaling of the resistive MHD model can be cast into the form

$$\beta_I = f\ (P_{tot}/P_{OH},\ S,\ q,\ a/R) \qquad (3)$$

where S is the magnetic Reynolds number and the other symbols have their usual meanings. It is assumed here that the plasma current is driven entirely by the transformer and that electron trapping is unimportant so that the Ohmic heating power is a consistent measure of the plasma resistivity. A simplified form of equation 3

$$\beta_I = 0.11((P_{tot}/P_{OH})\ (R/a)\ (b/a))^{0.5} \qquad (4)$$

is a quite good representation of the data [5] from several NBI dominated limiter experiments as shown in Figure 1. It is similar when transformed to a confinement time scaling to equation 2 and to the form expected of resistive ballooning mode turbulence [6].

3. THE NEO-ALCATOR TO AUXILIARY HEATING TRANSITION

The existence of a sharp transition between the neo-Alcator and auxiliary heating phases is indicated by several pieces of experimental data. The energy content of some 4MA, 3.4T ICRF heated JET plasmas is plotted against total power in Figure 2. The linearity and non-zero intercept imply the presence of an underlying confinement phase which supports most of the energy content. The propogation time of the sawtooth heat pulse was independent of input power for these discharges [7]. Furthermore, the thermal conductivity inferred from the beta pulse propogation is consistent with the characteristic time given by the slope in Figure 2. Therefore the thermal insulation has been broken down by the Ohmic heating and the application of auxiliary heating causes little or no further change. The transition becomes apparent when the energy content for Ohmic heating discharges with the same current and field are plotted against line average electron density. As can be seen in Figure 3, the transition is rather sharp and the energy content, becomes independent of density at high densities. The same behaviour has been observed in most machines.

Following the above comments, it is of interest to determine whether the transition to the high density Ohmic phase has any of the characteristics that might be expected of resistive MHD. The JET Ohmic heating data cluster around the transition and this results
in the reported weak density dependence of the energy confinement time [8]. Consequently, the JET data are well represented by the form of equation 3 as shown in Figure 4. The aspect ratio dependence is striking and must reflect the importance of toroidal coupling of modes or the edge plasma. It is tempting to ascribe the behaviour shown in Figure 4 to a threshold beta for MHD instability.

4. THE NATURE OF THE TRANSITION

Simple addition of the neo-Alcator and auxiliary heating loss rates is not consistent with the data. In order to match the sharpness of the transition, Goldston combined the loss rates by

$$\tau_E = ((1/\tau_{E,OH})^{\alpha} + (1/\tau_{E,aux})^{\alpha})^{1/\alpha} \qquad (5)$$

with $\alpha=2$. This suggests that each loss channel gains complete control of its own phase. The best match of the JET data to equations 1 and 2 can be obtained by taking $\alpha \to \infty$, or the maximum loss rate! Therefore it is unlikely that the confinement transition is due to the passage through a local critical point. Instead the data point to a global mechanism for switching from one loss process to the other [9].

Additional heating data from several machines [10] indicate that the current density profile or the shape of the electron temperature profile are held rigid by some, as yet, unexplained process. If this picture is correct, the temperature scale would be determined by the region with the worst loss rate in relation to the local power flow. A sharp confinement transition could then result form the switch of control between a region dominated by drift wave turbulence, for example, and another dominated by resistive MHD. Any model leading to the neo-Alcator scaling, in which the losses increase with electron temperature, would yield a confinement transition at a critical density which increases with heating power. Unfortunately the published data is rather sparse in this region. However there is some weak evidence in the JET data to suggest that the critical density increases slightly with power.

5. CONCLUSIONS

Complex, non-linear systems generally exhibit phenomena which can be described, at least phenomenologically, as phase transition. Tokamak plasmas are no exception and the transition from the neo-Alcator to auxiliary heating phases is a good example of such behaviour. The loss rate in the auxiliary heating phase and the critical beta in the Ohmic heating data are consistent with resistive MHD processes. However, the transition so sharp that local transport must be regulated by some global mechanism. This mechanics must reflect the dominance in tokamak plasmas of an unobserved phase transition associated with the shape of the electron temperature or current density profiles. A concerted experimental attack on the transition between the confinement phases would surely yield some insights into transport processes.

6. REFERENCES

1. See for example, H Haken, Rev. Mod. Phys., 47(1975)p67
2. R E Walz, Phys. Rev. Lett., 55 (1985)p1098
3. R J Goldston, Plas. Phys. and Cont. Fus., 26(1984)p87
4. J W Connor and J B Taylor, Nuc. Fus., 17(1977)p1047
5. The author gratefully acknowledges the use of data collected by S M Kaye and P J Lomas.
6. J W Connor, Plas. Phys and Cont. Fus., 26(1984)p1419
7. B Tubbing et al., Proc 12th EPS Conf. on Cont. Fus. and Plas. Phys., (Budapest 1985) Part 1, p215.
8. J G Cordey et.al, Proc 12th EPS Conf. on Cont. Fus. and Plas. Phys., (Budapest 1985) Part 1, p26.
9. B B Kadomstev, Comm. Plas. Phys and Cont. Fus., 9(1985)p227, has discussed a local switching of trasport processes.
10. J W Connor, Plas. and Cont. Fus., 26(1984)p1419.

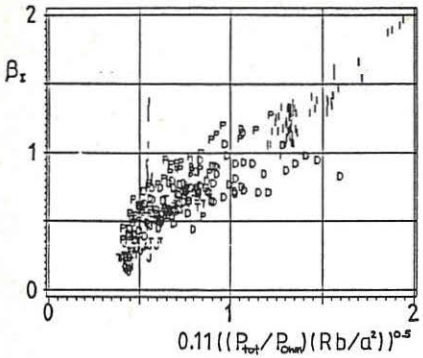

Figure 1: Equation 4 compared with data from DITE(C), DIII(D), ISXB(I), JET(J), PDX(P), TFR(F), and TFTR(T).

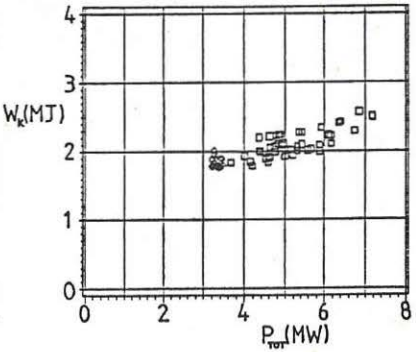

Figure 2: Total Plasma Energy vs total power for ◇ Ohmic and □ ICRF heated 4MA, 3.4T, $3.10^{19}m^{-3}$, a=1.2m JET discharges.

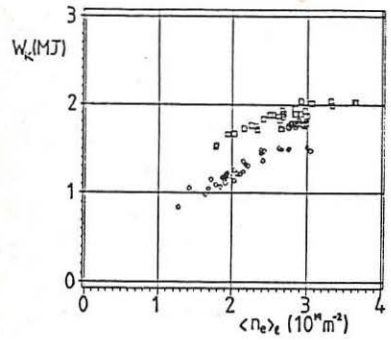

Figure 3: Total Plasma Energy vs. line average density for ◇ 3MA, 3.4T and □ 4MA, 3.4T JET discharges with a=1.2m and b/a = 1.4 - 1.55

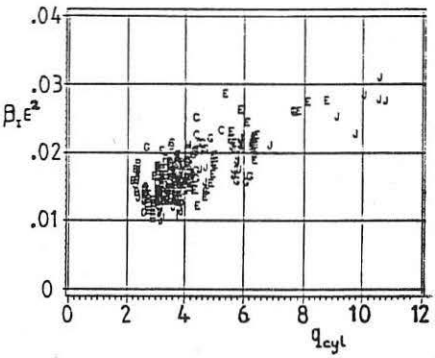

Figure 4: $\beta_T\varepsilon^2$ vs. Qcyl for JET OH discharges with toroidal field values A< 1.6T< B< 1.8T< C< 2.2T< D< 2.4T< E< 2.6T< F< 2.8T< G< 3.0T< H< 3.2T< I< 3.4T< J< 3.6T

HEATING PROFILE EXPERIMENT ON TFTR

R.J. Goldston, E. Fredrickson, K.McGuire, M. Zarnstorff, M. Bell, M. Bitter, C. Bush*, P. Efthimion, B. Grek, K. Hill, D. Johnson, H. Park, J. Schivell, S. Sesnic, G. Taylor
Princeton University Plasma Physics Laboratory, Princeton N.J. USA
*Oak Ridge National Laboratory, Oak Ridge Tenn. USA

Introduction

In early neutral beam injection experiments on PLT[1] it was observed that the electron temperature profile shape was not changed during injection, even at high densities where the heating profile was hollow. This was later quantified[2] using the temperature profile shape parameter $T_{eo}/\langle T_e \rangle_v$. Theoretically an ambiguity arises[3] because the sawtooth mechanism, in current profile equilibrium, dictates a maximum value for $T_{eo}^{3/2}/\langle T_e^{3/2} \rangle_v$, and if χ_e is sufficiently low in the core of the plasma relative to the edge, the plasma will seek this maximum. Thus it is difficult to tell if any other profile control mechanism is also active. In neutral beam heated discharges it is usually not possible to vary the beam deposition profile without changing the electron density[4,5] and thereby possibly χ_e, which makes the implication of profile consistency less clear. One alternative is to change the injected isotope[6], but because D^0 beams are observed to be more efficient at plasma heating than H^0, and thermal confinement also depends on plasma species, the penetration question is then mixed up with isotope effects.

Heating Profile Experiment - Initial results

We have begun experiments on TFTR to resolve the above ambiguities. By operating a plasma with R_0=2.36m, a=0.71m, we are able to inject 2 neutral beams with a total power of up to 2.5 MW aimed at tangency radii of 2.65 and 2.85m, to heat the edge of the plasma, or 1.76 and 2.05m, to preferentially heat the center. Thus the same target plasma and the same beam species and voltage can be used, giving very different heating profiles. With a plasma current of 1.2 MA and B_T = 5.1T, we obtain q_{cyl} = 4.5, and the sawtooth oscillations are relatively mild ($\Delta T_e/T_e \approx 10\%$ for "central" heating, 7% for "edge", $\tau_{st} \approx 35$ ms for both). The sawtooth inversion radius is at r = 0.16m and the prompt sawtooth effects are confined within r = 0.27m for both cases. Figures 1 & 2 show the calculated integrated beam heating profiles for "edge" and "central" heating, as well as the location of the q=1 surface (from ECE) and of the calculated q=2 surface.

With 0.5 sec of neutral beam injection, the electron density in these experiments rose from $\bar{n}_e = 2.4 \cdot 10^{19}$ m^{-3} to $3.8 \cdot 10^{19}$ m^{-3} in both cases. With "edge" heating, the central electron temperature rose more than with "central" heating during the first 0.2 seconds of injection, but then fell to the same final value as obtained in the "central" case. This might suggest that central fueling via a pinch mechanism is more favorable than via cold injected electrons. The time-dependent aspects of these discharges including particle balance, however, are still under investigation. $T_e(R)$ from Thomson scattering in each case at 0.45 seconds into injection is shown in figure 3. These profiles were both chosen to be at the midpoint of a sawtooth ramp. They are essentially identical - indeed if anything the "edge" heating cases are systematically very slightly narrower than the "central" cases. The density profiles from Thomson scattering overlay precisely. Table 1 summarizes the heating powers and final stored energies. The net beam heating, $P_{heat,b}$, and beam diamagnetism, $W_{dia,b}$, are calculated assuming the neutral density associated with $\tau_p = 0.2$ sec, comparable to τ_E. W_e is the electron stored energy from Thomson scattering, and W_{dia} is the stored energy from diamagnetism. Because of low metal content, X-ray Doppler broadening measurements of T_i had inadequate statistics. The central ion temperature was higher in the case of "central" heating but the value of T_i, and consequently of a neoclassical multiplier, is not well constrained by the error bars. The ion stored energy, W_i, is calculated assuming neoclassical ion thermal diffusivity with a large enhancement within the q=1 radius, although a multiplier of 5 on χ_i^{neo} does not violate the uncertainties in the stored energy measurements. Z_{eff} in these discharges was high, 3.6, as measured by X-ray PHA. These were among the first data shots taken after a machine opening. Z_{eff} due to metals was ≈ 0.01; thus central radiated power is anticipated to be low. Poloidal asymmetries in radiated power prevented us from measuring the local value inside of r = 0.3m, so p_{rad} was taken to be flat within this region.

Figure 4 shows the deduced χ_e profiles in "edge" and "central" heating cases as deduced from time-independent transport analysis. χ_e is reduced inside the region where the "edge" heating beams are deposited, but outside the region where sawteeth have a direct effect. This difference becomes more pronounced as the ion transport is increased in the analysis model. If we take χ_i to be neoclassical in the "edge" heating case, but 5 x neoclassical in the "central" case, the effect on the core χ_e is almost eliminated.

Radially dependent enhancements of χ_i during "central" heating could have a similar effect. Of course this means that the ions would then mediate profile consistency. However the measured $n_{eo}dT_{eo}/dt$ during sawteeth is 1.6 x greater in the "central" heating case than in the "edge" case, while the temperature gradients outside of the q=1 region are very similar. The calculated ratio of central electron heating powers for fixed χ_i/χ_i^{neo} is 1.75. This purely experimental result supports the idea that the mid-radius electron thermal diffusivity is lower in the "edge" heating case, despite the fact that $T_e(r)$ and $n_e(r)$ are identical.

Conclusions

Initial experiments indicate that $T_e(r)$ is remarkably fixed in shape and amplitude despite quite different heating profile shapes at a given total power. Coupled with Fredrickson's[7] result that $dlnT_e/dr$ in the mid-radius of full-size TFTR discharges is constant over a very wide range of parameters, these results point to the conclusion that $T_e(r)$ is constrained by more than just the direct action of the sawtooth. For the current series of experiments, however, better T_i and P_{rad} measurements are needed to improve the reliability of the calculated electron power balance. T_i profile measurements will help determine "profile consistency" of the ion temperature under these circumstances.

Acknowledgments

The authors thank the TFTR physics staff, operations staff, and beam group for their participation in these experiments. We also thank Dr. Harold Furth for his interest and encouragement. This work supported by US DoE Contract #DE-AC02-76-CHO3073.

Table 1

Case	P_{abs}	$P_{heat,b}$	P_{OH}	W_e	W_i	$W_{dia,b}$	W_{dia}
"center"	2.1	2.01	0.66	0.234	0.18	0.036	0.45
"edge"	2.32	2.15	0.66	0.219	0.15	0.017	0.39

References

1. R. Goldston et al., 2nd Joint Grenoble-Varenna Int. Symp. (1980), 711
2. R. Goldston, Plasma Physics and Controlled Fusion (1984) 26, 87
3. R.E. Waltz et al., GAT Report A18365 (1986)
4. M. Murakami et al., Plasma Physics and Controlled Fusion (1986) 28, 17
5. S. Milora et al., this conference
6. E. Speth et al., Proc. 12th Europ. Conf. Contr. Fusion and Plasma Phys., Budapest (1985) Vol II, 284
7. Fredrickson et al., this conference

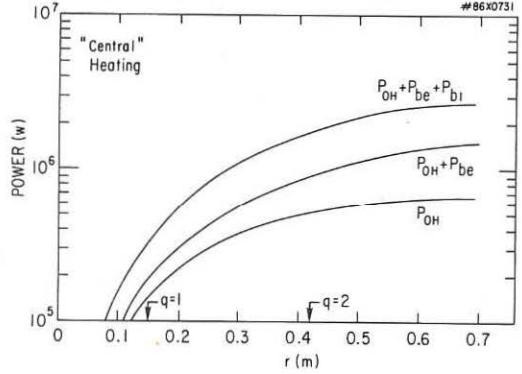

1. Volume integrated heating power - "Central" heating

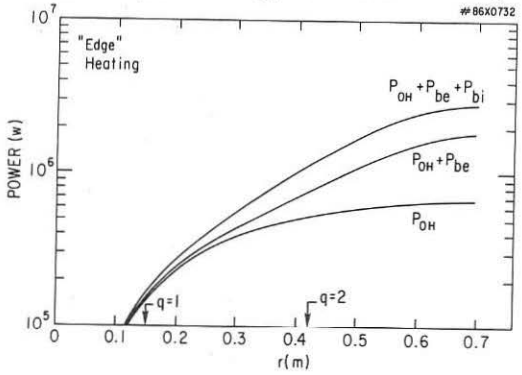

2. Volume integrated heating power - "Edge" heating

3. T_e profiles from Thomson scattering

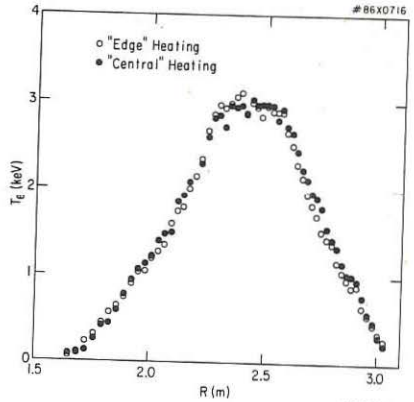

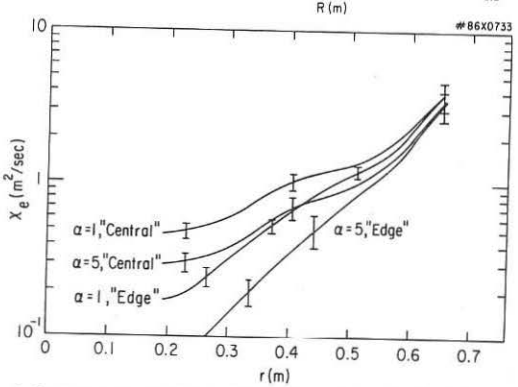

4. Deduced χ_e profiles. Error bars indicate shot to shot scatter of analysis results. $\alpha \equiv \chi_i/\chi_i^{neo}$

STABILITY OF HIGH PRESSURE PLASMA IN TOROIDAL TRAPS WITH A RIPPLED MAGNETIC FIELD

V.V. Demchenko, Yu.A.Zhdanov, A.Ya.Omel'chenko

Institute of Physics & Technology, the Ukrainian Academy of Sciences, Kharkov 310108, USSR

Closed magnetic traps with a spatial axis constitute an alternative concept to tokamaks, and they, too, can be used to form a basis for fusion-oriented reactor technology projects [1-2] . Recent advances in fusion experiment using such traps [3-4] have greatly stimulated the fusion community's interest in current-free magnetic systems featuring a complicated shape of magnetic axis [5-8] . The magnetic structure of the said devices is made up of spatial arrangements of the toroidal magnetic field coils (coil alignment). The number m of coils to generate such a field and thereby determine its magnetic structure which is inhomogeneous along the major azimuth of the torus (the ripple) can be several dozens, the ripple amplitude δ_m averaging several per cent from the value of the confining magnetic field.

The purpose of this study is to get an insight into the effects of the rippled magnetic field structure on the stability of Mercier modes and dissipative flutes (g-modes) in finite pressure plasmas produced in multi-form magnetic axis facilities. The stability analysis for such cases is based on the technique developed in [9,10] which takes into account both complex magnetic field geometry and longitudinal magnetic field ripple.

Let us assume that the magnetic axis of a toroidal fusion device is a spatial curve characterized by the curvature $k(\zeta)$ and torsion $\varkappa(\zeta)$ where ζ is the angular variable along the major radius of the torus. The stability of perturbations like Mercier and g-modes would be considered within the system of coordinates where the magnetic field lines of force are straight. Using such system of coordinates the stability criteria of the said modes can be shown as [11]

$$\mu'^2/4 + A_0 W - A_1 \mu' - A_0 A_2 + A_1^2 > 0, \qquad (1)$$

for the Mercier modes, and as

$$W - A_2 > 0 \qquad (2)$$

for the g-mode, all designations being standard.

In their general form the stability criteria (1) and (2) are too cumbersome to employ for a random plasma pressure distribution and a strong inhomogeneity of the magnetic field. With this in mind, we confine ourselves to the cases of an un-pronounced ripple of the longitudinal magnetic field:

$$B = \bar{B}/(1 + \textstyle\sum_m \delta_m e^{im\zeta})^2, \quad |\delta_m| \ll 1, \quad \delta_0 = 0 \qquad (3)$$

and parabolic plasma pressure distribution along the radius $P = P_0(1 - a^2/a_*^2)$. In which case the MHD criteria for the Mercier (1) and g-modes (2) in finite pressure plasmas in currentless

régime is as follows:

$$S_1 + S_2 - (a^2/R^2)\beta_\theta^3 \mu^6 S_3 < 0, \quad (4)$$

$$S_1 + S_2 + (a^2/R^2)\beta_\theta^3 \mu^6 S_4 < 0, \quad (5)$$

where $S_1 = \sum_n k_n^2$, $S_2 = -\frac{1}{2}\sum_n [k_n \tilde{k}_n^* + k_n \sum_m \delta_m^* k_{n-m}^* + k_n \sum_m \delta_m^* k_{n-m}^* + \text{c.c.}] \times$

$\times \frac{\mu - 2\varkappa - n}{\mu + n} + 3\sum_n n^2 |\delta_n|^2 + 8\varkappa^2 \sum_n |\delta_n|^2 - \frac{1}{2}\sum_n [k_n \sum_m \delta_m^* k_{n-m}^* \cdot m +$

$+ \tilde{k}_n \sum_m \delta_m^* k_{n-m}^* \cdot m + \text{c.c.}](\mu+n)^{-1}$, $S_3 = \frac{3}{16}\left[\sum_n \frac{|K_n|^2}{(\mu+n)^3} - \frac{1}{4}\sum_{n n_1 n_2}\left\{\left[-\frac{3}{2}\frac{1}{(\mu+n_1)(\mu+n_2)}\right.\right.\right.$

$+ \frac{5}{2}\frac{1}{(\mu+n)(\mu+n_2)} + \frac{1}{(\mu+n)(\mu+n_1)} + 4\frac{\mu+n+n_1-n_2}{(\mu+n)(2\mu+n+n_1)^2} + \frac{1}{2}\frac{(n-n_1)^2}{(\mu+n_1)(\mu+n_2)(\mu+n)^2}\left.\right] \times$

$\left.\frac{K_n^* K_{n_1}^* K_{n_2} K_{n+n_1-n_2}}{(\mu+n_1)(\mu+n_2)(\mu+n+n_1-n_2)^2} + \text{c.c.}\right\}$, $S_4 = S_3 - \frac{3}{16}\left[\sum_n \frac{|K_n|^2}{(\mu+n)^5}\right]^2$, $K_n = k_n + \tilde{k}_n$

k_n and $\varkappa$ being the Fourier components of curvature and torsion normalized to the torus major radius.

The results of numeric calculations of the mode stability criteria for the cases of Mercier [4] and g-modes [5] are given in Tables 1-4, while Tables 5-8 represent the cases of the devices the magnetic axes of which are simple spatial closed curves containing the minimum number of Fourier components needed to produce coupling which is two [12]. The type of the trap is assigned via the parameters N, M and $\varkappa$ which determine the Fourier components of curvature K_n and the spatial location of magnetic axis. The quantities N and M determine the number of turns of magnetic axis around the circumferential and direct line axes of the torus.

The principal stabilizing mechanism providing for Mercier mode stability for finite pressure plasmas in currentless devices is the action of the finite pressure plasma effects [13]. The de-stabilizing instances for those modes are the "anti-pit" and the ripple of the magnetic field. In the considered case of a small-scale ripple $m \geq 10$, the longitudinal inhomogeneity of magnetic field appears mainly as a de-stabilizing factor of the order $\sum_m m^2 |\delta_m|^2$.

Numeric calculations performed for various types of the devices with $\varkappa < 1$ and a prescribed value of β_θ indicate that the effects of the ripple can be neglected, if the ratio $(1 \div 2)(a/R)^2 \beta_\theta^3 > 3\sum_m m^2 |\delta_m|^2$ is fulfilled, and their influence upon the magnitude of the terms describing the effects of self stabilization is not great. In which case the stability criterion (4) gives rise to the ratio $\beta_{\theta r}^{cr}/\beta_\theta^{cr} \simeq (1 + 3\sum_m m^2 |\delta_m|^2 / \sum_n |k_n|^2)$ which is just another way of saying that for the cases considered the ripple is always a de-stabilizing factor. Here β_θ^{cr} and $\beta_{\theta r}^{cr}$ are the threshold values of β_θ which get the plasma stabilization going as far as excitation of the Mercier modes goes for the facilities with spatially homogeneous magnetic field rippled along the major azimuth.

An analysis of the stability calculations for g-mode in current-free devices (see Tables 5-8) with a rippled magnetic field gives an indication that the said-mode can be most dan-

gerous, because the condition for instability build-up in this case is satisfied when plasma pressure is random. The de-stabilizers here are "anti-pits", ripples of the confining magnetic fields proportional to $\Sigma_m m^2 |\delta_m|^2$ and finite pressure plasma effects serving to deepen the "anti-pit". The given numeric data tend to show that plasma finite pressures are the major de-stabilizing factors for the cases of currentless traps with $\varkappa > 1$ which holds true even at $\varkappa < 1$, if the condition $\beta_\theta \gtrsim (1{,}6 \div 1{,}9)(a/\alpha)^{2/3}$ is satisfied.

In conclusion, we bring your attention to the fact that the results of the calculations of Mercier and g-mode stability for the devices with spatial magnetic axes and a longitudinally inhomogeneous field as given in Tables 2, 7 are applicable to facilities which are being designed [7] or already operate [8].

REFERENCES

1. Glagolev G.M. et al. 10th Europ.Conf.Contr.Fus. & Plas.Phys. Moscow, 1981, v.1, rep.E-8
2. Георгиевский А.Б., Макеименко Б.П., Супруненко В.А. Атомная техника за рубежом, 1981, № I, с.20-29.
3. Funato J. et al.J.Phys.Soc.Jap.1980, v.48, no.6, 709-720
4. Bartlette D.V. et al. 8th Inter.Conf.Plas.Phys. and Contr. Nuc.Fus.Res., Vienna, v.1, pp.185-196 (Brussels) 1980
5. Yoshikawa Sa NF (1983), v.23, no.5, pp.667-669
6. Boozer A.H. et al. 9th Iner.Conf.Plas.Phys. & Contr.Nuc. Fus.Res., Vienna, v.3, pp.129-139 (Baltimore)1982
7. Harmeyer E. et al.12th Europ.Conf.Contr.Fus. & Plas.Phys., Budapest (1985), v.2, p.449-452
8. Hamberger et al. 12th Europ.Conf.Contr.Fus. & Plas.Phys. Budapest (1985), v.2, pp.429-432
9. Mikhailovskii A.B., Aburdshaniya Xh.D. Plas.Phys., 1979, v.21, no.2, pp.109-125
10. Михайловский А.Б. Физика плазмы, 1984, т.10, № I, с.83-91.
11. Михайловский А.Б. Неустойчивости плазмы в магнитных ловушках. М., Атомиздат, 1978.
12. Захаров Л.Е., Шафранов В.Д. Препринт ИАЭ-2789, М., 1977.
13. Михайловский А.Б., Шафранов В.Д. ЖЭТФ, 1974, т.66, № I, с.190-199.

Table 1: $N=5$, $M=1$, $\delta_m = 0.02$, $m=15$				
$\mathcal{R}$	k_0	k_5	$\beta_{0r}^{Tr}(R/a)^{-2/3}$	$\beta_{\theta}^{Tr}(R/a)^{-2/3}$
0.5	I.05	2.I3	I.48	I.44
I	I.II	2.9I	I.9I	I.88
I.5	I.I7	3.45	--	--
2	I.24	3.83	--	--
3	I.37	4.26	0.64	0.63

Table 2: $N=4$, $M=1$, $\delta_m=0.02$, $m=36$				
$\mathcal{R}$	k	k_4		
0.4	I.052	I.68	I.54	I.27
0.8	I.II	2.29	I.74	I.53
I.2	I.I7	2.7	--	--
I.6	I.23	2.99	--	--
2.4	I.35	3.28	--	--

Table3: $N=3$, $M=1$, $\delta_m=0.02$, $m=24$				
$\mathcal{R}$	k	k_3		
0.3	I.05	I.22	I.27	I.I
0.6	I.II	I.66	I.37	I.24
0.9	I.I7	I.94	--	--
I.2	I.22	2.I2	--	--
2.I	I.28	2.25	0.II6	0.I09

Table 4: $N=2$, $M=1$, $\delta_m=0.02$, $m=15$				
$\mathcal{R}$	k	k_2		
0.I	I.025	0.53	I.02	0.9I
0.2	I.05	0.73	I.04	0.95
0.4	I.I	0.98	I.07	0.99
0.6	I.I5	I.II	I.4	I.32

AXISYMMETRIC, RESISTIVE STABILITY AND CONTROL STUDIES FOR THE PROPOSED TCV TOKAMAK

J. DeLucia,* F. Hofmann, S.C. Jardin,* R. Keller, F.B. Marcus,
P. Marmillod and A. Perez
Centre de Recherches en Physique des Plasmas
Association Euratom - Confédération Suisse
Ecole Polytechnique Fédérale de Lausanne
21, Av. des Bains, CH-1007 Lausanne / Switzerland

* Present address: Plasma Physics Laboratory, Princeton University,
Princeton, N.J. 08544, U.S.A.

Abstract

Axisymmetric, resistive plasma stability and control in the proposed TCV tokamak have been studied with the Tokamak Simulation Code, which models the resistive time-scale evolution of a toroidal plasma, including its interaction with the poloidal field coils and the vacuum vessel. Realistic design parameters for the proposed TCV were used to study questions concerning active feedback response times and passive stabilization. It is shown that the plasma can be actively stabilized by power supplies with natural commutation thyristors operating at 100 Hz with 12 pulses.

Introduction

The Tokamak Simulation Code TSC is described in [1]. With this code, it has been demonstrated [2] that a tokamak plasma can be evolved continuously from a near-circular, cross-section shape to a 4/1 vertically elongated racetrack. All intermediate stages and the final state are stable to axisymmetric MHD modes. The stabilization is provided by the vacuum vessel walls on the ideal time scale and by an orthogonal active feedback system on the resistive time scale.

In subsequent studies with this code, it was found that the use of either a continuous vacuum vessel or a vessel with a toroidal gap resulted in very similar plasma evolutions. Also, the effects of diagnostics ports were studied by removing short poloidal sections from the toroidal symmetric vessel at port locations. Ideal stability was preserved, and the resistive growth rates did not significantly change. Based on these results, the vessel model used in the studies reported here is continuous poloidally and toroidally, with a resistivity equivalent to 1.0 cm thick INCONEL vessel walls plus strengthening ribs. In previous studies, the shaping coil supplies were ideal current sources. In what follows, the power supplies are natural commutation thyristor rectifiers, and the shaping coils are given the design values of resistance.

Feedback model for voltage source power supplies

For each shaping coil i at any instant of time t, the desired current I (i, t) is given by I (i, t) = $\sum$F(i, t, L) + C (i, t), where C (i, t) is the preprogrammed current to give the desired equilibrium and F (i, t, L) = G (i, L) E (t, L). For values of L=1-4, the coils produce radial, quadrupole, octupole, and vertical fields due to the current distribution G(i,L), which includes a gain factor. The error measurement E(t,L) is obtained by multiplying a state vectror for each of the four control systems by the flux loop measurements. The state vectors for the error measurements and resultant fields are othogonal, so that each feedback system is relatively independent of the others.

At any given instant of time, the difference D(i,t) between the desired current I(i,t) and the actual coil current I*(i,t) is D(i,t)≡I(i,t)-I*(i,t). The plasma and coil current solver in TSC advances the currents during a small time interval dt. We need to specify the coil voltage during this interval, V(i,t+dt) = V(i,t) + dV(i) where V(i,t) is the applied voltage during the previous interval and the change in voltage dV(i) us given by the feedback equation :

$$\frac{dV(i)}{dt} = A_I(i)\,\frac{V^{MX}(i)}{T(i)}\left[D(i,t)+A_P(i)\frac{dD(i,t)}{dt}+A_D\frac{d^2D(i,t)}{dt^2}\right]$$

where A_I, A_P, A_D are the integral, position, and differential gains for each coil, and $V^{MX}(i)$ and T(i) characterize the voltage source power supplies. $V^{MX}(i)$ is the maximum positive or negative voltage, and T(i) is the half-period, corresponding to the time to swing from maximum positive to maximum negative voltage. The command voltage from the feedback equation is therefore limited by

$$|V(i,t)| < V^{MX}(i) \quad \text{and} \quad \left|\frac{dV(i)}{dt}\right| < \frac{2V^{MX}(i)}{T(i)}$$

The resulting command voltage is applied to a model describing an ideal natural-commutation thyristor rectifier power supply for each coil. The thyristor supplies are taken to be 12 pulse and 100 Hz, which allows a commutation every 0.83 msec on average.

Results

The resistivity of each vacuum vessel element is 0.02*R ohms and the global value is 10^{-4} ohms, corresponding to 1.0 cm thick INCONEL plus strengthening ribs. The maximum supply voltages $V^{MX}(i)$ are 25 V/turn for outside coils, and 12.5 V/turn for the inner coils, correponding to the difference in self-inductances. (We note that because the coil grid size is 2.5 cm × 2.5 cm, the coils' self-inductances are larger than in the actual experiment.) For the inner coils (small major radius), the feedback coefficients are A_I = .00064/Amp, A_P = .004 sec, A_D = 0; for the outer coils A_I = .00024/Amp, A_P = .008 sec, A_D = 0. The plasma parameters for the simulation are central density and temperature $3 \times 10^{20} m^{-3}$ and 900 eV, safety factor ratio q_{edge}/q_0 = 2, and toroidal

field 1.5 Tesla. The Alfvén time is artificially enhanced by a factor of 600, so that the Alfvén time is still much less than the vessel time constant.

Examples of the results of a simulation with the above parameters are shown in Fig. 1. The plasma evolves from an elongation of 1.6 up to nearly 2.0 during 60 msec. A sample equilibrium is shown, with the positions of coils #7 and #8 indicated. The applied voltages and resulting coil currents are shown in Fig. 1 as a function of time. The initial conditions have the correct currents for the initial equilibrium, but the voltages are the resitive voltages only, and the plasma current density is not in resistive equilibrium. Thus the feedback model causes a large overshoot in the applied voltages as the plasma begins to evolve, but these are damped out later in time. An oscillation remains, superposed on the thyristor waveforms, because optimal feedback coefficients have not yet been determined.

Conclusions

The plasma is maintained in equilibrium for many 10's of milliseconds, whereas without feedback, it goes unstable on the millisecond time scale, indicating that the system response time is sufficient for the conditions considered.

Acknowledgements : We wish to thank Professor F. Troyon, Dr. R. Gruber and Dr. N. Pomphrey for useful discussions and comments. This work was partly supported by the Swiss National Science Fondation and by the U.S. Department of Energy through contract No. DE-AC02-76-CHO-3073.

References

[1] S.C. Jardin, Computational Techniques, ed. by B. Cohen and J. Brackbill (Academic, New York, 1985).

[2] F.B. Marcus, S.C. Jardin and F. Hofmann, Phys. Rev. Lett. 55, 2289 (1985).

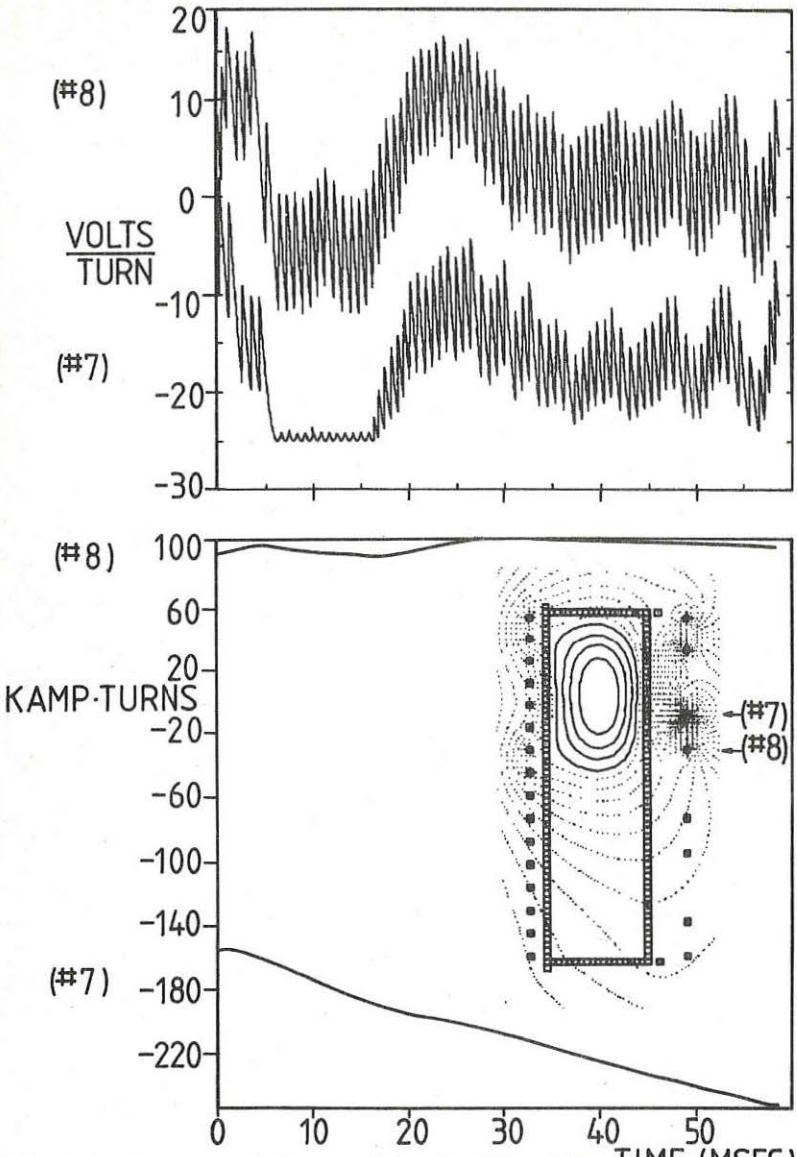

Fig.1 Voltage and Current, Coils #7and #8

RESISTIVE TEARING MODES IN THE PRESENCE OF EQUILIBRIUM FLOWS

M. Persson and A. Bondeson

Institute for Electromagnetic Field Theory
and EURATOM Fusion Research (SERC)
Chalmers University of Technology
S-41296 Göteborg, Sweden

It is generally recognized that the linear properties of tearing modes are sensitive to various corrections to the basic resistive MHD model because of their comparatively slow growth and the concentration of the dynamics to a thin resistive layer. One example of such corrections which is clearly relevant to tokamaks is due to the presence of equilibrium flows. The effects of equilibrium flows have been studied previously, notably in [1] and [2] for flows perpendicular to the magnetic surfaces and in [3] and [4] for sheared flows parallel to the magnetic surfaces. In [5] we reexamine and extend the results of [1 - 4], and the main results are summarized here.

The equations relevant to tearing modes in a large aspect ratio torus with small β can be separated into the usual force balance equation valid in the ideal region and one equation for the streamfunction in the resistive layer near the singular surface

$$\eta\rho\,[\nu\phi^{(4)}-c\phi'''-(\gamma+ir'y)\phi''\,] + F'^2y^2\phi = F'y(\gamma+ir'y)-F''\eta \qquad (1)$$

where we have considered slab geometry with the rational surface at $y = 0$, perturbations are of the form $\phi(y)\exp(ik_x x)$ and where the constant-ψ approximation was applied, $\psi(0) = 1$. In Eq. (1), γ is the growthrate, η the resistivity, ρ the mass density, ν the perpendicular viscosity, c the perpendicular flow speed, $r' = d(k_x v_{0x})/dy$ the shear parallel flow and $F = k_x B_{0x}(y)$. Matching of the external and internal solutions leads to the Δ' condition

$$\eta\Delta' = \int_{-\infty}^{\infty} (\gamma+ir'y-F'y\phi)dy \qquad (2)$$

Equation (1) is then Fourier transformed with respect to y whereby the inhomogeneous terms on the right-hand side give rise to jump conditions for the Fourier transform $\Phi(k)$ and its derivatives at $k = 0$. These jump conditions can be combined with the Fourier transform of Eq. (2) to restate the eigenvalue problem in the following compact way

$$\frac{2\pi\gamma}{\eta\Delta} = e^{-i\chi}/Y(0^-) - e^{i\chi}/Y(0^+) \qquad (3a)$$

where $\Delta e^{i\chi} = \Delta' - i\pi F''/F'$, $Y(k) \equiv d\Phi/\Phi dk$ and where Φ satisfies

$$\frac{d^2\Phi}{dk^2} - \frac{\eta\rho}{F'^2}\left[(\nu k^4+ick^3+\gamma k^2)\Phi - r'\frac{d}{dk}(k^2\Phi)\right] = 0 \qquad (3b)$$

for $k \neq 0$ and $\Phi(k)\to 0$ for $k\to\pm\infty$. In the following we use the normalized variables $P = \gamma (\eta^3\Delta^4F'^2/\rho)^{-1/5}$, $N = \nu (\eta^7\Delta^6\rho/F'^2)^{-1/5}$, $R' = r'(\eta\Delta^3F'^4/\rho^2)^{-1/5}$ and $C = c/\eta\Delta$, in which Eq. (3) can be written in dimensionless form. For the detailed computations we have subdivided the problem such that the plasma response is either inertial ($\nu = 0$) or viscous ($\gamma = 0$ in Eq. (3b)) and the flow is either perpendicular or parallel.

In the case of inertial plasma response and perpendicular flows numerical computation gives the diagram in Fig. 1. The solid lines give constant Re(P) and the dashed lines show constant Im(P) as functions of χ and C. For $|C|$ large the stability boundaries are $\chi = \arg(\Delta' - i\pi F''/F') = \pm\pi/2 + \mathrm{sgn}(C)\pi/10$, in agreement with [2]. However for small $|C|$ and $C\chi < 0$ there are regions in which the growth rate is complex. These regions can be demonstrated analytically by expanding $Y(0^{\pm})$ as a power series in $CP^{-5/4}$ or $PC^{-4/5}$. The small C expansion leads to

$$P^{5/4} \simeq \frac{\Gamma(1/4)}{4\pi\Gamma(3/4)}\left[\cos\chi \pm (\cos^2\chi + \frac{2\pi}{3} C \sin\chi)^{1/2}\right] \qquad (4)$$

It is valid in the vicinity of the endpoints $\chi = \pm\pi/2$, $C = 0$ of the curved parts of the marginal stability curve and reproduces both the complex growthrates and the form of the stability curve in this region. Similarly, around the other pair of endpoints

$$\chi = \mp 2\pi/5, \qquad C = \pm\frac{1}{3\pi}\cos\frac{\pi}{10} \qquad (5)$$

and also for $C \gg 1$, the large C expansion is valid

$$0.07071\cos(\chi + \frac{7\pi}{10})X^3 + 0.1612\cos(\chi + \frac{\pi}{10})X^2 + (\pi C + \frac{1}{3}\sin\chi)X = \Gamma(\tfrac{1}{5})\left[\Gamma(\tfrac{4}{5})\right]^{-1}5^{-3/5}\cos(\chi - \frac{\pi}{10}) \qquad (6)$$

where the expansion has been taken to third order in $X = PC^{-4/5}$. It is interesting to note that Eq. (23) of [2] gives the first order expansion of Eq. (6). However at the point (5) both the zeroth and first order terms of (6) vanish! The third order expansion allows us to determine the direction of the marginal stability curve through (5), the result agrees with the numerical stability diagram. Figure 2 shows the numerically determined stability limits and boundary between real and complex growth rates (solid) and the lowest order expansions to these curves obtained from Eqs (4) and (6) (dashed lines).

In the case of viscous plasma response and perpendicular flow, the growthrate is always real and the stability limit in χ is a smooth function of C, see Fig. 3. Analytic expansions in the limits $CN^{-5/6} \ll 1$ or $\gg 1$ give asymptotic results in agreement with the numerics.

The countour plots for perpendicular flows and inertial plasma response are shown in Fig. 4. Analytical expansions for $|R'| \ll 1$ or $\gg 1$ again agree with the numerics. In the flow dominated regime the expansion is :

$$P \simeq \left(\frac{R'}{2\pi} e^{i\chi}\right)^{1/2} + \frac{1}{2\pi} 3^{-2/3} R'^{-1/3} \Gamma\left(\frac{1}{3}\right) \cos\chi \qquad (7)$$

This is smaller by a factor $\sqrt{2}$ than the corresponding result of Paris and Sy (see discussion in [5]). Finally, the case of viscous plasma response and perpendicular flows is analytically solvable and the growthrate is given by

$$2\pi P = \frac{\Gamma(1/3)}{\Gamma(2/3)} 3^{-2/3} (4N + R'^2)^{-1/6}$$

$$\times\left[e^{-i\chi} \frac{\Gamma((1+\xi)/3)}{\Gamma((2+\xi)/3)} + e^{i\chi} \frac{\Gamma((1-\xi)/3)}{\Gamma((2-\xi)/3)}\right] \qquad (8)$$

where $\xi = R'(4N + R'^2)^{-1/2}$. The stability limit is unchanged by the flow, $\chi = \pm\pi/2$, but the flows increase the growthrates.

References

[1] D. Dobrott, S.C. Prager and J.B. Taylor, Phys. Fluids 20, 1850 (1977).
[2] R.K. Pollard and J.B. Taylor, Phys. Fluids 22, 126 (1979).
[3] I. Hofmann, Plasma Phys. 17, 143 (1975).
[4] R.B. Paris and W.N.-C. Sy, Phys. Fluids 26, 2966 (1983).
[5] A. Bondeson and M. Persson, CHT-IEFT/PP-1985-14 (internal report, submitted to Phys. Fluids).

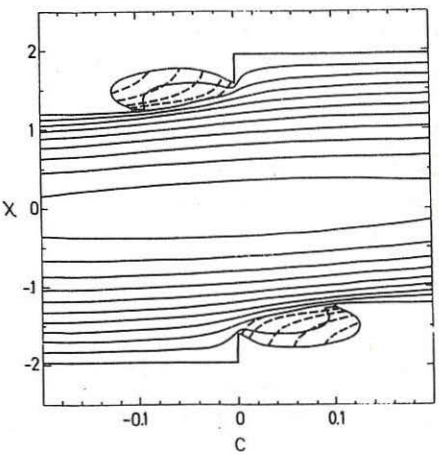

Figure 1. Level curves for Re(P) (—) and Im(P) (--) for perpendicular flow and inertial plasma response.

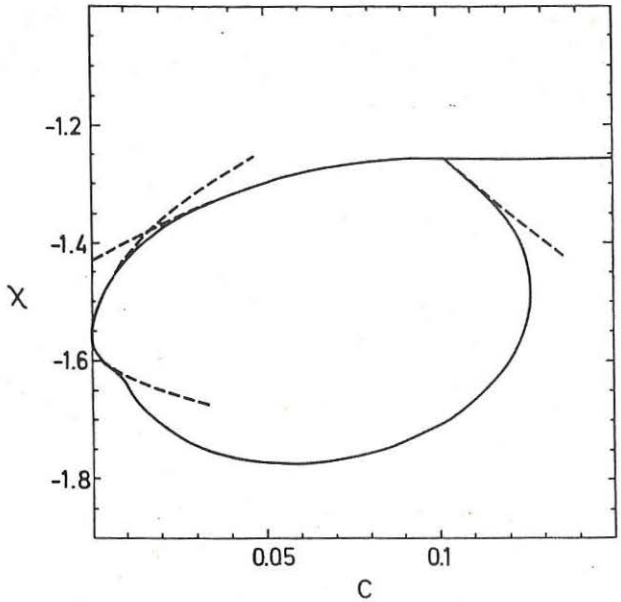

Figure 2. Boundaries of region with complex growthrate in Fig. 1. Dashed lines show analytical expansions based on Eqs. (4) and (6).

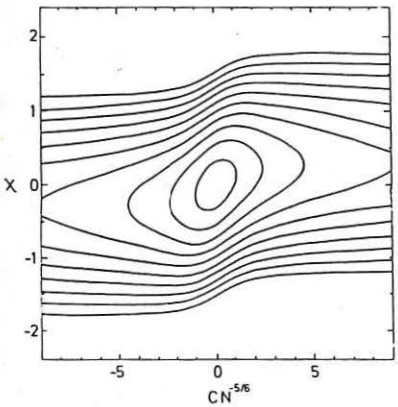

Figure 3. Growthrate plot for perpendicular flow and viscous plasma response.

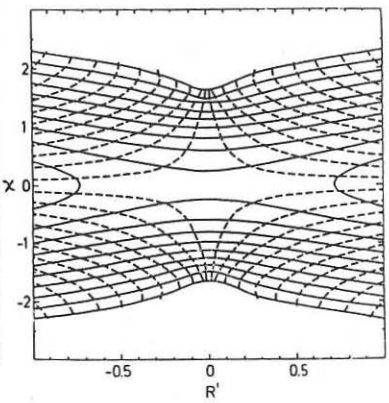

Figure 4. Growthrate plot for parallel flow and inertial plasma response.

FREE-BOUNDARY FLOW EQUILIBRIA FOR ASDEX AND ASDEX-UG

H.P. Zehrfeld

Max-Planck-Institut fuer Plasmaphysik
EURATOM Association, D-8046 Garching

Neutral beam injection into magnetically confined plasmas is connected with plasma flow and a corresponding alteration of the equilibrium characteristics of the discharge. In particular density variations on magnetic surfaces were observed in neutral beam heated plasmas. This has led to attempts to explain them by toroidal rotation of the plasma. It has turned out that in view of the measured Mach-numbers for this flow the mere effect of centrifugal forces caused by only toroidal rotation is too weak. However, taking into account the more involved effect of the combined action of both toroidal and poloidal plasma motion changes the situation qualitatively as well as quantitatively: Due to the finite rotational transform of the flow field accelerating forces in toroidal direction appear. In an equilibrium state, they must be balanced by corresponding components of jxB. This requires plasma currents across magnetic surfaces which together with the toroidal magnetic field maintain pressure gradients in magnetic surfaces. In order to demonstrate this effect quantitatively we have calculated corresponding MHD flow equilibria for the separatrix-bounded plasma configurations of ASDEX and ASDEX-UG. For this purpose the partial differential equation

$$R^2 \, div\left\{\frac{D\nabla\psi}{R^2}\right\} = \mathcal{P}(R,\psi,|\nabla\psi|,F) \quad , \qquad D = D(R,\psi,|\nabla\psi|,F) \tag{1}$$

must be solved for the poloidal flux ψ. D and $\mathcal{P}$ are given functions. F represents five profiles

$$F = (H_M, C_M, J_M, \Psi_M, \Phi_M) = F(\psi) \tag{2}$$

The first three quantities can be determined prescribing profiles for the density n, the temperature T and the poloidal current J on a straight line s leading from the magnetic axis ($\psi = \psi_A$) to the plasma boundary ($\psi = \psi_B$). Ψ_M is the poloidal mass flux, Φ_M the electric potential. We have chosen the distributions

$$n_s \sim (1-\gamma_n x)^\nu \quad , \quad T_s \sim (1-\gamma_T x)^\mu \quad , \quad J_s^2 = J_s^2(\psi_A) + (J_B^2 - J_s^2(\psi_A))\,G(x) \tag{3}$$

$$\Psi_M' \sim n_s T_s^{1/2} e^{-x} \quad , \quad \Phi_M' \sim T_s^{1/2} \quad , \quad ' \equiv d/d\psi \tag{4}$$

where $x = (\psi - \psi_A)/(\psi_B - \psi_A)$ and $G(x)$ ($0 \leq G(x) \leq 1$) some function describing the diamagnetism of the plasma. γ_n, ν and γ_T, μ are profile constants.

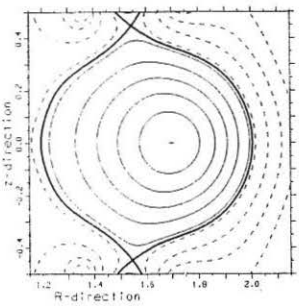

Fig.1 ASDEX flux surfaces

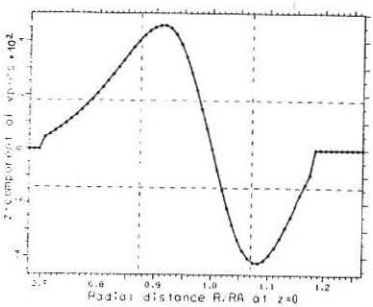

Fig.2 Radial v_p / c_s - profile

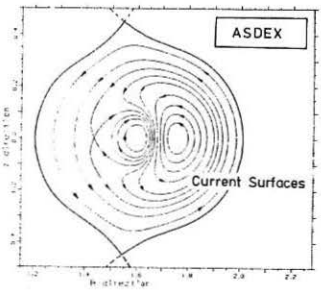

Fig.3 ASDEX current surfaces

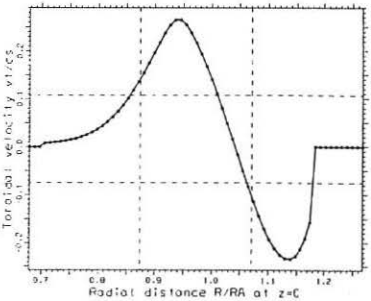

Fig.4 Radial v_T / c_s - profile

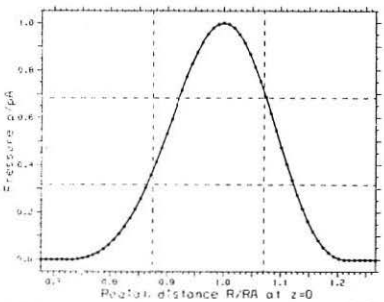

Fig.5 Radial pressure profile (static equilibrium)

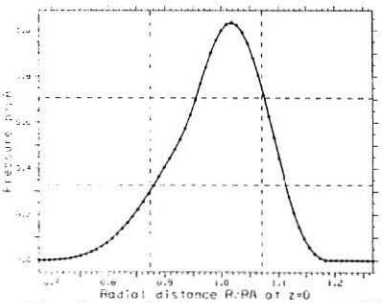

Fig.6 Radial pressure profile (flow equilibrium)

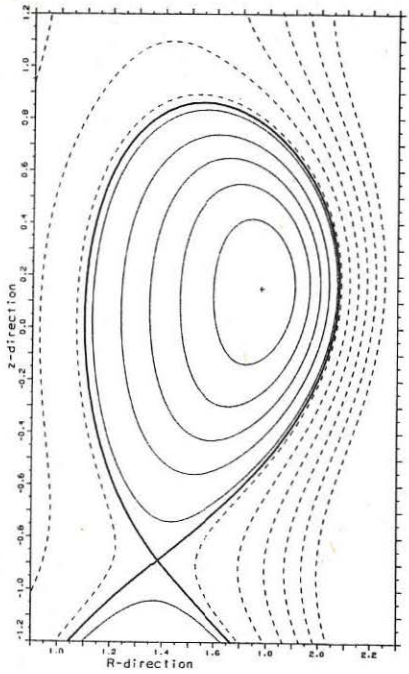

Fig.7 ASDEX-UG flux surfaces

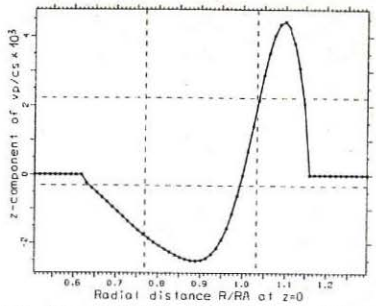

Fig.8 Radial v_p/c_s - profile

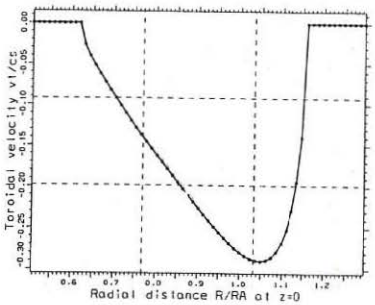

Fig.9 Radial v_T/c_s - profile

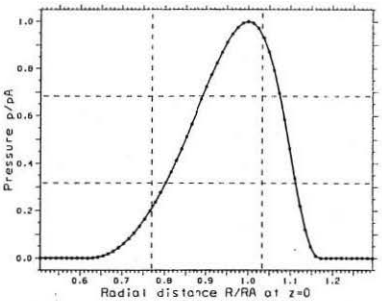

Fig.10 Radial pressure profile (static equilibrium)

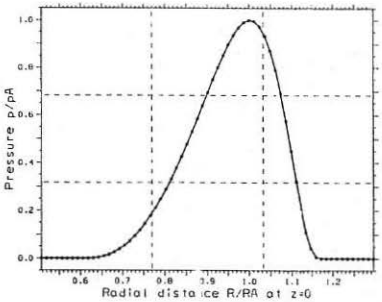

Fig.11 Radial pressure profile (flow equilibrium)

Fig.3 shows surfaces of constant J (the flux surfaces of the current density field) for an ASDEX case ($\beta_p \approx 1$). The poloidal components of the current density perpendicular to the magnetic surfaces are responsible for pressure variations along magnetic field lines. The corresponding mass density anomaly (i.e. a R-dependence of ρ if ρ is conceived as function of Ψ and R) at the magnetic axis is given by

$$\frac{R}{\rho}\frac{\partial \rho}{\partial R} = \frac{B^2 \Psi_M'^2/\rho^2 + 4\pi^2 R^2 \Phi_M'^2}{(1-(B\Psi_M'/\rho c_s)^2)c_s^2} \qquad (5)$$

The anomaly of the radial pressure profile is illustrated by Figs. 5 and 6. For the Mach-numbers for poloidal and toroidal flow indicated in Figs.2 and 4 we obtain pressure variations of about 20% on a magnetic surface. For ASDEX-UG, where considerable smaller values for the poloidal velocity have been used, the corresponding pressure distributions for the static and the flow case are barely discernable - purely toroidal flow at moderate Mach-numbers has only small effect on the density variation along magnetic field lines. The expression for the plasma flow field

$$v = \frac{\Psi_M'}{\rho} B_p + \left\{ \frac{\Psi_M'}{\rho} B_T + 2\pi R \Phi_M' \right\} R \nabla \varphi \qquad (6)$$

shows that for an appropriate choice of Ψ_M and Φ_M both velocity components can be small, whereas - approaching the boundary of the first elliptic regime of equation (1)

$$0 \leq \frac{\mu_0 \rho v_p^2}{B_p^2} < \frac{\beta}{1+\beta} \quad , \quad \beta = \mu_0 \gamma p / B^2 \qquad (7)$$

- the radial increase of the density (cf. equation (5)) may reach considerable values.

/1/ H.P. Zehrfeld, B.J. Green, "Stationary Toroidal Equilibria at Finite Beta", Nucl.Fusion 12 (1972), 569.

/2/ B.J.Green, H.P.Zehrfeld, "The Effect of Plasma Flow on the Toroidal Equilibrium Shift", Nucl.Fusion 13 (1973), 750.

/3/ S.Semenzato, R.Gruber, H.P.Zehrfeld, "Computation of Symmetric Ideal MHD Flow Equilibria", Computer Physics Reports 1 (1984),389.

/4/ S.Semenzato, R.Gruber, R.Iacono, F.Troyon, H.P.Zehrfeld, "Poloidal Asymmetry of the Density Profile Associated with a Flow in a Tokamak", LRP 258/85, 1985.

THE EFFECTS OF A RESISTIVE WALL ON RESISTIVE MHD INSTABILITIES

T C Hender, C G Gimblett and D C Robinson

Culham Laboratory, Abingdon, Oxon, OX14 3DB
(UKAEA/Euratom Fusion Association)

Introduction In this paper we study the effects of a finite conductivity wall on resistive MHD instabilities. The studies in the tokamak will focus on the destabilising influence of the wall resistivity when $q_a \lesssim 2.6$. The regime $q_a \lesssim 2.3$ which is difficult to access experimentally, is of particular interest from the viewpoint of increased ohmic heating and high-β limits. In present RFP's the need for a conducting wall is rather more intrinsic than in the tokamak, apparently being essential for gross stability. The OHTE RFP [1] and CLEO RFP [2] however have operated successfully with a thin wall, whose long time constant ($\tau_W \sim 1.5$ MS in OHTE) which is much shorter than the pulse length (~ 10ms). We shall study for OHTE parameters the linear spectrum of modes which are destabilised by the wall resistivity.

Numerics and Boundary Conditions Computationally we solve the reduced pinch equations [3]. These equations which are applicable to MHD stability in the RFP and tokamak have been shown to be a good approximation to solving the full compressible MHD equations [4] (at $\beta = 0\%$). Numerically we solve the linearised reduced pinch equations using an implicit scheme. The non-linear terms (which may optionally be suppressed) are included explicitly. A Fourier series representation is used in the poloidal and azimuthal (θ,z) directions and finite differences are employed in the radial direction (r). At the wall the boundary condition on the magnetic field is determined using a thin wall approximation (wall resistive skin depth >> wall thickness). This yields [5]

$$\frac{1}{r}\frac{\partial r b_r}{\partial r} = \left(\frac{m^2}{r^2} + k_z^2\right)\frac{K_m b_r}{K_m'} - \tau_W\left(\frac{\partial b_r}{\partial t} + ik_z V_z b_r\right) \qquad (1)$$

Here τ_W is the resistive wall time constant normalised to the Alfven time ($\tau_A = a\sqrt{\rho}/B_0$) and K_m is the modified Bessel Function. In this boundary condition (Eq 1) we have included the effect of a uniform toroidal rotation of the wall, with velocity V_z. This is equivalent to (but simpler than) adding a bulk toroidal rotation to the plasma. In the results given in the following section we shall convert to the frame of reference of the wall (i.e. the plasma rotates). The boundary condition on the velocity is taken as $V_r = 0$. This leads to the problem that we form a resistive boundary layer near the wall since as $V_r \to 0$ Ohm's law becomes $\partial b_r/\partial t = \eta(\nabla^2 \underline{b})_r$ (and $\partial b_r/\partial t \neq 0$ for a resistive wall). The $V_r = 0$ wall boundary layer however, has no effect on the marginal stability points.

Tokamak results We may derive an approximate dispersion relation for the resistive wall tearing mode by using the vacuum solution for b_r outside the resonant surface(r_s). In the tokamak limit the result is

$$\Delta' = \left[\frac{b_r'}{b_r}\right]_{r_s-\varepsilon}^{r_s+\varepsilon} = \Delta_\infty' + \frac{4m^2 r_s^{2m}}{r_s[1-r_s^{2m}][\tau_w(\omega+ik_zV_z)(1-r_s^{2m})+2mr_s^{2m}]} \qquad (2)$$

where ω is the growth rate (normalised to τ_A) and the subscript on the Δ' indicates the τ_w value. Examining Eq (2) for the non rotating case ($V_z=0$) we find if $\Delta'_0>0$ then by making ω small enough but still positive we can keep $\Delta'>0$ for all finite τ_w. In other words if the mode is unstable for $\tau_w=0$ then it is unstable for all values of τ_w and hence to determine stability it is sufficient to examine the case of $\tau_w=0$ (when $V_z=0$).

Figure 1 shows for the profile $q=1.1(1+[(q_a/1.1)^4-1]r^8)^{\frac{1}{4}}$ (which corresponds to a broad current profile) how Δ' varies with q_a. The lower plot shows the corresponding growth rates computed with the initial value code for $S=\tau_R/\tau_A=10^5$, $m=2$, $k_z=0.2$, $V_z=0$. For the superconducting wall case Δ' is negative when $q_a<2.6$ and the tearing mode is stable, whereas the resistive wall allows instability to persist. Calculations for finite τ_w in this case confirm the analytic result that a sufficient condition for instability is that the mode is unstable for $\tau_w=0$. The resistive wall tearing modes are however stabilised by sufficiently fast bulk toroidal rotation (if $\Delta'_\infty<0$). From Eq (2) in the limit $\omega<<k_zV_z$ we find that the frequency of the mode is given by k_zV_z and the growth rate is that of the $\tau_w=\infty$ mode. For most experiments with significant frequencies ($k_zV_z\tau_w \gtrsim 10$) rotation will stabilise the m=2 resistive wall tearing modes.

In the nonlinear regime the growth of the resistive wall tearing mode island (when $V_z=0$) is given by the normal relation [6]

$$\frac{dW}{dt} = 1.66\ \eta(\Delta'(\omega\tau_w)-\alpha W) \qquad (3)$$

but here Δ' is a function of $\omega\tau_w[\sim(2\tau_w/W)(dW/dt)]$ and is given by Eq (2). From Eq (2) we see that as the mode saturates and $dW/dt\to 0$, then $\Delta'(\omega\tau_w)\to\Delta'_0$ (for $V_z=0$); hence for all values of τ_w ($\neq\infty$) the eventual saturation width is that of the $\tau_w=0$ case when $V_z=0$. Computationally we find for the case shown in Fig 1 with $q_a=3$, that for the range $\tau_w=0$ to 10^4 the saturation width of the (2,1) island varies from 35% to 33% of the minor radius. Figure 2 shows the single helicity evolution of the (2,1) island for the same case as Fig 1 with $V_z=0$ and $q_a=2.5$, 2.75 and 3. For $q_a<2.8$ and $\tau_w=0$, the island actually touches the wall before it saturates and thus connects the outer~1/3 of the plasma to the wall. As discussed above this saturation width is approximately independent of τ_w but of course the nonlinear growth of the mode slows as τ_w increases.

RFP Results In the RFP the effects of the wall resistivity are greater than in the Tokamak. With a superconducting wall it is possible to achieve complete stability to ideal and resistive tearing modes with a vacuum region of up to 4% of the minor radius[7]. With a resistive wall however, complete stability to the tearing mode is not possible (when $V_z=0$). In addition ideal modes which are resonant at the magnetic axis or are just nonresonant are destabilised by the resistive wall. Their dispersion relation is

$$(ik_zV_z+\omega)\tau_w=\Delta'_w-\omega^{3/2}\sqrt{S}/\left|\vec{K}.\vec{B}\right|_{wall} \qquad (4)$$

where Δ'_w is evaluated at the wall. The $\omega^{3/2}$ term is due to the boundary

layer induced by the $V_r=0$ boundary condition; it is only important when $\tau_w \ll \sqrt{(\omega S)}$, a regime of little importance for present experiments.

Figure 3 shows how the growth rate of the m=1 modes within the field reversal surface vary with k_z for various τ_w with $S=5\times10^3$ and $\eta=(1+5r^2)^2$. The pitch profile in this case is $\mu=0.571(1-1.53r^2-0.375r^4)$ with a 2% vacuum region [7]. This profile is stable to all tearing and ideal modes in the limit $\tau_w=\infty$. The nonresonant modes ($k_z<1.75$) are ideal (twisting parity) and their growth rates are almost totally independent of S. The fastest growing modes for $\tau_w>20$ have $k_z\sim2.1$ and are tearing parity; their growth rate scales as $S^{-0.2}$ at $S=5\times10^3$. For OHTE, typical parameters are $S=5\times10^3$, $\tau_w=5\times10^3\tau_A$ and $\tau_A=3\times10^{-7}$ sec. For these parameters the fastest growing mode for the case shown in Fig 3 has a growth time of 600 μs. This tearing mode may be stabilised by the toroidal rotation effects if V_z is large enough. Figure 4 shows how the growth rate decreases as V_z increases for the same case as Fig 3 with $\tau_w=5\times10^3$ and Kz=2.2. For experimentally observed frequencies (~10KHz) $V_z=10^{-2}$ and the mode is stable. The ideal modes however are unaffected by bulk toroidal rotation up to near Alfvenic speeds; from Eq (4) we find that the mode locks to the wall and remains stationary as the plasma rotates. Computationally for the case shown in Fig 3 with $K_z=1.7$ and $\tau_w=5\times10^3$ the growth rate is unaffected by rotations up to $V_z=10^{-2}$. Hence for this case when rotation effects are taken into account the ideal modes are the most unstable; with this profile for OHTE parameters they have a growth time of ~3mS. The fact that these ideal resistive wall modes rotate very slowly (or not at all) needs to be taken into account when searching for these modes experimentally.

Conclusions In the Tokamak with $q_a\lesssim2.6$, the wall resistivity allows continued growth of tearing modes which would be stabilised by an ideal wall. For significant frequencies these modes can be stabilised by toroidal rotation. Nonlinear calculations indicate that the (2,1) island may touch the wall when $q_a<2.7$ (for the specific profile chosen). This behaviour could be related to the difficulty in operating Tokamaks at low q ($\lesssim$ 2). For the RFP it appears to be difficult to achieve complete stability to tearing and ideal modes with a resistive wall but, the growth rates of the resistive wall modes are easily reduced to relatively low values ($\sim 1/\tau_w$). For OHTE parameters the fastest growing internal mode when rotation effects are taken into account is an ideal, on-axis mode. Its growth time should make it apparent in the experiment if no other effects intervene (e.g. nonlinear, background turbulence, kinetic effects etc).

References

[1] R G Goforth et al, Bull Am Phys Soc 30, 9(85)1405
[2] D C Robinson et al, Culham report CLM-R222, 1982
[3] H R Strauss, Phys Fl 27 (84) 2580
[4] J A Holmes et al, Proceedings of the Sherwood Theory Meeting, 1985
[5] C G Cimblett, Nucl Fus to appear.
[6] R White, Phys Fl 12 (76) 1987; P Rutherford, 1985 Varenna Summer School
[7] D C Robinson, Nucl Fus 18 (78) 939

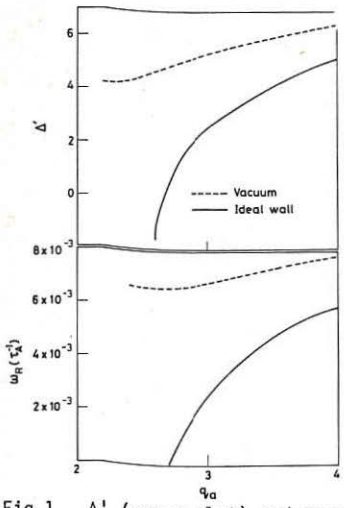

Fig 1 Δ' (upper plot) and growth rate (lower plot) v q_a for m=2, k_z=0.2.

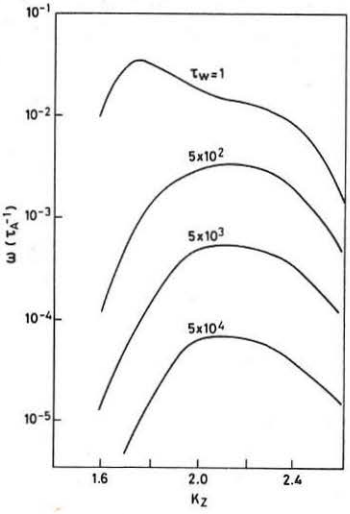

Fig 3 Growth rate of m=1 modes v k_z for various τ_w.

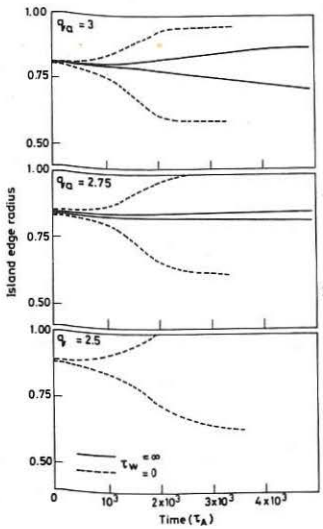

Fig 2 Single helicity m=2 island widths for τ_w=0 and ∞.

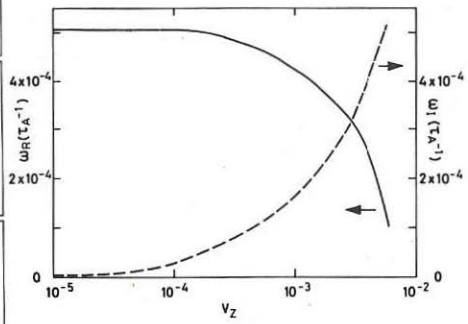

Fig 4 ω v V_z for same case as Fig 3 at τ_w=5x10³ and k_z=2.2.

THE EFFECTS OF FINITE-β AND SHAPING ON TEARING MODES IN JET

T C Hender*, D C Robinson* and R J Hastie*

JET Joint Undertaking, Abingdon, Oxon OX14 3EA, UK

*(UKAEA/Euratom Fusion Association) Culham Laboratory, Abingdon, Oxon, OX14 3DB

Introduction As the value of β in JET increases with the auxiliary heating it becomes important to understand the effects on the tearing mode. An analytic treatment of the tearing mode in toroidal geometry was given by Glasser et al [1]. They found a strong stabilising effect at finite-β, resulting from the influence of the average curvature on the tearing mode within the resistive layer. These average curvature effects are strongest in small aspect ratio, high magnetic Reynolds number (S) tokamaks, such as JET. Nonlinearly these curvature terms have also been shown to stabilise the tearing mode [2]. Thus the results presented here can remain valid in regimes where the linear resistive MHD equations appear to be inapplicable (eg Larmor radius > linear resistive layer width).

In this paper we present numerical studies of the effects of finite-β on tearing modes in JET. The next section gives details of the equations solved and numerics, and then in the following section the results are presented.

Numerics and Equations The compressible linear resistive MHD equations are solved in toroidal geometry with a version of the ORNL code FAR [3] modified to include the compressible terms. To achieve an efficient representation of the linear eigenfunctions an equilibrium flux coordinate system (ρ, θ, ζ)[4] is used. Where ρ is a flux surface label, θ is the straight field line poloidal angle and ζ is the geometric toroidal angle. These coordinates are generated from numerical toroidal equilibria and are an exact representation of the geometry with no ordering assumptions.

In the FAR code a stream function representation is used for the perturbed magnetic field ($\vec{b}$) and velocity ($\vec{v}$)

$$\vec{b} = \nabla\theta \times \nabla\chi + \nabla\zeta \times \nabla\psi; \quad \vec{v} = \nabla\theta \times \nabla\Lambda + \nabla\zeta \times \nabla\phi + \nabla\iota \qquad (1)$$

This form of the velocity separates the incompressible and compressible ($\nabla\iota$) parts of the perturbation. Equations for the evolution of χ and ψ are obtained from Ohm's law and equations for ϕ and Λ arise from the vorticity equation. An equation for ι is found by taking the divergence of the equation of motion and finally the perturbed pressure (P) is evolved compressibly. By setting ι=0 in these equations we obtain the incompressible MHD equations; the ability to solve either the fully compressible or incompressible equations is retained numerically. The equations for ψ, χ, Λ, ϕ, ι and ρ, which are equivalent to the primitive compressible MHD equations, are solved with a modified version of the FAR code. A finite difference representation is used in the radial direction (ρ) and a Fourier series decomposition is employed in the angular variables θ and ζ. The equations are solved with an implicit scheme which gives very rapid convergence to the

eigenfunction [3]. The boundary conditions are a non-porous superconducting wall at the last equilibrium flux surface.

Stability Results Figure 1 shows how the n=1 tearing mode growth rate (ω) varies as the central beta (β_o) is increased for a circular boundary JET equilibria with $q = 1.34(1 + (\rho/0.558)^8)^{1/4}$ and $P_{eq} \propto \psi^2$. For this case the ratio of the resistive time τ_R ($= a^2/\eta_o$) to the poloidal Alfven transit time τ_{Hp} ($= R_o\sqrt{\rho_m}/B_o$) is $S = 10^5$. This q profile is particularly unstable and has been used previously for disruption studies [5]. Despite this, a strong stabilising effect is evident in Fig 1 as β_o increases. Figure 2 shows the velocity flow pattern at $\beta_o = 2\%$ in the ζ=0 plane for the same case as Fig 1. The vortices at the q=2 surface are clearly evident and on the inboard side small vortices at q=3 and 4 are also evident. The compressible (ratio of specific heats $\gamma = 5/3$) results and incompressible ($\gamma = \infty$) results shown in Fig 1 are generally in good agreement. This is because the sound speed $\omega_s = \sqrt{(\gamma\beta_o P_{eq}/2q^2)}$ (normalised to τ_{Hp}) is greater than the growth rate for $\beta_o \gtrsim 1\%$. As $\beta_o \to 0$ however, $\omega_s \to 0$ (for $\gamma \neq \infty$) and the damping effect of the sound waves on the tearing mode disappears for the compressible case. Analytically at large aspect ratio we expect the compressible and $\gamma = \infty$ growth rates at $\beta_o = 0\%$ to differ by $(1 + 2q^2)^{1/5} = 1.55$ (for q=2); numerically this ratio is 1.72. For JET $\omega_s >> \omega$ is generally true and so this behaviour near $\beta_o = 0$ is of little practical importance.

The value of $S = 10^5$ used for Fig 1 is much lower than that in JET ($S \sim 10^8$). As we raise S for this case at $\beta_o = 2\%$, the growth rate initially decays as $S^{-3/5}$ and then for $S > 5 \times 10^5$ it decays more rapidly, and eventually becomes overstable (Fig 3). The departure of the growth rate from the normal $S^{-3/5}$ tearing scaling and the overstable behaviour are caused by the average curvature stabilisation which becomes increasingly important as S increases. At sufficiently high S the curvature terms stabilise the tearing mode, but we are unable to study this regime because our initial value method requires a growing solution. We can however estimate from the tearing mode dispersion relation given in [1] that for the case shown in Fig 3 ($\beta_o = 2\%$) the tearing mode is stable for $S > 10^7$. Since for $S = 10^5$, $\beta_o = 2\%$ the growth rate $\omega \propto S^{3/5}$ (Fig 3) we can conclude that the average curvature stabilisation effects are weak (at $S = 10^5$). Thus the stabilisation effect for $\beta_o < 2\%$ in Fig 1 ($S = 10^5$) is due to the changes in magnetic geometry and poloidal mode coupling associated with increasing β_o (and is not due to the average curvature).

For a less unstable circular boundary JET equilibrium with $q = 1.1\ (1 + (\rho/0.506)^8)^{1/4}$, we find that for $S = 10^5$ the n=1 tearing mode is almost completely stabilised by $\beta_o = 1.5\%$ (Fig 4). In Fig 4 incompressible results are shown for q(ρ) held constant as β_o is increased and also for $FdF/d\psi$ held constant (where F=equilibrium toroidal field). By raising β at constant q we are implicitly changing the current profile which itself effects the growth rate; the difference between the $FdF/d\psi$ and q constant curves (Fig 4) indicates that effects of finite-β equilibrium profile modifications are relatively small.

The results shown in Fig 4 are at the relatively low S of 10^5. At finite-β we again find as S increases that the favourable average curvature terms become more important and stabilise the mode. Figure 5 shows the growth rate trajectories as S is increased, in the complex ω-plane for the same case

as Fig 4 (q-constant) at β_0= 0.5%. Compressible and incompressible results are shown and can be seen to be in reasonable agreement. For this q (=1.1(1 + $(\rho/0.506)^8)^{1/4}$) at JET aspect ratio the ideal ballooning β-limit is β_0 = 6%. Thus at S = 10^5 there is a wide range, β_0 = 1.5-6%, of complete stability to the n=1 tearing mode and the ideal ballooning mode. At higher S the critical β for tearing mode stability will be even lower (β_0=0.24% at S=10^7).

Finally we study the effects of shaping on the finite-β tearing mode. We study a sequence of increasing D-shaping with the outer boundary defined by R = R_0 + a Cos (θ + δ Sinθ); Z = a κ Sinθ. We define the D-shaping sequence by κ = 1 + 2δ. Figure 6 shows how the growth rate varies as the D-shaping is increased for β_0 = 0% and 0.5% at S = 10^5. Results are shown for q held constant as (κ,δ) are varied and for FdF/dψ held constant (with q_0 = 1.1). The shaping results are strongly dependent on what is held constant, indicating that the effects of equilibrium profile modifications are important. The curves for β_0 = 0% and 0.5% are however, approximately parallel for both the q and FdF/dψ constant cases. This shows that for these relatively modest levels of shaping there is no marked change in the stabilisation of the tearing mode as β is increased. Although for the q constant case the reduction in growth rate as the shaping increases means that the curvature terms will stabilise the mode at lower β (or S). Increasing the D-shaping also raises the ideal ballooning β-limit.

Conclusions and discussion The finite-β properties of the tearing mode in JET have been studied computationally. The computations confirm the analytic results of Glasser et al [1]; there is a strong stabilising effect as β is raised which results from the favourable average curvature terms within the resistive layer. There is also a stabilising effect arising from profile modifications and poloidal mode coupling as β is raised. The importance of the stabilising average curvature terms increase as S (ie conductivity temperature) is raised. At large S the tearing mode growth becomes overtable and as S is raised still further the mode is completely stabilised. For moderately unstable q-profiles (Δ' ~ 5) we find that the n=1 tearing modes can be completely stabilised by β_0 = 1.5% at S = 10^5 (and β_0= 0.24% at S = 10^7). Since for these cases the critical β_0 for ideal ballooning is 6%, there is a considerable region of complete stability to the n=1 tearing mode and ideal ballooning mode (β_0 = 1.5 - 6% at S = 10^5). For modest shaping (κ = 1.4, δ = 0.2) there is no clear effect on the finite-β stability of the tearing mode. The critical β for ideal ballooning does however increase as the D-shaping is raised. Finally we note that critical-β for ideal ballooning scales as the inverse aspect ratio, whilst the critical β_0 which must be exceeded for the average curvature terms to stabilise the tearing mode scales as $(R_0/a^2)^{1/3}$ for n$\propto$T. Thus the region of stability to the tearin tearing mode and ideal ballooning mode shrinks as the aspect ratio is increased.

Acknowledgement We are indebted to the ORNL MHD group for providing us with a copy of the FAR code.

References

[1] A H Glasser et al, Phys Fl 18 (75) 875.
[2] M Kotschenreuther et al, Phys Fl 28 (85) 294.
[3] L A Charlton et al, to appear J Comp Phys (Feb 1986).
[4] J A Holmes et al, Phys Fl 25 (82) 800.
[5] B A Carreras et al, Phys Fl 20 (77) 1231.

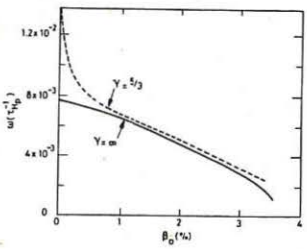

Fig 1 Growth rate (ω) v β_0

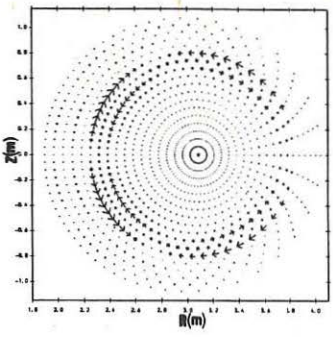

Fig 2 Velocity flow for same case as Fig 1 (β_0 = 2%)

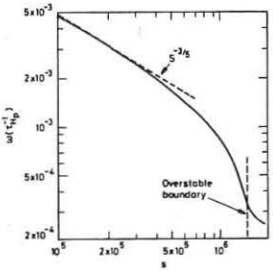

Fig 3 ω v S for same case as Fig 1 (β_0 = 2%)

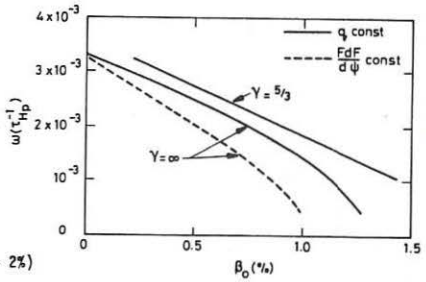

Fig 4 ω v β_0 for $q = 1.1\ (1 + (\rho/0.506)^8)^{\frac{1}{4}}$

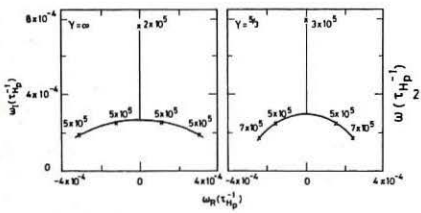

Fig 5 Growth rates in complex ω-plane for same case as Fig 4 at β_0 = 0.5%. The labels on the curves are the S values.

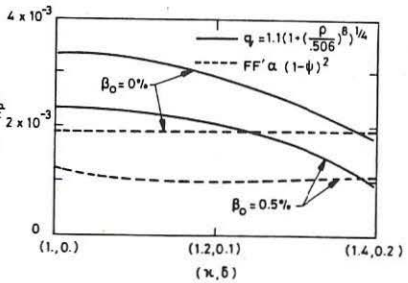

Fig 6 ω v D-shaping

TRANSPORT PROPERTIES AND SAWTOOTH RELAXATIONS IN THE FT TOKAMAK

F. Alladio, M. Ottaviani, G. Vlad

Associazione EURATOM-ENEA sulla Fusione, Centro Ricerche Energia Frascati, C.P. 65 - 00044 Frascati, Rome (Italy)

1. EVOLUTION OF THE SAFETY FACTOR PROFILE DURING SAWTOOTH ACTIVITY

The possibility that a magnetic trigger [1] is responsible for the sawtooth crash makes the attemp to calculate the evolution of the current density profile on the base of the available measured data rather attractive.

With such purpose we have solved, in cylindrical geometry, the coupled nonlinear equations for the evolution of the perturbed electron temperature and current density profile [2]. The solutions have been explored in a broad range of FT experimentally documented scenarios.

An interesting behaviour turns out to be characteristic of all discharges analyzed. We start after the sawtooth crash from a safety factor profile almost flat in the central region, as deduced from the Kadomtsev reconnection model [3]. The time evolution of the safety factor in the centre exhibits a rapid increase, which rises the q larger than one, followed by a slower decreasing phase. In the region between the centre and the mixing radius the safety factor profile turns out to have two q=1 resonances. The outer one $r = r_{s2}$ is calculated to be almost a fixed point at all times, whereas the inner one $r = r_{s1}$ is moving toward the centre $r = 0$ starting from the outer resonant surface $r = r_{s2}$ (see Fig. 1). In all the cases sofar analyzed the experimentally observed sawtooth repetition time τ_R turns out to be very near the time at which the inner resonance reaches the magnetic

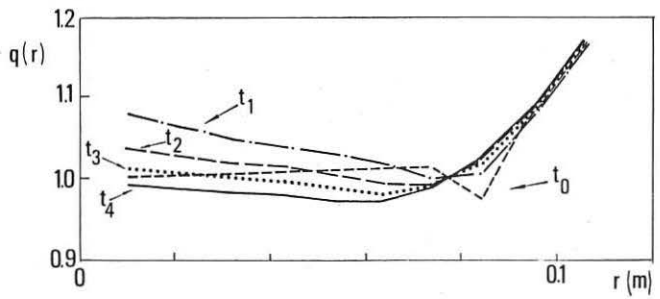

Fig. 1 q(r,t) profile for different times during the sawtooth period τ_R : $t_o = 0$ (after reconnection); $t_1 = \tau_R/4$; $t_2 = \tau_R/2$; $t_3 = 3/4\tau_R$; $t_4 = \tau_R$ (before reconnection).

axis and disappears. So we would be tempted to identify the magnetic trigger of the sawtooth crash with the simple condition $q(0) = 1$ on axis.

Although a detailed stability analysis has not yet been undertaken, such kind of result could be interpreted with the ideas expressed in Ref. [1]. The region in which a radial displacement ξ is predicted by the ideal MHD stability theory is the one in between the two resonances r_{s1} and r_{s2}. By enlarging such region the magnetic energy reservoir increases and is probably more susceptible to be depleted by the crash: however it is not clear to us why the crash should exactly coincide with the disappearance of the inner q=1 surface; on the other hand a more complete investigation is needed to have a full experimental evidence that this is the magnetic trigger.

2. ANALYTICAL MODEL

In order to make more explicit the dependence of sawtooth behaviour on the two characteristic times, the thermal diffusion time and the magnetic diffusion time, we have to introduce some simplifications.

Noticing that the relevant profile evolution happens inside a certain surface $r = r_k$, we can fix the boundary conditions for the perturbed q and T at r_k; the correct choice of r_k appears to be the point at which q is unchanged after a crash. For parabolic profiles this radius is related to the q=1 radius r_s through the relation [3] $r_k = 2/\sqrt{3}\ r_s$. In the limit $r_k^2/a^2 \ll 1$, where a is the minor radius of the plasma, we can neglect the contribution of the perturbation of the ohmic input in the perturbed temperature equation, since the associated characteristic time is just a^2/r_k^2 longer than the temperature evolution time inside the r_k surface. This fact decouples the temperature equation from the q equation.

We have been led to the following set:

$$\frac{\partial \tilde{T}(r,t)}{\partial t} - \frac{2}{3}\chi\left[\frac{\partial^2 \tilde{T}(r,t)}{\partial r^2} + \frac{1}{r}\frac{\partial}{\partial r}\tilde{T}(r,t)\right] = 0 \qquad (1)$$

$$\mu_o \frac{\partial \tilde{\mu}(r,t)}{\partial t} - \frac{1}{r}\frac{\partial}{\partial r}\left[\frac{1}{\sigma(T(r,t))}\frac{1}{r}\frac{\partial}{\partial r}(r^2\tilde{\mu}(r,t))\right] = \qquad (2)$$

$$= \frac{1}{r}\frac{\partial}{\partial r}\left[\frac{1}{\sigma(T(r,t))}\frac{1}{r}\frac{\partial}{\partial r}\left(\frac{r^2}{q_o(r)}\right)\right]$$

where $\tilde{T}(r,t)$ is the perturbed electron temperature, χ is the electron thermal conductivity (assumed radially constant inside r_k), $\tilde{\mu}(r,t)=1/q(r,t) - 1/q_o(r)$, $q_o(r)$ being the q profile after the crash, μ_o is the magnetic permability, $\sigma(T(r,t))$ is the electrical conductivity (assumed hereafter purely classical) and $T(r,t) = T_o(r) + \tilde{T}(r,t)$, $T_o(r)$ being the steady state electron temperature profile.

From the above discussion we can supplement Eqs (1,2) with the boundary conditions: $\tilde{T}(r_k,t) = 0$, $\tilde{\mu}(r_k,t) = 0$, $\tilde{T}(r,0) = T_o(r_k) - T_o(r)$, $\tilde{\mu}(r,0) = 0$.

Within the spirit of the approximation $r_k^2/a^2 \ll 1$ we can assume parabolic profiles:

$$\frac{\tilde{T}(r,0)}{T_o(r_k)} \sim -\frac{r_k^2}{a^2}(1-r^2/r_k^2); \quad \frac{1}{q_o(r)} \sim 1 - b^2 r^2/r_k^2, \text{ with } b^2 < \frac{3}{4}\frac{r_k^2}{a^2}$$

to allow sawtoothing (but an appropriate value should be $b^2 = 3/16\ (r_k^2/a^2)$ from Kadomtsev's model).

We also linearize the electric conductivity around the flat intial temperature profile. We get the following equation for $\tilde{\mu}(r,t)$:

$$\mu_o \frac{\partial\tilde{\mu}(r,t)}{\partial t} - \frac{1}{r}\frac{\partial}{\partial r}\left[\frac{1}{\sigma[T_o(r_k)]}\frac{1}{r}\frac{\partial}{\partial r}(r^2\tilde{\mu}(r,t))\right] = \tag{2'}$$

$$= \frac{1}{\sigma[T_o(r_k)]}\frac{1}{r}\frac{\partial}{\partial r}\left\{\left(1 - \frac{3}{2}\frac{\tilde{T}(r,t)-\tilde{T}(r,0)}{T_o(r_k)}\right)\frac{1}{r}\frac{\partial}{\partial r}\left(\frac{r^2}{q_o(r)}\right)\right\}$$

Equations (1) and (2') have been solved by standard methods in terms of radial Bessel functions. The results is conveniently written in the form:

$$\tilde{\mu}(r,t) = \tilde{\mu}(r)_{\text{asympt.}} - \frac{2r_k}{r}\sum_{1n}^{\infty}\frac{J_1(\mu_n^1\, r/r_k)}{[\mu_n^1 J_1'(\mu_n^1)]^2}\left\{L_n\, e^{-t/\tau_\sigma^n} + \right. \tag{3}$$

$$\left. + \sum_{1m}^{\infty}\frac{3}{2}C_m\, I_{mn}\left[(1-\tau_\chi^m/\tau_\sigma^n)^{-1}\, e^{-t/\tau_\sigma^n} + (1-\tau_\sigma^n/\tau_\chi^m)^{-1}\, e^{-t/\tau_\chi^m}\right]\right\}$$

with $\tilde{\mu}(r)$asympt. $= (-b^2 + 3/4\ (r_k^2/a^2)\ (1-r^2/r_k^2)$, $1/\tau_\chi^m = 2/3\ \chi\ (\mu_m^o/r_k)^2$; $1/\tau_\sigma^n = 1/(\mu_o\ \sigma[T_o(r_k)])\ (\mu_n^1/r_k)^2$ being the inverse characteristic diffusion times (μ_k^o and μ_k^1 are the k-th zeros of the Bessel functions J_o and J_1).

The coefficients L_n, C_m, I_{mn} are defined as follows:

$$L_n = \frac{8b^2 J_o(\mu_n^1)}{\mu_n^1}\ ; \qquad C_m = -\,8\,\frac{r_k^2}{a^2}\,\frac{1}{\mu_m^{o\,3}\,J_1(\mu_m^o)};$$

$$I_{mn} = \frac{2\mu_n^1\mu_m^o}{\mu_n^{1\,2} - \mu_m^{o\,2}}\ J_o(\mu_m^1)\ J_1(\mu_n^o)\ .$$

Figure 2 shows the dependence of the sawtooth repetition time τ_R on τ_χ^1, as obtained by Eq. (3) by imposing $\tilde{\mu}(0,\tau_R) = 0$ (that is $q(0,\tau_R) = 1$). Agreement with the more complete numerical code [2] is found. The curve shows an almost linear dependence of τ_R on τ_χ, while the dependence on τ_σ is weak. This is consistent with the density scaling observed in ohmic experiments. We have also run few cases with more peaked profiles $T \propto (1-r^2/a^2)^\nu$, $\nu > 1$ (Fig. 3), and we have found that the dependence of τ_R on τ_σ increases, according to what previously stated [2].

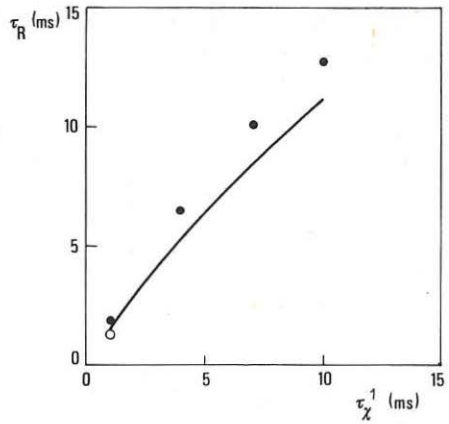

Fig. 2 Sawtooth repetition time τ_R vs τ_χ^1 as desumed by Eq. (3) by imposing $\tilde{\mu}(0,\tau_R) = 0$. $\tau_\sigma^1 = 10$ ms, $r_k/a = 0.4$, $b^{2\chi} = 0.2(r_k/a)^2$. Also shown are the complete numerical solution of the diffusive equations for $\tau_\sigma^1 \sim 10$ ms (full dots) and for $\tau_\sigma^1 \sim 1$ ms (open dot).

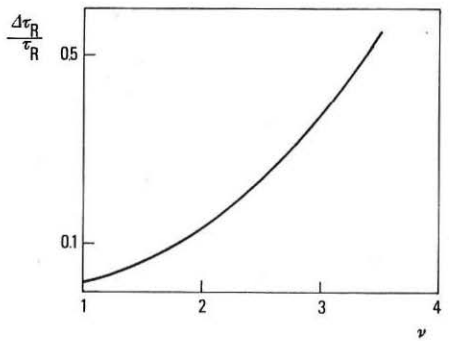

Fig. 3 Relative increase of sawtooth repetition time $\Delta\tau_R/\tau_R \equiv (\tau_R(\sigma_2)-\tau_R(\sigma_1))/\tau_R(\sigma_1)$, with $\sigma_2 = 2\sigma_1$, vs ν, as desumed by the complete numerical solution of the diffusive equations. $r_k/a = 0.4$, $\tau_\chi^1 \sim 1$ ms, $\tau_{\sigma_1}^1 \sim 5$ ms.

REFERENCES

[1] J. Wesson, Plasma Phys. 28, 1A, 243 (1986).
[2] F. Alladio, G. Mazzitelli, A.A. Tuccillo, G.Vlad, 12th European Conference on Controlled Fusion and Plasma Physics, Budapest, 9F, I, 138 (1985).
[3] B.B. Kadomtsev, Sov. J. Plasma Phys. 1, 389 (1975).

β LIMIT FOR ELONGATED CROSS-SECTION TOKAMAKS

A. Roy, O. Sauter, A.D. Turnbull, R. Gruber and F. Troyon

Centre de Recherches en Physique des Plasmas
Association Euratom - Confédération Suisse
Ecole Polytechnique Fédérale de Lausanne
21, Av. des Bains, CH-1007 Lausanne / Switzerland

Abstract

The scaling of the optimum β with current, in various elongated cross-section Tokamaks (elongation 2.5), is compared with a number of well-known scaling laws given in the literature. In particular, the effects of triangular and rectangular deformations (D and racetrack shapes) and of indentation of the poloidal cross-section are considered. Significant deviations from the known scaling laws are found and these are discussed with a view to constructing a configuration with the most favourable scaling.

Introduction

Plasma β optimization studies[1] against ideal MHD instabilities, which predict a remarkable linear scaling of β_{opt} with current I, have generally been limited to Tokamak cross section shapes of small to moderate (~1.6) elongation. For those cases considered, the linear scaling breaks down more or less abruptly when the safety factor at the surface q_s is in the vicinity of 2, so that the highest β that can be obtained occurs when q_s is a little above 2. By elongating the cross-section, the current for which $q_s = 2$ can be increased greatly and, if the linear scaling of β_{opt} remained valid, a proportionate increase in β_{opt} would result. It is therefore important to determine if the linear scaling can be extrapolated to cross-sections with large elongation. Recent optimization studies[2], restricted to stability against ballooning modes, suggest that the linear scaling does break down for elongations between 1.6 and 2.0. Nevertheless, these studies ignored low n kink stability and were, as are all optimization studies, restricted to particular class of plasma profiles.

An optimization procedure reported elsewhere[3] has been developed and applied to circular cross-section plasmas, with which a β limit that was 50% above that predicted by the linear scaling law was obtained. We apply that procedure to the problem of optimization of a 2.5 elongation racetrack cross-section Tokamak plasma. For this case, at low β, the operational regime in the (q_o, q_s) space is restricted to certain narrow windows just above the integer q_o values[4] (q_o is the value of q at the magnetic axis). We firstly show how the operational regime changes with finite β. The optimization study completes the picture. The optimized β limits against kink and ballooning modes, deviate strongly from the linear scaling law and, at moderate to high currents corresponding to q_s in the range 2 to 5, generally decrease with I.

If one assumes that kink modes could be stabilized by a nearby conducting shell, then the β is limited only by ballooning modes. We there-

fore also determine the ballooning limits. These are significantly higher than those for the full optimization, but are still well below the linear scaling predictions and follow the same overall trend as in reference 2. More optimistic results are obtained however, with regard to both ballooning limits, and to the complete stability limits by a strong triangularization (D shape) of the cross section.

Kink and Ballooning β Optimization

The optimization procedure used has been described elsewhere[3] but the key features can be summarized as follows:

i) The zero β stability is analysed thoroughly to determine the stability criteria for purely current driven modes and therefore determine a zero β "operating regime".
ii) The pressure gradient $p'(\Psi)$ and average current density $J(\Psi)$ over a flux surface are specified independently.
iii) The profiles $p'(\Psi)$ and $J(\Psi)$ are specified in piecewise differentiably continuous sections.

The operational diagram is shown in Fig. 1. The optimization proceeds at any given current, by increasing β_p from within the zero β stable windows. At finite β (constant β_p), the stable regime begins to close over and for $\beta_p = 0.4$, the new marginal stability line is indicated. Here, the β_p was increased by specifying a finite pressure gradient as described in ref. 3. Note that the window for $1 < q_0 < 1.16$ closes up very quickly for $q_s < 3$, suggesting that the highest β may be obtained at lower currents, although for constant β_p, the β is proportional to I.

Optimization curves for a family of current profiles with increasing current channel width are shown in Fig. 2 for a constant normalized current of $I_N = \mu_0 I/R_0 B_0 = 0.555$. The curves labelled A,B are always unstable; these are the most broad and have q_0 always in the unstable window for $1.16 < q_0 < 2$. The curve C is close to marginal stability at zero β and rapidly becomes unstable at any appreciable β. The curve labelled D is the optimum, having q_0 well within the stable window, and also q_s just above 3. As the current channel is narrowed further, q_0 drops below unity, the toroidal kink becomes unstable at zero β, and the curves never reache a stable point (E,F). The optimum stable β, obtained from this family of current profiles, at a O^2 criterion of 10^{-5}, is 1.85%, corresponding to the point marked x.

The results for β_{opt} vs I obtained from this study are shown in Fig. 3. The dips in β_{opt} correspond to the points where q_s drops below integer values. Overall, β_{opt} decreases with I. For the cases used in this study, kink stability almost always provides a more stringent restriction on β ballooning stability.

The results in Fig. 3 are sensitive to the parameters that were held constant, in the sense that the positions of the minima shift if different values for these parameters are taken. However, the overall behaviour appears to be unchanged. The parameters were chosen in this study so that the q profile is always quite flat in a large region, with large shear at the edge where the pressure gradient is finite. A limited optimization was also performed for the window at $q_0 > 2$, at one current with $q_s \sim 3$, the β limit was quite low (~0.25%) and it remains to be determined whether this improves at lower currents.

Ballooning optimization

For the calculations described above, no attempt to optimize the pressure profile against ballooning modes was necessary since the n = 1 kink mode was always unstable at a lower β than the ballooning modes. An optimization against ballooning modes was also carried out, with kink stability taken into account only to the extent that the equilibria were stable to current driven kink modes ($1.0 < q_0 < 1.16$). This optimization was done by locally adjusting the piecewise pressure profile until the ballooning and Mergier criterra were satisfied everywhere. The results are shown in Fig. 3. As found in [2], at high current, the ballooning linit is markedly inferior to the linear scaling predictions and begins to decrease with I. The highest β obtained in our case is 4.6% at a normalized current of $I_N = 0.55$.

If the restriction that $p' = 0$ at the edge is imposed thus preventing Pfirsch-Schlüter currents at the edge (the average current is alsways zero) this β is significantly lowered. For the full optimization this condition was imposed to reduce the number of free parameters and one could expect that, if it were relaxed, the β obtained could also be significantly higher.

Discussion and conclusions

The linear scaling law of [1] can not be extrapolated to large elongations above 2.04 The stability at high β is restricted by the encroaching unstable domain at $q_0 > 1$ as β is increase. The β limit that is obtained using a finite family of equilibria is generally dercreasing with current with pronounced minima when q_S is near integer values. If a larger dass of equilibria were used, the β limit would correspond to an envelope over a series of these curves so that the minima would be less pronounced but the overall trend would be expected to remain.

Ballooning stability alone yields substantially higher β values, especially if p' is non zero at the edge. Removing this restriction for the kink optimization (would) also improve (s) the β limits obtained.

More exotic current and q profiles may improve the β limits. The β limits are also dependent on the shape of the boundary. For exanple, for an elongated D shape the zero β operating diagram has no unstable window above $q_S = 3$, though is probably always unstable for $q_S<3$. With a limited kink optimization, the kink limit at one current of $I_N=0.565$ is already 3.7%. Ballooning limits are also improved at low currents, though, in contrast to the results of [2], we find that the improvement is not great at larger currents (Fig. 3). It is not yet clear whether the improvement for the D is due to the shape directly, or to the change in the current profile that is required to give the same q profile as we used for the racetrack. More exotic shapes, particularly indentation may improve this further still; certainly the ballooning linits should improve.

References

[1] F. Troyon, R. Gruber, H. Saurenmann, S. Semenzato and S. Succi, Plasma Phys. and Contr. Fusion 26, 209 (1984).

[2] K. Yamazaki, J. Amano, H. Nairov, Y. Hamada and M. Azumi, Nucl. Fusion 25, 1543 (1985).

[3] A.D. Turnbull and F. Troyon, Proc. 12th European Conf. on Contr. Fusion and Plasma Phys., Budapest (1985).

[4] A. Roy, A.D. Turnbull, O. Sauter, S. Nicli and F. Troyon, Proc. 13th European Conf. on Contr. Fusion and Plasma Phys., Schliersee (1986).

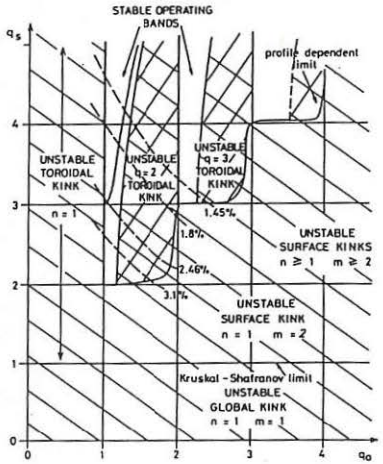

Fig. 1. $\beta_p = 0$ and $\beta_p = 0.4$ operating diagram

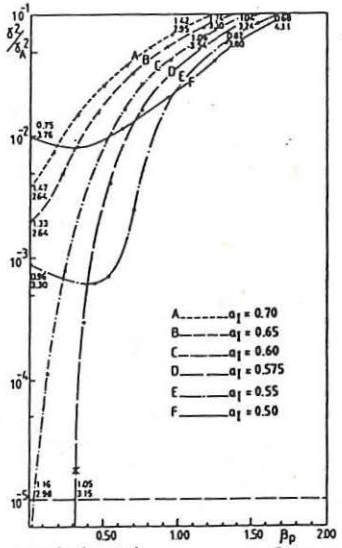

Fig. 2. Optimization curves for a constant current I_N=0.555

Fig. 3.

Kink and ballooning β limit vs. current $I = \mu_o I/RoBo$ (E=2.5). β_T is the Troyon limit.

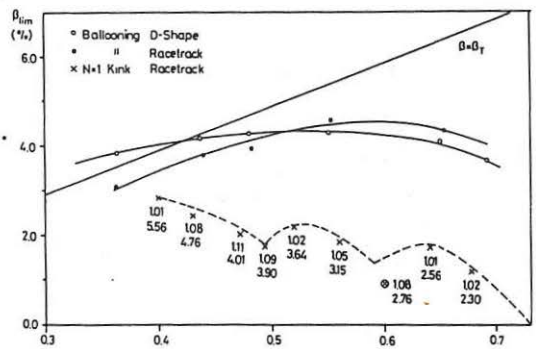

OPERATIONAL DIAGRAM FOR LOW β RACETRACK CROSS-SECTION TOKAMAKS

A. Roy, A.D. Turnbull, O. Sauter, S. Nicli and F. Troyon

Centre de Recherches en Physique des Plasmas
Association Euratom - Confédération Suisse
Ecole Polytechnique Fédérale de Lausanne
21, Av. des Bains, CH-1007 Lausanne / Switzerland

Abstract

The n = 0 axisymmetric mode and the n = 1 free boundary kink mode impose important constraints on the current configuration of Tokamak plasmas, even at low β. These contraints become more severe as the plasma cross-section is elongated in the vertical direction.

The n = 1 kink manifests itself in the form of various instabilities. These can be classified on a (q_0, q_s) operational diagram. We show how the stable operating regime of racetrack-shaped Tokamak plasmas varies with elongation at low β. The n = 0 mode can be stabilized by an active feedback system with a nearby conducting wall, but the proximity of the wall is limited by technological considerations, so this further restricts the stable operating regime.

Introduction

Optimization studies, which are used to determine the maximum β that can be acheived within the constraints imposed by ideal MHD stability in a particular Tokamak comfiguration, require a knowledge of the stability properties of the configuration at low β so that current-driven ideal MHD instabilities can be avoided from the outset. However, little is known about the kink stability of elongated plasmas so this must be determined as a first step to a β optimization study. The results of our study can be conveniently summarized on an operational diagram showing the marginal stability boundaries in a (q_0, q_s) space, where q_0 and q_s are the safety factor values at the magnetic axis and the plasma surface respectively.

Axisymmetric modes are also important for elongated cross-sections, and, although these can be stabilized by a combination of conducting shell and active feedback, the proximity of the wall is limited, thus imposing further restrictions on the plasma profiles. In general, axisymmetric stability requires a sufficiently broad current profile; a sufficiently low ratio q_s/q_0, whereas, for kink stability, this ratio must be sufficiently high. It is therefore important to determine if there is a region of the parameter space that is stable to both types of mode.

We consider the stability of a class of racetrack-shaped cross-section plasmas and show how the operational diagram changes with elongation and that, at large elongations, it becomes increasingly difficult to satisfy the stability constraints. A number of deformations, notably triangulation and indentation are also considered and compared.

n = 1 Kink Stability

The case of a circular cross-section Tokamak has been treated previously [1] and the stability can be summarized by the requirements that $q_0 > 1$ to avoid toroidal kink modes [1], $q_s > 2$ to avoid n = 1 m = 1 kink modes and $q_s/q_0 > \alpha(q_0)q_0$, where $1 < \alpha < 2$ depends on the current profile, to avoid higher m (and n) surface kinks. As the elongation is increased up to 2:1, this picture remains essentially unchanged, however, for elongations greater than 2.0, a new instability emerges which progressivley restricts the stable operating domain. The new instability is the q = 2 counterpart to the toroidal kink; it is unstable for $q_0 < 2$ and has the structure of a kink mode inside q = 2 with a large kinetic energy contribution in the vicinity of the q = 2 surface and little motion near the plasma edge. In fact, in this case, the mode appears to be truly internal. As q_0 approaches 2, the mode becomes less and less localised about the q = 2 surface. We call this mode a "q = 2 toroidal kink". Similar instabilities occur for $q_0 < 3$ and higher.

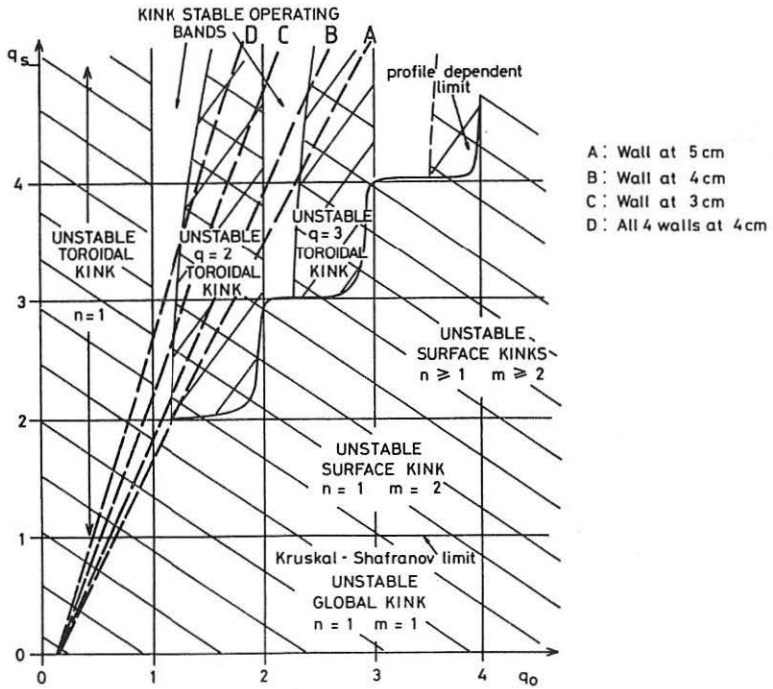

Fig. 1. N=1 kink and axisymmetric stability operating diagram.

The unstable region is shown on the operational diagram in Fig. 1 for the case of a 2.5 : 1 elongation racetrack plasma with aspect ratio 4.4. For the study described by this figure, we have used a family of current profiles, characterized by quite flat q profiles near the center and high shear only near the edge. The unstable region is somewhat profile dependent, varying with variations in the local shear of the q profile, and for some classes of current profile; those with more shear in the central region (but the same (q_0, q_s)), the stable region can vanish for $q_s<3$. For elongations greater than 3, we have not yet been able to find any stable region, however, this does not preclude the possibility if the right profiles are found.

Axisymmetric Stability

Previous studies [2] have shown that elongated racetrack plasmas can be stabilized by a reasonably close side wall and the top and bottom walls removed to a relatively large distance. This is the scenario envisaged for the Lausanne TCV Tokamak for which current designs allow elongations ranging from 1.0 to 4.0 in the same vessel. In Fig. 2, we show the maximum side wall distance d_{max} that is allowable for axisymmetric stability, at various values of (q_0, q_s), as a function of elongation E. Note that d_{max} becomes relatively insensitive to E for elongations E > 3 and even increases slightly. This is because the top and bottom walls begin to contribute to the stability at elongations E > 3.

The unstable regions for various wall configurations (3 cm, 4 cm and 5 cm and all four walls at 4 cm) are indicated on the operational diagram of Fig. 1 for E = 2.5. In particular, with a side wall at 4 cm or more, the stable region for $q_0 \sim 1$ $2 < q_s < 3$ is inaccessible. Nevertheless, if the side wall is less than 4 cm away, the high current region opens up and, if the top and bottom walls are also moved to within 4 cm, a substantial region is accessible. The TCV design in fact envisages that the stabilizing influence of the bottom wall is available in a non-symmetric configuration. Note that axisymmetric stability does not impose any constraints on the stable operating windows for $q_0 > 2$.

Conclusion

The n = 0 axisymmetric and n = 1 kink modes can impose quite severe constraints on the parameters at which an elongated Tokamak (E > 2) can operate in a stable configuration. Nevertheless, for elongations up to E ~ 2.5, stable windows are accessible and, in particular, high current operation is possible with $q_0 \sim 1$ and $q_s \sim 2$. (For a Tokamak of 80 cm major radius, aspect ratio 4.4 and toroidal field 1.5 T, this corresponds to 730 kA.) The stable windows can probably be widened further by a more judicious choice of the detailed q (or current) profiles. Furthermore for other elongated cross-sectional shapes the operational diagram can have a completely different character, for example, with a D-shaped modification, the unstable region for $q_0 < 2$ vanishes completely for $q_s > 3$ but it closes up completely when $q_s < 3$. This may prove more desirable if high

current operation is not necessary. Axisymmetric stability is also improved. With indentations in the poloidal cross-section, it appears that the stable windows for $k < q_0 < k + \delta$ (k integer) are replaced by stable windows for $k + \delta_1 < q_0 < k + \delta_2$. Combinations may therefore also prove effective.

References

[1] A.D. Turnbull and F.Troyon, Proc. 12th Eur. Conf. on Contr. Fusion, Budapest 1985.
[2] F. Hofmann, A.D. Turnbull and F.B. Marcus, to be published.

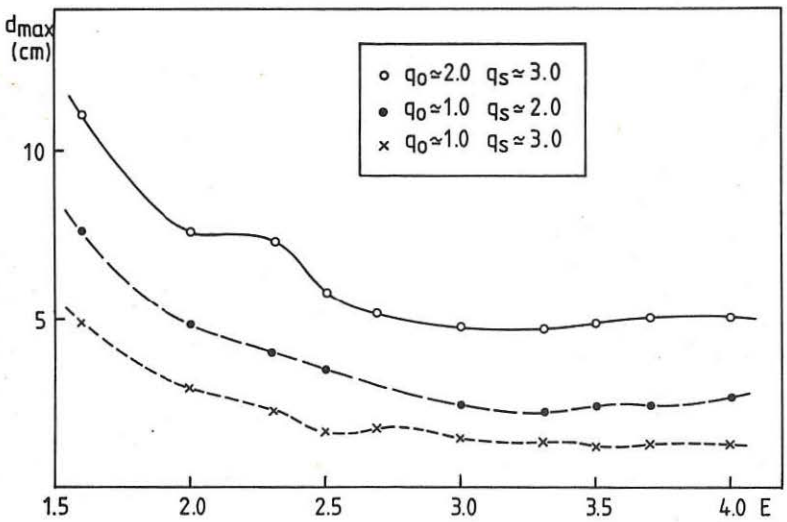

Fig. 2. Maximum side wall distance d_{max}, allowable for axisymmetric stability vs. elongation E at three different values of (q_0, q_s)

DIMENSIONALITY OF FLUCTUATIONS IN ASDEX

L. Battiston*, ASDEX-Team

Max-Planck-Institut für Plasmaphysik, EURATOM Association, D-8046 Garching, Fed. Rep. of Germany

*Istituto Dinamica Grandi Masse - C.N.R. Venezia S.Polo, 1364 (I)

INTRODUCTION

Dimensionality analysis of experimental series of data has revealed a new powerfull tool for a deeper understanding of turbulent physical systems. The analysis of the so-called strange attractors provides a tool to identify the fractal dimension ν of a time series. This fractal dimension is associated with the number of indipendent processes which characterize the system, and if it exists, it provides a distinction between deterministic chaos and noise /1/. Here it is used the well known definition of ν as the lim $R \to 0$ of the ratio $(d \log C(R))/(d \log R)$; $C(R) = 2/((N-1)N) \cdot \sum_{ij} H(R - |\overline{x}_i - \overline{x}_j|)$ where H is the heaviside function and $R_{ij} = |\overline{x}_i - \overline{x}_j|$ is the Euclidean norm between all pairs of $\overline{x}_i$ whose components are the values of the single time series signal at D different delayed times: $\overline{x}_i = \{x_i, x_{i+M}, x_{i+2M}, \ldots x_{i+(D-1)M}\}$ D is the so-called embedding dimension and M is the delay time factor. In the context of fusion research this method has been applied previously to the study of fluctuations on DITE, RFP, TOSCA and JET /2/, /3/, /4/. The present analysis exploits the poloidal divertor configurations of ASDEX and its strong additional heating power which give it access to the new favourable H-confinement regime and allow it to approach MHD Beta limits /5/. As a consequence a wider variety of fluctuation phenomena are observed by Mirnov coils and soft X-Rays diagnostics /6/.

CHOICE OF DIAGNOSTICS AND DISCHARGE PHASES

Different phases of a typical high power NI-heated discharge are analyzed. The important time traces of this discharge are shown in fig. 1. (Actually four shots are used of the same series because of the high time-resolution diagnostics (250 kHz) recovered over different shots, #18041, #18040, #18026, #18039.) The analysis is concentrated on the characteristic phases indicated in the same fig. 1. For comparison also an L-discharge is analyzed (#18024). Diagnostics used for characterization of the MHD fluctuations were soft X-Rays and Mirnov coils. For present analysis 5 signals are considered: SXF and SXJ which are central X-Rays signal ($q < 1$); SXL and SXA which are peripheral X-Rays signals ($q > 1$) and A8SSW which is a Mirnov signal from a coil located externally in the equatorial plane of the ASDEX torus.

In general 10 windows of 8 ms each corresponding to 2000 data are taken and analyzed for each shot in order to give account of different physical phases and to have enough data (at least if the dimensionality is low). For some specific situations, the windows could be taken different, for a better definition or much longer in order to have a better establishment of dimensionality or to distinguish between noise and chaos.

If the dimensionality is low it is found indipendent of the number of data from 1000 to 10000. Also for the delay time it is found a range of independence of results with $5 \lesssim M \lesssim 10$, for N = 2000 (e.g.), but in general M = 5 is taken.

ASDEX RESULTS

According to the preceding definitions results are presented phase by phase. During an H-shot one can distinguish approximately four phases: They are shown in fig. 1 on the bottom border.

Phase 1: Deep L-phase, after additional NI heating and before L → H transition. Combined results from #18041 and #18040.

SXF: $\nu \sim 1$ at the beginning and then increases to $\nu \sim 2$ through splitting of dimensionality: $\nu - \begin{cases} 1.22 \\ 0.8 \end{cases}$

SXJ: $\nu \sim 1$ at the beginning and then increases to $\nu \sim 2.25$ through splitting of dimensionality: $\nu - \begin{cases} 2.25 \\ 0.75 \end{cases}$

SXL and SXA: $\nu \sim 1$

A8SSW: value of dimensionality $2.25 < \nu < 3.5$

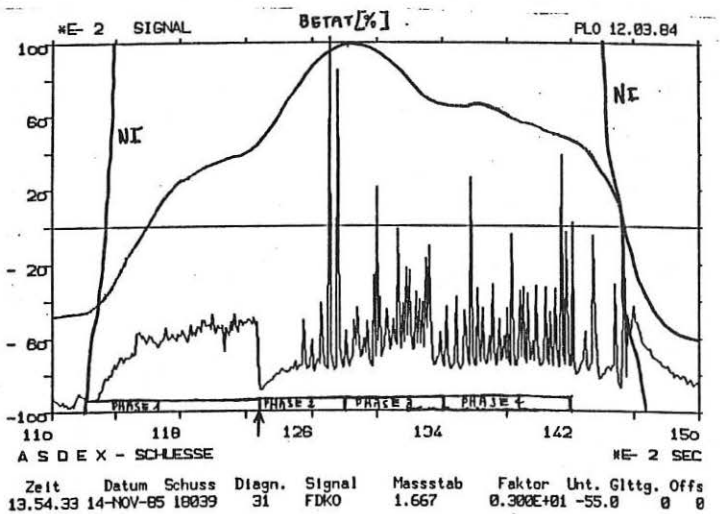

Fig. 1 shows some important parameters during a typical H-shot: NI is the neutral injection interval, FDKO is the signal connected with H_α activity which points the L → H transition (indicated with an arrow) and BETAT behaviour. In the bottom side the four phases of the analysis are reported.

Phase 2: After L→H transition, toward maximum BETAT. #18040. H-phase begins with sawtooth in edge region and fishbone like signal in central region.

SXF: $\gamma \sim 3.3$

SXJ: $\gamma \sim 0.75$

SXL and SXA: $\gamma \sim 1$

A8SSW: $\gamma \sim 3.5$

Phase 3: From BETAT maximum toward stationary phase with constant BETAT. #18026.

SXF: γ begins with value ~ 1 and then increases up to $\gamma \sim 3.6$

SXJ: $\gamma \sim 3$

SXL, SXA: $\gamma \sim 1$ in presence of well pronounced sawteeth

A8WNW: $2.6 < \gamma < 3.5$

Phase 4: Stationary H-phase at reduced but constant BETAT.#18039.

SXF: $\gamma \sim 1$ and after $2.5 < \gamma < 3.5$, Presence of a splitting of dimensionality at the beginning $\gamma \sim \begin{cases} 2.5 \\ 0.75 \end{cases}$

SXJ: noise

SXL: $\gamma \sim 0.85$, SXA: $\gamma \sim 1.2$ with well pronounced sawteeth (fig. 2 and 3)

A8SSW: $\gamma \sim 3.75$

In comparison an L-shot was considered (BETAT max ~ const.) #18024. In general the signals are very noisy and no definite values of dimensionality can be given.

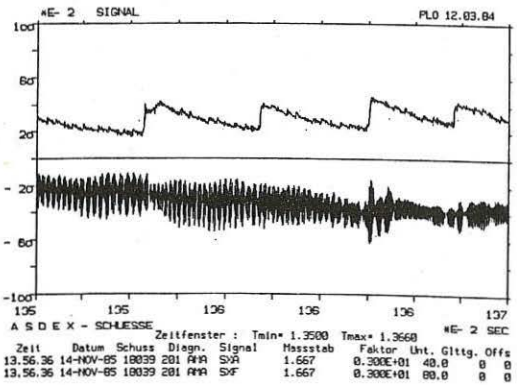

Fig. 2: Signals traces of two X-Rays chords during a time-window of 16 ms. SXA, the edge chord, shows definite sawteeth, while SXF, the core chord, exibits a fishbone-like structure. There seem to be no correlation between the two signals. #18039

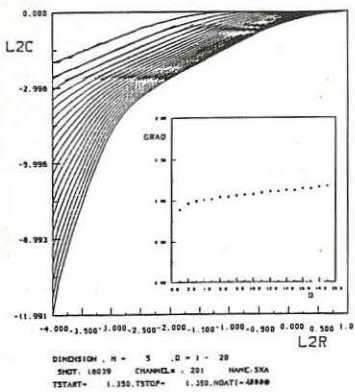

Fig. 3:
Dimensionality analysis for chord SXA signal. Same shot as in fig. 2 but for a longer period of 40 ms corresponding to 10000 data points. The result is identical for 1000 data point due to the very low dimensionality. M=5 is the delay time factor chosen. The embedding curves are simply connecting 50 calculated points (10 per decade). Logarithms in base 2 are used. The straight lines which show the D-depending slope are constructed with the least mean square method, starting from the same calculated points. In the square window the slopes, that is the gradients of the embedding curves as functions of embedding dimensions D are reported. The asymptotic saturation value of the slope is the dimension. $\gamma \sim 1.2$ in this case.

CONCLUSIONS

The MHD activity present in ASDEX NI heated divertor plasma configurations, has in general a low dimensionality: $\gamma < 3.75$. Signals with a non-strictly convergent saturation slope are ascribed to noise.
The edge soft X-Rays signals show a very low dimensionality: $\gamma \sim 1$ during all phases.
The central soft X-Rays signals, in general, develope a higher dimensionality passing from L to H-phase and $1 < \gamma < 3.5$.
The Mirnov coil signal seems to have an higher dimensionality in respect to other signals during all phases with $3 < \gamma < 3.75$.
In comparison the L-shot shows no information from edge signals and central signals because of their noisy-like structure.
Thus in general the MHD activity is characterized by fractal dimensionality associated with strange attractors.
The system seems to be characterized by two subsystems: a core region where at the end of the evolution a minimum of four indipendent processes is necessary, and an edge region where for the most of time a unique variable could be enough to characterize the system evolution reminding the theoretical example of the non-linear logistic map.
In some cases the central soft X-Rays signal splits into two different value of γ. An X-Ray signal is an integrated information that is it takes into account both central and edge X-Ray emission. Two different values of dimensionality should indicate that the two subsystems are physically indipendent /7/.
It is to be noted that a $\gamma = 1$ dimensionality value is obtained also in JET /3/, when soft X-Rays diagnostics exibits sawtooth activity.

REFERENCES

/1/ P.Grassberger, I.Procaccia, Physica 9D, 189 (1983).
/2/ S.J.Gee, J.B.Taylor, 12th Europ. Conf. Contr. Fus. and Plasma Physics, Vol. 2, 446 (1985).
/3/ A.Cotè et al., ibid, 450 (1985).
/4/ W.Arter, D.N.Edwards, ibid, 442 (1985).
/5/ M.Keilhacker, ASDEX-Team, Nuclear Fusion, Vol. 25, 9 (1985).
/6/ R.Stambaugh, J.Gernhardt, O.Klüber, F.Wagner, (IPP III/103) (1984).
/7/ J.P.Eckmann, D.Ruelle, Rev. Mod. Phys. 57, 3, 617 (1985).

ELECTRON HEAT TRANSPORT IN A STRONGLY MAGNETIZED PLASMA

Aldo Nocentini

The NET Team, c/o Max-Planck-Institut für Plasmaphysik,
Boltzmannstrasse 2, 8046 Garching bei München

Electron heat transport due to binary Coulomb collisions in a magnetically confined plasma has been widely studied. For toroidal plasmas this has led to the derivation of the "neoclassical electron heat conductivity", which, as is well known, in tokamaks is disproved by the experimental results, with respect to both its order of magnitude and its parametric dependence. It is pointed out here that the parameters of the tokamak plasmas studied experimentally are beyond the range of validity of the neoclassical electron transport theory. In fact, the usual assumption on which the neoclassical theory is based is that a binary Coulomb collision is a local (in space and time) change in the velocity of the two colliding particles. Actually, this assumption is a good approximation only if the Larmor radii r_L of the particles are much larger than the Debye length λ_D. In actual experiments in tokamaks this condition is fullfiled by the ion population, but not by the electron population. In fact, one has

$$r_L/\lambda_D = k \{N(10^{13}\ cm^{-3})\}^{1/2} / B(5\ tesla), \qquad (1)$$

where $k = 0.20$ for electrons and 8.7 for protons. Hence, in order to apply the theory to the experiments, one has to take into account what effect the presence of the magnetic field has on the dynamics of electron-electron collisions.

The properties of "binary drift collisions" among electrons, i.e. electron-electron scattering due to mutual electrostatic repulsion in the presence of a "strong" magnetic field (i.e. in the zero Larmor radius limit) are discussed here. It is shown that in plane geometry drift collisions among electrons lead, in the case $\lambda_D > r_{Le}$, to electron heat conductivities completely different from those of the usual theory based on binary Coulomb collisions /1/. In particular, for parameters which are typical of the plasma in front of the wall in tokamak experiments ($N \approx 10^{13}$ particles/cm^3, $B \approx 5$ tesla, $T \approx 100$ eV) the value of the perpendicular conductivity turns out to be much larger (by two orders of magnitude) and the value of the parallel conductivity of the perpendicular energy much smaller (by two orders of magnitude) than the corresponding classical values. These results should be taken into account in determining the transport properties of magnetically confined plasmas. Their consequences for tokamaks, a more detailed treatment and a comparison with preceding work /2/ are presented elsewhere /3/.

Firstly, we describe an electron-electron scattering event in the presence of a uniform, constant magnetic field (which we assume to point

in the z-direction) in the zero Larmor radius limit. The origin of our reference system is put in the center of mass of the two electrons. Let the distance ρ of the two lines of force on which the electrons lie before the collision (at $t \to -\infty$) be called the "scattering parameter", and their initial (at $t \to -\infty$) parallel speed (the parallel velocities being clearly opposite to each other) be denoted by v_{∞}. As far as the parallel (to $\underline{B}$) direction is concerned, the two electrons move towards the z=0 plane, slowing down under the action of the parallel component of their mutual electrostatic repulsion. If $mv_{\infty}^2 < e^2/\rho$ (where e and m denote the electron charge and mass, respectively), they are reflected before reaching the z=0 plane and return toward the region they came from, accelerating again. If $mv_{\infty}^2 > e^2/\rho$, they pass the z=0 plane and continue accelerating always in the same direction. As far as their motion in the plane perpendicular to $\underline{B}$ is concerned, they drift around the z-axis, in the positive direction, keeping their distance constant, under the action of the perpendicular component of their mutual electrostatic repulsion, i.e. with velocity $v_{D\mathcal{E}} = cE_{\perp}/B$, where c denotes the speed of light and E the electric field. At the end of this binary "drift collision" (at $t \to +\infty$) each electron has rotated around the z-axis by the angle

$$\Delta\theta = \frac{2c}{\rho B}\int_{-\infty}^{+\infty} E_{\perp}(t)\, dt = \frac{2ec}{B}\int_{-\infty}^{+\infty} dt\, \{4z^2(t) + \rho^2\}^{-3/2}\,, \qquad (2)$$

where z(t) denotes the (common) distance of the electrons from the z=0 plane at the instant t.

Hence, an electron-electron drift collision, in the laboratory system, causes an orthogonal (to $\underline{B}$) displacement of the two particles (with conservation of the perpendicular coordinate of the center of mass), and, possibly (if the parallel component of their relative velocity before the collision is smaller than $\Delta v_o = 2e/\sqrt{m\rho}$), an exchange of their parallel velocities (while the perpendicular energy is conserved). A collision operator describing this would be non-local, hence essentially different from the collision operator of the classical (and neoclassical) transport theory.

The perpendicular (to $\underline{B}$) electron heat conductivity due to electron-electron drift collisions is now evaluated for a plasma in thermal equilibrium, embedded in a uniform magnetic field and characterized by $\lambda_D > r_{Le}$. The evaluation is based on the simple stochastic argument which, for the perpendicular electron heat flux $q_{\perp}$, leads to the formula $q_{\perp} = N\chi_{\perp}^{D}\nabla_{\perp}T$ (where N and T denote, respectively, the number density and temperature of the electron population), where

$$\chi_{\perp}^{D} = \frac{1}{N}\int d\rho \int d\underline{v}_2 \int d\underline{v}_1\, f(\underline{v}_2)\,(v_2^2/2v_{th}^2)\, 2\pi\rho\,|v_{2\parallel}|\, f(\underline{v}_1)(\Delta r_{\perp})^2 \qquad (3)$$

denotes the perpendicular electron heat conductivity. In eq. (3) the label 1 is used for the target particle, $v_{th} = \sqrt{T/m}$ denotes the thermal speed of electrons, f denotes the (Maxwellian) electron distribution function and $\Delta r_{\perp}$ denotes the (orthogonal to $\underline{B}$) displacement of the particle 2 due to its drift collision with particle 1.

Equation (2) determines $\Delta r_\perp$. An approximate expression for it, for $\rho \lesssim \lambda_D$, can be obtained by multiplying the "interaction time" $2\rho/|v_{2\parallel} - v_{1\parallel}|$ by the typical drift velocity $ce/B\rho^2$ to yield

$$\Delta r_\perp \approx 2ce \,/\, B\rho\,|v_{2\parallel} - v_{1\parallel}| \quad . \tag{4}$$

The evaluation given by eq. (4) is valid if $|v_{2\parallel} - v_{1\parallel}| \gtrsim 2e/\sqrt{m\rho}$ and $\Delta r_\perp < \rho$. The first condition is taken into account in the integration in $v_{1\parallel}$ excluding the interval in which eq. (4) does not hold. The second condition is, in practical cases, much weaker than the condition $\rho > r_{Le}$, which has to be taken into account to justify the use of the drift approximation for the electrons in the bulk. From eqs. (3-4) it is seen that the main contribution to $\chi_\perp^D$ comes from drift collisions between electrons whose parallel velocities are such that during the collision they hardly pass each other in the parallel direction. Integrating over the velocities then leads to an integrand which depends on ρ as $1/\sqrt{\rho}$, showing that the main contribution comes from electrons having the largest scattering parameter. This raises the problem of the convergence of the integral, due to the long range of the Coulomb interaction. Note that the divergence is here stronger than the logarithmic divergence of the classical case of Coulomb collisions in the absence of a magnetic field, hence the dependence of the result on the upper limit of integration is here stronger then in the classical case. Cutting the integral on ρ at $\rho \approx \lambda_D$, we eventually get

$$\chi_\perp^D(\mathrm{cm}^2/\mathrm{s}) \approx 30\ \{N(10^{13}\ \mathrm{cm}^{-3})\}^{3/4}\ \{T(100\ \mathrm{eV})\}^{1/4}\ \{B(5\ \mathrm{tesla})\}^{-2}\ , \tag{5}$$

which should be compared with the classical value $\chi_\perp^C \approx 0.4\ NT^{-1/2}B^{-2}$ (where the same units have been used).

The parallel (to $\underline{B}$) conductivity of electron perpendicular energy due to electron-electron drift collisions is now evaluated as

$$\chi_\parallel^{D\perp} \approx \frac{1}{N} \int_{-\infty}^{+\infty} d\underline{v}_2\ f(\underline{v}_2)\ (v_{2\perp}^2/2v_{th}^2)\ |v_{2\parallel}|\,\lambda_{mfp}\ , \tag{6}$$

where $\lambda_{mfp} \approx |v_{2\parallel}|/\nu_\parallel^D$, $\nu_\parallel^D$ denoting the collision frequency relative to the parallel motion of electrons undergoing drift collisions, namely the inverse of the time a particle with parallel velocity $v_{2\parallel}$ needs to be stopped (in the $\parallel$-direction) by diffusion in the $\parallel$-velocity space.

Recalling that the characteristic step in the parallel velocity space is just $|v_{2\parallel} - v_{1\parallel}|$ if $|v_{2\parallel} - v_{1\parallel}| < \Delta v_o$ and zero otherwise, using the label 1 for the target particle we have

$$\nu_\parallel^D \approx |v_{2\parallel}| \int d\rho\ 2\pi\rho \int_{v_{2\parallel}-\Delta v_o}^{v_{2\parallel}+\Delta v_o} dv_{1\parallel} \int d\underline{v}_{1\perp}\ f(\underline{v}_1)\ (v_{2\parallel}-v_{1\parallel})^2/v_{2\parallel}^2\ . \tag{7}$$

Integrating over the velocities again leads to an integrand which depends on ρ as $1/\sqrt{\rho}$, showing that the main contribution comes from electrons having the largest scattering parameter. Again cutting the integral at $\rho \approx \lambda_D$, we eventually get

$$\nu_{\parallel}^{D}(v_{2\parallel}) \approx 27\ Ne^3\ \sqrt{\lambda_D}\ \exp(-v_{2\parallel}^2/2v_{th}^2)\ /\ v_{th} m^{3/2} |v_{2\parallel}| \ . \qquad (8)$$

The exponential dependence of $\nu_{\parallel}^{D}$ on $v_{2\parallel}$ is a consequence of the fact that an electron collides only with the electrons which are almost at rest with respect to it. Then, the integrand in Eq. (6) diverges for $v_{2\parallel} \to \infty$. Cutting the integral where the usual Coulomb collisions start to compete with the drift collisions (typically at $v_{2\parallel}/v_{th} \approx 4$), the parallel conductivity turns out to be

$$\chi_{\parallel}^{D\perp}(cm^2/s) \approx 10^{10}\ \{T(100\ eV)\}^{7/4}\ \{N(10^{13}\ cm^{-3})\}^{-3/4} \ , \qquad (9)$$

which should be compared with the classical value $\chi_{\parallel}^{C} \approx 1.4\ 10^{12}\ T^{5/2}/N$ (where the same units have been used).

It should be noted that these results, eqs. (5) and (9), are only qualitative. In fact, their reliability suffers from the many approximations made to obtain them. First of all, the fact that the main contribution comes from particles having large values of the scattering parameter necessitated the somewhat arbitrary assumption that λ_D is the maximum allowed scattering parameter, in order to obtain a finite result. The second important approximation directly affecting the numerical value in eq. (9) comes from the evaluation of the parallel velocities above which the diffusion in the parallel-velocity space due to the usual Coulomb collisions is stronger than that due to drift collisions. Finally, as far as the relevance of these results to actual situations is concerned, we have to note that in most of the present tokamaks the basic condition of applicability of the description presented here, $\lambda_D \gg r_{Le}$, is only fullfiled near the wall, while in the center it is often only marginally fullfiled, if at all.

Finally, we briefly discuss the influence of the magnetic field on electron-ion collisions. As has been seen, the main contribution of drift collision comes from the interaction of particles having very small relative parallel velocity. In typical cases, this velocity is much smaller not only than the electron thermal speed, but also than the ion thermal speed. Hence, electron-ion collisions are of the drift type (for the electrons) only for the very few electrons having parallel speed of the order of, or less than, the ion thermal speed, colliding with the few ions having perpendicular velocities much smaller than the ion thermal speed. Hence, we expect that, in typical cases, their inclusion should not modify the classical theory based on Coulomb collisions.

A useful discussion with F. Engelmann is gratefully acknowledged.

REFERENCES:

/1/ S.I. Braginskii, in Reviews of Plasma Physics (M.A. Leontovich Ed.) Consultants Bureau, New York, 1, 205 (1965).
/2/ C.T. Dum and D. Pfirsch, Proc. V Europ. Conf. on Controlled Fusion and Plasma Physics, Grenoble, 13 (1972).
/3/ A. Nocentini, NET-PM-86-001

CENTRAL MASS AND CURRENT DENSITY MEASUREMENTS IN TOKOMAKS USING THE DISCRETE ALFVEN WAVE SPECTRUM

G.A. Collins, J.B. Lister and Ph. Marmillod

Centre de Recherches en Physique des Plasmas
Association Euratom - Confédération Suisse
Ecole Polytechnique Fédérale de Lausanne
21, Av. des Bains, CH-1007 Lausanne / Switzerland

We report on the use of global modes of the Alfvén wave to obtain information on the central mass and current density in two tokamaks - TCA and PETULA.

Introduction

For many years the global eigenmodes of both the Alfvén wave and the fast compressional wave have been used as a diagnostic of low temperature plasmas. However their exploitation for the diagnosis of tokamak plasmas has been minimal. Global modes of the fast wave have frequencies that reflect global parameters, such as the average mass density, and, as their popular name "cavity mode" implies, their frequencies are sensitive to the boundary conditions. Even less attention has been given to global modes of the Alfvén wave since it was firmly believed that they only could be excited close to the ion cyclotron frequency ω_{ci}, hence the name Ion Cyclotron Wave. This belief was overturned by the early AWH experiments on TCA which revealed well defined peaks in the antenna loading spectrum at frequencies just below the thresholds of shear Alfvén wave continua, even at values of $\omega/\omega_{ci}<0.1$[1]. A more careful examination of mhd theory indicated that such global modes, labelled as the Discrete Alfvén Wave (DAW), existed at this low frequency due to the presence of the plasma current. This fact and its close association with the continuum threshold, which is usually defined by parameters at the centre of the tokomak discharge, makes the DAW interesting as a tokamak diagnostic [2,3], particularly to have access to information from the core of the discharge, such as the central current density, which is often difficult to obtain. In this paper we give a very brief theoretical background to the information available from the DAW spectrum and describe the experimental installation on two tokamaks - TCA ($a=0.18m$, $R=0.61m$, $B_\phi=1.5T$) and PETULA ($a=0.17m$, $R=0.71m$, $B_\phi=2.8T$). We present measurements of the effective mass $A_{eff}(0)$ made during impurity puffing experiments on TCA and estimates of $q(0)$ over a variety of discharges. From PETULA we present preliminary measurements intended to elucidate behaviour of the central current density during LHCD.

Theoretical Background

The shear Alfvén wave continium can be defined for a tokomak plasma in the large aspect ratio approximation as

$$\omega_A(r) = [1/v_A^2(r)\, k_\parallel^2(r) + 1/\omega_{ci}^2]^{-1/2} \qquad (1)$$

where $v_A(r)=B_\phi/[\mu_o\rho(r)]^{1/2}$, $k_\parallel(r)=[n+m/q(r)]/R$ and n, m are the toroidal and poloidal wavenumbers. The continuum threshold ω_{min} is defined by the minimum value of eq.(1) which is usually associated with a radius close to the magnetic axis. We are interested in the first radial eigenmode of the DAW spectrum which occurs at a frequency $\omega_1<\omega_{min}$. Naively we can assume that $\omega_1\sim\omega_{min}\sim\omega_A(0)$ and see from eq.(1) the

dependence of ω_1 on both $\rho(0)$ and $q(0)$. In reality the separation $\Delta\omega=\omega_1-\omega_{min}$ also depends on $q(0)$ as well as the ratio ω/ω_{ci} and the actual profiles of $\rho(0)$ and $q(0)$ near the axis. While some analytic approximations exist to predict $\Delta\omega$ for restrictive conditions we prefer to calculate ω_1 directly. We remain in cylindrical geometry and restrict ourselves to mhd theory with inclusion of ion cyclotron effects. This theory has proved adequate in predicting DAW frequencies even for those modes that are excited indirectly by toroidal coupling [4].

Experimental Description

Previous studies of the DAW spectrum on TCA have used the AWH antenna structure and the high power generator with its restricted frequency range [5]. For diagnostic purposes we use an antenna consisting of two parallel bars, separated by ~10cm, which encircle a poloidal quadrant either at the bottom of the plasma (TCA) or on the outside (PETULA). A 200 W amplifier provides 1-5A of antenna current via a wideband matching circuit, while detection is made 180° toroidally from the antenna with a magnetic field probe close to the vessel wall and protected by a ceramic tube. A heterodyne detection system allows adequate signal-to-noise with less than 10W coupled to the plasma. A typical scan of 2-10MHz in PETULA is shown in Fig.1. The peaks of the DAW spectrum can be identified by both the amplitude and phase relative to the antenna current. The toroidal field component b_φ is used since it is least sensitive to the localised waves that the antenna can excite in the scrape-off. Varying the electron density between discharges and scanning the frequency during 30-70ms allows us to plot the DAW frequencies as a function of line-averaged density, shown in Fig.2 for deuterium discharges in TCA (I_p=125kA) and PETULA (I_p=147kA). Also shown are the theoretical frequencies for constant model density and current profiles. In most cases we have found the dominant peaks to have wavenumbers m=-1 and n<0 since we restrict ourselves to $\omega/\omega_{ci}<0.5$.

Of more interest is the variation in the DAW frequencies. In Fig.3 we illustrate the sensitivity of the technique to variation in central plasma parameters during sawteeth activity in TCA. In this case the frequency was swept slowly over an extremely narrow frequency range to emphasize the change of DAW frequency as revealed by the detected phase. To follow a peak we can either sweep the frequency rapidly (in typically 5ms) over a narrow band around the nominal value, or use the phase information from the detector to track the peak, with a bandwidth up to 10kHz. In Fig.4 we show preliminary results for several peaks measured during LHCD at 3.7GHz in PETULA.

Effective mass during impurity puffing

Injecting a low Z impurity into a hydrogen plasma changes the effective mass $A_{eff}=\sum n_i A_i$ from a value close to 1.0 up to a maximum near 2.0 for fully stripped impurities. This lowers the DAW frequency ω_1 by decreasing the Alfvén velocity v_A and introducing lower ion cyclotron frequencies ω_{ci}. Calculating the dependence of ω_1 on impurity concentration produces the empirical scaling law illustrated in Fig.5. For the magnitude of frequency variations in this case, small variations in the profiles $\rho(r)/\rho(0)$ and $q(r)$ have minimal effect. The use of several peaks increases the accuracy of the measurement. In Fig.6 we show the derived value of $A_{eff}(0)$ for discharges in TCA where the electron density was increased by a factor >3 by the injection of nitrogen. For comparison we also show the value of $A_{eff}(0)$ as a function of density in "pure" hydro-

gen discharges and a predicted curve for $A_{eff}(0)$ if all the increase in electron density is due to nitrogen. Clearly the injection of nitrogen also causes an increase in hydrogen density. Such behaviour is confirmed by measurements of the radiated power profiles. We note for the future that since tritium has an anomalous A/Z=3 this technique offers an accurate way of measuring the D-T mixture as a fusion discharge evolves.

Central current density in Ohmic discharges

We present in Fig.7 the variation in DAW frequency as a function of plasma current in deuterium discharges in TCA (A_{eff}=2.0). As both q(0) and the profile q(r) can be modified by a change in I_p we have calculated the expected dependence for a crude variety of model profiles. FIR interferometer measurements indicate a peaking of $n_e(r)$ as I_p is reduced so this has been included in the calculations. An estimate of q(0) can be made with an uncertainty expressed as being related to q(0.5). Once again the use of several peaks increases the accuracy. In particular low-n DAW's are generally more sensitive to changes in the current profile than those of higher toroidal wavenumber. In Fig.8 we see the variation in DAW frequency at a constant value of I_p but with different values of $\dot{I}_p$. Peaking of the current profile at negative values of $\dot{I}_p$ is reflected in an increase in frequency.

Acknowledgments. We thank the PETULA group for their encouragement to develop this technique and the opportunity to use it on their tokamak. We acknowledge the support of Prof. Troyon and the TCA team, as well as the funding of the Fonds National Suisse.

References

[1] A. de Chambrier et al., Plasma Phys. 24 (1982) 893.
[2] B. Joye et al., "Discrete Alfvén Wave excitation as a tokamak plasma diagnostic", LRP 196/81, Lausanne (1981).
[3] A. de Chambrier et al., Phys. Lett. 92A (1982) 279.
[4] K. Appert et al., Phys. Rev. Lett. 54 (1985) 1671.
[5] G.A. Collins et al., to appear in Phys. Fluids.

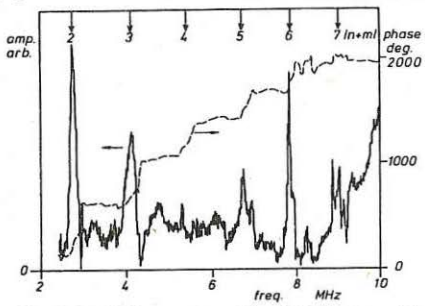

Fig.1 PETULA spectrum(I_p=147kA,$\bar{n}_{e13}$=3)

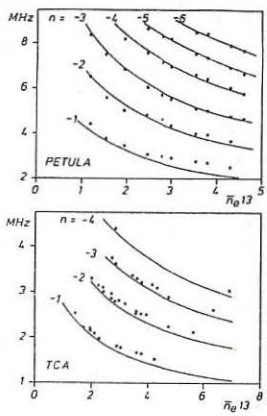

Fig.2 Density scans - measurements and theory(m=-1)

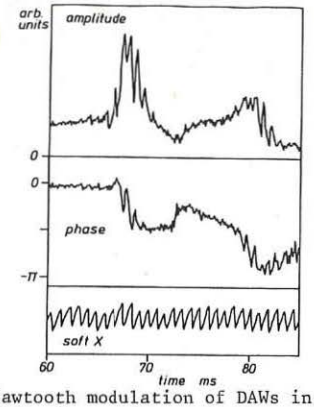

Fig.3 Sawtooth modulation of DAWs in TCA (10kHz/ms, $|n+m|=5$, $I_p=120$kA, $\bar{n}_{e13}=3$)

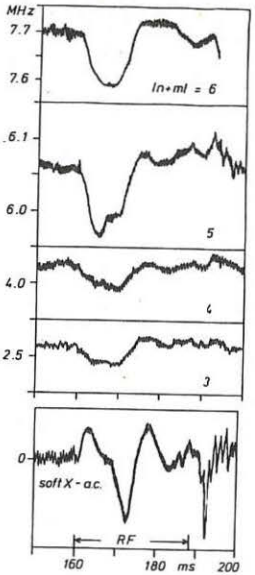

Fig.4 Frequency tracking during LHCD in PETULA

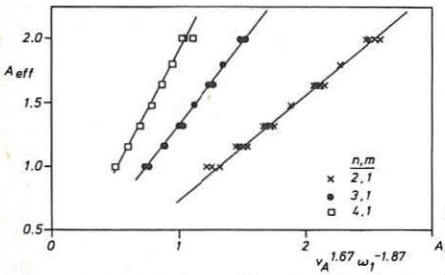

Fig.5 Theoretical scaling law for A_{eff}

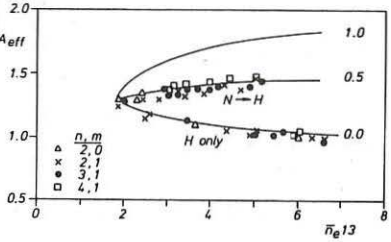

Fig.6 A_{eff} during nitrogen injection Curves calc. for diff. imp. fractions

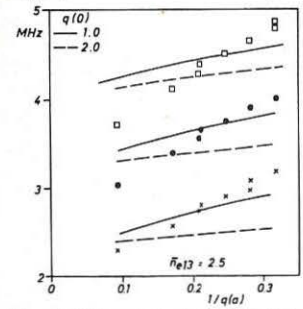

Fig.7 TCA current scan with curves from model profiles

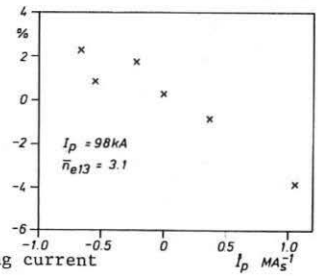

Fig.8 Change in (-2,-1) freq. with ramping current

MEASUREMENT OF PLASMA EMISSION PROFILES IN THE RANGE FROM 800 - 1000 nm FOR Z_{EFF}-ANALYSIS IN ASDEX

H. Röhr, K.-H. Steuer, D. Meisel, H. Murmann, G. Becker, H. S. Bosch, H. Brocken, A. Eberhagen, G. Fussmann, O. Gehre, J. Gernhardt, G.v.Gierke, E. Glock, O. Gruber, G. Haas, J. Hofmann, A. Izvozchikov[1], G. Janeschitz, F. Karger, M. Keilhacker[2], O. Klüber, M. Kornherr, K. Lackner, M. Lenoci, G. Lisitano, F. Mast, H. M. Mayer, K. McCormick, V. Mertens, E. R. Müller[2], H. Niedermeyer, A. Pietrzyk[3], W. Poschenrieder, H. Rapp, J. Roth, F. Ryter[4], F. Schneider, C. Setzensack, G. Siller, P. Smeulders[2], F.X. Söldner, F. Wagner, D. Zasche

Max-Planck-Institut für Plasmaphysik
EURATOM Association, D-8046 Garching

We report the attempt to use the 16-point ND-YAG Thomson scattering device on ASDEX (Fig. 1) for measurements of plasma radiation profiles as well. The system offers the possibility to measure three spectral ranges simultaneously: 780 - 880 nm, 900 - 970 nm and 985 - 1020 nm.

The plasma light can be analysed in two different ways:

As the Thomson scattering system is only transparent to high-frequency signals because of the AC coupling of the avalanche diodes, direct measurement of the plasma light calls for a fast chopping technique. This is achieved by a special chopper wheel (Fig. 2) in front of the large observation lens which interrupts the plasma radiation fast enough (chopper frequency 3 kHz).

On the other hand, without the installation of the wheel, it is possible to determine the plasma radiation by analysing the radiation shot noise signal (Fig. 3) which is necessarily detected during each Thomson measurement.

Both of the two possibilities have been applied. The first has the advantage of delivering the time evaluation of radiation profiles. The installation of the chopper wheel in the present form, however, doesn't allow simultaneous measurements of the Thomson scattering, and the lack of n_e, T_e profiles prevents direct comparison of the measured radiation with bremsstrahlung in the same discharge.

The second method yields averaged results during selectable time intervals of the order of a few 100 msec or more. The calibration of the noise signals is done by illuminating the avalanche diodes by LED's with different intensities. Owing to the simultaneously measured Thomson scattering profiles this method allows comparison with actual bremsstrahlungs profiles.

---

[1]Academy of Sciences, Leningrad, USSR; [2]Present address: JET Joint Undertaking, England; [3]Univ. of Washington, Seattle, USA; [4]CEN Grenoble, France

The two methods show rough agreement of the brightness profiles, which are nearly the same in the 3 spectral channels. In both cases the signals show relatively large statistical errors. The reason is the relatively weak plasma radiation in the infrared and the poor transmission of the electronics even at a chopper frequency of 3 kHz, on the one hand, and the small amplitude of the noise signals, on the other hand.

The absolute calibration of the measured plasma radiation can be done by comparing the signals with Thomson scattered signals in combination with the corresponding electron density and temperature. As the same observation system is used for Thomson scattering and plasma light measurements, only laser power in the observation volume and the length of the scattering volume must be known additionally.

Another method of Z_{eff} calibration is comparison with values gained by using the measured electron temperature profiles in conjunction with classical resistivity for well-defined ohmic plasmas.

As an example, we show the brightness and Z_{eff} profiles before and after pellet injection in ASDEX. Figure 4 shows the time behaviour of the central electron density measured simultaneously by Thomson scattering. About 12 pellets are injected into the discharge between 1.4 and 1.8 sec. After pellet injection the density keeps the high value for about 0.3 sec without any gas puffing. Figure 5a shows the Abel-inverted radiation profile averaged over the 3 spectral channels in the ohmic phase (averaged from 0.5 - 1.3 sec), and Fig. 5b the profile in the high-density phase from 1.7 - 2.0 sec. The radiation increases by a factor of more than 20 and scales as $n^2/\sqrt{T}$ (bremsstrahlung). The scaling already indicates that there is no essential change of Z_{eff} due to pellet injection. The corresponding Z_{eff} profiles are shown in Fig. 6a,b.

The results show that combined measurement of Thomson scattering and plasma radiation profiles is possible and reasonable. In a new system, e.g. for ASDEX Upgrade, we include this method by adding a second exit with dc-coupling for measuring plasma radiation directly without the complications of high-frequency coupling.

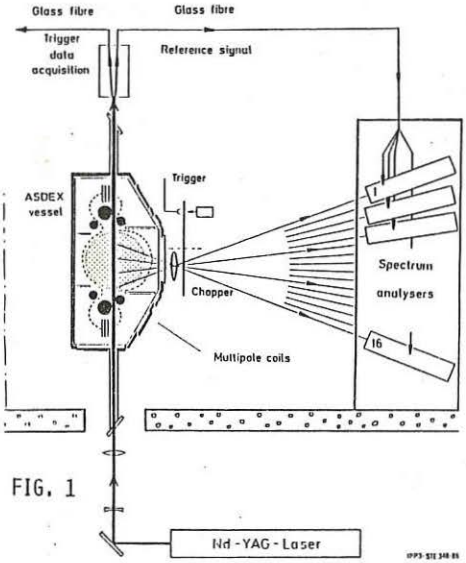

FIG. 1

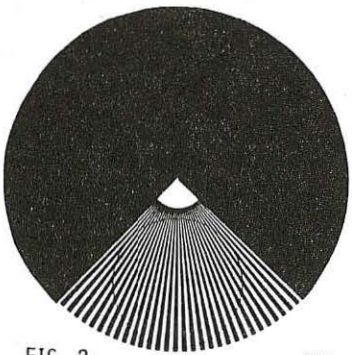

FIG. 2

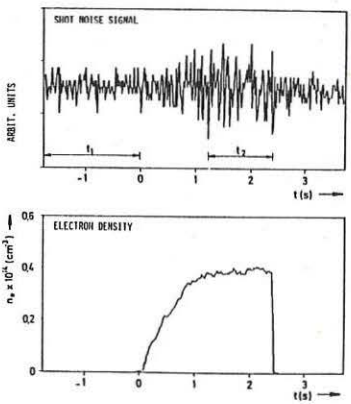

FIG. 3

PELLET INJECTION

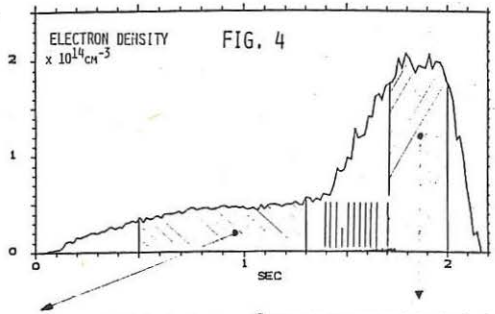

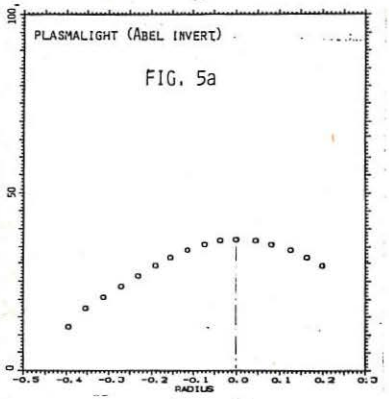

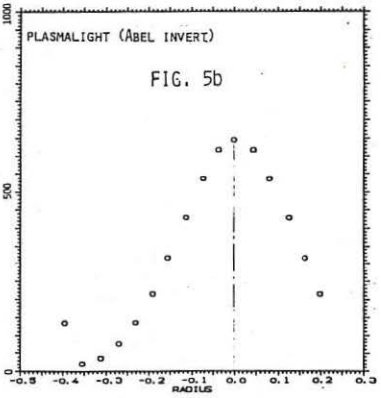

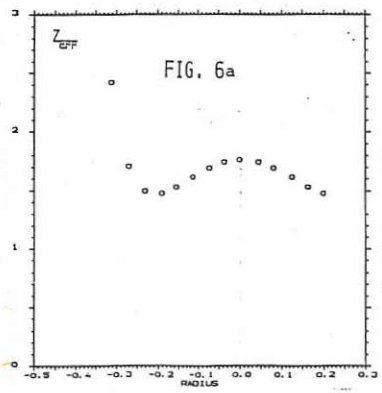

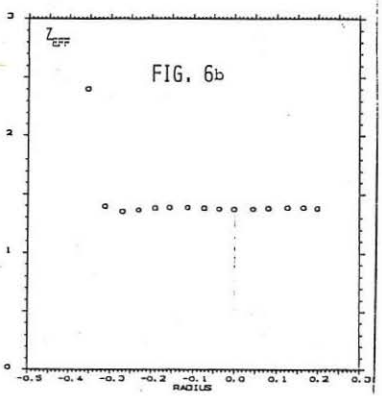

PERIODIC THOMSON SCATTERING DIAGNOSTIC WITH 16 SPATIAL CHANNELS ON ASDEX

D. Meisel, H. Murmann, H. Röhr, K.-H. Steuer, G. Becker, H.S. Bosch, H. Brocken, A. Eberhagen, G. Fussmann, O. Gehre, J. Gernhardt, G. v. Gierke, E. Glock, O. Gruber, G. Haas, J. Hofmann, A. Izvozchikov[1], G. Janeschitz, F. Karger, M. Keilhacker[2], O. Klüber, M. Kornherr, K. Lackner, M. Lenoci, G. Lisitano, F. Mast, H. M. Mayer, K. McCormick, V. Mertens, E. R. Müller[2], H. Niedermeyer, A. Pietrzyk[3], W. Poschenrieder, H.Rapp, J. Roth, F. Ryter[4], F. Schneider, C. Setzensack, G. Siller, P. Smeulders[2], F. X. Söldner, F. Wagner, D. Zasche

Max-Planck-Institut für Plasmaphysik
EURATOM Association, D-8046 Garching

The Nd-YAG Periodic Scattering System (PSS) was developped in teamwork with IPF of Stuttgart-University. At first a PSS with only one spatial channel was successfully tested in the ASDEX-Tokamak in 1982 /1/. Subsequently an upgraded system with 16 spatial channels was constructed. This new system is capable of measuring Te, Ne-profiles at 17 ms intervals during the entire ASDEX-Tokamak-discharge.
The PSS has been working successfully for the last one and a half years as a standard diagnostic method in the ASDEX-Tokamak. This means, that the measurement is being automatically performed during all plasma-discharges. The Te- and Ne-values are stored in the ASDEX-computer and every user has the possibility to get the Te(r,t), Ne(r,t)-data for his own needs.

The main purpose of the PSS at present time in the ASDEX is the determination of density- and temperature-profiles especailly in additional heating (Fig.3, 4,5) or pellet injection-experiments (Fig.6). With respect to the Single-Pulse-Ruby-Laser-Systems, the PSS has several advantages, the most important ones for Tokamak-physics are given below:

1. No series of reproducable discharges are necessary to evaluate the behavior of Te(r,t) and Ne(r,t).
2. The combination of Nd-YAG-Laser with detectors of high quantum-efficiency together with an optics of high luminosity, leads to a scattering device, where the photon-noise of the signals is sufficiently small at normal Tokamak-densities. The additional plasma-light-noise is also smaller than in Ruby-scattering devices, because plasma light is decreasing from the visible to the IR-region.
3. The large number of scattering and background signals can be used to make a calculation of the error-bars of the measurements. The PSS can reach an accuracy of about 5 % in Te- and 3 % in Ne-measurements in the normal Tokamak-regime.
4. The detectors (Si-Avalanche-Diodes) give an extremely linear response. Thus the PSS can work in a wide range without saturation effects, e.g. at high densities or high levels of plasma light. Magnetic fields do not influence the sensitivity of the diodes.

In some special discharges, the QSS is the only diagnostic method available for the reliable evaluation of Te, Ne-profiles, e.g. in the slide-away-region (Fig. 5) or during rapid density variations.

---

[1]Academy of Sciences, Leningrad, USSR; [2]Present address: JET Joint Undertaking, England; [3]Univ. of Washington, Seattle, USA; [4]CEN Grenoble, France

MAIN FEATURES OF THE PERIODIC THOMSON SCATTERING SYSTEM (PSS) ON ASDEX

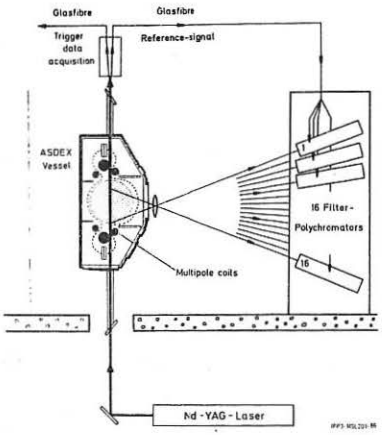

Fig. 1: Schematic of the optical set-up of the QSS.

The PSS simultaneously measures Te,Ne at 16 spatial points distributed over 3/4 of the diameter of the plasma-column (from z = -40 cm at the lower plasma-edge to z = 20 cm). The scattered light of every spatial point is spectrally divided into three parts by a separate polychromator (see Fig. 2). A small fraction of the transmitted laser-light is divided into 48 reference signals in order to calibrate the sensitivity of the detectors during the discharges. The main technical features of the PSS are:

Laser:
Nd-YAG at λ = 1.06 µm; 400 pulses with 0.8 Joule energy and 40 ns duration each. Repetition frequency 60 Hz.

Detectors:
Si-Avalanche-diodes; quantum efficiency up to 0.9; size 1.7 mm^2; NEP 1.6×10^{-13} $W/\sqrt{Hz}$.

Range of Te- and Ne-measurements of the ASDEX-PSS:
The PSS is capable of measuring kTe in the range of 150 eV (at the plasma-edge) up to 5 keV (in the plasma-centre) using two matched types of filter polychromators. The lower density-limit is a few x 10^{12} cm^{-3}. This limit can be further improved by averaging signals with respect to time.

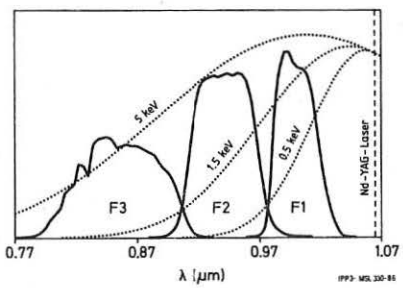

Fig. 2: Spectral sensitivity of the filter-polychromator for the central plasma region. The ratio of the signals F2/F1 is the basis for the calculation of kTe up to 1.5 keV; at higher Te, the ratio F3/(F1 + F2) is used. The system is density-calibrated by Anti-Stokes Raman-scattering in hydrogen /2/.

EVALUATION OF TE(r,t) AND NE(r,t) BY PSS DURING ADDITIONAL HEATING IN ASDEX

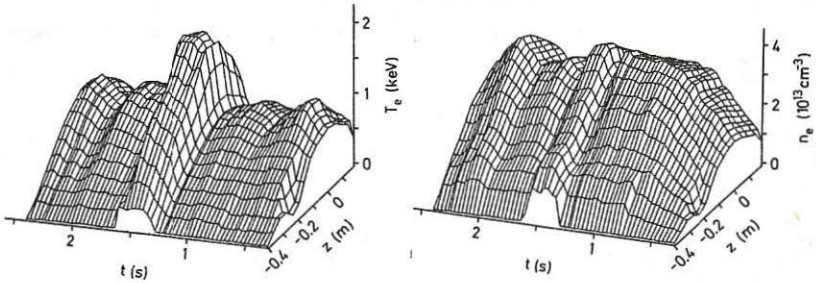

Fig. 3: Three-dimensional plots of Te and Ne of an ASDEX-discharge with Neutral Injection (P_{NI} = 3 MW). The behavior of Ne during Neutral-Injection indicates, that the discharge has changed from L- to H-regime.

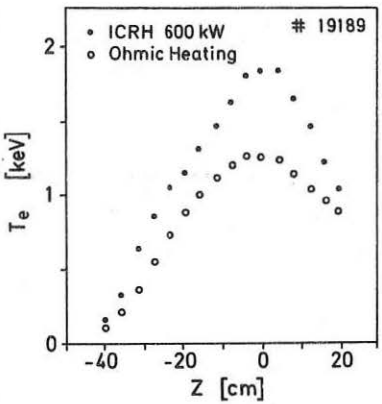

Fig. 4: Comparison of Te-profiles in an ASDEX-discharge during ohmic heating and during ICRH-minority heating (deuterium in hydrogen) with 600 kW RF-power.

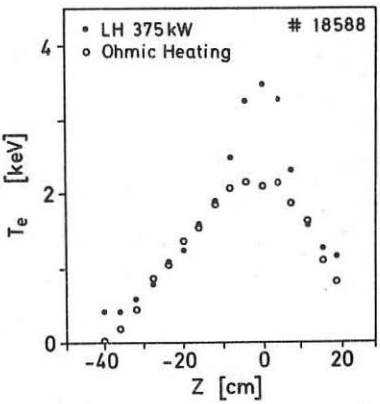

Fig. 5: Te-profile during LH-heating in ASDEX (open circles: ohmic profile before RF is switched on).

EVALUATION OF PLASMA-PARAMETERS DURING PELLET-INJECTION

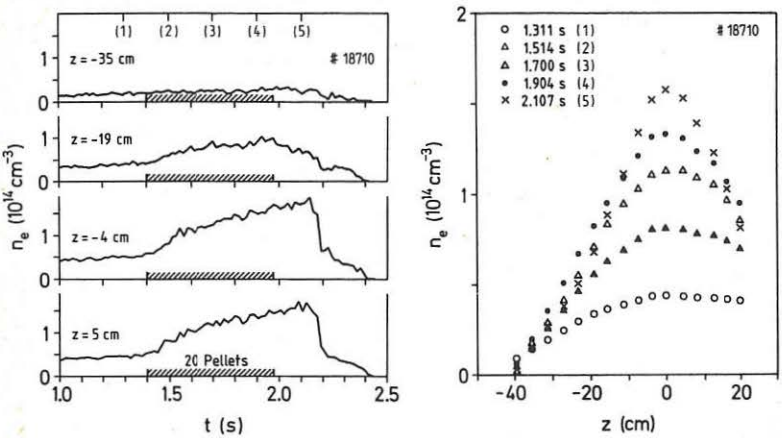

Fig. 6: Density increase of up to 1.5 x 10^{14} cm^{-3} by an injection of a series of pellets using a centrifuge. Time-evolution of Ne at different radii (Fig. 6a) as well as the corresponding Ne-profiles show, that the density raise occurs mainly in the plasma-centre, even when the pellet-injection has been discontinued.

The PSS-results are the basis for further calculations of plasma-parameters, e.g. heat-conductivity of electrons, diffusion-coefficients and so on. Profile measurements, which we have shown in a few examples, are necessary for any plasma-simulation by computer-codes or determination of the energy-balance of a Tokamak plasma. The PSS can deliver at present technical state the wanted parameters in a wide range of discharge-conditions.

References:

/1/ H. Röhr, K.-H. Steuer, G. Schramm, K. Hirsch, H. Salzmann, Nucl. Fus., Vol. 22, No. 8 (1982) 1099-1102.
/2/ H. Röhr, Phys. Letts., Vol. 81 A, No. 8 (1981) 451-53.

COMPARISON OF ICRH AND LH ACCELERATED HYDROGEN IONS IN NI HEATED ASDEX PLASMAS

F. Ryter[1], H. Brocken, A. Izvozchikov[2], F. Leuterer, H. Maaßberg, H.M.Mayer, F. X. Söldner, K. Steinmetz, G. Becker, H. S. Bosch, A. Eberhagen, D. Eckhartt, G. Fussmann, O. Gehre, J. Gernhardt, G.v.Gierke, E. Glock, O. Gruber, G. Haas, J. Hofmann, G. Janeschitz, F. Karger, M. Keilhacker[3], O. Klüber, M. Kornherr, K. Lackner, M. Lenoci, G. Lisitano, F. Mast, K. McCormick, D. Meisel, V. Mertens, E.R. Müller[3], H.Murmann, H.Niedermeyer, J.-M. Noterdaeme, A. Pietrzyk[4], W. Poschenrieder, H. Rapp, H. Riedler, H. Röhr, J. Roth, F. Schneider, C. Setzensack, G. Siller, P. Smeulders[3], E. Speth, K.-H. Steuer, O. Vollmer, F. Wagner, F. Wesner, D. Zasche

Max-Planck-Institut für Plasmaphysik
EURATOM Association, D-8046 Garching

Introduction

In ASDEX, ICRH /1/ and LHH or LHCD /2/ have been applied separately to NI preheated plasmas in the L regime ($H^0 \rightarrow D^+$, energy E_B). The coupling of these waves to beam ions (H^+) have been studied with charge exchange diagnostics. Possible synergetic effects are discussed in /3/. Shots were made with E_B = 29 keV and E_B = 42 keV and in the latter case P_{NI} or P_{RF} were scanned.

1. Experimental set-up

Measurements were carried out with two neutral particle analysers. One "tangential" analyser (E = 0.1 - 55 keV) viewing opposite to the NI beam direction with the same tangency radius R_T at which the beam is injected (R_T = 145 cm R_0 = 165 cm) and with one "perpendicular" analyser (E = 0.5 - 200 keV) which can be scanned vertically. Perpendicular measurements detect only particles with $V_{\parallel}/V \simeq 0$. Near the edge, however, banana ions are seen at the orbit tips. The energy upshift can be better studied in the case E_B = 29 keV because of the upper energy limit of the tangential analyser. For the 29 keV shots a diagnostic beam of hydrogen atoms was injected vertically in the poloidal plane of the perpendiular analyser and crossed the line of sight of the tangential one in the plasma centre.

2. Results

a) ICRH

The following features are observed with the tangential analyser when ICRH is applied: flux increase for $E > E_B$, flux decrease for $E < E_B$ (Fig.1). Fast atoms are detected in the highest energy channel (47 keV for E_B = 29 keV, 55 keV for E_B = 42 keV, Fig. 2). This signal has a rise time and a decay time of 30 ms. The diagnostic beam has no effect on this signal. In the perpendicular direction the active fluxes show a tail of fast ions up to 60 keV (Fig.3) and passive flux decay time is 30 ms at 40 keV. Passive fluxes at the plasma edge (r=a=40 cm) with E_B = 42 keV increase with P_{RF}/P_{NI} (Fig.4).

b) LH

In the tangential direction, fluxes increase for $E > E_B$, fluxes remain constant or increase (10 - 20 %) for $E < E_B$ (Fig. 1). Fast ions in the 47 keV channel, (55 keV for E_B = 42 keV) are detected (Fig. 2). This flux is twice as large for $\langle N_{\parallel} \rangle = 4$ than for $\langle N_{\parallel} \rangle = 2$. The decay seems to consist of a fast part (few ms) and a longer one (100 ms). For the E_B = 42 keV case, only the fast decay is clearly visible. As for ICRH the active flux is not

---

[1]CEN Grenoble, France; [2]Academy of Sciences, Leningrad, USSR; [3]Present address: JET Joint Undertaking, England; [4]Univ. of Washington, Seattle, USA

visible for $E > E_B$. In the perpendicular direction fluxes increase and ions are found till 60 keV. The 40 keV fluxes are twice as large for $\langle N_{\perp} \rangle = 4$ than for $\langle N_{\perp} \rangle = 2$ in the centre and equal at $r/a = 0.6$.

3. Discussion

Under our geometrical conditions ($R_T(NI) = R_T$ (Analyser) $= R_T$) and with NI alone, the tangential analyser receives only passing co-particles originating from the maximum of the ion distribution for each magnetic surface (Fig. 5). This is due to the relation, valid both for injection and detection: $R_T/R = v_{\perp}/v$ (R is the radius where the C.X. collision happens, $V_{\perp}$ the parallel velocity and v the total velocity). Then, for each position R, the ion distribution is peaked at the injection angle defined by $v_{\perp}/v = R_T/R$ which is the condition which must be fulfilled to receive neutrals from the position R. If the waves add perpendicular energy to some of the ions, a part of the distribution function is shifted to higher perpendicular velocities and the parallel analyser does not receive any more fluxes from the maximum for each magnetic surface. If no compensations occur from other regions, the signal for $E < E_B$ should drop. On the other hand, ions with $E > E_B$ must be found. They can be detected after acceleration and collisions which place them onto the detection line of the analyser, both geometrically and in velocity space. Estimation of the main collision times is given for the ICRH and LH cases for 30 keV ions ($n_e = 5 \cdot 10^{13}$ cm^{-3}, $T_e = 1.5$ keV and $n_e = 1.5 \cdot 10^{13}$ cm^{-3}, $T_e = 1.5$ keV correspondingly):

	slowing down on e^-	90^o scattering	charge exchange $n_o = 10^7$–10^8 cm^{-3})
ICRH	25 ms	50 ms	1s to 100 ms
LH	60 ms	115 ms	1s to 100 ms

These characteristic times as well as the confinement define the decay time of the signal after the RF turn off.
For the perpendicular analyser a general flux increase is expected. The experimental results show that both ICRH and LH waves add perpendicular energy to ions which are clearly accelerated to high energies and nevertheless remain confined as discussed in the following.

a) ICRH
Ions which fulfil the relation $\Omega_{ICRF}(R) - 2\Omega_{CH} = k_{\perp}.v_{\perp}$ can be accelerated in the perpendicular direction. It happens in the resonance layer ($R = R_o \pm 4$cm) if they have $v_{\perp} \simeq 0$. Some of them can be banana ions having their orbit tips in the resonance layer /4,5/. Ions can be accelerated outside of the resonance layer if they have enough $v_{\perp}$ to fulfil the relation given above. These are passing or banana particles with large $v_{\perp}/v$. Taking into account the $k_{\perp}$ spectrum of the wave, we calculate that acceleration is possible till $r \simeq 12$ cm for $E_{\perp} = 29$ keV and till $r \simeq 18$ cm for $E_{\perp} = 42$ keV. Therefore beam ions (passing particles) can be directly accelerated only outside of the resonance layer. Beam ions first scatter to larger $v_{\perp}/v_{\perp}$ before they can be accelerated in the resonance layer. Experimentally it is shown by the absence of active flux ($v_{\perp} = 0.85$ v) in the tangential analyser: ICRH does not affect passing ions in the centre but off-axis acceleration is found. On the other hand, observations made with the perpendicular analyser show that accelerated ions with large $v_{\perp}/v_{\perp}$ are present in the plasma centre.

b) LH
The LH interaction is not well located but particles must have enough perpendicular energy $E_{\perp}$ to fulfil the relation: $N_{\perp} \simeq 700\ (A/E_{\perp})^{1/2}$
($[E_{\perp}]$ = keV, A = atomic number)

The perpendicular index $N_\perp$ of the wave is calculated by ray tracing /6/ and the next tables compare the lowest $N_\perp$ values necessary for the interaction and the highest $N_\perp$ values given by the ray tracing method for different $N_\parallel$ values:

	$\langle N_\parallel \rangle$	2	4	resonance	$E_\perp$ 29 keV	42 keV
code	$N_\perp$	30-75	75-125	condition	$N_\perp$ 130	108

It appears that the $N_\perp$ values given by the code are too small to allow for interaction with beam ions particularly for the $\langle N_\parallel \rangle = 2$ spectrum. This general problem for the LH experiments will not be discussed here. As for ICRH the absence of active fluxes in the tangential direction shows that the interacting and accelerated ions in the centre have too large $E_\perp/E$ to be detected. This is confirmed by the perpendicular measurements which show an active flux increase in the centre due to LH.
Off axis acceleration happens and is enfavoured by the geometrical effect which provides the outer surfaces with beam ions having more $E_\perp$ than in the centre. The contribution of the non-central part to the fluxes could be large due to the high value of the neutral density and explain the flux increase for $E < E_B$. The life time of the ions generated off-axis is shorter due to higher losses (charge exchange, confinement) and could account for the fast part of the decay time. The non central effects are more favourable in the E_B =42keV case which provides the plasma edge with faster ions. Moreover interaction is expected further outside at higher density values. Shots made at 3×10^{13} cm^{-3} show flux increase of a factor 2 in the parallel direction for $E < E_B$ and very fast rise time and decay time. The perpendicular observations show large off-axis fluxes, similar to observed without NI /7/.

Conclusion

It appears from this analysis that for both the ICRH and the LH waves give perpendicular energy to beam ions:
- in the centre, to beam ions which have made 90° pitch-angle scattering
- off-axis, to ions which come almost directly from the beam. This contribution to the fluxes seems to be larger for the LH case.

For ICRH in particular, these two populations are separated both geometrically and in velocity space and cannot mix strongly according to the collision times. The second population might improve somewhat the ICRH heating efficiency for NI preheated plasmas compared to that obtained in ohmic plasmas, nevertheless both for ICRH and LH the contribution of the accelerated ions to ß is small /1,3/.
The clear patterns shown in Fig. 4 as a function of P_{RF}/P_{NI} (RF power per injected particle) indicate probably that the interaction occurs mainly with beam ions. They show the global increase of the perpendicular energy of the ion distribution. For ICRH the contribution of the fast ions to the impurity production is very probable as discussed in /8/.
This work has been made in the frame of a collaboration between IPP-Garching and CEA-DRFC-SIG (Grenoble), and project boards in both laboratories are gratefully acknowledged as well as the assistance of the technical staff.

References

/1/ K. Steinmetz, et al., this conference and EPS Conf., Budapest, 1985.
/2/ F. Söldner, et al., EPS Conf., Budapest, 1985.
/3/ F. Wagner, invited paper at this conference.
/4/ T. Hellsten, et al., EPS Conf., Budapest, 1985.
/5/ G. W. Hammett, et al., Pine Mountain Conf., 1985.
/6/ M. Brambilla, private communication.
/7/ D. Eckhartt, et al, Proc.4thInt.Symp.on Heating in Toroidal Plasmas, Rome 1984.
/8/ G.Janeschitz, et al., this conference.

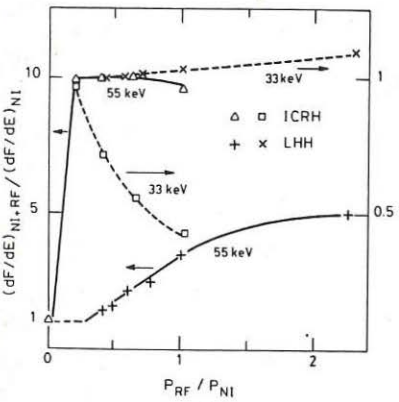

Fig. 1: H^0 normalised fluxes for the tangential analyser versus P_{RF}/P_{NI} (E_B = 42keV).

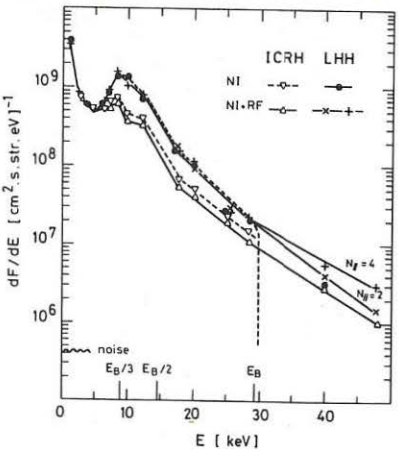

Fig.2: H^0 energy spectra for the tangential analyser (E_B = 29keV).

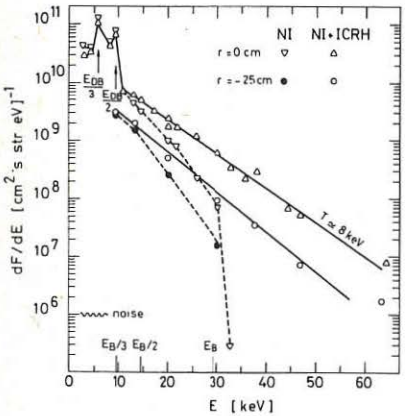

Fig. 3: Local H^0 energy spectra for the perpendicular analyser (E_B = 29keV).

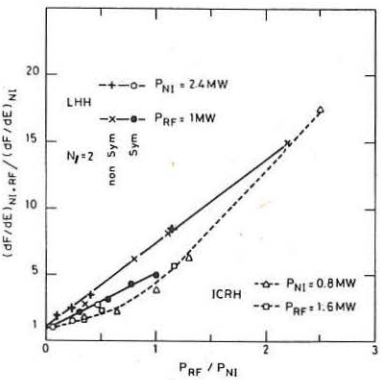

Fig. 4: H^0 17 keV normalized fluxes at r = 40 cm for the perpendicular analyser versus P_{RF}/P_{NI} (E = 17 keV is representative for the tail).

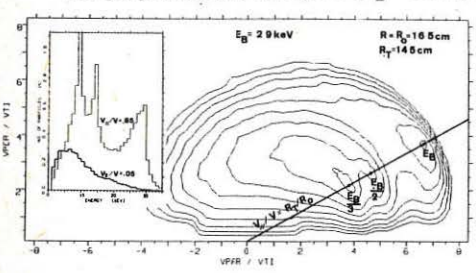

Fig. 5: Calculated ion distribution function with NI alone in the velocity space normalised to the thermal velocity. Energy spectra for two $v_{\parallel}/v$ values are enclosed.

FUSION PRODUCT MEASUREMENTS ON JET

G Sadler, P Van Belle, M Hone, O N Jarvis, J Källne,
G Martin+ and V Merlo

JET Joint Undertaking, Abingdon, Oxon, OX14 3EA, UK
+Association EURATOM-CEA-DRFC/TS. CEN Cadarache. France 13108

Neutrons from the D-D reaction and protons from the ^{3}He-D reaction have been used for diagnostic purposes during the past year of operation.

CODE CALCULATIONS OF FUSION PRODUCT SPECTRA (FSPEC)

It is well known that a measurement of the Doppler broadening of the 2.45 MeV neutrons from D-D reactions in a deuterium plasma affords a determination of the plasma ion temperature T_i. Several authors (refs 1-3) have shown that the Maxwellian ion energy distribution of a plasma in thermodynamic equilibrium leads to a neutron energy spectrum which is approximately Gaussian with a FWHM proportional to $\sqrt{T_i}$. These analyses include a number of approximations, e.g. the D-D reaction cross-section is usually assumed to be isotropic in the centre of mass (CM) system. The successful measurements of neutron spectra reported earlier (refs 4,5) have emphasised the need for a precise and reliable evaluation of the relationship between the neutron spectrum shape and ion temperature. A numerical simulation has been performed as follows.The birth energy spectrum of fusion products M_3 from the reaction $M_1 + M_2 \rightarrow M_3 + M_4 + Q$ taking place in a plasma is given by:

$$\frac{dN}{d\Omega_3 dE_3} = \int f_1(\vec{V}_1)\, f_2(\vec{V}_2)\, \frac{d\sigma}{d\Omega_3 dE_3 d\Omega_4 dE_4}\, \left|\vec{V}_1 - \vec{V}_2\right|\, dV_1^3\, dV_2^3\, dV_4^3$$

$$\text{where } \frac{d\sigma}{d\Omega_3 dE_3 d\Omega_4 dE_4} = \frac{d\sigma}{d\Omega_3 dE_3}\, \delta(E_3 - E_3^*)$$

$$\text{with } E_3^* = \tfrac{1}{2} m_3 V^2 + \frac{m_4}{m_3 + m_4}(Q+K) + \cos\theta\, V \sqrt{\frac{2\, m_3\, m_4}{m_3 + m_4}(Q+K)}$$

Q = Energy release in reaction, V = CM velocity, K = Kinetic energy of reactants in CM, θ = angle between relative velocity and velocity of fusion product in CM.

The above integral can be solved by Monte Carlo sampling on a computer. A code accepting numeric distribution functions of the form $f(\vec{V}) = f(V,\psi)$ has been developed, where ψ is the pitch angle of the reacting particle with respect to the total magnetic field. CPU usage is 7.5μs per sample on a Cray 1 (200μs on an IBM 3087). Neutron spectra from the anisotropic D-D reaction in a thermal plasma were calculated resulting in an almost perfect Gaussian shaped spectrum with a temperature dependent shift Δ and broadening $W = FWHM/\sqrt{T_i}$. A convenient representation for these

quantities, based on a series of calculations (each using $3 \cdot 10^7$ samples) is found to be:

$$W\ [\text{keV}^{1/2}] = 82.74 + 0.103\ T_i - 8.2\ 10^{-4}\ T_i^2 \pm 0.04 \text{ and}$$
$$\Delta\ [\text{keV}] = 2.94 + 3.41\ T_i - 0.034\ T_i^2 \pm 0.4 \qquad \text{for } 1 \leq T_i\ [\text{keV}] \leq 20.$$

APPLICATION TO NEUTRON MEASUREMENTS

Neutron spectra are obtained "routinely" during high yield discharges ($Y_n \geq 10^{14}$n/discharge) with a ^{3}He ionization chamber viewing the plasma vertically from the roof laboratory. The width of the spectrum is extracted by fitting the experimental data points (Fig. 1) with a gaussian convoluted with the detector response function using the maximum likelihood technique for Poisson distributions /4/. Computer simulations show that the correction which needs to be applied to the line of sight data to yield the central ion temperature is small (~9%) and depends only weakly (±1%) on profile shapes provided that the density profile is broader than the temperature profile.

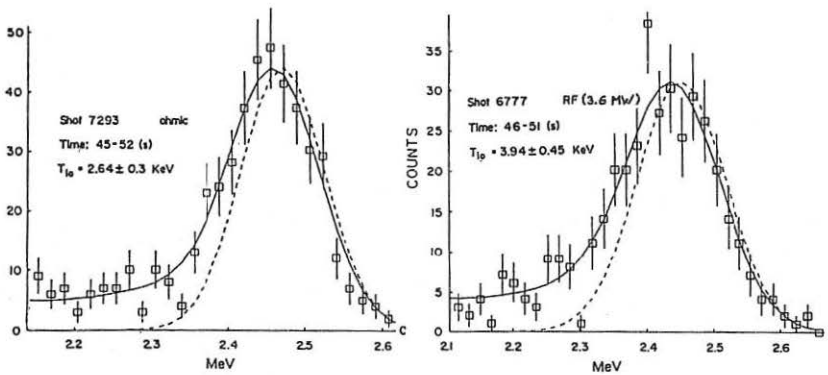

Fig. 1: Examples of measured pulse-height spectra and deduced central ion temperatures. The broken lines show the deduced neutron energy spectra.

The volume integrated neutron yield is measured with 3 pairs of absolutely calibrated fission chambers yielding a measurement of $\frac{1}{2}n_d^2 \langle\sigma v\rangle$ which can be used to deduce the deuteron density if $\langle\sigma v\rangle$ is calculated using the temperature measured with the spectrometer. This combination of measurements has shown that the ratio of $\hat{n}_d/\hat{n}_e$ for high yield discharges is noticeably low (between 0.8 and 0.3, reducing with $\hat{T}_e$). These results are obtained assuming the ion temperature profile is the same as the electron temperature profile.

One source of concern with the above analysis is that internal 'sawtooth' disruptions might lead to a preferential loss of fast ions from the central region of the plasma. A sensitivity analysis using FSPEC shows that the possible loss of all particles with E>27keV yields an overestimate of 10% in $\hat{n}_d$ for a T_i = 3keV case; a more gradual treatment, eg. exp-(ln2xE/12), or preferential loss of particles with high $V_\perp$ would lead to a systematic error of less than 5%.

14.7 MeV PROTON MEASUREMENTS

Protons from the D + ^{3}He → ^{4}He (3.6MeV) + p (14.7MeV) reaction have been observed with the experimental arrangement shown below. The ^{3}He ions originated either as reaction products (D + D → n (2.45MeV) + ^{3}He (0.82MeV) reaction) or from the bulk plasma (by ^{3}He gas puffing).

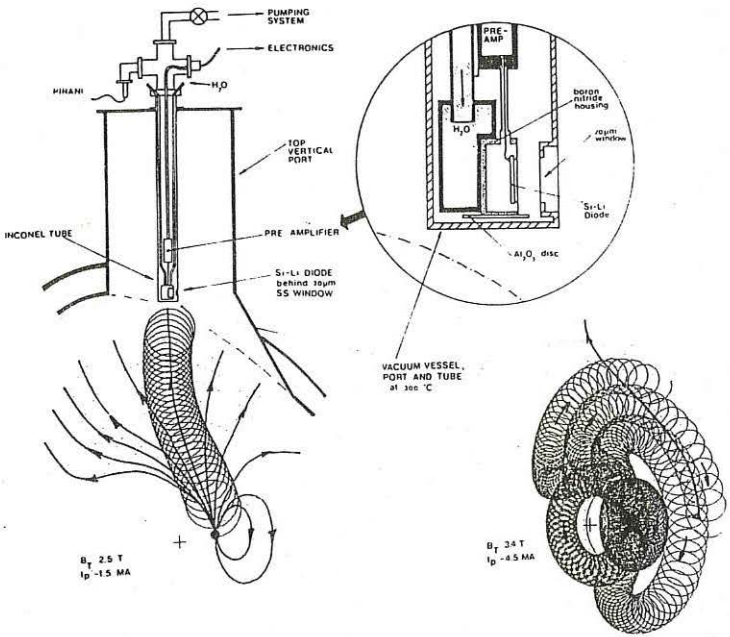

Fig 2: Detector arrangement with orbit examples at low and high current.

By collimation only protons with $V = V_\perp$ are accepted by the detector. The detector line-of-sight is determined with the help of an orbit code and depends strongly on the plasma current, the hot central core being visible only for currents below around 2.8MA (Fig. 2). The performance of the system was checked at plasma currents around 1.5MA (mainly during the current decay phase of discharges) yielding a Doppler broadening of the 14.7 MeV proton peak which was in agreement with other T_i measurements.

During H minority ICRF heating at low fields ($B_T \leq 2.6$T) and plasma currents ($I_p \leq 2.8$MA), protons originating from the central region of the plasma were observed. Enhanced sawtoothing could be clearly seen on the ECE signal (T_e) and the neutron yield. The proton yield, as derived from a single channel analyser showed the same trend but with less pronounced sawteeth. The 2.5MeV spread (FWHM) of the energy spectra around its nominal values was consistent with a 0.8MeV ^{3}He population slowing down in the plasma.

A systematic study of all discharges where data are available shows that the apparent ^{3}He burn-up fraction (= observed proton yield/ neutron yield) scales with T_e^7 while the expected burn-up fraction is proportional to $(n_d/n_e)T_e^{3/2}$, suggesting that the ^{3}He slowing down is influenced by the RF.

During ^{3}He ICRF minority heating the central part of the plasma is not visible but bursts of protons coinciding in time with the sawtooth collapse can be observed (Fig. 3). Spectra (Fig. 4) exhibit a downwards shift of ~1.5MeV which can be converted into a 75ms slowing down time for 15MeV protons (about half the sawtooth period) indicating that these protons were contained before being thrown out by the internal disruption. On the other hand the finite width (10-20 ms) of the proton bursts, being comparable to the decay time of the neutron sawteeth, rather suggests the burning up of expelled super thermal ^{3}He ions.

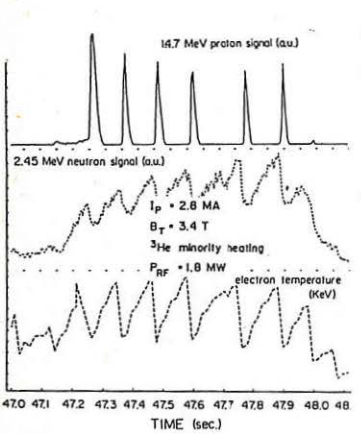

Fig. 3: Time dependence of 14.7MeV protons, neutrons and electron temperature during (^{3}He) ICRF.

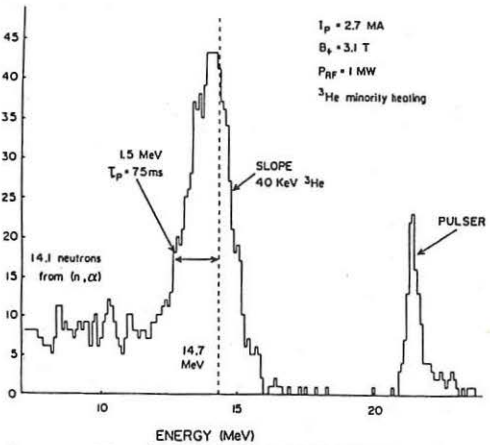

Fig. 4: 14.7MeV proton pulse-height spectrum during low power (^{3}He) ICRF heating.

SUMMARY AND CONCLUSIONS

* A highly efficient and exact code was used to calculate D-D neutron spectra from thermal plasmas.
* For high yields, $\hat{n}_d/\hat{n}_e$ ratios between 0.8 and 0.3 are measured.
* Intense bursts of 14.7MeV protons are observed at the collapse time of giant sawtooth disruptions during ^{3}He minority ICRF heating.
* The ^{3}He burn up fraction observed during ICRF(H) heating shows a very steep dependence on $\hat{T}_e$ indicating a possible interaction of the RF with the slowing down ions.

/1/ G Lehner and F Pohl Zeitschrift f Physik 207, 83, 1967
/2/ H Brysk, Plasma Physics, Vol 15, p 611, 1973
/3/ J Scheffel, Nuclear Inst. and Meth, Vol 224, No 3, p 519, 1985
/4/ V Merlo et al, Varenna, Course and Workshop, 26 Aug-3 Sept 1985
/5/ O N Jarvis et al, 12th EPS Conference, Budapest, Sept 1985

T_i PROFILE STUDIES DURING ICRF HEATING IN JET

S Corti, E Barbato*, G Bracco*, M Brusati, M Bures, A Gondhalekar*, F Hendriks, F Sand, A Taroni, F Tibone, V Zanza*

* JET Joint Undertaking, Abingdon, OX14 3EA, UK
* ENEA Euratom Association, Frascati, Italy

ABSTRACT

After a brief description of the analysis code used, some measurements performed with an array of four passive Neutral Particle Analysers are presented. The main result of this study is the evaluation of T_i profiles both during ohmic phase and ICRH phase of a JET plasma. A comparison of the experimental T_i profiles with those obtained from Transport analysis codes and a power balance computation performed using the JICS code are discussed.

This paper describes features related to the analysis of neutral particles and the ion temperature in JET as measured with an array of four passive Neutral Particle Analysers. Ten energies for two species (Hydrogen and Deuterium) are detected simultaneously in each analyser, so that the two energy spectra can be obtained at any time of a discharge and at different spatial locations. The neutral particles emitted by the plasma are ionised in a gas stripping cell and energy and mass analysed in a B//E geometry. The analysers have been absolutely calibrated both for H and D.

An analysis code /1/ taking into account all the relevant processes is available. This code, using the measured neutral particle fluxes, the measured T_e and n_e profiles, taking the edge neutral density as a free parameter allows to compute the neutral density and the T_i profiles. A value for n_i/n_e (ranging between 0.5 and 1) is assumed, constant in radius, throughout the calculation.

To start with, a T_i profile is assumed as a parabola best fitting the four points obtained performing a linear fit on the spectra given by the different operational analysers. An iterative process is then adopted taking the χ^2 of the fitting to the experimental spectra as the key parameter.

In order to check the consistency of the calculated profiles with the experimental data, the value of the derivative of the spectra (i.e. the value of the temperature) corresponding to the radial location of each energy measured experimentally is superimposed to the final profile. In doing that, the assumption is made that T_i be constant on a given magnetic surface, so that all energies, measured along different lines of sight, can be plotted on the same radial scale.

In Fig. 1 the profile obtained during the OHMIC phase of a discharge is shown. The horizontal error bars correspond to the halfwidth of the relevant source functions.

During Ion Cyclotron Resonance Heating the ion temperature profile is modified according to the location of the resonant layer and of the power deposition. By varying the value of the toroidal field it is possible to have the position of the resonant layer changed during the same discharge. Figs. 2 and 3 show respectively the profiles obtained in case of central and off-axis heating.
The experimental T_i profiles obtained in this way have been compared for the ohmic phase of a discharge with those resulting from transport code simulations. The standard transport model for JET has been used: i.e. neoclassical resistivity, $\chi_e = 2\chi_{eCMG}$ and $\chi_i = 5\chi_{iCH}$, χ_{iCH} being the neoclassical ion thermal conductivity given in /2/. The results are shown in Fig. 4. Good agreement is found between computed and measured profiles. The ion contribution to the energy replacement time in this case is half the electron contribution. This is mainly due to the deuterium depletion caused by impurities.

The same ion transport model is used to simulate the ICRH phase of the discharge. In this case a more detailed analysis is needed, especially at high RF power, where sometimes the consistency between the various T_i measurements failed. Results of the computation show that the NPA profiles can be consistent with the global power balance. However, when $P_{RF} \geq 2 \div 3$ P_Ω, they would imply that a substantial portion (~80%) of the auxiliary power is absorbed by the main ions. The radial dependence of the ion neoclassical conductivity allows to obtain, in these cases, T_i profiles rather broad in the intermediate plasma region ($|\nabla T_i| < |\nabla T_e|$) while the height of the central peaking is inversely proportional to the width of the RF power deposition profile. If this picture was confirmed, it would have rather drastic implications on the global plasma parameters (e.g. τ_e would be much higher, during RF, than estimated so far.)

The analysis of the power balance has been performed, both for the Ohmic and the RF cases, using the JET analysis code JICS /3/. Experimental profiles for electrons and ions have been used to infer power terms and local conductivities.
The power balance follows the general Tokamak pattern, with most of the input power being lost by conduction mainly through the electron channel. This picture is maintained (fig. 5) during additional heating: ie conduction losses scale with the total input power for both ions and electrons.

References.

(1) - G BRACCO, S CORTI, V ZANZA et al: JET Report JET-IR(84)04.

(2) - C S CHANGE, F L HINTON: AMPC Report 14-011, June 1985
(to be published in Physics of Fluids)

(3) - M BRUSATI et al. : Workshop on Diagnostics for Fusion
Research Conditions, Varenna, Sept. 1982, p.235

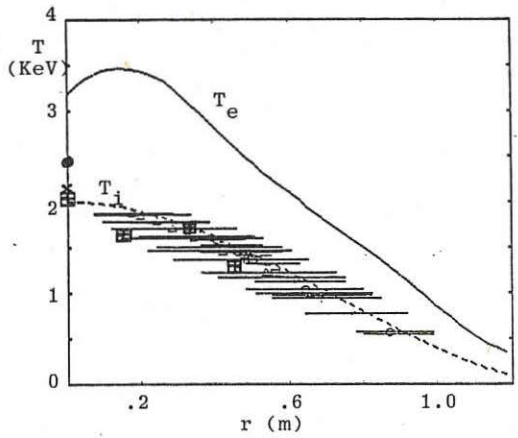

FIGURE 1 - T_i profile obtained during ohmic phase (shot 6850) (dashed line). The T_e profile from ECE measurements and the T_i values from x-ray spectroscopy on Ni (•) and from Neutron Yield (×) are also shown. The ⊞ represent linear fitting points.

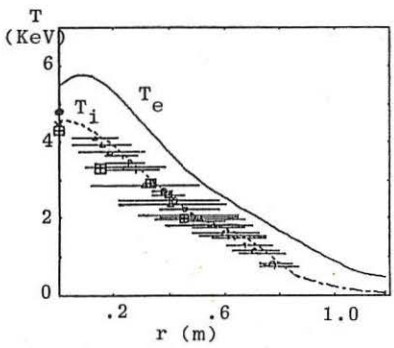

FIGURE 2 - As Fig. 1 but in case of ICRF central heating (shot 6850).

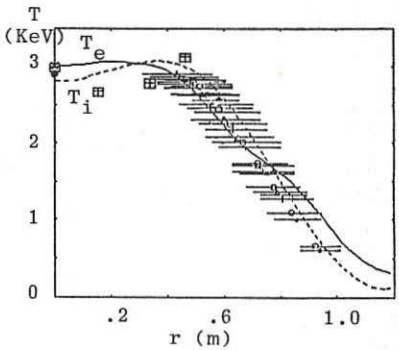

FIGURE 3 - As Fig. 1 but in case of ICRF off-axis heating (shot 6850) .

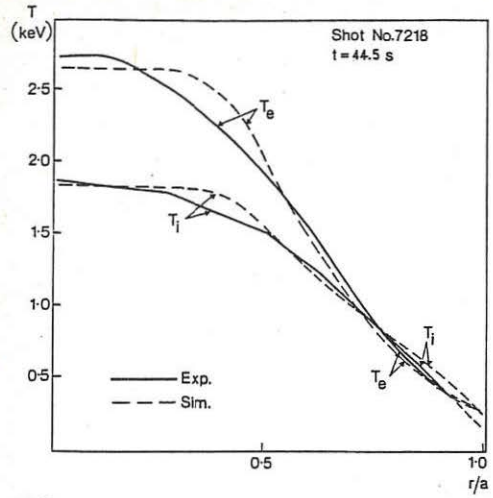

FIGURE 4

Comparison of experimental T profiles with those obtained by using Jet Transport Code in an ohmic case.

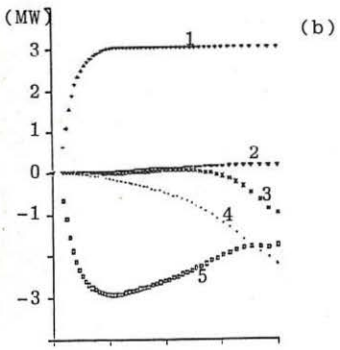

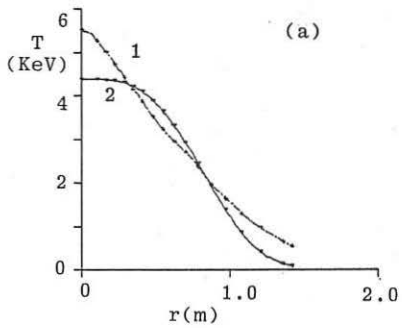

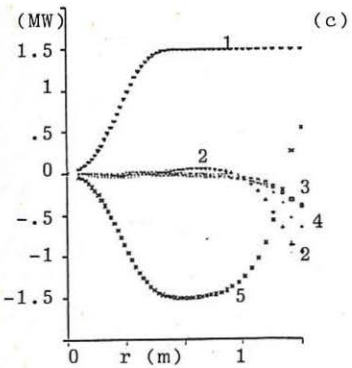

FIGURE 5 - Power Balance Analysis during ICRH (shot 7218).

(a)- Experimental profiles used. 1) T_i-NPA , 2) T_e-ECE

(b)-Electron Power Balance: 1) RF power, 2) ohmic power, 3) e-i transfer, 4) radiated power, 5) conduction

(c)-Ion Power Balance: 1) RF power, 2) e-i transfer, 3) c-x, 4) convection, 5) conduction

DETERMINATION OF POLOIDAL BETA IN JET

G Tonetti*, J P Christiansen, J G Cordey
JET Joint Undertaking, Abingdon, Oxon, OX14 3EA
*Euratom - CRPP Association, Switzerland

Abstract

Magnetic, diamagnetic, density and temperature measurements are used to calculate poloidal beta (β) by three independent methods. Comparison studies are made for a variety of plasma discharges in JET and error estimates are given. The results from the three methods are in good agreement for pulses with currents above 2MA.

1. Definitions and Relations

The poloidal beta (β), the internal inductance (ℓ_i) and the diamagnetic parameter (μ) are defined by the following integrals [1] over the plasma volume

$$\{\beta,\ \ell_i,\ \mu\} = \frac{4}{\mu_o I^2 R_o} \int \left\{p,\ B^2/2\mu_o,\ (B\phi_o^2 - B\phi^2)/2\mu_o\right\} dv \ . \qquad (1)$$

p, B, B_ϕ denote pressure, poloidal field and toroidal field; R_o is arbitary but in practice chosen to be the torus centre. If the plasma pressure is anisotropic and plasma flow is included values $\beta_\perp$, $\beta_{||}$, β_{ROT} are found from (1) by replacing the pressure p respectively with the perpendicular and parallel components of the pressure tensor and with the flow energy [2]. Neglecting the flow energy, two relations are derived [1,2] from (1).

$$\Lambda = \tfrac{1}{2}\beta_\perp + \tfrac{1}{2}\beta_{||} + \tfrac{1}{2}\ell_i = \tfrac{1}{2}S_1 + (1 - \tfrac{1}{2}\delta)S_2 \ , \qquad (2)$$

$$\beta_\perp - \mu = S_1 + \delta S_2 . \qquad (3)$$

The Shafranov integrals S_1, S_2 are evaluated on the plasma boundary via

$$\{S_1,\ S_2\} = \frac{4}{\mu_o I^2 R_o} \int B^2/2\mu_o \left\{r\ \bar{r}\cdot\bar{n},\ R_o\ \bar{R}\cdot\bar{n}\right\} R\ dl \ , \qquad (4)$$

the $\bar{}$ denoting unit vectors in the poloidal r, toroidal R and Z directions and $\bar{n}$ is normal to the boundary; δ in (2-3) is defined in [1]. In this paper we describe 3 calculations of β giving values referred to as follows:

$$\beta_{MHD} = \tfrac{1}{2}\beta_\perp + \tfrac{1}{2}\beta_{||} \ ; \quad \beta_{KIN} = \beta_\perp \ ; \quad \beta_{DIA} = \beta_\perp . \qquad (5)$$

These values are determined from (2), (1) and (3) respectively.

2. The MHD Beta

β_{MHD} is obtained from (2). Λ is given by the integrals (4) obtained from the plasma boundary calculations [3]. For an elongated plasma ℓ_i can be evaluated separately. An empirical formula for ℓ_i in terms of the elongation E, minor

radius a, major radius R_o and the current moment Y_2 has been given in [4].

$$\ell_i = \frac{2E}{1+E^2}\left(C_1 + C_2\,\frac{Y_2}{(E^2-1)a^2} + C_3\,\frac{\beta a^2 \Lambda}{R_o^2(E^2-1)}\,\frac{5+E^2}{4}\right) + C_4 \qquad (6)$$

The constants C_1 - C_4 are adjustable parameters. From a study of more than 1000 JET pulses the following values were determined

$$C_1 = 2.15 \qquad C_2 = 5.8 \qquad C_3 = 1 \qquad C_4 = -0.36\ . \qquad (7)$$

The values (7) have been obtained for JET pulses with $E>1.25$ and $0.9<\ell_i<2$.

3. The Kinetic Beta

The integral $\int p dv$ of (1) is written as

$$\int p dv = e\int_0^1 (n_e(x)\,T_e(x) + n_i(x)\,T_i(x))\,\Omega(x)dx\ , \qquad (8)$$

were $\Omega(x)$ is the volume between adjacent plasma surfaces described by the parameter $0 \leq x \leq 1$. The approximate geometry of the plasma surfaces is derived from the boundary geometry using the Lao-Hirshman parametric description [6]. The plasma profile quantities required to evaluate (8) are obtained or approximated as follows: T_e (x) directly from electron cyclotron emission; $n_e(x)$ from a parametric fit to data from 7 FIR interferometer channels; the ion temperature is assumed to be either

$$T_i(x) = T_{io}^{\text{neutrons}}\,\frac{T_e\,(x)}{T_e\,(0)} \quad \text{or} \quad T_i\,(x) = T_{io}^{\text{NPA}}\,(1-x^2)\ , \qquad (9)$$

where the central values T_{io} are calculated from the neutron emission and from the neutral particle analyser (NPA) data respectively; the ion density is $n_i\,(x) = f_{HD}\,n_e\,(x)$ with the fraction of hydrogenic species being fixed (usually $f_{HD} \sim 0.5$).

4. The Diamagnetic Beta

This is calculated directly from (3) using S_1, S_2 and δ as previously described. The diamagnetic parameter μ is

$$\mu = \frac{8\pi B_{\phi o}}{\mu_o\, I^2}\,\Delta\Phi\ . \qquad (10)$$

In (10) the flux change $\Delta\Phi$ is derived from the measurement $\Delta\Phi_M$ of a diamagnetic loop. The derivation includes compensation techniques implemented by hardware and software. The latter is

$$\Delta\Phi = \Delta\Phi_M - \Delta\Phi_{CX} - \Delta\Phi_{PF} - \Delta\Phi_I\ . \qquad (11)$$

In (11) the subscripts refer to flux change due to: toroidal field coil expansion (thermal and mechanical), coupling from the poloidal coil currents and from the plasma current. The hardware of the diamagnetic loop compensates for toroidal field and eddy currents in the vessel. Further details are given in [5].

5. Comparison of β values

In an isotropic plasma the 3 β estimates should be in close agreement. For a non-isotropic plasma (eg. with strong beam heating) the relations (5) would apply. On JET the values β_{KIN} corresponds to $\beta_\perp$ since the ECE and the NPA diagnostics measure $T_\perp$. For the JET pulses obtained so far non-isotropic effects are small and should not affect the comparison. Figure 1 shows the time evolution of β for 2 JET pulses with ICRH and neutral beam heating. All three methods are in good agreement on the increase of β. A large selection of β values for pulses with different current, field and plasma shape are shown in Figures 2 and 3; each symbol represents a value from one JET pulse chosen at the end of current flat top. Figure 2 shows a good agreement between β_{MHD} and β_{KIN} for the whole range of pulses. Figure 3 also shows a good agreement between β_{DIA} and β_{KIN} for currents above 2MA. For pulses with lower currents further studies of the coupling term $\Delta\Phi_I$ in (11) is needed.

The errors on β_{MHD} arise from the separation formulae (6-7) and are typically ± 0.05.

The errors on β_{KIN} are due to 1) approximate surface geometry ($\Omega(x)$ of(9)) in the axial region, 2) the density profile fit, 3) assumed profiles for n_i, T_i, 4) errors on raw data. The horizontal error bar in Figure 2, 3 assumes relative errors on T_e of 10% and on the density of 5%.

The error on β_{DIA} is proportional to B_ϕ/I^2 times the error on $\Delta\phi$. From measured residual fluxes the error $\Delta\beta_{DIA} = \pm 0.02$ is found for I = 4MA, B_ϕ = 3.4T. A systematic error related to $\Delta\phi_I$ is apparent at low plasma current (Fig 3).

6. Conclusion

For a variety of JET pulses with I>2MA the results from the 3 independent methods of determining β are found to be in good agreement. For I<2MA the compensation of the diamagnetic flux needs to be improved.

References

[1] V D Shafrancv, Plasma Physics 13 (1971)757
[2] L L Lao, H St John, R D Stambaugh, W Pfeiffer, GA report A117611 (1984)
[3] J P Christiansen, Integrated analysis of JET data. Submitted to J Comp Physics. JET Repoprt JET-R(86)04.
[4] J G Cordey, E Lazzaro, P Stubberfield, P Thomas, M L Watkins, Workshop on Transport Analysis codes PPL (March 1984)
[5] G Tonetti, J P Christiansen, L de Kock, 6th APS topical conf. on High Temperature plasma diagnostics, Hilton Head Island, South Carolina (March 1986)

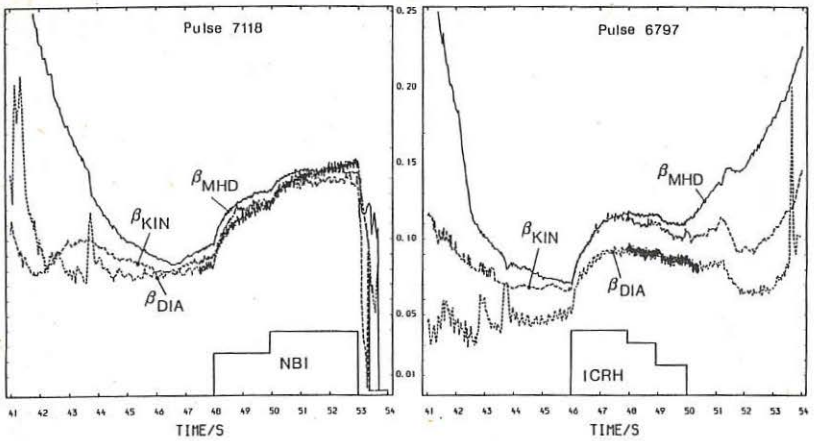

Fig. 1. Time evolution of poloidal beta for a neutral beam heated and an ICRH heated JET pulse. The increase in β is in good agreement for the 3 independent methods.

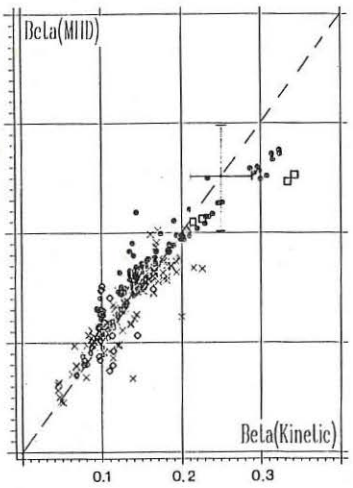

Fig. 2. Values of β_{MHD} vs β_{KIN} for the 1986 (Jan - March) JET pulses. The symbols denote different discharge parameters.

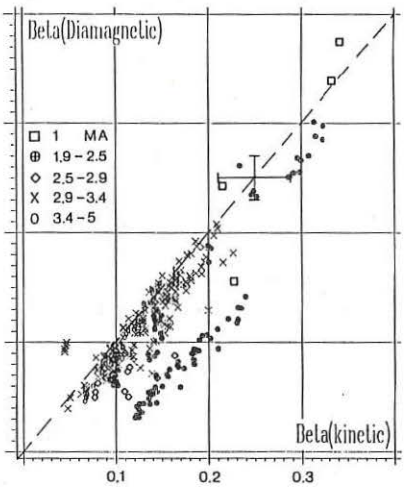

Fig. 3. Values of β_{DIA} vs β_{KIN} the points lying below the line correspond to pulses with currents under 2 MA.

CURRENT DENSITY DISTRIBUTION IN THE TJ-I FROM SINGULAR SURFACES POSITION DEDUCED FROM VISIBLE CONTINUUM PROFILES

C. Pardo, B. Zurro and TJ-I group

Division de Fusion, JEN, 28040 Madrid, Spain

Determination of current density distribution in tokamak plasmas is essential for confinement and stability studies. Among the different procedures used for its measurement, the one based on the location of q-rational surfaces appears as one of the most powerful methods. It has been applied until now using x-ray arrays data and tomographic techniques (1). They are quite sophisticated to be routinarely implemented and for this reason we are exploring in the TJ-I tokamak a similar method but using continuum profiles in the visible range and other spectroscopic features to locate the q-rational surfaces.

The existence of magnetic islands is closely related to the radial structure of bremsstrahlung continuum radiation: transport enhancement occurring through them makes small humps appear in the emission profiles close to the singular surface, due to impurity accumulation near the outer boundary of the island (2). This relationship has been confirmed through a perturbative experiment in the T-7 tokamak, for the q=2 case (3).

We have applied this procedure to ohmically heated discharges of TJ-I tokamak, a small device with R=30 cm, a=10 cm, operated for this experiment with a toroidal field of 1T, line average density $\bar{n}_e \simeq 2\times10^{13}$ cm^{-3} and peak current of 40 KA. Visible profiles were obtained with a 1 m monochromator provided with a fast rotating polygonal mirror that performs repetitive scans of the plasma in .4 msec. every 1.5 msec., with a spatial resolution better than 1 cm. A search in wavelength was done to look for spectral regions of minimum emission and free of line contamination. Data herein presented were obtained with a bandwidth of 4Å centered around 5233 Å.

Visible continuum and Thomson scattering profiles were measured at discrete times of this TJ-I discharge in order to compare the current density radial distribution obtained by two independent methods. Typical continuum measured profile is shown in fig. 1; the position of rational surfaces with q=1.5, 2 and 3 is indicated by arrows in this particular profile. The q-rational positions were fixed at the radii where emission inflexions take place. There are some facts supporting that these profiles in TJ-I contain information about q(r): humps appear at the same position for the same time through a serie of reproducible discharges, consecutive scans suggest island rotation and the structure in profiles is not always observed.

Current density distribution and q profiles deduced from continuum scans have been compared with those obtained from Thomson scattering

measurements assuming Spitzer model ($j(r) \propto Te(r)^{3/2}$). For the three studied cases, fairly good agreement between both q profile has been found, although, in general, q(o)'s extrapolated from continuum method tend to be higher than those predicted by Spitzer model. The less favourable comparison is shown in fig. 2.

Current density radial distribution obtained by these two methods are compared, normalized to their central value, in fig. 3. Peak Spitzer current is higher than that obtained by the other method, and thus central energy confinement times are smaller than those deduced from q-rational location. More significant differences between both analysis are found for Zeff spatial dependence, as is shown in fig.4.

In conclusion, sistematic radial structure in the visible continuum emission in the TJ-I tokamak has been interpreted as related to q-rational surfaces position. Current density profiles deduced from it are being compared with that from Thomson scattering data and Spitzer model. Until now, good agreement between them has been found for the studied cases.

Acknowledgements

The authors would like to thank a grant from IEN to one of us (C.P.).

References

1.- Sauthoff, N.R., Van Goeler, S., Stodiek, W.
Nucl. Fusion 18 (1978) 1445.

2.- Mirnov, S.V.,
Sov. J. Plasma Physics. 6 (1980) 127.

3.- Bagdasarov, A.A., Denisov, V.F., Ivanov, D.P., et al.
Plasma Phys. and Contr. Nucl. Fus. Res., Vol.3, IAEA, Vienna (1983), 281.

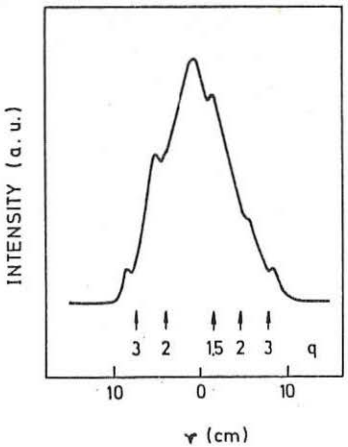

Fig. 1.- Visible continuum profile at the current peak. The rational surfaces position are indicated

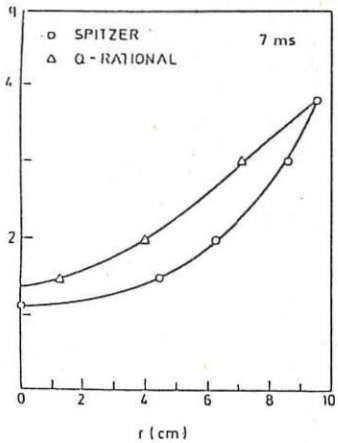

Fig. 2.- Comparison, in the less favorable case, between q profile obtained from Spitzer model and from visible continuum radial structure

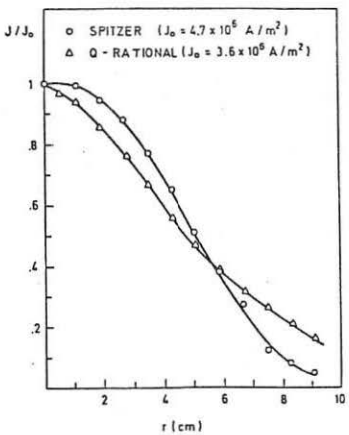

Fig. 3.- Comparison between current density radial distribution deduced from the above mentioned methods (at current peak).

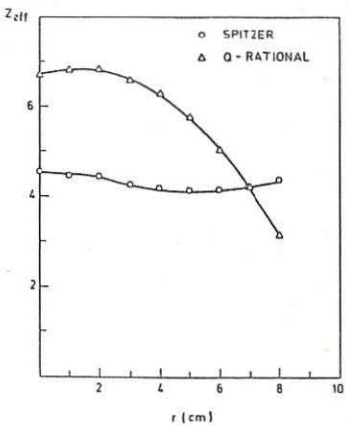

Fig. 4.- Zeff radial distribution found from Spitzer and q-rational location at current peak.

FIRST SPECTROSCOPIC CHARGE EXCHANGE MEASUREMENTS DURING NEUTRAL INJECTION ON JET

M G V von Hellermann, W W Engelhardt, L D Horton
P G Carolan*, M J Forrest*, N J Peacock*

JET Joint Undertaking, Abingdon, Oxon, OX14 3EA, UK
* EURATOM-UKAEA Association, Culham Laboratory, Culham, Oxon OX14 3DB,UK

INTRODUCTION During the first phase of neutral beam heating on JET advantage has been taken of using the heating beams to develop an active beam diagnostic system based on charge - exchange - recombination - spectroscopy (CXRS). The diagnostic is based on the charge exchange interaction of fast injected neutrals as H° and D° with thermal fully stripped atoms such as H^+, D^+, He^{2+}, C^{6+} and O^{8+}. The first two represent the bulk of a a JET plasma and the other the dominant light impurities. The charge exchange reaction is:

$$H^\circ_{beam} + Z^Z \rightarrow H^+_{beam} + Z^{Z-1,*}\ (n,\ell)$$

H° or D° are the injected high energy neutrals, Z^Z the thermal (fully) ionized impurity of charge z and $Z^{Z-1,*}$ (n,ℓ) the impurity atom excited in quantum state (n,ℓ).
The resulting recombination radiation can be analysed by suitable instrumentation. The most intense recombination lines are emitted from Δn=1 transitions and lie in the VUV or soft X-ray regions of the spectrum. At high beam energies (E_{beam} > 25keV/a.m.u.) there is appreciable recombination into high quantum states which emit in the visible region. The visible CXR lines have a particular appeal as diagnostic indicators in an active thermonuclear experiment such as JET since the collected light can be transferred via radiation hardened fibre guides into a remote diagnostic hall. CXRS enables diagnostic access to nuclei which are distributed widely throughout the bulk of the plasma, but which otherwise are not directly detectable in JET. In contrast to conventional line emission spectroscopy the geometric intersection of a line of sight and the neutral beam path determines a well defined active volume and hence gives a local measurement. The observed excited CXR flux is given by:

$$\frac{d\Phi(\lambda,L)}{d\lambda} = \frac{1}{4\pi} f(\lambda) \int_{-L/2}^{L/2} ds \cdot \{n_Z(s) \sum_E n_H(s,E)\ (\sigma v)^{n,\ell}_{cx}\ (E)\}$$

Where : $n_H(s,E)$ is the neutral particle density at fractional energy E and location s, $n_Z(s)$ the local (impurity) density, $\sigma v^{n,\ell}_{cx}(E)$ the effective charge exchange excitation rate at beam energy E and quantum numbers n and ℓ, taking into account cascading and ℓ - mixing processess (cf. FONCK. [1]). Finally L the length of emitting intersection volume along line of sight s and f(λ) is the spectral profile

$$f(\lambda) = \frac{1}{\sqrt{\pi}\lambda_D} e^{-((\lambda-\lambda_o)/\lambda_D)^2}$$

The Doppler width and Doppler shift allow a determination of the temperature and the bulk plasma velocity. The local fractional neutral beam particle density $n_{H^\circ}(R,E,t)$ can be derived by the recently developed PENCIL CODE (cf. WATKINS et al [2]). In addition to that code it is feasible to obtain the same information by measuring the electron impact excited and Doppler shifted Balmer-alpha spectra emitted by the fast injected neutrals (cf. PEACOCK et al [3]) The atomic physics data of the

involved excitation rates rely mostly on theoretical (cf. SUMMERS et al [4]) and partly on experimental data like those recently obtained from a CRX-experiment on ASDEX in pure helium discharges (PEACOCK et al [3]).

EXPERIMENTAL

The layout of the viewing chords and that of the heating neutral beams is described by Fig.1. At present two viewing chords are employed. A vertical line of sight in Octant 8 intersecting the neutral beams in the plasma centre (R=3.1m) and a second viewing line, which passes from a horizontal port in the adjacent Octant 1 to an intersection volume with the neutral beams at approximately half the minor radius (R=2.3 m). This viewing line enables measurement of toroidal plasma rotation. A multichord optical head, (8 fibres) which will allow a complete radial scan, will be installed during the next shut down of JET. The instrumental equip- ment is an optical head (F/1.6) followed by a 150m, PCS 1000, fibre link with an attenuation of 20 db/km at 500nm. The spectrometer is a 1m Czerny-Turner with a 2160g/mm grating. The 1024 element intensified detector array has a quantum efficiency of 8 photons/count at 500nm. The total sensitivity of the system was absolutely calibrated yielding a photon flux/count rate of 10^7 cm^{-2} sr^{-1} at the same wavelength.

RESULTS

The CXRS results obtained during the first NBI campaign have clearly demonstrated the potential for measurement of local ion temperature, toroidal plasma rotation and impurity concentration. The ion temperature derived from the Doppler broadened CX-line profiles of oxygen, carbon and helium agree reasonably with values determined by independent ion temperature diagnostics on JET. There seems to be a slight increase of derived ion temperature with increasing Z. This needs however, further systematic investigation. As an illustration of the CX characteristic features the time dependence of the oxygen 10 → 9 (6068A) spectrum before and during NBI is shown in Fig.2. Analysis of fitted line profiles and background level gives the ion temperature, line intensity and continuum intensity (Fig.3). A preliminary analysis of the calibrated photon fluxes making use of electron source rate data determined by the PENCIL code [2], excitation rates taking into account complete ℓ-mixing for the 10 → 9 transition [1], results in relative oxygen concentrations in the order of 2 % of the electron density. The concentration of oxygen relative to n_e appears to decrease during a NB pulse whereas the absolute level tends to increase slightly. This very preliminary analysis is based on the assumption that only the full energy component contributes to the CXR signal and that halo effects and excitation by meta stables from thermal atoms can be ignored.

Comparison of JET pulses with comparable NB and plasma parameters, the spectrometer being tuned to the spectra of O^{8+} and C^{6+} respectively, indicates a value n_C/n_O of 3 to 5 decreasing with increasing electron density during injection to ≈2. These values are in rough agreement with results obtained by the usual transport analysis (cf. BEHRINGER [5]). Further analyses are in progress which involve detailed modelling of the atomic physics and local neutral particle densities [2,4]. The tangential viewing line was used to measure temperature and toroidal plasma rotation at approximately half the minor radius (R = 2.3m). Typical values are in the order of a few times 10^6 cm/sec and the ratio of ion temperature Ti(R = 2.3m)/Ti (R = 3.0m)≈0.6 .

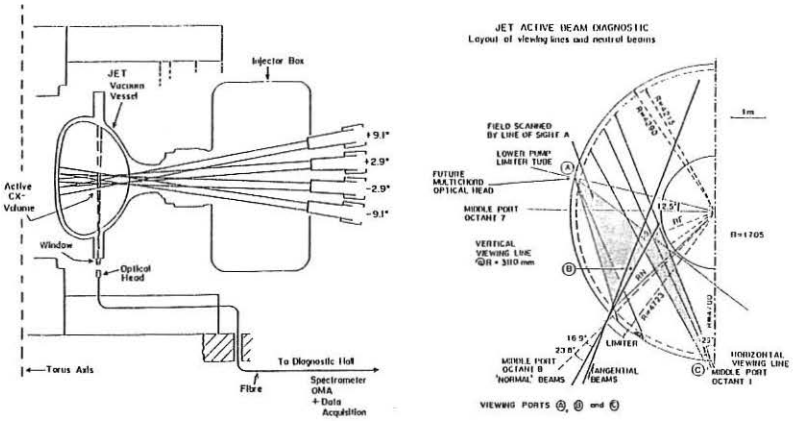

Fig. 1. Experimental layout showing viewing lines and neutral beams.

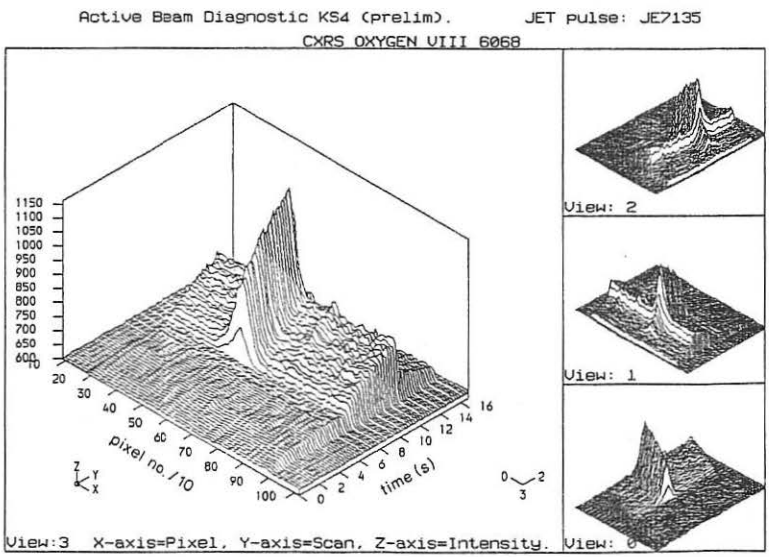

Fig 2. Time history of the O^{7+} (10 → 9) spectrum during NBI.

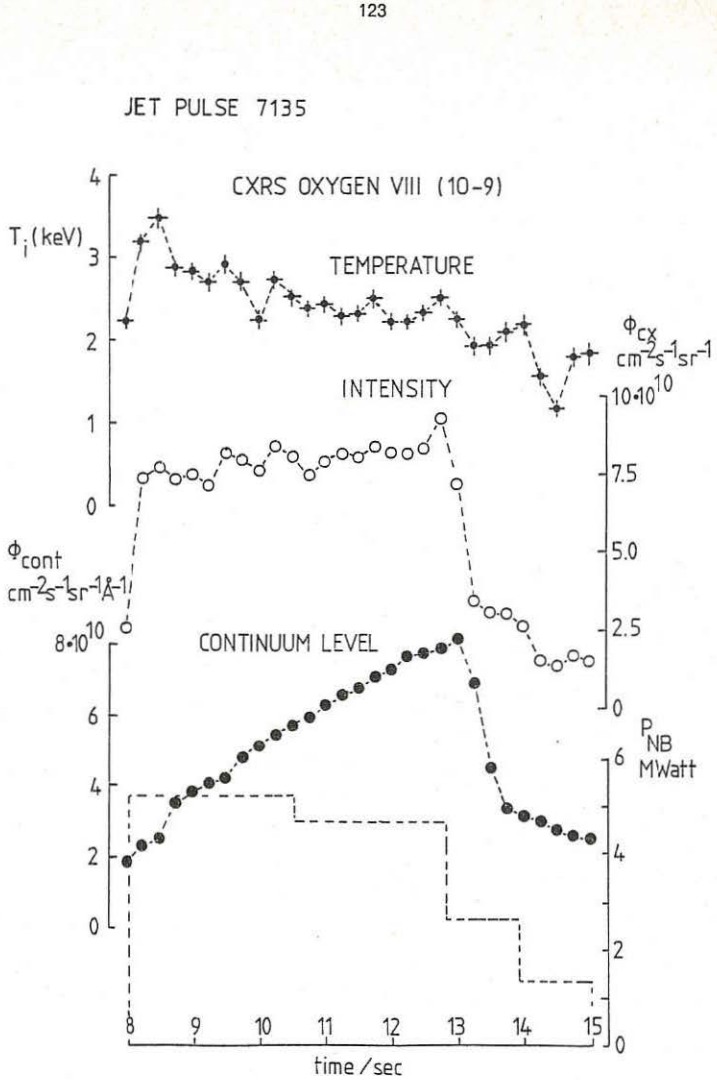

Fig 3. Calculated fit parameters a)CXR(O^{8+})-temperature b)CX-intensity, c)continuum intensity.

REFERENCES

[1]. FONCK el al, Phys. Rev. A29, 3288 (1983)
[2]. WATKINS et al, this conference
[3] PEACOCK et al, to be published
[4]. H.P. SUMMERS, JET Report 1986, P (86) 01
[5]. BEHRINGER et al, this conference

MEASUREMENTS OF CHARGED FUSION PRODUCTS IN ASDEX

H.-S. Bosch, U. Schumacher, G. Becker, H. Brocken, A. Eberhagen, D. Eckhartt, G. Fussmann, O. Gehre, J. Gernhardt, G. v.Gierke, E. Glock, O. Gruber, G. Haas, J. Hofmann, A. Izvozchikov[1] G. Janeschitz, F. Karger, M. Keilhacker[2], O. Klüber, M. Kornherr, K. Lackner, M. Lenoci[3], F. Leuterer, G. Lisitano, F. Mast, H.M. Mayer, K. McCormick, D. Meisel, V. Mertens, E.R. Müller[2], H. Murmann, H. Niedermayer, J.N. Noterdaeme, A. Pietrzyk[4], W. Poschenrieder, H. Rapp, H. Riedler, H. Röhr, J. Roth, F. Ryter[5], E. Speth, F. Schneider, C. Setzensack, G. Siller, P. Smeulders[2], F. Söldner, K. Steinmetz, K.-H. Steuer, O. Vollmer, F. Wagner, F. Wesner, D. Zasche

Max-Planck-Institut für Plasmaphysik
Association Euratom-IPP, D-8046 Garching

For normal deuterium operation in ASDEX (A = 4.1, I_p = 250 - 400 kA) the charged fusion products from the D–D reactions (3 MeV proton, 1 MeV triton and 0.8 MeV ^{3}He) escape from the plasma on helical orbits to the upper part of the vessel. Since slowing-down can be neglected in ASDEX, the protons and tritons escape on identical orbits, because the trajectory depends only on the product $m \cdot \vec{v}$. The measurements of the charged fusion products give information on the ion temperature, fusion yield, and plasma behaviour [1,2].

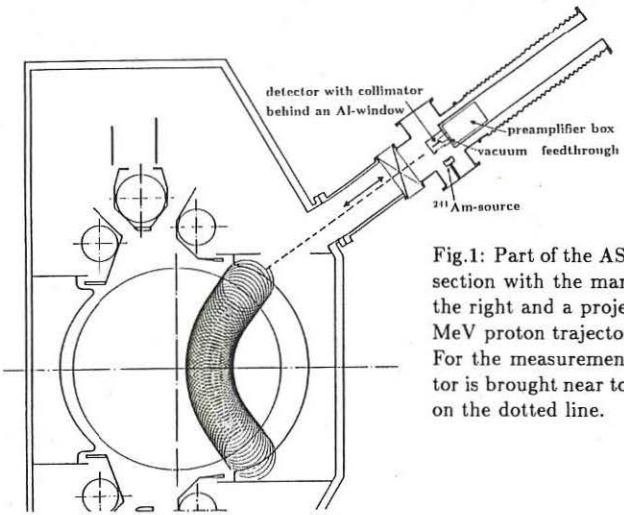

Fig.1: Part of the ASDEX cross-section with the manipulator on the right and a projection of a 3 MeV proton trajectory.
For the measurement the detector is brought near to the plasma on the dotted line.

The charged fusion products were measured for ASDEX deuterium plasmas by using a surface barrier detector or nuclear emulsion foils, installed on a manipulator. Figure 1 shows the ASDEX cross-section with the movable detector and a projection of a 3 MeV

[1]Academy of Sciences, Leningrad, USSR, [2]assigned to JET Joint Undertaking, [3]ENEA Frascati, Italy, [4]University of Washington, Seattle, USA, [5]CEN Grenoble, France

proton trajectory. For measurements with the surface barrier detector it is necessary to have sufficient electrical shielding and to keep the distance between the detector and the preamplifier short.

With the surface barrier detector , it is possible to measure the flux and the energy spectrum of the 3 MeV protons, and that of the 1 MeV tritons, either. The electric and magnetic distortions of the spectrum (about 50 keV) are monitored by a pulser signal, that is additionally fed into the preamplifier. By fitting the spectra with a Gaussian profile, we get a spectral width, that can be corrected with respect to the straggling in the Al foil and the noise broadening, which is measured by the width of the pulser peak. This corrected width, for the protons as well as for the tritons, is related to the ion temperature by the equation

$$\Delta E\ (FWHM) = 91.6 \cdot \sqrt{T_i}, \quad \Delta E, T_i\ in\ keV.$$

Figure 2 gives examples of a proton and a triton spectrum. The spectra demonstrate that both widths (not yet corrected for the straggling) are about the same, and hence they yield the same ion temperature. The time dependence of the temperature, evaluated from the proton spectra for a neutral-beam (H^0)-heated discharge in deuterium, is given in Fig. 3 in comparison with the temperature deduced from the neutron flux.

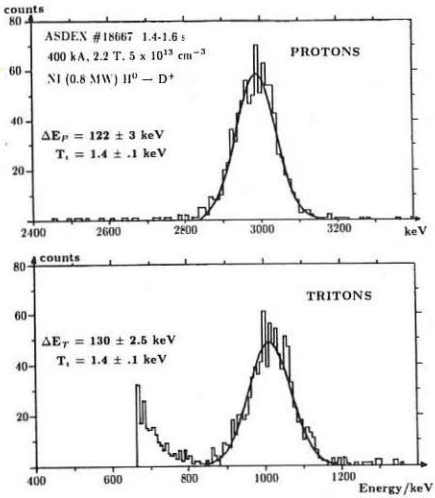

Fig.2: Spectra of protons and tritons

Fig.3: T_i from proton spectra and neutron flux

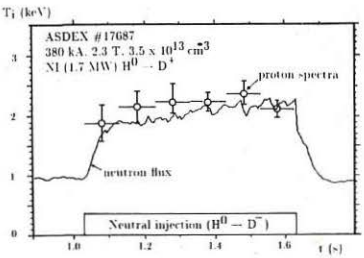

In principle, measurements of the tritons are of great interest, since their lower energy makes the spectrum more sensitive to the reaction conditions than the proton spectrum. However, the observation of the tritons is only possible in discharges with a low level of X-rays because these cause a background at the low energies that may cover the triton spectrum. Moreover, the surface barrier detector application is limited by the saturation of the preamplifier in discharges with high background levels.

Because of the influence of the strong magnetic fields in a tokamak the measurements of charged fusion products have to be supported by detailed particle trajectory calculations. They describe the phase space transformation of the charged fusion particles from the plasma to the detector. For measurements of the particle fluxes it is necessary to calculate the efficiency of the collimated detector [3], and for the spectra it is important to know which particles (characterized by birth radius and pitch angle) can reach the detector. To get this information about the phase space of the observed charged fusion particles, we calculate their trajectories in the opposite direction, i.e. from the detector into the plasma. For each point of the orbit the distance from the plasma centre and the pitch angle are calculated and then the point is stored in a matrix of these phase space coordinates. This is done for different directions through the collimator, weighted with the collimator transparency. Doing this, one gets a phase space probability for the measurement of charged fusion products that depends on the charge and energy of the particle, on the magnetic fields in the plasma, and on the orientation of the collimator. An example of such a probability calculation is given in fig. 4a, and it is obvious, that in this case the detector measures particles from the whole plasma volume, mainly starting perpendicularly to the plasma axis. In this case (pitch angle of about 90°) the influence of the poloidal field is very small, and so the details of the current distribution are of no importance. Measurements of the ion temperature are done with this collimator orientation.

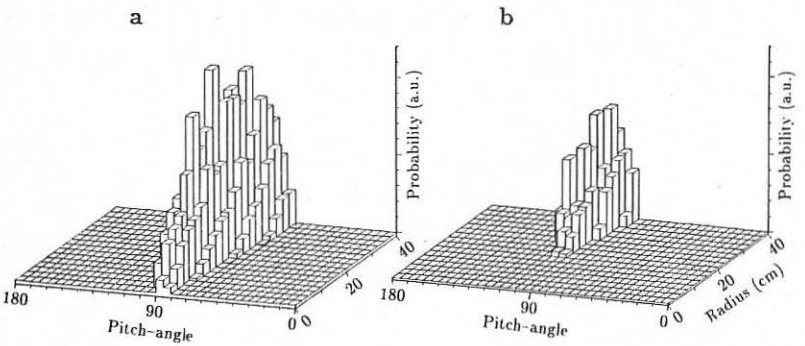

Fig.4a,b: Phase space probabilities for different collimator orientations
Calculation for ASDEX, I_P = 400 kA, B_T = 2.7 T, β_p= 0.5

Turning the collimator by 20° results in the probability distribution given in Fig. 4b. which measures only particles born at radii ≥20 cm, while the pitch angles are nearly the same as in Fig. 4a. This dependence of the phase space distribution on the collimator orientation can be used to deduce the fusion emission profile from the flux measurements at different orientations.

This procedure can be applied to look for the fast deuterium ions created by LH waves in ASDEX at densities above about 2.8 x 10^{13} cm^{-3} [4]. Figure 5a gives an example of a typical spectrum from such a discharge at a collimator orientation as in Figure 4a. The spectrum of the protons and that of the tritons show a superposition of a wide spectrum

on the expected thermal peak. These central peaks (ΔE about 100 keV) correspond to the Maxwellian plasma bulk with an ion temperature of about 700 eV. The wider parts of the spectra (about 600 keV wide) are produced by the fast ions generated by the LH waves. The velocity of these deuterium ions is mainly directed in the poloidal plane and their energy is in the range of 25 keV. Since the fusion reactivity at these energies is about 5 orders of magnitude higher than at 700 eV the number of these fast ions must be correspondingly smaller.

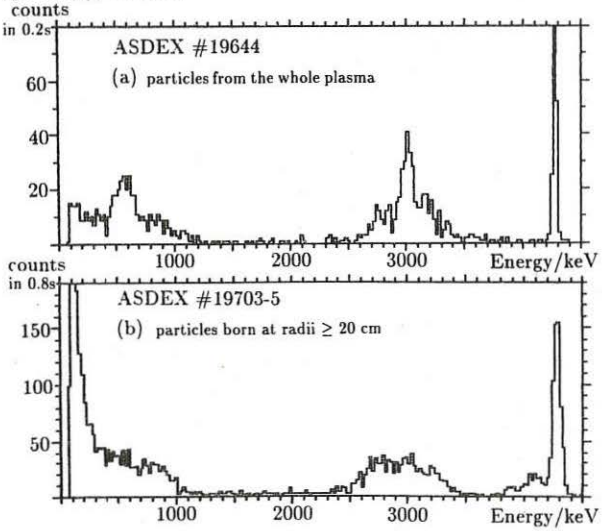

Fig.5a,b: Spectra for two ASDEX-discharges with different collimator orientations. I_P = 400 kA, B_t = 2.7 T, $n_e = 3.9 \times 10^{13}$ cm^{-3}, LH (1.3 GHz) P_{RF} = 900 kW

With a collimator orientation as in Figure 4b (where only particles from the outer regions are detected) we obtain the spectrum given in Figure 5b. As expected, the spectra generated by the bulk ions are not detected any more. Since the contribution of the fast ions appears nearly unchanged, however, one must conclude that the fast ions are created by the LH waves in the outer plasma regions, confirming the results from CX measurements [5].

References

1. Nagle D.E., Quinn W.E., Ribe F.L., Riesenfeld W.B., Phys.Rev. **119** (1960), 857–862.
2. Strachan J.D., in "Diagnostics for Fusion Reactor Conditions", EUR 8351-I-EN, Varenna, 1982, pp. 383–400.
3. Heidbrink W.W., Strachan J.D., Rev. Sci. Instr. **56** (1985), 501–518.
4. Eckhartt D., et al., 4th Int. Symp. Heating in toroidal Plasmas, Rome 1984 **I**, 501–512.
5. Ryter F., in "RF-Applications to Tokamaks", EUR 10333-EN, Varenna, 1985, pp. 746–751.

SIMULATIONS OF TOKAMAK DISRUPTIONS INCLUDING SELF-CONSISTENT TEMPERATURE EVOLUTION

A. Bondeson

Institute for Electromagnetic Field Theory
and EURATOM Fusion Research (SERC)
Chalmers University of Technology
S-41296 Göteborg, Sweden

Present address: Centre de Recherches en Physique des Plasmas, Association Euratom-Confédération Suisse, Ecole Polytechnique Fédérale de Lausanne, Lausanne, Switzerland

It is well known that tokamaks can be safely operated only within certain limits with respect ot the plasma current and density. If either of these limits is exceeded the discharge disrupts. The current is limited by the requirement that the safely factor at the plasma edge q_a be somewhat larger than 2 and the density limit is proportional to the average current density, $n[m^{-3}] < 10^{20}\ B_t[T]/(R[m]q_a)$. The density limit is generally thought to be connected with impurity radiation losses which cool the outer regions of the plasma so that the current density becomes small outside $q = 2$. Thus, the current profiles leading to density and current limit disruption are similar and are characterized by having very little current outside the $q = 2$ surface.

Waddell et al.[1] showed that many aspects of tokamak disruptions could be explained as the result of non-linear interactions of tearing modes of different helicities. Specifically they showed that the interaction of $m/n = 2/1$ and $3/2$ modes could be violent and lead to field line stochasticity and loss of confinement over some region of the plasma. However, violent interactions occurred only for equilibria sufficiently unstable to the 2/1 and 3/2 modes and the results of [1] leave open the question of how, or even if, such current profiles might arise.

The present simulations address the two interrelated questions of why and how disruptions occur and include selfconsistent evolution of the temperature and current profiles over transport timescales. The simulations intrinsically couple transport effects, which slowly change the equilibrium profiles, and resistive MHD instabilities occurring on shorter timescales. The stability of the MHD modes is determined by the equilibrium profiles and when an instability occurs it can quickly and drastically modify the profiles. The simulations show that sharply defined disruptive events, triggered by the 2/1 tearing mode occur when q at the boundary of the current channel is lowered towards 2. The disruptions are perhaps best described as shocks propagating inward from the $q = 2$ surface breaking up the magnetic surfaces and leaving turbulent plasma with poor confinement behind.

The model used is the lowest order reduced MHD system including a self-consistently determined temperature with a highly anisotropic thermal conductivity, Spitzer resistivity $\eta \propto T^{-3/2}$ and ohmic heating $\propto \eta j^2$. The boundary at $r = a$ is assumed nonconducting and the magnetic field is

matched to a vacuum solution. In the run described here, the resistivity at the centre was $\eta = 6\times10^{-6}$ and the heat conductivities were assumed constant $\kappa = 1.2 \times 10^{-5}$ and $\kappa_\parallel = 100$ (for details of normalization, see [2]). The system was integrated numerically with 120 radial grid points and 20 to 35 Fourier modes in the θ and z directions. A semi-implicit algorithm allows integration over transport timescales, using large timesteps when the level of perturbation is small.

In order to force the simulation into the disruptive regime, the toroidal electric field was adjusted so that the total plasma current was slowly increasing, $q_a(t) = q_a(0) \exp(-t/t_q)$, $t_q = 2\times10^5 t_A$, and q_a went from 2.74 to 2.49 in about 19000 Alfvén times.

Figure 1 shows the time history of the central temperature. During the first part of the run, when $q_a > 2.65$, sawtoothing occurs almost regularly and roughly in accordance with the Kadomtsev model[3]. The variations in the central safely factor q_0 are very small $|q_0-1|<0.02$ over the whole sawtooth period and the q-profile in the central region is very flat.

If the parallel thermal conductivity is made too small or the resistivity too large, the sawtoothing is replaced by a stationary m = n = 1 vortex in the central region. The vortex flattens the temperature profile and prevents q from going below unity anywhere. With a central resisitivity of 6×10^{-6} sawtoothing occurs for $\kappa_\parallel > 20$. The threshold in $\kappa_\parallel$ decreases with decreasing η so that large tokamaks are well into the region where the reduced MHD equations predict sawthoothing.

Figure 2 is a logarithmic plot of the total energies in the m/n = 2/1, 3/2 and 5/4 Fourier components. In the beginning of the run, when $q_a > 2.65$, the 2/1 and 3/2 modes exhibit mild oscillations with a period considerably longer than the sawteeth period. The amplitude of the oscillations is strongly dependent on q_a, the oscillations almost disappear when $q_a > 2.8$ and, as seen in Fig. 2, become very violent when $q_a < 2.6$ eventually leading to the three disruptive events at t/t_A =12600, 15800 and 18100. The oscillations are connected with periodic changes in the equilibrium profiles. When the current density at q = 2 is low, the m = 2, n = 1 tearing mode is unstable if the current density increases rapidly inside the q = 2 surface. The 2/1 mode then grows and creates an island at q = 2. If the island is sufficiently large it destabilizes the 3/2 mode primarily by displacing the current gradient and the q = 3/2 so that the current gradient becomes steep inside the q = 3/2 surface[4]. This causes the 3/2 mode to grow and produce at least partially stochastic field lines. Consequently the radial thermal transport increases and the temperature profile is flattened between q = 3/2 and q = 2. Figure 3 shows the temperature profile at t = 7300 when the 2/1 mode is growing (dashed line) and at t = 9125 after the phase of increased transport (solid line). At the later time the gradient just inside q = 2 have decreased, the 2/1 mode is stable and the q = 2 magnetic island shrinks. The cycle repeats when the equilibrium broadens resistively so that the current gradients increase near q = 2.

At later times these oscillations become more and more violent because with a lower q_a, giving a lower current density at q = 2, the 2/1 mode becomes increasingly unstable. When $q_a < 2.6$ disruptive events occur in the form of shocks propagating from the q = 2 surface toward the center of the plasma. During its inward motion the shock is carried by modes with a decreasing ratio m/n = q to remain in resonance with the magnetic field. In

particular, modes with m = n+1, n increasing, are strongly destabilized. Inside the shock, confinement is still good, whereas behind the shock, the flux surfaces have broken up and the plasma is turbulent. Figure 4 is a contour plot of the current density at the end of the first shock, t/t_A = 12550. In the subsequent disruptions, the shock reaches further into the plasma and involves even higher m and n components.

In these simulations the shock invariably stops when it reaches the q = 1 surface and leaves the central region relatively untouched. When the shock reaches q = 1, the current profile is close to a step function with the constant value $j = 2B_t/\mu_0 R$ inside the q = 1 region and j = 0 outside. This profile is marginally stable to all modes with m = n and m = n+1 but stable to all other modes of the lowest order RMHD system.

It is the author's opinion that the stopping of the front is a property special to the lowest order reduced MHD equations. The temperature and pressure profiles in the final stage are similar to the current profile and fall off very sharply at the q = 1 surface. In the presence of toroidal and pressure effects, such an equilibrium would be strongly ballooning unstable and it appears justified to assume that full MHD effects would lead to penetration of the q = 1 barrier and the final broadening of the current profile observed experimentally in major disruptions.

References

[1] B. V. Waddell, B. Carreras, H. R. Hicks and J. A. Holmes, Phys. Fluids 22, 896 (1979).

[2] A. Bondeson, Nucl. Fusion (to appear).

[3] B. B. Kadomtsev, Sov. J. Plasma Phys. 1, 389 (1975).

[4] R. G. Kleva, J. F. Drake and A. Bondeson, Phys. Fluids 27, 769 (1984) and A. Bondeson, Phys. Rev. Lett. 51, 1668 (1983).

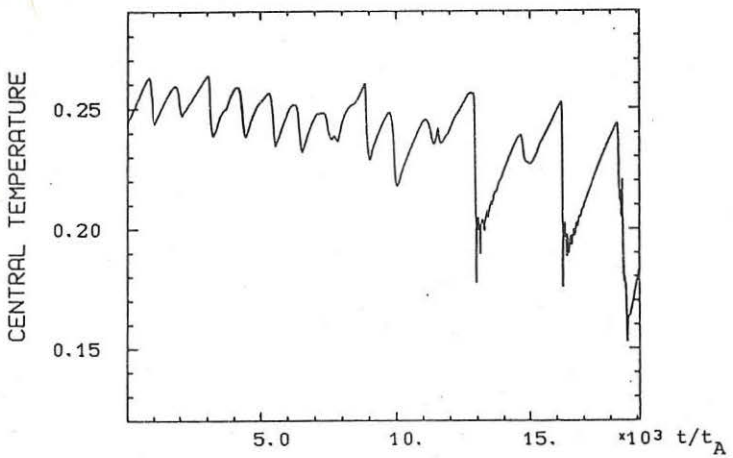

Figure 1. Time evolution of central temperature

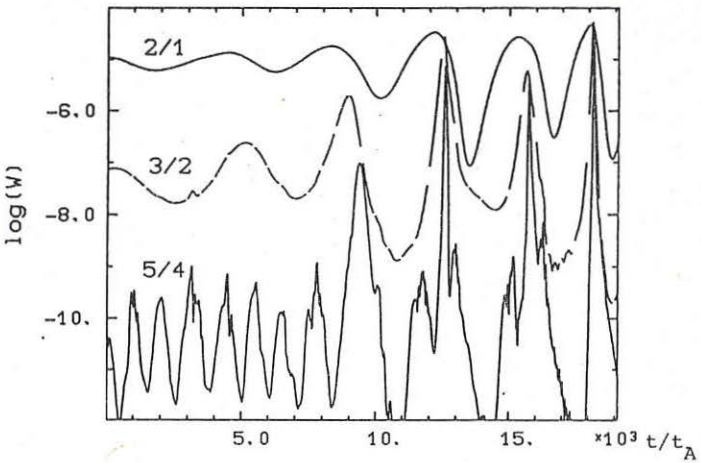

Figure 2. Mode energies vs. time in a run where the plasma current is slowly increasing

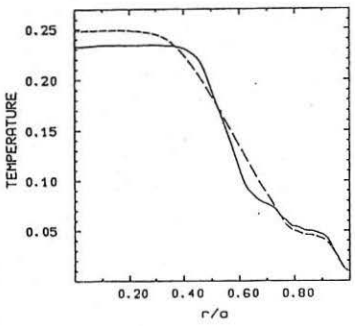

Figure 3. Temperature profiles at t/t_A=7300 (--) and 9125 (—).

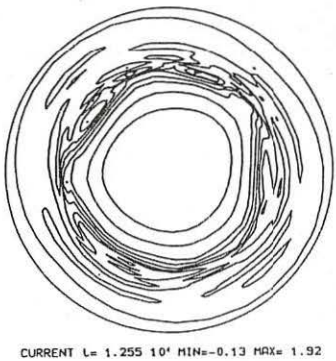

Figure 4. Current density near end of first disruption.

SAWTEETH: A CRITICAL COMPARISON OF TWO MODELS

E. Westerhof and W.J. Goedheer

Association Euratom-FOM, FOM-Instituut voor Plasmafysica "Rijnhuizen"
Nieuwegein, The Netherlands

INTRODUCTION

Sawteeth are a phenomenon widely studied in tokamaks, but the underlying physical processes are still unclear. This is reflected by the number of different models proposed to explain the sawtooth oscillations, see e.g. [1-6]. The present paper is intended as an attempt to answer some of the questions on the underlying physics. The emphasis here will be on the period and amplitude of the sawteeth. For this purpose two discharges of the T10 tokamak [7] were selected and simulated with the transport code ICARUS [8], in which models for the sawtooth oscillation were incorporated. Both discharges are heated by electron cyclotron waves, but have a different toroidal magnetic field and thus a different power deposition profile.

Two different models were used to describe the sawtooth dynamics, each being representative of a certain class of models. The first [2] belongs to the class of models which ascribe the internal disruption to the mixing which accompanies the fast reconnection of helical flux in or around the centre of the plasma. This model will be called the reconnection model. The second [6] belongs to the class of models which ascribe the internal disruption to an enhancement of radial transport, as caused by e.g. micro-turbulence generated by a degeneration of the X-point of an m=1, n=1 island into a line [5]. This model will be called the turbulent model.

THE TRANSPORT MODEL

The transport code solves the following set of equations by a Cranck Nicolson scheme [8]

$$\frac{\partial}{\partial t} B_\theta = + \frac{\partial}{\partial r} \frac{\eta}{r} \frac{\partial}{\partial r} r B_\theta, \tag{1a}$$

$$\frac{\partial}{\partial t} n_e = + \frac{1}{r} \frac{\partial}{\partial r} r \left[D_n \frac{\partial}{\partial r} n_e - n_e v_{an} \right] + S_n, \tag{1b}$$

$$\frac{\partial}{\partial t} p_e = + \frac{1}{r} \frac{\partial}{\partial r} r n_e \chi_e \frac{\partial}{\partial r} T_e + P_{OH} - P_{ei} - P_{rad} + P_{ECH}, \tag{1c}$$

$$\frac{\partial}{\partial t} p_i = + \frac{1}{r} \frac{\partial}{\partial r} r n_i \chi_i \frac{\partial}{\partial r} T_i + P_{ei}, \tag{1d}$$

where η is the neoclassical resistivity for $Z_{eff} = 2.2$, D_n and v_{an} are the anomalous particle transport coefficient and inward drift, respectively, defined by

$$D_n = c_D \chi_e; \quad v_{an} = - c_v 2 D_n \frac{r}{a^2}, \tag{2a,b}$$

S_n is the particle source, χ_e is the anomalous electron heat conductivity, taken to be [7]

$$\chi_e = \begin{cases} \chi_o & r < .15 \text{ m} \\ \chi_o + \dfrac{r - .15}{.325 - .15}(\chi_m - \chi_o) & r \geq .15 \text{ m}, \end{cases} \tag{3}$$

P_{OH}, P_{ei}, P_{rad} and P_{ECH} are the heating sources and losses (Ohmic, electron-ion energy equilibration, radiation, and electron cyclotron heating, respectively) and χ_i is the ion heat conductivity taken to be a multiple of the neoclassical value. During additional heating χ_o was multiplied by 1.5.

THE SAWTOOTH MODELS

In the reconnection model [2] an m = 1, n = 1 island starts growing when q < 1. The island growth is exponential and the growth rate, γ, is given by the linear growth rate of the m = 1, n = 1 tearing mode in the undisturbed plasma, which is [9] a solution of

$$\gamma^3 - i\gamma^2(\omega_{*e} + \omega_{*i}) - \gamma\omega_{*e}\omega_{*i} = 1/\tau_R\tau_H^2 , \tag{4}$$

where $\omega_{*e(i)}$ is the electron (ion) drift frequency and $\tau_{R(H)}$ is the resistive (Alfvén) time. In the transport code this growth rate is multiplied by a phenomenological constant, c_γ, in order to be able to reproduce the observed sawtooth period. If the island fills the region with q < 1, i.e., if $\delta = r_s$, a disruption occurs on a timescale equal to γ^{-1}, during which particles, energy and flux are redistributed according to Kadomtsev [1].

In the turbulent model [6] an m = 1, n = 1 island grows, when q < 1, on a resistive timescale as appropriate for the nonlinear regime of the m = 1, n = 1 mode [5],

$$\frac{d}{dt}\delta^2 = 3\eta. \tag{5}$$

When the island reaches its critical size δ_c, [6], given by

$$\delta_c = A\hat{s}^{-2}; \quad \hat{s} \equiv \left[r\frac{dq}{dr} \right]_{r_s}, \tag{6}$$

where A is chosen so as to reproduce the observed sawtooth period, an internal disruption occurs during which the radial transport of praticles and energy is enhanced in the region inside and around the q = 1 surface by a factor (10 to 10^3) and the m = 1, n = 1 island disappears (or is reduced substantially). The duration of the internal disruption is a free parameter, taken from the experiment.

RESULTS AND DISCUSSION

Both discharges were simulated with roughly the same transport model and basic plasma properties. These data are given in Table I. In the turbulent model we took A = .085 for both discharges. In the reconnection model we used c_γ = .06 (.05) for discharge nº 23517 (-594). The resulting evolution of the central temperature is displayed in Figs. 1 and 2. In the case of central heating the turbulent model predicted a decrease of the sawtooth period, as seen in the experiment, while the reconnection model predicted an increase. Also, the amplitude is clearly too large in the reconnection model during heating.

For off-axis heating the sawtooth disappeared altogether in the turbulent model, because $\hat{s}$ was strongly reduced. In contrast, in the reconnection model the period hardly changed, but the amplitude vanished while the q = 1 surface shifted inwards. Thus both models reproduced the observations equally well: the former because the period became effectively infinite and the latter because the amplitude vanished.

In the case of central heating the turbulent model clearly simulates the observations better. The reconnection model, however, could be improved by using a different trigger criterion for the internal disruption. A simulation

adopting a fixed value of q on axis (e.g., $q_o = .9$) as a criterion for an internal disruption did not lead to a significantly smaller sawtooth period during central heating. Instead, an increase of the period was again predicted.

One is led to the conclusion that the trigger for sawtooth collapse has to be a very sensitive function of the shear (in the turbulent model the period is proportional to $\hat{s}^{-4}$). The energy redistribution is better described in terms of enhanced transport than by reconnection, the latter giving rise to too large an amplitude in the case of central heating. This is related to the fact that reconnection leads to hollow (or completely flat) temperature profiles immediately after the internal disruption, whereas the profiles preserve a maximum on axis in the experiment [7].

Table I: Basic plasma and transport variables.

	T10-23517			T10-23594		
	Exp.	reconn.	turb.	Exp.	reconn.	turb.
B_ϕ(T)	3.0	3.0	3.0	3.3	3.3	3.3
I(kA)	335	335	335	335	335	335
Z_{eff}	2.2	2.2	2.2	2.2	2.2	2.2
$\langle n_e \rangle$ (m^{-3})	$5\ 10^{19}$	$4.9\ 10^{19}$	$4.9\ 10^{19}$	$5\ 10^{19}$	$5.0\ 10^{19}$	$5.0\ 10^{19}$
χ_o	-	0.3	0.3	-	.275	.3
χ_m	-	2.0	2.0	-	2.2	2.0
c_D	-	0.35	0.35	-	0.35	0.35
c_v	-	0.9	1.0	-	0.8	0.8
$\chi_i/\chi_{n.cl}$	-	3	3	-	3	3

REFERENCES

[1] B.B. Kadomtsev, Sovjet Journal of Plasma Physics **1** (1975) 389-391.
[2] G.L. Jahns et al., Nuclear Fusion **18** (1978) 609-628.
[3] V.V. Parail and G.V. Pereverzev, Sovjet Journal of Plasma Physics **6** (1980) 14-17.
[4] W. Pfeiffer, Nuclear Fusion **25** (1985) 673-679.
[5] M. Dubois and A. Samain, Nuclear Fusion **25** (1980) 1101-1109.
[6] E. Westerhof and W.J. Goedheer, in 'Magnetic Reconnection and Turbulence'. M.A. Dubois et al. editors (Éditions de Physique, Orsay, 1985), p. 243-248.
[7] R. Sillen et al., Nuclear Fusion **26** (1986) 303-327.
[8] M. Watkins et al., in 'Methods in Computational Physics' **16** (1976), eds. J. Killeen et al. (Academic Press, New York).
[9] F. Pegoraro and T.J. Schep, accepted for publication in Plasma Physics.

ACKNOWLEDGEMENT

This work was performed under the EURATOM-FOM association agreement with financial support from ZWO and EURATOM.

FIGURE CAPTIONS

Fig.1: Evolution of $T_e(o)$ in case of central heating.
a) experiment; b),c) simulation with the reconnection and turbulent model, respectively.

Fig.2: Evolution of $T_e(o)$ in case of off-axis heating.
a),b),c) as in figure 1.

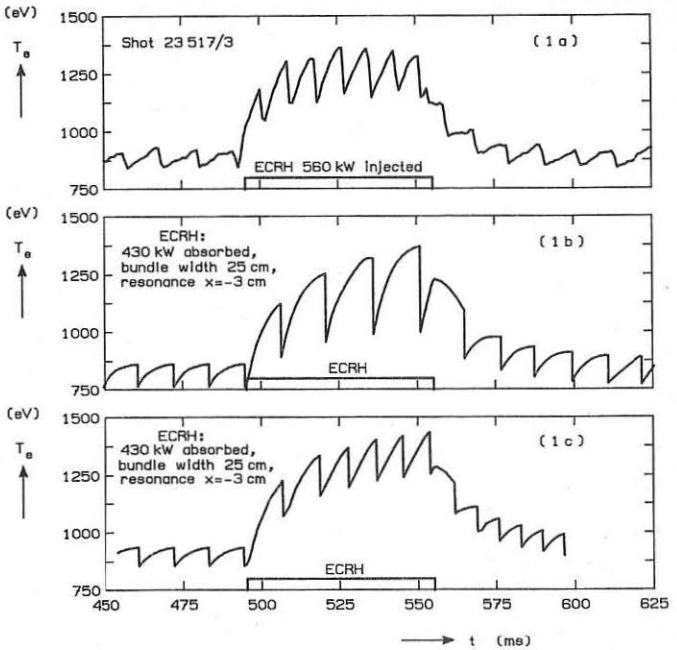
(eV)
T_e
1500
1250
1000
750
Shot 23517/3
(1a)
ECRH 560 kW injected
(1b)
ECRH:
430 kW absorbed,
bundle width 25 cm,
resonance x=-3 cm
ECRH
(1c)
ECRH:
430 kW absorbed,
bundle width 25 cm,
resonance x=-3 cm
ECRH
450
475
500
525
550
575
600
625
t (ms)

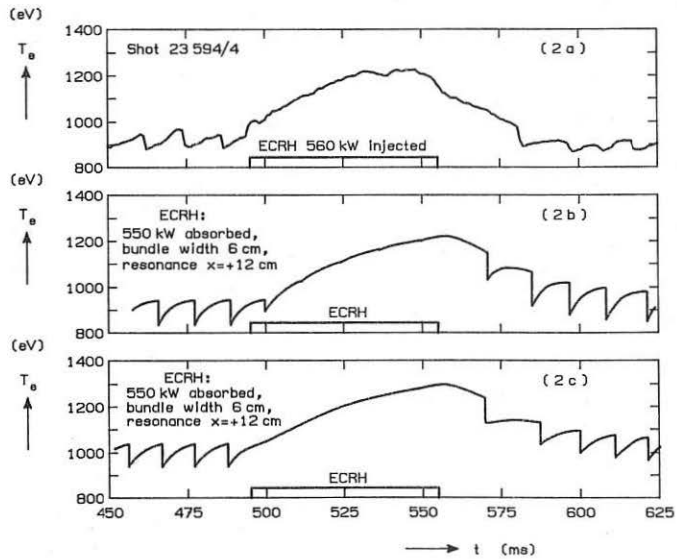
(eV)
T_e
1400
1200
1000
800
Shot 23594/4
(2a)
ECRH 560 kW injected
(2b)
ECRH:
550 kW absorbed,
bundle width 6 cm,
resonance x=+12 cm
ECRH
(2c)
ECRH:
550 kW absorbed,
bundle width 6 cm,
resonance x=+12 cm
ECRH
450
475
500
525
550
575
600
625
t (ms)

MHD CHARACTERISTICS OF ASDEX H-TYPE DISCHARGES APPROACHING THE ß LIMIT

O. Klüber, J. Gernhardt, K. Grassie, J. Hofmann, M. Kornherr, R. Stambaugh[1], H. P. Zehrfeld and G. Becker, H. S. Bosch, H. Brocken, A. Eberhagen, G. Fussmann, O. Gehre, G.v.Gierke, E. Glock, O. Gruber, G. Haas, A. Izvozchikov[2], G. Janeschitz, F. Karger, M. Keilhacker[3], K. Lackner, M. Lenoci, G. Lisitano, F. Mast, H. M. Mayer, K. McCormick, D. Meisel, V. Mertens, E. R. Müller[3], H. Murmann, H. Niedermeyer, A. Pietrzyk[4], W. Poschenrieder, H. Rapp, H. Riedler, H. Röhr, J. Roth, F. Ryter[5], F. Schneider, C. Setzensack, G. Siller, P. Smeulders[3], F.X. Söldner, E. Speth, K.-H. Steuer, O. Vollmer, F. Wagner, D. Zasche

Max-Planck-Institut für Plasmaphysik
EURATOM Association, D-8046 Garching

1. Introduction

Due to the favourable confinement properties of the H regime, ß values close to the Troyon limit can be achieved in the ADSEX device at a neutral injection power level ~3 MW. In many cases, the ß limit is a soft one, i.e. ß attains a maximum and then decays smoothly up to the end of the injection pulse. Disruptions, however, may occur both during the rise and fall of ß.

2. Temporal evolution of MHD activity in the case of soft ß limit

The investigations presented below are mainly based on the analysis of Mirnov probe signals. Due to the divertor geometry, only a fraction of the poloidal circumference could be covered, namely 102° at the outside and 44° at the inside of the torus symmetric to the midplane. The toroidal mode number n is obtained from 5 probes placed in the midplane at the outer side distributed over a toroidal angle of 156°. Apart from a few n=2 cases not discussed in this paper, always n=1 is observed.

In ohmically heated ASDEX divertor discharges, MHD activity is very weak apart from disruptive ones; in this case the common m = 2, n = 1 precursor is seen. Application of neutral beam heating at sufficient power level (maximum 3.5 MW in the case of H_0 injection) leads to a continuous mode which develops during the L phase and attains a steady state lasting up to the end of the injection pulse if the discharge remains in the L regime. In the case of transition into the H-type confinement regime, however, the amplitude of the continuous mode decreases at some time after the H transition to a low level; in the further course of the discharge bursts occur as shown in Fig. 1. It is seen from Figs. 2 and 3 that these bursts have a fishbone-like character, i.e. increase and decrease of amplitude with a half-width of a few oscillations; they are referred to as fishbones in what follows.

It is well known that H-type discharges exhibit another quite different kind of MHD activity, too, namely the so-called ELMs. The most prominent manifestation of an ELM is the sudden change of the equilibrium position of the plasma column by typically a few mm (indicating a sudden decrease of the

---

[1]GA Technologies, San Diego, Calif., USA; [2]Academy of Sciences, Leningrad, USSR; [3]Present address: JET Joint Undertaking, England; [4]Univ. of Washington, Seattle, USA; [5]CEN Grenoble, France

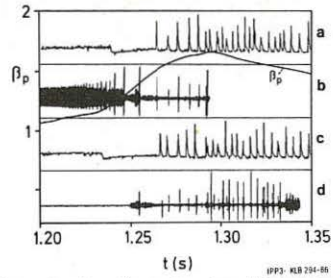

Fig. 1: β_p, H_α emission (traces a,c) and β_θ (traces b,d) versus time for shots No. 18030 (a,b) and 18034 (c,d). Injection starts at 1.13 s and stops at 1.43 s. The temporal evolution of β_p is practically the same for both discharges.

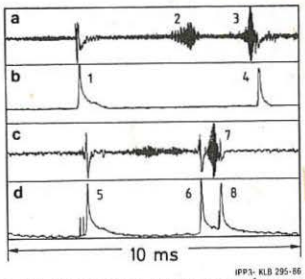

Fig.2: Examples for ELMs (events No. 1,4,5,6,8) and fishbones (events No. 2,3,7) recorded by Mirnov probes (traces a,c) and H_α monitor (traces b,d).

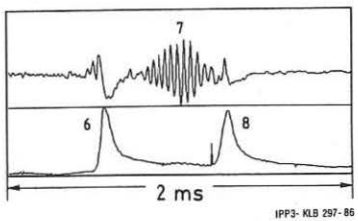

Fig. 3: Expansion of the sequence 6-7-8 from Fig. 2.

equilibrium parameter $\beta_p + l_i/2$) and a peak in the H_α emission. ELMs do not manifest, however, in the records of the Mirnov probes apart from the inward motion.
It is seen from Fig. 2 that ELMs and fishbones may occur independently from each other; on the other hand, fishbones appear to be triggered by ELMs in some cases and, more frequently, ELMs appear to be triggered by fishbones.

There are several features which are common to the continuous and the fishbone-like mode, namely

- The amplitudes measured at the outer side of the torus are much larger than those at the inner side. Amplitude ratios of 15 - 25 are typical; in many cases, the ratio must be even larger since no signals from the inner probes are obtained. Obviously, the determination of the poloidal mode number is particularly difficult in this situation.
- The frequency recorded by the soft X-ray diode cameras coincides with that of the Mirnov probe signals. During the continuous mode, an m = 1, n = 1 structure with frequency doubling is clearly seen. In the case of the fishbone-like events, the amplitudes are much smaller. In some cases, doubling of frequency was observed in near-center channels which indicates that the q = 1 surface may still be present.
- The mode propagates according to the toroidal rotation of the plasma applied by the unidirectional co-injection. Doppler shift measurement can only be obtained from a small zone at $R \sim R_o + 3a/4$. The velocity calculated from the mode frequency is systematically by a factor of 1.4 larger than the spectroscopic one. This discrepancy increases if an additional motion of the mode due to the diamagnetic drift is assumed. Thus, the mode frequency appears to be governed by the central rotation velocity.

It is seen from Fig. 1 that the repetition rate of the ELMs does not vary appreciably during the rise and the fall of ß. Fishbones appear more frequently in the ß decay phase. The duration of a fishbone-like burst, however, is less than 1 ms and the island size estimated from the amplitude of $\dot{B}$ is typically of the order of a few cms. Hence, for this type of shots, the observed MHD activity does not explain the decay of ß.

3. Discharges dominated by an m=2, n=1 mode

Another type is characterized by a dramatic change of the mode structure. A typical example is shown in Fig. 4. It is seen that at 1.29 s a continuous mode develops the amplitude of which increases suddenly at the inner side of the torus. A temporal expansion of this event is shown in Fig. 5. The change

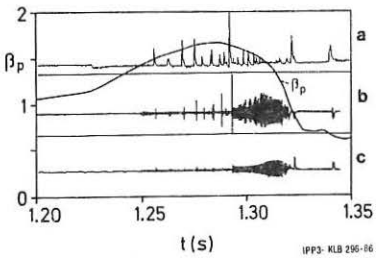

Fig. 4: $ß_p$ versus time for shot No. 18033. Injection starts at 1.13 s. The first disruption occurs at 1.32 s. Trace a: H_α emission. Trace b: $\dot{B}_\theta$ from a Mirnov probe located in the midplane at the outside of the torus. Trace c: Same for the inside.

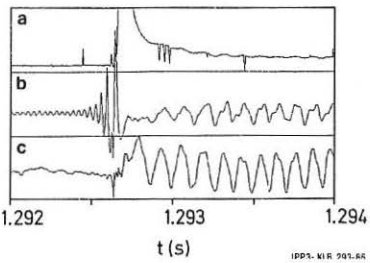

Fig. 5: Onset of the m=2 oscillation in shot No. 18033. Trace a: H_α signal (diode saturates). Trace b: Mirnov signal, midplane outside. Trace c: Mirnov signal, midplane inside. The amplitude is enhanced by a factor of 4 as compared to trace b.

of the mode structure is initiated by an ELM which is preceded by a fishbone. It is seen from Fig. 4 that the amplitude of the H_α spike of this particular ELM exceeds by far that of the preceding and the following ones. After the transition, the mode continues to propagate in the direction given by the toroidal rotation; the frequency of it decreases, however, by a factor between 2 and 4. Most remarkably, the ratio of the frequencies before and after the transition is close to an integral number. Furthermore, it is seen that the frequency recorded before the tansition remains with a small amplitude which lasts for typically 10 ms. Later on, only the "slow" mode is recorded. It is clearly an m = 2, n = 1 mode, as shown in Section 4.
In the case presented in Fig. 4, the m = 2 mode leads to a disruption after 30 ms. In the last ms before the onset of the disruption, the signal frequency decreases drastically. In other discharges, the m = 2, n = 1 mode may attain a saturated level and persist up to the end of the NI pulse. In both cases, the island size is large and may amount up to 20 % of the minor radius of the plasma column. It is seen from Fig. 4 that the onset of the m = 2, n = 1 mode leads to a violent decrease of $ß_p$.
Most frequently, the onset of the "large" m = 2 mode occurs nearly at the time at which ß attains its maximum. In some cases, however, this mode develops already in the phase of ß rise, in particular, if q_a is low.

4. Discussion of the poloidal mode structure

In the discharges considered here, the boundary q value is $3.5 < q_a < 4.5$. Hence the mode numbers m = 2,3 and 4 (if $q_a > 4$) are the candidates for the explanation of the mode structure. In a previous paper /1/, one of the authors investigated the effect of the toroidal curvature on the poloidal mode structure. In this model, the modes are created by surface currents flowing on rational magnetic surfaces parallel to the magnetic field. Typical examples for the modes m = 2,3 and 4, n = 1 are plotted in Fig. 6 where the phase is chosen such, that a maximum is located in the midplane at the outer side of the torus. It is seen that the amplitudes at the outer side of the torus exceed those at the inner side considerably. The amplitude ratio depends, of course, on $\beta_p + l_i/2$, on the aspect ratio of the resonant surfaces and on the position of the plasma column and may amount up to 5. It is further seen that the mode structure is distorted towards the inner side of the torus where the distortion is rather moderate in the case m=2 but increases drastically with increasing mode number.

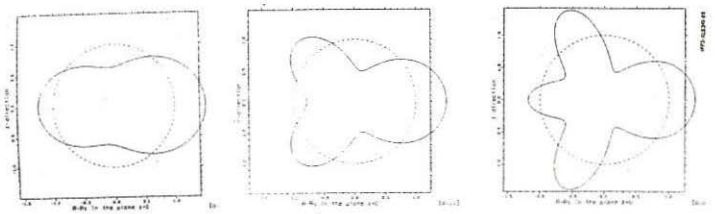

Fig. 6: Polar diagrams of the modes m = 2,3,4. The torus axis is on the left-hand side.

While the m=2 mode discussed in the preceding section fits quite well into this picture, the continuous and the fishbone-like mode cannot be explained by this model. The observed out-in amplitude ratios of 15 - 25 might be ascribed to the occurrence of two modes, an even and an odd one, coupled such that two maxima coincide in the midplane at the ouside. It is seen from Fig. 6, however, that all three modes pretend an m=2 structure as far as the outer side of the torus is concerned. This contradicts to the observed phase relations according to which phase reversal is obtained at poloidal angular distances between 45° and 60° (which would indicate a superposition of m=3 and m=4 if the geometry were cylindrical).
Obviously, rational magnetic surfaces with m > 4 are also present due to the separatrix. They are located, however, in a region with very large shear and hence very small island sizes. It is unlikely, therefore, that modes with appreciable amplitudes develop in this region.

5. Summary

- Three types of MHD oscillations were observed, a continuous, a fishbone-like and an m=2, n=1 mode.
- The decay of ß can be attributed to observable MHD activity only in the cases in which a strong m=2, n=1 mode develops.
- The continuous and the fishbone-like mode cannot be ascribed to currents flowing parallel to the magnetic field on rational surfaces.

Reference:

/1/ G.Fussmann, B.J.Green, H.P.Zehrfeld, Plasma Phys.and Contr.Nucl.Fus.Res. 1980 (Proc.10th Int.Conf.Brussels, 1980), Vol.I,IAEA, Vienna (1980) 353.

MHD-EFFECTS WITH NI AND ICRF HEATING ON ASDEX

M. Kornherr, A. Eberhagen, J. Gernhardt, O. Klüber, F. Wagner, G. Becker, H. S. Bosch, H. Brocken, G. Fussmann, O. Gehre, G.v.Gierke, E. Glock, O. Gruber, G. Haas, J. Hofmann, A. Izvozchikov[1], G. Janeschitz, F. Karger, M. Keilhacker[2], M. Kornherr, K. Lackner, M. Lenoci, G. Lisitano, F. Mast, H. M. Mayer, K. McCormick, D. Meisel, V. Mertens, E. R. Müller[2], H. Murmann, H. Niedermeyer, J.-M. Noterdaeme, A. Pietrzyk[3], W. Poschenrieder, H. Rapp, H. Riedler, H. Röhr, J. Roth, F. Ryter[4], F. Schneider, C. Setzensack, G. Siller, P. Smeulders[2], F.X. Söldner, E. Speth, K.Steinmetz, K.-H. Steuer, O. Vollmer, F. Wesner, D. Zasche

Max-Planck-Institut für Plasmaphysik
EURATOM Association, D-8046 Garching

Introduction

With high power auxiliary heating at increased plasma pressure many new MHD phenomena occur which can be studied most suitably by observation of the soft X-ray ("SX") radiation. In the plasma centre NI excites large m=1, n=1 oscillations, the detailed behaviour of which depends on external parameters. In divertor discharges with NI power $\lesssim$2 MW their occurrence is repetitive and terminated by sawteeth. When NI is combined with ICRH the m=1 mode often disappears after a first strong sawtooth which is followed by "precursor-free" large sawteeth.

The hot spot model

Detailed studies of the m=1 mode and of sawtooth activity have been made in ASDEX mainly based on the analysis of the signals of two SX diode cameras. In the case of a toroidal rotating plasma and disregarding a possible poloidal rotation these signals represent the projection of an asymmetric and helical radiation profile into the viewed poloidal cross section. From comparison with ECE measurements we conclude that the oscillating SX signals are mostly caused by varying electron temperatures.

Figure 1 shows an example of an m=1 mode during NI rotating opposite to the electron drift direction. The behaviour of the signals (doubled frequency, phase relations) can be well described by a rotating hot spot with an extension 2D, which is much larger than the distance Δ of its centre to the magnetic axis (Fig. 2). The hot spot centre describes a circle with radius Δ around the magnetic axis, the off-axis rotation of the hot spot affects a plasma roughly within the q = 1 zone.

Assuming growing values of Δ (at fixed D) we can distinguish three possibilities concerned to a chord with distance Z to the magnetic axis. These three cases and their characteristic different features are exhibited schematically in Fig. 3a,b,c (the dashed curves belong to parallel but opposite to the axis positioned chords with the same distance Z).

---

[1]Academy of Sciences, Leningrad, USSR; [2]Present address: JET Joint Undertaking, England; [3]Univ. of Washington, Seattle, USA; [4]CEN Grenoble, France

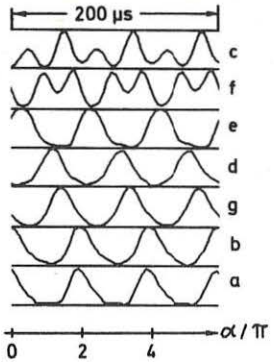

Fig. 1: SX traces of a m=1 mode with positions shown in Fig.2.

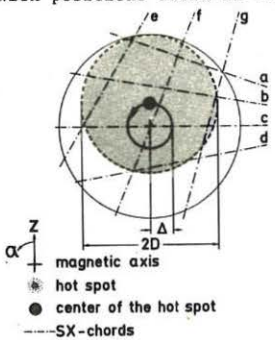

Fig. 2: The hot spot model.

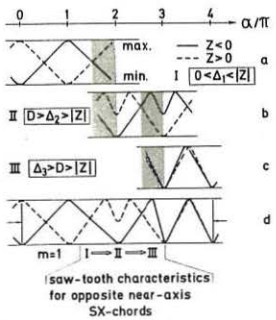

Fig. 3: Characteristics of the hot spot model for different cases with transitions (sectors hatched).

The sawtooth collapse

Near-axis SX chords show even during the conventionally defined period of the sawtooth collapse an oscillatory structure which seems to evolve from the m=1 mode with typical deviations from it. Such traces were interpreted as relaxation into an m=0 mode or a sudden change of direction of rotation.

With the assumption of a growing Δ, however, the observed behaviour as seen in the near-centre chords can well be described by the hot spot model.

Figure 3d exhibits the characteristic behaviour of two opposite chords during such a growth phase. The picture is "constructed" with the assumption of a transition from case I to case II and finally to case III each in a half period. Measured signals from two opposite SX channels with a radial distance R = 2.5 cm ($\approx$ Z) agree very well with this model - Fig. 4b demonstrates an example.

Another example is presented in Fig. 5 (an expended section of Fig. 6). While the central chord points toward a precursor-free sawtooth the near-axis chords show clearly the development of a weak m=1 mode which is followed after two periods by the sawtooth transition with the typical evolution described above (Fig. 5a). Opposite chords with a larger distance R from the axis exhibit this transition one half period later.

Heat wave propagation

The developed picture based on the hot spot model explains the spikes in the SX traces and their irregular nature as often seen when SX signals are plotted on a large time scale (Fig. 6). The traces of this example document that the hot spot does not reach the plasma edge and the mode is damped. The hot spot decays and a heat pulse propagates to the plasma edge on a time scale roughly two orders of magnitude larger than the collapse time and with a velocity of about 10^4 cm/sec.

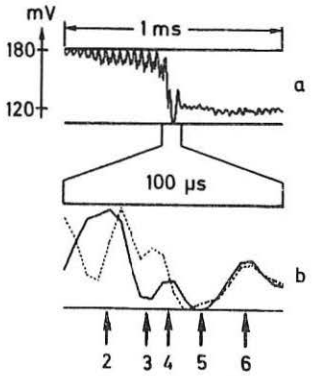

Fig. 4: a) The central signal from a sawtooth event with preceding m=1 mode. b) Vertically opposite near-axis signals during this sawtooth transition. The expended interval corresponds to the marked segment (by arrows) in Fig. 3d.

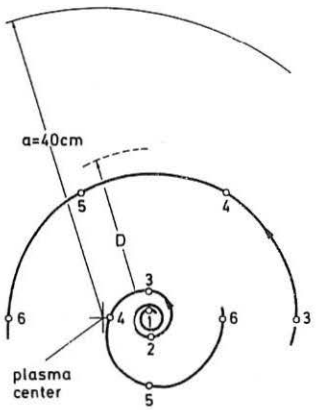

Fig. 7 The inner spiral represents the path of the hot spot centre during a sawtooth transition, the outer curve describes the movement of a second hot spot centre which is assumed to originate from the first one. The marked time points correspond to the arrows of Fig. 4b and 8.

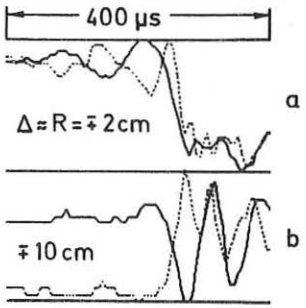

Fig. 5: A sawtooth transition after a weak but rapidly developing m=1 mode, shown for opposite channels at different distances from the magnetic axis.

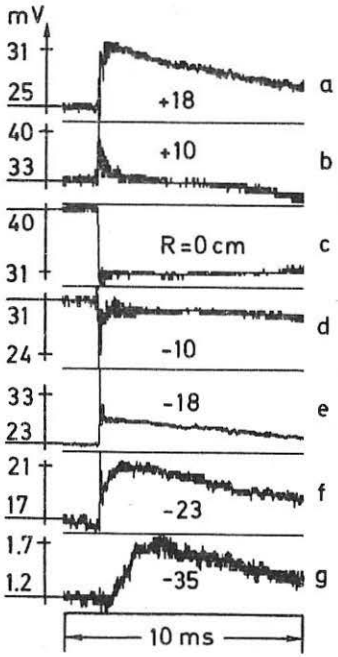

Fig. 6: A sawtooth collapse with typical spikes and the propagating heat pulse.

MHD activity

Together with the signals of a second camera the movement of the hot spot from the example described in Fig. 4 was reconstructed. Fig. 7 shows the path of the centre of the hot spot, which starts from an m=1 mode (marked time point 1) and roughly describes a spiral. After the time point 4 the determination of Δ becomes uncertain. From time point 3 on a second hot spot is clearly seen which rotates at a larger radius. The phase relation between both hot spots is well described by the assumption of a frequency ratio 3/2. Within the sawtooth transition the phase velocity of the inner hot spot decreases to about its half original value. During the m=1 mode Δ is smaller than 2 cm, the centre of the mode activity is clearly shifted outwards from the plasma centre and the mode structure is observed up to $r \approx 14$ cm.

Within the transition 2 to 3 the value of Δ increases to about 6 cm and the mode structure extends to $r \approx a/2$. The central channel shows at time point 3 a first distinct minimum and does not reach again its maximum value when the hot spot passes the horizontal channel at time point 4. It is assumed that the original hot spot is deformed and breaks up simultaneously when Δ starts to increase. Its absolute minimum shows the central channel at time point 5 and a last clear relative maximum is observed at time point 6.

In the following phase the MHD activity within a/2 becomes complicated but remains regular and ends finally in a stationary low frequency m=3 mode.

A thermal wave on a equilibrium transport time scale does not develop in this case. Beginning from time point 3 the outer plasma region ($r > a/2$) shows growing signals. Already at time point 5 these signals reach a first maximum at the top and bottom of the plasma. These maxima are followed by a somewhat larger signal at the top and a tremendous burst at the bottom region rising only 50 µsec after the beginning of the sawtooth transition with a duration of 200 µsec (Fig. 8). In this case the energy transport from the plasma core to the edge caused by a sawtooth event occurs on an ideal MHD time scale.

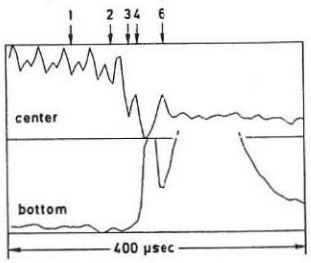

Fig. 8: SX signals from the central and edge chord during and after the sawtooth transition of Fig. 4b.

The sawtooth events discussed before were observed at the following experimental conditions. Fig. 4/7/8:
I_p = 380 kA, $q_{a,cyl}$ = 2.7;
$\bar{n}_e = 2.4 \cdot 10^{13}$ cm^{-3} increased from $1.5 \cdot 10^{13}$ cm^{-3} by means of a strong Ne puff;
NI power 3.4 MW; L-mode discharge with m=1 frequency of 26 kHz;
sample frequency 200 kHz.
Fig. 5/6:
I_p = 380 kA; $q_{a,cyl}$ = 2.9;
$\bar{n}_e = 3.5 \cdot 10^{13}$ cm^{-3}
NI power 1.7 MW + ICRH with 400 kW;
sample frequency 100 kHz.

CHARACTERISTICS OF BROADBAND MAGNETIC AND DENSITY FLUCTUATIONS IN THE TCA TOKAMAK

Ch. Hollenstein, R. Keller, A. Pochelon, M.L. Sawley, W. Simm and H. Weisen

Centre de Recherches en Physique des Plasmas
Association Euratom - Confédération Suisse
Ecole Polytechnique Fédérale de Lausanne
21, Av. des Bains, CH-1007 Lausanne / Switzerland

Abstract

The results of studies of broadband magnetic and density fluctuations during ohmic discharges in the TCA tokamak[1] are described.

Introduction

Three different diagnostics have been employed to investigate the broadband spectrum of fluctuations observed at frequencies greater than the Mirnov frequency (≃ 10kHz in TCA): (i) magnetic probes placed at various poloidal and toroidal locations in the shadow of the limiters, (ii) a triple Langmuir probe for scrape-off plasma measurements, and (iii) a novel CO_2 laser phase contrast diagnostic[2] that yields line-integrated density fluctuations along selected vertical chords of the plasma cross-section.

In Fig. 1 is shown an example of the power spectrum of the magnetic fluctuations. By rotating a probe, ensuring precise measurement of the probe angle with respect to the static field B_ϕ, the fluctuation field has been determined to be polarized in the plane normal to the total magnetic field at the probe position ($\tilde{b}_\parallel/\tilde{b}_\perp \lesssim 10^{-2}$). The level of the magnetic fluctuations, measured 4 cm behind the limiter, is in the range $[\tilde{b}_\theta(f>40kHz)/B_\theta]_{rms} = 10^{-5}$-$10^{-4}$. It is found to scale inversely with energy confinement time, suggesting a possible relation with confinement.[3,4]

The Langmuir probe measurements in the scrape-off layer show a high relative level of fluctuation ($\tilde{n}_e/n_e \simeq$ 50-100%). Correlation between the fluctuations in density and potential yields an outward-directed transport, which is dominated by the low frequency contribution (see Fig. 2).[5]

From the phase contrast diagnostic it has been determined that the absolute level of the chord-averaged fluctuations is rather constant for $r/a < 0.5$. This suggests that the fluctuation level is largest in the gradient region ($\tilde{n}_e/n_e \simeq$ 10% is estimated for $r/a = 0.75$).

Comparison between diagnostics

The results obtained from the three diagnostics can be compared with respect to their spectral and spatial characteristics and also their dependence on the plasma parameters.

All three diagnostics yield power spectra that exhibit an $f^{-\alpha}$ dependence above a roll-off frequency f_c. Spectra determined from the phase contrast diagnostic viewing a central chord are considerably

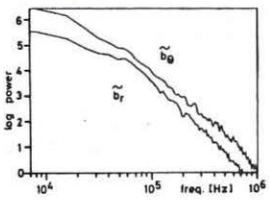

Fig. 1

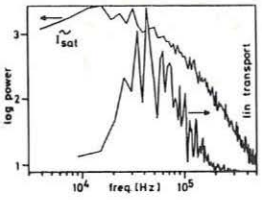

Fig. 2

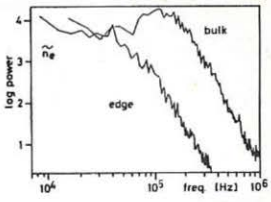

Fig. 3

broader than those obtained from the Langmuir probe, but quite similar for an edge chord that does not probe the bulk plasma (Fig. 3). Figure 4 shows that f_c gradually decreases from ~150kHz for a central chord to the low values (30-80kHz) measured by the Langmuir probe in the scrape-off layer. This figure also shows that the spectral index α for density fluctuations is only weakly dependent on position. The spectral indices for both density and magnetic fluctuations are not strongly dependent on the plasma parameters. (For the parameters of Fig. 4, $\alpha \simeq 3$ for $\tilde{b}_\theta$.)

Correlation measurements using the Langmuir probes yield poloidal phase velocities in the range $1 - 5 \times 10^5$ cm s^{-1} (ion diamagnetic direction), while about 5×10^5 cm s^{-1} is obtained from the phase contrast diagnostic (undetermined direction).

Evidence of significant coherence over long distances has been obtained from both the phase contrast diagnostic and the magnetic probes. Figure 5 shows the spatial autocorrelation function of the density fluctuations obtained from two scannable detectors. For frequencies up to 100 kHz, sizable coherence is observed between chords separated up to 7 cm. In fact, more than half the spectral power of the density fluctuations is associated with long wavelengths; $kr_s = kc_s/\omega_{ci} \lesssim 0.1$ (edge) and $kr_s \lesssim 0.3$ (bulk). These values are comparable to those predicted by strong drift wave models.[6] Although the poloidal coherence length for magnetic fluctuations is only a few centimeters, the examples shown in Fig. 6 demonstrate that significant levels of coherence have been observed from probes in diametrically opposite poloidal ($\Delta\phi=0$, $\Delta\theta=\pi$) and toroidal ($\Delta\phi=\pi$, $\Delta\theta=\pi/2$) planes. This substantial coherence is measured up to ~400 kHz, well above the discernible harmonics of the Mirnov frequency. (A somewhat irreproducible measured phase relation has hampered interpretation in terms of

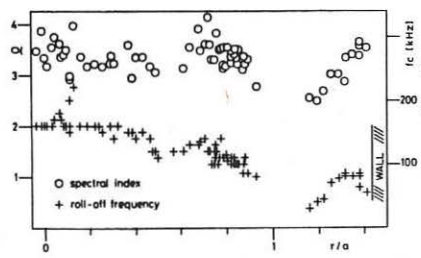

Fig. 4

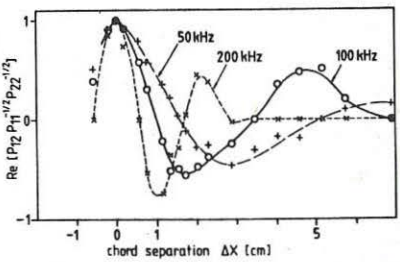

Fig. 5

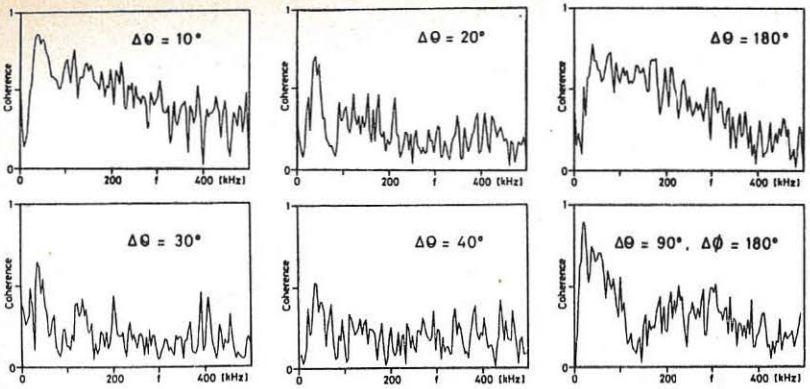

Fig. 6

wave propagation, as for the other two diagnostics.) Despite this observation of long coherence lengths, presumably along the total magnetic field direction, we have found no evidence of significant linear coherence between signals measured by the different diagnostics.[7]

The parametric dependence of the level of density fluctuations measured along a central chord (Fig. 7(a)) constrasts with that measured for $\tilde{b}_\theta$ (Fig. 7(b)). Although $\tilde{n}_e$ increases linearly with n_e, a decrease in $\tilde{b}_\theta$ is measured if n_e is increased. Also, $\tilde{n}_e$ does not exhibit the dependence with plasma current that is observed for $\tilde{b}_\theta$.

Finally, the correlation dimension[8] of the fluctuations has been studied. Signals from each of the three diagnostics, filtered above 40 kHz, yield a high dimension; $\nu > 8$ for the available resolution. For signals containing a large low frequency component, no reliable estimate of the dimension could be obtained.

Conclusions

Long coherence lengths have been measured for both density and magnetic fluctuations. The possible importance of these measurements is stressed by the Langmuir probe results that show that the fluctuation-induced transport is dominated by the long wavelength contribution. Although density and magnetic fluctuations exhibit similar spectral characteristics, no direct connection between them has been observed. The scaling of the density fluctuation level, $\tilde{n}_e/n_e \approx$ constant, does not indicate the same dependence on energy confinement time as measured for $\tilde{b}_\theta/B_\theta$. However, a more definite statement would require detailed measurements of the fluctuation-induced transport in order to determine the role of the observed fluctuations in energy confinement in tokamaks.

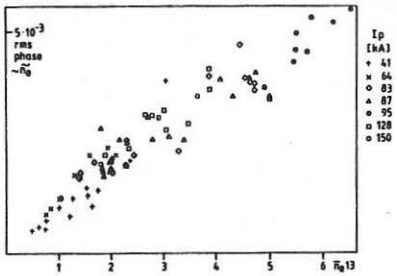

Fig. 7(a)

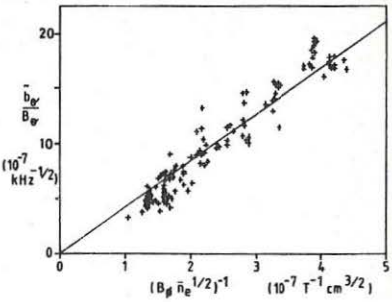

Fig. 7(b)

Acknowledgements

This work was partially supported by the Swiss National Science Foundation.

References

[1] TCA Team, Nucl. Fusion 25, 1041 (1985).
[2] H. Weisen, Infrared Phys. 25, 543 (1985).
[3] P.A. Duperrex et al., Phys. Lett. 106A, 133 (1984).
[4] M.L. Sawley et al., Proc. 12th Europ. Conf. Controll. Fusion and Plasma Phys., Budapest, Vol. I, 291 (1985).
[5] S.J. Zweben et al., J. Nucl. Mat. 111, 39 (1982).
[6] P.C. Liewer, Nucl. Fusion 25, 543 (1985).
[7] S.J. Zweben and R.J. Taylor, Nucl. Fusion 21, 193 (1981).
[8] P. Grassberger and I. Procaccia, Phys. Rev. Lett. 50, 346 (1983).

PROFILE CONSISTENCY ON TFTR

E. Fredrickson, K. McGuire, R. Goldston, S. Hiroe*, M. C. Zarnstorff, M. Bell, N. Bretz, J. D. Callen**, P. C. Efthimion, B. Grek, D. Johnson, D. McCune, G. Taylor, N. Sauthoff, F. Stauffer, and R. Wieland

Princeton Plasma Physics Laboratory, Princeton N.J., USA

*Oak Ridge National Laboratory, Oak Ridge Tenn. USA

**University of Wisconsin, Madison Wisconsin USA

Introduction

It has been observed on many tokamaks that the shape of the electron temperature profile is not strongly affected by other plasma parameters, but is only a function of the edge safety factor, q_a; the so-called principle of profile consistency [1]. Recently there has been renewed interest in this viewpoint, because of its strong implications for the next generation of tokamaks. This paper presents an analysis of electron temperature profile consistency in TFTR, and the results of experiments to elucidate the role of the current profile in profile consistency.

Equilibrium Electron Temperature Profiles

Approximately one hundred TFTR equilibrium electron temperature profiles, with $2.5<q_a<10$, $0<P_{Beam}<13$MW and $0.1<n_e(0)(x10^{20})<2.5$, were examined for systematic variations of the profile shape. It was found that the profile shape outside q=1.2 was only dependent on the minor radius, and was roughly independent of all other quantities, e.g., q_a, auxiliary heating, and density. This was also found for heavily beam heated low density discharges that showed evidence of significant beam driven current, and for discharges with very different beam deposition profiles [2].

For full bore (a=0.8 m) discharges, the inverse scale length, $-d(\ln T_e)/dr$, is $\approx 3\pm1$ m^{-1} independent of density, beam power and, most interestingly, of q_a in the range $2.5<q_a<10$ (Fig. 1). The profile shape was approximately exponential for $T_e > 1$ keV outside the sawtooth mixing radius.

In contrast, smaller minor radius plasmas (a= 0.55 m) have more nearly Gaussian T_e profiles outside the sawtooth mixing radius and within $T_e>1$ keV, as observed in previous experiments. For TFTR reduced minor radius discharges $T_e \propto \exp(-r^2/2\sigma^2)$ in this region, where $a^2/\sigma^2 \approx 4.5$. It was not possible to determine a scaling of σ with q_a.

In a tokamak, the current density, J, and T_e profiles are coupled in

steady state by the plasma resistivity. Thus, the observed constancy of the T_e profile shape might be due to constraints on the current profile shape [3]. To study the hypothesis that the electron temperature profile is strongly controlled by the contraints of tearing mode stability, a code which calculates $\Delta'_{m,n}$ from the equation $\nabla_\perp^2 \tilde{\Psi} = (mqR_0/(rB_T(m-nq))) (dJ/dr) \tilde{\Psi}$ is used to test current density profiles (calculated from the observed time dependant T_e profiles and neoclassical resistivity) for stability to tearing modes. These inferred current profiles for normal (non-disruptive) TFTR plasmas are generally found to be marginally stable.

Current Ramp Experiments

In an attempt to perturb the T_e profile, and the relationship between T_e and J, the plasma current was rapidly increased (at up to 3MA/sec) after achieving flattop, with and without neutral beam heating. The penetration of the current into the discharge was calculated using a time dependent transport code using the measured surface voltage and $T_e(t)$ profiles, and assuming neoclassical resistivity. The calculations were able to reproduce the observed Λ (Fig. 2). If all the extra current was localized at the edge of the plasma edge, the Λ would have dropped to about 0.2. If the current profile remained in equilibrium with the temperature profile, Λ would have just dropped to the final value. There is no evident need to invoke an anomalous resistivity to simulate available measurements of the current penetration.

During the current ramp, at high ramp rates, several bursts of MHD activity were observed as low order rational surfaces moved through the edge of the plasma (q_a=5.0, 4.5, 4.0). The burst at q_a=4 was an m/n=4/1 mode which caused a fast drop in the edge Te and a jump in Λ (which was reproduced by the resistive current penetration calculation). The Δ' stability calculations using the calculated current profiles during the current ramp show reasonable agreement with the observed instability occurances (Fig. 3). At all other times during the current ramp, the Δ' calculations show the current profile to be stable.

Even though the current ramp produced strong perturbations in the inferred J profile, including reversal of dJ/dr, the observed perturbation to $d(\ln T_e)/dr$ was extremely small (Fig. 4), except due to the 4/1 MHD burst at the plasma edge. Thus, in TFTR, the T_e profile shape must not depend on such local quantities as J and q, or their gradients.

Conclusions

It is found that in TFTR the electron temperature profile shape is constant outside the sawtoothing region and for $T_e > 1$ keV. For full bore discharges this shape is roughly exponential, with an inverse scale length of 3 m^{-1}, independent of all other factors, including q_a. Smaller minor radius discharges show approximately Gaussian profiles. Further, by rapidly ramping the plasma current, this profile shape is seen to be independent of such local quantities as the current density and q(r), or their derivatives.

Acknowledgements

The authors thank the TFTR physics staff, operations staff and beam group for their participation in these experiments. This work supported under DoE Contract #DE-AC02-76-CH03073.

References

[1] Comments on Profile Consisteny, R. E. Waltz GAT Report A18365

[2] Heating Profile Experiments on TFTR, R.J. Goldston, et al., this conf.

[3] A Simple Model of Energy Confinement in Tokamaks, N. Oyabu and J.K. Lee, GAT Report GA-A17890.

Figure 1. Inverse gradient scale length of T_e vs. minor radius for equilibrium full bore TFTR discharges for $T_e > 1$ keV outside the sawtooth mixing radius.

Figure 2. (a) Plasma current vs. time during a current ramp.
(b) Measured and calculated Λ vs. time during current ramp.

Figure 3. (a) Plasma current vs. time during a current ramp. (b) Bursts of coherent MHD activity observed on the Mirnov loops during a fast current ramp. (c) Calculated Δ' vs. time from the inferred current density profile.

Figure 4. Variation of $d/dr(\ln T_e)$ with time during a current ramp, for different shots and for radii from 0.3 to 0.5 meters.

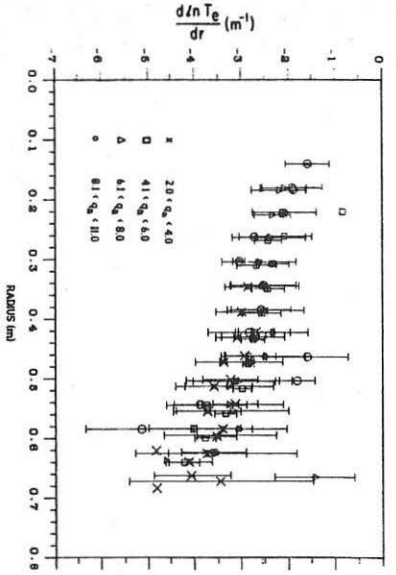

Figure 1.

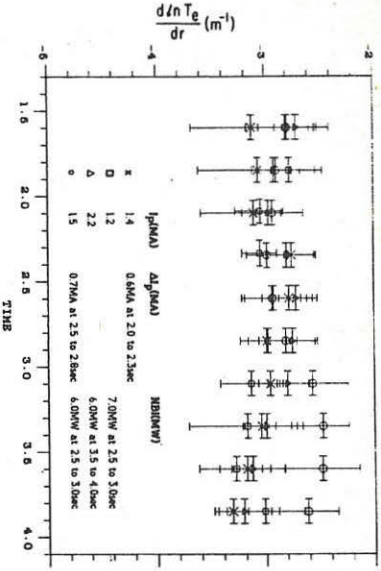

Figure 4.

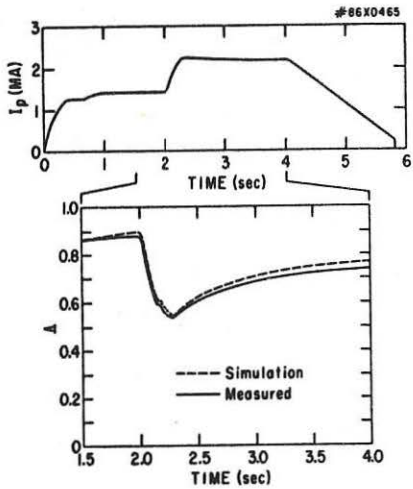

Figure 2.

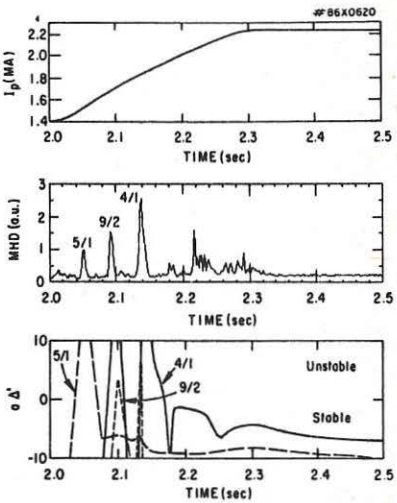

Figure 3.

A COMPARISON BETWEEN THEORY AND EXPERIMENT FOR MULTIPLE HELICITY MODES DURING AUXILIARY HEATING ON JET

J A Snipes*, P S Haynes*, T C Hender*, A W Morris‡, D C Robinson* and G Tonetti•

JET Joint Undertaking, Abingdon, Oxon, OX14 3EA, UK

*(UKAEA/Euratom Fusion Association) Culham Laboratory, Abingdon, Oxon, OX14 3DB

‡University of Oxford, present address Princeton Plasma Physics Laboratory, Princeton, USA

•On attachment from EURATOM-SUISSE Association, CRPP, CH-1007, Lausanne

Introduction Initial RF and NB heating experiments on JET exhibit enhanced sawtooth activity accompanied by multiple helicity MHD modes. The activity observed on internal coil signals has been compared with solutions of the resistive MHD equations in full toroidal geometry including plasma shaping effects with no ordering assumptions by means of the FAR code.[1] Multiple helicity locked modes are also observed, which grow approximately linearly in time up to a critical amplitude that triggers the disruption.

Multiple m Mode Coupling During centrally heated RF and NB heated discharges, the internal m=1, n=1 activity observed on ECE and soft X-ray diagnostics often becomes strongly coupled to higher m modes observed on magnetic pick up coils at the wall. While the frequency of the internal and external oscillations is the same, the poloidal phase variation of the external mode is typically that of m=3 or m=4, depending on q_ψ, with n=1 dominant. The amplitude can reach levels greater than 10^{-4} B_θ (wall), especially for low q, high auxiliary heating power discharges. The observed in/out ratio of the tangential field fluctuations decreases (increased ballooning) with increasing NB power at fixed q_ψ.

FAR code calculations of multiple m mode coupling effects are in broad agreement with experiment. For an equilibrium with q_ψ=6, q_o = 0.9 and an elongation of 1.4, the code predicts that an internal m=1 resistive mode will exhibit poloidal magnetic fluctuations with m=3 at the boundary and an in/out ratio of 0.2. This is to be compared with the observed ratio that varies from 0.2 to 0.6, depending on q_ψ. For the particular current distribution chosen, q_o=0.9, and S=10^6, the code predicts a fluctuation level of 10^{-4} B_θ(wall) for an m=1 island width of 10% of the minor radius. The predictions are, however, quite sensitive to the details of the current distribution. Increasing β_p in the calculations decreases the in/out ratio of the poloidal field fluctuations in agreement with observations during NB heating.

Multiple n Mode Coupling Nonlinearly coupled modes of different toroidal mode number n having frequencies proportional to n have been observed. By combining coils from six toroidal locations with carefully chosen weighting factors that enhance a particular Fourier harmonic and reject the other harmonics, combinations selecting n=1, 2 and 3 modes were constructed. During the current rise, $\tilde{b}_\tau(n=2) \approx 5\%\ \tilde{b}_\tau(n=1)$ and $\tilde{b}_\tau(n=3) \approx 1\%\ \tilde{b}_\tau(n=1)$. Before disruptions, the ratios increase to $\tilde{b}_\tau(n=2) \approx 25\%\ \tilde{b}_\tau(n=1)$ and $\tilde{b}_\tau(n=3) \approx 5\%\ \tilde{b}_\tau(n=1)$, typically. During MHD activity associated with enhanced sawteeth due to RF or NB heating, the ratios become $\tilde{b}_\tau(n=2) \approx 10\%\ \tilde{b}_\tau(n=1)$ and $\tilde{b}_\tau(n=3) \approx 3\%\ \tilde{b}_\tau(n=1)$.

The n=1 frequency in OH and RF discharges is usually between 500 and 1500 Hz. With additional momentum from the NB in the opposite direction to the apparent direction of toroidal mode rotation, however, the mode rotation reverses and the frequency may increase up to ~5 kHz, depending on the NB power and density. This is consistent with a toroidal rotation velocity of more than 9×10^4 ms^{-1}.

Disruption Precursors Preceding all disruptions studied thus far on JET with Ip>500 kA, a stationary n=1 mode grows, often linearly, until disruption (Fig 1). From the poloidal variation of both the amplitude and phase of the radial and tangential fields as the oscillating mode slows and finally locks, the dominant mode was found to be m=2, n=1 with m=1, n=1 and m=3, n=1 sidebands at ~30% $\tilde{b}$(m=2) and even higher order sidebands, eg m=0, n=1 at ~5% $\tilde{b}$(m=2). The relative strength of the sidebands increases with time.

The mode locks when the oscillating amplitude at the wall reaches $\tilde{b}_\theta \sim 10$G, then grows to a level, depending on q_ψ, of 1% B_θ(wall) for q_ψ=5. The length of time for which the mode is locked depends on I_p and can be as short as 30 msec for low currents or $\gtrsim$ 1 sec for high currents.

The observed disruption precursor activity compares well with m=2 dominated FAR code calculations. Figure 2 shows a FAR calculated field line tracing plot with $q_o > 1$, exhibiting large m=2 and m=3 islands when $\delta b_\theta / B_\theta$ (wall) ~ 1%, which occurs shortly after mode lock in Fig 1. For $\delta b_\theta / B_\theta$ (wall) $\gtrsim$ 2% these islands overlap and destruction of the magnetic surfaces occurs. The calculated poloidal variation in the amplitude of tangential field fluctuations reproduces the observed in/out ballooning asymmetry that arises from interference between the dominant m=2 harmonic and its principal sidebands. The calculated poloidal phase variation of the magnetic fluctuations also agrees with experiment.

Background MHD Level The amplitude of low frequency (<5 kHz) MHD activity between sawtooth collapses can remain as low as 3×10^{-5} B_θ independent of RF and NB input power and the position of the heating zone. However, the precursor MHD activity, which may last for 50 msec, and sawtooth induced magnetic perturbations rise substantially with NB power, often reaching 10^{-4} B_θ(Fig 3). The growing n=1 mode coinciding with the sawtooth collapse, whose

growth time is $\lesssim$100μsec [2], can reach an amplitude as high as 2×10^{-3} B_θ (wall) and be observed on the loop voltage [3]. RF heating generally shows less activity than NB heating, especially if heated off axis, though MHD levels of $\sim10^{-4}$ B_θ(wall) have occasionally been reached.

Conclusions Both RF and NB heating exhibit enhanced sawtooth activity correlated with edge magnetic fluctuations that are combinations of multiple helicity MHD modes produced through coupling due to toroidicity and shaping with the driven m=1, n=1 internal mode. The observed mode coupling effects are reproduced by the FAR code. In some cases, there is detailed agreement for the amplitude and phase variations of the mode activity [4]. Locked n=1 modes occur and grow prior to disruption, always locking in the same location, with the spectrum in m increasing prior to disruption. Only a low level of n=2 activity is present before disruption. The apparent direction of rotation of the MHD activity reverses with NBI. The background MHD level between sawtooth collapses can remain as low as 3×10^{-5} B_θ independent of RF and NB input power and the location of the heating zone. Generally, however, the average MHD activity is an order of magnitude higher during NBI than during RF or OH alone.

References

[1] L A Charlton et al, to appear J Comp Phys ($\gtrsim$ March1986)

[2] D C Robinson, Proc Conf on Physical Processes in Toroidal Confinement, Varenna, 1985, to be published.

[3] D C Robinson, Proc Workshop on Magnetic Reconnection, Corsica, p259, 1985

[4] T C Hender et al, "The effects of finite-β and shaping on tearing modes in JET", this conference

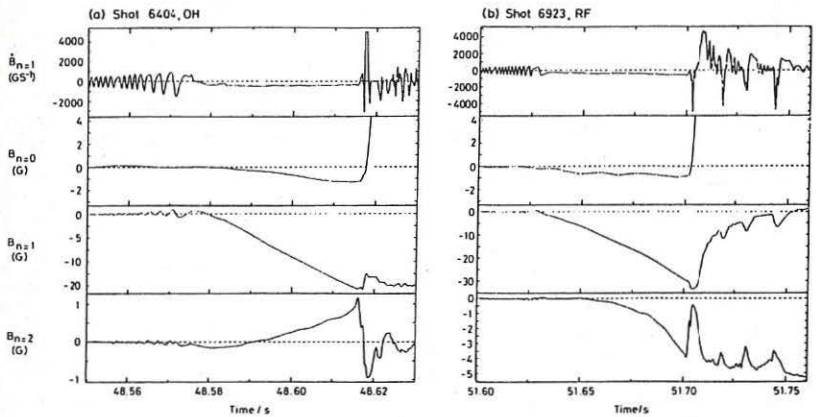

Fig 1 n=0 (equilibrium), and locked n=1, 2 modes prior to disruption in (a) OH at I_p = 1.5MA, q_ψ = 7, (b) RF heated at P_{RF} = 2.1 MW, q_ψ = 5.0.

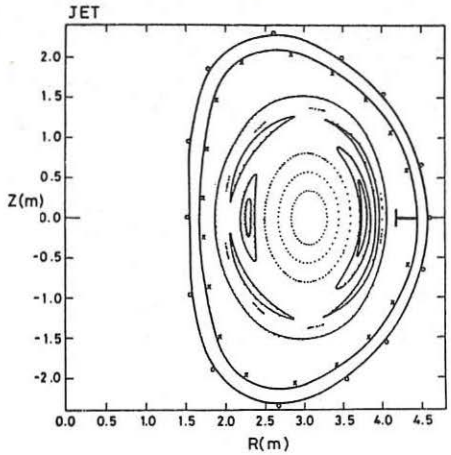

Fig 2 FAR code simulation fieldline tracing with q_0 = 1.1, q_ψ = 4.3, S = 10^5, β_0 = 0.12 and $\delta B_\theta \simeq 1.0\%\ B_\theta$ at the boundary.

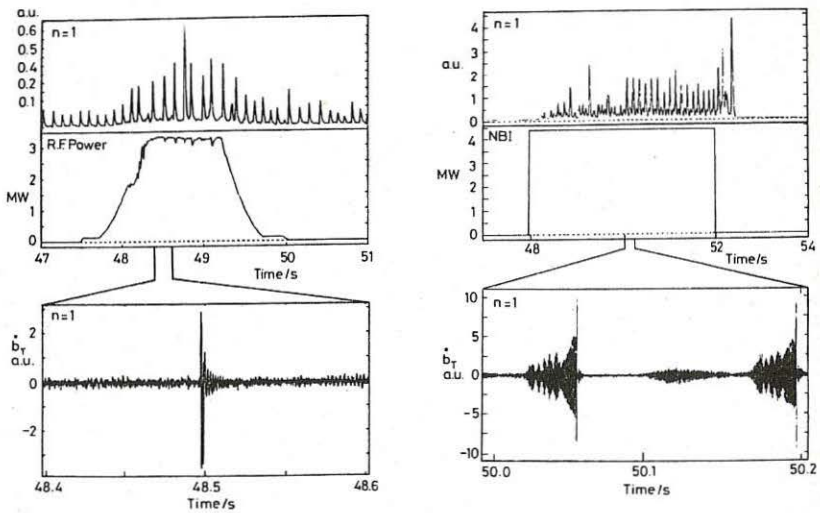

Fig 3 Comparison of background MHD levels on the n=1 combination monitor during (a) central RF heating, I_p=3MA, q_ψ=4.3, b/a=1.45 and (b) NB heating, I_p=3MA, q_ψ=4.8, b/a=1.45, this discharge disrupted at 52.4sec.

PREDICTIVE STUDIES OF NEUTRAL BEAM AND PELLET INJECTION ON JET

M L Watkins, W A Houlberg*, P Kupschus, P M Stubberfield, A Taroni.

JET Joint Undertaking, Abingdon, Oxon, OX14 3EA, UK.
*Oak Ridge National Laboratory, Oak Ridge, Tennessee, 37831 USA.

1. INTRODUCTION

A 1½-D transport code is used to examine the importance of energy confinement degradation, beam deposition profile, central plasma fuelling and edge pumping in JET plasmas with neutral beam and pellet injection.

2. MAIN FEATURES OF THE TRANSPORT MODEL

The transport models used to simulate JET ohmic plasmas (including target plasmas for neutral beam injection and pellet injection) are basically those used previously [1-3] and include: anomalous electron thermal diffusivity of the ALCATOR-INTOR or Coppi-Mazzucato-Gruber form ($\chi_{eAI} = 5.10^{19} n_e^{-1}$ or $\chi_{eCMG} = 3.10^{15} a B_T n_e^{-0.8} (RqT_e)^{-1} A_p^{-0.5}$); ion thermal diffusivity of the Chang and Hinton form [4]; anomalous diffusive and convective particle fluxes; oxygen/carbon and nickel impurities; neoclassical resistivity; classical energy transfer between electrons and ions; and the K a d o m t s e v reconnection model for sawteeth.

Following [2,3], a full calibration of the ECE temperature measurement removed the need for excessively high anomaly factors ($\alpha_i \geq 10$) on the ion thermal diffusivity, thereby allowing a "conventional" transport model with $\chi_i \leq 5\chi_{iCH} \leq \chi_e$ to be acceptable. The present calculations use $\alpha_i = 4$.

3. NEUTRAL BEAM INJECTION

Neutral beam heating of JET plasmas is simulated using a multiple pencil beam model for additional power and particle sources and by increasing the transport coefficients over their ohmic values.

The birth profile of fast ions is obtained from the attenuation of many filamentary neutral currents by electron impact ionisation, proton ionisation and charge exchange, including capture by impurities. The energy partition to the background ions and electrons is obtained by solving a Fokker Planck equation for the slowing down of fast ions. The power mix assumed for hydrogen and deuterium injection at different energies is given in the Table.

Table

Full Energy/Species (E_o)	Power		
	Fractions at E_o: $E_o/2$: $E_o/3$ (%)	At full energy (MW)	Total (MW)
65kV/H	69:23:8	3.7	5.4
80kV/H	63:29:8	4.2	6.6
80kV/D	76:17:7	7.8	10.3

Confinement degradation during NBI is simulated by increasing outside the q = 1 region the electron thermal diffusivity for ohmic plasmas [2,3] by either a fixed factor, $\alpha_e \leq 2$, or a power-dependent factor, $\alpha_{ep} = \alpha \int^V P_{total,e} dV / \alpha \int^V P_{OH} dV$.

Simulations of the ohmic deuterium discharges of [2,3] but with hydrogen or deuterium neutral injection at 80kV indicate that maximum central temperatures are reached after only 0.8-1.3s of additional heating and subsequently decrease as the centre is shielded from the neutral beams with increasing density from beam fuelling. The highest temperature is achieved at the lowest starting density and with deuterium injection. These effects have been observed in the first experiments with NBI on JET. In particular, simulation of the medium density discharge (JET Pulse #7145) fuelled to high densities by neutral injection at 65kV shows the subsequent fall in the electron temperature from its peak after approximately 0.5s of heating (Figure 1). The calculated beam deposition profiles at the beginning and end of injection are shown in Figure 2. High ion temperatures have been achieved in low density plasmas by pumping the edge particle flux by moving the plasma off the outer limiters, towards the inner wall. The low density discharge (JET Pulse #7155) heated to high ion temperatures by neutral injection at 65kV is also well simulated (Figure 3). Even higher ion temperatures are predicted with the above models with deuterium injection at 80kV, provided beam fuelling is compensated by edge pumping (Figure 4).

4. PELLET INJECTION

The penetration of frozen hydrogenic pellets is calculated using a model that has been tested against TFTR, ISX-B and ALCATOR-C data [5]. The pellet surface is protected by a neutral gas shield of thickness given by the hydrodynamic solution of the gas expansion assuming spherical symmetry [6] and a "tube" of cold ionised plasma, which extends along the magnetic field. The heat flux to the pellet surface is calculated from convective flows of electrons along the magnetic field through both the tube of cold plasma and the dense neutral gas shield and fast neutral beam ions normal to the magnetic field only through the neutral gas shield, which they can enter since their gyro-orbits are larger than the effective pellet ionisation radius.

Calculations using the stand-alone code for pellet injection indicate that pellets up to 6mm diameter and speeds up to at least $10 kms^{-1}$ are necessary to penetrate to the centre of JET discharges with central densities and temperatures up to $10^{20} m^{-3}$ and 10keV respectively. Solid curves in Figure 5 show the penetration for electron ablation only and a fixed ratio between the thickness of the ionised plasma tube and the cold neutral gas shield. It should be added that when the thickness of the ionised plasma tube is kept fixed at 0.35cm (as derived from TFTR bench mark tests) smaller gains in the penetration depth are found with increasing pellet speed. For these cases, the penetration of low speed pellets, in particular, is strongly reduced by ablation by fast ions from 10MW of deuterium injection at 160kV (dashed curves).

Full transport code calculations indicate that lower edge recycling fluxes are achieved with peaked density profiles maintained by continuous pellet injection and pumping. However, radiated power losses equal to the ohmic input power can result after relaxation of the density profile, and although this situation can be avoided by additional heating, when all this power has been used to reach conditions close to ignition, reheat of the plasma is not possible with this model in which pellet injection does not lead to improved confinement.

5. CONCLUSIONS

The expectations of neutral beam injection theory and confinement degradation are borne out by NBI on JET, with respect to both high density plasmas, in which the electron and ion temperatures are similar and the energy confinement is severely reduced and high temperature plasmas, in which the ion temperature exceeds the electron temperature and energy confinement is little affected when pumping the edge particle flux allows low densities to be maintained.

The predictions of pellet injection on JET indicate that a push towards $10kms^{-1}$ appears to be warranted for JET, with somewhat improved penetration in the absence of fast ion effects and as a means of recovering penetration to the central plasma in the presence of fast ions. The potential disadvantages, including substantial radiation losses and the failure to recover ignition-like conditions after pellet injection (unless confinement improves) should be considered together with the potential benefits, including lower edge fluxes, peaked densities and high edge temperatures obtained with continuous pellet injection and pumping.

ACKNOWLEDGEMENTS

We are indebted to members of the JET Experimental Department for the experimental data we have presented or quoted.

REFERENCES

[1] Behringer, K.H. et al, in Plasma Physics and Controlled Nuclear Fusion Research (Proc. 10th Int. Conf., London, 1984) 1, IAEA, Vienna (1985)291.
[2] Taroni, A. et al, Proc. 12th Eur. Conf. on Cont. Fusion and Plasma Physics, Budapest, 1985, 9F(I), EPS (1985)22.
[3] Taroni, A. et al, Varenna Workshop August/September 1985 (1985).
[4] Chang, C. S. and Hinton, F. L., AMPC Report 14-011 (To be published in Physics of Fluids) (1985).
[5] Houlberg, W.A. et al, Bull. Am. Phys. Soc. 30 (1985)1630.
[6] Milora, S.L. and Foster, C.A., IEE Trans. Plasma Sci. PS-5 (1978)12.

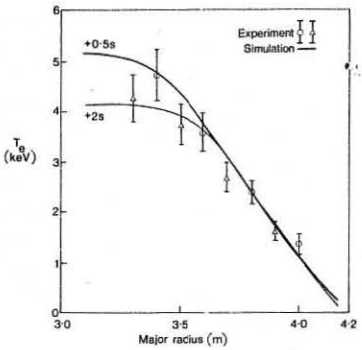

Fig 1: Comparison between theory and ECE measurements of the electron temperature profile for JET pulse #7145 after (a) 0.5s of NBI, model $2\chi_{eCMG}$ and α_{ep} and (b) 2s of NBI, model $0.4\chi_{eAI}$ and α_e=1.5.

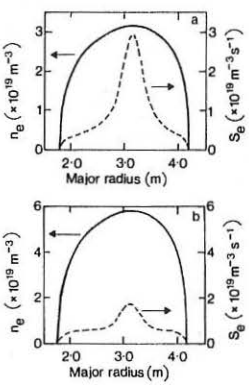

Fig 2: Density profiles and particle source rates at (a) the beginning and (b) the end of neutral injection.

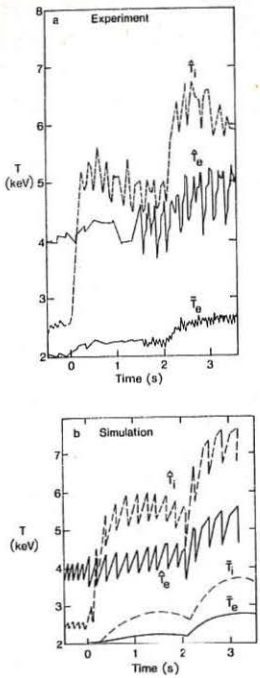

Fig.3: Comparison between experiment and theory for the temporal variation of the peak and mean electron and ion temperatures for JET pulse #7155 (a) ECE and NPA measurements, and (b) simulation with $4\chi_{eCMG}$ and α_{ep}. 2.7MW is applied at 0s and a further 2.7MW at 2s.

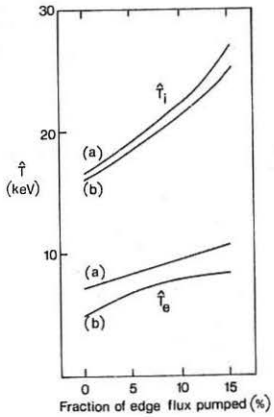

Fig.4: Predicted peak ion and electron temperatures with deuterium injection at 80kV and various levels of edge pumping for (a) $0.4\chi_{eAI}$ and α_e=1.5 and (b) $4\chi_{eCMG}$ and α_{ep}.

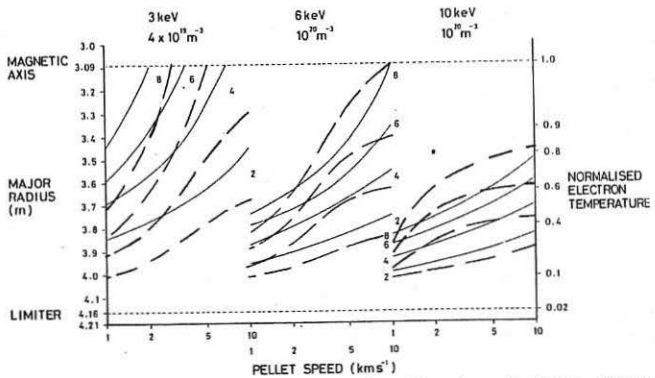

Fig.5: The position of maximum source density immediately after pellet injection when the thickness of the tube of cold plasma is fixed (a) relative to the thickness of the cold gas shield (—) and (b) at 0.35cm (- - -).

PROFILE CONSISTENCY AND ELECTRON ENERGY TRANSPORT MODELS

A. Taroni and F. Tibone

JET Joint Undertaking, Abingdon, Oxon. OX14 3EA, UK

INTRODUCTION

Results from several tokamaks have been recently interpreted invoking the concept of "Profile Consistency" (PC) first introduced by B. Coppi [1].

There does not seem to be a unique definition of PC (see for example [2-6]). Here we adopt the following definition: in tokamaks, with and without auxiliary heating, the plasma relaxes to a state with a "canonical" temperature profile

$$T_e(r) = T_{e2}\, f(r,\alpha), \tag{1}$$

T_{e2} being the temperature at a radius r_2 close to the plasma boundary and outside which atomic processes and transport not related to PC dominate [5,7]. α represents a "shape" parameter that can depend on global parameters such as q_a (safety factor at the boundary), I_p (total plasma current), B_t (toroidal field), poloidal or toroidal β. The family

$$f(r,\alpha) = \exp\left[\alpha\left(1 - \frac{r^2}{r_2^2}\right)\right] \tag{2}$$

was originally proposed [2] as "canonical" shape, and we shall mainly refer to it. However, we assume eq(1) to be valid in general only outside the region dominated by sawtooth activity ($r > r_1 \approx r(q=1)$). Thus other expressions for f may turn out to be more appropriate. Theory and/or experimental results are supposed to provide the information necessary to determine $f(r,\alpha)$. A first analysis of JET data is presented in [8].

2. DERIVATION OF χ_{ePC}

Our approach will be an empirical one. We assume PC with some $f(r,\alpha)$ and derive a series of consequences for thermal conductivity models used in transport codes, modifying and somewhat clarifying previous work in this direction [3].

Following [2,3,9] we derive χ_e from the steady-state electron thermal energy equation:

$$\chi_e(r) = -\frac{\int_{r_1}^{r}(P_\Omega + P_{aux} + S_e)r\,dr + \Phi_1}{r\, n_e(r)\, \partial T_e/\partial r} \tag{3}$$

where P_Ω is the ohmic input term, P_{aux} is the auxiliary heating term for electrons and S_e includes all other local sources and sinks in the equation. Φ_1 is proportional to the electron heat flux at $r=r_1$ and convection is neglected.

Eq.(1) can be used to eliminate $\partial T_e/\partial r$ from eq.(3) [3,9]. Furthermore, for any $f(r,\alpha)$ it is possible to eliminate T_{e2} by introducing $T_e(r)$, thereby obtaining a transport coefficient constrained by PC and expressed in terms of local quantities, α and integral quantities.

Clearly χ_e derived in this way (χ_{ePC}) cannot be expected to be valid far from the relaxed state. We assume it to be valid after the current distribution has relaxed (e.g. flat top of I_p in JET).

If the profile shape (2) is assumed, one obtains

$$\chi_{ePC} = \frac{1}{2\alpha} \frac{r_2^2}{r^2} \frac{\int_{r_1}^{r} (P_\Omega + P_{aux} + S_e) r dr + \phi_1}{n_e(r)\, T_e(r)} \qquad (4)$$

Notice that P_{aux} is treated on the same footing as P_Ω in this expression. If one considers a clean ohmic plasma with $T_e \simeq T_i$, and $r_1 = 0$, then

$$\chi_{ePC} = \frac{1}{4\pi\alpha} \frac{r_2^2}{r^2} \frac{E\, I(r)}{n_e(r)\, T_e(r)} = \frac{r_2^2\, V\, B_t}{4\pi\alpha\, \mu_o R^2 n_e(r)\, T_e(r)\, q(r)} \qquad (5)$$

where E is the (radially constant) electric field, I(r) the current inside r, V the resistive loop voltage, R the plasma major radius and μ_o the vacuum magnetic permeability. Eq.(5) gives essentially the Coppi-Mazzucato -Gruber coefficient [10], which approximates the χ_e derived in [2].

The main difference between χ_{ePC} (5) and the coefficients proposed in [2,3] is due to the further assumption of a scaling, including a weak n(r) dependence, for some global quantity (e.g. V) made in [2,3]. It seems to us that if PC holds any global scaling - including V, the energy replacement time and its degradation with auxiliary heating - must follow (for a given density, resistivity model, impurity content and ion transport model) from:

- a choice of $f(r,\alpha)$ and possibly a scaling of α (i.e. numerical coefficient in χ_e) in terms of global quantities (PC contribution);
- the plasma boundary model (or in its absence a scaling for r_2 and T_2);
- the effects of sawtooth activity.

The problem of connecting the PC region of the plasma with the sawtooth dominated region needs further investigation. Sawtooth activity can be reconciled with steady state only considering time averages over a sawtooth period. For example one can assume $\phi_1 = \int_o^{r_1} (P_\Omega + P_{aux} + S_e) r dr$. This prescription is consistent with the simplest model of sawtooth activity: an enhanced χ_e for $r < r_1$. It can be used also with "reconnection" models and other choices of χ_e for $r < r_1$. However other expressions of $\phi_1 = \phi_1(t)$, possibly more consistent with a "pulsating" model of sawteeth, are to be looked for. Notice the connection between the choice of $\phi_1(t)$ and the problem of the velocity of propagation of the heat pulses induced by a sawtooth collapse.

We observe that other empirical transport coefficients are closely related to PC. For example the assumption $f(r,\alpha) = 1 + (\alpha/T_2)(1 - r/r_2)$ leads, under the same approximations used to derive eq.(5), to $\chi_e = \frac{r_2 V B_T r}{\alpha \mu_o R^2 n(r) q(r)}$. This coefficient is close to the Neo-Alcator one.

3. NUMERICAL RESULTS

The coefficient χ_{ePC} given by eq.(4) has been extensively and successfully tested for JET ohmic discharges. Encouraging preliminary results have been obtained also for a number of RF heated discharges.

Figure 1a shows the temperature profiles computed with χ_{ePC} in our transport code, for ohmic discharges at different densities. They have been obtained with $r_2 = a$ (the plasma radius) and prescribing T_{e2} according to the observed experimental trend (Fig.1b); $\alpha = 2.85$ has been used.

The influence of the plasma boundary transport model is illustrated in Fig. 2. We assumed $\chi_{eb} \propto \chi_{eBohm}$ when $r > r_2$ (= .8a). In this case T_{e2} changes by changing χ_{eb} and the entire temperature profile follows.

Figure 3 shows results obtained with χ_{ePC} and RF heating. Again T_{e2} was prescribed according to the experimental trend and $\alpha = 2.85$.

The acceptable agreement between computed and experimental temperature evolution implies that χ_{ePC} can indeed be used outside steady state.

4. CONCLUSIONS

Simple considerations allow to derive a transport coefficient χ_{ePC} that we regard as being "genuinely PC". In comparison, coefficients derived in [2,3,9] are to be considered as "quasi-PC". A particular choice of χ_{ePC} has been successfully tested in the simulation of JET discharges.

Our analysis shows that the success of $\chi_{eCMG} \approx \chi_{ePC}$ in simulating ohmic discharges in completely different devices can be explained by:

- the underlying "canonical profile" is close to reality and no strong change of α is needed in different cases;
- a "hidden" scaling is introduced in computations using χ_{eCMG} when the boundary value of T_e is changed. This aspect has always been disregarded in the past.

Choices other than (2), possibly less optimistic, are however possible for the "canonical profile", leading to other expressions for χ_{ePC}.

In the absence of a quantitative theory and of more detailed experimental observations on PC, our analysis and results are to be considered only as indications that transport models can be modified to introduce the constraint of PC. This must and can be done taking into account appropriate models for the central and the boundary plasma region.

REFERENCES

[1] B. Coppi, Comments Pl. Phys. and Cont. Fus. 5, 261 (1980)
[2] B. Coppi and E. Mazzucato, Phys. Letters 71A, 337 (1979)
[3] B. Coppi, Sov. Journal of Plasma Physics 11(1), 49 (1985)
[4] P.H. Rebut and M. Brusati, Pl. Phys. and Cont. Fus. 28, 113 (1986)
[5] H. Furth, Proc. Varenna Workshop on Fusion Plasmas, 1985
[6] B.B. Kadomtsev, Pl. Phys. and Cont. Fus. 28, 125 (1986)
[7] R.J. Bickerton et al., Royal Society Meeting on the JET Project, 1986
[8] D. Bartlett et al., this conference
[9] F. de Luca et al., 27th An. Meeting of Division of Plasma Physics of APS, San Diego, USA, 4-8 November 1985
[10] O. Gruber, Nuc. Fus. 22, 1349 (1982)

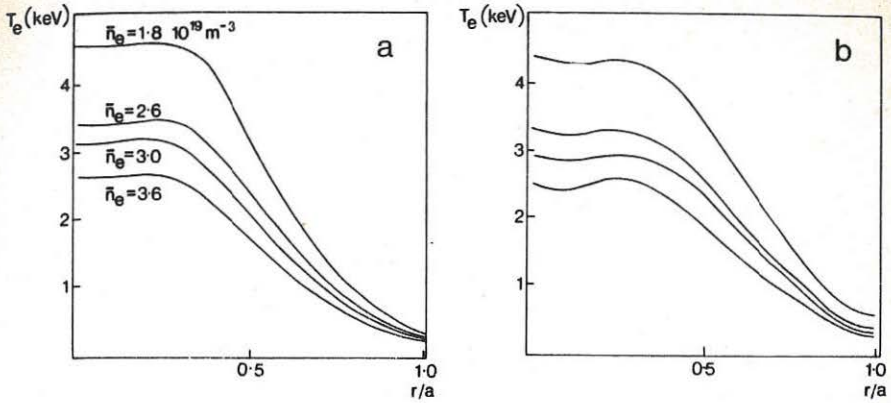

Fig.1 - Steady-state (sawtooth averaged) electron temperature profiles for a density scan at B_t= 3.4 T , I_p= 4.0 MA in JET : a) computed using $\chi_e(0<r<a) = \chi_{ePC}$; b) experimental data (ECE).

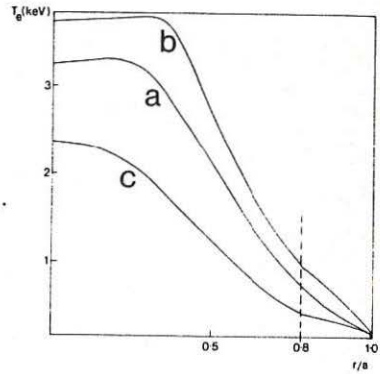

Fig.2 - Profile sensitivity to changes in the boundary model: three numerical experiments were performed using χ_{ePC} given by eq.(4), α=2.85 and
a) r = a
b) r = 0.8a and $\chi_e(r>r_2)$=0.1 χ_{eBohm}
c) r = 0.8a and $\chi_e(r>r_2)$= 2 χ_{eBohm} .

Fig.3 - Experimental data from ECE and numerical results (thicker lines) for an RF-heated JET discharge with $P^{tot}_{aux}/P_\Omega \sim 3$:
a) time evolution of peak and volume-averaged electron temperature ;
b) T_e-profiles before and during RF (three ECE profiles during the same RF-heated sawtooth are shown) .
In the simulation $\chi_e(r<r_1) \propto \chi_{eBohm}$ and T_{ea} is increased by 50% during RF.

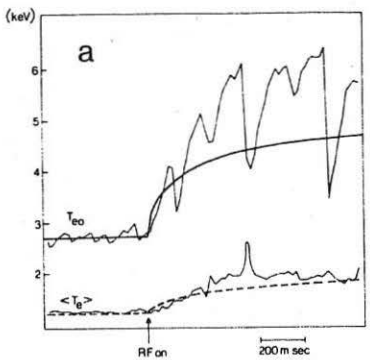

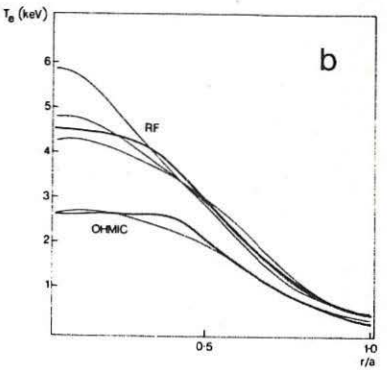

3-D MONTE-CARLO COMPUTATIONS OF THE NEUTRAL TEMPERATURE AND DENSITY DISTRIBUTION IN JET DISCHARGES

R. Simonini, A. Taroni

JET Joint Undertaking, Abingdon, Oxon., OX14 3EA, UK

INTRODUCTION - Detailed knowledge of the density and temperature of background neutrals in the JET bulk plasma is necessary for the interpretation of measurements such as charge-exchange emission spectra for NPA analysis. On the other hand, transport codes need averages of those quantities for evaluating source and sink terms.

The purpose of this work is to calculate as accurately as possible the distribution of the neutrals by means of 3-D Monte-Carlo codes, including the effects of toroidicity, non-circularity of the plasma cross-section and poloidal and toroidal asymmetries due to the limiters.

The results are used to assess the validity of simpler and faster models based on assumptions such as circular cylindrical plasma symmetry. Such codes are routinely used both for predictive and interpretative computations at JET.

Typical ohmic JET discharges at low and high plasma densities have been considered. For the calculations, the 3-D Monte-Carlo code NIMBUS [1] and an upgraded (3-D) version of the 1-D Monte-Carlo code AURORA [2] code have been used. For comparison with simpler models, the 1-D code FRANTIC [3] (upgraded so as to include a model of wall interactions) and the model for neutrals used in the ICARUS code [4] were selected.

GEOMETRY - The plasma and the chamber 3-D structure are considered in the following "complementary" way in codes AURORA and NIMBUS. NIMBUS does not allow for an exact treatment of toroidicity, but is otherwise very flexible in its geometry: it can model a general straight cylinder, with a largely arbitrary configuration in the poloidal plane; different materials can be assigned at various heights, with possibly periodic boundary conditions. Particle motion is fully 3-D. AURORA on the other hand can only model poloidal cross-sections defined by two matching semi-ellipses to allow for some degree of triangularity, but with full toroidicity. Taking into account these features, a configuration of eight 3-D limiters have been considered in NIMBUS, neglecting essentially only the toroidal curvature. In AURORA these limiters are replaced by a 2-D belt lying on the wall, thus the main approximation is the absence of any limiter shadow both in the toroidal and radial coordinate.

For the 1-D calculations, the toroidal elliptical shells are replaced by area-preserving cylindrical circular shells. The limiters are taken into account only for ion recycling, while their area is neglected for neutral reflection which is considered to take place on walls only.

PHYSICAL MODEL - The physical model in all codes assumes that the plasma characteristics remain fixed in the calculation. Electron temperature and density profiles are read from JET Processed Pulse File (PPF). The ion density profile is obtained by scaling the electron density by a depletion factor (typically, $n_i/n_e = 0.6\text{-}0.8$). The ion temperature is made up by

taking the axial and average temperatures and then setting up a profile that follows that of the electrons.

Test particles are neutral atoms or molecules (these for NIMBUS only). Target particles are electrons or deuterium ions. Impurities are only taken into account by assuming different densities for electrons and ions. No interaction neutral/impurity is considered.

Wall and limiters are assumed to be fully saturated, and the total ion flux to the first wall is considered to be one tenth of the total flux, the rest going to the limiters.

The neutrals are created either by recombination or by interaction of the scrape-off layer plasma with the carbon limiters and the chamber wall. Interactions with the chamber wall and the limiters are simulated by instantaneous backscattering or re-emission. NIMBUS allows for re-emission in both atomic and molecular state. The processes considered for neutral ion interactions are charge-exchange, ionisation by electron impact, recombination. In NIMBUS, also molecular dissociation and ionisation.

RESULTS AND DISCUSSION - We report here results from two typical ohmic shots, one at low density, $n_e = 8.4 \times 10^{12} cm^{-3}$, and one at high density, $n_e = 3.2 \times 10^{13} cm^{-3}$. Since NIMBUS and AURORA feature complementary approximations to a "full" 3-D geometry, a cross-check of their results has been performed to assess the relevance of these approximations. As for toroidicity for JET, AURORA has been run with different aspect ratios. It turns out that toroidicity plays a negligible role, all the discrepancies being well within the statistical errors. As for the importance of the 3-D structure of the scrape-off layer, comparisons of results from AURORA with results with NIMBUS averaged over the toroidal direction show that the presence of a 3-D scrape-off leads to an increase on the boundary neutral density of about 25%. Here NIMBUS was run with the option of re-emission in atomic state. One may add at this point that re-emission in molecular state leads to a decrease in neutral density of about 30%.

Poloidally averaged neutral density profiles computed by NIMBUS, namely $n_H(r,\phi)=1/(2\pi)\int n_H(r,\phi,\theta)d\theta$, are plotted in Figs. 1,2 along the toroidal direction as functions of the distance from the limiter centre. A molecule is counted as two atoms. At limiter level, the neutral density drops by almost two orders of magnitude over a distance of 1.5m.

The toroidally averaged neutral density profiles obtained by AURORA at various radii are shown in Figs. 3,4 for different minor radii at the mid-plane, as functions of the poloidal angle. A marked poloidal asymmetry is present. In this case, an asymmetry is present even in the neutral temperature. In the high-density case, the asymmetry is more localised in front of the limiter, and practically negligible as far as neutral temperature is concerned.

Poloidal and toroidal averages of neutral densities from 3-D AURORA are compared with 1-D (i.e. cylinders with circular cross-section) results in Figs. 5,6, including AURORA in the 1-D mode. For the Monte Carlo simulations, the statistical errors for the computed radial profiles are of the order of few percent at the boundary, and 15% at the centre of the discharge. We see that the shape of the plasma has some bearing in the case of low density. Here the circular 1-D AURORA overestimates the neutral density at the boundary and underestimates it at the centre by about 50%, due probably to the larger distance between source and centre in this boundary-recycling dominated case. For the same shot, the FRANTIC code

overestimates the central neutral density when compared to 1-D AURORA. ICARUS, instead, estimates the density well, but the central neutral temperature is somewhat overestimated. At high density, the agreement of the models is generally better, except for the density from ICARUS, which is overestimated by about 70%.

SOME SENSITIVITY RESULTS AGAINST BACKGROUND ASSUMPTIONS - The details of the plasma profiles in the scrape-off do not influence noticeably the toroidally and poloidally averaged neutral profiles in the bulk plasma (about 10% for relative variations of the scrape-off e-folding length from 0.5 to 2). In addition, variation of the ratio deuterium/electrons (keeping the electron concentration constant) from 0.8 to 0.5 amounts to negligible variations in the low-density case. For this case the neutral density is also rather insensitive to quite large (30%) changes in the temperature profiles by constant factors. At high density the sensitivity to both changes is larger: 15% at the centre for the variation of the depletion factor, 40% for the variation of the plasma temperature (recombination effects).

Finally, the neutral profiles are not very sensitive to the wall composition, the differences between cases with pure nickel or pure carbon wall being just above the statistical errors.

CONCLUSIONS - Toroidicity and the 3-D structure of the limiters do not appear to have a strong effect on poloidally and toroidally averaged neutral profiles in the bulk plasma, at least for the typical ohmic JET discharges examined.

The simple 1-D models reproduce sufficiently well the radial neutral profiles. This justifies the use of such models in transport codes where only averaged values of neutral profiles are required for source and sink terms. In such codes other inaccuracies are more relevant than those related to uncertainties in neutral profiles of the order estimated above.

However, strong poloidal and toroidal asymmetries in neutral profiles are indeed present. They could play a role that remains to be assessed for problems where only the local neutral density or an average over particular lines of sight is to be considered, e.g. the determination of the ion temperatures from NPA measurements.

REFERENCES -

[1] E. Cupini, A. de Matteis, R. Simonini, "NIMBUS - Monte-Carlo simulation of neutral particle transport in fusion devices", NET Report EUR XII - 324/9.

[2] M.H. Hughes, D.E. Post, "A Monte-Carlo algorithm for calculating neutral gas transport in plasmas", Princeton University Report, PPPL-1335 (1977).

[3] See for instance S. Tamor, "ANTIC: a code for calculation of neutral transport in cylindrical plasmas", JCP 40,104 (1981).

[4] M.L. Watkins et al., Plasma Physics and Controlled Nuclear Fusion Research, 1980 (Proc. 8th Int. Conf., Brussels, 1980) 1, IAEA, Vienna. (1981) 639.

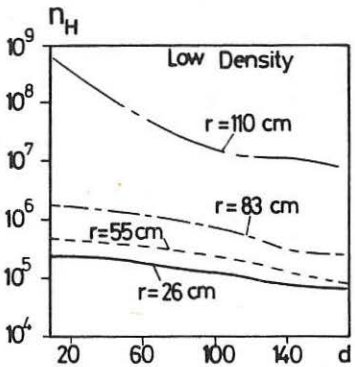

Fig.1 Toroidal neutral density as function of distance from limiter

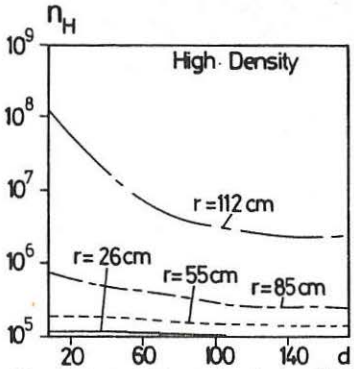

Fig.2 Toroidal neutral density as function of distance from limiter

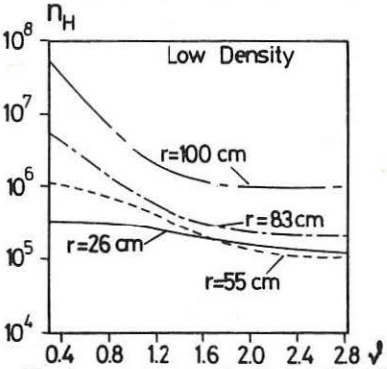

Fig.3 Poloidal neutral density at various radii.

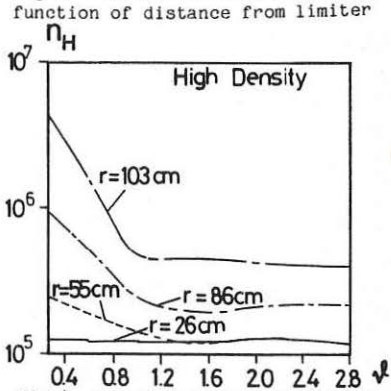

Fig.4 Poloidal neutral density at various radii.

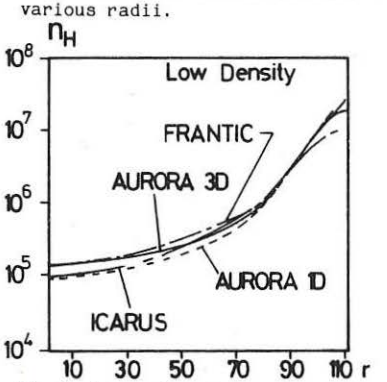

Fig.5 Comparison between models.

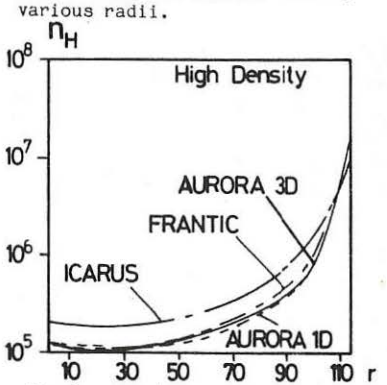

Fig.6 Comparison between models.

INCREASE OF THE DENSITY LIMIT IN ASDEX BY REPETITIVE PELLET INJECTION

H. Niedermeyer, K. Büchl, M. Kaufmann, R. Lang, V. Mertens, W. Sandmann, G. Vlases[1], G. Becker, H. S. Bosch, H. Brocken, A. Eberhagen, G. Fussmann, O. Gehre, J. Gernhardt, G. v. Gierke, E. Glock, O. Gruber, G. Haas, J. Hofmann, A. Izvozchikov[2], G. Janeschitz F. Karger, M. Keilhacker[3], O. Klüber, M. Kornherr, K. Lackner, M. Lenoci, G. Lisitano, F. Mast, H. M. Mayer, K. McCormick, D. Meisel, E. R. Müller[3], H. Murmann, A. Pietrzyk[1], W. Poschenrieder, H. Rapp, H. Riedler, H. Röhr, J. Roth, F. Ryter[4], F. Schneider, C. Setzensack, G. Siller, P. Smeulders[3], F.X. Söldner, E. Speth, K.-H. Steuer, O. Vollmer, F. Wagner, D. Zasche

Max-Planck-Institut für Plasmaphysik
EURATOM Association, D-8046 Garching

Introduction: Investigations performed on ASDEX in a large range of plasma parameters with and without neutral beam heating showed that the density limit is normally caused by energy losses at the plasma boundary /1/. The stronger gas influx needed to achieve higher densities leads to increasing recycling losses and increasing radiation at the edge. At a certain average density the discharge becomes unstable. It seems to be obvious that more efficient refuelling deeper inside the discharge, e.g. by injection of fast pellets, should result in a higher density limit. High densities have been achieved in several experiments by a fast density ramp up with a few pellets /2/,/3/,/4/,/5/. In ASDEX also slow ramp up with a large number of pellets was applied and pellet injection was switched off or continued with reduced frequency before the density limit was reached. Very high densities, favourable peaked density profiles and improved energy confinement were obtained even after stopping pellet injection. We conclude that pellet injection can change the transport properties of the plasma fundamentally.

The experiment: In ohmically or beam heated divertor discharges the deuterium density was first ramped up by gas puffing to a value safely below the limit. Then deuterium pellets were injected to further increase the density as slowly as possible until a disruption was detected. Gas puffing during the pellet injection phase has been optimized in contrast to earlier work /6/ where it has been attempted to minimise recycling. The pellets (diameter 1.0 mm, length 1.0 mm) are cut from an extruded rod of frozen deuterium and accelerated by a centrifuge to a velocity of typically 650 m/s /7,8/. They can be individually triggered with a minimum time interval of 20 ms. The mass of each is measured with a microwave interferometer system developped by the RISØ National Laboratory. One rod is sufficient for 80 pellets which may be injected in one burst. Normally 20 to 30 pellets were injected with a repetition rate of one per 30 ms. In some discharges the repetition rate was reduced after a few pellets or injection was switched off to keep the plasma density constant. The $5 \cdot 10^{19}$ particles of one typical pellet correspond to a volume averaged density of $1 \cdot 10^{13}$ cm^{-3}.

Line averaged densities: Figure 1 shows a Hugill plot of divertor discharges at the density limit. All ohmically heated discharges in non-carbonised

---

[1]University of Seattle, DOE contract; [2]Academy of Sciences, Leningrad, USSR; [3]Present address: JET Joint Undertaking, England; [4]CEN Grenoble, France

vessel with gas refuelling lie close to the solid line. The points marked with figures indicate the best discharges achieved so far with pellet refuelling in three different scenarios: ohmically and beam heated plasmas in non-carbonised vessel and ohmically heated plasma in carbonised vessel. For optimization the pellet frequency and the amount of additional gas puffing have been varied. The benefit of wall carbonisation for chmically heated pellet discharges is clear and much higher than for gas puffed discharges (not shown in Fig. 1). Low power beam heating increased nR/B_T to about 9 in pellet refuelled discharges without wall carbonisation. It was not yet possible to exceed this value with wall carbonisation. High power co-injection did not permit to reach high densities without heavy gas puffing, so that no substantial improvement could be achieved with pellet injection at high beam powers.

Profiles: Pellet injection permits a much larger relative increase of the fusion relevant central density than of the line averaged density usually plotted in Hugill diagrams. A comparison of density and electron temperature profiles from two shots close to the density limit, one with gas puffing alone, the other one with pellet refuelling, reveals dramatic differences (Fig. 2). Density profiles with efficient pellet refuelling are strongly peaked in contrast to the rather flat gas puffing profiles. T_e profiles of gas puffing shots normally stay peaked up to the disruptive end while T_e profiles of pellet shots flatten shortly before the disruption. The time evolution of a pellet refuelled discharge which was driven close to but not into the density limit is shown in Figs. 3 and 4. Before pellet injection (A) we observe a flat n_e and a peaked T_e profile. The radiation profile (P_{rad}) is peaked at the edge with negligible radiation on axis. During pellet injection (B) the density profile peaks, the central radiation increases exponentially, the T_e profile stays peaked as long as the radiation profile is hollow. These characteristic features are observed during the pellet injection phase and even a few hundred milliseconds after its end. Finally (C) the central radiation has strongly increased to a value comparable to the local power input and flattened the temperature profile. T_e- and n_e-profiles are similar to the ones at the density limit shown in Fig. 2. Now the discharge disrupts at a density below the limit reached with continuous density increase. The radiation source has been spectroscopically identified as iron. An increase of low-Z impurities is not being observed, Z_{eff} stays close to 1.

The disruption: In contrast to gas refuelled shots a further increase of the density with pellets is not prevented by edge effects but by central radiation. With flattening T_e-profile the current density profile flattens until a stability limit is violated. A stability calculation based on fitted n_e- and T_e-profiles states that the ballooning limit is being reached. Wall carbonisation reduces the level of iron in the discharge by an order of magnitude, so that the critical level of central radiation is reached later at a higher density. It has been found that additional gas puffing also permits to reach a higher density at a certain level of radiation. We have identified high-Z impurity radiation as the limiting factor. The level of radiation observed cannot be explained by the higher density, but an increase of impurities has to be assumed. Enhanced impurity release can be excluded from spectroscopic measurements. The only possible explanation is accumulation of impurities.

Particle transport: The initial idea was to obtain peaked density profiles by moving the particle source from the boundary to the centre, but the measured profiles cannot be explained by a peaked source term. The pellets penetrate to slightly inside half the minor radius only. In the discharge phase after pellet injection the only particle source is at the edge. Assuming that the particle transport may be described by a diffusion term with a diffusion coefficient D(r) and an inward drift term with a drift velocity v(r), we analysed nearly stationary phases of a pellet shot (C in Fig. 4) and of a gas refuelled high density discharge (Fig. 2). One finds that the gas puffing profile is very well approximated with $v/D \sim r^3$, the pellet profile with $v/D \sim r$, however. Pellets, though not penetrating to the centre, apparently change the transport coefficients throughout the plasma. The effect begins with pellet injection and lasts until a few hundred milliseconds after its end, the magnitude of the effect varies, however, during the density ramp up: the density gain associated with each pellet scatters and is not proportional to the pellet size (the first ones are normally very efficient). High power co-injection seems to prevent switching of the transport properties. The impurity accumulation observed may be explained by an inward drift as well, if the ratio of drift velocity to diffusion constant is much higher for high-Z impurities than for deuterium. Because saturation has never been reached in the experiments a quantitative description is not possible.

Energy confinement: The modified transport properties do not only result in good particle confinement but also in strongly improved energy confinement. Improvement of the energy confinement is not caused by higher densities but is switched on by pellet injection as we see in Fig. 3. Absolute values of up to 160 ms were achieved in other discharges. An improvement of the global energy confinement time of 80 % was observed in ohmic discharges only. High power co-injection prevents an improvement of the energy confinement as it prevents peaking of the density profiles.

Conclusions: Pellet injection is able to switch the confinement properties of a tokamak discharge fundamentally. This switching is possible with pellets penetrating to the half-radius (there are indications that even much smaller penetration depths are sufficient). Improved particle confinement and triangular density profiles permit to achieve extremely high central densities. Substantially improved energy confinement is provided in this transport regime. The problem of impurity accumulation has to be solved which prevented to sustain this transport mode stationarily and a way has to be found to sustain the regime with high heating power.

References:

/1/ H. Niedermeyer, et al., Proc. 12th European Conf. on Contr. Fusion and Plasma Physics, Budapest 1985, part 1, p. 159.
/2/ M. Greenwald, et al., Proc. 11th European Conf. on Contr. Fusion and Plasma Physics, Aachen 1983, part 1, p. 7.
/3/ G.L. Schmidt, et al., Proc. 12th European Conf. on Contr. Fusion and Plasma Physics, Budapest 1985, part 2, p. 674.
/4/ S. Sengoku, et al., Nuclear Fusion, Vol. 25, No. 10 (1985), p. 1475.
/5/ R.J. Fonck, et al., Journal of Nuclear Materials 128 & 129 (1984), p.330.
/6/ G. Vlases, et al., submitted to Nuclear Fusion.
/7/ W. Amenda, R.S. Lang, Proc. 13th Symp. on Fusion Technology, Varese 1984, p. 243.
/8/ W. Amenda, R.S. Lang, to be published in J. Phys. E: Sci. Instrum. (1986).

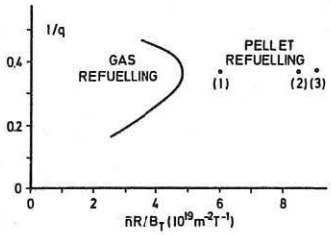

Fig. 1: Hugill plot of discharges at the density limit with gas refuelling (ohmic heating, solid line) and pellet refuelling
(1) OH non-carbonised wall
(2) OH carbonised wall
(3) NI 0.43 MW non-carbonised

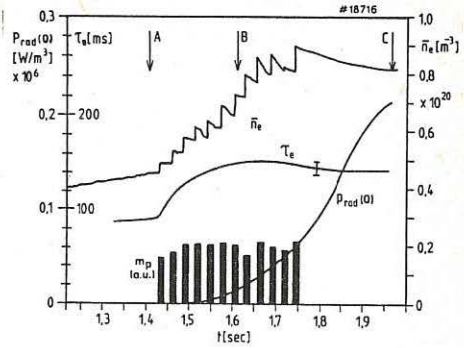

Fig. 3: Time evolution of the line averaged density n_e, radiation density on axis P_{rad}, global confinement time τ_E and pellet mass during a discharge with injection of 12 pellets.

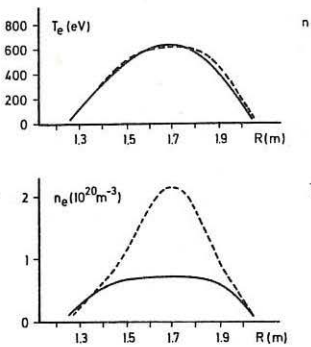

Fig. 2: T_e- and n_e-profiles of high density discharges with gas puffing (solid lines) and pellet injection (dashed lines).

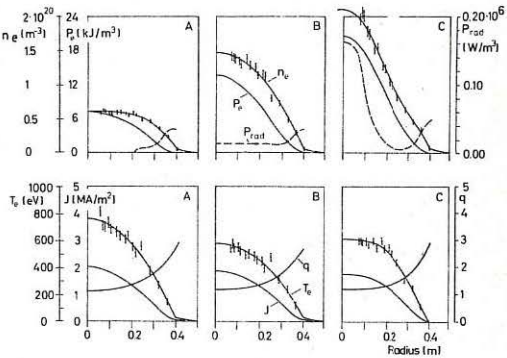

Fig. 4: Profiles of the electron density n_e, electron pressure p_e, radiation density P_{rad}, current density J, safety factor q at three times as indicated in Fig. 3.

EVOLUTION OF RADIATION POWER PROFILES IN ASDEX H-MODE DISCHARGES

E. R. Müller[1], G. Janeschitz, P. Smeulders[1], G. Fussmann, M. Kornherr, K. F. Mast, G. Becker, H. S. Bosch, H. Brocken, A. Eberhagen, O. Gehre, J. Gernhardt, G.v.Gierke, E. Glock, O. Gruber, G. Haas, J. Hofmann, A. Izvozchikov[2], F. Karger, M. Keilhacker[1], O. Klüber, K. Lackner, M.Lenoci, G. Lisitano, H. M. Mayer, K. McCormick, D. Meisel, V. Mertens, H. Murmann, H. Niedermeyer, A. Pietrzyk[3], W. Poschenrieder, H. Rapp, H. Riedler, H. Röhr, J. Roth, F. Ryter[4], F. Schneider, C. Setzensack, G. Siller, F. X. Söldner, E. Speth, K.-H. Steuer, O. Vollmer, F. Wagner, D. Zasche

Max-Planck-Institut für Plasmaphysik
EURATOM Association, D-8046 Garching

Abstract

The paper compares the impurity radiation behaviour of two types of H-mode discharges. In the normal H-mode that reaches a quasi-stationary state the energy (and particle) losses within the outer plasma half-radius are characterized by the repetitive burst-like exhaust into the divertor and constantly moderate radiation power losses. In contrast, the burst-free variant of the H-mode with superior confinement properties is dominated by radiation losses growing continuously up to 100 % of the heating power. The time evolution of the impurity concentration and the associated radiation losses at the plasma centre is hardly influenced by the kind of H-mode. If the concentration of medium-heavy metals in the burst-dominated H-mode plasma is raised to sufficiently high values, e.g. by the accumulation of intrinsic iron, the burst-free (or burst-deficient) H-mode is triggered which after a new accumulation period usually ends by a radiation collapse.

1. Introduction

During the normal H-mode /1/ of neutral-injection heated divertor discharges in the tokamak ASDEX the energy and particle flow from the main plasma volume into the divertor is modulated by highly repetitive bursts. While typical bursts exhibit pulse lengths of around 0.5 ms and power amplitudes of the order of 1 MW, the energy exhaust into the divertor is almost blocked during the quiescent intervals between bursts /2/.

In order to investigate the influence of the bursts, a discharge with a long-lasting burst-free H-mode (shot # 11447) has been produced /3/ and is contrasted with that kind of H-mode endowed with the usual burst-pattern (shot # 11338). Both discharges have identical parameter settings at the beginning of the NI-heating interval (I_p = 320 kA, B_t = 2.17 T, $\bar{n}_e$ = 3.5 x 10^{13} cm^{-3}, $P_{OH} + P_{NI}$ = 3.3 MW, $H^0 \rightarrow D^+$ (40 kV) tangential injection in co-direction) except for the 4 cm outward shift of the plasma needed to establish the long-lasting burst-free H-phase. The time history of various plasma parameters ($\bar{n}_e$, β_p, τ_E^* etc.) is discussed in Ref. /3/.

Figure 1 shows that the bolometrically measured total volume power losses within the divertor (RAD_{DIV}) /4/ drop instantly at the L-to-H mode transition (t = 1.16 s) and remain at the low level of the ohmic phase throughout the burst-free H-mode, whereas they recover time-averaged over the bursts

---

[1]Present address: JET Joint Undertaking, Culham, England; [2]Academy of Sciences, Leningrad, USSR; [3]Univ. of Washington, Seattle, USA; [4]CEN Grenoble, France

with growing burst activity during the second variant of H-mode. The total radiation power losses of the main plasma volume (RAD) are considerably higher in the burst-free H-discharge, even during the preceding L-phase. This radiation enhancement indicates an impurity contamination of the plasma produced by its shift to the outer stainless-steel protection limiters. The burst-free H-mode is terminated when, after a continuous radiation increase accelerated by a simultaneous rise of plasma density, the value of the main plasma radiation (RAD) equalizes the total heating power.

2. Radiation power profiles

Figure 2 compares the two types of H-mode discharges at two discrete times with regard to their chord-intensity profiles measured with a 19-bolometer array, and Fig. 3 presents the time development of the respective radial profiles of radiation power density ($P_{RAD}(r)$) derived by Abel-inversion method. During each kind of H-mode the radiation profiles evolve towards shapes peaked at the plasma centre. The repetitive burst-like release of plasma energy due to the Edge Localized Modes (ELMs) /3,5/ prevents any long-term increase of radiation power at plasma radii between a/2 and a. In this case, the growth of the central radiation peak is restricted to the inner half-radius and at t = 1.260 s it is reversed into a decay towards an equilibrium profile identical to that at t = 1.215 s. In contrast, during the burst-free H-mode, where the energy outflow into the divertor is permanently suppressed, the radiation power losses grow unimpeded over nearly the whole plasma cross-section until the radiation collapse converts the discharge back into the L-mode. The burst activity and the radiation enhancement thus act mutually exclusively as additional important energy loss mechanisms within the outer plasma half-radius and, depending on the class of H-mode, both quantitatively substitute each other. The main plasma radiation becomes the dominant energy loss channel in the burst-free H-mode. Therefore, the energy flow into the divertor (see e.g. RAD_{DIV} signal in Fig. 1) keeps low and does not restore the previous L-mode level as one would expect for transport-dominated losses after the plasma equilibrium (with improved confinement) is re-established.

It is important to note that the chord-intensity profile of the burst-dominated H-mode which ends up quasi-stationary stays always, even during its transient central peaking, distinctly below the base profile from which the fatal radiation increase of the burst-free H-mode starts at t=1.215s (Fig.2).

3. Radiation and impurity accumulation at the plasma centre

Correlation of the bolometric radiation profiles (Fig. 3) with those from VUV spectroscopy, soft X-ray tomography, temperature and density measurements makes evident that the radiation emission at the plasma centre is completely dominated by line radiation of highly ionized iron /3/ and that the central peaking of the radiation profiles reflects an impurity accumulation taking place irrespective of the type of H-mode. Figure 4 demonstrates that the presence or absence of bursts hardly influences the evolution in time of the local radiation power density at the plasma centre ($P_{RAD}(0)$), particularly the time-constant of the exponential rise after the L-to-H-mode conversion. The absolute magnitude of $P_{RAD}(0)$, however, is at any instant, including the preceding L-phase, about three times higher in the burst-free H-discharges as compared with the burst-dominated one, due to the initial iron contamination. The iron concentration at the plasma centre, displayed in Fig. 5, is derived from $P_{RAD}(0)$ by applying the temperature-dependent radiative power loss function for iron $P_{Fe}(T_e)$ /6/, that includes charge-exchange recombination with beam neutrals ($n_o/n_e = 10^{-5}$).

4. Internal triggering of the burst-free H-mode

Shot # 12218 (Figs. 6 and 7) shows that the burst-dominated H-mode with moderate radiation losses may turn into the burst-deficient H-mode with disastrous consequences. The mode conversion occurs when the accumulation of intrinsic metal impurities during the burst-dominated H-phase raises the bolometric centre-chord intensity up to the threshold value of the burst-deficient H-mode. The first and the last step in the profile evolution depicted in Fig. 7 resemble strikingly their burst-dominated and burst-free counter-parts in Fig. 2, respectively, because the burst frequency in the burst-deficient H-mode seems to be too low to slow down the impurity accumulation. Our interpretation that a sufficient degree of plasma contamination with medium-heavy metals is needed to establish the long-lasting burst-free H-mode agrees with the experimental observation that the burst-free H-mode can be triggered externally by the laser blow-off injection of metals such as chromium and copper /7/.

References:

/1/ Wagner, F., et al., Phys. Rev. Lett. 49 (1982) 1408.
/2/ Müller, E.R., et al., Journ. Nucl. Mat. 121 (1984) 138.
/3/ Keilhacker, M., et al., in Plasma Physics and Contr. Nuclear Fusion Res. (Proc. 10th Int. Conf. London, 1984) Vol.1, IAEA, Vienna (1985) 71.
/4/ Müller, E.R., Behringer, K., Niedermeyer, H., Nucl. Fus. 22 (1982) 1651.
/5/ Wagner, F., et al., Phys. Rev. Lett. 53 (1984) 1453.
/6/ Hulse, R.A., Post D.E., Mikkelsen, D.R., J. Phys. B: Atom. Molec. Phys. 13 (1980) 3895.
/7/ Keilhacker, M., et al., Plasma Phys. and Contr. Fusion, 28, (1986) 29.

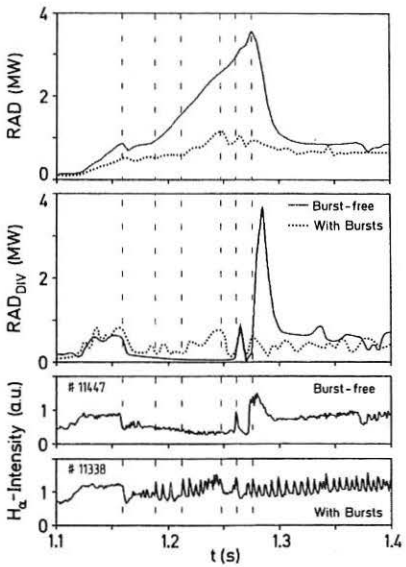

Fig. 1 (left): Time history of the bolometer signals RAD and RAD$_{DIV}$ (electronic integration-time ≈10 ms) for both kinds of H-mode discharges.

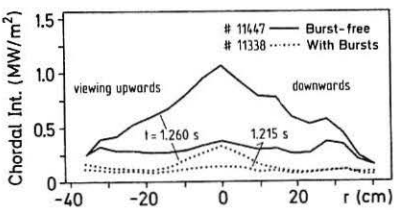

Fig. 2 (above): The bolometric chord-intensity profiles characteristic of either type of H-mode at two discrete times.

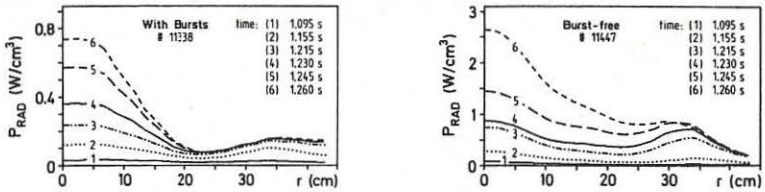

Fig.3: Time evolution of the radial profile of radiation power density during the burst-dominated (left) and the burst-free (right) H-mode discharge (note the different radiation scales).

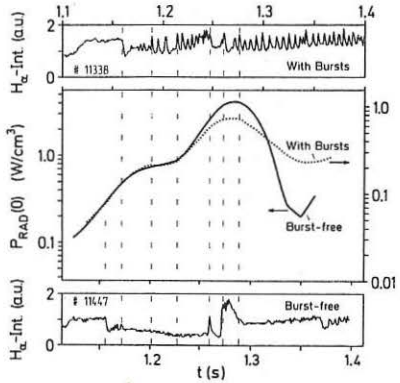

Fig. 4: Dynamic behaviour of the radiation power densities at the plasma centre.

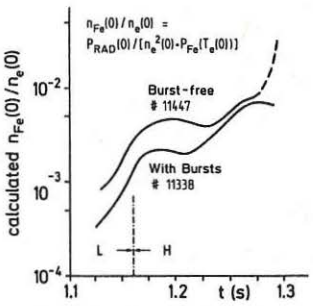

Fig. 5: Variation in time of the calculated iron concentrations at the plasma centre.

Fig. 6 (right): Time development of various plasma parameters during shot #12218 converting from a burst-dominated into a burst-deficient H-mode.

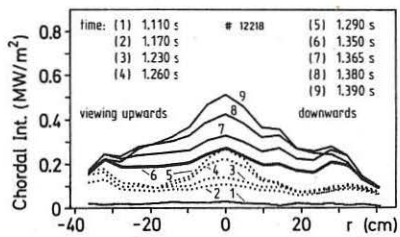

Fig. 7 (above): The evolution of the bolometric chord-intensity profile during shot #12218.

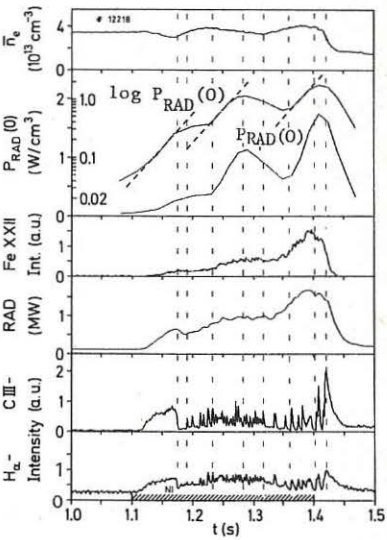

METAL SOURCES AND GENERAL IMPURITY BEHAVIOUR IN JET PLASMAS DURING ICRH

K H Behringer, B Denne, M J Forrest*, N C Hawkes*, A Kaye, P D Morgan, N J Peacock*, M F Stamp, H P Summers and G Tallents

JET Joint Undertaking, Abingdon, Oxon, UK
* EURATOM-UKAEA Association, Culham Laboratory, Abingdon, Oxon, UK

INTRODUCTION

The behaviour of impurities during ICRF heating after heavy carbonisation has been reported on before /1/. Further investigations have been carried out with modified antennae, clean limiter carbon tiles and an uncarbonised vessel.
Presently three ICRF antennae are installed in JET. Their Faraday screens are made of nickel; one of the screens (2D antenna) is chromium plated. The antennae are protected by surrounding carbon tiles. The vessel consists of Inconel 600 (72% nickel, 16% chromium, 8% iron). The discharges are operated either on eight poloidal carbon limiters or on the inner wall carbon protection tiles.

ORIGIN AND MIGRATION OF METALS DURING ICRH

During ICRF heating, an increase of Cr line brightness from the bulk plasma is observed when the 2D antenna is active; an increase of Ni intensity accompanies operation of the other antennae (2B or 6B). Thus it is evident that the antennae screens are the original sources of these metals. Observation of the 2D screen by visible spectroscopy proves the existence of chromium influx during RF manifesting itself in intense Cr I line radiation. In the course of operation with ICRH, screen material is deposited onto limiters and antennae protection tiles and subsequently eroded by the plasma. This is demonstrated by the behaviour of Cr I and Ni I lines in the respective visible spectra. As a consequence, the metal fluxes and concentrations in subsequent pulses increase in the ohmic part of the discharge before RF and higher concentrations result during RF for a given power. For constant RF energy, an equilibrium is established after a few pulses (Fig. 1 for the case of Cr). Lower RF energy or purely ohmic discharges lead to cleaning of the respective surfaces (Fig. 1). A beneficial result of the metal contamination is a reduction of oxygen influxes and oxygen concentrations in the plasma (gettering).

Cr INFLUXES AND RELEASE MECHANISM

Absolute Cr influx densities have been derived from Cr I intensities. They are roughly proportional to RF power and decrease during some months of operation. Indications are that H minority heating leads to somewhat higher Cr fluxes than ^{3}He minority heating.
Combining an analysis of Cr densities in the plasma and total influx (using the antenna area) results in a Cr replacement time τ_D of ≈ 20ms. This value agrees with simulations of the plasma edge conditions, if the Cr atom energy is some eV (ie sputtering, not evaporation). No significant shift (<0.1 A) of Cr I lines in the visible spectrum could be detected, which means that the energy of the atoms is < 50 eV. Visible

He II line profiles yield an edge ion temperature of ≈ 80 eV which is not affected by the RF pulse. Concluding from these observations, the release mechanism of Cr is probably neutral atom or ion sputtering, but the details are not clear.

PARAMETER DEPENDENCE OF METAL DENSITIES

An estimate of the increase in Ni and Cr density during RF is provided by taking the incremental increase in Ni XXV and Cr XXII line intensities, corrected for the change in electron density, $\bar{n}_e$, by dividing the line intensity by $\bar{n}_e$. The behaviour of nickel as a function of RF power coupled to the plasma for a variety of conditions is shown in Fig. 2. Open symbols denote H-minority heating whereas filled symbols indicate ^{3}He-minority heating. In the ^{3}He-case it is seen that, for a given electron density, higher plasma current leads to a somewhat larger increase in nickel density (3/4 MA, 3 x $10^{19}m^{-3}$). Lower $\bar{n}_e$ leads to a higher nickel density, even at a lower plasma current (2 MA, 2 x $10^{19}m^{-3}$). This behaviour is also evident in the H-minority data (2 MA, 1.5/2 x $10^{19}m^{-3}$). H-minority heating leads to higher metal densities than ^{3}He heating, but the comparison in Fig. 2 overemphasises this fact because of lower $\bar{n}_e$ in some H cases. For several pulses the nickel concentration following from a detailed analysis is also shown in Fig. 2.

A study of the Cr density behaviour shows a steeper dependence on RF power than nickel does which is possibly due to the previous carbonisations of the nickel screens.

A heavy carbonisation (48 hrs, 17% CH_4) in 1985 led to a reduction of the OH metal concentrations by about a factor 100 and a very small increase during RF. Recovery to the usual behaviour was observed after about 200 plasma pulses, indicating an erosion of carbon layers on both antennae and limiters. The results measured towards the end of this campaign (reported in /1/) fit into the present data set (pulse 5486 in Fig. 2) obtained many months after the carbonisation.

IMPURITY CONCENTRATIONS AND RADIATED POWER

In spite of a substantial increase of metal line radiation during RF, the metal contribution to Z_{eff} and P_{rad} is relatively small (Table 1 and Fig. 3). Impurity concentrations and contributions to radiated power are derived from VUV line intensities using an impurity transport code /2/. About 20% of the radiated power during RF is due to metals. The local radiation in the plasma centre amounts to ≈ 10 mW/cm^3, as supported by bolometer and soft X-ray results/3/.

SUMMARY

The Faraday screens of the RF antennae have been identified as the original sources of metal impurities during ICRH in JET. Migration of metal impurities from the antennae screens to the limiters and protection tiles has been observed, leading to a build-up of metal concentrations in ohmic plasmas and aggravating the increase during RF. It has been observed that the limiters and protection tiles are cleaned by operation without RF within a few pulses.

Carbonisation leads to a temporary reduction of metals before and during RF heating.

In all cases, radiated power and Z_{eff} of the plasma are dominated by contributions from light impurities (C,O), and metals only contribute ≈ 20% to P_{rad}.

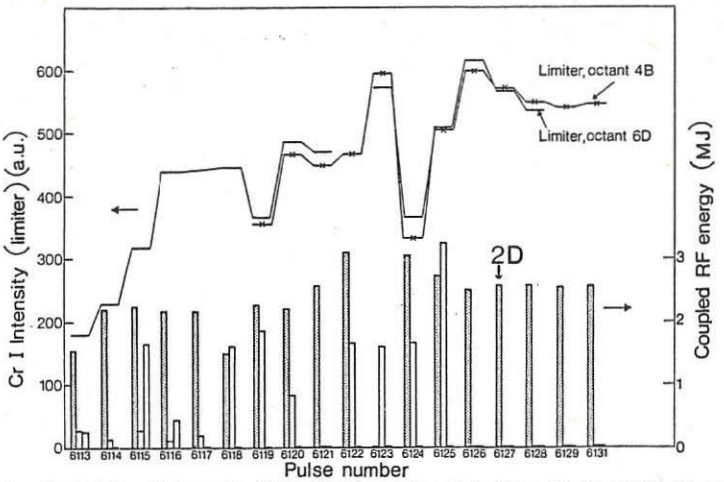

Fig.1 Cr I line intensity (two limiter views) before RF demonstrating the contamination and cleaning of the limiters as a function of preceding 2D antenna operation.

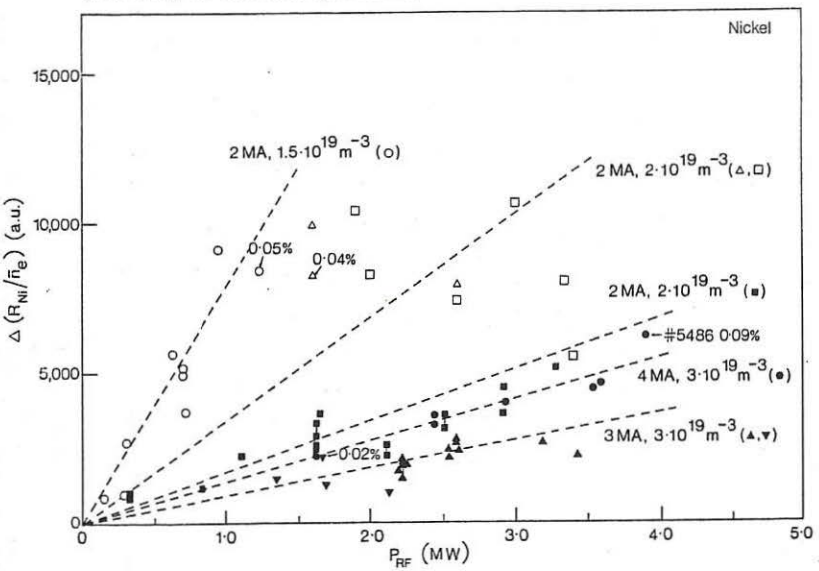

Fig. 2 Increase of Ni XXV 117.9-Å line intensity divided by $\bar{n}_e$ during ICRH as a function of RF-power from the 2B and 6B antennae. The dashed lines are drawn to guide the eye only.

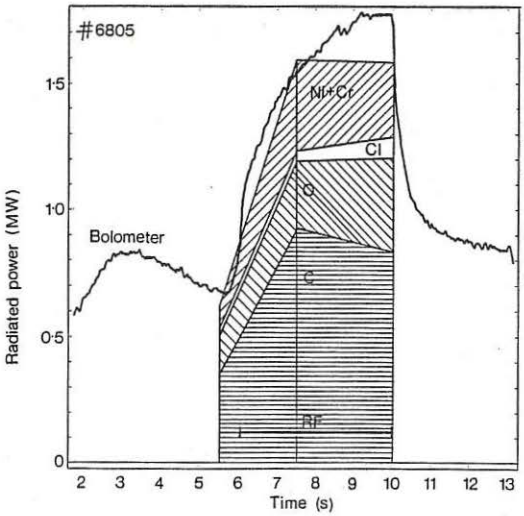

Fig.3
Calculated contributions from carbon, oxygen, chlorine and metals (nickel + chromium) to the total radiated power.
The calculation has been made for one time point before RF and two time points during RF. The result is compared with the total radiated power as measured by bolometry.

#6805
(^{3}He)D, 3.4 T, 2.0 MA, P_{RF} = 1.66 MW

	Before RF (t=5.5 s)	During RF (t=10.0 s)
C :	4.0% of n_e	4.7
O :	1.0	1.3
Cℓ:	0.04	0.06
Ni:	0.03	0.04
Cr:	0.02	0.02
Z_{eff}^{calc} :	3.2	3.6
Z_{eff}^{brems} :	4.0	3.5
$n_e(0)$:	1.93×10^{19} m^{-3}	2.79×10^{19} m^{-3}

Table 1 Analysis of the impurity content of JET pulse 6805 before and during RF heating. Z_{eff} is calculated from the impurity mixture for comparison with Z_{eff} from visible bremsstrahlung.

REFERENCES

/1/ B Denne et al., M F Stamp et al., Proc. of the 12th European Conf. on Contr. Fusion and Plasma Phys.I, p.379 and II, p.539, Budapest (1985)

/2/ K H Behringer et al., JET Preprint JET-P(85)08 (1985)

/3/ H Jäckel et al., this conference

RADIATION BEHAVIOUR DURING ADDITIONAL HEATING OF JET PLASMAS

K Behringer, A Edwards, H-U Fahrbach[+], R D Gill, R Granetz, N Gottardi, H Jaeckel[+], G Magyar, E R Mueller[+], A Weller[+] and D Zasche[+]

JET Joint Undertaking, Abingdon, Oxon OX14 3EA, UK
[+]EURATOM-IPP Association, Garching

Abstract

Additional heating in JET with ICRH or NBI leads to an increase of the total radiated power. This is partly due to the density increase caused by the applied heating method. The relative power loss P_{rad}/P_{tot} reaches higher values with RF heating. The density increase can be partly controlled when the plasma is attached to the inner wall.

Radiation sources at the plasma edge lead to asymmetric radiation flux profiles. For this case the local emissivities can be derived from the bolometer measurement by a tomographic reconstruction method. Reliable values for the central radiation can be evaluated from the soft X-ray diagnostic when measuring with a 4.4 µm Be filter.

The radiative power loss of the JET plasma can be measured by bolometers in the energy range 5 eV $\leq E_{ph} \leq$ 9 KeV and with surface barrier diodes (soft X-ray diagnostic) in the range 300 eV $\leq E_{ph} \leq$ 10 KeV. The lower threshold energy of the diodes can be shifted to higher values by using Be-filters of different thickness. For both diagnostics two camera systems are available, viewing the plasma from the bottom ("vertical cameras") and the side ("horizontal cameras") on the same ports. In the immediate vicinity two RF antennae are installed which generate local radiation sources due to their interaction with the plasma. These sources contribute to the bolometer signal as well as to the soft X-ray signal (provided the latter is operated without filter). This may lead to an overestimation (up to about 10%) of the total radiated power derived from the vertical bolometer camera.

At present additional heating on JET with RF or NB provides similar maximum power levels ($P_{AH} \leq 5.5$ MW). The evolution of the electron density and hence of the radiated power during additional heating depends sensitively on whether the plasma is attached to the outer limiters or to the inner wall carbon protection plates. A strong increase of the electron density (particularly with NB-heating) and of the radiation loss is observed when the plasma is attached to the outer limiters. In inner wall operation, the density increase can be reduced or the density can even be kept constant. High radiation peaks may occur at the plasma edges. Fig.1 shows the radiation flux distribution for two NB-heated (Fig. 1a, 1b) and two RF-heated discharges (Fig. 1c, 1d) for limiter operation (top) and inner wall operation (bottom). The sudden appearance of a pronounced radiation peak at the inner plasma edge during the limiter bound discharge of Fig.1 is due to a shift of the plasma to the inner wall.

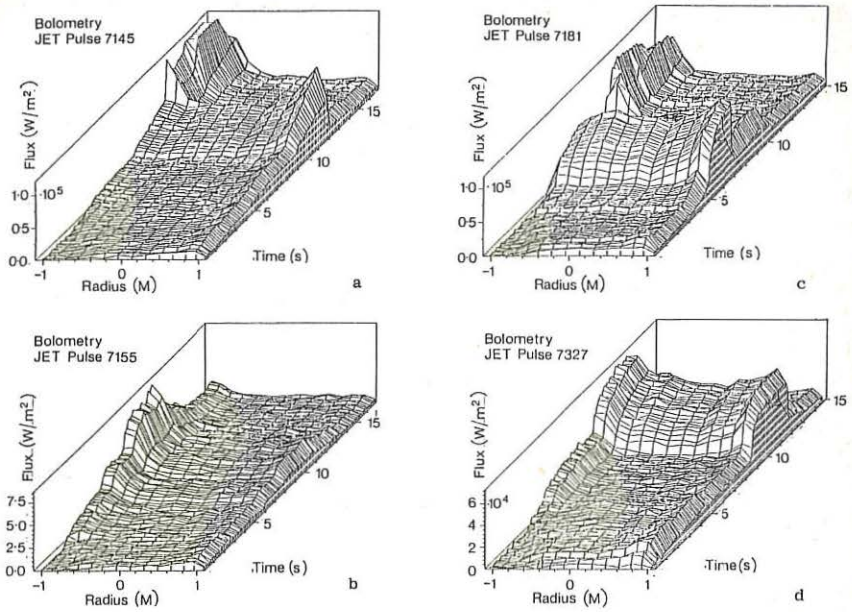

Fig. 1 Brightness distribution measured by the vertical bolometer camera for NB- (left) and RF-heated (right) discharges.

The relative power loss reaches 70% in the case of RF-heating (high <ne>). It can be kept quite low for NB-heating, when the density increase is controlled by shifting the plasma to the inner wall (Fig.2). Even in the high density NB-heated discharges the relative power loss is only about half of that in the corresponding RF-heated discharge.

The local emissivities can be evaluated by Abel inversion only for radially symmetric flux profiles. Using a tomographic reconstruction method /1/ one can derive local emissivities also when m = 1 and m = 2 deviations from the poloidal symmetry occur. Fig. 3 shows the emissivity distribution obtained from a tomographic reconstruction and from an Abel inversion (dashed curve) of the flux profile of the vertical bolometer camera. In the latter case the channels which are affected by the outer local radiation source have been omitted.

The emissivity in the centre cannot be derived accurately when asymmetries or hollow flux profiles occur. In that case the central emissivities can be obtained from soft X-ray measurements. Using a 4.4 µm Be filter ($E_{ph} \geq 750$ eV) leads to an attenuation of the radiation predominantly from the plasma edge and hence to radially almost symmetric emissivity profiles (Fig.4). In this case the m = 0 component gives reliable values for the central radiation. For the hollow radial profile shown in Fig.4 the contribution to the soft X-ray signal can arise from resonance lines of H-

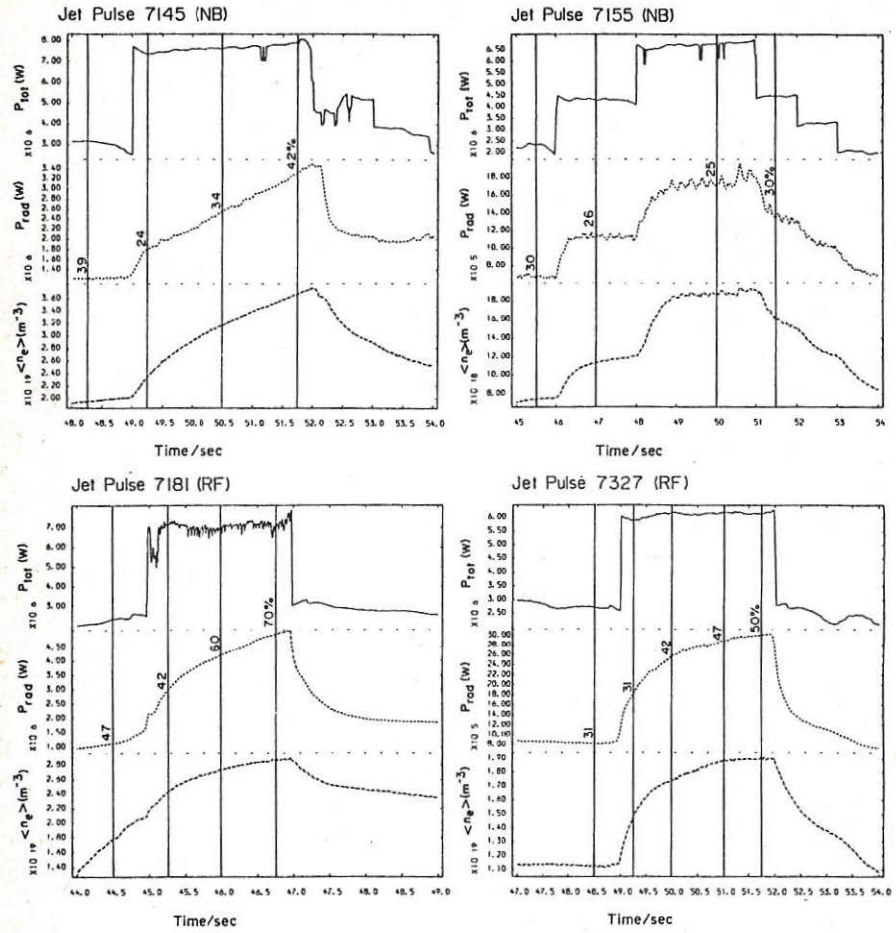

Fig. 2: Time history of the total radiated power (middle curves) and the volume averaged density <ne> (lower curve) for the input power given in the upper curves. The numbers at the middle curves give the relative power loss P_{rad}/P_{tot}.

and He- like oxygen and/or from metallic impurities in Ne- to Li-like states. Carbon line radiation is almost completely supressed by the 4.4 µm Be filter. For the discharge of Fig.4 a concentration of ~ 0.09% metallic impurties estimated from the soft X-ray measurements are in agreement with spectroscopic results /2/. For oxygen line radiation transport calculations usually show the radiation shell closer to the plasma edge than one would derive from the soft X-ray emission profile.

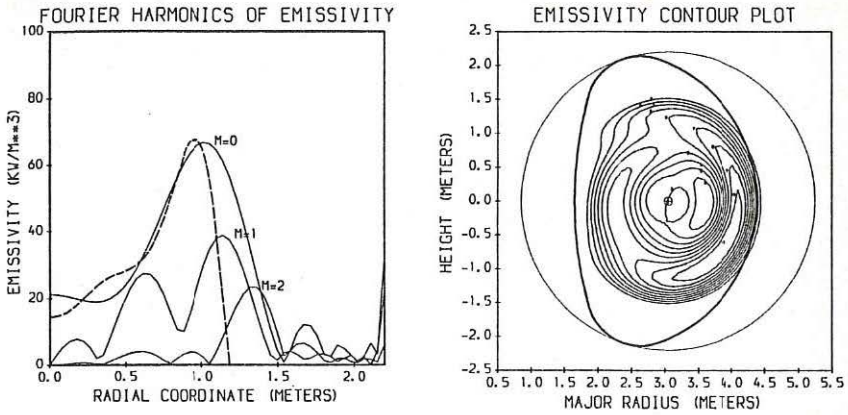

Fig. 3: Emissivity distribution of an RF-heated discharge derived by a tomographic method and by Abel inversion (dashed curve).

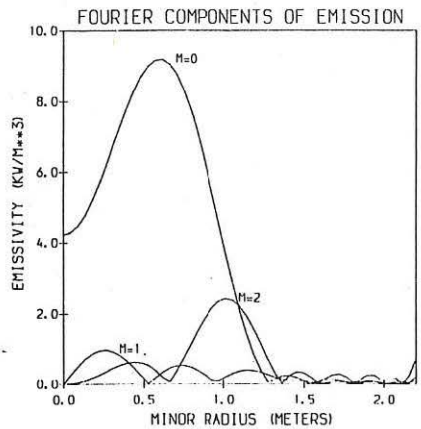

Fig. 4: Fourier components of the emissivity obtained from a soft X-ray measurement using a 4.4 µm Be filter.

References

/1/ R.S. Granetz and J.F. Camacho, Nucl. Fus. 25, 727 (1985)
and
J.F. Camacho and R.S. Granetz, Rev. Sci. Instr., 52, 417 (1986)

/2/ B. Denne, et al., this conference.

STUDY OF LINE RADIATION ASYMMETRIES IN THE TJ-1 TOKAMAK

B. Zurro, C. Pardo and TJ-1 Group
División de Fusión. J.E.N. 28040 Madrid. Spain

Observations of poloidal asymmetries in hydrogen isotopes and impurity line emission, (1) (2) (3) (4) and (5), from tokamak plasmas have motivated reconsideration of particle transport processes in plasmas (4). Poloidal and toroidal line radiation asymmetries have been also observed in stellarator plasmas (6) but they have been exclusively atributed to wall inhomogeneities.

In this work, results of the spatial distribution of hydrogen and ionized impurities states in the TJ-1 tokamak are presented. This is a small device (R = 30 cm, a = 10 cm) toroidally limited, operated for this experiment with a toroidal field of 1 T, line average density between 1 - $3x10^{13}$ cm^3 and peak current of 40 KA. This device offers some advantages for this measurements, since plasma cross section can be scanned at two 90º separated views, and, high ionized states radiate from the inner core, due to the TJ-1 plasmas temperature range ($T_e \lesssim 400$ eV).

TJ-1 plasma emission profiles between 200 - 600 nm were measured with a 1 m monochromator provided with a fast rotating polygonal mirror (Fig. 1) that performs repetitive plasma scans in .4 msec, every 1.5 msec. The optical system forms the entrance slit image (90º rotated) at the quartz window to get the maximum spatial resolution. Emission profiles are temporarily stored in the diskette unit of a digital oscilloscope to be later transferred to a PDP-11/44.

Typical H_β emission profiles obtained through TJ-1 side and

bottom ports are shown in Fig. 2. Side profile Fig. 2a, shows a maximum around the equatorial axis chord, monotonically decreasing towards the up and down plasma edges. Hydrogen emission profiles measured from the bottom window exhibit a systematic peaking on the outside boundary, Fig. 2b. Similar behaviour has been also observed for spatial scans of H_β - wing radiation.

Line emission from low ionization states of impurities (OII, CIII, CrI, ...) radiating from the plasma edge present side emission profiles, Fig. 2c, similar to those of hydrogen. They peak around the equatorial plane where the interaction between the plasma and the toroidal limiter is stronger. This type of emission, in contrast with hydrogen, when viewed through the bottom port shows typical two edge peak structure, Fig. 2d, in this case the in-out asymmetry changing along the discharge depending on small variations of plasma positioning. This horizontal asymmetry tends to be more important for emission of lower ionized elements, like is shown in Fig. 3.

Significant vertical asymmetries have been observed in higher ionized elements like OV, when probes were placed in the upper boundary at the same toroidal sector as this spectral diagnostic. This asymmetry was consistent with $B \times \nabla B$ drift, see Fig. 4, since its sense changed by reversing the toroidal field. This asymmetry, that was not due to a local source of oxygen, disappeared without probes.

In conclusion, poloidal asymmetries in TJ-1 line plasma radiation have been observed, most of them seems to be related like in (2) and (6) to geometrical asymmetries in the vacuum chamber and diagnostics of TJ-1.

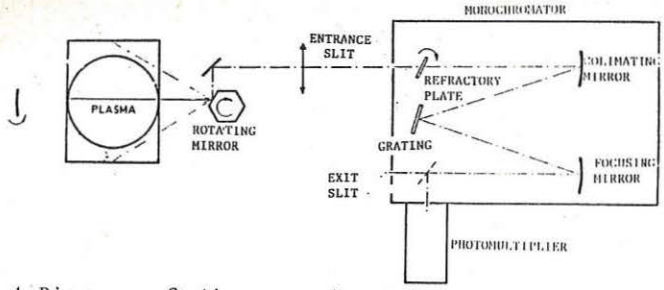

Fig.1 Diagram of the experimental set-up. The whole system can be brought down to scan the plasma through the bottom port using an auxiliary mirror.

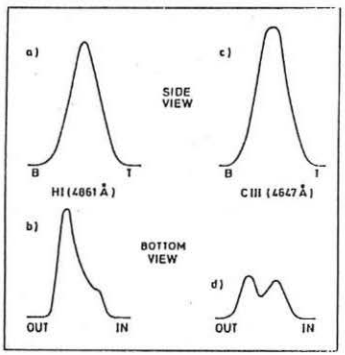

Fig. 2 Typical emission profiles of hydrogen and low ionization stages in TJ-1.

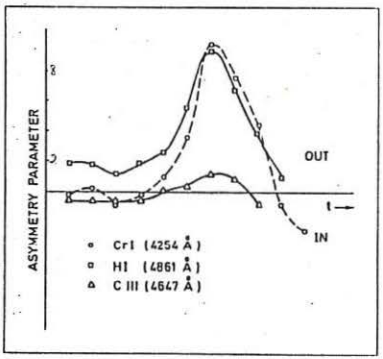

Fig. 3 IN-OUT asymmetry parameter for three spectroscopic features in TJ-1.

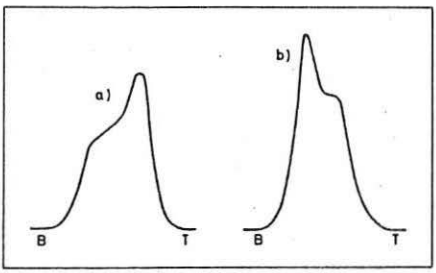

Fig. 4

Observation of vertical asymmetries in OV (2781 Å) emission. Toroidal field was reversed from a) to b).

References

(1) J.L. Terry, E.S. Marmar, K.I. Chen and H.W. Moos
Phys. Rev. Lett. 39, 1615 (1977).

(2) S. Suckewer, E. Hinnov and J. Shivell
Rapid scanning of spatial distribution of spectra line intensities in PLT tokamak. Report PPPI-1430 (1978).

(3) K.I. Chen and M.E. Huber,
Bull. Am. Phys. Soc. 27, 8, Part II, 1060 (1982).

(4) K. Brau, S. Suckewer and S.K. Wong,
Nucl. Fus. 23, 12, 1657 (1983).

(5) Axdex Team, Proc. XII Eur. Conf. Cont. Fus. Plas. Phys. 53 (1985)

(6) WVII-A Team, Proc. IX Eur. Conf. Cont. Fus. Plas. Phys. BP-29 (1979).

RESPONSE OF THE ALT-I-PUMPLIMITER TO DIFFERENT PLASMA CONDITIONS IN TEXTOR

D.Reiter (1), G.A. Campbell (2) and the ALT-I-Group

1. Institut für Plasmaphysik der Kernforschungsanlage Jülich
   Association EURATOM-KFA, P.O.B. 1913, D-5170 Jülich;

2. University of California at Los Angeles,
   Los Angeles, CA USA

1) Introduction

The main objective of the Advanced Limiter Test-I (ALT-I) programme is to study the capabilities of pumplimiters for particle removal as an alternative to magnetic divertors. The ALT-I arrangement consists mainly of the exchangeable ALT-I pumplimiter heads, the vacuum chamber (Volume=700 l) and the pumping system ($S \leq 1.5 \cdot 10^4$ l/s).

Maximum particle removal rates of $6 \cdot 10^{20}$ particles/s were achieved, enough to allow an active density control. The removal efficiency $P \cdot S/Q_{in}$ (Q_{in}: particle flux at the throat entrance, P: pressure) is found in the range 0.5 - 1.0, and, assuming $\tau_p = \tau_e$ the estimated exhaust efficiency $P \cdot S/(Ne/\tau_p)$ is 15%.

Recent progress in pumplimiter modeling /1/ has led to a better understanding of the performance of pumplimiters in general. The ability to reproduce experimentally observed pressure rises in the pumping chamber vs. different boundary plasma conditions within a few percents by a fairly simple and well understood theoretical model for the neutral gas encourages the step from the reproducing "interpretative modeling" to the predictive type of modeling. In this paper we will identify the important assumptions made in creating the model and those to which the results are less sensitive, by comparing experimental results from the ALT-I pumplimiter experiments in TEXTOR /2/,/3/ with data obtained with the Monte Carlo Code EIRENE /4/.

2) Pump Limiter Geometry

One of the minimum requirements of the model is to reproduce precisely the vacuum conductances for backstreaming from the pumping chamber to the main plasma region. It turned out that a fairly detailed 3D description of the limiter head geometry, comprising the throat and duct region (figs./1/,/2/) was necessary, even including a discontinuity in the crossection at the connection of the throat and duct components. The throat with a rectangular crossection (3.75 × 22.5 cm^2) has a lenght of 28.6 cm. A duct is mounted perpendicular to it, with a rectangular crossection (28.5 × 7.4 (narrow) or 13.5 (wide duct)) and 84 cm long. This duct points outward and leads particles into the cylindrical pumping chamber.

Vacuum conductances (H_2 molecules, 300 Kelvin) have been computed for several geometries similar to the one of the ALT-I-VG head, and the actual value for the narrow duct (wide duct) VG-head, 565 l/s ± 2% (880 l/s ± 2%), is in perfect agreement with the value determined for ALT-I-VG from the Helium pressure decay rate in the pumping chamber in gas puff experiments without plasma in TEXTOR (570 l/s, /5/).

3) Neutral-Plasma Interaction

Simulation was facilitated considerably by the fact that for the different geometrical configurations we are mainly interested in global quantities. Since the code can handle continuously varying plasma parameters within one mesh cell, no mesh discretization of the 3D volume was necessary (/4/,Append.). In the throat region (shaded area in fig./2/) a plasma is defined by the numbers n_e, n_i, T_e, T_i, λ_{n_e}, λ_{n_i}, λ_{T_e}, λ_{T_i} and M, which are the mean electron density, ion density, electron and ion temperature, the radial decay lengths for these parameters and the Machnumber of the flow parallel to **B** onto the deflector plate, respectively. The reaction rates for neutral-plasma interactions, which are selected from a data-library, are only those which can expected to have influence for the case studied. The range of relevant throat plasma parameters points to only three important reactions, namely ionisation of H-atoms by electron impact, charge exchange $H+H^+ \rightarrow H^+ + H$ and dissociation of H_2-molecules (via different channels leading to $2 \cdot H$, $H+H^+$ or $2 \cdot H^+$).

Fig.3 shows the pressure (mtorr) in the pumping chamber vs. T_e and n_e, for $n_i = n_e$, $T_i = T_e$, $\lambda_{n_e} = 1.5$, $\lambda_{T_e} = \infty$, M = 0.3, for no pumping /3a/ and for 7000 l/s pumping speed /3b/ in the chamber using "standard geometry" of the ALT-I-VG head (narrow (7.4 cm) duct, wide (3.75 cm) throat). In /1/ these results are compared with experimental data, interpreted and discussed concerning their relevance for future pumplimiter design. We should point out here that the shape of the profile in fig./3/ has a strong dependence on electron temperature for $T_e < 20$ eV. This is a result of the steep increase of the production rate for ion-electron pairs from neutral particles H and H_2 with increasing electron temperature (fig./4/) and much more distinct in the unpumped than in the pumped case (note the different pressure scales in fig. 3a and 3b).

4) Wall Reflection Model

Ions impinging at the deflector plate and neutrals hitting the walls are treated as prescribed by the "Behrisch Matrix" /6/, which has empirically been extended for nonperpendicular incidence /7/. We have crosschecked the results with those from runs where the "Marlowe"- database /8/ and the "Trim"- database /9/ have been applied instead. Within both the experimental error margins and the statistical scattering in the Monte Carlo results no significant change (less than 10%) in the global values could be observed. This can be understood from the fact that in the very narrow throat and duct a neutral particle experiences many (> 100) collisions with the wall during its lifetime in the system. Thus it does not carry over the details of one single wall collision into its contribution to e.g. the mean pressure in the pumpchamber. The same (and from the point of view of modeling helpful) observation was made with respect to the assumptions for the distribution (in both physical and velocity space) of ion flux hitting the neutralizer plate.

Of course, more detailed but experimentally not observable features of the model, like energy spectra of the neutrals in regions close to the deflector plate, are sensitive to these more complex boundary conditions. On the other hand, they lead to much higher computation times (up to a factor 2), thus we routinely apply the simpler but still fairly complete "Behrisch-Matrix", using the "Trim"-data only occasionally for crosschecking.

5) Design Considerations, Conclusions

Three different geometries of the pumplimiter head have been used in the experiments by now. They made accessible different throat lengths and both open and closed configurations. In the calculations an even wider range of geometries could be evaluated.

We consider the effective conductance of the plasma filled throat for backstreaming from the neutralizer plate into the bulk plasma and the conductance of the duct and pumping system.

It is clearly demonstrated by both real and numerical experiments (/1/,/3/) that high removal efficiencies require small ratios of the two conductances mentioned above. The conductance of a plasma filled rectangular throat decreases with increasing electron temperature. This "plasma antiplugging" via electron-neutral interactions is counteracted to some extend by the action of the ions, the "plasma plugging" (charge exchange). In the calculations the latter effect depends on the assumptions made for the velocity distribution of the ions in the throat volume. Until now we always assumed a shifted but otherwise isotropic maxwellian distribution. First numerical results seem to indicate that in cases with high pumping (i.e. low neutral pressure in the throat) more realistic, anisotropic distributions can have a significant (+25%) effect on the pressure built-up in the pumping chamber.

/1/ G.A. Campbell, D.Reiter et al., to be published

/2/ W. Bieger et al., Proc Int Symp. on Plasma Wall Interactions Jülich (1976), 609

/3/ A.E.Pontau et al.,J.Nucl. Mat 128 & 129 (1984),434

/4/ D.Reiter,Jül - 1947, (1984)

/5/ G.Thomas, Sandia Livermore, private Communication

/6/ R. Behrisch, Summer school of Tokamak reactors, Erice (1976)

/7/ D. Reiter,A. Nicolai, J.Nucl. Mat 128 & 129 (1984),458

/8/ G.Bateman, PPPL Applied Physics Report No. 1

/9/ W.Eckstein, IPP Garching, private Communication

Fig. 1

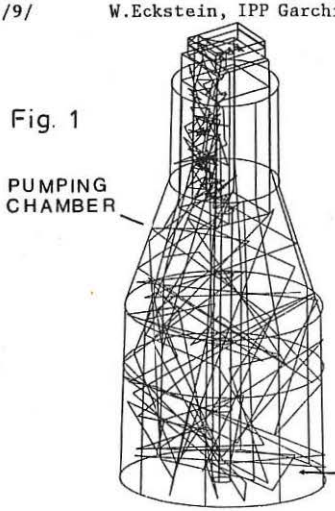

Fig. 2

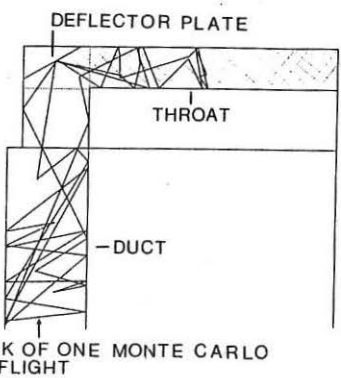

Fig. 3a

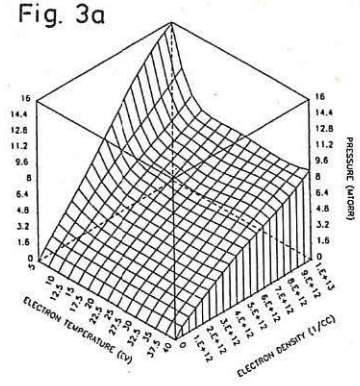

Fig. 3b

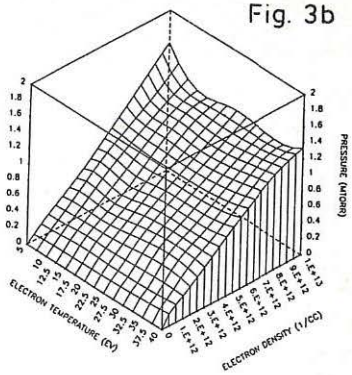

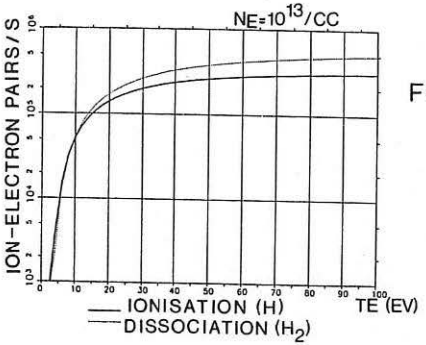

Fig. 4

Fig. 5

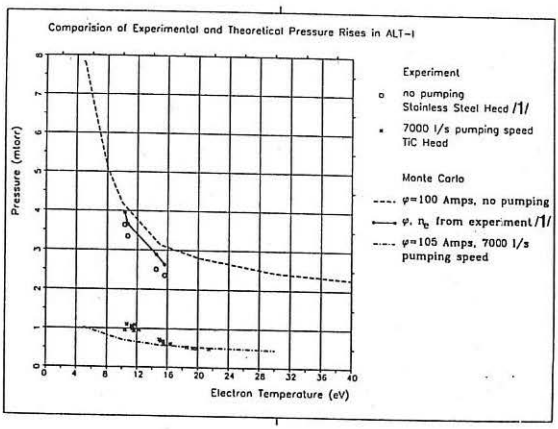

PERFORMANCE OF TEXTOR WITH OHMIC HEATING IN THE PRESENCE OF GRAPHITE LIMITERS

G. Fuchs, G. Waidmann and the TEXTOR-Team

Institut für PLasmaphysik, KFA-Jülich, Assoziation EURATOM-KFA
5170 Jülich, F.R.G.

Abstract
The operational limits of Ohmic heating in TEXTOR with graphite as limiter material have been explored up to plasma currents of 0.5 MA. The results are compared with former experiments using stainless steel as the main limiter material. The parametric dependence of the global energy confinement time τ_E follows the Goldston scaling. The poloidal β_{pol} scales proportional to $\bar{n}_e/I_p$. A saturation effect was observed in the high density regime.

Introduction

In the field of plasma wall interaction studies on confined tokamak plasmas TEXTOR has paid special attention to the influence of limiter and liner materials on plasma performance. After the demonstration of metal impurity removal from the core of the plasma by in situ surface carbonisation /1/ the stainless steel limiters were exchanged against graphite limiters. One objective was to show that the transient behaviour caused by decarbonisation could be avoided and the exclusion of metallic impurities could be extended over longer periods of experimental work.

The TEXTOR machine was operated at full lay-out values: I_p = 0.5 MA, B_T = 2T and current pulse durations of more than 3 sec. More recently the magnetic field was increased to B_T = 2.6 T allowing operation at a higher safety factor. With graphite limiters the loop voltage dropped below 1 Volt resulting in a pulse duration of 4 sec. Cylindrical q_L = 2 values were reached. The q=1-surface had a diameter of $2r_s$ = 34 cm for I_p = 480 kA showing a regular sawtooth activity with a period between 7 and 40 msec depending on machine operating conditions. Metallic impurities could be suppressed effectively at the expense of an increased carbon impurity concentration. Average densities $\bar{n}_e$ = 5.3 x 10^{13} cm^{-3} were obtained for Ohmic heating and $\bar{n}_e$ = 5.7 x 10^{13} cm^{-3} for plasmas with additional ICR-heating.

Operational Regime of TEXTOR

The operational limits of TEXTOR in case of Ohmic heating are shown in Fig. 1 for different wall and limiter conditions. Operation with graphite limiters is presented by the symbols ◇ > ∧ . (◇ density disruption, > ∧ stable discharges). The symbol □ stands for a disruption with carbonized steel limiters and carbonized liner, + for density disruptions in the current ramp down phase. The circles ● show for a comparison the situation obtained before with cleaned metal walls and steel limiters. After a perioc of intense cleaning and repetitive baking the performance with graphite limiters gradually improved so that similar density limits were obtained as found before with carbonized limiters and wall surfaces. A maximum value of $M = \bar{n}_e \cdot R/B_T$ = 4.9 · 10^{19} $m^{-2}T^{-1}$ was reached compared to M = 4.5 · 10^{19} $m^{-2}T^{-1}$ reported earlier /1/.

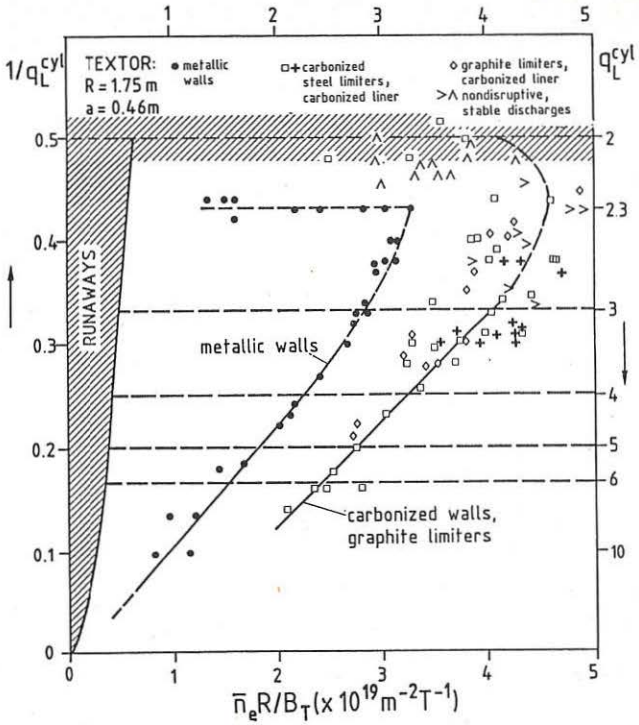

Fig. 1 Operational regime of TEXTOR for metallic limiters and walls •, carbonized limiters and walls □ + and graphite limiters and carbonized walls ◇>∧.

The density limit showed again a linear dependence on plasma current up to a transition region where the q-limitation enters in the vicinity of $q_1 = 2$. A clear improvement is seen with respect to the steel limiter situation where only $q_1 = 2.3$ was reached as the q_1-limit /2/. No memory effect after hard disruptions was observed when working near the critical limits. However, the graphite limiters store and release gas during a discharge cycle and influence strongly the density obtained in subsequent discharges. The source and sink properties of graphite limiters play an important role in the particle balance. The electron temperatures measured on axis by ECE $T_e(Ro)$ are given in Fig. 2 in the form of a scaling law. T_e increases with plasma current and decreases inversely to the square root of average density from 1.3 to 0.6 keV.

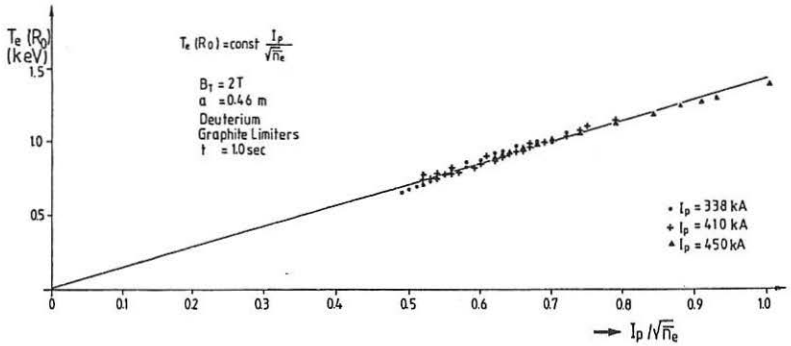

Fig. 2 Electron temperature on axis versus the ratio of plasma current to the square root of electron density.

Scaling Laws for Ohmic Heating

The plasma β_{Pol} was measured by means of a compensated magnetic loop. Its parametric dependences were studied experimentally. β_{Pol} increases linearly with the average density $\bar{n}_e$ and decreases with the plasma current I_p. For the highest density a slight deviation is seen after the linear increase, indicating a saturation. For the linear part a scaling law of the form

$$\beta_{Pol} = 4.8 \times 10^{-9}\ \bar{n}_e/I_p\ (cm^{-3} \cdot A^{-1})$$

was deduced (s. Fig. 3). A comparison with the situation of carbonized steel limiters gave a similar but somewhat lower scaling value $\beta_{Pol} = 4.3 \times 10^{-9}\ \bar{n}_e/I_p$. The saturation effect, however, was not evident in these experiments.

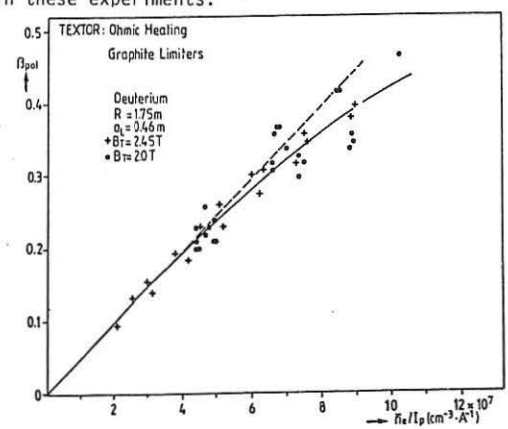

Fig. 3
β_{Pol} versus $\bar{n}_e/I_p$

The global energy confinement time τ_E was also studied as a function of average electron density and plasma current. τ_E increases at first linearly with density and tends to saturate for $q_L \gtrsim 4$. For smaller q_L-values this effect is less clearly visible. With graphite limiters a pronounced detachment effect of the plasma from the limiters was observed for the higher densities. Especially in the early state of graphite limiter operation of TEXTOR, when larger amounts of impurities were released, a retraction of the plasma from the limiters was recognized. The power loading on the limiters was strongly reduced and a major energy loss due to radiation from the boundary plasma was measured /3/. The dependence of τ_E on q_L is shown in Fig. 4. The scaling law of Goldston /4/ is included as solid curve. A good agreement is demonstrated. The data favour a square root dependence on q_L. Maximum values τ_E = 100 msec were recorded similar to the situation observed already for carbonized stainless steel limiters.

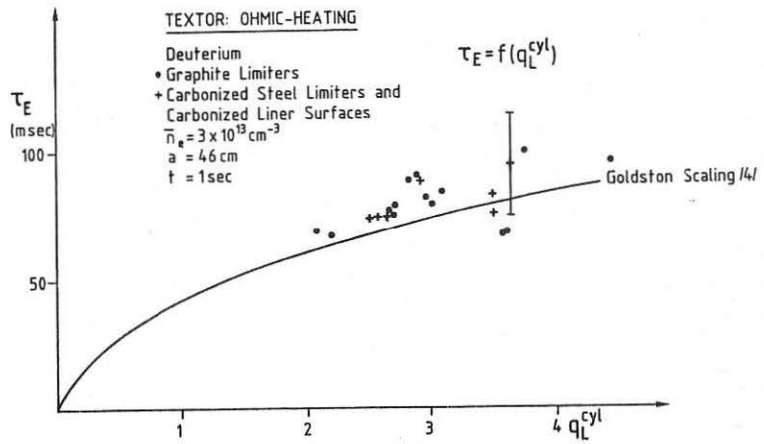

Fig. 4 Global energy confinement time τ_E versus q_L

References

/1/ J. Schlüter et.al., 12th Europ. Conf. on Controlled Fusion and Plasma Physics, Budapest 1985, Vol II, 627

/2/ G. Waidmann et.al., Plasma Physics and Controlled Nucl. Fus. Res. 1984,; Nuclear Fusion Suppl., Vienna (1985) Vol 1, 193

/3/ U. Samm et.al., 11th Symp. on Plasma Engineering, Austin, Texas, 1985

/4/ R.J. Goldston, Plasma Phys. and Contr. Fusion, 26, No. 1A, 1984, 87

Wall Carbonization in ASDEX: A Collation of Characteristic Results

W. Poschenrieder, G. Fußmann, G. v. Gierke, F. Mast, H. Niedermeyer, J. Roth, F. Söldner, K. Steinmetz, H. Verbeek, F. Wagner. G. Becker, H.S. Bosch, H. Brocken, K. Büchel, A. Eberhagen, D. Eckhartt, O. Gehre, J. Gernhardt, E. Glock, O. Gruber, G. Haas, J. Hofmann, A. Izvozchikov[1], G. Janeschitz, M. Kaufmann, F. Karger, M. Keilhacker[2], O. Klüber, M. Kornherr, K. Lackner, R.,S. Lang, M. Lenoci[3], F. Leuterer, G. Lisitano, H.M. Mayer, K. McCormick, D. Meisel, V. Mertens, H. Murmann, J.N. Noterdaeme, A. Pietrzyk[4], H. Rapp, H. Riedler, H. Röhr, F. Ryter[5], W. Sandmann, F. Schneider, C. Setzensack, G. Siller, P. Smeulders[2], E. Speth, K.-H. Steuer, O. Vollmer, F. Wesner, D. Zasche.

Max-Planck-Institut für Plasmaphysik, EURATOM-Association
D-8046 Garching/München, FRG

The aim of this presentation is to describe the procedures of carbonization and decarbonization followed on ASDEX, and to summarize the most significant changes of discharge parameters observed under the various experimental conditions with carbonized walls.

Carbonization and Decarbonization.

Carbonization, a method originally proposed by the Jülich IPP Group /1/ has been employed before on TEXTOR /2/ and JET /3/ to reduce high Z impurities from the wall material in discharges. In contrast to the philosophy on TEXTOR and JET, where carbonization was executed with wall temperatures above 150°C, room temperature conditions were used on ASDEX, without any obvious disadvantage. From August 85 to March 86 nine carbonization and five decarbonization runs were done. The walls were in carbonized condition on thirteen experiment days. The system for glow discharge cleaning /4/ was also employed here. Methane was admitted to the D_2 or H_2 discharge via the divertors to prevent local overconcentration. Typical discharge parameters during carbonization were $p(D_2) = 4.10^{-1}$ Pa and $p(CH_4) = 9.10^{-2}$ Pa with the discharge off. When the discharge is switched on (U = 400 V, I = 2.0 A) the partial pressures change as depicted in Fig. 1. The exponential transitions are reasonably well described by a first-order differential equation with the time constant given by $\tau^* = V/S$ for "off" and $\tau^* = V/(S_V + S^*)$ for "on". V is the vessel volume (26 m^3), S_V is the speed of the vacuum pumps, and S^* represents the speed by which CH_4 disappears from the gas phase caused by the discharge. H_2 shows practically the same time constants as CH_4 and is obviously produced by cracking of CH_4. The time constants yield S_V = 2600 l/s (only 1/4 of the full pumping system was employed) and S^* = 1500 l/s. The latter corresponds to a "cracking rate" of $3.5\ 10^{19}$ molec./s, while the current of 2A is equivalent to $1.2 \cdot 10^{19}$ ions/s. An analysis of the ions leaving the discharge by a time-of-flight analysis indicates that the current is mainly carried by hydrocarbon ions. Consistent with this is the observed deposition rate based on the table of interference colors as given by the Jülich group /5/. Obviously, CH_4 is more cracked than is directly deposited. The radicals

---

[1]Academy of Sciences, Lenigrad, USSR; [2]Assigned to JET Joint Undertaking, England; [3]ENEA Frascati, Italy; [4]University of Washington, Seattle, USA; [5]CEN Grenoble, France.

formed in the gas phase do not lead to carbonization on contact with the wall but seem to react to C_mH_n as indicated by the mass spectrum. A detailed particle balance was not attempted, but summing up the partial pressures of fig. 1 yields a slight increase of total pressure with the discharge on. It also explains the simultaneous drop in the ionization gauge indication since CH_4 is replaced by H_2 and HD.

The carbon deposition was limited to the plasma chamber, and not homogeneous owing to its geometry with corners and protrusions. Film thickness judged by the interference colors varied from 500 to 1500 Å, with a mean value of about 1000 Å after 6 hours carbonization. The deposited film were not analyzed otherwise, but all observations suggest they were the typical amorphous a-C:H layers /1/. Effect and behavior of the deposits during discharges are shown in fig. 2 for the radiation of C and Fe. Typically, one carbonization lasted for 50 shots (one experiment-day) with ICRH being most abrasive. The second carbonization was for 2h on top of the old layer.

Decarbonization in pure H_2 turned out to take about ten times as long as carbonization, i.e., 60 hours. But, the presence of a few permille of oxygen from residual H_2O, a leak or deliberate admission was found to considerably speed up the cleaning. A mixture of 0.5 % O_2 in H_2 reduced the time to 12 h, but lead to an increase of residual H_2O. A mixture of 5 to 10% O_2 in He cleaned the machine in less than 3 hours. It was followed by a deoxidation phase in a mixture of He and D_2 and pure D_2. (The best deoxidant is CH_4.) However, discharges after this procedure were characterized by poor density limits and other deviations from normality. Still, global radiation and O radiation were normal, but unusually high radiation of fluor (probably from decomposition of teflon) was found. So far, the actual origin of the problem remains unresolved.

The effects of carbonization on discharges

As already experienced previously with the large toroidal graphite limiter in ASDEX, the presence of large amounts of carbon in the plasma chamber can significantly affect the recycling behavior of hydrogen. Obviously, hydrogen atoms stick to the carbon surface without a high probability for recombination, as compared to steel at room temperature, thus large amounts of hydrogen stay in the vessel between shots. But, in contrast to JET, only minor problems with density control at very low densities were experienced. This is certainly due to the fact that the divertors, which dominate the recycling flux, remained uncarbonized.

ICRH: The success of carbonization reported from TEXTOR /2/, especially with respect to ion cyclotron resonance heating, was a strong motivation also to investigate carbonization on ASDEX. Indeed, concomitant with a reduction of central radiation from Fe by a factor of ten, the total ICRH power of 2.4 MW could now be launched. Without carbonization and only ohmic preheating the power limit was 1.1 MW due to disruptions caused by strong central Fe radiation. Typical values of P_{rad}/P_{tot} = 20 % were found and the improvement in radiation losses is also evident from Fig. 3 showing the fractional radiation increase per ICRH power coupled into the plasma for various wall conditions. Also, the degradation in τ_E during 1 MW of ICRH was only down to 70 % of the ohmic value, instead of 60 % for uncarbonized walls. A comparison of radiation profiles shows slightly increased boundary radiation for the carbonized case being mostly due to C radiation.

OH+NI: In the ohmic phase preceeding neutral injection, spectroscopic data show a 2.5-fold increase in C-radiation with carbonization, a slight decrease in O-radiation and a reduction of Fe-radiation by a factor of ten, still, the global radiation is little affected. Increased τ_E in the saturation regime ($n_e > 3\ 10^{19}\ m^{-3}$) as depicted in figure 4 indicates a reduced share of central radiation. This is fully corroborated by the radiation profiles showing the shift of major radiation to the boundary. Also for NI the degradation of energy confinement in the L-regime was less severe (figure 4), and the power limits for obtaining the H-regime in D_2-discharges were hardly influenced by carbonization. However, the H-regime was not of the same quality showing a higher and more stochastic ELM frequency. The difference is particularly obvious in the values of the poloidal beta, which reached only values of 55 % of the critical value instead of 70 % before carbonization. This behaviour might be associated with the increase in global radiation which is essentially due to high boundary radiation of C under carbonization.

LH: Also lower hybrid heating has profited from carbonization extending the working range to $5\ 10^{19}\ m^{-3}$. Radiation showed now a much smaller increase with $\bar{n}_e$ and LH-Power. Previously, the strong influence of Fe, caused by generated fast ions at higher density ($\bar{n}_e > 2\ 10^{19}\ m^{-3}$), had led to disruptions at $\bar{n}_e \approx 3.5 \times 10^{19}\ m^{-3}$. Problems with density control below $1.2\ 10^{19}\ m^{-3}$ limited the operation regime for experiments with current drive.

Pellet injection: Extremely high central densities of $2.2\ 10^{20}\ m^{-3}$ could now be reached as the reduced Fe-influx eliminated the thermal collapse observed without carbonization. The regime, thus attained, showed unusually long energy and particle confinement. The Murakami-parameter $\bar{n}\ R/B_T$ for $q = 2.7$ increased from $6\ 10^{19}\ m^{-2}\ T^{-1}$ (without carbonization) to $8.5\ 10^{19}\ m^{-2}\ T^{-1}$.

In conclusion, we see ICRH as the main beneficiary of carbonization but the reduced influx of heavy wall impurities extended the operational range quite generally. Only in the quality of the H-regime are negative effects of the increased boundary radiation seen. Carbonization can be regarded as a rather simple and efficient tool to change wall conditions and study plasma wall interaction. Though divertor discharges are less susceptible to impurities the results on ASDEX confirm those of TEXTOR and JET, all of which show that, for the time being, carbon is the best wall material.

References

/1/ Winter, Waelbroeck, Wienhold, Esser, Könen, Banno, Rota and Clausing, Journal of Nuclear Materials 122/123 (1984) 1187.
/2/ Schlüter, Graffmann, Könen, Waelbroeck, G. Waidmann, J. Winter and TEXTOR-Team, Proceed. 12th Europ. Conf. Controlled Fusion and Plasma Physics, Budapest (1985).
/3/ Bickerton et al. JET Report JET-P(85) 15.
/4/ Poschenrieder, Staudenmaier and Staib, Journal of Nuclear Materials 93/94 (1980) 322.
/5/ Winter, Wienhold, Besocke, Littmark, Esser, Banno, Waelbroeck, Kaleck and Tschersich, to be published.

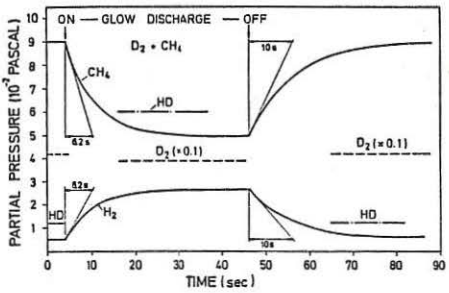

Fig.2: Variation of partial pressures of a D_2 + CH_4 mixture under stationary flow conditions, when the discharge is switched on.

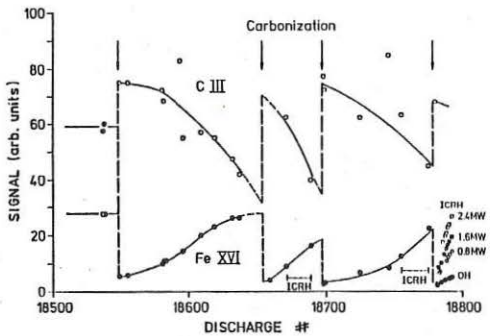

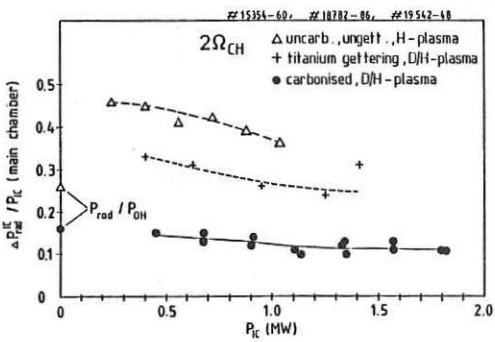

Fig. 3: Reduction of radiation increase during ICRH with carbonization.

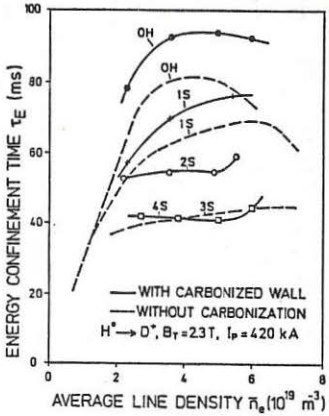

Fig. 4: Improvement of energy confinement with carbonization for OH- and NI-discharges (S: number of sources).

Fig.2: Effect of discharges on the carbon deposit, shown for Fe- and C-radiation. Points represent ohmic standard discharges where not indicated otherwise.

PELLET INJECTION INTO TFR PLASMAS : MEASUREMENT OF THE ABLATION ZONE

TFR Group
(presented by H.W. DRAWIN)

Association Euratom-CEA sur la Fusion
Département de Recherches sur la Fusion Contrôlée
Centre d'Etudes Nucléaires
Boite postale n°6, F-92265 FONTENAY-AUX-ROSES CEDEX, FRANCE

Abstract

Photographies of deuterium pellet ablation clouds show luminous striations extending along the magnetic field lines. Measurement of the angle of inclination of the striations with respect to the toroidal magnetic field direction yields the safety factor $q(r)$. Spectroscopic measurements lead to electron densities of $n_e \gtrsim 10^{23}$ m^{-3} and temperatures ranging from T = 1.6 eV to 20 eV near the ablation center. It sometimes happens that photographies show for an individual pellet striations under angles incompatible with the picture of "classical magnetic islands" imbedded in otherwise well-behaved magnetic surfaces, suggesting a more complicated structure.

Experimental set-up

Frozen deuterium pellets were injected into plasmas of the Fontenay-aux-Roses Tokamak TFR (major radius R_o = 0.98 m, plasma radius a = 0.18 to 0.19 m) during the current plateau using a single-shot pellet injector delivered by the RISO National Laboratory (Danemark) [1] . The pellet parameters are : length ≈ 2 mm, diameter ≈ 0.6 mm, velocity ≈ 600 m/s, average number of deuterium atoms per pellet entering the plasma $\gtrsim 8.10^{18}$. The pellets were partly doped with neon (1 %) in order to increase the visible light intensity (contribution from ionised atoms to the emission).

The pellets are injected in radial direction, perpendicularly to the magnetic surfaces. The injection plane is slightly inclined with respect to the horizontal plane.

The pellet trajectory is observed under an oblique angle β (r) with respect to the injection plane, see figure 1. The injection plane is either focused on a photographic film or on the plane of the entrance slit of a spectrograph. A photomultiplier equipped with a Dβ -filter and connected to a fast acquisition device (100 ns/sample) yields a high time resolution of the D β-emission. Fast electro-mechanical shutters ensure that light is only measured during pellet injection.

Results

1. Photographic measurements : The time-integrated photographic pictures of the luminous trajectories show zones of strong and weak emission. These bright and dark zones extend in form of striations along the magnetic field direction. The whole ablation cloud shows a drift in the direction of the electron current of the discharge. We could obtain unstriated, bent pellet trajectories as shown in Fig. 2 of Ref [2] for very low plasma currents I.

Figure 2 shows densitogrammes of an ablation cloud for 12 equidistant toroidal positions.

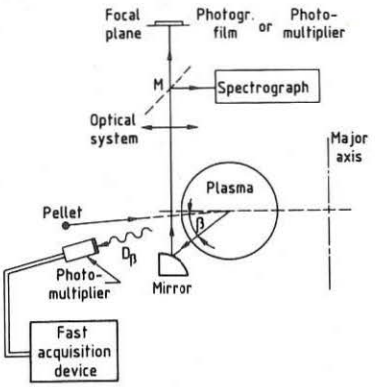

Fig.1 Experimental set-up

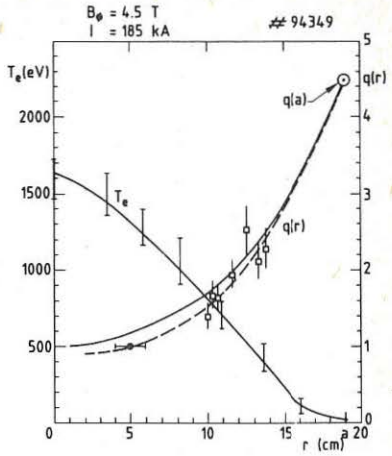

Fig.3 Safety factor q(r) and electron temperature T_e

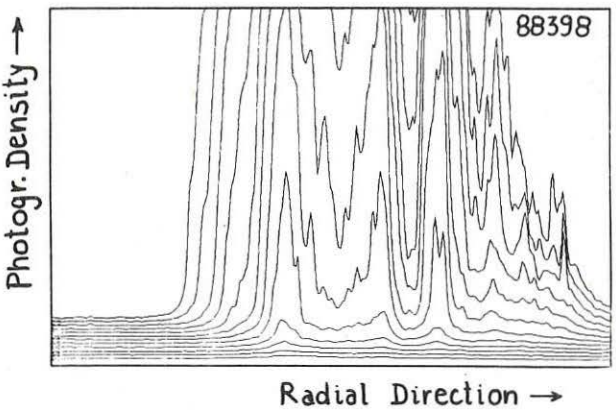

Fig.2 Densitogrammes of striations, discharge N° 88398

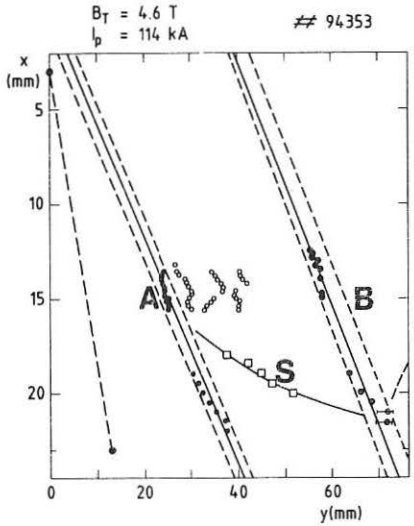

Fig.4 A secondary striation S connects the main striations A and B.The broken line which connects the two dots is the toroidal reference line

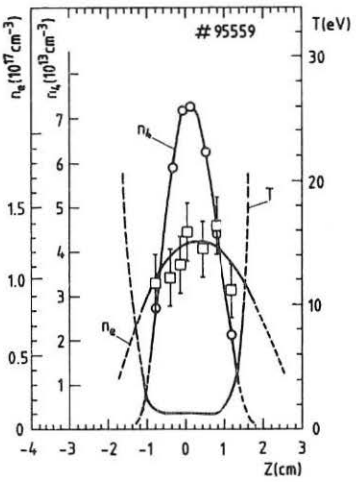

Fig.6 Electron density n_e, particle density n_4 and temperature T along a striation.z=0 has been fixed arbitrarily

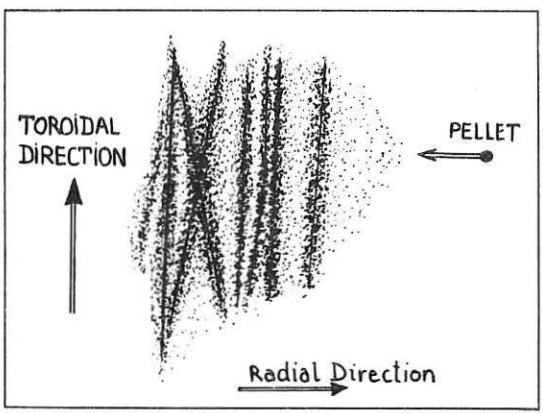

Fig.5

Schematic presentation of a series of striations interrupted by two striations crossing each other and forming an X

On each photography appear, together with the ablation cloud, machine-internal reference points indicating the toroidal direction. We measured a radially dependent inclination of the striations with respect to the toroidal direction. Reversal of the direction of the toroidal magnetic field (without changing the current direction) reversed the angle of inclination. The striations thus seem to follow the magnetic field direction. We have tried to determine from the angle of inclination the safety factor $q(r)$. An example is shown in figure 3. The squares refer to the inclination, the dot at $q = 1$ is from soft-X ray measurements, $q(a)$ is from the total plasma current I. The broken curve is qualitative interpolation. The continuous curve has been calculated with the Spitzer electrical conductivity using as input data the measured values of electron temperature $T_e(r)$, electron density $n_e(r)$, current I and radius a.

It happens that photographies show "well behaved main striations" which are connected by "secondary striations", as if magnetic surfaces at different radii were linked by magnetic channels with strong radial components. An example is shown in figure 4.

In extreme cases, a series of "well-behaved main striations" is locally interrupted by striations forming an X. This is schematically shown in figure 5 (original photography presented in the poster session).

The observed angles between the crossing striations (pertaining to the same pellet) are much too large to be compatible with the direction of the magnetic field lines in the X-points of classical magnetic islands.

It might be that these features visualize particular, still unknown properties of the magnetic structure during a short time interval. Another explanation could be that the plasma column undergoes during a short moment a kind of very fast oscillatory movement.

2. Spectroscopic measurements : By aligning the entrance slit of a spectrograph parallel to the magnetic field lines, i.e., parallel to the striations, we were able to obtain time-integrated spectra of individual striations along the magnetic field direction z. The strongly Stark-broadened D β-line yields the electron density $n_e(z)$ along the striation. Integrating over the D β- profiles yields the (relative) particle density $n_4(z)$ in quantum state $n = 4$ of D^0. Assuming a degree of ionisation of 10^{-4}%, the local thermodynamic equilibrium relations yield $T(z)$. The results of the spectroscopic measurements are summarized in figure 6. The high degree of ionisation explains why the striations are aligned parallel to the magnetic field.

From $n_e(z)$ and $T(z)$ follows $\beta(z) \ll 1$ along the visible part of the striation, i.e. thermal expansion of the ablation cloud pushing away the magnetic field does not take place.

The observations cannot be explained by the "neutral shielding model" [3] nor by the "energy transduction model" [4].

[1] H. Sörensen et al., Proc. 9th Intern. Vacuum Congress and 5th Intern Conf. on Solid Surfaces, 26-30 sept.1983, Madrid, paper I.10.OR2, p. 196

[2] V. Andersen, Proc. 12 th Europ. Conf. Contr. Fusion and Plasma Phys. 2-6 sept.1985, Budapest, Contr. Papers, Part II, p.648

[3] P.B. Parks, R.J. Turnbull, Phys. Fluids 21 (1978) 1735

[4] F.J. Mayer, Phys. Rev. Lett. 55 (1985) 1673

BETA AND CURRENT LIMITS IN THE DOUBLET III TOKAMAK

E.J. Strait, M.S. Chu, G.L. Jahns, J.S. Kim, A.G. Kellman, L.L. Lao, J.K. Lee,
R.W. Moore, H. St. John, D.O. Overskei, R.T. Snider,
R.D. Stambaugh, and T.S. Taylor
GA Technologies Inc., P.O. Box 85608, San Diego, CA 92138, USA

Neutral beam heated discharges in Doublet III exhibit an "operational" beta limit,[1] as shown in Fig. 1, which is in good agreement with a simple theoretical scaling law:

$$\beta(\%) \leq C \frac{I\ (\mathrm{MA})}{a\ (\mathrm{m}) B\ (\mathrm{T})} \tag{1}$$

where I is the plasma current, a is the minor radius of the discharge, and B is the toroidal magnetic field, and in the experiment C is about 3.5. Major disruptions have prevented operation of discharges beyond this limit, despite numerous attempts where the available heating power would have permitted it. These disruptions appear to be due to a low mode number kink or tearing instability. Similar operational limits have been reported in other tokamaks,[2–4] although these limits are not always due to disruptions.

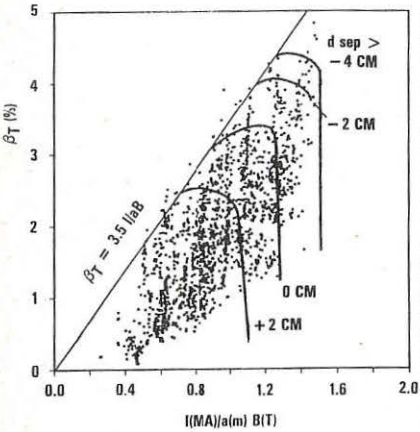

FIG. 1. Beta vs. I/aB for many Doublet III discharges, from MHD equilibrium fits. Operational limit of $\beta = 3.5\ I/aB$ is shown. Maximum attainable I/aB decreases as the distance from limiter flux surface to separatrix varies from negative (limiter) to positive (divertor).

The observed beta limit in Doublet III follows Eq. (1), independent of discharge shape, over a wide range of discharge elongation κ (1.0 to 1.6), triangularity δ (−0.1 to +0.7), safety factor q (1.7 to 6) and topology (limiter, single- and double-null divertors). Plasma shape and separatrix topology enter indirectly by determining the maximum value of I/aB and thus the maximum beta which can be reached within the constraints of Eq. (1). Elongation in particular allows a larger I/aB for a fixed value of q: for Doublet III, $I/aB \propto \kappa^{1/2}(\kappa^2+1)/2q$. Limiter discharges were obtained with $\kappa \leq 1.6$ and q as low as 1.7.[5] Such discharges form the right-hand boundary of the data in Fig. 1, with $I/aB \approx 1.5$. Major disruptions which may be due to the ideal external kink instability prevented operation at lower q. Similar disruptions restricted divertor discharges to lower currents, corresponding to $I/aB \lesssim 1.1$ for well-diverted configurations.

Several expressions approximated by Eq. (1) have been reported recently for the theoretical beta limit of a tokamak with respect to ideal MHD instabilities.[6–10] The coefficient C, which contains the explicit dependence on plasma shape, is either a very weak function[8] or independent of shape. For ideal external kink modes with low toroidal mode number n, and no wall stabilization,[6,7] the predicted value of C ranges from 2.8 to 3.2. For ideal infinite-n ballooning modes,[7–10] the value of C ranges from 3.7 to 4.4. A conducting wall at a distance from the plasma surface of half the minor radius raises the kink mode limit to

equal the ballooning mode limit.[7,8] The experimentally observed value of C falls in the middle of this relatively narrow range of predictions, making it impossible to distinguish by the value of C alone which instability is responsible. Therefore we must examine the detailed behavior of the discharge near the beta limit.

Major disruptions are the only phenomena clearly and universally identified with the operational beta limit in Doublet III. These disruptions have a number of features in common, most of which are illustrated by discharge 46167 (Fig. 2). The sequence of events can be divided into three phases: a triggering event, a predisruption phase, and the disruption itself.

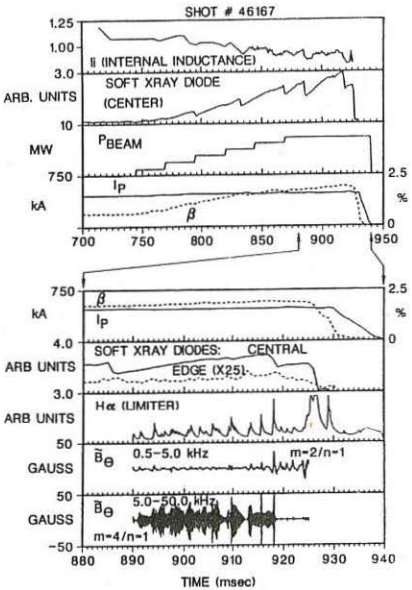

FIG. 2. Behavior near the beta limit in a typical discharge (46167): I=0.48 MA, B=1.73 %, κ=1.0 (circular), q=3.1, β_p=1.21, β=1.89%, $\beta\, aB/I$=3.0. Lower traces show $\tilde{B}_\theta$ obtained by numerical filtering and integration of Mirnov loop signal.

The triggering event is usually the fall of a sawtooth (918 msec in Fig. 2) although occasionally a neutral beam switching on or off seems to provide the trigger. There may be an unusually large precursor to the triggering sawtooth and a large burst of H_α light at the limiter. In discharges with $q \geq 3$, the inversion radius of this sawtooth is often significantly larger than that of earlier sawteeth, occurring close to the q=2 surface. This suggests destabilization of the m=2/n=1 mode, and in such cases this event might better be termed a minor disruption.

The predisruption interval typically has a duration of less than half a sawtooth period, and is sometimes very short in discharges with $q < 3$. Energy confinement becomes poorer, resulting in constant or slowly decreasing beta in constant beam power. In discharges with $q \geq 3$, this seems to be due to a deterioration of confinement outside of the q=2 surface, as shown by the soft x-ray emission from this region declining continuously. This is consistent with the presence of a slowly growing 2/1 island. The more abrupt character of the disruptions when q is below 3 may be due to the proximity of the island to the limiter. A rise in H_α light at the limiter and/or nickel line radiation indicates a stronger interaction with the limiter. The MHD activity is characterized by an n=1 mode rotating at low frequency (less than 5 kHz). The poloidal mode number observed in the interior by the soft x-ray diodes is m=1, while the Mirnov loops usually detect m=2.

In some cases the soft x-ray diodes also show m=2 near the plasma edge. In some cases the rotation of both the plasma and the MHD mode slows down continuously from 10–20 kHz in the beam injection direction to near zero during the predisruption phase. This mode may be seen at low amplitude long before the last sawtooth, but begins to grow at or soon after the sawtooth, with small or zero real frequency and a growth time of a few milliseconds, until the final disruption.

The behavior observed before and during these disruptions seems consistent with a model which has been previously proposed for low beta disruptions:[11,12] The fall of a sawtooth oscillation creates a steepened current density profile inside the q=2 surface. This destabilizes an m=2/n=1 tearing mode. In the ensuing predisruption interval, the 2/1 island causes poor confinement near the plasma edge. Interaction with the limiter cools the edge of the discharge, causing further growth of the island. Growth of the 2/1 island may also destabilize the 1/1 mode. The zero or near-zero rotation velocity reduces the stabilizing effect of the resistive ($L/R \sim 1$ msec) vacuum vessel wall. Rapid growth of the mode then results in disruption. The unstable mode becomes more kink-like for $q < 3$ as the q=2 surface approaches the plasma edge.

The identification of the disruption as a 2/1 kink or tearing mode is supported by a linear stability analysis of several discharges near the beta limit with the resistive MHD code CART,[13] using profiles from MHD equilibrium fits.[14] The safety factor q ranged from 2.2 to 5.3, but the q=2 surface was always found at a minor radius of greater than $0.8a$. In all cases, the structure of the unstable mode was predominantly 2/1 for the magnetic perturbation, while the pressure perturbation appeared as 1/1 near the center and 2/1 near the edge. This is in qualitative agreement with Mirnov loop and soft xray data. These results were insensitive to variations of the plasma or vacuum resistivity in the simulations.

Detailed analyses of ideal MHD stability were performed for a number of discharges using pressure profiles consistent with both kinetic and magnetic data.[1] The ideal external kink mode was found to be stable. However, the discharge with highest beta in Fig. 3 was calculated to be unstable with respect to ideal high-n ballooning modes inside 0.6 of the plasma's minor radius. In some discharges near the beta limit, including this one, an oscillation with unusually high toroidal mode number (n=3 to 5) is observed inside 0.8 of the minor radius, which may represent the low-n end of an unstable spectrum of ballooning modes. The higher n part of the spectrum would be very difficult to detect with Mirnov loops and soft x-ray diodes due to limited toroidal resolution of the detectors and small signal size.

In neutral beam-heated Doublet III discharges, the current profile broadens with increasing $\beta\, aB/I$, as shown by decreasing internal inductance ℓ_i (Fig. 4), and the current

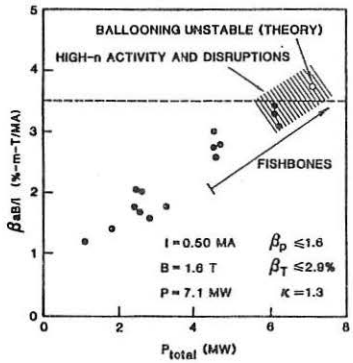

FIG. 3. Typical power scan for fixed parameters. $\beta\, aB/I$ is plotted vs. total input power. Regimes of theoretical instability and observed MHD activity are shown.

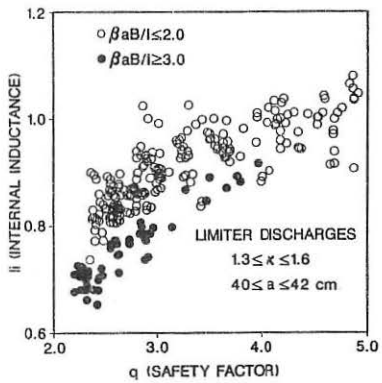

FIG. 4. Internal inductance ℓ_i vs. safety factor q, showing decrease of ℓ_i with increasing $\beta\, aB/I$. Intermediate values of $\beta\, aB/I$ are omitted for clarity.

density gradient at the edge increases. ℓ_i is not the fundamental parameter for the beta limit, since it depends on q and discharge shaping, but it does provide an indication of profile peakedness. Broad current profiles have larger shear, which is favorable for stability to pressure driven kink modes[15] and ballooning modes,[16] but may be more unstable to tearing modes. A sawtooth oscillation may finally trigger the instability by causing an additional downward excursion of ℓ_i (Fig. 2).

In all power scans, beta rises linearly with heating power (constant $d\beta/dP$), until the limit is reached (see Fig. 3). There is no evidence of the saturation which is predicted by models in which ballooning modes cause progressive deterioration of energy confinement as beta increases, and greater portions of the profile reach marginal stability. However, ballooning modes in the interior could drive the discharge toward broader pressure and current profiles, accounting for the decrease in ℓ_i at high beta. The tearing mode may be destabilized before a change in global energy confinement becomes detectable.

In summary, the maximum beta values attained in Doublet III discharges are in good agreement with the scaling law $\beta \leq CI/aB$, with C=3.5. The discharges which reach this limit generally terminate in disruptions. Phenomena observed before and during a beta limit disruption are very similar to those for disruptions at low beta associated with current limits: $q \sim 2$ for limiter discharges and $q \sim 3$ for divertor discharges. Within any set of similar discharges, the maximum values of $\beta\ aB/I$ are found for the discharges with the lowest values of ℓ_i. This suggests that both types of disruption are due to a current-driven kink or tearing mode, which becomes unstable as the current profile broadens due to low q or high beta. Ballooning modes may play an indirect role by causing the current profile broadening observed at high beta.

This is a report of work sponsored by the Department of Energy under contract no. DE-AC03-84ER51044.

References

[1] R.D. Stambaugh et. al., in Plasma Physics and Controlled Nuclear Fusion Research (Proc. Tenth Int. Conf., London, 1984) Vol. I, IAEA, Vienna (1985), 217.
[2] M. Keilhacker et. al., in Plasma Physics and Controlled Nuclear Fusion Research (Proc. Tenth Int. Conf., London, 1984) Vol. I, IAEA, Vienna (1985), 71.
[3] K. McGuire et. al., in Plasma Physics and Controlled Nuclear Fusion Research (Proc. Tenth Int. Conf., London, 1984) Vol. I, IAEA, Vienna (1985), 117.
[4] H.G. Neilson and A.J. Wootton, Bull. Am. Phys. Soc. **29** (1984), 1352.
[5] K.H. Burrell et. al., Nuclear Fusion **23** (1983), 536.
[6] F. Troyon et. al., Plasma Physics and Controlled Fusion **26** (1984), 209.
[7] T. Tuda et. al., in Plasma Physics and Controlled Nuclear Fusion Research (Proc. Tenth Int. Conf., London, 1984) Vol. II, IAEA, Vienna (1985), 173.
[8] L.C. Bernard et. al., Nuclear Fusion **23** (1983), 1475.
[9] P. Rutherford, in U.S. Contribution to the INTOR Phase-2A Workshop, USA FED-INTOR 82-1, Georgia Institute of Technology, Atlanta, GA (1982).
[10] A. Sykes et. al., in Controlled Fusion and Plasma Physics (Proc. Eleventh European Conference, European Physical Society, Aachen, 1983), Part II, 363.
[11] R.B. White, et. al., Phys. Rev. Lett. **39** (1977), 1618.
[12] M.F. Turner and J.A. Wesson, Nuclear Fusion **22** (1982), 1069.
[13] J.K. Lee, Phys. Fluids (to be published, 1986).
[14] L.L. Lao, et. al., Nuclear Fusion **25** (1985), 1611.
[15] J. Manickam, Bull. Am. Phys. Soc. **30** (1985), 1479.
[16] J.A. Wesson and A. Sykes, Nuclear Fusion **25** (1985), 85.

MODELLING OF H-MODE DISCHARGES BY THE CONFINEMENT AMELIORATION FROM A LOCALIZED REDUCTION OF FIELD ERGODICITY

A. Nicolai and G.H. Wolf

Institut für Plasmaphysik der Kernforschungsanlage Jülich GmbH, Association EURATOM-KFA, P.O.Box 1913, D-5170 Jülich

1. Introduction

The electron energy confinement time is significantly lower than predicted by neoclassical theory. This applies to H-mode and even more to L-mode discharges. Attempts to explain this behaviour include drift instabilities, island formation by tearing modes and the development of regions with field line ergodization. In particular, resistive MHD activities cause major magnetic islands in the vicinity of rational flux surfaces, and at higher β_p, pressure driven modes may evoke numerous small islands /1/. Their common feature is an erosion of the system of nested flux surfaces in certain plasma regions characterized by a low shear and a high pressure gradient allowing dissipation by MHD activities. This results in an enhancement of the effective radial transport caused by transport parallel to ergodic magnetic field lines being inclined relatively to the toroidal direction. In case of divertor configurations in the vicinity of the separatrix a shear-stabilized layer can be expected, because the safety factor q varies strongly there. This layer provides the enhanced confinement during the H-mode, especially for the electron energy.
In the present paper an attempt is made to account for these effects within the frame of a 1d-transport code by introducing a mean inclination angle of the ergodized field lines $\varepsilon(r) = \langle B_r/B \rangle$ with a local minimum at the effective separatrix radius ($r=r_s$) (Fig.1). (B is the total magnetic field strength, B_r the radial field component and $\langle \ldots \rangle$ denotes the average over an otherwise unperturbed flux surface). The angle $\varepsilon(r)$ used earlier already /2-4/ for the description of a deliberately ergodized boundary layer replaces those anomaly factors which are generally used in transport codes to simulate the observed electron "cross field" transport. In case of limiter configurations without separatrix values around 10^{-4} lead to a suggestive agreement of the computed parameters with the experimental results for both, ohmically and additionally heated plasmas.

2. Magnetic field structure

The following assumptions concerning the magnetic field structure are employed in the 1d-transport code /2-4/.

1. The island structure/ergodization does not cause major disruptions or otherwise influence the dynamics of the discharge.

2. The mean inclination angle $\varepsilon(r)$ varies with radius. It is mainly given by the value at the plasma center ε_0, the bulk value ε_b and the the separatrix value ε_s. Specifically, $\varepsilon_0 = 10^{-4}$, $\varepsilon_b = 2 \times 10^{-4}$, $\varepsilon_s = 10^{-5}$ were employed in Fig. 1.

3. The parameters ε_0, ε_b are assumed to be timeindependent; however, for ε_s which can be treated as a constant as well, a 2nd option is foreseen by introducing a timedependence via the shear parameter Λ. The latter is defined as in the Mercier criterion by

$$\Lambda = \mu_0 \dot{\iota}' \chi'^2$$

μ_0 is the vacuum permeability, ι the rotational transform and χ the toroidal flux function; the prime denotes the derivative with respect to the volume V. The timedependence

$$\varepsilon_s = \varepsilon_{s_0} \left(\frac{\Lambda_0}{\Lambda}\right)^2 \qquad (2.1)$$

is assumed in this option accounting for the fact that increasing shear enhances the stability at $r=r_s$. It was expected, that by this way the onset of the H-mode /5,6/ might be explained: The initial shear Λ_0 provides some barrier against heat conduction thus steepening the temperature and the current density profile at $r = r_s$ if sufficient power is deposited in the core plasma. This yields a further increase in Λ if we assume in a 1st step that the derivative $\dot{\iota}'$ at $r = r_s$ is proportional to the local current density there. Hence a mutual reinforcement of the confinement improvement and of the toroidal current density at the boundary occurs. Saturation is reached when the current density becomes flat.

3. Transport model

The model of ref. /7/ had been adopted throughout. In this model an averaging along the unperturbed flux surfaces was introduced and the effective radial particle, electron and ion energy flux densities were derived from the parallel flux densities.

4. Results

The calculations are based on ASDEX parameters /8/: major radius R = 164 cm, minor radius a = 41.5 cm, toroidal field B_t = 22 kG, plasma current I_p = 300 kA and maximum density $n_{max} = 8 \times 10^{13}/cm^3$. For the independent ε-values of Fig.1 the temperature profiles at t = 500 ms are displayed in Fig.2; neutral injection heating with the power P_b = 3.5 MW was started at t = 200 ms. Although the profiles are flatter than those obtained experimentally, the core plasma

temperature is 2.4 keV, in rough agreement with the experiments /8/. In Fig.2 the difference between T_i and T_e arrises from the model assumptions with dominant electron energy losses. For timedependent ε_s the evolution of the current density (a) and of the electron temperature (b) are shown in Fig.3 ($\varepsilon_o = \varepsilon_b = 2 \cdot 10^{-4}$, $\varepsilon_{s_\bullet} = 0.25 \cdot 10^{-4}$). The initially peaked current density flattens because of the uniform resistivity. However, this flattening starts already during the OH-phase so that an abrupt triggering during the NI-phase, as observed experimentally, could not yet be reproduced.

The calculations show, that the striking difference between the L and H mode can be attributed to significant changes of the electron thermal transport, as has been concluded from the experimental data already /8/. Our model explains the enigmatic reduction of the electron transport at the edge by the shear stabilization in the vicinity of the separatrix which locally reduces the radial field components and thus the mean inclination angle. Even if this reduction initially might be small, the resulting flattening of the current density increases the shear and thus improves the confinement. It seems however, that at least an artificial lower limit of the resistivity is required to prevent the current density from becoming frozen in.

References

/1/ B.A. Carreras et al., 9th Int. Conf. on Plasma Physics and Contr. Nucl. Fusion, Baltimore, IAEA-CN-41/P-4 (1982)

/2/ G.H. Wolf, KFA-Report Jül-1666, ISSN 0366-0885 (1980)

/3/ W. Feneberg and G.H. Wolf, Nucl. Fusion 21, 669 (1981)

/4/ A. Nicolai and D. Reiter, J. of Nucl. Mat. 111/112, 428 (1982)

/5/ F.L. Hinton, Nucl. Fus. 25 (1985) 1457

/6/ C.E. Singer et al., Nucl. Fus. 25 (1985) 1555

/7/ A. Nicolai, G.H. Wolf, Proc. of the 11th Europ. Conf. on Contr. Fus. and Plas. Phys., Aachen, Vol. II 319, (1983)

/8/ F. Wagner et al., Nucl. Fusion, 25 (1985) 1490

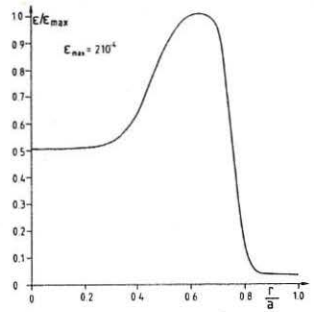

Fig. 1

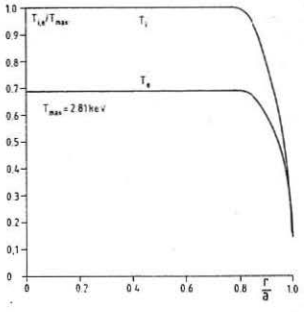

Fig. 2

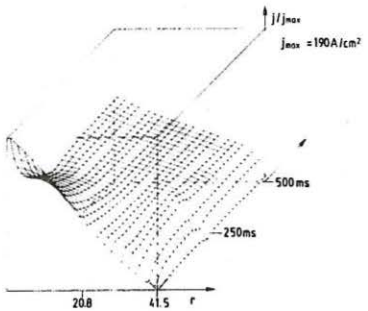

Fig. 3a

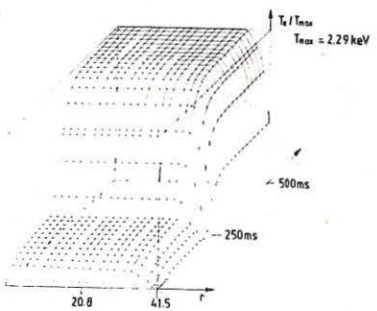

Fig. 3b

Figure captions

Fig. 1: Mean inclination ε angle versus radius.

Fig. 2: Electron and ion temperature versus radius.

Fig. 3: Time-evolution of the current density (a) and of the electron temperature (b).

A PHENOMENOLOGICAL INTERPRETATION OF TRANSPORT LIMITS AND SLOW-TIME EVOLUTION IN TOKAMAKS

F.A.Haas and A. Thyagaraja
Culham Laboratory, Abingdon, Oxfordshire, OX14 3DB, UK
(EURATOM/UKAEA Fusion Association)

1. INTRODUCTION

Tokamak discharges have been run with and without auxiliary heating for pulse lengths long compared with particle and energy confinement times. Their gross behaviour can be summarised in terms of experimentally measured temperature and density profiles and global quantities such as current. These slow-time evolution phenomena are the subject of the present investigation. The key difference between our model and many previous 1-D or 3/2-D (Hugill 1983) models of transport in tokamaks is the explicit and crucial use of the pressure-balance and poloidal-Ohm's law. While there is no direct measurement of the resistivity perpendicular to the magnetic field, it can be shown that the law of conservation of momentum for electrons and ions is incompatible with Spitzer-like poloidal resistivity and the observed particle flux. This was first pointed out by BICKERTON (1978), who showed the poloidal resistivity to be 100 times Spitzer in order to match experiment.

2. EQUATIONS AND PHENOMENOLOGICAL BASIS

We consider a cylindrical plasma of minor radius "a" and periodicity length $2\pi R$. We set $T_e = T_i$, and neglect radiation in comparison with anomalous thermal conduction. Given the sources and appropriate boundary conditions, the variables $n(r,t)$, $T_e(r,t)$, $v_r(r,t)$, $p(r,t)$, $B_\theta(r,t)$, $B_z(r,t)$ are determined from the equations below. Thus

$$\frac{\partial n}{\partial t} + \frac{1}{r}\frac{\partial}{\partial r}(rnv_r) = S_p(r,t) \quad , \tag{1}$$

with the energy equation expressed as

$$\frac{3}{2} n \left\{\frac{\partial T_e}{\partial t} + v_r \frac{\partial T_e}{\partial r}\right\} + nT_e \frac{1}{r}\frac{\partial}{\partial r}(rv_r)$$
$$= \frac{1}{r}\frac{\partial}{\partial r}\left(rn\chi_{\perp e}\frac{\partial T_e}{\partial r}\right) + \eta_z j_z^2 + \eta_\theta j_\theta^2 + P_{aux}(r,t) \quad . \tag{2}$$

The radial momentum balance is

$$\frac{\partial p}{\partial r} = \frac{1}{c}\left(j_\theta B_z - j_z B_\theta\right) \quad \text{with } p = 2nT_e \tag{3}$$

The poloidal and toroidal components of Ampère's & Ohm's equation are

$$\frac{4\pi}{c} j_z = \frac{1}{r}\frac{\partial}{\partial r}(rB_\theta) \quad , \quad \frac{4\pi}{c} j_\theta = -\frac{\partial}{\partial r} B_z \quad . \tag{4}$$

$$-\frac{v_r B_z}{c} = \eta_\theta j_\theta \quad , \quad -\frac{1}{c}\frac{\partial A_z}{\partial t} + \frac{v_r B_\theta}{c} + E_{ext}(t) = \eta_z j_z \quad , \tag{5}$$

with η_θ and η_z the poloidal and toroidal resistivities, respectively. Using Equations (3) and (5) we have

$$v_r = -\frac{D}{n}\frac{\partial n}{\partial r} - U \quad , \tag{6}$$

where

$$D = \frac{c^2 p \eta_\theta}{B_z^2} \quad \text{and} \quad U = \frac{c^2 \eta_\theta p}{B_z^2} \frac{1}{T}\frac{dT}{dr} + \frac{c\eta_\theta j_z B_\theta}{B_z^2} \tag{7}$$

Coppi and Sharky (1981) have proposed on purely empirical grounds that the plasma velocity should take the form of Eq.(6), with however, $D \sim \chi_{\perp e}$. Taking η_z to be Spitzer this leads to

$$\frac{\eta_\theta}{\eta_z} \sim \frac{\chi_{\perp e} B_z^2 ne^2 \tau_e}{c^2 m_e p}, \tag{8}$$

which has the value of order 10^2 under typical tokamak conditions. By a more general consideration of our basic equations, we are in fact, led to setting $\eta_\theta/\eta_z \sim B_z^2(a)/B_\theta^2(a)$ which is of comparable order. This implies from Eq.(7) that $D_{max} \sim c^2 \eta_z$.

3. STEADY-STATE ANALYSIS

We begin by considering the ohmic case with negligible particle sources and sinks, so that the diffusion driven current $v_r B_\theta/c$ is small. The anomalously large η_θ ensures that the poloidal diffusion driven current makes a negligible contribution to the radial pressure balance. Thus

$$\frac{dp}{dr} = -\frac{B_\theta E_{ext}}{c\eta_z} \tag{9}$$

We follow the experimenter's procedure of writing the radial energy balance as

$$\frac{1}{r}\frac{d}{dr}\left(rn\chi_{eff}\frac{dT_e}{dr}\right) + E_{ext} j_z = 0 \quad , \tag{10}$$

where χ_{eff} is an effective thermal diffusivity. These equations lead to

$$\frac{2\pi}{c^2}\frac{\chi_{eff}}{\eta_z} = 1 + \frac{d(\ell n\, n)}{d(\ell n\, T)} \quad . \tag{11}$$

Since we have shown that $D \sim c^2\eta_z$ it is clear that $D \sim \chi_{\perp e} \sim c^2\eta_z$. Combining Eq(10) with toroidal Ohm's law and setting $j_z = I_p/\pi a^2$, then

$$\chi_{eff} \propto \frac{I_p^2}{n} T_e^{-5/2} \quad . \tag{12}$$

Experiment shows that $\chi_{eff} = \text{const}/n$, and hence we obtain $T_e \propto I_p^{4/5}$ and (by Eq(11)) $n \propto I_p^{6/5}$, for the ohmic scalings.

We next consider auxiliary heated discharges. We have found that the degradation in $K_\perp (= n\chi_\perp)$ for ISX-B can be most simply represented by taking $K_\perp = K_{\perp ohm} A_1 (\frac{nT}{B_\theta^2})^2$, where A_1 is a constant order unity. Replacing scale-lengths by "a", using $B_\theta = 2I_p/ca$, $P_{aux} = P_{tot}/2\pi^2 a^2 R$ and introducing $r\Sigma(r) = \int_o^r rS_p dr$, our basic equations lead to the scalings

$$\tau_{conf} = \frac{nT}{P_{tot}} = \frac{I_p^{12/7}\, P_{tot}^{-9/14}\, \left(\frac{\Sigma}{\eta_0}\right)^{1/7}}{c^2 (K_{\perp\, ohm} A_1)^{5/14}\, a^{11/7}\, R^{5/14}}\, C,$$

$$T_e = \left(\frac{\eta_0}{\Sigma}\right)^{2/7} \frac{I_p^{4/7}\, P_{tot}^{2/7}\, a^{-6/7}}{(K_{\perp\, ohm} A_1)^{2/7}\, R^{2/7}}\, C'', \quad n = \frac{I_p^{8/7}\, P_{tot}^{1/4} \left(\frac{\Sigma}{\eta_0}\right)^{3/7}}{c^2 (K_{\perp\, ohm} A_1)^{1/14} a^{5/7} R^{1/14}}\, C''' \qquad (13)$$

where C, C", C"' are geometrical constants and η_o is defined through $\eta_z = \eta_o T_e^{-3/2}$:. We observe that the confine-confinement time degrades like $P_{tot}^{-0.63}$ whilst ISX-B (NEILSON et al., 1983) report, $P_{tot}^{-0.66}$. It scales with current as $I_p^{1.7}$ while ISX-B quote $I_p^{1.5}$. The temperature-current scaling of $I_p^{0.6}$ is somewhat worse than the ohmic scaling of $I_p^{0.8}$. The density current relation is very similar to ohmic, the particle source controlling the slope of the line in the Hugill diagram. Finally, we note that DOUBLET II, PDX and ASDEX are best represented by a linear β_{pol} dependence for $K_\perp$. However, the scalings for T_e and n in Eq.(13) are not significantly affected, while τ_{conf} shows L-mode scaling.

4. INTERPRETATION OF SLOW-TIME PHENOMENA IN TOKAMAKS.

We have applied the above model to ISX-B, DITE and ASDEX; in the present paper, however, we shall only report the results relating to the latter two experiments. In simulating discharge no. 16129 for DITE no attempt is made to describe the start-up phase. Instead the total plasma current is specified to be I_p = 110 kA and is held fixed throughout the calculation; the other parameters are B_{tor} = 13.5 kG, beam power P_{aux}= 685 kW, a=25 cm, R=120 cm and Z_{eff}=1.2 (HUGILL et al. 1983).

The initial plasma density profile is taken as parabolic while the initial temperature profile is a gaussian. The edge values of n and T are held fixed throughout the calculation. The evolution is carried out for 150 ms and during this time we have a uniform gas feed rate $S_p(r,t)$. This is not available from experiment, but is obtained from $S_p = \frac{n(o,o)}{\tau_p}$, where τ_p is taken as 25 ms. It must be stressed that this is a free parameter and its choice is justified by the qualitative agreement of the calculated wave forms with the observations. The form for $\chi_\perp$ is that suggested by GRUBER (1982), namely

$$\chi_\perp = C_1 n^{-1}(r,t)\; T_e^{1/2}(o,t) T_e^{-1/2}(r,t) cm^2 s^{-1}$$

with C_1=4.8 x 10^{17}. We take η_z to be Spitzer and $\eta_\theta/\eta_z = (B_z(a)/B_\theta(a))^2$

Fig.1 shows the line-averaged density $\bar{n}_e$ calculated as a function of time. After the density "clamp" sets in $\bar{n}_e$ falls slightly to the end of the simulation. Considering the simplicity of the model, agreement with experiment is remarkably good, as it is for the β_{pol}, $T_e(o,t)$ and the loop voltage $V_\ell(t)$. When neutral beams are injected into an ohmically heated target plasma in ASDEX, the first 10-100 ms of the injection phase always show a deterioration of the particle and energy

confinement compared with the ohmic values. After this low confinement (L-phase) the discharge either evolves into a high-confinement (H-phase) or remains in the L-mode depending on the experimental conditions. (KEILHACKER et al., 1984). We are able to simulate many of the features of this L-H transition without invoking divertor action or changes in edge physics. The parameters pertaining to discharge no.9910 are: I_p=380 kA, $\bar{n}_e$ =4 x 10^{13} cm^{-3}, B_{tor}= 2.2 T and P_{aux} = 2.9 MW. In this case it is necessary to take $S_p = 3.5 \times 10^{13} - n(r,t)/\tau_p$ where τ_p= 0.05 s, and η_θ/η_z takes the same form as DITE. The degradation of $\chi_\perp$ with beam-power is most simply represented as a linear β_{pol} dependence. Thus

$$\chi_\perp = n^{-1}(r,t) K_{\perp ohm} \left(\frac{T_e(o,t)}{T_e(r,t)}\right)^{1/2} \left(1 + \frac{8\pi nT}{B_\theta^2(a)}\, 1.5\right) \text{ with } K_{\perp ohm} = 3 \times 10^{17}\ cm^{-1}\ s^{-1}.$$

The results show that up to 30 ms from the start of the beam $\bar{n}_e$ falls slightly (see FIG 2), while T_e and β_{pol} rise sharply. The subsequent behaviour also follows experiment very closely. Our results suggest that the L-phase is a density clamp analogous to that seen in DITE.

REFERENCES

BICKERTON R. J. (1978) Journal of Physics D- Applied Phy. II, p.1781.
COPPI B. and SHARKY N. (1981) Nuc. Fusion 21, 1363.
GRUBER O. (1982) Nuc. Fusion 22, 1349.
HUGILL J. et al. (1983) Culham Laboratory Report CLM-R239.
HUGILL J. (1983) Nuc. Fusion 23, 331.
KEILHACKER M. et al. (1984) Plasma Physics and Controlled Fusion 26, 49.
NEILSON G. H. et al. (1983) Nuc. Fusion 23, 285.

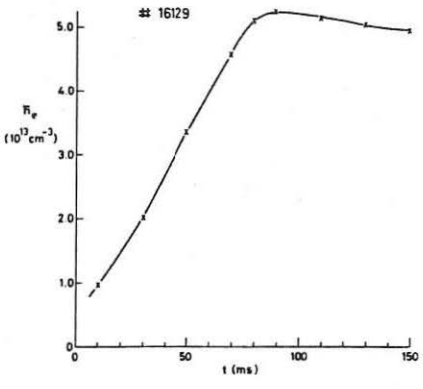

Fig.1. Computed time-dependence of line averaged density, $\bar{n}_e$, for DITE discharge (No.16129).

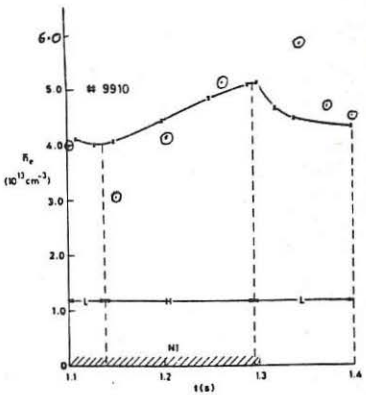

Fig.2. Calculated time-dependence of line-averaged density in ASDEX during the neutral injection phase (1.1<t<1.4s). The experimental points (o) are obtained from Fig.1 of KEILHACKER et al.

ANALYSIS OF THE INVARIANCE PROPERTY OF THE ELECTRON TEMPERATURE DURING AUXILIARY HEATING IN ASDEX

H. Murmann, F. Wagner, G. Becker, H. S. Bosch, H. Brocken, A. Eberhagen, G. Fussmann, O. Gehre, J. Gernhardt, G.v.Gierke, E. Glock, O. Gruber G. Haas, J. Hofmann, A. Izvozchikov[1], G. Janeschitz, F. Karger M. Keilhacker[2], O. Klüber, M. Kornherr, K. Lackner, M. Lenoci, G. Lisitano, F. Mast, M. H. Mayer, K. McCormick, D. Meisel, V. Mertens, E. R. Müller[2], H. Niedermeyer, A. Pietrzyk[3], W. Poschenrieder, H. Rapp, H. Röhr, J. Roth, F. Ryter[4], F. Schneider, C. Setzensack, G. Siller, P. Smeulders[2], F.X. Söldner, K.-H. Steuer, D. Zasche

Max-Planck-Institut für Plasmaphysik
EURATOM Association, D-8046 Garching

A crucial and still unsolved problem in tokamak physics is the understanding of anomalous heat transport across the magnetic field via heat conduction of the electrons. All efforts to establish a universal expression for the diffusivity χ_e as a function of local plasma parameters which is valid also for auxiliary heating have failed so far. The problem has become even greater since it became evident that plasma confinement deteriorates during additional heating in a parameter range that is still very close to ohmic heating conditions. The conventional way of thinking is that additional heating of plasma affects its temperature locally according to the energy deposition profile. Consequently the electrical conductivity $\sigma \propto T^{3/2}$ will rise and thus the current density profile takes a new shape determined by the power deposition profile. This statement is, however, in clear contradiction to the experimental finding: electron temperature profiles exhibit a remarkable invariance to external influences and possess a very characteristic shape. An example is given in Fig. 1 showing temperature profiles as taken with a new Thomson scattering device with relatively high spatial resolution using a 60 Hz Nd:YAG laser. The profiles are normalized to the central value and represent four different cases: Ohmic heating (OH) alone, OH with additional neutral beam injection (NI) with different power deposition. In one case 29 keV D^o-particles were injected into a relatively high density target plasma. The beam power is then deposited at radii of 25 ... 30 cm. This is compared to the case of 40 keV D^o injection in a low density plasma with peaked power deposition. Although the central T_e values rise appreciably, the relative T_e-profile shapes remain unchanged. This profile invariance has been further checked in discharges with addition of Ne impurities, which clearly documents that rather $1/T \cdot dT/dr$ and not dt/dr keeps constant. Profile consistency has also been confirmed in cases with and without sawtooth activity. Despite the lack of sawteeth the T_e profiles are found to be consistent and are still affected by q_a. The electron density profile $n_e(r)$, however, becomes steeper in this case. Another example of this disparity is a discharge with pellet refuelling during which the $n_e(r)$ profile is changed enormously while the T_e-profile shape keeps practically fixed (Fig. 2).

It is well-known, on the other hand, that T_e-profiles can easily be influenced by the choice of the safety factor q_a, i.e., the ratio of the

---

[1]Academy of Sciences, Leningrad, USSR; [2]Present address: JET Joint Undertaking, England; [3]Univ. of Washington, Seattle, USA; [4]CEN Grenoble, France

toroidal magnetic field to the plasma current. Amazingly, this statement has also proved to hold for additionally heated plasma discharges: the T_e-profile shapes are influenced in the same manner by q_a as in the OH case, regardless where the heating power is deposited. This is demonstrated in Fig. 3 for two cases with identical plasma current but variable toroidal field with q_a = 2.9 and 4.7, respectively. Profiles are normalized to the peak value again and do not change shapes when NI-power is applied. The dependence on q_a, however, is quite evident and can be summarized impressively for a large variety of plasma conditions in a plot of $T_e(0)/\langle T_e\rangle$ versus q_a, where $\langle T_e\rangle$ is the volume averaged electron temperature (Fig. 4). $T_e(0)/\langle T_e\rangle$ represents a measure for the peakedness of a T_e profile and shows a characteristic q-dependence. The tendency is similar for $n_e(r)$ profiles but many exemptions exist which do not fit to the same characteristics, e.g. discharges with pellet injection or witout sawtooth activity /1/.

So far we concentrated on OH an NI conditions. When the plasma is additionally heated by high frequency radiation e.g. ion cyclotron resonance heating or lower hybrid heating, the profile invariance has to be restricted to a region $r > r_1$, where r_1 might be interpreted as the radius of the q = 1 surface. In both cases the heating effect is higher in the plasma center. Obviously this region $r \lesssim r_1$ is a confinement region of its own, and has to be treated separately in comparison to the region $r > r_1$. But if the T_e-profiles are normalized to a value at a radius where the influence of the q = 1 surface is negligible one observes that all profiles coincide amazingly for $r > r_1$ within the error bars of the diagnostic and yield an almost constant slope

$$(1) \qquad \frac{1}{T_{r/a = 0.45}} \cdot \frac{dT}{dr} = (4 \pm 0.3)\ m^{-1} \text{ for } r > r_1 \cdot \sqrt{2}$$

for all discharge conditions (see Fig. 5). If we apply the same procedure to merely OH and NI heated discharges, we note that eq. (1) is valid as well. In this case the deviation from eq. (1) for radii $r < r_1$ is only due to the different q_a values (Fig. 6). Thus, the profile steepening for large q_a values (Fig. 4) is mainly caused by phenomena within the q = 1 surface. Then the plasma turns into the high confinement regime during neutral injection (NI(H)) the T_e-profiles deriate slightly from the general shape due to an additional edge temperature rise.

The dominant role of q alone to constitute the T_e profile shape is quite obvious and points to the current density profile as a leading quantity to be invariant. This is also supported by the observation that the inversion radius of sawteeth is only a function of q_a and otherwise remarkably constant /2/. Via the coupling $T_e(r) \propto j(r)^{2/3}$, the temperature profile is then forced to become invariant, too. There are indeed reasons for j(r) to take a "natural shape" arising from very basic principles as minimization of magnetic field energy in a plasma column with a given toroidal current I.

References

/1/ Gehre, O., et al., this conference
/2/ Wagner, F., Phys. Rev. Letters, to be published

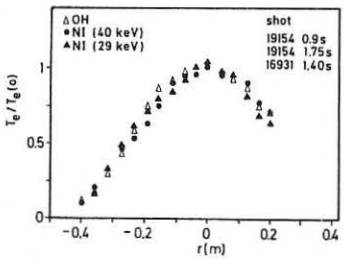

Fig. 1:
Variation of the deposition profile
Δ ohmic heating (OH)
q = 2.9; $T_e(0)$ = 0.65 keV
• 2 MW neutral injection (NI) D^o (40 keV) $\rightarrow H^+$ $\bar{n} = 2.9 \cdot 10^{13} cm^{-3}$; $T_e(0)$ = 1.68 keV; q = 2.9
▲ 1.3 MW NI, D^o(29 keV) $\rightarrow D^+$; q = 2.6 $\bar{n} = 5.6 \cdot 10^{13} cm^{-3}$; $T_e(0)$ = 1.1 keV

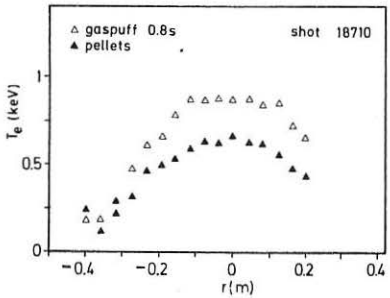

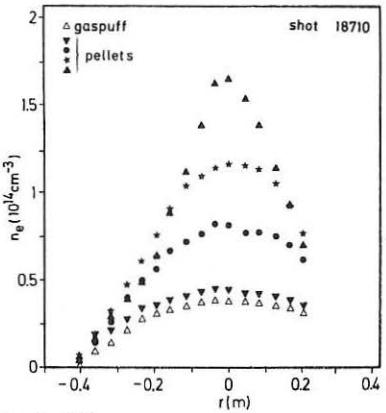

Fig. 2: Comparison: gasfuelling - pelletfuelling
left: $T_e(r)$ with gasfuelling (Δ) and after a series of 20 pellets (▲)
right: $n_e(r)$ during gasfuelling (Δ) and pellet fuelling (dark symbols) showing the time evolution of $n_e(r)$; (t = 1,3-1,5-1,7-2,1 s).

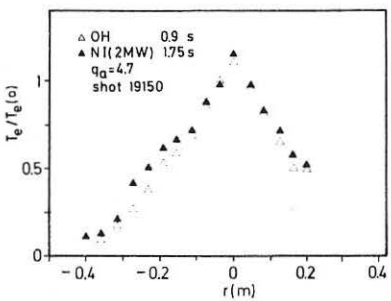

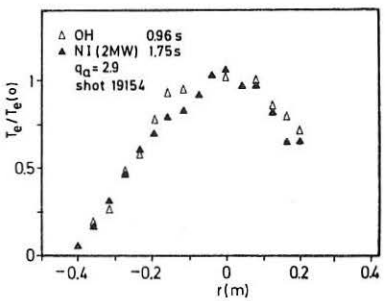

Fig. 3: Comparison of T_e profile shapes during ohmic heating (Δ) and 2 MW neutral injection (▲) at q_a = 2.9 and q_a = 4.7

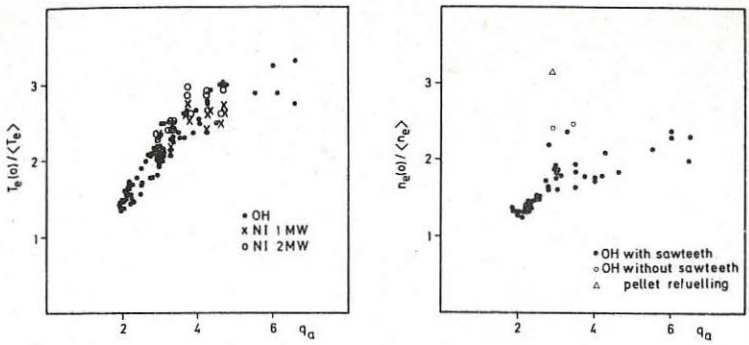

Fig. 4: left: peakedness $T_e(0)/\langle T_e\rangle$ of temperature profiles vs. q_a at different heating powers
• OH, x 1 MW(NI), o 2 MW(NI)
right: $n_e(0)/\langle n_e\rangle$ vs. q_a

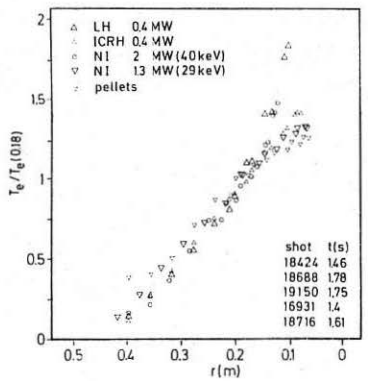

Fig. 5: different cases of additional heating

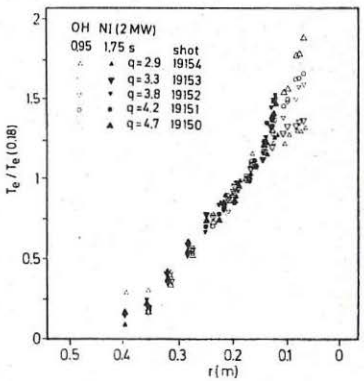

Fig. 6: OH and NI heated discharges with $2.9 \leq q_a \leq 4.7$

Fig. 5 and 6: Temperature profiles normalized to the T_e value at r = 0.18 m vs. radius r of the flux surface at which T_e is measured. The ß-shift of the flux tubes is taken into account. A small area around the magnetic axis is not covered by the laser beam of the scattering diagnostic.

PARTICLE CONFINEMENT IN OHMICALLY HEATED ASDEX PLASMAS

O. Gehre, G. Becker, A. Eberhagen and H. S. Bosch, H. Brocken, G. Fussmann, J. Gernhardt, G.v.Gierke, E. Glock, O. Gruber, G. Haas, J. Hofmann, A. Izvozchikov[1], G. Janeschitz, F. Karger, M. Keilhacker[2], O. Klüber, M. Kornherr, K. Lackner, M. Lenoci, G. Lisitano, H. M. Mayer, F. Mast K. McCormick, D. Meisel, V. Mertens, E. R. Müller[2], H. Murmann, H. Niedermeyer, A. Pietrzyk[3], W. Poschenrieder, H. Rapp, H. Röhr, J. Roth, F. Ryter[4], F. Schneider, C. Setzensack, G. Siller, P. Smeulders[2], F.X. Söldner, K.-H. Steuer, F. Wagner, D. Zasche

Max-Planck-Institut für Plasmaphysik
EURATOM Association, D-8046 Garching

Abstract: The anomalous particle transport in ohmic deuterium and hydrogen discharges is investigated by scans of the plasma current, density and toroidal magnetic field. At smaller current or larger ion mass more peaked density profiles are found. The flux-surface-averaged transport is analysed by computer simulations. It is shown that the inward drift velocity is independent of the poloidal and toroidal magnetic field and the ion mass number but inversely depends on the density and electron temperature. Empirical scaling relations for the electron heat diffusivity and the diffusion coefficient are also presented.

Introduction: Anomalous diffusion and inward drift in ohmically heated (double-null divertor) discharges are investigated in the ASDEX tokamak by extensive parameter studies. For deuterium and hydrogen plasmas the variation of the density profile with plasma current I_p, toroidal magnetic field B_t and line-averaged density $\bar{n}_e$ is explored. Several series of discharges are studied in which only one of these parameters has been scanned. In all cases, data measured during long current and density plateaus are analysed.

Diagnostics: The electron density n_e is measured by a multichannel HCN-laser interferometer /1/ working at a wavelength of 337 μm. Figure 1 shows the arrangement of the viewing chords with respect to the ASDEX plasma. The electron density profile $n_e(r)$ is constructed by a fit procedure for the measured line densities of the horizontal channels. A modified parabola of the form $n_e(r) = n_e(0)\,[1 - (r/a)^{\beta}]^{\alpha}$ describes the profile inside the separatrix while an exponential function with a typical decay length of 2 cm is used outside. For the rather smooth profiles found in ohmically heated discharges, this method yields good accuracy.

The electron temperature T_e is derived from the extraordinary mode of the second harmonic of the electron cyclotron emission (ECE) from the plasma. Its intensity is registered by a four-channel polychromator, constructed to observe simultaneously four slightly different wavelengths between $2.0 \lesssim \lambda \lesssim 3.0$ mm corresponding to four radial positions in the plasma about 6 - 8 cm apart from one another. The complete T_e profile can be established by a sequence of at least two identical discharges with properly varied wave

---

[1]Academy of Sciences, Leningrad, USSR; [2]Present address: JET Joint Undertaking, England; [3]Univ. of Washington, Seattle, USA; [4]CEN Grenoble, France

length settings of the polychromator. For details of the ECE diagnostic employed see e.g. Ref. /2/.

Analysis of the particle transport by computer modelling: The steady-state particle balance equation with anomalous outward diffusion and anomalous inward convection reads

$$- D \frac{dn_e}{dr} + v_{in}\, n_e = \Gamma_i, \qquad (1)$$

where Γ_i is the flux density due to ionization of cold atoms which mainly takes place near the plasma edge.
The experiments are simulated with the BALDUR transport code /3,4/. For deuterium and hydrogen plasmas the computations fit the measured $n_e(r)$ and $T_e(r)$, the central ion temperature $T_i(0)$ from CX diagnostics and the poloidal beta β_p from the diamagnetic loop. The following expressions for the electron heat diffusivity χ_e and the diffusion coefficient D are to be used for best fits in ohmically heated plasmas:

$$\chi_e(r) = 1.61 \times 10^{16}\, A_i^{-1/2}\, B_t\, n_e(r)^{-1}\, T_e(r)^{-1}\, q(r)^{-1}\ \mathrm{cm^2\ s^{-1}} \qquad (2)$$

$$D(r) = 0.2\, \chi_e(r), \qquad (3)$$

where B_t is in kG, n_e is in $\mathrm{cm^{-3}}$ and T_e is in keV. A_i denotes the ion mass number. Note that the ion mass dependence given holds under pure deuterium and hydrogen plasma conditions after glow-discharge cleaning. The ion heat diffusivity χ_i used is one time the neoclassical values according to Chang and Hinton. For the anomalous inward drift velocity $v_{in} = \gamma(r/r_w)^2$ is applied instead of the Ware pinch. γ is a factor whose parameter dependences are investigated by scanning I_p and $\bar{n}_e$, and r_w is the wall radius (r_w = 49 cm). As illustrated by Fig. 2, this model yields the measured profile variation, characterized by $n_e(0)/\langle n_e\rangle$, on I_p, where $\langle n_e\rangle$ is the volume-averaged density. For deuterium $v_{in} = -550\ (r/r_w)^2$ cm $\mathrm{s^{-1}}$ is used while for hydrogen $v_{in} = -710\ (r/r_w)^2$ cm $\mathrm{s^{-1}}$ is applied. The inward drift velocity is found to be independent of the plasma current. In Figs. 3 and 4, examples of computed density and temperature profiles from these scans are compared with the measured results for deuterium and hydrogen, respectively.

Results of the density scan are presented in Fig. 5. For a given electron temperature the inward drift exhibits an inverse $\bar{n}_e$ scaling. Scanning the toroidal magnetic field (see Fig. 6) yields a weak rise of the measured $n_e(0)/\langle n_e\rangle$ values with increasing B_t which is ascribed to the variation of the q=1 radius. These scans show that v_{in} is independent of the poloidal magnetic field B_p, B_t and A_i but it depends inversely on n_e and T_e. Equations (2) and (3) and $B_t/q = R_o\, B_p/r$ yield

$$\frac{v_{in}(r)}{D(r)} \simeq - A_i^{1/2}\, B_p(r)^{-1}\, f(r) \qquad (4)$$

independently of B_t, n_e and T_e. Smaller currents and larger ion mass correspond to higher $|v_{in}|/D$, i.e. more peaked density profiles, in agreement with the measurements. The v_{in} scaling given by Eq. (4) differs from the previously used relation $v_{in}/D \simeq -2\alpha\, r/a^2$ with α being a constant. An explicit dependence of χ_e, D and v_{in} on Z_{eff} was not identified in the scans.

References

/1/ Gehre, O., Int. Journal of Infrared and Millimeter Waves, Vol. 5 (1984) 369.
/2/ Eberhagen, A., Campbell, D.J., Kissel, S.E., Mertens, V., EC-4, Fourth Int. Workshop on ECE and ECRH, Roma, 1984, p. 115.
/3/ Becker, G., ASDEX Team, Neutral Injection Team, Rep. IPP III/98 (1984).
/4/ Post, D.E., Singer, C.E., McKenney, A.M., PPPL Transport Group, TFTR Physics Group, Rep. 33 (1981).

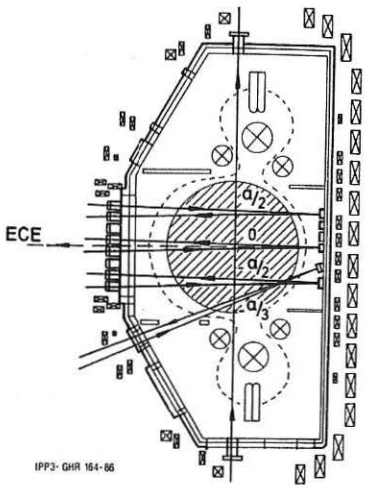

Fig. 1: Cross-section of the ASDEX device, showing the viewing chords of the HCN-laser interferometer (solid lines) and ECE diagnostics (dashed line).

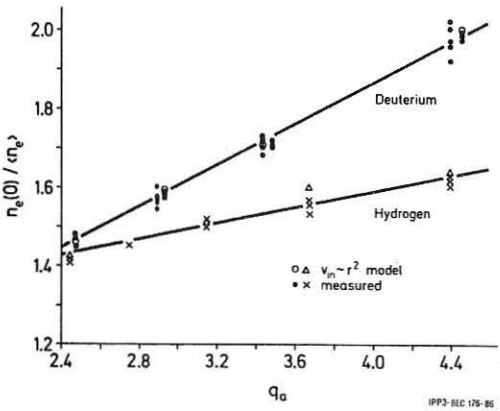

Fig. 2: $n_e(0)/\langle n_e \rangle$ versus q_a by scanning the plasma current between 250 and 450 kA (B_t = 2.25 T, $\bar{n}_e$ = 2.7 x 10^{13} cm^{-3}.

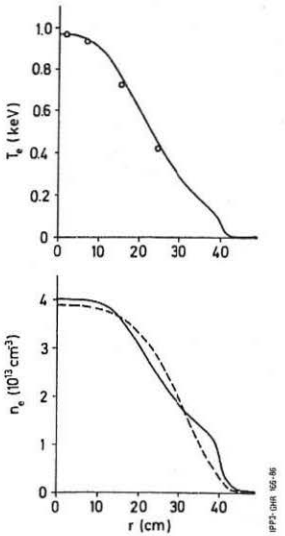

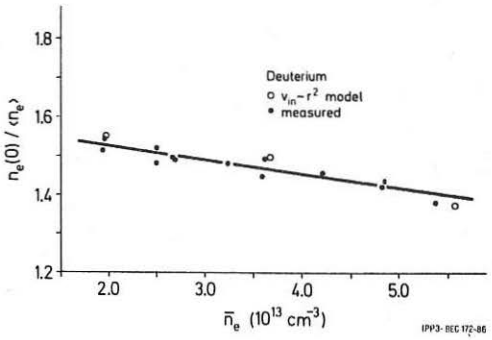

Fig. 5: Measured and computed $n_e(0)/\langle n_e \rangle$ versus $\bar{n}_e$ (I_p = 420 kA, B_t = 2.18 T).

Fig. 3: Measured density (dashed curve) and electron temperature (circles) profiles compared with computed results (solid curves, I_p = 320 kA and deuterium plasma).

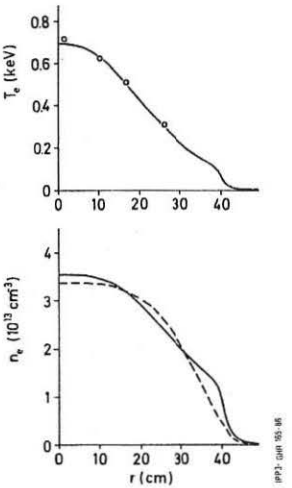

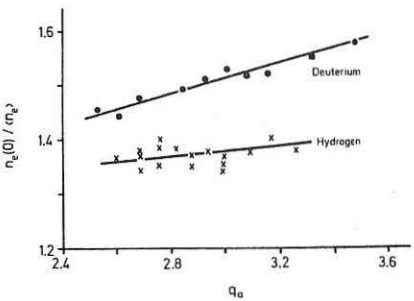

Fig. 6: Measured $n_e(0)/\langle n_e \rangle$ versus q_a by scanning the toroidal magnetic field (I_p = 380 kA).

Fig. 4: As in Fig. 3, but I_p = 350 kA and hydrogen plasma.

LOCAL TRANSPORT IN TOKAMAKS WITH OHMIC AND INJECTION HEATING

G. Becker

Max-Planck-Institut für Plasmaphysik
EURATOM Association, D-8046 Garching

Abstract: The anomalous electron heat diffusivity χ_e is investigated by a power scan of the injection heating and by the time evolution of L (low confinement) discharges. It is shown that deviations from the ohmic scaling occur if the non-ohmic electron heating locally exceeds the ohmic power density. The change in scaling is attributed to the injection heating with its different dependence on the plasma parameters rather than to other instabilities or saturation effects. Constraints on χ_e are derived from the electron and ion energy equations and the shape of the measured electron temperature profiles. For small injection power complex χ_e scalings result which cannot be represented by superposing the ohmic and L scalings.

Introduction: As reliable microinstability-based diffusivities are not available at present for tokamaks with ohmic and auxiliary heating, preference is given to empirical scalings determined by means of transport modelling of many series of discharges. The flux-surface-averaged electron heat diffusivity χ_e and the diffusion coefficient D exhibit a scaling in injection-heated plasmas which greatly differs from that with ohmic heating /1-4/. It was demonstrated that the ohmic transport scaling is not a universal plasma quality which is independent of the heating method. One possible explanation for the different scaling is that neutral injection changes the transport mechanism, i.e. the underlying instabilities and/or saturation effects. There might exist a threshold parameter which distinguishes between the confinement regimes. Another possibility is that the transport mechanism itself remains unchanged and the χ_e scaling is modified by the injection heating with its different variation with the plasma parameters. These questions will be pursued by studying the transition between ohmic and L transport and by following the time evolution of L discharges /5/. The paper deals with the anomalous transport in the ohmic, L and intermediate regimes. Results from transport computations (with the BALDUR code /6,7/) are used.

Constraints on χ_e with ohmic and injection heating: The steady-state electron and ion energy equations and measured T_e profile shapes are used to derive constraints for the electron heat diffusivity. In the stationary ohmic and neutral-beam-heated phases of ASDEX characteristic shapes of $T_e(r)$ are observed. This is illustrated by Fig. 1, which shows an example of the time evolution of the electron temperature profile in an L discharge with an injection period of 400 ms and an absorbed beam power P_{abs} = 2.0 MW. As can be seen, a Gaussian shape is found during the stationary ohmic phase. After the beginning of neutral injection (t_{on} = 1.12 s), the T_e profile changes to an approximately triangular shape which is then maintained during the whole injection period. The 'confinement zone' (hatched in Fig.1) is defined by $r_{q=1} < r < 0.9a$, where the plasma radius a is equal to the separatrix radius of 40cm.

Neglecting the ion heat conduction, the steady-state electron and ion energy equations yield

$$\frac{1}{r}\frac{d}{dr}\left(rn\,\chi_e\,\frac{dT_e}{dr}\right) + \eta j_t^2 + P_b \approx 0 \qquad (1)$$

with $\eta j_t^2 = E_t j_t$. The power density of the ASDEX neutral injection system can be approximated by $P_b(r) = \alpha_b/r$ with $\alpha_b = P_{abs}/(4\pi^2 R_o a)$ and major radius R_o. After integration it follows that

$$\chi_e(r) = \left[\frac{c}{4\pi} E_t B_p(r) + \alpha_b\right] n(r)^{-1} \left|\frac{dT_e}{dr}\right|^{-1} . \qquad (2)$$

With $P_b = 0$ and $T_e(r) = T_e(0)\exp(-\alpha r^2/a^2)$ one obtains the constraint

$$\chi_e^{OH}(r) = \frac{c}{8\pi}\,\frac{a^2}{\alpha}\,E_t\,\frac{B_p(r)}{rn(r)T_e(r)} . \qquad (3)$$

Large injection power and $T_e(r) \simeq T_e(0)(1-r/a)$ yield the constraint

$$\chi_e^{L}(r) \simeq a\,\alpha_b\,T_e(0)^{-1}\,n(r)^{-1} . \qquad (4)$$

Comparing the constraints shows that the χ_e scalings depend on the heating method and its variation with the plasma parameters. Neutral injection does not introduce a $B_p(r)$ dependence in contrast to ηj_t^2. Owing to $j_t(r) \sim T_e(r)^{3/2}$ the ohmic heating and electron temperature profiles are stongly coupled, whereas $P_b(r)$ depends on the target density and injection energy. It is obvious from Eq. (2) that the transport in the intermediate range cannot simply be represented by superposing the ohmic and L scalings, but that rather complex, mixed χ_e scalings occur. The beam heating modifies the ohmic contribution by changing E_t and the T_e profile shape and the ohmic heating modifies the beam contribution.

Transition between ohmic and L transport: The confinement in the intermediate range between OH and L scaling is studied by simulating a series of discharges at $\bar{n} = 2.5 \times 10^{13}$ cm^{-3}, $I_p = 380$ kA, $Z_{eff} = 1.5$ and $P_{OH} = 0.52$ MW with various injection powers. Figure 2 shows the increase of the electron heat diffusivity with rising absorbed beam power. Obviously, at small P_{abs} equal to 0.3 and 0.6 MW the χ_e values clearly exceed the ohmic result (cross) in the middle of the confinement zone at $r = 2a/3$. This explains the observed decrease of the global energy confinement time τ_E /2/. The χ_e profiles with ohmic heating and $P_{abs} = 0.6$ MW are presented in Fig. 3. Special attention is paid to the local ratio of the injection and ohmic heating power densities. Results for various absorbed beam powers are shown in Fig. 4. It is obvious that $P_b/(\eta j_t^2) \simeq 0.3$, where the influence of beam heating should become important, is already exceeded with $P_{abs} = 0.3$ MW. As shown above, the corresponding χ_e and τ_E are indeed found to deviate from the ohmic scaling. With $P_{abs} = 0.6$ and 0.9 MW, neutral injection becomes dominant in the confinement zone. This explains the observed fast transition of τ_E to the L scaling. For $P_{abs} \gtrsim 1.2$ MW the beam power density is large compared with ηj_t^2, which agrees with the essentially pure L confinement found. The power scan shows that the transition to the L regime correlates with the ratio $P_b/(\eta j_t^2)$. Both the deviation from the ohmic scaling and the approach to the L confinement occur at power density ratios which agree with the expected values. According to the electron energy equation, injection powers of this level perturb the ohmic state. The associated change in

confinement suggests that the χ_e scaling responds to the auxiliary heating. The fact that the coupling between the ohmic heating profile and $T_e(r)$ is broken up with neutral injection should play an important role. As the smallest injection power scarcely modifies the plasma parameters, such as density and temperature gradients and poloidal beta, a transition to other instabilities and/or saturation effects, i.e. to a different transport mechanism, is very unlikely.

Transport behaviour after neutral injection: A characteristic time development of the diffusivities χ_e and D in L discharges was found by means of transport simulations /1,2/. It was shown that the L phase persists for about 100 ms after the end of injection. As the slowing-down time of the fast beam ions is only about 10 ms, the injection power rapidly decays. It is thus concluded that the L transport does not require the presence of injection heating, beam fuelling and direct ion heating. Simulations of many L discharges revealed that the phase with the ion-electron energy transfer rate $P_{ie} > 0$ also lasts for a time span of about 100 ms, which suggests that the L phase is maintained by non-ohmic electron heating.

The time development of the electron temperature profiles measured after injection is shown in Fig. 5. Although the beam power is negligibly small, the Gaussian-shaped T_e profiles typical of the ohmic phase are only reached after about 80 ms. The central steepening of the profiles results from the electron heating due to P_{ie}, which is largest in the plasma centre. Profiles of $P_{ie}/(nj_t^2)$ after neutral injection which were determined by simulating the L discharge with P_{abs} = 2.1 MW in Figs. 2 and 4 are presented in Fig. 6. The absorbed beam power is negligibly small at $t-t_{off}$ = 43 ms, so that the only non-ohmic heating is due to P_{ie}. Owing to P_{ie} a transport scaling different from the ohmic one should thus persist in a considerable fraction of the plasma cross-section. Close to the end of the L phase, however, the ratio of the power densities has become so small that the scaling becomes almost purely ohmic. It is concluded that deviations from the ohmic scaling occur if the non-ohmic electron heating (due to neutral injection or ion-electron energy transfer) locally exceeds the ohmic power density.

References

/1/ Becker, G., ASDEX Team, Neutral Injection Team, Nucl. Fusion 22 (1982) 1589.
/2/ Becker, G., Campbell, D., Eberhagen, A., Gehre, O., Gernhardt, J., et al., Nucl. Fusion 23 (1983) 1293.
/3/ Becker, G., Nucl. Fusion 24 (1984) 1364.
/4/ Kaye, S.M., Goldston, R.J., Bell, M., Bol, K., Bitter, M., et al., Nucl. Fusion 24 (1984) 1303.
/5/ Becker, G., Report IPP III/109 (1986).
/6/ Post, D.E., Singer, C.E., McKenney, A.M., BALDUR: A One-dimensional Plasma Transport Code, PPPL Transport Group, TFTR Physics Group, Report 33 (1981).
/7/ Becker, G., ASDEX Team, Neutral Injection Team, Report IPP III/98 (1984).

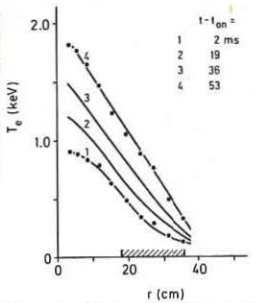

Fig. 1: $T_e(r,t)$ after the beginning of neutral injection (t_{on} = 1.12 s) measured by multi-pulse Thomson scattering in an L discharge with $\bar{n}$ = 2.4 x 10^{13} cm^{-3}, I_p = 280 kA and P_{abs} = 2.0 MW. The hatched area denotes the confinement zone.

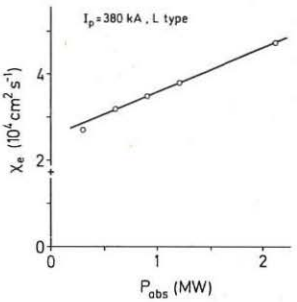

Fig. 2: Approximately homogeneous electron thermal diffusivity from simulations versus absorbed beam power ($\bar{n}$ = 2.5 x 10^{13} cm^{-3}). For comparison, the ohmic χ_e (2a/3) value (cross) is shown.

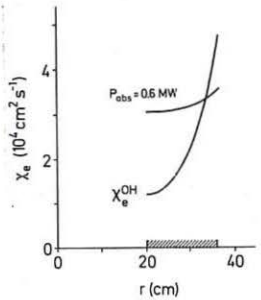

Fig. 3: $\chi_e(r)$ in the confinement zone (hatched) with ohmic heating and neutral-beam heating with two sources.

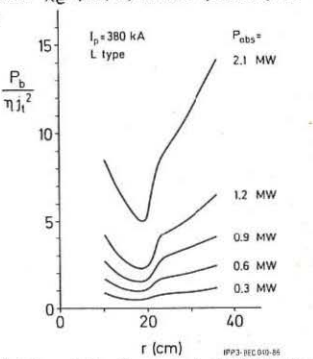

Fig. 4: Ratio of the beam and ohmic power densities versus radius from simulations of the power scan of Fig. 2.

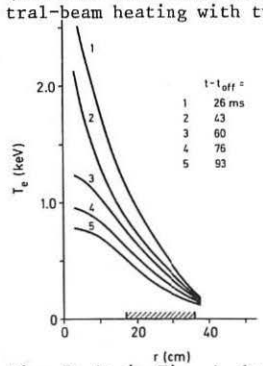

Fig. 5: As in Fig. 1, but after the end of neutral injection (t_{off} = 1.52 s).

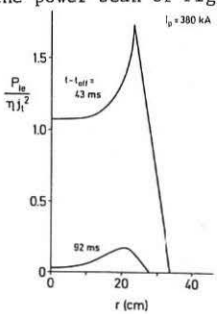

Fig. 6: Ratio of the power densities of ion-electron energy transfer and ohmic heating versus radius after t_{off}.

ENERGY AND PARTICLE TRANSPORT IN MEDIUM-DENSITY ASDEX PELLET DISCHARGES

O. Gruber, W. Jilge, V. Mertens, G. Vlases, M. Kaufmann, R. Lang, W. Sandmann, K. Büchl, H.S. Bosch, H. Brocken, A. Eberhagen, G. Fussmann, O. Gehre, J. Gernhardt, G. v. Gierke, E. Glock, G. Haas, J. Hofmann, G. Janeschitz, F. Karger, M. Keilhacker, O. Klüber, M. Kornherr, K. Lackner, M. Lenoci, G. Lisitano, F. Mast, H. M. Mayer, K. McCormick, D. Meisel, E. R. Müller, H. Murmann, H. Niedermeyer, W. Poschenrieder, H. Rapp, H. Röhr, F. Ryter, F. Schneider, C. Setzensack, G. Siller, P. Smeulders, F. X. Söldner, K.-H. Steuer, F. Wagner, D. Zasche.

Max-Planck-Institut für Plasmaphysik, EURATOM Association,
D-8046 Garching, Fed. Rep. Germany.

1. INTRODUCTION

In ASDEX a comparison of ohmically heated divertor discharges with gas fuelling (GF) and pellet fuelling (PF), without any gas puffing after a gas puff "start-up" phase, has been done [1].

With a large interval between successive pellets ($\Delta t_p \approx 40$ ms) the density stayed below $2 \cdot 10^{19}\,\mathrm{m}^{-3}$ and only small differences resulted in the radial plasma parameter profiles and the transport behaviour comparing PF and GF discharges at the same density. With $\Delta t_p \approx 35$ ms a medium density of $\overline{n}_e \approx 3.3 \cdot 10^{19}\,\mathrm{m}^{-3}$ resulted where the pellet penetration depth increased up to ≥ 25 cm, primarily a consequence of the continuously falling electron temperature (shot PM). The PM density profiles are much more peaked than the profiles of the gas-fuelled discharge GC at the same density $\bar{n}_e$, whereas the PM T_e profiles become only slightly broader compared with the GC T_e profiles (see Fig. 1). The corresponding $T_e(o)/\langle T_e\rangle$ values for both discharges are still within the scatter of the data showing pofile consistency at the corresponding $q_a^* = 3.4 : T_{e0}/\langle T_e\rangle = 2.2 \div 2.7$ [2]. In the PM discharge a distinct increase of the totally radiated power and of the radiation power density in the plasma centre is observed and sawteeth are absent after 1.1 s. With still further reduced $\Delta t_p < 33$ ms the density is limited to $< 5 \cdot 10^{19}\,\mathrm{m}^{-3}$ by a radiation collapse and is comparable with the density limit of a GF discharge. Only combining pellet injection and gas puffing and using wall carbonization considerably higher densities can be obtained [3].

This paper deals with a detailed comparison of the radial transport of the PM and the GC discharges with the transport analysis code TRANSP [4] using the measured radial profiles of n_e, T_e and radiation losses.

2. PARTICLE TRANSPORT

In the PF discharges the particle fluxes Γ inside $r < 0.75a$ are solely determined by the decrease of the particle content after the pellet injection event, which is equal to the pellet fuelling rate there. Only for larger $r > 3/4a$ has the particle recycling flux (and the gas puff rate in GF discharges) to be considered as an additional source term. From the calculated Γ at $r = 30\,\mathrm{cm}$ (Fig. 2) a $\dot{N} = \Gamma \cdot 2\pi R \cdot 2\pi r = 10^{21} s^{-1}$ is obtained therefore, which is equal to $\Delta N_{pellet}/\Delta t_p$. The total particle confinement time has been estimated from pressure measurements in the divertor chamber to increase from 60 ms (GC) to about 100 ms (PM), yielding only a small recycling flux $2 \cdot 10^{19}\,\mathrm{m^{-2}\,s^{-1}}$ at $r = a$ in the latter case.

The particle flux Γ can be modelled by the ansatz $\Gamma(r,t) = -D\frac{\partial n}{\partial r} - nv_{in}$, where v_{in} is an anormal "inward drift" velocity. Fits have been tried to yield a consistent description of D and v_{in} over a pellet cycle by using 1) $v_{in} = v(a)r^2/a^2$, yielding D(r,t), 2) $v_{in} = 3\frac{r^2}{a^3}D$, yielding D, 3) $D = 4000\,\mathrm{cm^2/s}$, yielding v(r,t) and 4) $D = 0.2 \div 0.4\chi_e$, yielding again v. The electron thermal diffusivity χ_e was determined from the energy transport analysis (s. Sec. 3). In practice scatter is large, but model 3) can be excluded and models 2) and 4) give about equal results for D and v, correspondingly. The same model, $D = 0.3\chi_e$ and $v_{in} = 3\frac{r^2}{a^3}D$, describes also GF discharges with constant or rising density [5].

3. ENERGY TRANSPORT

The global energy confinement time $\tau_E^* = W_{pl}/(P_{heat} - \dot{W}_p l)$ are degraded in the PM discharge from 72 ms (GC) to a pellet-cycle-averaged value of 44 ms due to three effects:

1. The total plasma energy is smaller in PM as the temperatures are decreased and the density profiles are strongly peaked (accounting for 20% of the decrease in τ_E^*).
2. Radiation losses are increased from 110 kW (GC) to 160 kW (PM) (accounting for 10%) (see Fig. 3).
3. Non-adiabatic fast losses ($\Delta W \leq 2\,\mathrm{kJ}$) occur after each pellet event constituting a time-averaged loss rate of about 50 kW for the quasi-steady PF discharge state (accounting for 10%). This energy loss is an order of magnitude higher than the energy required to ionize all injected particles. It is further equal to the time-averaged energy increase during the pellet cycle shown in Fig. 3a for the quasi-steady discharge phase.

Due to the deep pellet fuelling the convective energy losses $P_{conv} = \frac{5}{2}k(T_e + T_i)\Gamma$ exceed the electron conduction losses throughout the plasma in contrast to the GF discharges ($P_{cond,e} \gg P_{conv}, P_{rad}$ for $\bar{n}_e < 3 \cdot 10^{19}\,\mathrm{m^{-3}}$; Fig. 3b). The cycle-averaged β and $\beta_p + li/2$ values of the kinetic analysis agree with the magnetic measurements.

The local transport analysis shows further that within the error bars the cycle-averaged thermal heat diffusivity $\bar{\chi}_e^t$ can be described by the scaling $\chi_{CMG} \sim (n_e^{0.8} T_e q)^{-1}$ derived from GF discharges [5], showing no major change in the anomalous transport mechanism. But χ_e is larger than χ_{CMG} just after the pellet injection event ($t = t_p$) and smaller at the end of

the pellet cycle ($t = t_p + \Delta t_p$) (Fig. 4). On the other hand, the ohmic input power is strongly changing over one pellet cycle, too, due to the T_e decrease at the pellet injection event and the corresponding increase of the loop voltage U_L (e.g. t_p+5 ms: $P(\mathrm{OHM}) = 650\,\mathrm{kW}$, $t_p + \Delta t_p$: $P(\mathrm{OHM}) = 450\,\mathrm{kW}$). Therefore a description $\chi_e \sim (P_{cond,e}/2\pi R)/(n_e T_e \frac{r}{T_e}\frac{\partial T_e}{\partial r})$, where $P_{cond,e}$ is a certain fraction of the input power $P(\mathrm{OHM}) = U_L \cdot I$ and $\frac{r}{T_e}\frac{\partial T_e}{\partial r} \sim \frac{r^2}{r^{*2}}$ is fixed by the profile consistency (s. Fig. 1; r^* may be the $q = 2$radius), is strongly suggested and supported by the results given in Fig. 4b. One then obtains a local diffusivity $\chi_e \sim B_t U_L r^{*2}/(R^2 n_e T_e q)$ which is derived under the assumption of profile consistency and is essentially equal to $\chi_{GMG} = 3.4 \cdot 10^{15} B_t a/(R n_e^{0.8} T_e q)$ [$\mathrm{m^2/s}$, T, m , keV] with $U_L \sim a \cdot R/r^{*2}$. The ion heat conductivity is about one to two times the neoclassical one and much smaller than χ_e both for PM and GC discharges.

REFERENCES

[1] G. Vlases et al, Proc. 12th Europ. Conf. on Contr. Fusion and Plasma Physics, Budapest 1985, **1** (1985) 78.

[2] F. Wagner, O. Gruber et al, submitted to Phys.Rev.Letters.

[3] H. Niedermeyer et al. and M. Kaufmann et al, (Invited paper), this conference.

[4] R. Hawryluk, in *Physics of Plasmas Close to Thermonuclear Conditions*, Vol. 1, Varenna (1979) (EUR-FU-BRU/XII/476/80).

[5] O. Gruber, Proc. Invited Papers, Int. Conf. on Plasma Physics, Lausanne (1984) Vol. 1, p. 67.

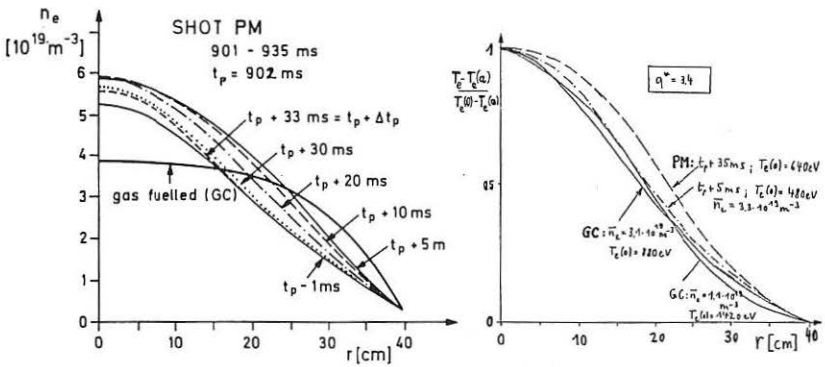

Fig. 1 Radial density and normalized temperature profiles for pellet-fuelled (PM) and a gas-fuelled (GC) discharge.

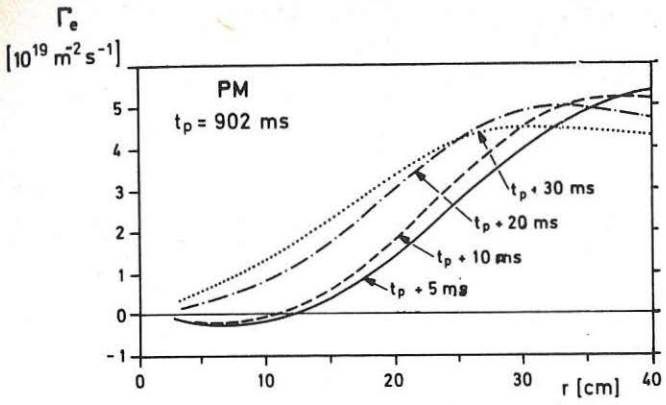

Fig. 2 Particle fluxes $\Gamma(r,t)$ for PM discharge.

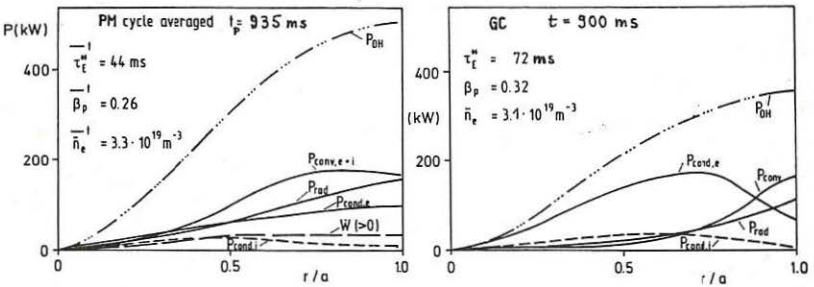

Fig. 3 Radial power balance for PM (time-averaged over a pellet cycle) and GC

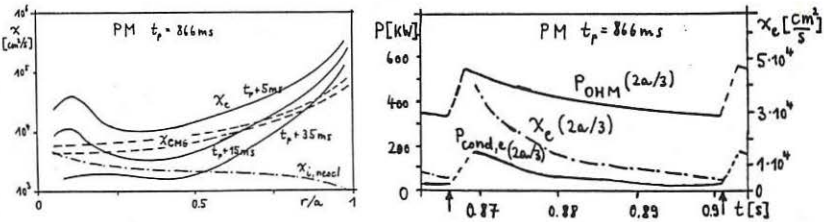

Fig. 4a Radial profiles of electron thermal diffusivity χ_e, χ_{CMG} [5] for the measured plasma parameters and the neoclassical ion heat conductivity $\chi_{i,neocl}$ (PM)

Fig. 4b Time dependence of ohmic heating power P_{OHM} within $r = 2a/3$, electron thermal conduction loss $P_{cond,e}$ and χ_e at $r = 2a/3$ (PM discharge).

DIRECT MEASUREMENT OF THE ELECTRON DIFFUSION COEFFICIENT ON JET USING A MICROWAVE RELECTOMETER

A Hubbard* D Ward* and T E Stringer

JET Joint Undertaking, Abingdon, OX14 3EA, UK
*On attachment from Imperial College, London, UK

ABSTRACT

A fixed frequency reflectometer on JET is used to make localized measurements of density changes. During sawtooth oscillations, the effects of the central density collapse are clearly seen outside the mixing radius. The timing of these density pulses is compared with model predictions to derive the particle diffusion coefficient, D_p. Values of D_p = 0.5 - 0.8 m^2/s are derived, in good agreement with those obtained by other means.

EXPERIMENT

Measurements of electron density changes are made using a microwave reflectometer which launches waves at a fixed frequency F_o in the ordinary mode ($\underline{E}//\underline{B}$) /1/. Total reflection occurs where F_o equals the local plasma frequency. This corresponds to a critical density $n_c = F_o^2/80.6$ (MKS units). A simple interferometer detects movements in this layer throughout the plasma pulse. Gunn oscillators with frequencies of 20, 34.5, 49 and 60GHz have been used on different pulses to probe density layers at 5.10^{18}, 1.5×10^{19}, 3×10^{19} and 4.5×10^{19} m^{-3} respectively. In recent JET experiments the central density n_o was typically $3 - 5 \times 10^{19}$ m^{-3}, so that a 35GHz beam reflects well outside the sawtooth mixing radius.

The reflectometer uses a single antenna to launch and receive waves along the horizontal mid-plane (Figure 1). A long, oversized (WG10) transmission line directs radiation to a tunable crystal detector, which measures the interference signal. Signal/noise ratios of up to 200 are obtained. Using a low-pass filter to reduce the effect of MHD fluctuations with f > 500Hz, the delayed effect of the sawtooth collapse is clearly observed.

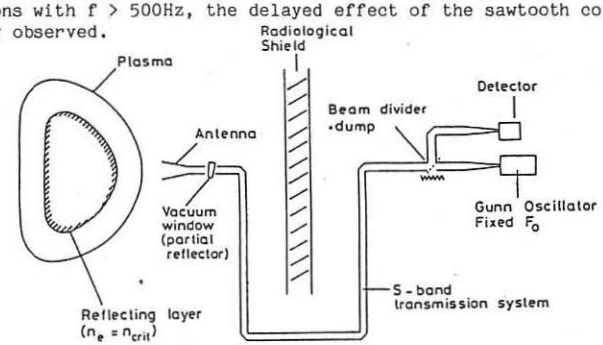

Fig. 1 Schematic of JET Reflectometer.

MODEL OF DENSITY PULSE PROPAGATION

A 1-dimensional numerical model is used to simulate the density profile of a sawtoothing plasma. First, an equilibrium is allowed to evolve assuming full recycling with a realistic neutral penetration depth, a uniform diffusion coefficient D_p and an anomalous pinch term $V_p = D_p\, r/a^2$. This gives a profile in good agreement with JET measurements. The sawtooth activity is now included by a periodic instantaneous flattening of the density profile in the central region out to the mixing radius R_m. This central perturbation then evolves on a diffusive time scale. The effect on the density at different radii is shown in Figure 2. For the region of interest, we find the time of arrival of the maximum density change (T_p) scales linearly with the distance from R_m.

In previous similar work on the propagation of the sawtooth temperature perturbation /2,3,4/, the time for the pulse to reach the edge, $T_p(a)$, was short compared to the sawtooth period τ_{st}, and consequently each pulse behaved independently. For density perturbations, however, the two times are comparable (both ~100ms on JET). This leads to a sensitive dependence of T_p on τ_{st}, which is summarized in Figure 3. Similar curves have been plotted for the time at which the pulse is first seen (T_1 in Figure 2), which has a different scaling with radius.

The influence of the assumed pinch velocity on our results has been tested by using two different values: $V_p = 2D_p r/a^2$ and $V_p = 0.2D_p r/a^2$. The predicted delay times for these cases vary by less than five percent while the equilibrium density profiles are of course very different. This shows that the derived D_p is not sensitive to variations in the pinch term.

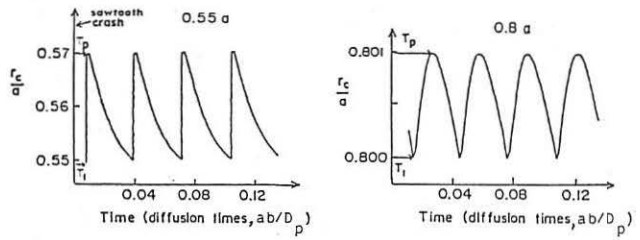

Fig. 2 Predicted movements of density layers at different radial positions across a sawtoothing plasma. ($r_c = R_c - R_o$).

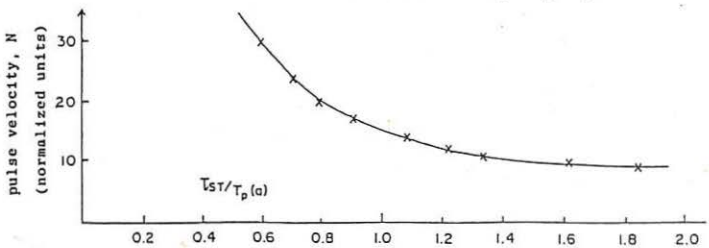

Fig. 3 Dependence of $N = (R - R_m)/T_p$ on sawtooth period.

DATA ANALYSIS AND RESULTS

To derive the diffusion coefficient we use density pulse times measured by the reflectometer during a series of similar sawteeth. Information from other diagnostics is also required. Data used for the ohmically heated JET discharge 7010 (I_p = 3MA, B_T = 2.9T) are summarized below.

Parameter	Value	Diagnostic
a	1.07m	Magnetics
b/a	1.45	
$R_c(1.5 \times 10^{19}m^3)$	4.04m	Multichannel FIR interferometer
R_m	3.75m	ECE grating polychromater, Soft X-rays
T_1	8ms	
T_p	51ms	Reflectometer and 2mm transmission
τ_{st}	93ms	Interferometer

T_p is compared to the model prediction as discussed above. For this case D_p = 0.81m²/s. Using this value, we also fit the first arrival time T_1 to within 1ms. Figure 4 shows the good agreement between the measured and predicted pulse shape. This gives confidence in the model as well as the values of R_m and R_c. For pulse 6276, which has higher density due to RF heating, we find D_p = .62 during heating and .48 afterwards. So far we have analysed insufficient data to determine whether there are systematic changes with RF heating or plasma parameters. Varying R_m, R_c and the delay times within experimental tolerances, we estimate an uncertainty of ± 30%. This could be improved significantly by using 2 or more frequencies simultaneously, reducing the sensitivity to R_m. Such an experiment is planned in the near future.

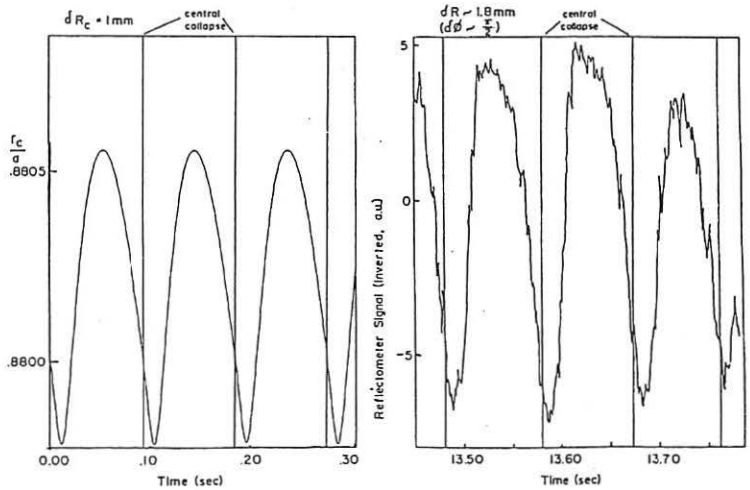

(a) Modelled Pulses (r_m = .6a, τ_{ST} = .104 ms) (b) Observed Pulses, Shot 7010

Fig. 4 Comparison of observed and predicted movements of R_c (Pulse 7010, D = 0.81 m²/s).

CONCLUSIONS

- A simple fixed frequency reflectometer is able to make localised measurements of density perturbations in the outer regions of the discharge due to the sawtooth collapse. The shape and amplitude of the observed pulses agree with predictions of a numerical model. This gives a new and more direct technique of measuring particle diffusion.

- Detailed analysis of an ohmically heated JET discharge (pulse 7010) gives a value of $D_p = (0.81 \pm 0.25) m^2 s^{-1}$. On other discharges D_p falls in the range 0.5 to $0.8 m^2 s^{-1}$. No scaling with plasma parameters has yet been attempted.

- The cumulative effect of the sawtooth density perturbations is found to be important. With only one measurement point, the value of D_p is sensitive to experimental errors, in particular to error in the radius of the critical density, R_c. Thus we have at present an estimated uncertainty of ± 30% on D_p. This error would be reduced by having a larger number of data points (more reflectometer frequencies). A multichannel reflectometer is planned on JET.

- The results obtained are in good agreement with the mean values for D_p derived from density profile changes during RF heating /5,6/.

REFERENCES

/1/ A E Hubbard, A E Costley and C W Gowers, JET-PC(85)32 (Submitted for publication)

/2/ G L Jahns et al, Nuclear Fusion 18, 609 (1978)

/3/ J D Bell et al, Nuclear Fusion 24, 997 (1984)

/4/ H W Piekaar et al, 27th Annual Meeting of the Division of Plasma Physics of the APS (San Diego, 1985); JET-P(85)31/9.

/5/ A Gondhalekar et al, 27th Annual Meeting of the Division of Plasma Physics of the APS (San Diego, 1985); JET-P(85)31/3.

/6/ A Gondhalekar et al, this conference.

FIGURE CAPTIONS

Fig. 1 Schematic of JET Reflectometer.

Fig. 2 Predicted movements of density layers at different radial positions across a sawtoothing plasma. ($r_c = R_c - R_o$).

Fig. 3 Dependence of $N = (R - R_m)/T_p$ on sawtooth period.

Fig. 4 Comparison of observed and predicted movements of R_c (Pulse 7010, $D = 0.81\ m^2/s$).

INVESTIGATION OF ELECTRON TEMPERATURE PROFILE BEHAVIOUR IN JET

D V Bartlett, H Bindslev, M Brusati, D J Campbell, J G Cordey, A E Costley, S E Kissel, N Lopes-Cardozo*, B van Milligen*, P E Stott

JET Joint Undertaking, Abingdon Oxon OX14 3EA, UK
* FOM Institute for Plasmaphysics, Rijnhuizen, Netherlands

1. INTRODUCTION

The characteristics of the electron temperature profile in JET have been examined for a wide variety of plasma conditions. Both ohmically heated plasmas ($2.1 < B_T < 3.5$ Tesla, $1 < n_e < 4 \times 10^{19}$ m^{-3}, $1 < T_{eo} < 5$ keV, $1 < I_p < 5$ MA) and those with strong additional heating (RF and Neutral Beam powers up to about 5 MW) have been studied.

The temperature data have been obtained from electron cyclotron emission measurements. The spatial and temporal resolution of the diagnostic systems employed permit a detailed study of the profile behaviour to be made.

In this paper, both global information (volume averaged quantities) and local information (eg. temperature gradients) are examined to see if they show any scaling with other plasma parameters, and whether this can be related to any of the theories of profile consistency [1,2,3].

2. THE ELECTRON TEMPERATURE DIAGNOSTICS

All the temperature data presented here have been obtained from measurements of the second harmonic (extraordinary mode) of the electron cyclotron emission (ECE). The observation direction is along a major radius on, or close to, the plasma mid-plane. These measurements provide reliable temperature information for all plasma conditions of interest here across a major radius range from just inside the plasma centre to almost the plasma edge (ie. R = 2.8 to ~ 4.0m). The measuring instruments and techniques used in the JET ECE diagnostic system have been described in detail elsewhere [4]. Two instruments are used in the present study:

1) All the temperature profiles are produced by an absolutely calibrated Michelson interferometer which measures the whole ECE spectrum about 300 times during each JET discharge. The spatial resolution of the profile both parallel and perpendicular to the line of sight is about 0.15 m, and the time taken for each measurement is 15 ms. An important characteristic of this instrument for the current investigations is that the temperatures deduced are absolutely calibrated to within ±10%, and the relative systematic error within any profile is about ±5%. Despite this accuracy, the uncertainties in the spectral response of this instrument are a limiting factor in the present analysis.
2) A 12-channel grating polychromator gives the time dependence of the temperature at fixed positions in the plasma. Its spatial resolution, about 0.06 m along the line of sight, and its response time, about 5 μs, are well suited to the present task.

3. GLOBAL TEMPERATURE BEHAVIOUR

Figure 1 shows the ratio of the peak temperature to the volume average as a function of q_{edge} for a large number of discharges with ohmic, ICRH and neutral beam heating. These data were taken at the end of the current flat top when the plasma was in a steady state and sawteeth were present. Although the peak electron temperature depends on a number of plasma parameters, the shape of the profile appears to be strongly linked to the safety factor at the edge of the plasma, q_{edge}. Also shown in figure 1 is the time development for a typical 4 MA (q_{edge} = 3) pulse. It is only when the plasma has reached a steady state with the current fully penetrated (about 3 seconds into the flat top) that the correlation of T_{eo}/T_{av} with q_{edge} is observed. The inductance shows similar correlation with T_{eo}/T_{av}.

The scatter in the T_{eo}/T_{av} plot is not due to sawteeth since the data is averaged over a time longer than the sawtooth period. It is probably related to the net input power profile (input power minus radiated power), the temperature profile being much narrower when the total radiated power is 90% of the input power. Plasmas of this type are shown by the crosses on figure 1. There is also an apparent tendency for the profile to be narrower during ICRH where the heating profile is very peaked (*), and broader during neutral beam heating which has a less peaked deposition profile (Δ).

The radius at which q = 1 (which we equate approximately to the sawtooth inversion radius measured by the 12 channel grating polychromator) is also closely correlated with q_{edge} as shown in figure 2. This, of course, is not surprising since the current density profile is determined by the temperature profile once the electric fields have fully penetrated the discharge. The confinement inside q = 1 is largely determined by sawtooth activity and the region of prime interest for confinement lies between q = 1 and q_{edge}. The parameter T_{eo}/T_{av} may be a fairly coarse measure of the profile shape in this confinement region and in particular scatter in the experimental data could mask significant differences in profile shape. We have therefore looked in more detail at the actual shape of the profiles.

4. LOCAL TEMPERATURE BEHAVIOUR

Figure 3a compares three temperature profiles measured in the steady state of ohmic plasmas with difference values of q_{edge}. Due to the different ohmic power inputs and densities the peak temperatures for these three discharges vary considerably. The gradients ($\nabla T_e = dT_e/dR$) of these three profiles are shown in figure 3b: again there are large differences. In part c) of the figure, the ratio $\nabla T_e/T_e$ is plotted. These curves show a trend with q_{edge}: across a wide region outside q = 1, the slope decreases with increasing q_{edge}. To examine this behaviour, it is convenient to fit a straight line to these curves (outside q = 1), which implies a Gaussian fit to the profiles. Figure 4 shows the slope of the fitted line as a function of q_{edge} for a number of ohmic discharges. Although the quality of the fit becomes poor at high q_{edge} (when the profile becomes more triangular) there is a correlation with q_{edge}.

With additional heating the picture becomes more complicated. The localised deposition of ICRH power inside the q = 1 surface produces greatly enhanced sawteeth, but little change in the electron temperature outside q = 1. Figure 5 shows an example of a plasma with 5 MW of ICRH (plus 2 MW of ohmic heating) and q_{edge} = 4. Even in this case, where the additional heating gives a slight increase in both the temperature and its gradient outside q = 1, the $\nabla T_e/T_e$ ratio remains constant.

With neutral injection, the temperature can increase across the whole profile. When the injected power is comparable to the ohmic input power, the $\nabla T_e/T_e$ shows a change of shape, as shown in figure 6. Since a number of plasma parameters are being changed simultaneously (eg. density), it is not clear which is responsible for this effect.

5. CONCLUSIONS

The analyses made so far on the JET data permit some tentative conclusions to be made. A range of temperatures and temperature gradients are obtained for different plasma conditions. The profile shape, represented by T_{eo}/T_{av} or the slope of $\nabla T_e/T_e$, also shows considerable variation but appears to be correlated with q_{edge}. A Gaussian fit to the profile shape outside $q = 1$ works well only at low and moderate values of q_{edge}. The changes in profile shape with additional heating are small, and more detailed analysis is required to determine their cause. Further work on these points is in progress.

6. REFERENCES

[1] B Coppi, Comments on Pl. Phys. and Cont. Fus. 5, 261 (1980)
[2] P H Rebut and M Brusati, Pl. Phys. and Cont. Fus. 28, 113 (1986)
[3] B B Kadomtsev, Pl. Phys. and Cont. Fus. 28 125 (1986)
[4] A E Costley et al, 27th Meeting of APS, San Diego, USA (1985)

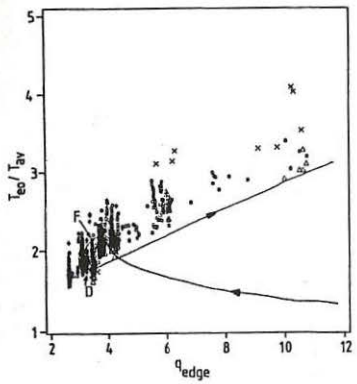

Figure (1): The ratio of peak to volume average electron temperature as function of q_{edge} for a large number of JET pulses. The symbols are:

- o Ohmic plasmas
- * With ICRH
- Δ With NB
- x High radiated power

The curve shows the time evolution for a typical $q_{edge} = 3$ plasma. The plasma current reaches its flat top at the point marked F, and begins to decay at D.

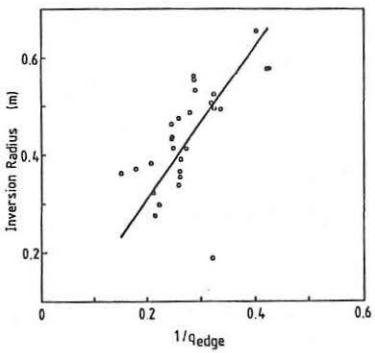

Figure (2): The sawtooth inversion radius as a function of q_{edge} for a number ofJET ohmic plasmas. The inversion radius is obtained by examination of the data from the twelve channel ECE polychromator.

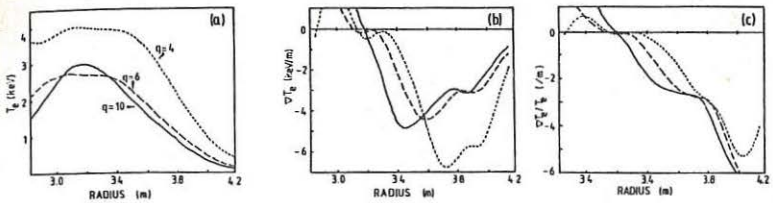

Figure (3): Variation of the profile shape with q_{edge}. The electron temperature (a), its gradient (b), and the ratio of the two (c) are plotted for 3 values of q_{edge}: solid line: q = 10, long dashes: q = 6, short dashes: q = 4

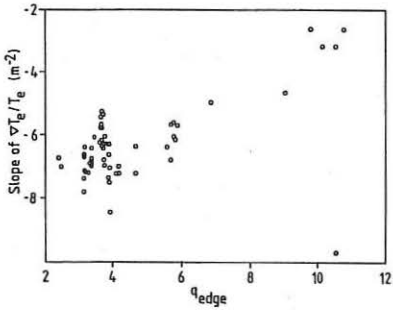

Figure (4):
The slope of the $\nabla T_e/T_e$ curve as a function of the cylindrical q at the edge of the plasma (q_{edge}) for a number of ohmic pulses.

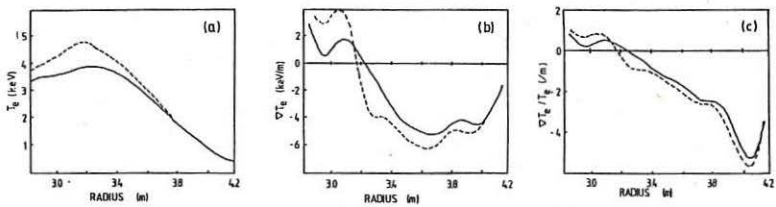

Figure (5): Variation of the profile shape with ICRH heating. The solid curve is the ohmic phase and the dashed curve 1 second after the start of 5 MW of ICRH. Although T_e and ∇T_e change, the $\nabla T_e/T_e$ curve shows only a slight outward shift.

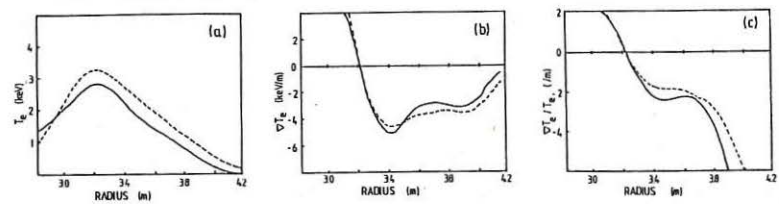

Figure (6): Variation of the profile shape with neutral beam heating. The solid curve is the ohmic phase and the dashed curve 1 second after the start of 5 MW of heating (several times the ohmic power). In this case the $\nabla T_e/T_e$ curve shows a distinct change of shape.

ELECTRON DENSITY TRANSPORT IN JET

A Cheetham, J P Christiansen, S Corti, A Gondhalekar, F Hendriks
J Hugill*, P D Morgan, J O'Rourke and M Watkins

JET Joint Undertaking, Abingdon, Oxon OX14 3EA, UK
* Culham Laboratory, Abingdon, Oxon OX14 3DB, UK

This study is based upon absolute measurements of H_α or D_α emission at various locations, of electron density using a 7-channel FIR interferometer and of neutral particle effluxes using a NPA. Plasma fuelling with auxiliary heating is investigated and transport coefficients determined for a range of plasma parameters.

FUELLING AND PLASMA EDGE BEHAVIOUR

During an OH discharge, the density evolution closely follows that of the plasma current, [1]. The application of auxiliary heating pulses of duration a few seconds produces an increase in the electron inventory, ΔN_e, which scales approximately linearly with the additional power, Fig.1,while dN_e/dt falls throughout the heating pulse. During NBI, asymptotically the ratio of increase in electron inventory to the number of electrons injected by the beam, $\Delta N_e/N_{NBI}$, does not vary appreciably with N_{NBI}, Fig. 2, and is ~ 0.8. In contrast, starting from the same initial conditions, admitting $N_g \approx 2.8 \times 10^{21}$ atoms into the torus by gas puffing produces a relative increase $\Delta N_e/N_g$ of ~ 0.4.

During both ICRF and NBI, the global particle confinement time τ_{pg} drops during the heating pulse, consistent with the plasma being more impermeable to the recycled neutrals, due to its higher edge density. For a series of shots in which only the density is varied, and where the vessel has been conditioned by a number of discharges, τ_{pg} at current flat top varies inversely with $\bar{n}_e$ at densities $\gtrsim 1.5 \times 10^{19}\ m^{-3}$, (1). At lower densities the reverse dependence has been seen. However, for the same settings of the discharge parameters, the values of τ_{pg} obtained for a large collection of OH shots over a period of many months show a significant spread at a given $\bar{n}_e$, varing by a factor of 2 or more. Apart from uncertainties concerning the spatial uniformity of the H_α/D_α emission, the spread in τ_{pg} can be understood in terms of a shot-to-shot variation in the neutral influx from the limiters Φ_H^L, at fixed $\bar{n}_e$, depending on the recent history of the machine, Fig. 3.

ELECTRON DENSITY TRANSPORT IN JET

Density Profile Constancy is a striking feature of electron density build-up in JET. Figs. 4(a) and 5(a) show the line integrated density along seven vertical chords through the plasma. Fig. 4(a) is for a plasma with ICRF. Fig. 5(a) is for a similar plasma with NBI. Observe that, in both cases, after the plasma current and aperture become stationary, the ratios among the seven line integrated electron density signals remain nearly constant (within less than 5%) as the discharge evolves in time, indicating that the density profile shape remains nearly constant - see Figs. 4(b) and 5(b). This indicates that the magnitude of the electron density transport coefficients adjust themselves as the plasma heating source, electron source and electron density change, so as to maintain a nearly constant density profile.

In order to determine the electron density transport coefficients, the density transients as shown in Fig. 4(a) and Fig. 5(a) have been analyzed. The continuity equation governs the density evolution:

$$\frac{\partial n_e}{\partial t}(r,t) = S_e(r,t) - \nabla \cdot \Gamma_e(r,t).$$

The spatial form of the radial electron source function $S_e(r)$ is calculated using the neutral density profile arising from edge neutrals only, recombination neutrals do not contribute to the electron source. $S_e(r)$ is then normalized at the edge using the absolute H_α measurement. Ionization of impurities is also a source of electrons. We have simplified this by multiplying by a factor (usually 1.6) the electron source due to ionization of neutrals. Fig. 4(c) shows such a computation. This gives us a measurement of the radial electron flux.
In NBI discharges the electron source consists of, in addition to ionization of edge neutrals, ionization of beam neutrals. Fig. 5(c) shows the electron source function at the start of NBI. This source is strongly time dependent; as the plasma density increases, the beam-generated source flattens.

The measured electron flux $\Gamma_e(r)$ is interpreted in terms of a model of electron transport consisting of diffusive and convective driving terms, [2]:

$$\Gamma_e(r) = - D(r) \frac{\partial n_e(r)}{\partial r} + n_e(r)\, V_p(r).$$

$D(r)$ and $V_p(r)$ are assumed not to change during auxiliary heating. The magnitude of the diffusion coefficient D determined above is in agreement with that determined by analysis of density sawtooth propagation [3].

The analysis described has been performed for a large number of RF heated and a few NBI discharges, covering a large parameter range in B_ϕ, I_ϕ, P_{aux} and $\bar{n}_e$, Fig. 6.

CONCLUSIONS

1. ICRF and NBI heating produce increases in the plasma electron inventory, which are comparable under similar conditions, despite the differences in fuelling. The increase scales approximately linearly with applied power.
2. Hysteresis behaviour in the variation with $\bar{n}_e$ of the H or D influxes from the limiters leads to a spread in particle confinement time. Vacuum vessel conditions influence recycling and particle confinement.
3. The results of the electron density transport analysis, whilst yeilding credible results do not provide a detailed insight into the transport mechanisms. The transport coefficients do not depend in any systematic way on the externally controllable parameters. It seems plausible that transiently, the transport coefficients assume a magnitude so as to prevent the density profile deviating far from a preferred shape. Work is in progress to explore if the measured electron flux $\Gamma_e(r,t)$ is related to other driving terms such as the plasma pressure and its gradient.

REFERENCES

[1] P D Morgan et al, Proc 12th European Conf. on Controlled Fusion and Plasma Phys. Budapest 1985, Vol II, p.535

[2] B Coppi and N Sharky, Nuclear Fusion 21, 1981.

[3] A Hubbard et al., this conference.

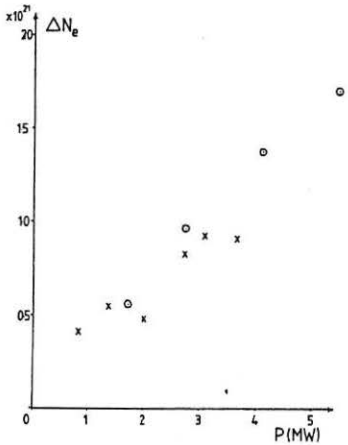

Fig. 1. Variation of increase in plasma electron inventory, ΔN_e, with auxiliary power, P, for discharges with ICRF (X) and NBI (O). I_p = 2 MA, B_ϕ = 3.4 T, D, plasma, ^{3}He minority or 65 keV H beam, length of auxiliary power pulse = 2 s.

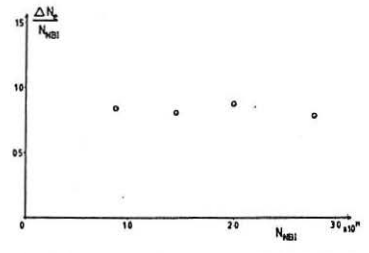

Fig. 2. Variation of ratio of increase in plasma electron inventory during NBI to total number of injected beam atoms, $\Delta N_e/N_{NBI}$, with number of injected atoms, N_{NBI}. I_p = 2 MA, B_ϕ = 3.4 T, D, plasma, 65 keV H beam, length of NBI pulse = 3.5 s.

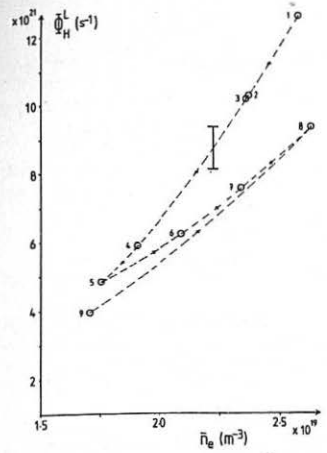

Fig. 3. Variation of total D influx from limiters, Φ_H^L, with average plasma density, $\bar{n}_e$, for a sequence of consecutive discharges. I_p = 3 MA, B_ϕ = 2.6 T, D_2 plasma. Φ_H^L exhibits hysteresis behaviour. The machine had not been operated previously for 3 days.

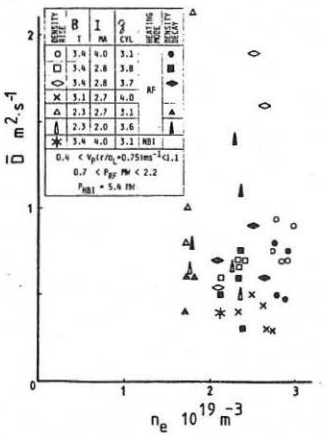

Fig. 6. The volume averaged diffusion coefficient $\bar{D}$, versus average electron density $\bar{n}_e$, for various plasma conditions.

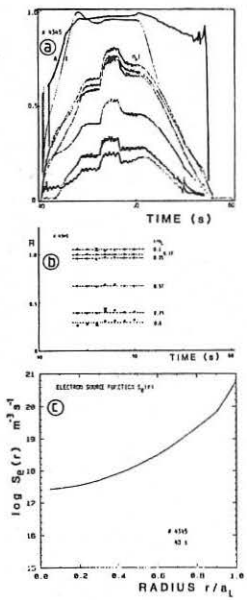

Fig. 4. Plasma discharge in deuterium, B_T = 2.3 T, b/a = 1.4. 2 MW ICRF applied at 46.1 sec, for 2 sec, in hydrogen minority heating mode.
(a) Temporal evolution of plasma current, I, (2.1 MA full scale), plasma aperture, A, (5.86 m² full scale), and seven vertical line-integrated measurements, $n_e\ell$, (6.53 x 10^{19}m^{-2} full scale).
(b) Ratios of the seven line-integrated density measurements to a central value, versus time. The constancy of these ratios indicates the constancy of the electron density profile during ICRF.
(c) Electron source versus normalized radius.

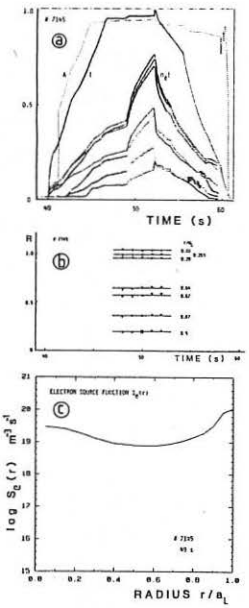

Fig. 5. Plasma discharge in deuterium, B_T = 3.5 T, b/a = 1.46. 5.4 MW of 65 keV hydrogen NBI at 49 sec, for 3 sec.
(a) Temporal evolution of plasma current, I, (4.1 MA full scale), plasma aperture, A, (7 m² full scale), and seven vertical line integrated measurements, $n_e\ell$, (19.5 x 10^{19}m^{-2} full scale).
(b) Ratios of the seven line-integrated density measurements to a central value, versus time.
(c) Electron source (including beam contribution) versus normalized radius.

HYDROGEN ION TRANSPORT IN TOKAMAK PLASMAS

K.W. Gentle, B. Richards and F. Waelbroeck

The University of Texas, Austin, Texas USA

The response of a system to a slow change near equilibrium is a natural way to observe transport characteristics. In particular, the response of a tokamak discharge to an oscillating density source is a sensitive indicator of particle transport.[1] A strong modulation of the small continual gas feed required to maintain a plateau tokamak discharge directly produces a small modulation of the edge density where the neutrals are ionized. The amplitude and phase of the perturbation as it propagates toward the interior depends distinctively on the transport coefficients. Experiments have been done on the TEXT tokamak[2] (R = 1m, a = .27m) over a broad range of discharge parameters: $1T<B_T<3T$, $100\ k_a \le I_p \le 400$ kA, and $1 \le n \le 6 \times 10^{19} m^{-3}$. The external gas feed has been modulated at frequencies from 10 to 40 Hz and the density response observed with a six-channel FIR interferometer along vertical chords at -16, -8, 0, 8, 16, and 24 cm with respect to the major radius.

The experiments are analyzed with the standard model of diffusion and inward convection. Although simple, it is generally quite satisfactory. The observations can be fit well with appropriate choices of V and D, and values of best fit are uniquely determined. The flux and particle conservation equations in this model are

$$\Gamma_r = -D\frac{\partial n}{\partial r} - V\frac{r}{a}n \tag{1}$$

$$\frac{\partial n}{\partial t} = \frac{1}{r}\frac{\partial}{\partial r}\left(rD\frac{\partial n}{\partial r}\right) + \frac{1}{r}\frac{\partial}{\partial r}\left(rV\frac{r}{a}n\right) + P(r,t) \tag{2}$$

where P(r,t) is the production rate, averaged poloidally and toroidally. In steady state, Eq. (2) can be fully integrated to express the density as

$$n_0(r) = e^{-Sr^2/2a^2}\int_r^a \frac{\Gamma_0(\rho)}{D} e^{S\rho^2/2a^2} d\rho \tag{3}$$

$$\Gamma_0(r) = \frac{1}{r}\int_0^r P(\rho)\rho d\rho \tag{4}$$

with $\Gamma_0(r)$ being the radial flux from the sources inside r, and S=aV/D. Since ionization rates are significant only near the edge, the profile from Eq. (3) is Gaussian in the interior, with a shape determined only by S. To facilitate comparison with experiment, the chord integrals of n(r) are computed as a function of radius to provide curves upon which the experimental points should lie. The adequacy of this fit is illustrated in Fig. 1, which compares the best fit of Eq. (3) with the experimental points for chord averages. There are only two free parameters: n(o), set by a multiplier on the production rate, and S; the shape

of P(r) was fixed by H_α profiles. The equilibrium density profiles can thus be used to obtain one constraint on D and V by determining a value of S. A value of best fit is typically determined with an accuracy of ± 20%.

The time-dependent analysis is more difficult. Assuming a separable time dependence $e^{i\omega t}$ for the perturbation, Eq. (2) can be solved in the source-free interior in terms of confluent hypergeometric functions:[3]

$$\tilde{n}(r) = \tilde{N}_0 M(i\omega a/2V, 1, Sr^2/2a^2)\, e^{-Sr^2/2a^2} \tag{5}$$

The region of ionization at the edge is neither observable with sufficient spatial resolution to permit analysis nor tractable mathematically. The net effect of the sources is simply to provide a boundary condition for Eq. (5) at a radius where sources become significant, r~24 cm here. Although simple to impose mathematically, this boundary value is not observable experimentally. A solution for the edge region must be developed to obtain chord integrals for comparison with experiment. Since the neutrals permeate the ionization region quickly, a simple but plausible assumption is that the source term retains its equilibrium form and has a uniform phase independent of radius. A solution to Eq. (2) may then be constructed from the Green's function and manipulated to a form similar to Eq. (3) as

$$\tilde{n}(r) = M(r)e^{-Sr^2/2a^2} \int_r^a \frac{\tilde{\Gamma}(\rho) e^{Sr^2/2a^2}}{M^2(\rho)} d\rho \tag{6}$$

$$\tilde{\Gamma} \equiv \frac{1}{r} \int_0^r \frac{P(\rho)}{D} M(\rho)\rho d\rho \tag{7}$$

from which chord integrals can be obtained for comparison with experiment. The arguments of M are those of Eq. (5). For convenience, the results are normalized to the central channel as unit amplitude and 0° phase.

Typical comparisons with experiment are shown in Figs. 2 and 3, which show the chord-integrated amplitude and phase of the oscillations as a function of radius. The points are observed values, and the solid lines the result from Eq. (6) for the values of V and D which fit best. The model is certainly adequate in the sense that the curves of best fit are generally within the experimental errors. The largest error is generally in the amplitude of the outermost channel, which may be partly explained by sensitivity of this point to plasma position and may also indicate an oversimplification in the treatment of the edge. Optimal values of D and V may be obtained from nonlinear fitting routines, but formal error analysis remains impractical. One useful measure is illustrated in Fig. 2, however, in which the broken lines represent results from Eq. (6) for somewhat different values of the transport parameters; the fits are clearly worse.

Although Eq. (6) can be taken to the asymptotic limit of pure diffusion and the fact that the best fits do not occur in that region implies significant inward convection, the strength of that inference is illustrated in Fig. 3, where the broken lines represent attempts to fit the data with purely diffusive transport. The failure is clear. It is often impossible to produce phase differences as great as those observed. At best, the value of D which best fits phase implies completely wrong amplitudes, and a reasonable fit to amplitude implies phases much too small. Inward convection is essential to explain both the equilibrium profiles and the time response.

Over the range of discharge conditions, S =2±1. Density profiles are always peaked with modest variations in degree. The values of D and V show considerably greater variation. The results do not fit a simple relation, but some patterns are clear. For a set of discharges differing only in density, both D and V vary as n^{-1}. There are also variations with current and toroidal field. The best regression fit to the data is that for both D and V varying as $(nq)^{-1}$, which is plotted in Fig. 4. The trends as well as the scatter are clear. These are scalings in terms of the global discharge parameters; there is no evidence to suggest that they be taken as local scalings.

These results may be compared with various other transport processes. The inward convection is generally stronger than the neoclassical prediction by more than an order of magnitude; diffusion is even larger. The values for D and V are generally similar to those inferred for impurity transport in TEXT,[4] although the scalings differ. Comparing with thermal transport,[2] the scalings are similar with $\chi_e \sim$ (2-4)D.

A few discharges in deuterium have also been analyzed. The diffusion coefficient is systematically lower than in hydrogen, but no other consistent pattern is evident.

Although this simple D and V model characterizes the large-scale particle transport well in many cases, it is inadequate in some cases. It clearly fails as the density approaches the density limit,[5] above which the discharge disrupts, or if the discharge is strongly perturbed by being moved hard against the inside or outside limiter. Such discharges appear to have significantly enhanced values of D and V at the edge, preserving the value of S for the equilibrium profile, coupled with reduced values in the center. The core behavior may be consistent with V = 0 or neoclassical pinch.

Work supported by the U.S. Department of Energy.

1. A.A. Bagdasarov, *et al.*, Nucl. Fusion (Supplement) 1985, **1**, 181.
2. R.V. Bravenec, *et al.*, Plasma Physics and Controlled Fusion **27**, 1335 (1985).
3. K.W. Gentle, *et al.*, Plasma Physics and Controlled Fusion **26**, 1407 (1984).
4. W.K. Leung, "Impurity Transport in TEXT," Ph.D. Thesis, University of Texas, 1985.
5. R.C. Isler, W.L. Rowan and W.L. Hodge, Phys. Rev. Letters **55**, 2413 (1985).

Figure 1.

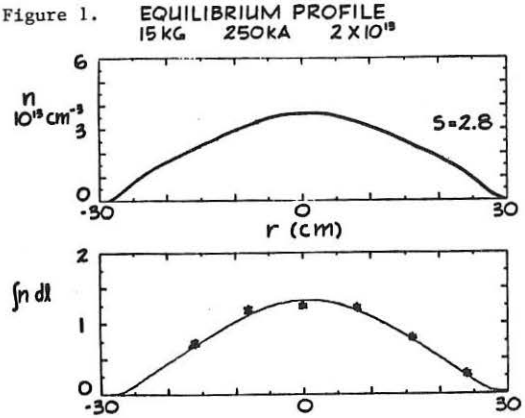

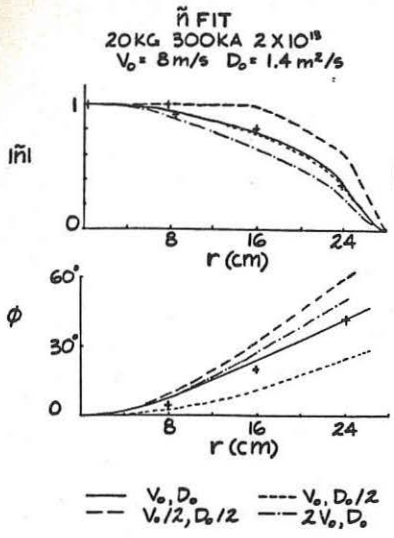

Figure 2.

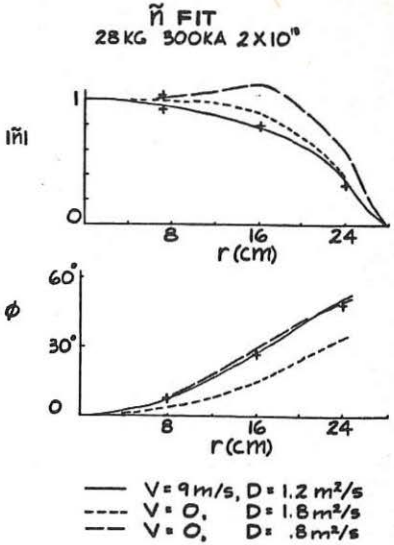

Figure 3.

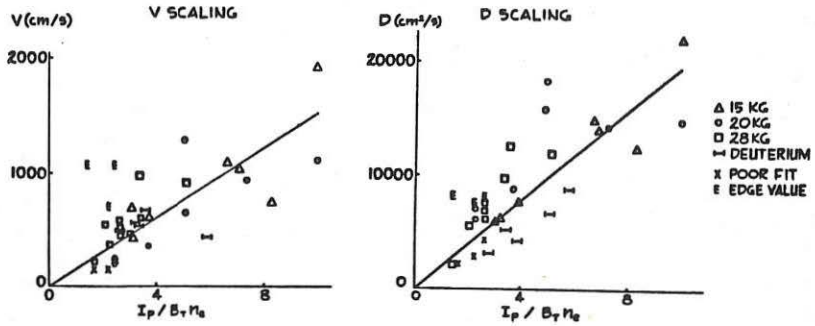

Figure 4.

TRANSPORT IN BEAM-HEATED ASDEX DISCHARGES BELOW AND IN THE VICINITY OF THE BETA LIMIT

O. Gruber, W. Jilge, H.S. Bosch, H. Brocken, A. Eberhagen, G. Fussmann, O. Gehre, J. Gernhardt, G. v. Gierke, E. Glock, G. Haas, J. Hofmann, G. Janeschitz, A. Izvozchikov, F. Karger, M. Keilhacker, O. Klüber, M. Kornherr, K. Lackner, M. Lenoci, G. Lisitano, F. Mast, H. M. Mayer, K. McCormick, D. Meisel, V. Mertens, E. R. Müller, H. Murmann, H. Niedermeyer, W. Poschenrieder, H. Rapp, H. Riedler, H. Röhr, J. Roth, F. Ryter, F. Schneider, C. Setzensack, G. Siller, P. Smeulders, F. X. Söldner, E. Speth, K.-H. Steuer, O. Vollmer., F. Wagner,

Max-Planck-Institut für Plasmaphysik, EURATOM Association,
D-8046 Garching, Fed. Rep. Germany.

1. INTRODUCTION

Radial transport and confinement properties of ohmically and beam-heated ASDEX discharges are studied using the PPPL transport analysis code TRANSP[1] and measured radial plasma profiles and global parameters. Results are that the anomalous electron thermal transport is dominating in low-density ohmic as well as "L" beam-heated ASDEX plasmas. It leads, however, for these regimes to different scaling laws of the global energy confinement time [2]. At high-density ohmic and "H" mode beam-heated discharges the neoclassical ion heat conductivity and convective losses (H mode) are comparable to the electron losses and tend to dominate the energy balance.

The ion heat conduction χ_i is described by two times the neoclassical value calculated by C. Chang and F. Hinton in all discharge phases (OH, L, H, H^*). Thereby a χ_i of three times $\chi_{i,neocl}$ fits the central ion temperature measured by the energy spectrum of CX neutrals whereas a $\chi_i = \chi_{i,neocl}$ yields for the calculated T_i profiles the measured neutron fluxes.

Experiments show that the electron temperature profile shape in ohmically and beam-heated "L" discharges is only influenced by the safety factor $q^*(a)$[3]. According to this concept the elctron thermal diffusivity $\chi_e(r)$ depends directly on the electron thermal conductive loss $P_{cond,e}$ across the magnetic surface with radius r, which is a certain fraction of the input power. From the definition $\chi_e = -(P_{cond,e}/2\pi R)/(n_e T_e \frac{r}{T_e}\frac{\partial T_e}{\partial r})$ and from the "profile consistency" argument $\frac{r}{T_e}\frac{\partial T_e}{\partial r} \simeq -\alpha\frac{r^2}{r^{*2}}$ (where r^* may be the $q = 2$ radius, and α is a function of $q^*(a)$) one obtains $\chi_e(r) \sim P_{cond,e}(r)/(n_e(r)T_e(r)r^2)$. The definition of a local χ_e which depends on local plasma parameters does not seem to be appropriate. In this paper the χ_e values deduced from the transport analysis of OH, L and H mode discharges are used to show which description is applicable.

2. PROFILE CONSISTENCY IN OHMIC AND BEAM-HEATED "L MODE" PLASMAS

In nearly steady-state ohmic discharges χ_e can be described by a local parameter dependence $\chi_e(OH) = \chi_{CMG} \sim (B_t a/R)/(n_e^{0.8} T_e q)$ [2]. But in ohmically heated pellet discharges only the χ_e values averaged over one pellet cycle agree with χ_{CMG}, whereas a description in agreement with "profile consistency" depicts also the time-resolved χ_e measurements and yields an explanation for the scaling given by χ_{CMG} [4].

L-mode discharges at $q^*(a) \approx 2.6$ have been studied using $H^o \rightarrow D^+, D^o \rightarrow H^+, D^o \rightarrow D^+$ injection with 14.5–40 keV maximum energy/nucleon yielding about the same normalized T_e profiles (Fig. 1a), despite quite different heat deposition profiles (see Fig. 1b), total heating powers ($P_h = P_{bi} + P_{be} + P_{OH} = 1.5 \div 4.1 MW$) and densities ($\bar{n}_e = 4.10^{19} \div 11.3 \cdot 10^{19}\,\mathrm{m}^{-3}$). The electron heating ($P_{be} + P_{OH}$) exceeds slightly the ion heating (P_{bi}) and $T_i \gtrsim T_e$ is obtained. Accordingly the central confinement times $\tau_E^* = W_{pl}/(P_h - \dot{W}_{pl})$ are increasing with off-axis heating deposition, whereas the global confinement times are about the same. The deduced $\chi_e(r)$ values given in Fig. 1d can well be described by $\chi_e \sim P_{cond,e}/(n_e T_e r^2)$ for $r_{q=1} < r < 0.8a$ for individual discharges, and at a fixed radius of $r = 2a/3$ the relation $(\chi_e n_e T_e)\,|_{2a/3} \sim P_{cond,e}(2a/3)$ holds for different discharges too. At that radius $P_{cond,e} \approx (0.5 \div 0.65) P_h$ holds, showing the dominance of electron thermal transport in the L mode over the entire density range.

Despite this good agreement a fit of χ_e depending on the local plasma parameters I_p, n_e and T_e has been tried with the limited data base at present available (not only the discharges described here). Good agreement is obtained with a scaling $\chi_e(L) \sim r^2/(I^{1.5}(r) n_e^{0.3}(r) T_e(r) A_i)$, where A_i is the ion mass. This parameter dependence will be tested using a simulation code to reproduce the measured temperatures. We are aware of the "explosive" nature of the $1/T_e$ dependence and that the limited parameter set may give a misleading tendency with inherent correlations of the chosen local parameters.

3. H-MODE CONFINEMENT BELOW AND AT THE BETA LIMIT

Beam-heated ASDEX discharges with $D^o \rightarrow D^+$ show an H mode confinement of $\tau_E^*(a) = 0.2 I$[MA, s] independent of the heating power for plasmas with $\beta < 0.9\beta_c$ and $\beta_c = 0.028 I/aB_t$[MA, m, T]. Reaching the β_c limit the energy confinement times decrease with increasing heating power. This confinement factor of 0.2 s/MA is more than a factor of 2 better than reported from D III and PDX discharges. At higher plasma currents ($I_p > 400$kA) or lower q^* values (< 3) the confinement factor is decreased ($\tau_E^*(a) \lesssim 60ms \lesssim 0.15 I_p$) [5]. Together with $H^o \rightarrow D^+$ and $H^o \rightarrow H^+$ injection results, a scaling $\tau_E^*(H) = 0.1 I A_i$ is deduced.

At these high confinement times and therefore high plasma energies (see Fig. 2a) the convection losses ($P_{conv}/P_h \approx \frac{5}{2}\Gamma k(T_e + T_i)/\Gamma\langle E\rangle$, with the particle flux Γ and the medium energy $\langle E\rangle$ of the injected neutrals) and the ion conduction losses are comparable to the elctron conduction losses (see Fig. 2b). These are now only between $0.25 ((I_{pl} = 310kA, q^*(a) = 4)$ and $0.4 (I_p = 410kA, q^*(a) = 2.7)$ of the total heating power over a large part of the plasma

cross-section. At the higher plasma current the neoclassical ion heat losses are reduced ($\chi_i \sim 1/I^2$). The ion heating by the beams exceeds the electron heating with $D^o \rightarrow D^+$ injection ($P_{bi} \lesssim 3P_{be}$) and the contribution of the beams to the total β value is about 25%. This fact results in the difference of the τ_E^* values with and without the beam contribution given in Fig. 2c. The confinement time τ_E includes only the conductive and convective losses and shows the influence of the radiation and CX losses on τ_E^*.

For these H-mode discharges no description compatible with "profile consistency" is available at present. But the local parameter dependence of $\chi_e(L)$ given above fits also the $\chi_e(H)$ values covering now a parameter range of $0.6 \lesssim \chi_e(L,H) \lesssim 3.7 m^2/s, 200 \lesssim I \lesssim 350\,\mathrm{kA}, 2.8 \cdot 10^{19} \lesssim n_e \lesssim 11 \cdot 10^{19}\,\mathrm{m}^{-3}, 300 \lesssim T_e \lesssim 1100\,\mathrm{eV}, 1.3 \lesssim A_i \lesssim 2$. The χ_e for the discharge near the β limit described in Fig. 2 is above this scaling derived from discharges below the β limit.

4. CONCLUSIONS

In OH and L mode discharges the concept of "profile consistency" is supported by pellet injection and strongly varied deposition profiles, respectively. In H-mode discharges no consistent picture has evolved up to now. But also a dependence of χ_e on local parameters seems possible in both L and H mode. $D^0 \rightarrow D^+$ injection provides high confinement times with a scaling $\tau_E^* = 0.1 I A_i$[s, MA] for $q^*(a) > 3$ and with strong ion heating. At the β limit confinement degrades with increasing χ_e compared with χ_e below the β limit.

REFERENCES

[1] R. Hawryluk, in *Physics of Plasmas Close to Thermonuclear Conditions*, Vol. 1, Varenna (1979) (EUR-FU-BRU/XII/476/80).

[2] O. Gruber, Proc. Invited Papers, Int. Conf. on Plasma Physics, Lausanne (1984) Vol. 1, p. 67.

[3] F. Wagner, O. Gruber, K. Lackner et al, submitted to Phys.Rev.Letters.

[4] O. Gruber et al, this conference.

[5] M. Keilhacker et al, Plasma Phys. Contr. Fusion **28** (1986), 29

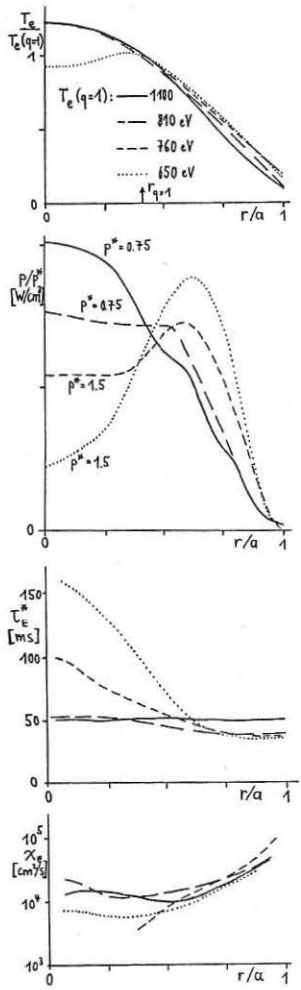

Fig. 1 Normalized T_e, heating power density p, energy confinement time τ_E^* and χ_e radial profiles of L-mode discharges with $q^*(a) = 2.6$.

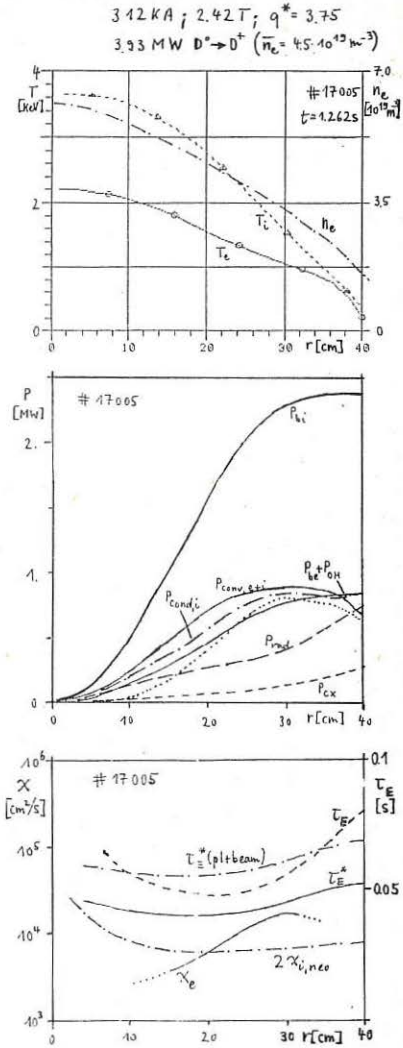

Fig. 2 Radial profiles of T_e, T_i and n_e, volume-integrated power balance, τ_E^* with and without beam contribution, $\tau_E = W_{pl}/(P_{cond}+P_{conv})$, χ_e and χ_i of H-mode discharge at the β limit ($\beta/\beta_c = 0.95$).

STABLE REGION OF FEEDBACK CONTROL IN TOKAMAK DEVICE

Z.Shen, S.Zheng, L.Wang

Institute of Physics, Chinese Academy of Sciences,
Beijing, China

Abstract: An experiment of feedback control has been conducted in CT-6B tokamak, on which the Ohmic heating and equilibrium field are controlled. A stable region of feedback control in the parametric space consisting of four feedback gain factors is found and compared with the prediction of a linear feedback theory. It is shown that the experimental stable region is less than that predicted by the theory.

Introduction: Feedback controls of the position of plasma column or/and other plasma parameters have been implemented on a number of tokamaks/1-7/. Classical or optimal control models applied on these control systems were formalized on the basis of a linearized treatment of the dynamic equations. To examine the linear control theory, an experiment has been conducted in CT-6B tokamak on which both the Ohmic heating and vertical field coils are controlled to maintain the plasma current and the plasma horizontal position at their desired values. The experimental results about stable regions are compared with the numerical results of a theoretical model.

Theoretical model: For reason of simplicity, we make the following assumptions: 1, The vertical displacement of plasma column is neglected. 2, The effect of the eddy current induced in conducting shell or vacuum chamber on the plasma is described by an equivalent electrical circuit equation, in which only dipole current component(cosine function distribution) is taken into account. 3, The iron-core transformer is regarded as a linear element.

The dynamics of the system can be formulated by using a equilibrium equation along with the circuit equations which

include the plasma channel(p), primary winding of transformer(t) vertical magnetic field coil(v) and conducting shell(s)

$$\frac{d}{dt}\left[L_p I_p - M_{pt} I_t - M_{pv} I_v - M_{ps} I_s\right] = -R_p I_p$$

$$\frac{d}{dt}\left[-M_{pt} I_p + L_t I_t - M_{tv} I_v - M_{ts} I_s\right] = U_t - R_t I_t - k_1 (I_p - I_{p0}) - k_2 (X - X_0)$$

$$\frac{d}{dt}\left[-M_{pv} I_p - M_{tv} I_t + L_v I_v - M_{vs} I_s\right] = U_v - R_v I_v + k_3 (I_p - I_{p0}) + k_4 (X - X_0)$$

$$\frac{d}{dt}\left[-M_{ps} I_p - M_{ts} I_t - M_{vs} I_v + L_s I_s\right] = -R_s I_s$$

$$F_x = 2\pi \times 10^{-7}\left(\ell_n \frac{R}{a_p} - 1.5 + \beta_l - \frac{l_i}{2}\right) I_p^2 - \left(\frac{\partial M_{pt}}{\partial X} I_t + \frac{\partial M_{pv}}{\partial X} I_v - \frac{\partial M_{ps}}{\partial X} I_s\right) I_p = 0$$

where $R = R_0 + X$ and k_i ($i=1,2,3,4$) are feedback gain factors; the desired equilibrium values are identified by the subscript "0"; F_x is the resultant force acting on the plasma column. If the deviations of the state variables from their equilibrium values, which are denoted by small letters, are much less than the equilibrium values, the above mentioned equation set can be linearized as the follows:

$$H_0(1,1)\frac{di_p}{dt} + H_0(1,2)\frac{di_v}{dt} + H_0(1,3)\frac{di_s}{dt} + H_0(1,4)\frac{dx}{dt} = \Delta_1 - k_1 i_p - k_2 x$$

$$H_0(2,1)\frac{di_p}{dt} + H_0(2,2)\frac{di_v}{dt} + H_0(2,3)\frac{di_s}{dt} + H_0(2,4)\frac{dx}{dt} = \Delta_2 - R_v i_v + k_3 i_p + k_4 x$$

$$H_0(3,1)\frac{di_p}{dt} + H_0(3,2)\frac{di_v}{dt} + H_0(3,3)\frac{di_s}{dt} + H_0(3,4)\frac{dx}{dt} = -R_s i_s$$

$$H_0(4,1)\frac{di_p}{dt} + H_0(4,2)\frac{di_v}{dt} + H_0(4,3)\frac{di_s}{dt} + H_0(4,4)\frac{dx}{dt} = \Delta_4$$

where the elements of matrix $H_0(i,j)$ and $\Delta_1, \Delta_2, \Delta_4$ can be represented through the equilibrium values of the state variables. The stability criterion of the system is that the real part of the solution of the equation

$$\begin{vmatrix} H_0(1,1)\omega + k_1 & H_0(1,2)\omega & H_0(1,3)\omega & H_0(1,4)\omega + k_2 \\ H_0(2,1)\omega - k_3 & H_0(2,2)\omega + R_v & H_0(2,3)\omega & H_0(2,4)\omega - k_4 \\ H_0(3,1)\omega & H_0(3,2)\omega & H_0(3,3)\omega + R_s & H_0(3,4)\omega \\ H_0(4,1) & H_0(4,2) & H_0(4,3) & H_0(4,4) \end{vmatrix} = 0$$

is less than zero. Therefore a feedback stable condition can be calculated for a set of plasma parameters and a stable region can be found in the parametric space consisting of four feedback gain factors k_i.

Experiment: CT-6B is a small conducting-shellless iron-core transformer tokamak. The main device and plasma parameters are: main radius R=45cm; radius of limiter a=12.5cm; toroidal field B_t=13kGs; skin time of vacuum chamber τ_v=0.3ms; plasma current I_p=30kA; electron temperature T_e=250ev; electron density n_e= (1-2)*$10^{13}cm^{-3}$. The plasma current and horizontal plasma displacement are measured by a Rogowskii coil and cosine wound coils respectively.

The feedback control is carried out by two analog power supply systems. The feedback control power supply for the heating field is a capacitor bank, which discharge current can be adjusted by a current controller consisting of a compensating regulator in parallel with a linear regulator. The maximum output current is 0.1-0.2 I_p/N, where N is the turn number of the primary winding of the transformer. The feedback control system for the vertical field consists of two group of feedback coils and a quick responce power supply. The power supply is a six-phase full wave rectifier, which output current can be regulated by a high power regulator. The system can generate 20% of needed vertical field for maintaining the plasma equilibrium. The two feedback systems, having 1ms responce time, are driven by the signals of plasma current and horizontal plasma displacement, which output are proportional to the deviations of the signals from desired equilibrium values taken at a given moment. Changing the weights of two input signals for the two feedback systems, the four gain factors can be chosen for the study of the stable region.

The stable and unstable experimental points are plotted in k_1-k_4 and k_3-k_4 planes respectively as shown in Fig.1 and Fig.2. The boundarys of the stable regions calculated theoretically are shown in the same diagrams. It is apparent that the stable region obtained in the experiment is less than the theoretical prediction. In the above mentioned formulation, some state variables are not taken into account, in which the interaction of the plasma with the limiter and its effect on the change in the plasma density would be the most important factor, which is hard to be described by a physical model.

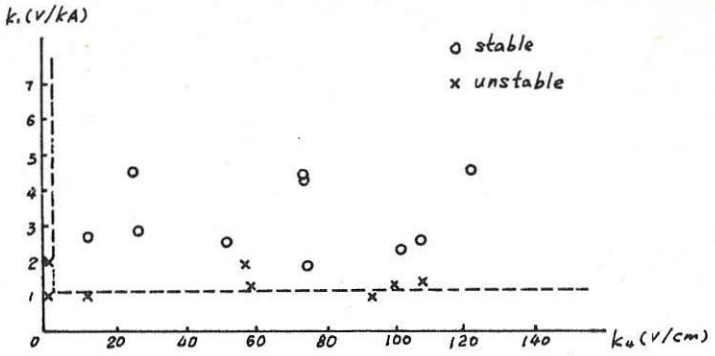

Fig.1 $k_2=0$, $k_3=23$V/kA case

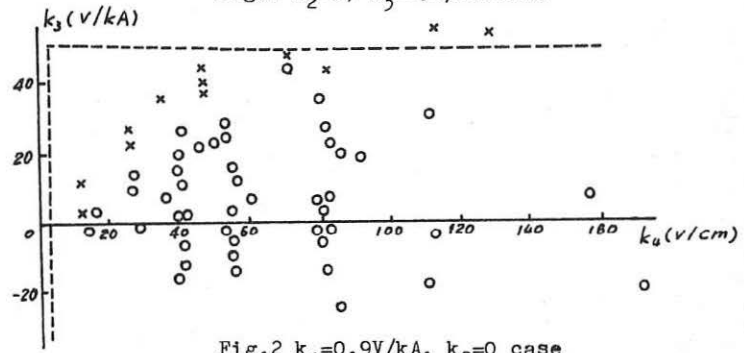

Fig.2 $k_1=0.9$V/kA, $k_2=0$ case

References:

/1/ J.Hugill, A.Gibson, Nucl. Fusion, 14(1974) 611.

/2/ M.Fujiwara et. al., IPPJ-T-22(1974).

/3/ J.L.Anderson et. al., Nucl. Fusion, 16(1976) 629.

/4/ J.Blum, Proc. 8-th Symp. Eng. Prob. Fusion Res., Vol.IV(1979) 1873.

/5/ Y.Matsuzaki et. al., ibed, 1899.

/6/ R.Gran et. al., Proc. 7-th Symp. Eng. Prob. Fusion Res., Vol.I(1977) 104.

/7/ D.B.Albert, IPP 111/61(1980).

THE TOKOLOSHE CURRENT-CARRYING LIMITER EXPERIMENT

D.E. Roberts, D.P. Coster, J.A.M. de Villiers, J.D. Fletcher,
P.B. Kotze, G. Nothnagel, J.R. O'Mahony and D. Sherwell

Plasma Physics Group
Atomic Energy Corporation of South Africa

INTRODUCTION

The present program of experiments and related theoretical studies on the low aspect ratio tokamak, "Tokoloshe", centres on the perturbation of $\simeq$100 kA reference plasmas by the current pulse in a single fully poloidal coil. Among the effects to be studied are:

(i) Changes in recycling of both fuel and impurity ions caused by strong radial field components near the coil. We remark that the perturbing field is never strong enough to give a separatrix of the toroidal field in the present work (Fig. 2(a)).

(ii) Magnetic island formation, particularly m/n = 1/1 and 2/1. Islands are induced by a simple poloidal current (Fig. 6) because of the very low aspect ratio of Tokoloshe.

The influence of (i) and (ii) on both internal and major disruptions is of particular interest.

Here we report preliminary experimental results and calculations for a perturbing coil within the fully poloidal limiter. (Poloidal Limiter Coil, PLC). Later, it is intended to install another coil external to the vacuum chamber and at a different toroidal location (Poloidal External Coil, PEC) in order to facilitate separation of effects (i) and (ii) (see Fig. 1).

EXPERIMENTAL RESULTS

Most experiments to date have been with limiter coil pulses of $\geqslant$10 ms duration starting at t = 15 ms with $B_{PLC}/B_{\phi} = \pm 0.085$. Characteristic field penetration time to the q = 2 surface ($r \simeq 17$ cm) and the q = 1 surface ($r \simeq 9$ cm) are $\simeq$2 ms and $\simeq$15 ms respectively.

With $B_{PLC}/B_{\phi} = 0.085$, the signal from a moveable Langmuir probe biased at -50 V located 40 mm in the toroidal direction from the limiter (Fig. 1) increases by 2 to 4x (Fig. 3) for $0.23 \leqslant r \leqslant 0.25$ m (the inside radius of the limiter and the wall radius are 0.24 m and 0.28 m respectively). This arises from inward radial displacements of field lines by $\lesssim 0.025$ m in the region of the limiter (Fig. 2(c) - calculations for a filamentary limiter current). There are little or no changes to the H_{α} and visible radiation signals or to the MHD activity, but the OVI 1032A intensity increases dramatically by up to $\simeq$100x (Fig. 3).

For $B_{PLC}/B_\phi = -0.085$ the Langmuir probe signal decreases in the vicinity of the limiter (Fig. 4). The H_α signal is found to decrease slightly but there is little effect on the OVI signal. If the H_α intensity is below a critical level at the time the limiter coil is switched on, a major disruption is always precipitated. This is apparently a result of the change in edge conditions rather than 2/1 island formation by the limiter coil since the observed 2/1 mode amplitude at coil switch-on time can vary over quite a large range without influencing the disruption. The latter proceeds in the normal way i.e. with a slowing down of the 2/1 mode, considerable growth of the island width which probably leads to 'short-circuiting' to the limiter (Fig. 5). When the limiter coil is switched on at 30 ms, at which time sawtoothing is visible as a modulation of the m = 2 mode, the modulation is clearly suppressed (Fig. 3). This again appears to be due to a change in edge conditions.

CALCULATIONS

Field line calculations were performed with the PLC field superimposed on the field approximating an ideal MHD equilibrium for Tokoloshe at t = 30 ms. For this case ($q_\psi(a) = 4.4$, $q(o) \simeq 0.7$) island formation is seen for B_{PLC} antiparallel to B_T and with axial $B_{PLC}/B_\phi \gtrsim 0.01$ (Fig. 6(b)). In particular m/n = 1/1 and 2/1 modes are excited, consistent with the results of a Fourier power spectrum of $B_\perp$ on the equilibrium magnetic surfaces. Large scale regions of stochasticity are seen near the limiter for $B_{PLC}/B_\phi \gtrsim 0.05$.

For B_{PLC} parallel to B_ϕ much weaker island formation is seen with the 1/1 island now on the inside of a poloidal cut at the limiter ($\phi = 0$) (Fig. 6(a)). The island formation in this case is a result of the strong outward displacement of the flux surfaces in Tokoloshe.

As a first step in interpretation of the effect of the poloidal current on existing tearing mode islands, calculations have also been performed with the limiter coil field ($B_{PLC}/B_\phi = -0.05$, Fig. 6(b)) superimposed on a quadrupole field ($B_{Quad}/B_\phi = 0.002$, Fig. 7(a)) orientated to produce islands shifted in θ with respect to the limiter coil islands (Fig. 7(b)). Here we see a distinct shift in θ of the resultant 1/1 island with respect to both the PLC and quadrupole 1/1 islands when these islands are of comparable size. Note that the quadrupole field imposed on a low aspect ratio machine creates an extensive stochastic region near the edge (Fig. 7(a)).

CONCLUSIONS

Preliminary experimental results have shown the PLC produces marked changes in edge conditions which can influence MHD behaviour. The calculations indicate that the formation of large islands can be expected. These should become more apparent after a planned increase of 2x in the amplitude/duration of the PLC, longer plasma current pulses and the addition of the PEC.

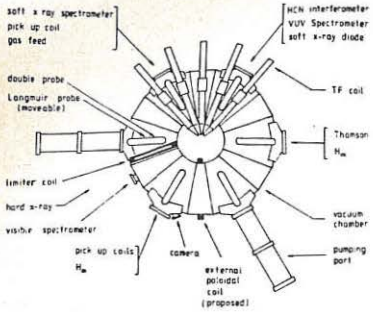

$R_o = 0,52m$
$a = 0,24m$
$B_\phi = 0,6T$

Fig. 1 Experimental Layout

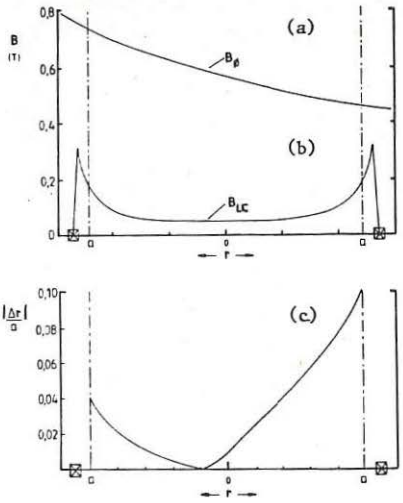

Fig. 2 B_ϕ, B_{PLC} and $|\Delta r|$ versus r, midplane, no plasma current. Here $\Delta r = r(\phi=0)-r(\phi=\pi)$ on a field line

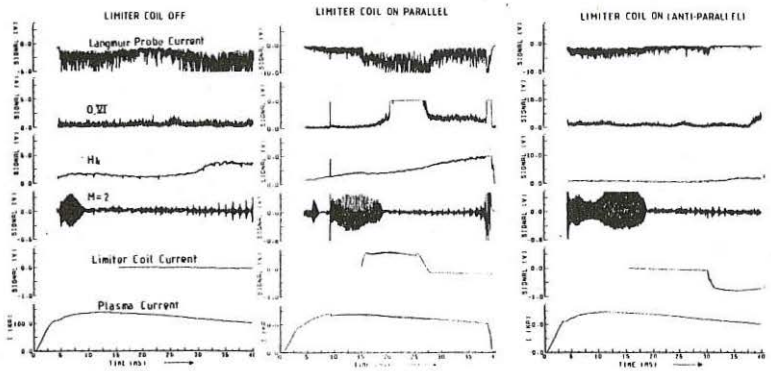

Fig. 3 Experimental results for $B_{PLC}/B_\phi = 0$ and ± 0.085

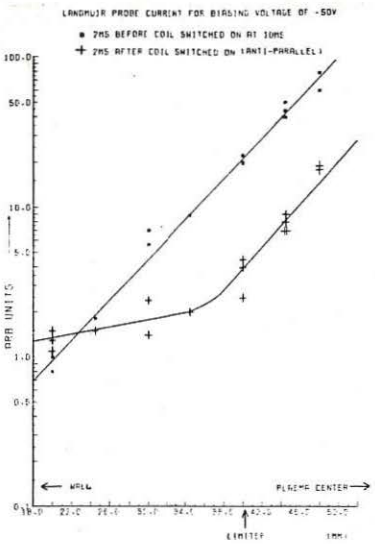

Fig. 4 Langmuir probe current vs minor radius for $B_{PLC}/B = -0,085$

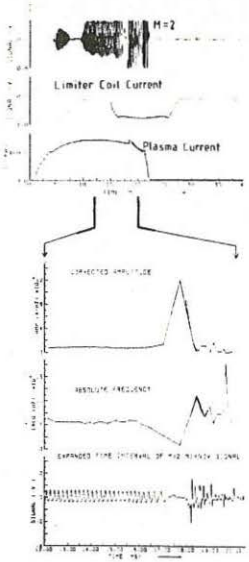

Fig. 5 Disruption caused by PLC

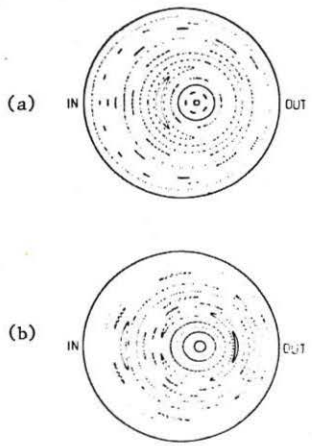

Fig. 6 Poincare plots of field lines at the limiter for a model equilibrium with q(a) = 4.4, q(o) = 0.7 and (a) B_{PLC}/B_ϕ = +0.05 (b) B_{PLC}/B_ϕ = -0.05

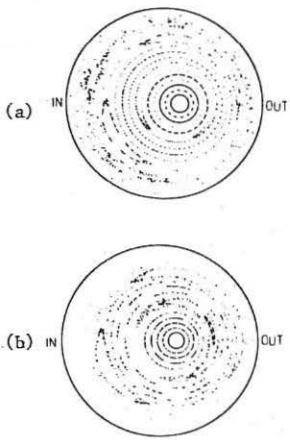

Fig. 7 Poincare plots for equilibrium field plus (a) quadrupole field with B_Q/B_ϕ = +0.002 and (b) Both Limiter field with B_{PLC}/B_ϕ = -0.05 and quadrupole field with B_Q/B_ϕ = +0.002

RESONANT HELICAL WINDINGS IN TOKAMAKS*

A.S.Fernandes[x], M.V.A.P.Heller, I.L.Caldas
Instituto de Física - Universidade de São Paulo
C.P. 20.516, 01498 - São Paulo, SP, Brazil

ABSTRACT: The Chirikov condition has been applied to estimate the helical winding current threshold for ergodization of the magnetic field lines in large aspect-ratio tokamaks. Overlapping of magnetic islands created by external windings and by a helical surface current on a rational magnetic surface has been considered. Toroidal corrections have been also considered.

We consider a large aspect-ratio tokamak with circular cross-section, represented by a periodical cylinder with length $2\pi R$, and assume the tokamak scaling $B_z/B_\theta \simeq R/a$, where a is the minor plasma radius. B_z is uniform and $\vec{j} = j_0(1 - r^2/a^2)^\gamma \hat{z}$, where j_0 and γ are constants.

The magnetic surfaces are given by

$$\vec{B} \cdot \nabla\psi = 0 \quad , \quad \psi = \psi_0 + \psi_1 \quad . \tag{1}$$

We consider $|\psi_1/\psi_0| \ll 1$ and the linear superposition of an unperturbed equilibrium described by $\psi_0(r)$ with a resonant helical perturbation described by $\psi_1(r,u)$, where $u=\theta - \alpha z$ and $\alpha = \frac{n}{mR}$. ψ_0 is given by

$$\psi_0 = \int_0^r dr' \, \frac{r'}{a} \left(nB_z - \frac{mR}{r'} B_\theta\right) \tag{2}$$

and

$$\psi_1 \simeq \frac{\mu_0 mRI}{\pi a} \left(\frac{r}{b}\right)^m \cos mu \tag{3}$$

or

$$\psi_1 \simeq \frac{\mu_0 J_0 R r_{m,n}}{2a} \left(\frac{r}{r_{m,n}}\right)^{\pm m} \cos mu \quad . \tag{4}$$

Eq. (3) corresponds to perturbations created by external currents I flowing (with opposite directions in adjacent conductors) in m pairs of helical windings, equally spaced, with radius b[1,2]. Eq. (4) corresponds to spontaneous tearing perturbations due to the resonant helical current sheet

$$\vec{J} = J_0 \, \delta(r - r_{m,n}) \cos mu \, (\hat{\theta} \cos\nu + \hat{z} \operatorname{sen}\nu), \tag{5}$$

where $\operatorname{cotg}\nu = \alpha r_{m,n}$. The resonant perturbations create m magnetic islands around the rational magnetic surface with $q(r_{m,n}) = m/n$.

We suppose that soft disruptions observed in tokamaks are caused by the superposition of magnetic islands created by different resonant fields. The helical winding current thresholds for ergodization of the magnetic field were estimated applying the Chirikov condition

$$\Delta_{m,n} + \Delta_{m',n'} > | r_{m,n} - r_{m',n'} |, \qquad (6)$$

where $\Delta_{m,n}$ is the island half-width. The condition (6) is satisfied for I greater than the values plotted in the Figs. (1) and (2) as a function of q(a). $\Delta_{m,n}$ was calculated in two different ways: taking into account the changes in ψ_0 and ψ_1 over the islands width and also neglecting these changes. All magnitudes were adjusted to fit TBR data[3] (a=8cm, b=11cm, R=30cm, $B_z \doteq 0,4T$) and the dependence of J_0 with q(a) is in agreement with the data reported in the Ref. (3).

On a large aspect-ratio tokamak the major effect of the coupling between helical field and the toroidal curvature is the appearance of $m' = m \pm 1$ magnetic islands on the rational surfaces with $q = m'/n$. The toroidal corrections were taken into account by multiplying the constant B_z by the factor $(1 + \frac{r}{R}\cos\theta)^{-1}$. Expanding the differential equations for the magnetic field lines in terms of the aspect ratio we obtained

$$\vec{B} \cdot \nabla\chi = 0 \quad , \quad \chi = \chi_0 + \chi_1 \qquad (7)$$

where

$$\chi_0 = \int_0^r dr' \, (\frac{r'}{a})^{m'-m} \, (nB_z - \frac{m'R}{r} B_\theta) \qquad (8)$$

and

$$\chi_1 = \frac{\mu_0 m I r^{m'}}{2\pi a^{m'-m} b^m} \cos m'u' \qquad (9)$$

for the winding perturbations and

$$\chi_1 = \frac{\mu_0 J_0 r^{m'}}{4a^{m'-m} r_{m,n}^{m-1}} \cos m'u' \qquad (10)$$

for the current sheet perturbations, where $u' = \theta - \frac{nz}{m'R}$.

χ was used in the same manner as the stream function ψ to calculate the width of m' magnetic islands at the q=m'/n surfaces. An example of winding currents required for ergodization, due to toroidal corrections, is plotted in the Fig. (3) as a function of q(a).

REFERENCES

(1) Pulsator Team, Nuclear Fusion 25, 1059 (1985).
(2) A.S.Fernandes, I.L.Caldas, Report IFUSP/P-539 (1985).
(3) I.H.Tan, I.L.Caldas, I.C.Nascimento, R.P. da Silva, E.K. Sanada, R.Bruha,

to be published in IEEE Trans. Plasma Science, June (1986).

ACKNOWLEDGEMENTS

One of the authors (I.L.C.) would like to thank Drs.F.Karger, K. Lackner, W.Feneberg and H.P. Zehrfeld for useful initial discussions.

* This work was partially supported by CNPq and CAPES.
+ On leave from Setor de Ciências Exatas, UFP, Curitiba, PR, Brazil.

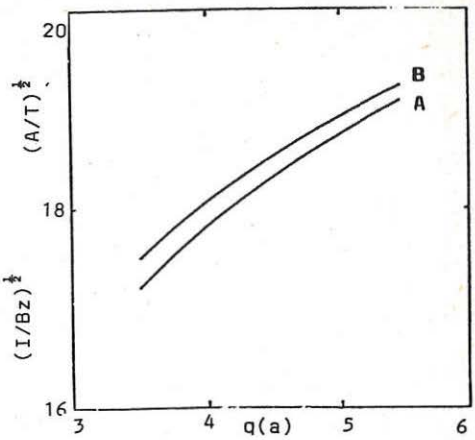

Fig.1- Helical current in two sets of helical windings for overlap of $m_1=2$ and $m_2=3$ resonances. The curves A and B were obtained neglecting and taking into account the r-dependence of Ψ over the island width[$q(0)=1, I_p=10$kA]

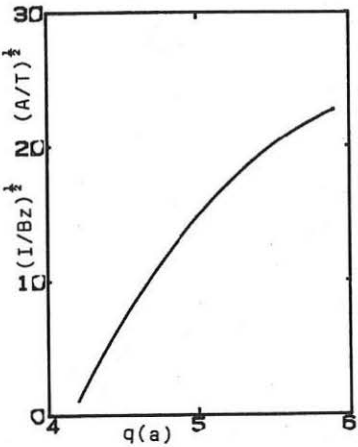

Fig.2- Helical winding current for overlap of m=3 induced islands and m=2 spontaneous islands observed in the tokamak TBR[13] [$q(0)=1$, $I_p=10$ kA, $n=1$]

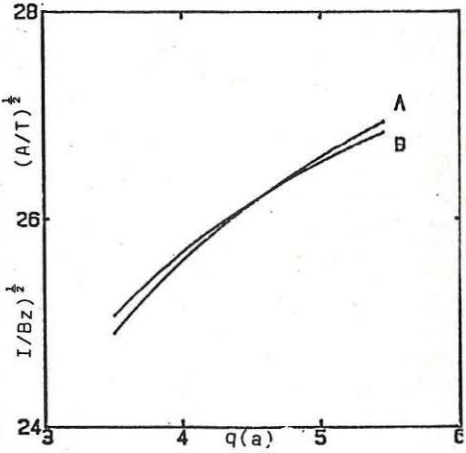

Fig.3- Helical winding current (m=2/n=1)for overlap of m=2 and m'=3 resonances due to toroidal corrections ($q(0)=1, I_p=10$ kA). The curves A and B were obtained neglecting and taking into account the r-dependence of χ over the island width.

EFFECTS OF MAJOR RADIUS COMPRESSION IN JET

A Tanga, N Gottardi, A Hubbard, E Lazzaro, P Noll,
E Springmann, A Taroni.

JET Joint Undertaking, Abingdon, Oxon, OX14 3EA

Introduction

Major radius compression in tokamaks is a tool for achieving high plasma pressure [1,2,3,4]. Its attractiveness depends also on the fact that the compression can be made "adiabatic" and then the plasma quantities are expected to change according to simple laws ([1]).

In JET the application of a fast increase of vertical field has produced a displacement of the plasma column in major radius with the toroidal field constant in time. Typically the time necessary to detach the plasma from the limiter, until it reaches the final state in the contact with the inner wall, was 0.15 → 0.2s while the global energy confinement time was 0.5 → 0.7s. Parameters of the discharges analysed are presented in table I. Since the vertical field is not completely decoupled from the plasma, the increase of the vertical field causes an increase of poloidal flux. When the plasma is compressed the increase of plasma current is due for one third to the effect of the compression and for the rest to the increase of poloidal flux. The situation is illustrated in the figures 1,2,3. Fig 1 shows the flux contour as obtained by the equilibrium code INDENT B ([5]) before the radial compression. Fig 2 shows an analogous plot for the plasma, 0.19s later after the compression. The plasma is in contact with the inner wall and the cross section is hardly changed. The expected result in an ideal adiabatic case starting from the configuration of Fig 1 is shown for comparision in Fig 3. Here the equilibrium configuration was calculated using the code ESCO ([6]). The fluxes on the vacuum vessel are the same as in Fig 2 but the q profile and the toroidal and poloidal fluxes inside the plasma have been conserved and the adiabatic constraints ([7]) have been verified. It is evident that a pure adiabatic compression would have produced a smaller plasma. Moreover the increase in plasma current would have been only ~ 110kA against the ~ 360kA observed experimentally. The variation of flux as given in the table is in agreement with the changes in plasma current and variation of inductances.

Changes in plasma parameters

In terms of other plasma parameters a noticeable increase of the peak and of the volume average electron temperature has been measured by electron cyclotron emission and it is shown in Fig 4. It should be noticed that the increase of the peak and average electron temperatures is more slow than the compression which takes place between t = 8 and t = 8.2 seconds.

Some enhancement of the sawteeth activity is also present. The time evolution of the ion temperature, as deduced from neutron emission is shown in Fig 5. In Fig 6 the radial profile of the electron density is shown as obtained by Abel inversion of the interferometer data. There is a noticeable peaking of the electron density profile subsequent the radial compression. It should be also mentioned that n_e scales approximately as C^2, C being the initial major radius divided by the final one, as it is expected from the adiabatic scaling. The total radiated powers as obtained by the integration of the multichord bolometer camera, during the compression shows only a small variation (in this case a reduction), compared to the global input power. This fact would suggest that the resistive losses are not substantially enhanced by the radial compression.

Conclusions:

According to the adiabatic laws the temperature should scale with the compression ratio to the 4/3. Thus one would have expected a 10% increase in Te and Ti while the experimental values are respectively an increase by 20% and 30% shown in Table 1. This is probably due to the appreciable ohmic contribution as it is shown by the analysis of the magnetic data. It is obviously difficult to quantify in detail the balance of the power fluxes in a transient, however the increase of both the ion and electron central temperature is much faster than the resistive skin time and may this suggest the presence of an anomalous penetration of the plasma current which may contribute to the increase of the plasma temperature. The elctron density scales in agreement with the adiabatic scalings. It should be stressed that, despite the elative changes in plasma parameters being small, there seems to be an enhancement in the thermal content of the discharge which seems to originate both from the flux variation and from the radial compression.

References

1) H P Furth and S Yoshikawa Phys of Fluids 13 2593 (1970)

2) V E Golant Plasma Physics and controlled Fusion 26 N° 1A, 77 (1984).

3) G Tait et al. in Plasma Physics and Controlled Nuclear Fusion Research London, Sep 12-19, 1984 (IAEA, Vienna, 1985) vol I, pp 141-154.

4) A Airoldi-Crescentini, G Grosso, G Lampis, L Lanzavecchia and E Lazzaro. Proc of the 2nd Joint Genoble-Varenna. Int. Symp. 1980 Vol II p 1059.

5) M Brusati et al. Comp. Phys. Rep 7-8, 345 (1984).

6) A Cenacchi, E Springmann, A Taroni to be published.

7) F L Hinton and R D Hazeltine Rev. of Mod. Phys. Vol. 48 N. 2 pp 305, 306. (1976)

TABLE I

	Ip	t	B_T	ϕ_T	ψ	q_b	Li
Before Compression	2.03	8.02	2.92	1.6	6.95	5.4	1.15
After Compression	2.39	8.19	2.92	1.8	7.34	5.6	1.09

Compression ratio C = 1.07

Adiabatic scalings(1)

$$T \rightarrow C^{4/3} = 1.09; \quad n \rightarrow C^2 = 1.15; \quad Ip \rightarrow C = 1.07$$

Experimental values

$$\frac{T_{e_2}}{T_{e_1}} = 1.20; \quad \frac{T_{i_2}}{T_{i_1}} = 1.30 \quad \frac{n_{e_2}}{n_{e_1}} = 1.16$$

B_T = Toroidal field in tesla

t = time in seconds

ϕ_T = toroidal flux

ψ = poloidal flux

$T_{i1(2)}$ = ion temperature before (after) the compression

Ip = plasma curretn (MA)

q_b = safety factor at plasma boundary

β_p = poloidal beta

li = internal inductance

$T_{e(2)}$ = electron temperature before (after) the compression

$n_{en(2)}$ = electron density before (after) the compression

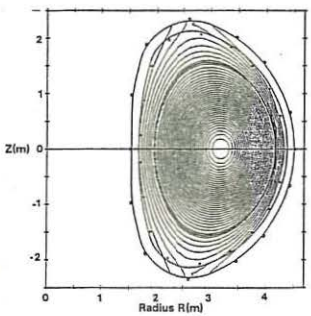

Fig 1

Poloidal flux contour of the plasma before the compression.

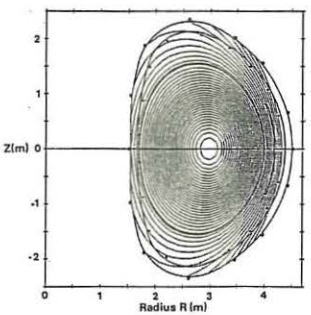

Fig 2

Poloidal flux contour of the plasma after the compression.

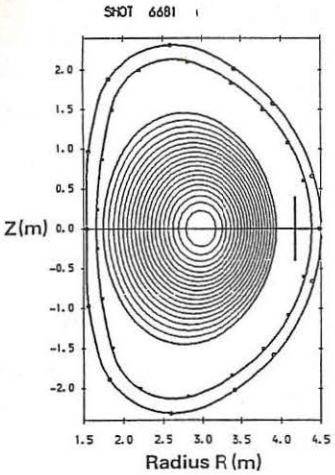

Fig 3

Poloidal flux contour of the plasma as it should have been if the compression were purely adiabatic.

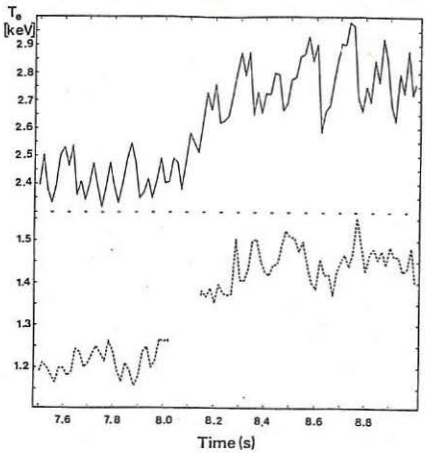

Fig 4

Time evolution of the peak electron temperature (top) and average electron temperature (bottom).

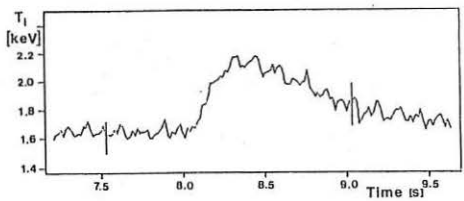

Fig 5

Time evolution of the peak ion temperature.

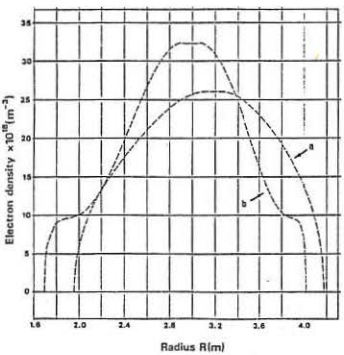

Fig 6

Electron density profile before compression (curve a) and after compression (curve b).

ANALYSIS OF CURRENT AND TEMPERATURE PROFILE FORMATION IN JET

D.J. Campbell, J.P. Christiansen, E. Lazzaro, A.W. Morris+, M.F.F. Nave, F.C. Schueller and P.R. Thomas

JET Joint Undertaking, Abingdon,Oxon, OX14 3EA, UK
+Balliol College, Oxford University

INTRODUCTION - The study of of current formation in a tokamak is important both at the practical operation level and at the fundamental level of identifying basic transport mechanisms and regimes. Here an analysis of observations on the formation of tokamak temperature and current profiles in JET is presented. The time evolution of these profiles has been studied for a large number of plasma discharges using the equilibrium identification codes IDENTC and FAST, and the ECE measurements of electron temperature profiles.

It is found that plasma resistivity is neoclassical during the current flat-top, from which we deduce that ECE temperature profile measurements are consistent with current profiles deduced independently from magnetic signals by the equilibrium codes. The effective resistivity is substantially higher than neoclassical during the initial stage of the current rise and, as a result, the current penetration occurs on a timescale which is much shorter than the neoclassical skin time. The penetration enhancement depends on the current and density ramp rates. Furthermore, during this early stage of the discharge substantial MHD activity is observed. The association between this activity and the process of current penetration has been investigated by analysing the path followed by typical discharges in the parameter plane (q_o, q_a), where q_a is the safety factor.

CURRENT PENETRATION BY RESISTIVE DIFFUSION

MAGNETIC ANALYSIS - The toroidal component of Ohm's law can be written

$$\eta_{eff} = E_\phi / J_\phi, \qquad (1)$$

where η_{eff} includes the resistive effects of any instabilities which may occur. For steady toroidal fields, this may be written

$$\eta_{eff} = \mu_o \frac{\partial \psi}{\partial t} \Big/ \left[R \frac{\partial}{\partial R} \frac{1}{R} \frac{\partial}{\partial R} + \frac{\partial^2}{\partial Z^2} \right] \psi. \qquad (2)$$

Equation (2) is solved for a time sequence of inverse Grad-Shafranov equilibria fulfilling Dirichlet boundary conditions plus an optimal fit of Neumann conditions [1] with current density profiles taken in the functional class:

$$J_\phi(R,\psi) = I_o \left[\alpha \, R/R_o (1-\psi+b(1-\psi)^2) + (1-\alpha) R_o/R (1-\psi+a(1-\psi)^2) \right], \qquad (3)$$

where a, b, α are the parameters to be determined. Once the calculation is validated by checks of compatibility with other diagnostics, the accuracy of the evaluation of q_o is of the order of 20% if the error in the data is 3%.

PLASMA RESISTIVITY - Profiles of plasma resistivity are derived from local parameters obtained by diagnostic measurements. The principal data are $T_e(r)$ from ECE [2], $n_e(r)$ from microwave or far-infrared interferometry, and Z_{eff} from visible Bremsstrahlung measurements. 'Spitzer' resistivity is calculated from

$$\eta_s = 1.034 \times 10^{-4} \, Z_{eff} \, \alpha(Z_{eff}) \, \ell n \, \Lambda / T_e^{3/2}, \qquad (4)$$

where T_e is in eV, and the neoclassical resistivity from

$$\eta^* = g \eta_s, \qquad (5)$$

where

$$g = \left(1 - f_T/(1+\xi\nu_*)\right)^{-1} \left(1 - C_R f_T/(1+\xi\nu_*)\right)^{-1}. \qquad (6)$$

Explicit forms of the coefficients $\alpha(Z_{eff})$, ξ, C_R, the electron trapping factor f_T, and the collisionality ν_* are given in [3]. The principal sources of error in these calculations arise from the measurement of $T_e(r)$ (±10%), and Z_{eff} (the profile is assumed to be flat).

RESULTS - The evolution of the principal parameters of a pulse selected for analysis is shown in figure 1. Figure 2 shows a comparison of radial profiles of η_{eff} (crosses), η_s (full line) and η^* (dashed line) at several times during the rise phase and flat top of this discharge. Once the plasma current has reached its equilibrium value, the profiles of resistivity derived from magnetic analysis and from temperature measurements are in very good agreement [4]. However, during the first 2s there are significant differences between the two, and particularly during the first 0.7s, where η_{eff} is significantly higher than η^*. Thus, the current penetration occurs more rapidly than can be explained by neoclassical resistivity, which leads to this enhancement in the calculated value of η_{eff} over η^*. This might be explained by magnetic relaxation, as discussed in the next section.

ROLE OF MHD INSTABILITIES IN CURRENT PENETRATION

TYPE OF INSTABILITIES PREDICTED FOR THE CURRENT RISE - to investigate the relationship between the observed MHD activity and the processes affecting current penetration, we have analysed the evolution of typical discharges in the parameter plane (q_o, q_a) [5]. By drawing the boundaries of various MHD instability regions, obtained from the model of [6], in this plane, it is possible to interpret the processes accompanying current penetration. Figure 3 shows a scatter plot of a sample of JET pulses in this plane. Several time points are included for each pulse. It is remarkable how few points lie centrally in the 'stable' region.

For clarity we discuss the trajectory of a particular pulse (2214) which, as shown in figure 4, passed through all regions of the plane. Identification of the times of interest which are labelled in the figure can be obtained from the plasma current trace in figure 1. Detailed magnetic equilibrium calculations show that the current profile initially exhibits a significant skin effect, and that it becomes gradually more peaked as the trajectory reaches the equilibrium state. It is also found that the trajectory reaches $q_o \sim 1$ at approximately the same time as sawteeth appear, and that it remains in this condition during a substantial period of the current decay. Thus, there is qualitative agreement between the form of the J (and q) profiles at various times and the region in which the trajectory lies.

This relationship between the J profiles and the regions of the (q_o, q_a) plane is further illustrated the two other cases shown in figure 4. These trajectories show very distinct patterns of evolution. Pulse 2442 starts in the $q_a < q_o$ sector and then remains entirely in the 'kink' sector before disrupting during the flat top. Its current density profile starts hollow and peaks 3s after breakdown, the trajectory then being in the 'kink' region. This is in contrast to pulse 2214 which has a similar slow rise, but enters the 'kink' region earlier and also becomes fully peaked earlier (after 2s), terminating within the 'tearing-internal' band. The third example (shot 2044) is rather unusual, but interesting, because it always has a peaked current profile and, as expected, it crosses only the 'tearing' region.

CURRENT REDISTRIBUTION BY MAGNETIC RELAXATION - The trajectories described here show a significant correlation with the spectra of MHD activity observed. Figure 5 shows the magnetic activity signal for pulse 2442 plotted as a function of the safety factor, q_a. Investigation over many pulses during the current rise shows that trajectories lying in the 'double-tearing'/'kink' regions exhibit MHD actvity spectra of this form,

i.e. with distinct peaks close to rational values of q_a, that is $q_a = m/n$ with n = 1 or, sometimes, n = 2. Evidence for the redistribution of J for pulses such as 2442 is shown in the plot of ℓi versus q_a (fig.6). This is further supported by observation of negative spikes in dI/dt. Trajectories which have crossed into the 'tearing' region have MHD spectra which are generally less structured with peaks of the signal often uncorrelated to integral values of q_a. The same is true for the evolution of ℓi.

CONCLUSIONS - The evolution of current and temperature profiles in JET may be understood in terms of the trajectory of the discharge in the (q_o, q_a) plane. It is found that the plasma evolves through regions in this plane which are predicted to be MHD unstable. While substantial MHD activity is observed, which is correlated with rapid current penetration, the occurrence of MHD instabilities generally has no deleterious effect on the flat-top performance. As the MHD activity decays, current penetration approaches the neoclassical value, and becomes neoclassical as the current plateau value is reached. Generally the plasma current flat-top is reached with $q_o \sim 1$, and this state is maintained into the decay phase.

REFERENCES

[1] J. Blum, B Thooris and J. Le Foll, JET Contract 9008.
[2] A.E. Costley et al. in Controlled Fusion and Plasma Physics (Proc. 12th Europ Conf., Budapest, 1985), 9F-I, 227 (1985).
[3] S.P. Hirschman and D.J. Sigmar, Nucl. Fus. 9, 1077 (1981)
[4] J.P. Christiansen, et al., in Controlled Fusion and Plasma Physics (Proc. 12th Europ Conf. Budapest, 1985) 9F-I 327 (1985)
[5] E. Lazzaro and M.F. Nave, JET-DN-T(85)24.
[6] J.A. Wesson, Nucl. Fus. 18 87 (1978)

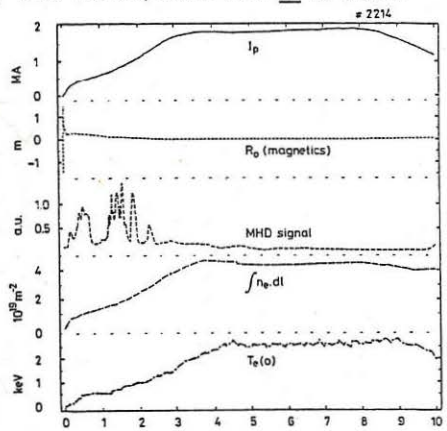

Figure 1 Evolution of several principal parameters during a JET pulse: plasma current, I ; magnetic axis, R_o; MHD activity signal; line integral of density, $\int n_e dl$; central electron temperature, $T_e(o)$.

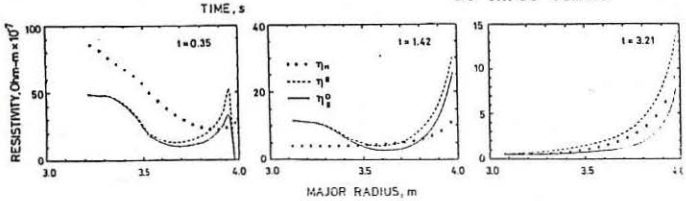

Figure 2 Comparison of radial profiles of η_{eff} (effective resistivity), η^* (neoclassical resistivity) and η_s (Spitzer resistivity) at three times.

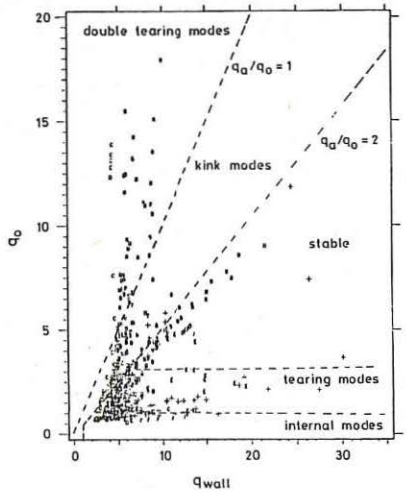

Figure 3 Scatter plot of JET pulses in the plane (q_o, q_a). The stability boundaries for various forms of MHD activity (derived from [6]) are superposed.

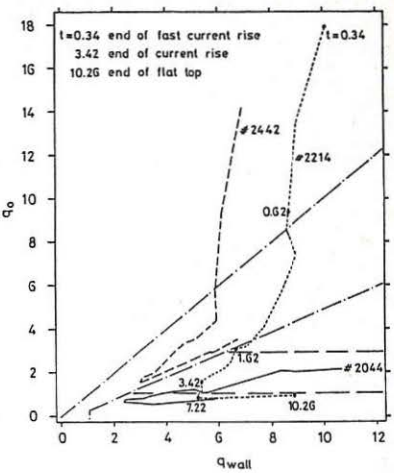

Figure 4 Trajectories of 3 JET pulses during their evolution and decay.

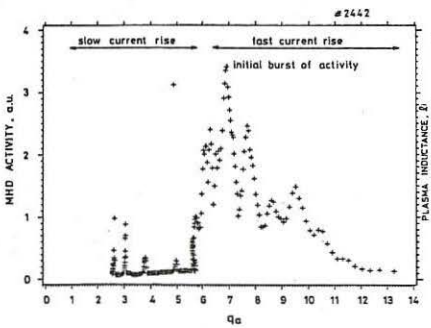

Figure 5 MHD activity signal for pulse 2442, plotted as a function of q_a.

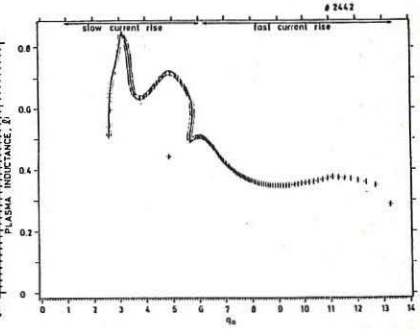

Figure 6 Internal inductance ℓi versus q_a for #2442.

RUNAWAY ELECTRON CONFINEMENT STUDIES IN THE TJ-I TOKAMAK

L. Rodriguez, A.P. Navarro and TJ-I Group

Division de Fusion, JEN, 28040 Madrid, Spain

INTRODUCTION

Runaway electron study is an important topic not only because of their potential deleterious effects on any device but for the possibility to use them as a heating method (1) or to stabilize heliacs, as the proposed TJ-II by JEN, in achieving the second stability regime (2).

On the small tokamak TJ-I (Ro=.3 m, a=.1 m, b=.12 m, B< 1.8 T, $I_p \leq$ 80KA), runaway electron behaviour has been studied using a collimated scintillation detector (3 cm ϕ, INa(TL)) by measuring the energy distribution of the photons due to runaway electron bremsstrahlung. The typical experimental setup was modified so pulses could be temporaly resolved and up to four different spectra accumulated during the TJ-I discharge so runaways could be studied during the build-up, plateau and rundown of the discharge. The system was calibrated using a Cs^{137} source resulting 10 KeV/ch and, previously to the measurements, the angular distribution of the radiation was determined to optimize the detector position to get the maximum count rate, obtaining R $\sim 10^4$ c/s for a midplane position 20° out of the perpendicular.

THEORY

For spectrum interpretation a model, assuming only the toroidal component of the electron velocity and including relativistic effects, has been developed. Solving, for the tail of the assumed maxwellian distribution of thermal electrons in the plasma, numerically the equation:

$$d(\gamma m_e V)/dt = -\left\{(\Lambda n_e / V^3 m_e)(\gamma + 1/\gamma) + (\Lambda n_i / V^3 m_i)((m_i \gamma / m_e) + 1)\right\} . V - eE(t)$$

where $\Lambda = e^4 n_e \ln\Lambda / 4\pi\varepsilon_o^2$, $\gamma = (1 - v^2/c^2)^{-1/2}$, $n_{e(i)}$ is the electron (ion) density, $m_{e(i)}$ is the electron (ion) mass, v the toroidal velocity of the electrons and E(t) the applied electric field, it is possible to deduce the energy distribution of the runaway electrons. Figure 1 shows the two extreme cases: gaussian when the confinement time (τ_R) is shorter than the thermal equilibration time (τ_{eq}) and "slide-away" for $\tau_R \gg \tau_{eq}$. Because of the photon energies in TJ-I are always moderate, below 500 KeV, the thin target approach can be assumed for the runaway electron interactions in the simulation of the hard-X-ray spectra for the above mentioned distributions. Figure 2 shows the simulation result for a slide-away distribution. No clear differences appear for the spectrum of a gaussian distribution, only different slope as it is shown at figure 3 where the assumed τ_R in the simulation is plotted vs. the inverse of the slope of the obtained

spectrum. In order to determine the type of distribution the deduced must be compared with τ_{eq}, that can be estimated from (3):

$$\tau_{eq} = \left(\frac{m^{1/2}}{J\pi\sqrt{2}e^4}\right)(Te^{3/2}/n_i)$$

that for TJ-I plasmas is in the order of 40 μs.

EXPERIMENTAL RESULTS

On the TJ-I tokamak runaway confinement time and density (n_R) have been measured for different operational conditions: I_p scan (from 20 to 60 KA) and B_T scan (from 0.7 T to 1.5 T). Figure 4 presents the measured photon spectra for the different times along the discharge in one of these series (44 KA, 1T). The results from the hard-X-ray spectrum analysis using the above mentioned model are sumarized in Table I.

B_T (T)	I_p (KA)	time interval (ms) 2-6	6-10	10-14	14-18	
1	20	.7 1.8	.8 3.2	.6 4.0	- -	τ_R (ms) n_R (x10^{11} cm^{-3})
1	44	.5 0.7	.5 5.5	.6 3.9	.5 7.7	τ_R n_R
1	58	1.4** 0.2	.7 1.8	.6 3.2	.4 32	τ_R n_R
0.7	36	.6 1.1	.8* 1.2	.7 3.0	.6 1.8	τ_R n_R
1.5	44	- -	- -	.6 1.8	.65 3.5	τ_R n_R
$\Delta\tau_R = 0.2 \times \tau_R$, $*\Delta\tau_R = 0.3 \times \tau_R$ $\Delta n_R = 2. \times n_R$, $**\Delta\tau_R = 0.5 \times \tau_R$						

TABLE I.

τ_R is obtained from the spectrum slope using the dependence shown at figure 3. n_R is deduced from the total measured spectrum area, the geometrical parameters of the detection set-up and the measured angular distribution of the radiation.

From these results it follows that τ_R is almost constant along the discharge and its value is similar to τ_p, particle confinement time, in TJ-I and that n_R increases along the shot. B_T scan shows no τ_R dependence on B_T and a systematic decrease of n_R when B_T increases. Similarly, I_p scan shows no τ_R dependence on I_p; only high I_p produces better confinement

during the initial build up of the plasma but, after a systematic appearance of fluctuations in the total flux of hard-X-rays, as shown in figure 5, the confinement lowers to the values of smaller I_p, n_R decreases when I_p increases.

Hard-X-ray fluctuations have been found in almost any discharge. These fluctuations are accompanied by spikes in the loop voltage and precede the appearance of MHD activity in the discharge, and they seem to follow Parail's model (4). In an attempt to characterize them, a camac controlled digitizing system, with sampling frequency up to 500 KHz, was used to store hard-X-ray and other plasma signals ($\tilde{B}_\theta$, $\tilde{n}_e$, $\tilde{\varphi}_p$, etc) as shown at figure 5. From Fourier analysis of these data a dominant frequency around 10 KHz was obtained for the runaway fluctuation and no clear correlation with the other magnitudes.

SUMMARY

Runaway electron confinement time in TJ-I seems to be independent of I_p and B_T and when, in plasma build up, higher τ_R appears it returns to the normal value following a sudden appearance of hard-X-ray fluctuations. Runaway density decreases when B_T or I_p increases.

REFERENCES

(1) G.C. Goldenbaum, et al. Phys. Rev. Letters, 32 ,830 (1979)

(2) Miller, R.L., Bull. Am. Phys. Soc. 30 ,1574 (1985)

(3) Trubnikob, "Particle interaction in fully ionized plasmas", Rev. Plasma Phys. I, 105 (1965).

(4) Parail, V.V., Pogutse, O.P., Nucl. Fusion, 18 , 303 (1978).

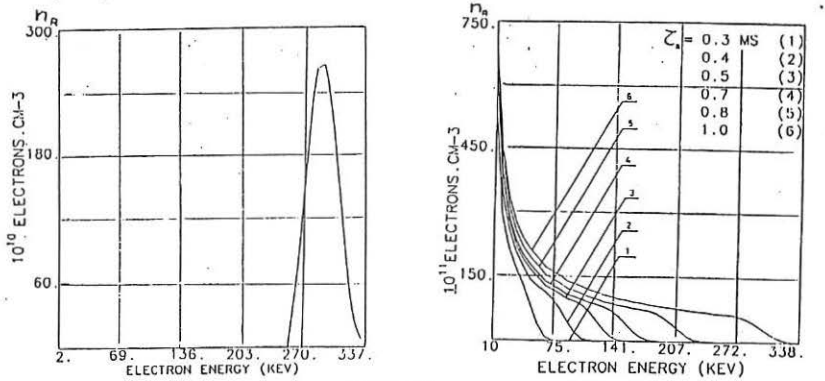

Figure 1.
a) Gaussian Distribution ($\tau_R < \tau_{eq}$) - b) Slide-away distributions ($\tau_R \gg \tau_{eq}$) for $\tau_{eq} = 40\ \mu s$

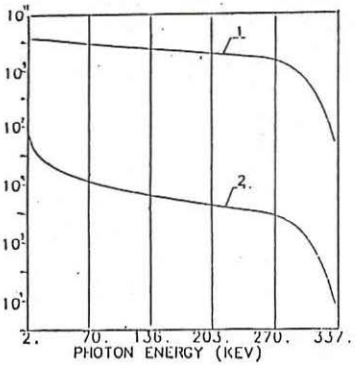

Figure 2
Simulated spectra (intensity (1), photon (2)) for a gaussian distribution

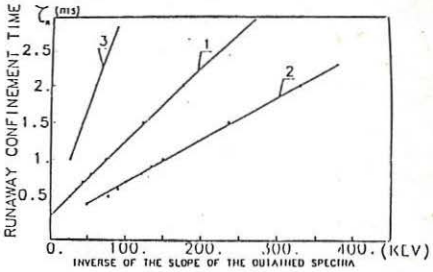

Figure 3
Runaway confinement time for
1- Slide-away distribution (4V)
2- Gaussian distribution (4V)
3- Slide away distribution (2V)

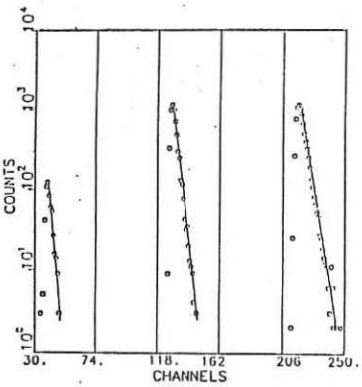

Figure 4
Photon spectra along the discharge for I_p=44kA and B_T=1T

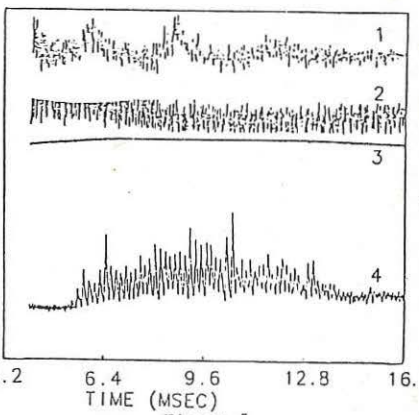

Figure 5
Plasma signals stored in a camac controlled digitizing system ($\bar{\varphi}_p$ (1), B_θ (2), I_p(3), HXR(4))

TURBULENT HEATING OF THE TORTUR TOKAMAK BY FAST CURRENT PULSES

TORTUR TEAM: N.J. Lopes Cardozo, C.J. Barth, B. de Groot, H.A. van der Laan, H.J. van der Meiden, W. van Toledo, W.A. de Zeeuw, H. de Kluiver.

Association Euratom-FOM,
FOM-Instituut voor Plasmafysica, Rijnhuizen, Nieuwegein, The Netherlands

In the TORTUR tokamak ($R = 0.46$ m; $a = 0.085$ m; $B_{max} = 3.0$ T) turbulent heating effects, due to fast (10 μs) toroidal current pulses from a high voltage bank superimposed on the plateau current, have been investigated. The additional heating across the column could also be used to determine the thermal diffusivity χ_e as a function of r.

Evolutions of various plasma parameters are shown in Fig. 1. During stage I the electrons are rapidly heated, presumably due to ion-acoustic turbulence invoked by the large current increment. This is due to the discharge of capacitor C_1 (1 mF; 5000 V) coupled to the 0.25 Vs iron core transformer. $\dot{I} \approx 3\times10^7$ A/s; $E_{tor} \leq 25$ V/m. $E_{tor}/E_{RA} > 0.1$; $(\omega_{ce}/\omega_{pe})^2 = 4$. ($E_{RA}$ is the runaway field strength.) Then current-driven ion-acoustic turbulence can occur [1,2,3].

A plateau state (II in Fig. 1a) is maintained up to 40 ms. (Bank $C_2 = 0.4$ F; 500 V; $I_p \leq 60$ kA.) Maximum β-values are near Troyon's limit. Density and temperature profiles are rather broad. Now the turbulent heating due to the fast current pulses (III in Fig. 1a and the following) is discussed. Bank C_3 (25 μF, 50 kV) is connected to a copper shell. A thin liner (0.15 mm) ensures fast field penetration (< 1 μs). Pulse parameters are: $\tau_{rise} = 5$ μs; $E_{tor} \leq 1$ kV/m; $\Delta I_p \leq 60$ kA; $E/E_{RA} \leq 40$. Then, (probe measurements [4,5]) strong dissipation occurs initially in a skin-current region, of about 2 cm. Conductivity is strongly reduced typically: $\sigma/\sigma_{Cl} \approx 2.4\times10^{-3}$. Dissipation is probably due to scattering of unstable electrostatic ion-cyclotron and ion-acoustic modes, together with the scattering interactions of tail-accelerated electrons ($v \gg v_{th}$) with bulk plasma modes via the anomalous Doppler effect [6]. On a log-time scale Figs. 2e and 2f show the tail temperatures and partial densities of non-thermal electrons near the skin as derived from accurate 90°-Thomson scattering. Increase in T_e is found near the axis, together with density increase ($\Delta n/n \approx 20\%$) already during the pulse. (Retardation < 4 μs.)

Our explanation is the collapse of the unstable skin-current profile which leads to current transport to the centre and plasma heating by adiabatic compression and wave transport [3]. In the following decompression the temperature and density increases are apparently lost, especially near the edge ($\Delta t \approx 10$ μs). These losses are small (< 30%) compared to the dissipated energy. The bulk is thought to be stored as extra poloidal magnetic energy of the peaked-up current profile which remains after the implosion and removal of the current pulse. During this removal, again, a skin region is formed, even with local current reversal [4]. In Figs. 1d and 2a, T_e and T_i increase again, reaching real thermal maxima in about $\Delta t \approx 2$ ms, followed by a characteristic decay time from which $\tau_\varepsilon \approx 2$ ms is obtained, comparable with τ_ε of the stationary fase. Evolution of the plasma kinetic energy is modelled by

$$\frac{dW_k}{dt} + \frac{W_k}{\tau_\varepsilon} = \int_0^t I_p \Delta V_\ell e^{-t'/\tau_\varepsilon}\, dt' + \frac{\Delta W_p}{\tau_M} e^{-t/\tau_M} - \frac{\partial W_B}{\partial t} ,$$

W_k is the energy of the plasma ($\int 3/2\, n_e k(T_e+T_i)dV_p$; τ_M the relaxation time of the distorted magnetic profile; ΔW_p the energy dissipation of the high-voltage pulse; V_p the plasma volume; $\partial W_B/\partial t$ the power losses to the wall (about 2× bolometer values). Best fit (Fig. 3) is for $\tau_M \approx 1$ ms and $\tau_\varepsilon \approx 2$ ms (is very reasonable in view of $\Delta L/\Delta R_p$, changed self-inductance/changed plasma resistance).

Fig. 4 shows the density fluctuation spectrum during plateau (stage II), obtained from scattering of 4-mm waves at r = 65 mm under 90° [7]. Waves between 20-700 kHz can be interpreted as unstable electrostatic drift waves in a tokamak [8]. Real frequencies are around electron-drift frequency: $\omega^*_e/2\pi$. Periodic growth and quenching (≈ 0.6-1.5 kHz) are close to 0.01 ω^*_e, the expected growth rates [8]. Similar modulations are found in V_ℓ, the ECE-spectra and the in periodic formation of non-thermal tails in $F(v_\perp)$. Amplitude modulations with comparable periodic times are also found for waves of 1-3 MHz and 10-50 MHz (Fig. 5d,f). The first is tentatively connected to magnetic (Alfvén and magnetosonic) waves. On the Thomson spectra satellites are found near the Alfvén speed. Their amplitudes δ show a similar time behaviour (Fig. 5e). The highest frequency regions (Fig. 5f) could be the density-gradient type of current-driven instabilities due to formation of runaway electron tails near 100 keV (occasionally confirmed by X-ray and ECE spectra [3]). Because all regions show about the same period, a coupling is suspected, made plausible by the estimation of about the same $k_\parallel$-values and growth maxima ($k_\perp \rho_i \approx 0.2$) for all regions.

The fast - and different - variations of fluctuation spectra, X-rays, etc., will be discussed now. In the first 5 μs of the compression period after starting the pulse, strong current-driven fluctuations enhance the spectra first near 10-100 MHz, followed by the 1-3 MHz Alfvén wave region (see also X-ray burst: runaways seem to be lost to the wall, Fig. 6). While these spectral regions are totally quenched, the drift waves are strongly growing to a maximum in about 200 μs, and then decline to the plateau values. This growth occurs in the relaxation period of the current profile. During the decrease of the 20-700 kHz waves the non-thermal (runaway) tails are formed again and the 1-3 MHz and 10-20 MHz regions are growing in intensity. (See also Thomson-scattering satellites in Fig. 5e).

The radial temperature increment due to the turbulent heating pulse, as obtained from ECE-spectra, and the subsequent decrease in time can be used to deduce $\chi_e(r)$. For $r \leq 40$ mm the decay time is independent of r, only determined by τ_ε. Thus the diffusion equation could be separated into space and time. Near the axis $\chi_e = 0.6$ m²/s, slowly increasing towards the outside ($n_e(o) = 6\times10^{19}$ m^{-3}). Carerras-Diamond's model for the resistive ballooning modes results in $\chi_e = 0.5$ m²/sec [9].

Acknowledgement This work was performed under the Euratom-FOM association agreement with financial support from ZWO and Euratom.

References

[1] E.D. Volkov et al., "Collective phenomena in current-carrying plasmas"; Kiev: Naukova Dumka 1978. English version: Gordon and Breach Comp. 1985.
[2] H. de Kluiver et al., Phys. Lett 94A (1983) 156.
[3] N.J. Lopes Cardozo, Rijnhuizen Report 85-160 (1985).
[4] H.W. Kalfsbeek, Rijnhuizen Report 78-114 (1978).

[5] Y. Nishida et al., Phys. Rev. Lett. 38 (1977) 653.
[6] B.B. Kadomtsev et al., Sov. Phys.-JETP (Engl. transl.) 26 (1968) 1146.
[7] F. Huussen et al., Plasma Physics and Contr. Fusion 27 (447) 1985.
[8] M. Venema et al., Rijnhuizen Report 84-152 (1984).
[9] B.A. Carreras et al., Phys. Rev. Lett. 50 (1983) 503.

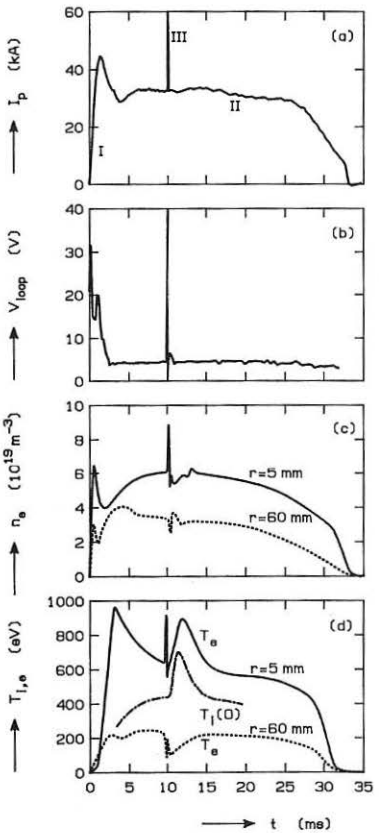

Fig. 1.
Time development of I_p, V_{loop}, n_e and $T_{e,i}$.

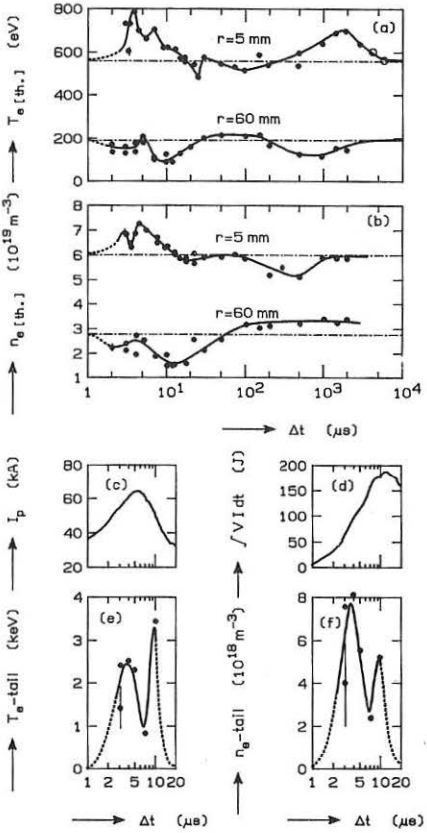

Fig. 2.
Evolution on log-time scale in μs after the current pulse: T_e, n_e, I_p, the pulse energy (a,b,c,d) and T_e, n_e of the non-thermal tail (e,f).

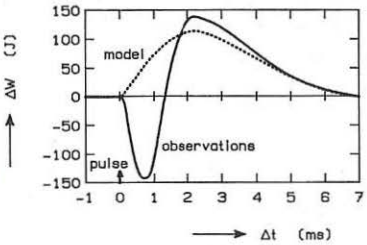

Fig. 3. The increase of W_K with respect to the basic level of 375 J.

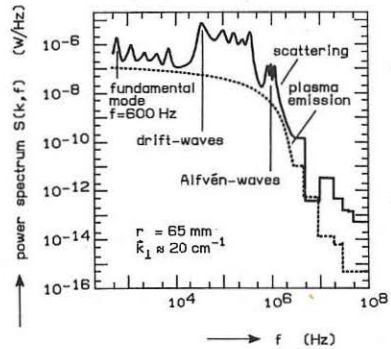

Fig. 4. Power spectrum of density fluctuations.

Fig. 5. Evolution of different plasma parameters: $T_{e,i}$(a); $\tilde{n}$(b,d,f); P_{rad} (c) and amplitude δ of satellites on Thomson spectra (e).

Fig. 6. Fast increase of hard X-rays and 1-2 MHz waves after the current pulse.

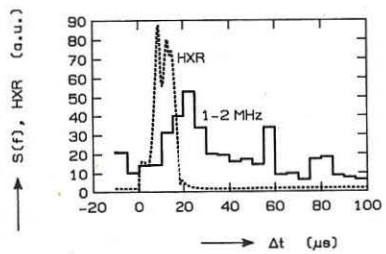

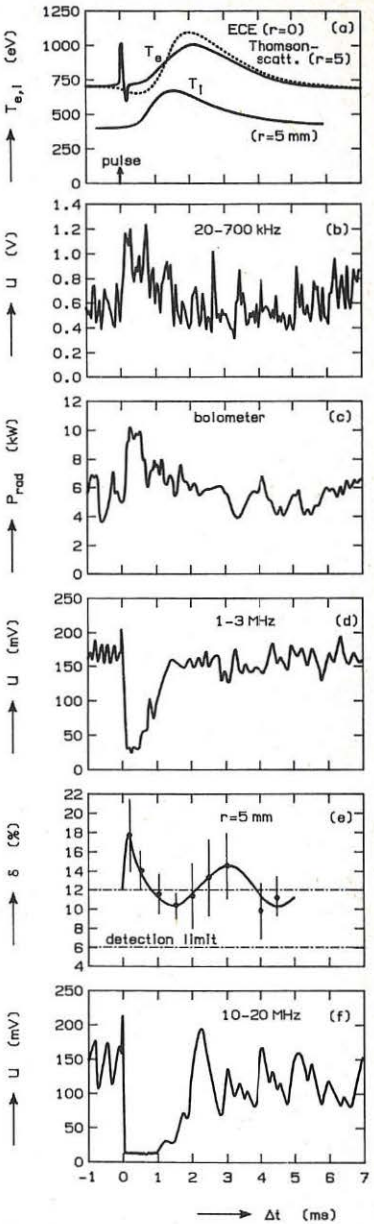

Stellarators

Finite β and Vacuum Field Studies for the Helias Stellarator

P. MERKEL, J. NÜHRENBERG, R. ZILLE
Max-Planck-Institut für Plasmaphysik
IPP-EURATOM Association
D-8046 Garching bei München

The achievement of magnetohydrodynamically stable stellarators with medium $\langle\beta\rangle$ values ($\gtrsim 0.05$) at medium aspect ratio $A(10 \lesssim A \lesssim 20)$ is a major challenge to stellarator research. In continuation of earlier configuration studies [1] a class of $\ell = 0, 1, 2, 3$ stellarators is described which is called Helias [2] because it combines features of W VII-AS and Heliac. It comprises stellarators with $A = 12$ which are stable to Mercier, resistive interchange, and ballooning modes at $\langle\beta\rangle = 0.05$ as is discussed below. In addition, Helias vacuum field studies are presented.

The geometry of Helias equilibria is given by their aspect ratio A, number of periods N, and 8 parameters which define the shape of the plasma boundary as

$$\begin{aligned} R =& A + R_{0,1}\cos V + (1 - \Delta_{1,0} - \Delta_0 \cos V)\cos U + \Delta_{2,0}\cos 2U \\ & - \Delta_{1,-1}\cos(U - V) + \Delta_{2,-1}\cos(2U - V) + \Delta_{2,-2}\cos(2U - 2V) \\ Z =& \quad Z_{0,1}\sin V + (1 + \Delta_{1,0} - \Delta_0 \cos V)\sin U + \Delta_{2,0}\sin 2U \\ & + \Delta_{1,-1}\sin(U - V) + \Delta_{2,-1}\sin(2U - V) - \Delta_{2,-2}\sin(2U - 2V) \end{aligned}$$

Here, R, Z, ϕ ($V = \phi N$) are cylindrical coordinates; U is the poloidal parametrization. Thus, $R_{0,1}$ and $Z_{0,1}$ define the radial and vertical displacements of the plasma column, i.e. the $\ell = 1$ content, Δ_0 the $\ell = 0$ content, $\Delta_{1,0}$ the $\ell = 2$ axisymmetric content, $\Delta_{1,-1}$ the $\ell = 2$ stellarator content (elliptical cross-section turning 180^0 per field period), $\Delta_{2,-2}$ the $\ell = 3$ stellarator content (triangular cross-section turning 240^0 per field period), $\Delta_{2,0}$ and $\Delta_{2,-1}$ the indentation.

Figures 1 and 2 show a Helias equilibrium with the above parameters given in the caption.

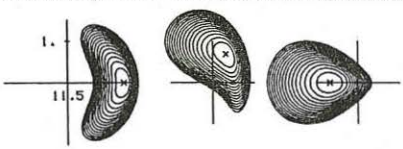

Fig.1: Flux surface cross-sections at $V = 0, \frac{\pi}{2}, \pi$ of a Helias equilibrium obtained with the BETA code [3] with $N = 5$, $A = 11.5$, $R_{0,1} = 0.8$, $Z_{0,1} = 0.4$, $\Delta_{1,0} = 0.1$, $\Delta_0 = 0.07$, $\Delta_{2,0} = 0.05$, $\Delta_{1,-1} = 0.29$, $\Delta_{2,-1} = 0.24$, $\Delta_{2,-2} = 0.07$. $\langle\beta\rangle = 0.05$. The pressure profile is characterized by $p = p_0(1 - s)$.

The equilibrium shown has no net toroidal current (more precisely, $J(s) \equiv 0$, where J is the toroidal current and s the flux label), $\langle\beta\rangle = 0.05$ with a parabolic (in radius) pressure profile so that the peak β-value is 0.1, and a finite-β well depth of about 0.09. The twist per period ι_P lies in the range $0.1 < \iota_P < 0.14$ so that low-order rational values of the

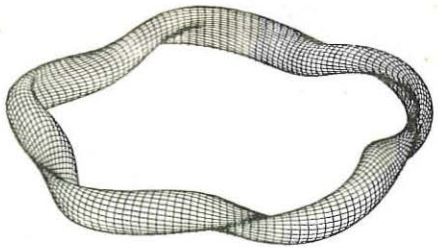

Fig.2: Perspective view of the Helias plasma boundary.

twist per period are avoided (only $\iota_P = \frac{1}{9}$ and $\frac{1}{8}$ are crossed), on the one hand, and the lowest-order rational values of ι_T $\frac{1}{2}$ and 1 are avoided as well, $0.5 < \iota_T < 0.7$. The parallel current density is strongly reduced as compared with an $\ell = 2$ stellarator, as evidenced by $\langle j_\parallel^2 / j_\perp^2 \rangle \lesssim 1$. The reduction is also significant if compared with W VII-AS, where the corresponding number is 4. The equilibrium is stable or marginally stable to all local stability criteria which have been evaluated hitherto. Figure 3 shows the evaluation of Mercier's criterion, which appears to be safely stable except for the narrow regions around $\iota_P = \frac{1}{9}$ and $\frac{1}{8}$.

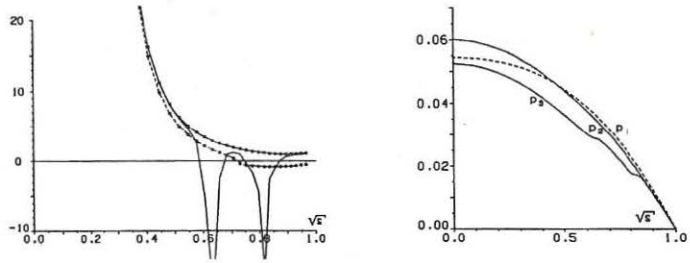

Fig.3: Values of the Mercier (solid line with circles) and the resistive interchange (broken line with circles) criteria as functions of $\sqrt{s}$, which represents the normalized average flux surface radius. The ordinate is taken as the exponent (shifted by $\frac{1}{2}$) occurring in the asymptotic theory of local ballooning modes; negative values represent imaginary exponents. The solid line without circles shows the Mercier criterion with the $\frac{1}{9}$ and $\frac{1}{8}$ resonance included. The BETA run evaluated here has NS, NU, NV = 30, 48, 36; extrapolation to zero mesh size just slightly lowers the curves.

The righthand side shows three pressure profiles as functions of $\sqrt{s}$. p_1 is the profile used for the results shown in the lefthand part; p_2 is the profile corresponding to marginal resistive interchange stability excluding resonance effects; p_3 is the profile including the $\iota_P = \frac{1}{8}, \frac{1}{9}$ resonances.

These formal violations of stability criteria involving the parallel current density are really manifestations of the existence problem of 3D equilibria and can be eliminated by small regions of flattened pressure profile. Helias configurations with smaller shear avoiding these resonances could also be realized if more refined MHD theory showed this to be of advantage. With the value of Mercier's criterion at $s = \frac{1}{2}$ as a reference value, it

is concluded that a substantial improvement in stability is obtained in comparison with Heliac results [4] (in the normalization used in [4] the Helias and the Heliac values are 0.03 and -0.03, respectively). Also shown in Fig.3 is the resistive interchange criterion, which, of course, is more stringent but still approximately marginal in this configuration.

The resistive interchange criterion is, for the case of vanishing net longitudinal current, identical with the applicability condition of a sufficient stability criterion [5] and with the stability condition for peeling modes [6], which adds significance to its use for selecting viable finite-β stellarators. Moreover, it has been shown [7] that island growth (as a function of β) is connected with resistive instability. Thus, the occurrence of the resonances may be presumed to be harmless under these circumstances. As illustrative information three different pressure profiles are shown in Fig.3.

The profile p_1 is the one actually used in the equilibrium computation. The second profile is obtained from marginal resistive interchange stability in the following way: excluding resonance effects, we calculate $p_2 = \int_1^s ds'(V''/\langle \vec{j}^2_{nonres}/p_1'^2 |\nabla s|^2\rangle)$. Thus, p_2 is too optimistic (pessimistic) for an unstable (stable) value of the resistive interchange criterion, because the decrease (increase) of the well depth is not taken into account in the above formula. Closeness of p_1 and p_2 indicates a marginal situation more clearly than the actual values of the criteria. The third profile p_3 is obtained by taking into account resonant effects in $\vec{j}$ and defining $p_3 = \int_1^s ds'(p_2' \langle \vec{j}^2_{nonres}/|\nabla s|^2\rangle / \langle \vec{j}^2_{res}/|\nabla s|^2\rangle)$. In the present context of evaluating stability this regularization of the parallel current density is more natural than Boozer's method based on the classical diffusion argument [8]. Both ways are of course closely related and lead to the same analytical behaviour of the pressure profile near the resonances. Narrowness of the flattened regions and, correspondingly, closeness of the profiles (and β-values) alleviates the doubts connected with the 3D nature of the equilibrium. The above arguments also rely on the dependence of ι on β. Figure 4 shows the $\langle\beta\rangle = 0$, 0.05 twist curves. Finite β has little effect on ι in contrast to the situation in ATF and W VII-AS.

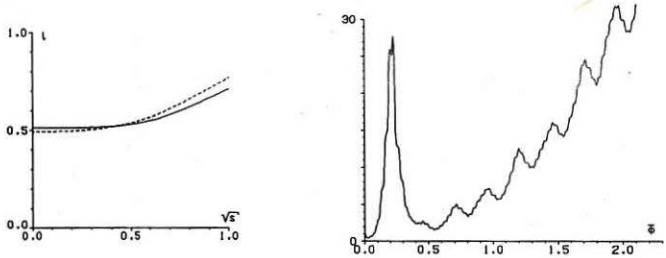

Fig.4: The total twist values ι_T as functions of $\sqrt{s}$ for the $\langle\beta\rangle = 0$ and $\langle\beta\rangle = 0.05$ cases. The righthand side shows the solution F of the one-dimensional ballooning equation for the equilibrium of Fig.1 evaluated at $\iota_T = \frac{4}{7}$. The variable $\bar{\phi}$ is the contracted toroidal variable which varies between 0 and 1 as the field line closes on itself, which corresponds to 35 field periods of the equilibrium. The field line starting at $U = V = 0$ is considered. A zero of F would indicate ballooning instability.

Figure 4 (righthand side) shows the evidence for ballooning stability. Here, we evaluate the one-dimensional ballooning equation [9] at $\iota_T = \frac{4}{7}$, i.e. we consider a localized $m = 7, n = 4$ mode (which should not be influenced by resonance effects within one period)

on the full torus. The potentially dangerous oscillatory curvature terms (apart from the favourable average magnetic well) manifest themselves in the minimum of the ballooning solution but are apparently not strong enough to drive a ballooning instability. This result is in accordance with our previous result [9] that ballooning instability occurs in stellarators only if the Mercier criterion is violated.

The choice of the parameters of the particular Helias configuration presented in Fig.1 may be characterized as follows: A decrease of any of the 9 parameters A, $R_{0,1}$, $Z_{0,1}$, $\Delta_{1,0}$, Δ_0, $\Delta_{2,0}$, $\Delta_{1,-1}$, $\Delta_{2,-1}$, $\Delta_{2,-2}$ decreases the Mercier and resistive interchange stability. Thus, while one may want to decrease all of these parameters, e.g. for easier realization, this imposes a penalty on the stability properties. Apparently, the nature of stellarator optimization is such that the optimum occurs at the boundary of the optimization domain, this boundary being given by side conditions, e.g. minimum acceptable β-value, maximum acceptable aspect ratio, maximum acceptable geometrical distortion.

Since finite-β 3D codes do not yet provide a reliable insight into the quality of magnetic surfaces, vacuum field calculations for Helias were performed with NESTOR [10]. Figure 5 shows the Poincaré plots of three Helias vacuum fields; despite the strong three-dimensionality of the configuration the quality of the surfaces appears to be very good and the radial extent of the detectable islands small if the occurence of the lowest order resonances (e.g. $\frac{1}{7}$) in the outer region of the confinement domain is avoided. In particular, a strong decrease of island size is observed for $\iota_p < \frac{1}{7}$.

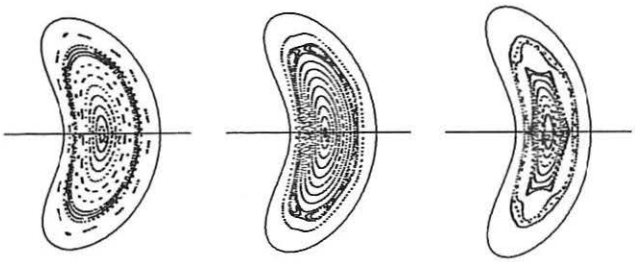

Fig.5: Poincaré plots of Helias vacuum fields with the surface parameters as given in Fig.1, except $\Delta_{1,-1} = 0.27, 0.32, 0.39$.

References

[1] J. Nührenberg, Proc. of Int. Symp. on Stellarators with Three-dimensional Magnetic Axis, Sendai, Japan (1979) 1; IPP Annual Report 1984

[2] J. Nührenberg, R. Zille, Phys. Lett. 114A, 129 (1986)

[3] F. Bauer, O. Betancourt, P. Garabedian, Equilibrium and Magnetohydrodynamic Equilibrium and Stability of Stellarators (Springer, New York, 1984)

[4] O. Betancourt and P. Garabedian, Phys.Fluids **28** (1985) 912.

[5] D. Lortz, E. Rebhan, and G. Spies, Nucl.Fusion **11** (1971) 583.

[6] D. Lortz, Nucl.Fusion **15** (1975) 49.

[7] J.R. Cary and M. Kotschenreuther, Phys.Fluids **28** (1985) 1392.

[8] A. Boozer, Phys.Fluids **24** (1981) 1999.

[9] J. Nührenberg, R. Zille, Proc. 12th European Conf. Contr. Fusion and Plasma Phys., Budapest, 1985, Part I, 445 - 448

[10] P. Merkel, Proc.5th Int.Workshop on Stellarators, Vol.I, 387

INFLUENCE OF SHEAR, $\Delta\iota/\iota$ ON THE CONFINEMENT IN THE W7A STELLARATOR

H. Renner and W7A Team*, ECRH Group**, NI Team***
Max-Planck-Institut für Plasmaphysik,
EURATOM Association, D-8046 Garching

* G. Cattanei, D. Dorst, A. Elsner, V. Erckmann, U. Gasparino, G. Grieger, P. Grigull, H. Hacker, H.J. Hartfuß, H. Jäckel, R. Jaenicke, J. Junker, M. Kick, H. Kroiss, G. Kühner, H. Maaßberg, C. Mahn, G. Müller, W. Ohlendorf, F. Rau, H. Renner, H. Ringler, F. Sardei, M. Tutter, A. Weller, H. Wobig, E. Würsching, M. Zippe

** W. Kasparek, G. Müller, E. Räuchle, P.G. Schüller, K. Schwörer, M. Thumm, R. Wilhelm (Inst.f.Plasmaforschung, Univ. Stuttgart)

*** K. Freudenberger, W. Ott, F.-P. Penningsfeld, E. Speth

Introduction

The plasma behaviour at the W7A stellarator (l=2, m=5; almost shearless $\Delta\iota/\iota < 0.01$) has been shown strongly dependent on the magnetic twist number $\iota = 1/q$. So far "resonances" with a deterioration of the confinement are identified at rational twist numbers of $\iota = m/n$; e.g. 1/2, 1/3, 2/3. For rational twist numbers at the plasma edge strong losses have been found. Island formation and convective losses may be responsible for these perturbations, especially with strong influence at low temperature edge conditions. Shear hence modifies the position and extension of such islands. Shear can be introduced by internal effects: An inhomogeneous current density distribution of the remaining current J_p and the plasma pressure distribution vary the twist number profile.

The influence of shear on the confinement has been demonstrated for "currentless" discharges maintained by ECF 70 GHz (200 kW, 0.1 s pulse duration) and by NI at higher β /1, 2/.

A detailed analysis seems rather difficult, since no direct measurements of the ι profiles are available. Some indications from temporally and spatially resolved measurements of ECE temperatures and soft X radiation for varied ι profiles seem in agreement with the picture of perturbation by quasistationary islands. Optimum confinement has been found for values of the twist numbers close to but not at $\iota = m/n$; e.g. 1/3, 1/2, 2/3. In these regions the low order m/n resonances are less dense. Numerical studies of the magnetic configurations perturbed by error fields confirm, that even the vacuum magnetic surfaces of these ι values are rather insensitive to perturbations. By control of the edge value far from main resonances the confinement can be optimized: Either the remaining plasma current or the current of the helical windings has to be programmed.

Torsatron operation of W7A

The W7a stellarator with 2 sets of helical windings allows to produce vacuum configurations with variable shear. By unbalanced currents $\delta J_{Hx} \neq 0$ to the helical windings positive or negative shear up to $\Delta\iota/\iota < .2$ can be realized. The otherwise almost shearless W7A stellarator field can be modified by the superposition of a l=4 Torsatron field determined by δJ_{Hx}, Fig. 1. Depending on the sign of δJ_{Hx} the central values of ι_0 can be larger or smaller than the edge value. Keeping δJ_{Hx} constant ι-scans can be carried out. Proportional to δJ_{Hx} the toroidal and vertical field components of the helical system have to be compensated.

Mode of operation

For various magnetic configurations the confinement has been investigated. Due to technical constraints arising from the interaction forces between the various coil currents the experiments are restricted to a main field B_o = 1.25 T. To avoid loop voltages the plasma is generated and heated at steady magnetic field by the application of rf at 70 GHz. For the second harmonic heating the power absorbed by the plasma is roughly $P_{IN} \sim$ 120 - 150 kW. During the discharge with $\Delta t \lesssim$ 100 ms the plasma density increases by gas puffing for optimum confinement close to the cutoff density $n_{eo} \lesssim 3 \cdot 10^{13}$ cm^{-3} /3/. Shot by shot the central value of ι_o is controlled by variation of the J_{Hx}.

Vacuum shear $\Delta\iota/\iota = \pm .1$

Starting at low density, low ß and low current Ip Fig. 2 summarizes the energy content W depending on the central twist number ι_o for various $\Delta\iota/\iota$. The minima correspond to the location of $\iota = 1/2$ at the edge. The small plasma current Jp contributes to the edge value with $\iota_p = .032\ J_p$ (J_p kA). The current increases almost linearly during the discharge to $J_p \lesssim +1$ kA. In Fig. 3 the energy content W is plotted in a similar way with $\Delta\iota/\iota = .1$ for ι_o at different time delay Δt. With increasing J_p the edge value 1/2 is reached at lower ι_o values. Consequently also the perturbation according to t = 1/2 is reached at lower t_o values. In addition to the edge effect also the perturbation according to $\iota_o(0) = 1/2$ is indicated. For edge value $\iota = 1/2$ the reduction of W is caused by smaller densities. Apparently the perturbation is localized at the edge, thus an increase of the external gas flux can counteract: Fig. 4 shows, that the dependence of W on the density is almost at the optimum. In Fig. 5 the case $\Delta\iota/\iota = -.1$ is given for comparison. The plasma current J_p reduces now the vacuum shear $\Delta\iota/\iota$. At higher densities the discharge becomes unstable and shows periodically a rapid decrease of the energy content, as indicated by the shadowed regions. Similar to the case, where the negative shear has been produced by induced currents, in Fig. 4 for higher densities and ß values the confinement becomes worse. The persistence of the perturbations for $\iota_o = 1/2$ at the centre for Figs. 3 and 5 indicates, that the current distributions must be hollow. Such current density distributions are expected for the bootstrap current peaked at the pressure gradients dp/dr.

Conclusion

For the described experiment the central pressure is limited to $ß(0) \lesssim .5$ %. So far plasma driven instabilities seem not indicated. Concerning the variation of the confinement only modifications of the equilibrium by the plasma pressure are important. Resonances at the edge and in the entire plasma lead to perturbations and have to be avoided for optimum confinement: Thus shear has to be restricted. Comparing the confinement properties of W7A close at $\iota = 1/2$ for various shear the positive shear with $\Delta\iota/\iota \sim .1$ is favourable. A hollow current density profile may indicated as predicted for the bootstrap current. Consequently the unstable conditions at $\iota_o = 1/2$ for negative shear may be explained by a reduction of the shear depending on Jp. With higher ß an increasing net current and the secondary currents influence the ι profile /4/. Due to the link of pressure profiles, transport and ι profiles a control of optimum confinement will be difficult. But nevertheless by shaping ι of the vacuum configuration some corrections are possible and for the advanced

stellarator a further decrease of the parallel component of the secondary currents, pressure effects may be reducible.

References

/1/ W7A-Team, ECRH Group, 12. Europ. Conf. Contr. Nucl. Fusion and Plasma Physics, Budapest,Vol. 1, 393 (1985)
/2/ G. Grieger and W7A Team, NI Team, ECRH Group Plasma Phys. and Contr. Fusion 28, 43 (1986)
/3/ V. Erckmann and W7A Team, NI Team, ECRH Group, Invited paper, 13. Europ. Conf. on Contr. Fusion and Plasma Physics, Schliersee (1986)
/4/ H. Wobig, J. Kißlinger, 12. Europ. Conf. on Contr. Nucl. FLusion and Plasma Physics, Budapest, Vol. 1, 453 (1965).

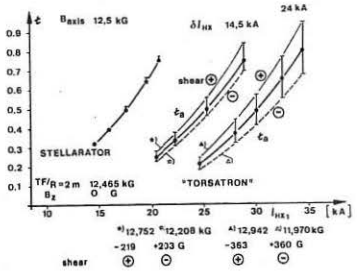

Fig. 1 W7A Stellarator/Torsatron ι and shear variable by J_{Hx1} and J_{Hx2}, δJ_{HX} as parameter.

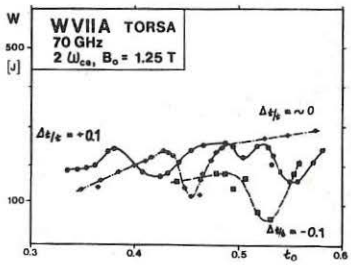

Fig. 2 Energy content versus r_0 for different $\Delta r/r$. Discharge at low ß and J_p with ECF heating 70 GHz: $2\omega_{ce}$ at 1.25 T.

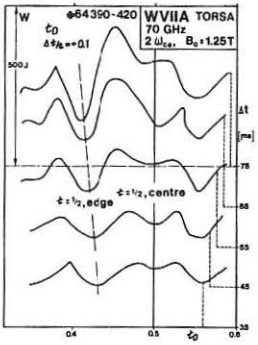

Fig. 3 Energy content versus t_o for $\Delta t/t = .1$ vacuum field. Delay time Δt as parameter. Note the density increases with time.

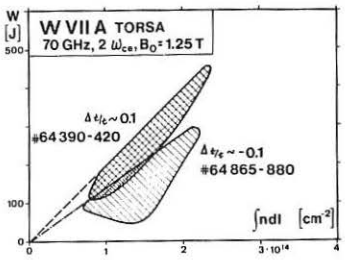

Fig. 4 Energy content versus line density for $\Delta t/t = \pm .1$.

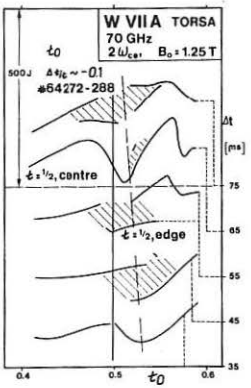

Fig. 5 Energy content versus t_o for $\Delta t/t = -.1$ of the vacuum field. Compare to Fig. 3.

A TRANSPORT MODEL OF ECR-HEATED PLASMAS IN WVII-A

H. Wobig, WVII-A TEAM*

Max-Planck-Institut für Plasmaphysik, EURATOM Association
D-8046 Garching, FRG

Introduction

Currentless plasmas produced by ECRH have been extensively investigated in the WVII-A stellarator /1/ and the Heliotron E device /2/. Electron temperatures of up to 2.5 keV could be reached, the electrons being in the long-mean-free-path regime. Ions stay at a much lower temperature because they are heated only by the electrons. Since ions and electrons are largely decoupled in ECRH discharges and ion thermal losses are small compared with electron losses, these discharges are appropriate for studying the electron power balance. Furthermore, the radiation losses in ECRH discharges are not as dominant as they are in NBI-heated discharges. In contrast to ohmically heated discharges, plasmas with ECR heating do not show tearing modes and sawtooth oscillations. We therefore expect the electron thermal conductivity to be determined by Coulomb collision processes or high-frequency turbulence only. Unfortunately the electron power deposition is only vaguely known in ECRH discharges. Either one has to rely upon the results of a ray-tracing code with a classical absorption mechanism or to extrapolate the radial power deposition from the measurements of the non-absorbted power at the wall opposite the antenna. Such measurements were made in WVII-A , so that a rough picture of the radial power deposition is available.

The Transport Model

In the following paper, the analysis of the electron power balance is done with measured data from WVII-A. The measurements were taken at a magnetic field of 1T and 2.5 T. With the power of one gyratron, the parameter regime could be extended to $T_e \leq 2.5\,keV$ and a maximum density of $5.4 \times 10^{13}\,cm^{-3}$. Radiation losses are measured by bolometers and are taken into account in the power balance. The TEMPL transport code solves a coupled system of second-order differential equations for the ion and electron temperatures with the density profile taken from the experiment. A steady-state solution is obtained with given boundary values for density and temperatures. The independent variable is the effective plasma radius r, corrections due to the elliptical shape of the magnetic surfaces being neglected. The system of equations is

$$-\frac{1}{r}\frac{\partial}{\partial r} r n \chi_e \frac{\partial T_e}{\partial r} = Q_e(r) - P_{Rad} - P_{ei} \tag{1}$$

$$\frac{1}{r}\frac{\partial}{\partial r} r n \chi_i \frac{\partial T_i}{\partial r} = P_{ei} \tag{2}$$

In these equations χ_e and χ_i are the coefficients of thermal conductivity. In our model neoclassical transport coefficients as given by Shaing et al. are used /3/. These coefficients are the sum of neoclassical losses $\chi_{e,HH}$ (Hazeltine - Hinton) and ripple losses and they provide a smooth transition from the Pfirsch-Schlüter regime to the plateau and the long-mean-free-path regime.

In fig. 1 the neoclassical electron thermal conductivity with different temperatures is shown as a function of collisionality.

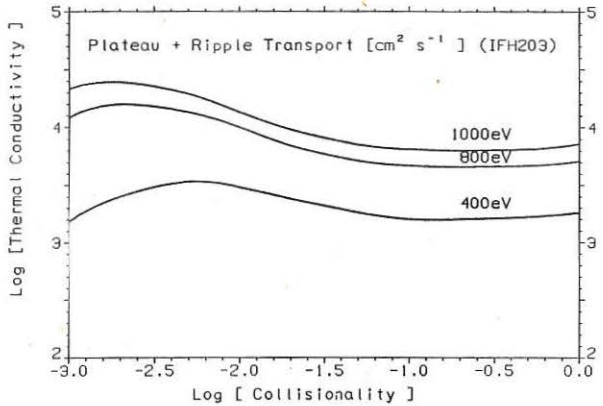

Fig. 1: Neoclassical electron thermal conductivity, $r = 5\,cm$, $\iota = 0.1$

The anomalous electron thermal conductivity as found in ohmically heated plasmas in W VII-A is added to the neoclassical terms. The hypothesis is made that the same anomaly is also present in net current free plasmas. As discussed by Gruber /4/, the coefficient in front of χ_e may depend on the magnetic field and aspect ratio of the ohmically heated plasma. This relation is suggested by comparing several tokamak experiments:

$$\chi_{e,an} = \text{const}\, B_0 \frac{a}{R} \frac{1}{n T_e^{2/3}} \tag{3}$$

In W VII-A the anomaly coefficient C_{an} is $C_{an} = \text{const}\, B_0\, a/R = 3 \times 10^{18}$ at $B_0 = 3\,T$.

$Q_e(r)$ is the power deposited into the electrons, in principle it has to be calculated self-consistently as a function of the plasma parameters. In the present model, however, the deposition profile $Q_e(r)$ is described in the following form

$$Q_e(r) = Q_e(0)\,(1 - r^2)^{\beta_e} \tag{4}$$

where β_e is a profile parameter which allows one to describe either a centrally peaked profile (large β_e) or broader profiles (small β_e). The central value of the heating power is calculated from the measured total heating power, which ranges between 50 and 140 kW. P_{ei} is the power delivered from the electrons to the ions and P_{Rad} is the radiated power. The radiation power is modelled according to the experimental data.

Results and Conclusions. The results of the simulations show that plasma losses can be described by a combination of neoclassical transport and anomalous transport where the anomalous thermal conductivity is the same as found in ohmically heated discharges of W VII-A. Owing to the $(nT^{2/3})^{-1}$ -dependence of $\chi_{e,an}$ this transport mechanism clearly dominates the outer regions of the plasma column, where temperature

and density are small. With neoclassical transport coefficients the calculated electron temperature profiles show a parabolic shape, the more bell-shaped experimental profiles only being reproducible if the anomalous transport coefficient is included. In the central region neoclassical effects play the dominant role, especially if the collisionality is low and electrons approach the long-mean-free-path regime, where ripple losses begin to dominate. In fig. 2a temperature profile taken at $B = 1\,T$ is shown together with the calculated profile. The transport coefficients shown in fig. 3 indicate the dominating role of the ripple losses in the inner regime of the plasma column. The neoclassical transport coefficients also become large at small values of the rotational transform. Since $\chi_{e,HH}$ is proportional to $1/\iota$, it dominates over the other terms at small iota. The analysis of a discharge with $B = 2.5\,T$ and $\iota = 0.1$ (fig. 4) shows that in the central region of the plasma the coefficient $\chi_{e,HH}$ is the dominating one. In discharges with temperatures below $1.5\,keV$ and high density ($n(0) = 2 - 4 \times 10^{13}\,cm^{-3}$) the anomalous thermal conductivity is the dominating term all over the plasma radius.

By comparing discharges at $B = 1\,T$ and $B = 2.5\,T$ it is possible to draw conclusions about the dependence of the magnetic field. Reducing the field from $2.5\,T$ to $1\,T$ conciderably enhances the neoclassical losses, whereas the anomaly factor C_{an} either stays constant or is even reduced following the formula (3). In all discharges at $B = 2.5\,T$ the anomaly factor $C_{an} = 2.5 \times 10^{18}$ gave a rather good fit to the experimental profiles. Simulation of discharges taken at $B = 1\,T$ with the same anomaly factor gives poor agreement with the experimental findings, the temperatures yielded by the calculations being too low. In order to reproduce profiles at $B = 1\,T$, C_{an} has to be chosen smaller than 2.5×10^{18}. The best fit of discharges # 42222-... was obtained with $C_{an} = 1 \times 10^{18}$ which, supports the linear dependence of C_{an} on the magnetic field.

If instead of the anomalous thermal conductivity as given by the WVII-A formula an Intor-like dependence with $\chi_{e,an}$ proportional to $1/n$ is used it is difficult to obtain a good fit to the experimental profiles. By a proper choice of the factor it is easy to reproduce the central value of the electron temperature, but the profile fit is poor in the outer plasma region.

Although all conclusions on the transport mechanisms have to be considered with care and caution there is no doubt that the anomalous thermal conduction plays a large role in ECR-heated plasmas, especially in the boundary region. The exact scaling laws are not yet known, since power deposition is not known accurately enough and parameter dependences have not yet been investigated as has been done in OH discharges. Since in the central region neoclassical effects and anomaly effects are comparable, distinguishing between the two and derivation of scaling laws are particularly difficult. Another problem for analysing the transport mechanisms is the scatter of the experimental data due to the reproducibility of the discharges as can be seen from the figures. This makes it difficult to decide which theoretical profile is the best fit. The error bars coming from the reproducibility of the discharges also introduces error bars on conclusions about transport mechanisms. In spite of these objections, there have been not yet any contradictions to the hypothesis that $\chi_{e,an}$ is the same as in ohmically heated discharges. A consequence of this result would be that $\chi_{e,an}$ is not caused by the ohmic heating current and therefore could appear in any net current-free stellarator. If the favourable temperature scaling of

$\chi_{e,an}$ persists, however, this loss mechanism would be negligible under reactor conditions.

REFERENCES:

/1/ R.Wilhelm et al. WVII-A Team, Plasma Physics and Contr. Fusion, Vol. 26, No. 1A, 1984, p. 259.

/2/ K.Uo et al. Proc. 9th Int. Conf. Plasma Phys. and Contr. Nucl. Fus. Research, Baltimore. 1982 Vol. II p. 209

/3/ K.C.Shaing et al. 10th Int. Conf. Plasma Phys. and Contr. Nucl. Fus. Research, London 1984, Vol. II, p. 189

/4/ O. Gruber: Nuclear Fusion , Vol. 22, No. 10 (1982) p.1349

*) see paper of H. Renner, this conference

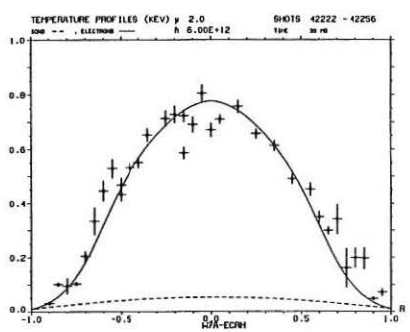

Fig. 2

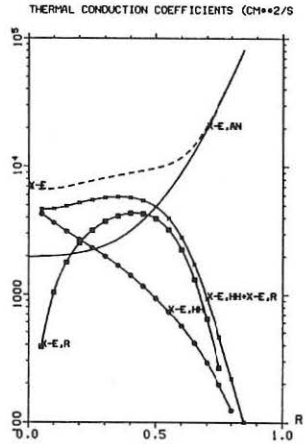

Fig. 3

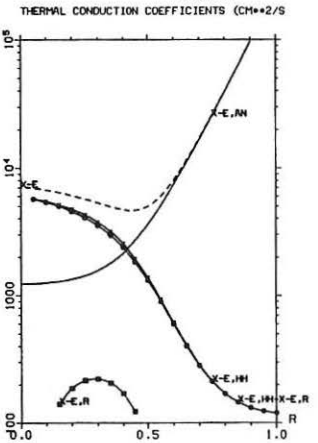

Fig. 5

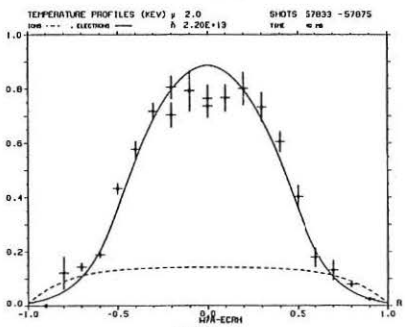

Fig. 4

HELIAC-TORSATRON TRANSITION IN A 8-PERIOD HELICON

J. Guasp and J.A. Fabregas

Junta de Energia Nuclear (JEN). Madrid, Spain.

As it has been described elsewhere [1,2] the Helicon device is a helical axis configuration of "Heliac" type who emerged as a lateral result during the TJ-II configuration search phase [3,4]. It consists of an l=1 external helical coil that creates the toroidal magnetic field and at the same time produces the magnetic axis helicity. This coil is wrapped around the central structure (the hard core) formed by two more coils: a circular one, placed at the helix centre, and another l=1 internal helical coil with the same period than the outer one but shifted half a period. In this way the Helicon differs from TJ-II only in the replacement of the 32 TF coils by a single helical coil, minimizing the total number of coils. From another point of view it can be considered also as an l=1 torsatron with two "Pusher" coils placed at the device center.

In a former study [1,2] the 4,8 and 12 period cases were explored finding good magnetic surfaces of "heliac" type for the 4 and 8 period devices and of "torsatron" type for 8 and 12 periods, In addition flexibility properties were shown also, as well as the very high resultant ι values and the difficulty to obtain configurations with magnetic well, except for the 8-period case that in consequence was considered as the most promising case.

In consequence we have continued the study of the configuration properties for this 8-period case stressing this time the possibility to pass, almost continuously, from configurations with "heliac" surfaces to that of the "torsatron" type by changing only the current setting of the different coils. "Heliac-kind" surfaces correspond to magnetic configurations that wrap around the hard core leaving it inside the helix described by the magnetic axis (Fig.1 and 2). On the other hand "Torsatron-like" surfaces do not encircle the hard core but instead leave it outside the helical path of the magnetic axis (Figs. 3 and 4). Both kind of surfaces can be found in the 8-period Helicon.

Schematic upper views of the 8-period Helicon are shown in Figs. 1 and 3, the dimensions have been scaled-up to the final size of TJ-II, for the radius of the outer l=1 helical coil and 6.4 cm for the radius of the inner one. To produce an average magnetic field of 1 T a 938 KA current is needed in the outer coil. Two supplementary circular vertical field coils, 2.25 m of radius, placed at $\pm$ 0.56 m high, allow to shift the magnetic axis position.

With these global parameters we have done extensive scans allowing variations of the circular and helical coil currents (Icc and Ihc) as well as modifications of the magnetic axis position (Rax) controlled by the VF

coil) current (Ivf).

The scans show the existence of three non overlapping regions, they are shown in the diagram of Fig.5 plotting the values for the hard core current (It=Icc+Ihc) and arbitrary hard core current ratio (Ihc/It). The first region (Rax $\lesssim$ 1.85 m, It $\gtrsim$ 500 KA) corresponds to "Heliac" surfaces, the second one (Rax $\gtrsim$ 1.74 m, It $\lesssim$ 700 KA) to "torsatron" surfaces. Separating both regions there is a "forbidden" zone where no magnetic surfaces exist. As it can be seen from the plot simultaneous changes in both VF coil and hard core currents allow the crossing of the forbidden region and in some cases the jump is possible even maintaining one of the constant parameters (for ex. vertical line It = 600 KA in Fig. 5).

The best heliac surfaces are found around It $\sim$ 675 KA and Rax $\sim$ 1.74 m. Figs. 1 and 2 represent the case Icc = 641 KA, Ihc = 34 KA and Ivf = -159 KA (Rax = 1.74 m), average plasma radius is more than 16 cm and there is a slight magnetic well (2%). Toroidal disymmetry is rather large (>7 cm) and very visible. High rotational transforms at axis are reached for these configurations ranging from 2.2 up to almost 6 (4.10 in the case of Fig. 2) and, as it was shown in [1,2], the ι values depend strongly on the hard core current distribution (Ihc/It ratio), nevertheless average radius shrinks quickly leaving only a narrow window of useful Ihc/It values for each It and Rax couple.

On the other hand the "torsatron" surfaces are obtained for larger Rax values that correspond, mainly, to VF coil currents of the same direction than It. The best configurations are obtained around It~250 KA and Rax~2.14 m, Figs. 3 and 4 show the case Icc=325 KA, Ihc=-75 KA, Ivf=+54 KA (Rax=2.14 m) (note that Ivf has now the same direction as It). For the shown case average plasma radius is more than 18 cm, helical excursion surpasses 32 cm and small magnetic wells may appear in some cases. Nevertheless flexibility is now almost lost: very slight variations are observed in all magnitudes when the current ratio (Ihc/It) is changed.

In addition an extremely high magnetic ripple at axis is observed in these cases (78% for the Fig. 4 case compared with 25% for Fig.2) originated by the so external situation of the magnetic surfaces. This high ripple value should have adverse consequences on equilibrium and transport properties for torsatron-kind configurations.

REFERENCES

[1]. J.Guasp, J.A. Fabregas, 12th EPS Conference, Budapest 1985. Eur. Conf. Abstr. Vol. 9F, Part I, p. 437.

[2]. J. Guasp, J.A. Fabregas, to be published in Nucl. Fus.

[3]. J. Guasp, J.L. Alvarez Rivas et al., 12th EPS Conference, Budapest 1985, Eur. Conf. Abstr. Vol. 9F, Part I, p. 441

[4]. S. Yoshikawa, Nucl. Fus. 23 (1983) 667.

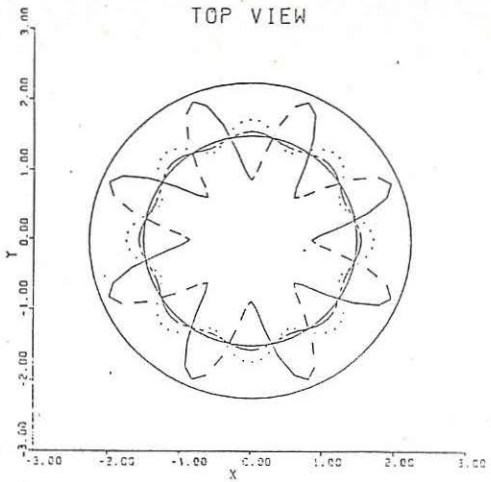

Fig 1. Top view of 8-period Helicon (Heliac surfaces)

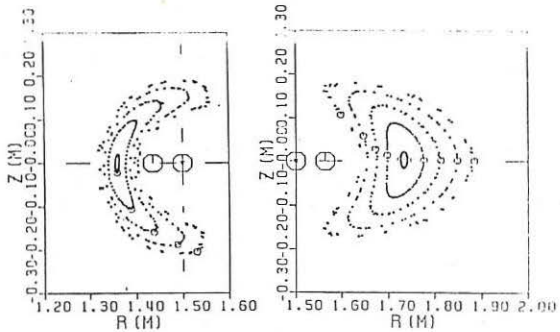

Fig 2. Magnetic surface cross-sections for 8-period Helicon (Heliac type)

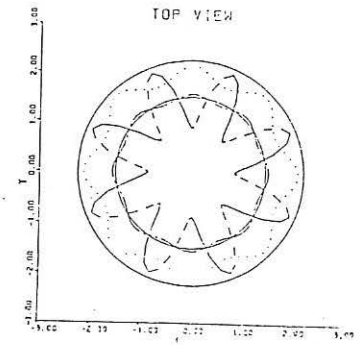

Fig 3. Top view of 8-period Helicon (Torsatron surfaces)

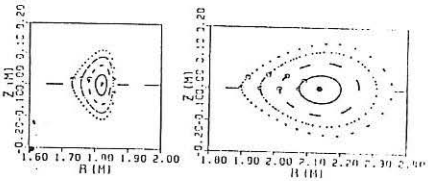

Fig 4. Magnetic surface cross-sections for 8-period Helicon (Torsatron type)

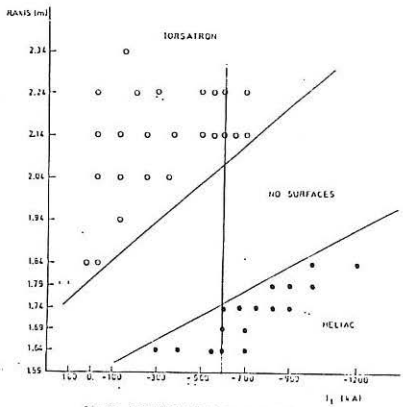

Fig 6. DIFFERENT TYPES OF SURFACES FOR SEVERAL HARD CORE CURRENTS AND MAGNETIC AXIS POSITIONS

EVALUATION OF CONFINEMENT TIMES FOR THE FLEXIBLE HELIAC TJ-II

J. Guasp

Junta de Energia Nuclear (JEN) Madrid, Spain.

The TJ-II is a helical axis stellarator of Heliac type, endowed with a very high flexibility, to be built at JEN [1], (Fig.1). In order to have some estimations for the expected plasma parameters in the device, preliminary evaluations of confinement times have been done using a simple model. Such evaluations complement deeper transport studies that are now under development [2].

We have used a simple analytical model for the magnetic field intensity near the magnetic axis: that of a straight Heliac [3], [4], taking in account only the first helical harmonic and with first order toroidal corrections added. The resulting coefficients are adjusted to fit the magnetic axis position and the ripple dependence with TF coil current modulation for the TJ-II configuration.

As transport model we have chosen the expresions for particle and heat fluxes given for Stellarators by Kovrizhnykh [5], [6] that allow the possibility to include selfconsistent radial ambipolar electric field effects, the selfconsistent electric field value can be obtained by cancelation of the total particle flux. Finally we assume parabolic radial profiles for density and temperatures.

The results of the model for the different heating scenarios planned for the TJ-II are the following:

a) For 400 KW of ECRH, a central density of 2×10^{13} cm^{-3} and Te/Ti=3.33 the global energy confinement time τ_E decreases steadily with the central value of Te (Fig.2) giving 4 ms at 700 eV. Below 400 eV τ_{Ee} remains higher than τ_{Ei} but at 700 eV τ_{Ei} surpasses τ_{Ee} in 20%.

The influence of the electric field is very high, indeed a change of $e\phi/Te$ from 0. to +1. produces an increase of τ_E by factor 2.1 at 700 eV. When selfconsistent E-field is used (Fig.2) its value goes from $e\phi/Te$=-0.59 at 100 eV up to -0.10 at 700 eV. The three usual roots: ionic, electronic and unstable [6], [7] appear at 670 eV. The electronic root gives a higher τ_E value (~10 ms) but remains unaccesible below 1.9 KeV.

The dependence with density for the same Te/Ti ratio is shown at Fig.3, τ_E increases with density for Te lower than ~2 KeV reversing its behaviour at higher temperatures when the electronic root is reached.

The quoted results corresponds to absence of toroidal current modulation, that is with a value for the magnetic ripple at axis of 10%, when a 15% factor in modulation is used ripple decreases to 1% and our model predicts a clear increase of τ_E. Nevertheless this effect has lesser

influence than the E-field, this fact is illustrated at Fig.3 where relative losses, evaluated from the particle confinement time for ions at $ne(0)=3x10^{13}\ cm^{-3}$ $Te(0)=700$ eV and $Te/Ti=3.33$, are represented versus the E-potential for three modulation factors. In addition this modulation dependence seems to be much weaker when more complicated models, now on development, are used.

b) For 1 MW NB injection at $ne(0)=3x10^{13}\ cm^{-3}$ and $Te/Ti=0.48$ a similar behaviour appears, at Te=700 eV τ_E amounts to 9.0 ms.

We have calculated also the equilibrium temperatures at several heating powers and densities using a global simplified code (zero-dimensional, static, frozen radial profiles including Bremmstrahlung losses and electron energy transfer) leading to the following results:

a) For 400 kW ECRH, $ne(0)=2x10^{13}\ cm^{-3}$ and no modulation, we obtain $Te(0)=700$ eV, $Ti(0)=190$ eV, $\tau_E=4.3$ ms, $\beta_o=0.72\%$ the selfconsistent E-potential $e\phi/Te$ is about -0.10.

These results are compatible with direct extrapolations from experimental data published for other Stellarators [8].

b) For 1 MW NB injection, 80% efficiency, no modulation and $ne(0)=3x10^{13}\ cm^{-3}$, we obtain:

$Te(0)=700$ eV, $Ti(0)=1470$ eV, $\tau_E=9.0$ ms, $\beta_o=2.6\%$

In addition for every MW of NB absorbed, the increase in β_o is about 2%, so that the apparent equilibrium limit of the device, that seems to be about $\beta_o \sim 9\%$ should be attained around 5 MW.

Direct scaling-up to the configuration predicts that Lawson criterion should be fulfilled for a major radius device of 12 m and a 6 T magnetic field.

Calculations for microwave penetration have shown that the most favourable position is found at a toroidal angle of 16° injected from below. For 28 GHz and 1T (1st harmonic) the X-cutoff does not interfere with the resonance at average line densities lower than $1.1x10^{13}\ cm^{-3}$ (Fig.5), the same situation appears at 53.2 GHz (2nd. harmonic) for average densities lower than $1.6x10^{13} cm^{-3}$ (Fig.6). Higher densities bring the cutoff ahead the resonance and can impair the penetration at plasma centre. This means that for higher densities supplementary heating will be needed.

NB penetration has been studied also, extremely favourable tangential directions have been found (Fig.1) giving a total path inside the plasma of 2.3 m and a value for $\int ne.dl=669x10^{13}\ cm^{-2}$ at an average density of $2x10^{13}\ cm^{-3}$, this means that an absorption efficiency higher than 80% could be attained widely (a value of about 250 is required for 27 KeV beams). Finally the effective beam width is about 10 cm.

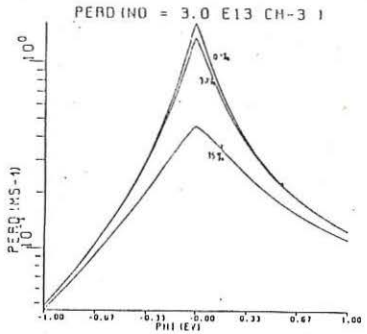

FIG 3

DEPENDENCE OF LOSSES WITH CURRENT MODULATION AND WITH ELECTRIC FIELD

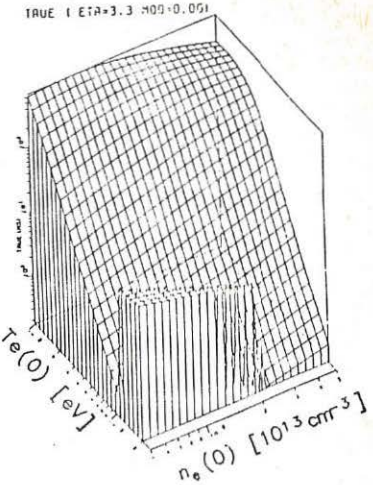

FIG 4 Dependence of τ_E with central n_e and Te.

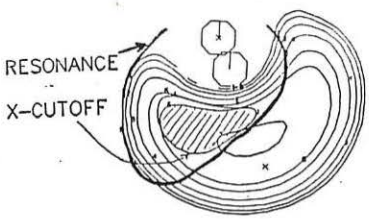

FIG 5

28 GHZ (1ST HARMONIC)

$\bar{n}_e = 1.1 \times 10^{13}\ CM^{-3}$

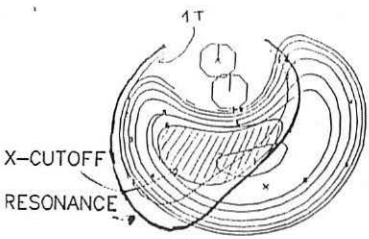

FIG 6

53.2 GHZ (2ND HARMONIC)

$\bar{n}_e = 1.6 \times 10^{13}\ CM^{-3}$

REFERENCES

[1]. J. Guasp, J.L. Alvarez-Rivas, et. al., 12th EPS Conference, Budapest 1985. Eur. Conf. Abstr. Vol. 9F, Part I, p.441.
[2]. E.R. Solano, to be published.
[3]. N.M. Zueva, L.S. Solov'ev, Plasma Phys. 8 (1966) 765.
[4]. J.H. Harris, J.L. Cantrell et al., Nucl. Fus. 25 (1985) 623
[5]. L.M. Kovrizhnykh, Nucl. Fus. 24 (1984) 435.
[6]. L.M. Kovrizhnykh, Nucl. Fus. 24 (1984) 851.
[7]. D.E. Hastings, T. Kamimura, J. Compt. Phys. 61 (1985) 286
[8]. Heliotron-E Group, Proc. 5th Int. Conf. Stellarators Schloss Ringberg 1984. EUR-9618EN. Vol.I, p. 145.

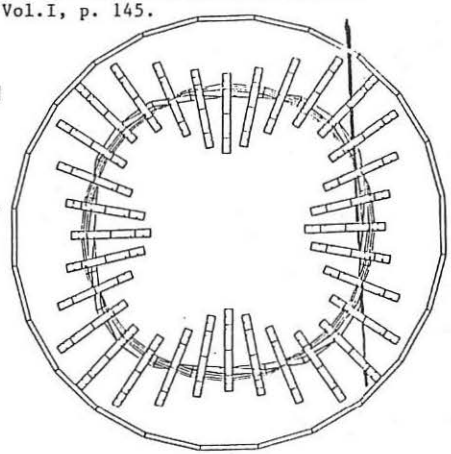

FIG 1. Top view of TJ-II and best NB position.

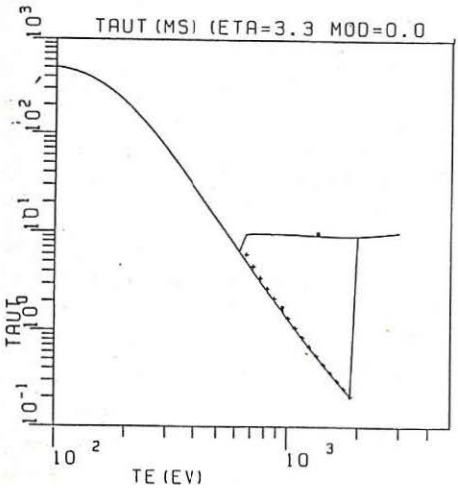

FIG 2.
Dependence of τ_E with central Te.

OPTIMIZATION OF RF PLASMA HEATING IN URAGAN 3 TORSATRON

N.I. Nazarov, V.V. Plyusnin, T.Yu. Ranyuk, V.T. Tolok, O.M. Shvets, V.V. Bakaev, B.V. Kravchin, Yu.K. Mironov, O.S. Pavlichenko and A.S. Slavnyj

Kharkov Institute of Physics and Technology, Ukrainian SSR Academy of Sciences, 310108 Kharkov, USSR

Our earlier papers [1,2] were devoted to the development of an efficient method of currentless plasma production and heating with ion cyclotron and Alfven waves excited by unscreened helical frame-type antennae in the URAGAN 3 torsatron. It was shown that similar antennae could be used to produce a low-temperature, yet sufficiently dense plasma by launching a fast magnetosonic wave (FMSW) near the cut-off frequency [3]. The plasma thus created is used in URAGAN 3 to clean the surfaces of the RF antennae and helical winding casings in the vacuum tank.

This report describes the attempts to optimize the RF plasma parameters in URAGAN 3 through exploration of the effect of the RF conditioning, gas pressure in the vacuum tank and RF pulse duration.

The experiments were carried out with a frame-type antenna fed with RF current at 5.4 MHz which permitted a spectrum in the range from 35 to 200 cm to be obtained.

Effect of RF Conditioning on Plasma Parameters

The RF conditioning was performed by means of RF discharges created in hydrogen under gas filling to a pressure of 1×10^{-4} Torr in the tank pre-evacuated to 5×10^{-7} Torr. The pulse duration (τ_{RF}) and repetition rate were 20 ms and 0.2 pulse/s, respectively. The confining magnetic field $B_o = 0.2 \div 0.5$ kG and absorbed RF power $P \simeq 100$ kw permitted the plasma of average density $n_e \simeq 1 \times 10^{12}$ cm^{-3} and electron temperature $T_e \simeq 10$ eV to be created using FMSW.

The effect of the number of RF discharges (after evacuating

the tank) on the plasma parameters was studied under the following operating conditions: B_o=4.8 kG, p=1.4x10^{-5}Torr, P = 500 kw, and τ_{RF}=3 ms. The mass-spectrometric analysis revealed that at the start of the RF conditioning procedure the discharges facilitated the formation of molecules of water, carbonic oxide and hydrocarbons as a result of plasma-wall interactions. As the cleaning proceeded further, the CIII and OII intensities gradually decayed, the plasma energy built up and soft X-radiation increased (Fig. 1). The time variation of the plasma parameters at the start of the cleaning (a) and after 5x10^3 cleaning discharges (b) is shown in Fig. 2. It can be seen that after 5x10^3 RF discharges the plasma parameters are stabilized, the initial pressure simultaneously decreasing to 1.5x10^{-7}Torr. The RF conditioning now precedes all RF plasma experiments on URAGAN 3.

Plasma Parameters as a Function of Pressure

While the vacuum tank (70 m^3) is being filled with gas, on the outside of the plasma column there is a permanent fairly dense gas blanket ($n_{H_2} \simeq 1x10^{12}$cm^{-3}) which provides a constant influx of molecular hydrogen to the plasma edge during the discharge. Together with the molecular hydrogen to the plasma edge flows a certain amount of light and heavy impurities present in the tank in the gaseous phase or released from the metal walls exposed to the plasma. The contributions of the hydrogen and impurity influxes to the particle and energy balance would change as the gas pressure is changed. To ascertain the role of the atomic processes resulting from these fluxes, in the particle and energy balance the plasma parameters were measured for the hydrogen pressure varied in the range (1.4÷6)x10^{-5}Torr after long RF discharge conditioning. Fig. 3 represents the plasma parameters (at t= 3 ms) measured versus the hydrogen pressure: average electron density, OII and CIII intensities, electron temperature from soft X-R. measurements, total plasma energy content as measured with γ-loops [2], and energy confinement time $\tau_E = \frac{nT}{\frac{d}{dt}(nT)}$, determined at the end of the RF pulse. It can be seen that as the gas pressure decreases, the OII and CIII intensities

decay while the total plasma energy content, electron temperature and energy confinement time increase, with the electron density changing negligibly. The observed build-up of the plasma energy content and energy confinement time can be ascribed to lower power losses by hydrogen excitation, ionization and charge exchange due to the decreased hydrogen influx to the plasma edge. Less clear are the decreased OII and CIII intensities. It is evident, however, that the maximum plasma parameters can be realized under certain (optimum) hydrogen pressure. In this case the plasma energy content and plasma confinement time increase with the increasing RF power input (Fig. 4), and $\overline{\beta} = \frac{8\pi n \overline{T}}{B_0^2} \simeq 0.5\%$.

Effect of RF Pulse Duration on Plasma Parameters

It was not possible to maintain the plasma parameters reached by the third millisecond: as the RF pulse duration increased, the plasma energy, electron density and energy confinement time decreased, with the OII and CIII intensities increasing (Fig. 5). Whether the observed deterioration of the plasma parameters results from the plasma cooling due to the radiation losses is the subject of our further investigations.

1. O.M. Shvets, A.G. Dikij et al., In: Heating in Toroidal Plasmas (Proc.4th Int.Symp., Rome, 1984) 1, p.513.
2. V.V. Bakaev, S.P. Bondarenko et al., In: Plasma Physics and Controlled Nuclear Fusion Research (Proc.10th Int.Conf., London, 1984) Paper IAEA CN-44/D-1-3.
3. S.S. Kalinichenko, P.I. Kurilko, A.I. Lysojvan et al., Fizika Plazmy, 3, N 1, 118, 1977.

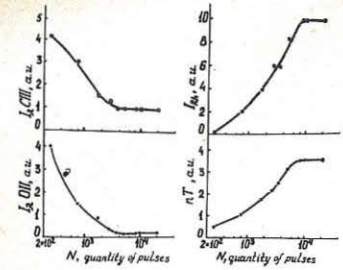

Fig.1 Plasma parameters vs RF conditioning

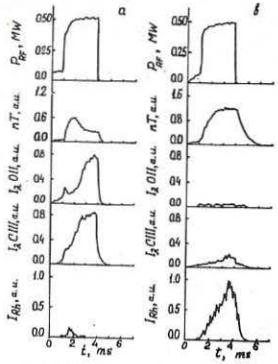

Fig.2 Time variation of plasma parameters:
a) at the start of RF conditioning, b) after RF conditioning.

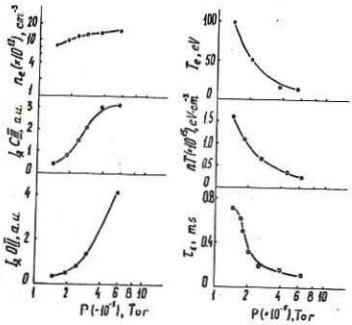

Fig.3 Plasma parameters vs hydrogen pressure

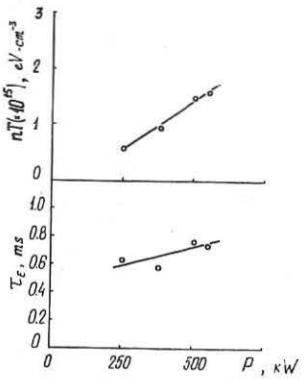

Fig.4 nT and τ_E vs power input

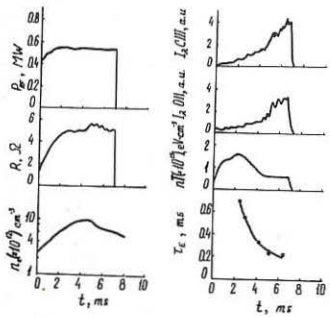

Fig.5 Plasma parameters vs RF pulse duration

BEAN-SHAPED ADVANCED STELLARATORS WITH MODULAR COIL SYSTEMS

F. Herrnegger and F. Rau

Max-Planck-Institut für Plasmaphysik
IPP-EURATOM Association
D-8046 Garching bei München

Abstract

Bean-shaped Advanced Stellarator configurations with a nearly plane magnetic axis, small shear, an aspect ratio of $A = 10 - 12$, and $m = 5$ field periods around the torus are investigated. These configurations are given by Dommaschk potentials. Associated modular coil systems with a coil aspect ratio of about 5.5 and 18 to 6 coils per field period are derived. For such vacuum field configurations with a magnetic well, values of $\langle j_\parallel / j_\perp \rangle = 0.8$ to 2.2 are obtained at $\iota = 0.48$ to 0.31. By comparison, the corresponding values of W VII-AS are $\langle j_\parallel / j_\perp \rangle = 2.2$ to 1.9 at $\iota = 0.39$.

1. Introduction

Advanced Stellarator configurations [1] with an average magnetic well are characterized by a reduced drift of particles away from a magnetic surface, reduced secondary currents, and thus by a reduced Shafranov shift of the magnetic surfaces compared with a classical stellarator. Configurations like the Advanced Stellarator Wendelstein W VII - AS [2] are shown by numerical computation to allow an average value for the equilibrium-β of up to approximately $\langle \beta \rangle \approx 5\%$[3], whereas calculations of the stability-β yield considerably lower values. On the other hand, spatial axis configurations like Helias [4] afford prospects of stability-β values of up to 5%.

In the present paper, Bean-shaped Advanced Stellarators with a nearly plane magnetic axis and associated modular coil systems are introduced where the magnetic field is represented by Dommaschk [5] potentials. Modular coil systems are derived from these potentials. Typical parameter values are $m = 5$ field periods, aspect ratio of the last closed magnetic surface $A = R_T/a = mL_P/2\pi a \simeq 10$ to 12 (a is the average minor radius of the last closed magnetic surface and R_T the major torus radius), a magnetic well of the vacuum field $(V' - V_0')/V_0'$ down to -2.5%, twist (rotational transform) at the magnetic axis around $\iota_0 = 0.4$, and small shear.

2. Configuration Studies

We consider three different examples of Bean-shaped Advanced Stellarator configurations (see Fig.1), which are characterized by a certain indentation of the vertically elongated magnetic surfaces at the beginning of a field period (FP). The dependence of the twist $\iota(r)$ and the specific volume $V' = \oint d\ell/B$ (normalized to its value on the magnetic axis) on the average minor radius r of the magnetic surfaces is shown in Figs.2 and 3. Configurations with labels FZH are given in Dommaschk potentials, those with FFR are from a system of 9 twisted coils per FP. For comparison, the standard case of W VII-AS is entered, too. All configurations have a magnetic well ($V'' < 0$).

As a figure of merit in comparing the different configurations we use the average ratio $\langle j_\parallel / j_\perp \rangle$ and the quantity $J^* = \langle (B_0^2/B^2)[1 + (j_\parallel/j_\perp)^2] \rangle$, where B_0 is the reference magnetic field at R_T and $\langle \ldots \rangle$ denotes the average on a magnetic surface. J^* is a measure of the Pfirsch-Schlüter currents and also appears in the stability criterion of resistive interchange modes. The ratio $\langle j_\parallel / j_\perp \rangle$ is obtained from the poloidal variation of $\int dl/B$ taken along a field line over one field period. The quantities $j_\parallel$ and $j_\perp$ are the absolute values of the secondary and the diamagnetic current densities, respectively, which scales

as $2/\iota$ for a standard stellarator like W VII-A and are reduced by a factor of about 2 in the Advanced Stellarator device W VII-AS.

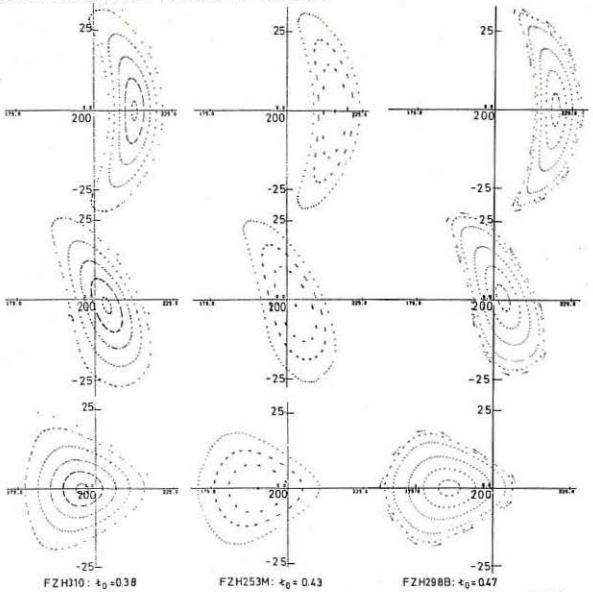

Fig.1 Cross-sections of the magnetic surfaces at 0, $L_P/4$, $L_P/2$ of a field period (R_T = 200 cm).

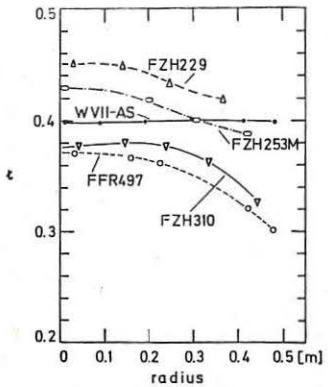

Fig.2 Twist profile.

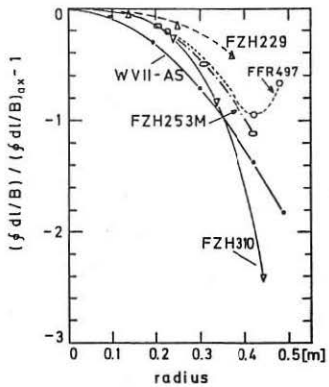

Fig.3 Specific volume.

The configuration FZH310 (see Figs.1 - 3) is characterized by a twist number at the magnetic axis $\iota_0 = 0.38$, a small field modulation $\delta = (B_{max} - B_{min})/(B_{max} + B_{min}) \sim 10\%$ and a deep magnetic well of $\Delta V'/V_0' = -2.5\%$; the reduction of the secondary currents is comparable to the W VII-AS configuration in the boundary region and is

moderately improved near the magnetic axis: $\langle j_\parallel / j_\perp \rangle_{ax} \simeq 1.70$. The configuration FZH298B has $\iota_0 = 0.425$, a field modulation at the axis $\delta \sim 25\%$, and a small parallel current density of $\langle j_\parallel / j_\perp \rangle_{ax} \simeq 0.82$. The configuration FZH253M is characterized by $\iota_0 = 0.43$, a moderate field ripple on axis $\delta \sim 12\%$ and $\langle j_\parallel / j_\perp \rangle_{ax} \simeq 1.37$.

3. Modular Coil Systems

Modular systems of non-planar coils are derived for such configurations with a coil aspect ratio of around $A_c = 5.5$ and a number of coils per FP of 18, 9, or 6. For a typical number of 9 or more coils per FP the original configurations are reproduced with sufficient accuracy, whereas with 6 coils per FP a slight magnetic hill of the vacuum field is developed.

In the following example, a coil system representing the configuration FZH253M is given. As a first step, a toroidal surface with elliptical cross-section and an aspect ratio $A_c = 5.5$ is defined, where the elongation of the ellipses varies between 1.6 (at the beginning of a FP) to 1.2 (middle of a FP). The geometric centre of the cross-sections moves radially inward and outward by an amount of $\Delta R/R_T = 0.07$. On this surface 18 surface current lines [5] are computed. The discretization of this surface current distribution for a modular system of 18, 9, or 6 coils per FP is made straightforward by choosing the corresponding current lines as coil centres. At a major radius of $R_T = 500$ cm we use radial and lateral coil dimensions of 36.4 cm and 20 cm for the system with 9 coils per FP. At a gross current density of $j_{eff} = 30\text{MA/m}^2$ the total coil current of 2.2 MA introduces a magnetic induction of $B_{ax} = 3.7$ T at the magnetic axis.

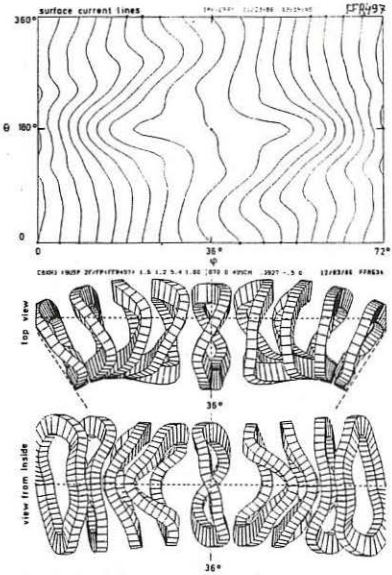

Fig.4 Angular map of surface current lines (top graph). View of coils from top (middle graph) and from inside (bottom; φ, θ are toroidal and poloidal angles).

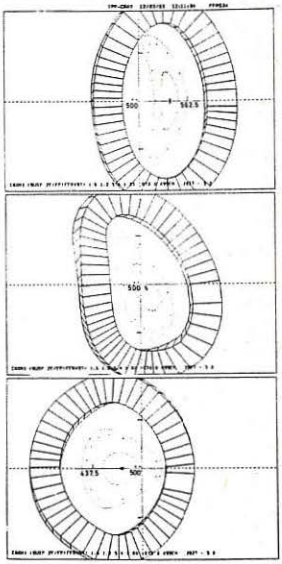

Fig.5 Cross-sections of the magnetic surfaces and shape of the adjacent coils at 0, $L_P/4$, $L_P/2$ of a field period.

The top plot of Fig.4 shows the shape of the 18 surface current lines of one field period in an angular plot (φ, θ are the toroidal and poloidal angles); the second and third plots show the top and inside views of the modular system of the non-planar coils. There are 5 different coil shapes in the set of 9 coils per FP. The triangular cross-section of the magnetic surfaces is at $\varphi = 36°$. The toroidal excursion of the coils is kept moderate by choosing an adequate aspect ratio of the surface where the surface current distribution is calculated. Configurations with other twist numbers $\iota_0 = 0.37 \ldots 0.46$ at the magnetic axis are obtained for different values of the coil aspect ratio $A_c = 5.6 \ldots 5.3$ which gives an extended parameter range compared to the original configuration FZH253M. Figure 5 shows the cross-sections of the magnetic surfaces and the shapes of the adjacent coils at toroidal positions 0, $L_P/4$, $L_P/2$ for $\iota_0 = 0.37$ (configuration FFR497). In comparison with W VII-AS, the coil aspect ratio is increased.

4. Summary and Conclusions

As shown in Fig.6, the Bean-shaped Advanced Stellarators (aspect ratio A = 10 – 12) provide improved values of $\langle j_\parallel / j_\perp \rangle$ *versus* ι compared to W VII-AS. For comparison, the corresponding curve for W VII-A and the relationship $2/\iota$ are also given. Configurations with best values $\langle j_\parallel / j_\perp \rangle_{ax} = 0.82$ and $J^*_{ax} = 1.72$ are found for $A \simeq 12.4$ with a marginal magnetic well.

The BETA/BBG [6] code is used to compute the finite-β magnetohydrostatic equilibria. An example is shown in Fig.7 for FZH747, a data set similar to FZH298B. Preliminary finite-β computations have shown the expected reduction of the Shafranov shift accompanied by a small change of the twist profile.

The influence of the bean shape of the magnetic surfaces on the stability remains to be studied.

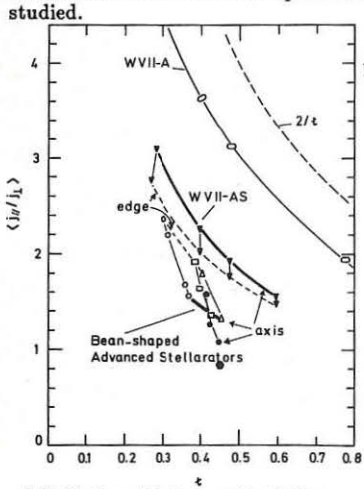

Fig.6 Average normalized parallel current density $\langle j_\parallel / j_\perp \rangle$ as a function of twist ι for various stellarators (R_T=200 cm).

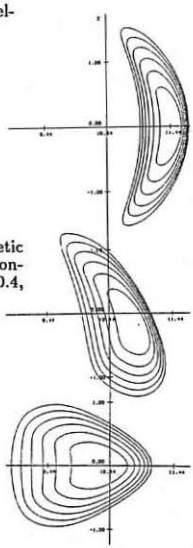

Fig.7 Cross-sections of the magnetic surfaces at $\beta_0 = 0.07$ for configuration FZH747 ($A = 10.4$, $\iota_{0vac} = 0.39$).

1 R. Chodura, W. Dommaschk, F. Herrnegger, W. Lotz, J. Nührenberg, and A. Schlüter, IEEE Trans.Plasma Science PS-9 (1981) 221.

2 B. Brossmann et al., Proc. 9th IAEA Conf. Baltimore, Vol. III, 141, 1982

3 E. Harmeyer, F. Herrnegger, J. Kißlinger, F. Rau, H. Wobig, 4th Tech. Comm. Meeting and Workshop Fusion Reactor Design and Technology (Yalta, USSR) 26 May – 6 June 1986, Paper submitted.

4 J. Nührenberg, R. Zille, Phys.Lett. **114A** (1986) 129.

5 W. Dommaschk, Z.Naturforsch. **37a** (1982) 867.

6 F. Bauer, O. Betancourt, P. Garabedian, Magnetohydrodynamic Equilibrium and Stability (Springer Verlag, New York 1984).

Calculation of the Influence of Suprathermal Electron Radiation on ECE Spectra,with oblique Direction of Observation

M.Tutter,WVIIA-Team *
Max-Planck-Institut für Plasmaphysik, EURATOM Association
D-8046 Garching, FRG

The plasma is considered with respect to the electrons as consisting of a thermal main part and a small optically thin suprathermal part. The thermal part is described on the basis of temperature and density profiles as measured via Thomson scattering. Concerning energy and density distribution of suprathermal electrons, the following assumptions seemed most practicable [1] :

(1) exponential shape of energy distribution function, being zero below a certain energy ,
(2) ratio $q = v_{\parallel}/v_{\perp} = const$,
(3) arbitrary density profile.

The emission of the thermal main part is calculated by means of the optical depth and Kirchhoff's law,that of the suprathermal part by means of the single particle radiation formula. The latter emission is partly absorbed in the thermal background on its way to the observer.

For the optical depth of the thermal plasma expressions given by several authors [2] – [6] are used . The calculation is done onedimensional with sheath model.

The total radiation of a suprathermal electron per solid angle unit in

direction Θ with respect to the B-field is [7] :

$$\xi = \frac{e^2\omega^2}{8\pi^2\epsilon_0 c}\sum_{l=1}^{\infty}\left(\underbrace{(\frac{cos\Theta-\beta_\parallel}{sin\Theta})^2 J_l^2(x)}_{o\text{-}mode} + \underbrace{\beta_\perp^2 J_l'^2(x)}_{x\text{-}mode}\right)[W] \quad , \quad x = \frac{l\beta_\perp sin\Theta}{1-\beta_\parallel cos\Theta}$$

The distribution funktion is:

$$f(E) = \frac{1}{EO}\cdot e^{-\frac{E-ECO}{EO}} \quad \text{for} \quad E \geq ECO$$

The emission of an electron gas of density n (radiation power per volum unit, frequency unit and solid angle unit in direction Θ) is calculated from the line radiation, as energy per frequency interval :

$$j(\omega) = \xi\cdot\left|\frac{dn}{d\omega}\right| \quad , \quad \left|\frac{dn}{d\omega}\right| = \frac{dn}{dE}\cdot\left|\frac{dE}{d\omega}\right| = n\cdot f(E)\cdot\left|\frac{dE}{d\omega}\right|$$

$$\omega = \frac{l\omega_b}{\gamma - a\sqrt{\gamma^2-1}} \quad , \quad a = \frac{cos\Theta}{\sqrt{1+\frac{1}{q^2}}}$$

$$\left|\frac{d\omega}{dE}\right| = \frac{l\omega_b}{m_0c^2}\frac{\pm 1}{\gamma^2(1-\beta_\parallel cos\Theta)^2}\left(1-\frac{a\gamma}{\sqrt{\gamma^2-1}}\right) \quad \text{for} \quad \begin{cases}\gamma < F_{UMK}\\ \gamma > F_{UMK}\end{cases}$$

$$F_{UMK} = \sqrt{\frac{1+q^2}{1+q^2 sin^2\Theta}}$$

Fig.1 shows the o.mode lines ξ for $\Theta < \pi/2$ for growing energy E starting at $ECO = 0$: at first the positiv Dopplershift dominates (the gyrating electrons approach the observer) the relativistic decrease of frequency, it is $\omega/\omega_b > 1$. For

$$E > E_{UMK} = m_0c^2\cdot(F_{UMK}-1)$$

the resulting increase of frequency decreases again. The line density there gets infinity, caused by the assumption $q = const$. For

$$E > m_0c^2\cdot\frac{2a^2}{1-a^2}$$

$\omega/\omega_b < 1$ holds.The curves show $j(\omega)$ for both modes. From $q \approx 2$ on F_{UMK} is already near its asymptotic value $1/sin\Theta$; so even when electrons with a distribution in pitchangle are present a pronounced maximum of emission near $1/sin\Theta$ can be expected. Because the frequency there is greater than $l\omega_b$ at the point of emission , no reabsorption by the thermal background plasma takes place on its way outside to the observer across the decaying B-field of a toroidal machine, and as its frequency has a nearly constant distance to $l\omega_b(r)$ for $q > 2$ (for $q = const$ exactly constant), one can get an image of the suprathermal density distribution superposed to the thermal temperature profile obtained from the measured spectrum, at least in the case when its energy distribution is independent of radius (s.fig.2).

In reality the energy distribution of the suprathermals is hardly independent of the radius; but a measurement with $\Theta \neq \pi/2$ should at least give a clear indication on the presence of such electrons with $v_{\parallel} \neq 0$.

Literature:

[1] C.M.Celata,D.A.Boyd, Nuclear Fusion 17 (1977) S.735

[2] R.Cano,A.A.Bagdasarow,A.B.Berlizov,E.P.Gorbunov, G.E.Notkin, Fontenay EUR-CEA-FC-983 (Dez.1978)

[3] M.Bornatici,F.Engelmann, Rijnhuizen P.P.78/03 (Mai 1978)

[4] R.Cano,A.A.Bagdasarow,A.B.Berlizov,E.P.Gorbunov, G.E.Notkin, Nuclear Fusion 9 (1979) S.1415

[5] M.Bornatici, Rijnhuizen I.R.80/023 (April 1980)

[6] F.Engelmann,M.Curatolo, Nuclear Fusion 13 (1973) S.497

[7] G.Bekefi, Radiation Prcesses in Plasmas J.Wiley,N.Y.1966

* see H.Renner, this conference

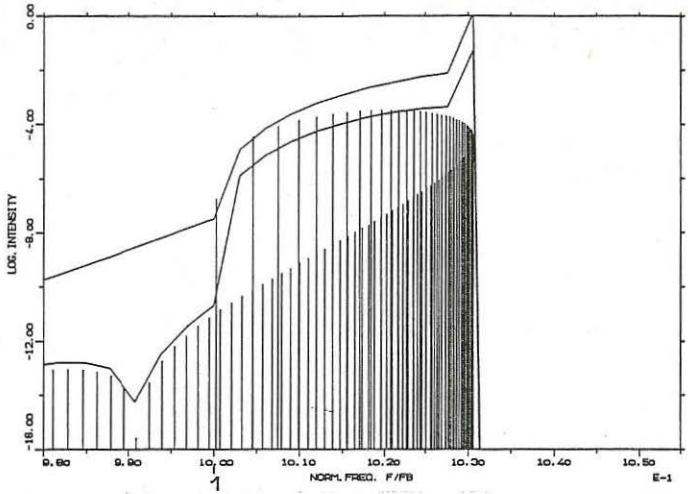

Fig.1: O.mode lines ξ for $\Theta = 70^0$ and frequency spectrum around a cyclotron harmonic FB for both modes; B-field = constant.

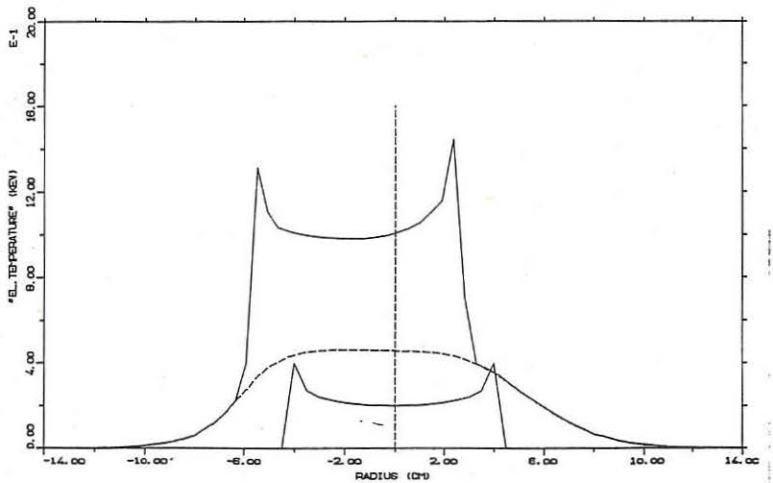

Fig.2: Computed profile (by $r \sim 1/F$ from the frequency spectrum). Lower curve : shape of the (arbitrarily chosen) suprathermal density distribution , upper one: the addition of the undamped suprathermal emission upon the thermal one (dashed).

EXPERIMENTAL DETERMINATION OF THE LOCAL HEAT CONDUCTIVITY COEFFICIENT $\chi_e(r)$ IN THE W VII-A STELLARATOR

H.J. Hartfuß, H. Maaßberg, M. Tutter, W VII-A Team*
Max-Planck-Institut für Plasmaphysik,
EURATOM Association, D-8046 Garching, FRG

ECRH Group**
Institut für Plasmaforschung der Universität Stuttgart
D-7000 Stuttgart 80, FRG

The local electron thermal conductivity coefficient $\chi_e(r)$ has been measured applying a modulation and correlation technique to the stellarator plasma of Wendelstein VII-A ($R = 2.0$ m, $a = 0.1$ m, $l = 2$, $m = 5$). The method is based on the fact that the power deposition of electron cyclotron heating (ECH) is locally well defined in the plasma centre. If the deposited power is modulated with proper frequency and amplitude, a heat wave is generated whose outward propagation is dominated by electron thermal conductivity and which is detectable by temperature sensitive diagnostics. Amplitude, $\Delta T_e(r)$, and time lag, $\Delta t(r)$ (or phase), relative to the generating signal as function of distance, r, to the plasma centre determine $\chi_e(r)$, the quantity of interest /1/.

We used a single gyrotron (70 GHz, 200 kW, 100 ms) for plasma build-up and heating. Its output power, P_{No}, was square wave modulated with amplitude ΔP_N after reaching quasistationary plasma parameters. The transient electron temperature, $T_e(r)$, has been determined at eight discrete radii, r_i ($i = 1...8$), on the high field side, $r < 0$ ($-a \leq r \leq +a$), of the plasma column by means of a multichannel heterodyne radiometer /2/ measuring the electron cyclotron emission (ECE).

The time lag $\Delta t(r_i)$ of the electron temperature modulation $T_e(r_i,t) = T_{eo}(r_i) + \Delta T_e(r_i)\cdot e^{i\omega t}$ was evaluated via Fourier transform of the cross-correlation function interconnecting the modulating signal and the response to it. Different modulation frequencies $\omega/2\pi$ between 100 and 1000 Hz and different types of discharges (see below) have been investigated.

The evaluation of the experimental data is based on the following theoretical model: In an axisymmetric geometry the balance equation for the electron energy W is used: $\partial W/\partial t = \mathrm{div}\, Q + P_N - P_L$, where the perpendicular heat flow Q is given by $n(r)\,\chi_e(r)\,\mathrm{grad}\,T_e(r)$ (n being the time independent electron density). P_L are the power losses via ion channel and radiation. All transport processes not related to the electron temperature gradient are neglected. Purely sinusoidal power modulation $P_N(r,t) = P_{No}(r) + \Delta P_N(r)\cdot e^{i\omega t}$ and electron temperature response as given above are assumed. Electron temperature dependence for both the heat conductivity coefficient $\chi_e(r)$ and the power loss P_L is considered by lowest order Taylor expansion in time. Since the temperature modulation is small, $\Delta T_e/T_{eo} \approx$ some per cent, the balance equation splits into an equation for the electron temperature $T_{eo}(r)$ (stationary balance) and an equation for the complex modulation amplitude $\Delta T_e(r)$ which is solved numerically and fitted to the experimental quantities to gain $\chi_e(r)$.

*, ** see H. Renner et al., this conference

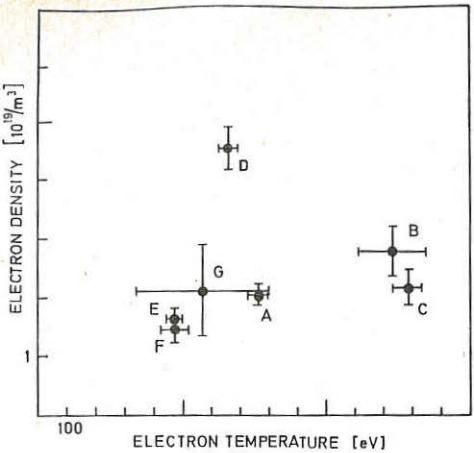

Fig. 1: The parameter range of the different types of discharges investigated.
Discharge A: $\iota < 0.5$, $I_p = -4$ kA, B: $\iota < 0.5$, $I_p = +4$ kA, C: $\iota > 0.5$, I_p = free, D: $\iota < 0.5$, I_p = free, E: $\iota = 0.2$, $I_p = -2$ kA, F: $\iota = 0.2$, I_p = free, G: $\iota < 0.5$, I_p = free.

Different types of discharges have been investigated to check the χ_e-dependence on rotational transform and shear and on the main toroidal field. Figure 1 gives central electron temperature and density for six different types and the corresponding changes during the discharges (bars). The changes are usually monotonic. Discharges A to F correspond to 2.5 T main field, first harmonic ordinary mode EC-heating. Type G is conducted at 1.25 T, second harmonic extraordinary mode ECH. Except in case D, the discharges are guided well below the cut-off density, $6.2 \cdot 10^{19}/m^3$ for A-F and $3.1 \cdot 10^{19}/m^3$ for G respectively, to avoid significant refraction of the ECH beam. It is a crucial experimental condition for the applicability of the modulation method that clear separation between the power deposition and the zone of observation is accomplished. In Wendelstein VII-A with plasma radius < 10 cm, this condition is difficult to fulfill. The power deposition profile is at least 5 cm wide, so heat wave propagation can be observed only between 3 and 8 cm in maximum. The electron temperature profile should have its gradient regime clearly outside the deposition zone and the electron density profile should, according to the model, be as broad as possible. In addition electron temperature and density should be high enough to assure high single pass absorption of the ECH beam to avoid wall reflections with subsequent boundary layer absorption.

The rigorous experimental demands are verified best with type A. The results are discussed in detail in reference /3/. Beyond that Figure 2 presents the results in comparison to theoretical results on the basis of neoclassical transport /4/, clearly demonstrating the usefulness of the method. Only an upper bound for the local transport coefficient can be derived at best from the other discharge types investigated. Only small

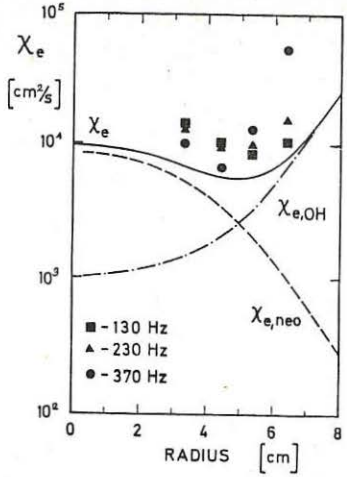

Fig. 2: χ_e-results obtained with type A discharge for different modulation frequencies in comparison to theoretical studies based on neo-classical theory, $\chi_{e,neo}$. An anomalous contribution as found in OH discharges, $\chi_{e,OH}$, is included. # 57829 - 57896.

time lag is found in type E and F discharges which is even decreasing for $r > 5$ cm due to incomplete single pass absorption followed by wall reflections and diffuse power deposition in the plasma boundary layers. Still stronger decrease is observed with type D because ECH beam refraction doesn't allow for localized deposition in the plasma centre. Discharges B and C have rather narrow electron temperature profiles with gradient regime not sufficiently separated from the deposition zone for clear conclusions.

Figure 3 gives the evaluation of discharge type G, ECH at 2nd harmonic X-mode. Unfortunately the discharge is not as stationary as types A-F. Both central electron temperature and density vary by more than a factor of two during the modulated heating phase. In addition they are connected with profile changes. The rather large discrepancy to the results evaluated from the stationary balance, based on the profiles as measured at the beginning of the modulated phase, may be due to these imperfect experimental conditions.

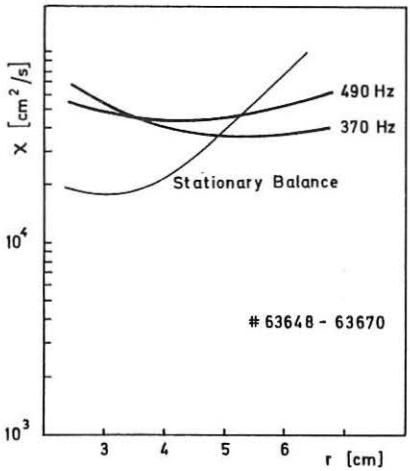

Fig. 3: $\chi_e(r)$ evaluated for a 1.25 T, type G, discharge heated with 2nd harmonic ECH. Included is the result obtained from the stationary balance.

REFERENCES
/1/ G.L. Jahns, S.K. Wong, R. Prater, S.H. Lin, S. Ejima, Nucl. Fusion 26 (1985) 226
/2/ H.J. Hartfuß, M. Tutter, Rev.Sci.Instr. 56 (1985) 1703
/3/ H.J. Hartfuß, H. Maaßberg, M. Tutter, W VII-A Team, and ECRH-Group, Nucl.Fus. 26 (1986), number 5
/4/ H. Wobig, paper TU-51, this conference.

CX-RECOMBINATION SPECTROSCOPY DURING NBI HEATING OF ECRH TARGET PLASMAS IN W VII-A STELLARATOR AND COMPARISON WITH A TRANSPORT MODEL

M. Kick, H. Ringler, F. Sardei, A. Weller, W VII-A Team*, NI Team**

Max-Planck-Institut für Plasmaphysik
EURATOM Association, D-8046 Garching, FRG
ECRH Group***
Institut für Plasmaforschung der Universität Stuttgart
D-7000 Stuttgart 80, FRG

Radiation in most of the Wendelstein VII-A plasmas has been dominated by oxygen impurities. In discharges that have been sustained by NB heating, starting from OH-target plasmas, beam injected oxygen along with some oxygen influx from the walls of the vacuum vessel has been shown to account for the observed radiation losses. In some particular cases also high Z radiation (Fe) was observed to yield some contribution to the radiation losses at late times during the discharge, when the electron temperature drops. These experimental results were summarized in /1/ and compared with transport calculations.

The knowledge of time history and radial distribution of the relevant ionization stages are thus of large interest, in particular in connection with numerical transport studies. In this paper we will report on measurements of time history and to some extent also on spatial information of O^{8+} and O^{7+} intensities.

The plasma under consideration starts out from an ECR (70 GHz) produced target plasma, which is further heated and sustained by NB injection ($\sim$ 750 kW) after the ECH power has been switched off.

Central densities up to 8 x 10^{13} cm^{-3} and electron temperatures between 300 and 600 eV, with ion temperature slightly above the electrons, have been achieved. (For a more detailed description of NB heating from ECR target plasmas see paper /2/ at this conference.) Figure 1 shows some parameters of such discharges, but with a second ECRH pulse applied in the late NB-injection phase. During the time interval shown, spectroscopic measurements of O^{7+} and O^{8+} will be compared with code simulations.

By injection of energetic neutral hydrogen atoms from a separate diagnostic injector (E_o = 26 kV, I_o = 6.5 A, species mix $E_o:E_o/2:E_o/3$ $\sim$ 20:30:50, half width $\sim$ 4 cm and Δt = 15 ms) highly excited O^{7+*} ions originate from CX-recombination ($H_o + O^{8+} \rightarrow H^+ + O^{7+*}$) /3/. Radiation from the $8^2H_{9/2} \rightarrow 7^2G_{7/2}$ transition at λ = 2976 Å was observed spectroscopically from the intersection volume between the line of sight of the spectrometer and the diagnostic beam. The intensity of this radiation is given by

$$B_\lambda^{CX} = \frac{1}{4\pi} \sum_{j=1}^{3} \langle\sigma v\rangle_j^\lambda \int n^{O^{8+}} n_j^H \, dl \qquad [\text{Photons/cm}^2 \text{ s sterad}]$$

where $\langle\sigma v\rangle_j^\lambda$ is the rate coefficient for excitation, j denotes the 3 beam components with density n_j^H and the integration is across the diameter of the diagnostic beam.

There is no temperature dependence in $\langle\sigma v\rangle$ and from n_e-profiles and line density measurements also n_j^H is calculated to show little variation throughout the beam cross-section. Therefore from the observed signal we can derive $\int n^{O^{8+}} dl$ as a function of time. Moreover since the n_e and T_e

profiles are flat within the beam cross-section with steep gradients outside, this line integral is also a measure of the behavior of the central density of n^{08+} and can be compared with a transport model.

On the other hand, the same transition is also observed with the diagnostic beam off. In this case it must be due to electron collisional excitation and thus this signal is proportional to the O^{7+} density

$$B_{\lambda}^{e-} = \frac{1}{4\pi} \int_0^L n_e(r)\, n(r)\, q(r)_{1s\to np}\, B\, dl \quad [\text{Photons/cm}^2\ \text{s sterad}]$$

where $q_{1s\to np}$ is the rate coefficient for electron collisional excitation, B the branching ratio and L the plasma diameter.
It is interesting to note that Doppler temperature measurements from the passive (electron excited) and active (beam excited) signal lead to the same ion temperature and support the interpretation of the signal as being due to electron excitation.

COMPARISON OF MEASUREMENTS WITH SIMULATIONS

The total soft X-radiation from the intrinsic impurities for this discharge type is shown in Fig. 2a. The increase of the central raditaion is described reasonably well by the O VII + O VIII radiation calculated with our neoclassical transport code SITAR /1/ with a 1 % oxygen beam contamination and a wall influx of O raising from 1.9×10^{18} to 4.7×10^{18} s^{-1} during the discharge (Fig. 2b). At the late stage of the discharge, however, the soft X-radiation is not correctly reproduced by the oxygen simulation. In order to reduce the discrepancy, high Z material has been included in the simulations for this discharge type (Fig. 2c). In fact, oxygen radiation cannot account for the drop of the soft X-radiation observed late in the discharge, as T_e decreases. In addition high Z material in low density neutral beam sustained discharges seems very likely, since local Fe-fluxes of about 2×10^{17} s^{-1} originating from sputtering by fast ions on lost orbits at the vacuum vessel wall have been measured earlier /5/. The code results of Fig. 2c were obtained with a Fe influx increasing from 1.9×10^{17} to 4.7×10^{17} s^{-1} during the discharge. The steep increase of the calculated O VII + O VIII radiation at $\simeq$ 105 ms is essentially a consequence of the T_e drop observed after switching off the ECH pulse. The related decrease of the O^{8+} density is clearly confirmed by CX-recombination measurements (active signal) mentioned above. The measured and calculated O^{8+} densities are shown in Fig. 3.

The time evolution of the electron excited passive signal for the same discharge type is shown in Fig. 4. The simulated signal has been obtained by using the equation for B_{λ}^{e-} given above with the electron density and temperature taken from Thomson scattering measurements, the rate coefficient from calculations by P.R. Summers /4/ and the O^{7+} densities from the transport simulations.

The time evolution of the signal is very well reproduced by the model up to 90 ms. The small discrepancy shown at later times is believed to be caused by the uncertainties in the electron temperature due to temperature interpolations between the measured temperature profiles.

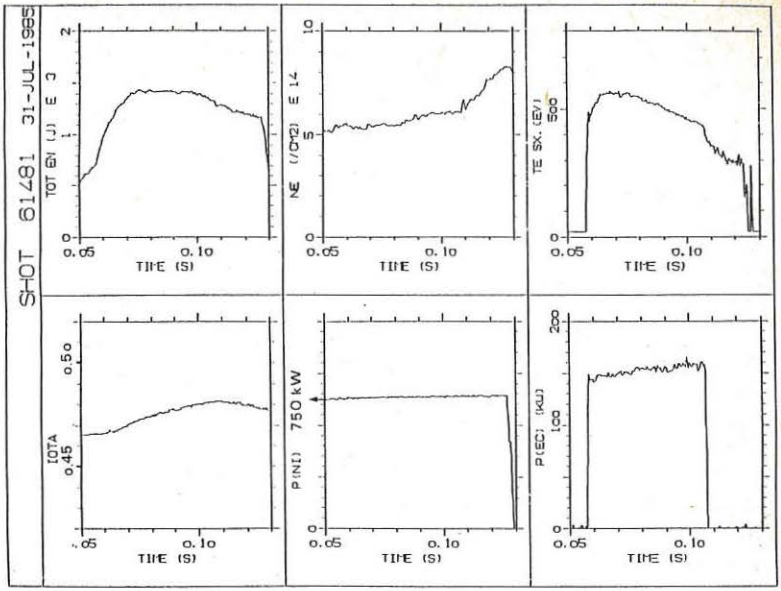

Fig. 1: Plasma energy, line integrated density, electron temperature, edge value of iota, neutral injection power and ECH power during the second ECH pulse (t $\simeq$ 58 - 108 ms).

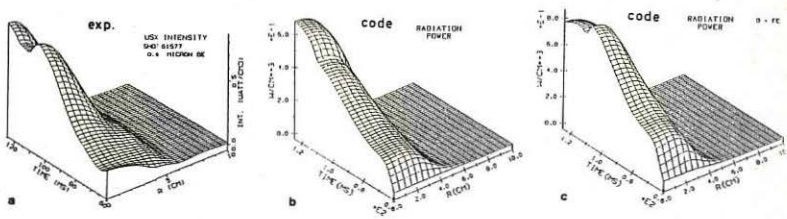

Fig. 2: a) Evolution of soft X-radiation for the NI+EC heated discharge shown in Fig. 1.
b) Code simulation with oxygen impurities and neoclassical transport fluxes
c) Same as b) but with additional iron impurities.

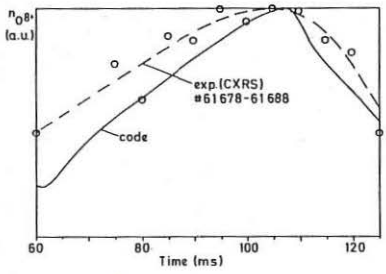

Fig. 3 Central O^{8+} density (a.u.) vs. time from active CXRS measurements in comparison with code calculations.

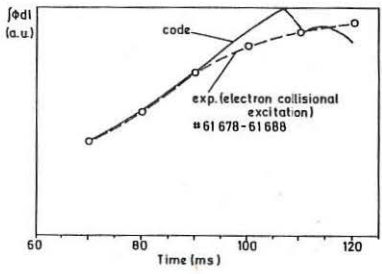

Fig. 4 Flux of O VIII (2976 Å) line intensity (a.u.) (electron excitation) vs. time in comparison with code calculations.

REFERENCES

/1/ Nuclear Fusion 25 (1985) 1593
/2/ Invited paper V. Erckmann, this conference
/3/ R.F. Fonck et al., PPPL-2067 (1983)
/4/ H.P. Summers, private communication
/5/ W VII-A Team, NI Group, 5th Int. Workshop on Stellarators, Vol. 1, CEC Brussels (1984) 259.

*, **, *** see H. Renner et al., this conference.

MAGNETIC FIELD STUDIES NEAR SEPARATRIX

E. Harmeyer, J. Kißlinger, H. Wobig and F. Rau

Max-Planck-Institut für Plasmaphysik, EURATOM Association
D-8046 Garching, FRG

Abstract

Vacuum magnetic fields are studied in the vicinity of the separatrix of modular Advanced Stellarator coil configurations with reactor dimensions. A modular divertor appears to be not feasible because of the complicated field structure. Rational ι-values inside of and near the plasma edge should be avoided. A system with comparatively small islands at $\iota = 5/11$ outside of the separatrix is seen to be relatively insensitive against a m = 1 perturbation and should allow the use of pumped limiters for edge control.

Introduction

In stellarators, the closed magnetic surfaces are separated from the region of outer open field lines by a usually well defined separatrix. It was often proposed to use this characteristic of the stellarator topology for a "natural" divertor, in order to achieve an edge control of the plasma. For toroidal systems with $\ell = 3$ modular non-planar coils, flux bundles of the separatrix region were found to encircle the coils at particular positions / 1 /, and the UWTOR-M fusion reactor / 2 / is designed with a modular divertor.

For modular Advanced Stellarators like the Garching experiment Wendelstein VII-AS, magnetic vacuum fields and also finite-β topologies / 3 / inside the separatrix were published so far. Details near and outside of the separatrix are of interest, in order to study the question of a modular divertor in such fields with reduced secondary currents. Vacuum fields of modular coil systems in fusion reactor dimensions are considered, having major radii of $R = 25$ or $20\,m$, and 6 coils in each of the 5 field periods. Figure 1 shows a schematic of such systems. In the first part of the paper, the spatial structure of the magnetic field outside of the separatrix is investigated numerically by following field lines. The second part concentrates on the presence of "natural" magnetic islands in the vicinity of the separatrix at rational values of the rotational transform, gives evidence of their removal by the fields of resonant currents, and shows effects of superimposed perturbation fields.

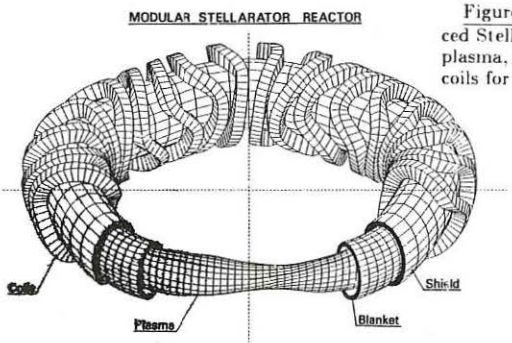

Figure 1: Schematic of a modular Advanced Stellarator, showing the contours of the plasma, of blanket and shield, as well as the coils for three of the five field periods.

Flux Bundles Outside of Separatrix

For a modular coil system similar to that of Figure 1 with $R = 25.5\,m$ and average radii of the coil centers, $r_c = 5.8\,m$, a number of 100 field lines is launched outside of the separatrix, at distances of 10 to 20 % of the average separatrix radius, $r_s \approx 1.6\,m$. (Starting points in 10 equally spaced toroidal planes within a field period, at 10 poloidal positions of approximately equal angular and locally different radial distance; integration step width small compared to the grid size of stored local field values). The intersection points of the field lines are marked on elliptically shaped outer surfaces. At a surface with average radius $r \approx 2 \cdot r_s$, the symmetry pattern of the starting points is still visible. The field lines merge at $r = 3.5\,m$, see top left of Figure 2, (abscissa = 1 field period, ordinate = 1 minor circumference). They show a reasonable concentration at $r = 3.8\,m$ (lower left part of the Figure), where 70 intersection points are obtained after 2 minutes CPU time of the Garching CRAY-1 computer. At $r = 5\,m$, one of the field line clusters is absent and 15 minutes CPU time are required for about the same number of intersections. Reversing the direction of integration, the pattern is mirror reflected as expected, but only 10 % more intersection points appear after a doubling of the CPU time. The lengths of the field lines for this case range between 3.5 and 100 times the circumference $2\,\pi\,R = 160\,m$.

In conclusion of this part: The initially poor field line concentration, their different lengths, and the change of the position of the intersection points when varying the aspect ratio of the boundary surfaces, makes such magnetic structures undesirable as to connect the plasma edge to divertor plates.

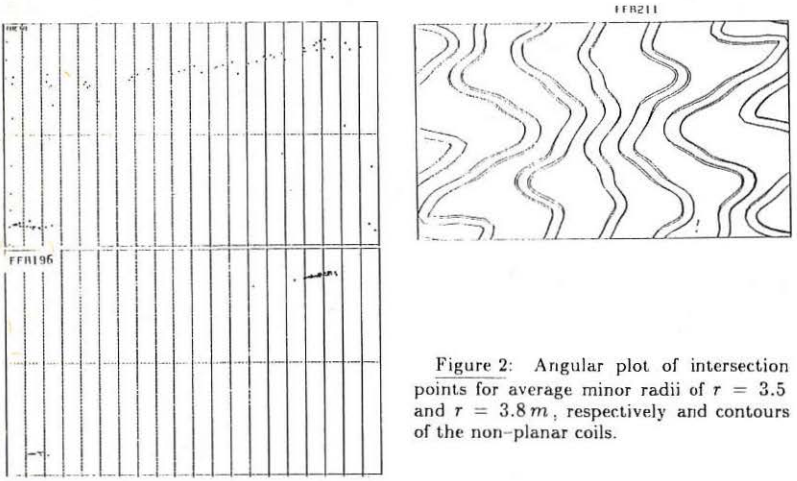

Figure 2: Angular plot of intersection points for average minor radii of $r = 3.5$ and $r = 3.8\,m$, respectively and contours of the non-planar coils.

"Natural" Magnetic Islands near Separatrix and Perturbation Fields

The Advanced Stellarator properties of the magnetic vacuum fields depend on the specific shapes of the coil bores and of the contours of the toroidal excursions. The coils provide a rotational transform ι which can be easily changed in the computations by a small variation of the coil aspect ratio. Systems with a low number of e.g. 6 coils per field period tend to show some negative shear. Already without the influence of external perturbations, "natural" magnetic islands can be seen near the plasma edge, at a rational value of the rotational transform $\iota = 5/N$, with integer $N = 9 \ldots 13$. Such islands were demonstrated / 4 / in the vacuum field studies for WVII-AS.

An example of 10 comparatively large islands is shown in the left part of Figure 3, for the toroidal positions of 0 and 1/2 field periods. In this particular case, outside of each X-point (O-point), further O-points (X-points) exist in an otherwise open field topology. In order to reduce the size of the natural islands, small currents outside of the islands and "resonant" with $\iota = 5/10$ were considered by A. Schlüter and W. Lotz[1]. These currents reduced the island size in the case of WVII-AS, at resonant $\iota = 5/10 \ldots 5/13$.

Following that approach, resonant currents are applied for the above example. Two current polygons are obtained by an outward projection of the inner O- and X-points, towards points at a radial distance of about 80 % of the separatrix radius, see insert of Figure 3. The whole chain of inner islands is removed by currents which introduce about 0.2 % of the average magnetic field at the position of the neighbouring island. The outer O-points are still present, see top of the right half of Figure 3. Increasing the currents in the same current polygons from 30 to 50 kA, removes the islands of a similar case at $\iota = 5/9$. In these two examples, the aspect ratio of the resulting configuration is approximately the same as that of a configuration with a neighbouring irrational value of the rotational transform.

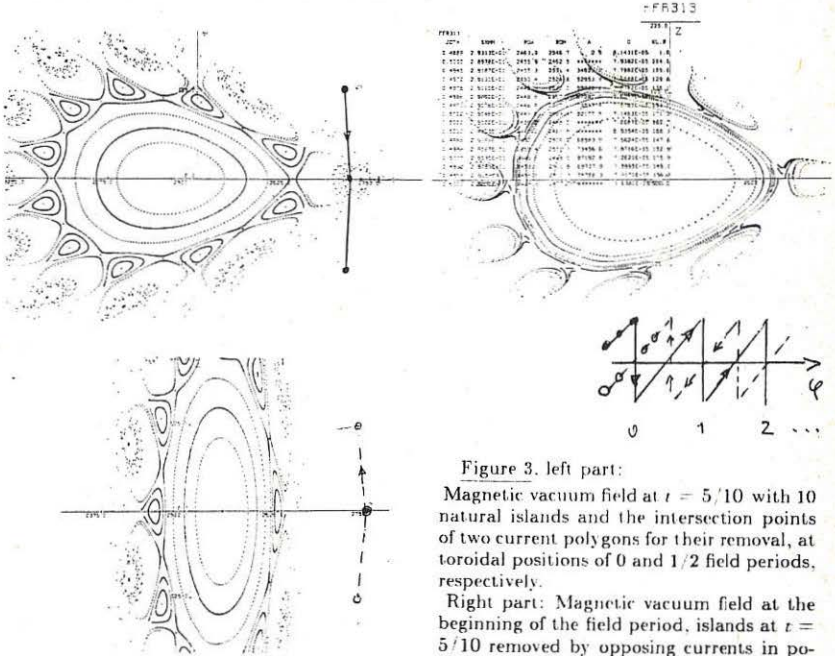

Figure 3, left part:
Magnetic vacuum field at $\iota = 5/10$ with 10 natural islands and the intersection points of two current polygons for their removal, at toroidal positions of 0 and 1/2 field periods, respectively.
Right part: Magnetic vacuum field at the beginning of the field period, islands at $\iota = 5/10$ removed by opposing currents in polygons as shown schematically in the insert

[1] W.Lotz and A.Schlüter :
private communication of their unpublished results for the fields of Wendelstein VII-AS

The effect of a homogeneous horizontal perturbation field is studied for the above configuration at $\iota = 5/10$, and for a different system, ASRA6C with $R = 20\,m$ and $r_c = 4.57\,m$. Whereas in the first case a homogeneous horizontal perturbation field $B_y/B = 4 \cdot 10^{-4}$ introduces a drastic reduction of the separatrix radius, ASRA6C with a prime number of 11 islands outside of the separatrix allows perturbation fields up to a value of 0.2 % of the average field $B = 5.3\,T$, at a small reduction of the separatrix radius, as shown in Figure 4.

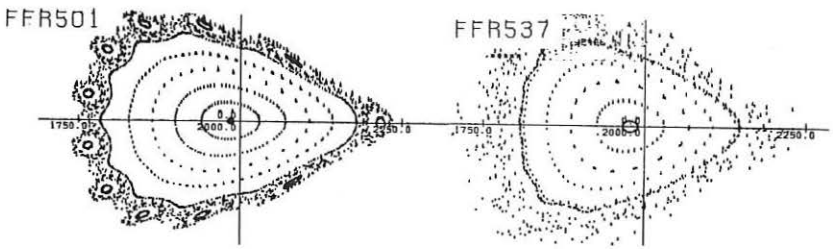

Figure 4: Magnetic vacuum field of ASRA6C showing 11 natural islands outside of separatrix at a value of $\iota = 5/11$, and effect of a homogeneous horizontal perturbation field $B_y/B = 0.2\%$ introducing a small reduction of the separatrix radius.

Summary and Conclusions

From the observed complicated structure of vacuum field lines outside the separatrix it appears that a modular divertor is not feasible in Advanced Stellarators as studied so far, unless the field topology could be changed by the action of further and yet unknown external currents. Magnetic islands at rational ι can be efficiently removed by small outer resonant currents, but the aspect ratio of the resulting configuration is not improved. Therefore, configurations at a neighbouring irrational rotational transform are preferred, avoiding inside and near the plasma edge rational $\iota = M/N$, with low integer values of M and N. Several such data sets are known. An example with comparatively small islands at $\iota = 5/11$ outside of the separatrix is seen to be relatively insensitive against a m = 1 perturbation and should allow the use of pumped limiters for edge control.

References

/ 1 / D. T. Anderson et al., Proc. 12^{th} Eur. Conf. Budapest, Vol. I, 465, 1985
/ 2 / B. Badger et al., UWTOR-M, Univ. of Wisconsin Report UWFDM-550, 1982
/ 3 / B. Brossmann et al., Proc. 9^{th} IAEA Conf. Baltimore, Vol. III, 141, 1982
/ 4 / J. Kisslinger et al., IPP Garching Report 2/259, 1982

RADIATIVE LOSS IN CURRENTLESS PLASMAS OF HELIOTRON E

S. Besshou, S. Morimoto, O. Motojima, H. Kaneko, K. Kondo, T. Mizuuchi, T. Mutoh, H. Okada, F. Sano, M. Sato, S. Sudo, Y. Takeiri, H. Zushi, T. Baba, K. Hanatani, M. Nakasuga, T. Obiki, A. Iiyoshi and K. Uo

Plasma Physics Laboratory, Kyoto University
Gokasho, Uji, Kyoto, Japan.

Abstract

This paper describes recent measurements on radiative loss in the Heliotron E currentless plasmas. A bolometer array with seven channels and wide angle bolometers are used to estimate the profile of total radiative loss. Electron cyclotron resonance heating (53 GH_z, 500 kW) and NBI (4 MW, 150 ms) produce and heat the currentless plasma simultaneously. In low density regime ($\bar{n}_e \leq 3 \times 10^{13} cm^{-3}$), steady state radiative loss power is 40 % - 60 % of estimated absorbed NBI power, where radiative loss at plasma boundary is dominant. In higher density regime ($\bar{n}_e \geq 5 \times 10^{13} cm^{-3}$), the central radiative loss often increases with time. Volume integrated radiative loss increases generally with absorbed neutral beam power.

1. Introduction

The Heliotron E device (major radius R=2.2m average minor radius of plasma $\bar{r}_p$=0.2m) is an asymmetric toroidal system with large rotational transform and shear [1,2]. The radiation losses of the plasma depend strongly on the heating method (NB or ECRH). In the NB-heated currentless plasma, the total radiation losses increase up to 40~80 % of absorbed NB power, thus often effecting on total energy balance. This paper describes further development of bolometric measurements in Heliotron E after the previous preliminary report [3].

2. Bolometers and Experimental Setup.

The metal-resistor bolometers (10 kΩ, 10 μm stainless steel absorber) are of the type described in Ref. [4]. Figure 1 shows the arrangement of a bolometer array which looks the plasma horizontally. The time resolution is about 3 msec and the detection limit in plasma discharge is approximately 0.2 $mW \cdot cm^{-2}$ at a 300 H_z band width. As the 7-channel system is mounted at a position (unperturbed porthole far from NB, ECH and gas puff) which is assumed to be representative of the plasma, the total radiation power and,

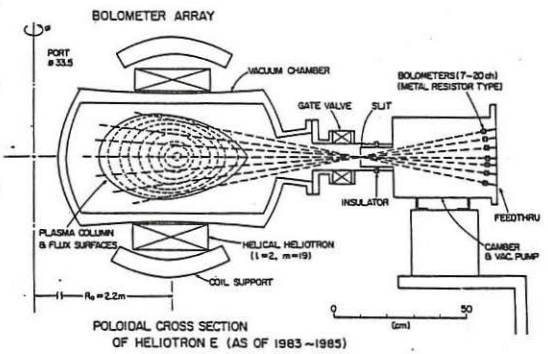

Fig.1 Arrangement of bolometer array in HELIOTRON E

local radiation levels are derived from measurements. A local emissivity is obtained through assumptions on the geometry of toroidal isoemissivity flux surfaces.

The other bolometers are also set in toroidally separeted positions(a bolometer array in three vertical chords, and two wide angle 2π bolometers at wall). These bolometers are necessary to find both toroidal and poloidal asymmetry of heat flux to wall. The wide angle 2π bolometers have faster time resolution (≤1 ms) with higher heat flux to detect rapid energy loss to walls [3].

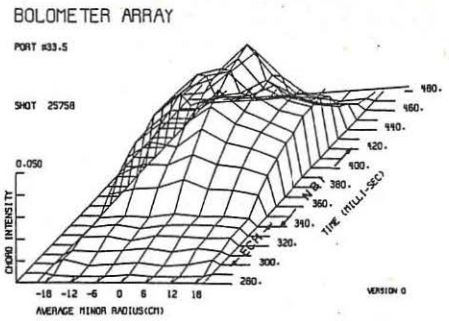

Fig. 2(a) Chord intensity of bolometers in low density ECH+NBI case.

The bolometers with thin nickel resistor and SiO_2 insulator are reliable in high hard x-ray dose in Heliotron E($\leq 10^4$ rad, $\leq$ 1 rem/shot). Bolometer systems have measured total radiative loss power(VUV photons and neutral particles) in currentless plasmas during 1983 - 1985.

3. Results

3.1 Radiation loss in low density case($\bar{n}_e = (2\text{-}3)\times 10^{13}$ cm^{-3})

Figure 2(a) shows the chord intensity of bolometer array in currentless ECH + NBI (3 MW in port, $H^0 \rightarrow H^+$) at high field 1.9 T. Figure 2(b) is the power signal of bolometers. Figure 2(c) is the profile of emissivity after inversion. At the start of NBI (t=360ms) emissivity is high at plasma boundary. During NBI central radiation gradually increases higher with time. In this low density case, however, total radiation loss is not severe for total energy confinement. A long pulse (~150msec) NBI heating is feasible. Figure 3 shows the total radiative loss and plasma parameters. Total radiation is about 450kW. Electron density increases with time due to fueling of NBI and internal energy does not saturate.
The total radiative loss is 50% of calculated absorbed NBI power, 900 kW. A 2πbolometer also indicates 450-550 kW of total radiation independently. Central emissivity,0.3 W cm^{-3} is not severe in central power balance. However total radiation becomes volume loss(flat profile) during NBI.

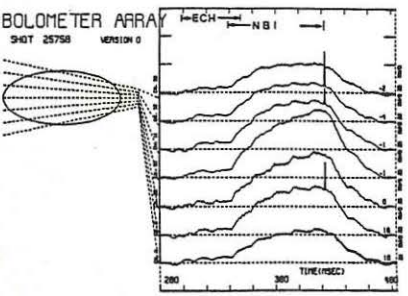

Fig. 2(b) Power signals of bolometers.

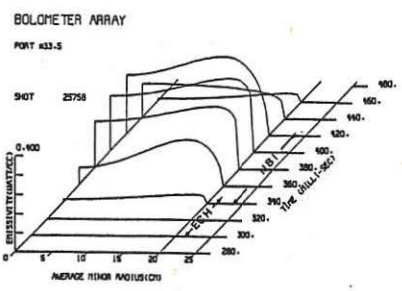

Fig. 2(c) Profile of emissivity.

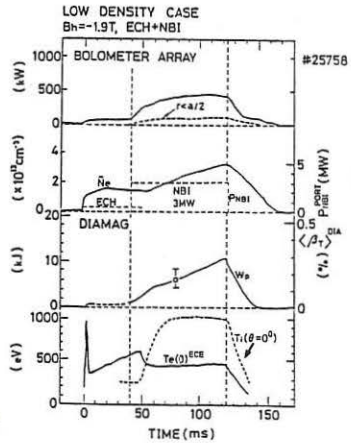

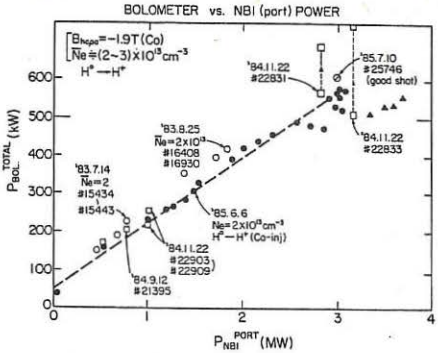

Fig.3(b) Total radiative loss vs. NBI port power in low density and high field

Fig.3(a) Plasma parameters in low density case. B_h=1.9 T.

Shine through power is 50%-60% of NBI port through power in this low density case. Three neutral beam lines, BL-2($\theta=28^0$), BL-3($\theta=0^0$, perpendicular) and BL-5($\theta=0^0, 11^0$) have nearly perpendicular injection angles. Impurities(Fe) from beam dumper(stainless steel) can be the source. Internal energy by diamagnetism[5] increases up to 10 kJ. Steady state temperatures, Ti($\theta=0$)=1000 eV and Te(0)=450 eV, are observed. Figure 3(b) shows the total radiative power vs. NBI port power in low density case. Data points include typical shots in 1983-1985 year after sufficient titanium gettering to wall. Detected bolometric power is almost in proportion to NBI port power. Considering that calculated absorbed power is 30%-40% of NBI port power, about 50% of total absorbed power is radiated in low density regime.

3.2 Radiation loss in high density case ($\bar{n}_e$=5x10^{13}cm^{-3})

Radiative loss in high density currentless plasma often shows the accumulation of impurities at plasma center. Figure 4(a) shows the profile of emissivity in ECH+NBI (2.6MW) at average density 5x10^{13}cm^{-3}. The emissivity at plasma center increases with time up to about 0.8MW·cm^{-3}, which is about half of deposited power of NBI. Figure 4(b) shows the total radiative loss power vs. time and plasma parameters. The total radiation increases up to 750kW (about 68% of absorbed NB power), where absorbed NB power, P_{abs}, is estimated by the decay of internal energy ($-\frac{\partial W_p}{\partial t}$ =1.1MW). In this case, central radiation within half a radius increases linearly with time.

The bolometric central chord intensity increases linearly with time, which is well correlated with the central chord of the soft x-ray emission and the intensity of the FeXVI line. VUV spectroscopy shows that radiation from iron impurity amounts to 40% of the bolometer power. Poloidal magnetic fluctuation often appears when stored energy exceeds about 15 kJ at 1.9T. The increase of impurity source with density & stored energy is possible.

3.3 Radiation loss in low field (B_h=0.94T) and high density case ($\bar{n}_e \geq 5\text{x}10^{13}\text{cm}^{-3}$).

Radiation losses in low field case have severe effect on plasma energy.

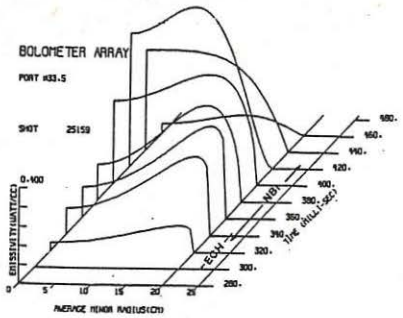

Fig. 4(a) Profiles of emissivity in high density ECH+NBI at 1.9T.

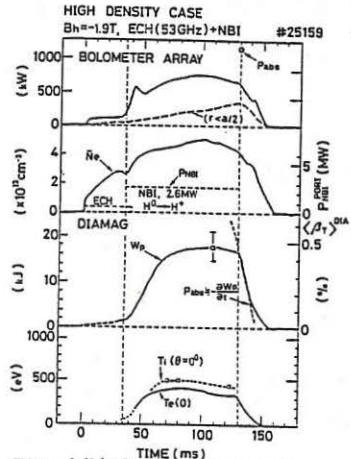

Fig. 4(b) ECH+NBI at 1.9 T.

Figure 5 shows the total radiative loss power vs. time and plasma parameters. Electron cyclotron resonance at 2nd harmonics produces hydrogen plasma and total 3.6MW NBI power heats plasma further. The density increases up to $6\times10^{13}cm^{-3}$ with gas puffing. When total NB power (3.6MW) is injected through ports, total radiative loss increases sharply with time. Considering that effective absorbed NB power is about 500kW from $(\partial W_p/\partial t|_{t=100ms})$ the increment of radiation loss (400-500kW) during t=100ms~120ms is almost equal to absorbed NB power. Energy loss to wall is often observed by a 2π bolometer and ion saturation current within 1 msec after onset of spikes in poloidal magnetic field (about 0.5-1% at 20kHz). Thus the MHD activity is one of the candidates for radiation enhancement.

Titanium gettering to both walls and NB ion sources is effective, but not sufficient to reduce impurity (F_e, and O). Further reduction of impurity radiation is necessary to study MHD property in currentless high density plasmas.

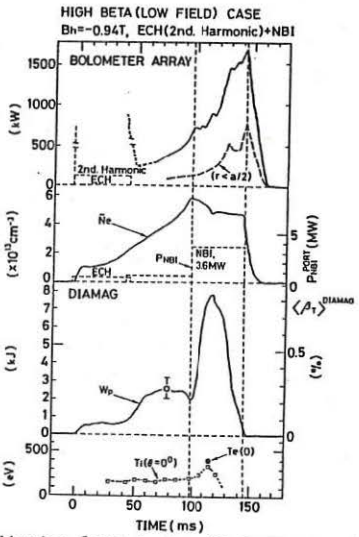

Fig. 5 Radiative loss in low field(0.94 T)

References

[1] K. UO, A. Iiyoshi, et al. Nucl. Instr. and Meth. 207 (1983) 151
[2] A. Iiyoshi, M. Sato, O. Motojima, et al. Phys. Rev. Lett. 48 (1982) 745
[3] S. Besshou, S. Morimoto, et al. Nucl. Fusion 26 (1986) 114
[4] S. Besshou, S. Morimoto, et al. Japanese J. App. Phys. 23 (1984) L 839
[5] S. Besshou, C. E. Thomas, et al. PPLK-R-5(Plasma Physics Lab. Kyoto University Report) (Dec. 1985)

ECRH EXPERIMENT ON HELIOTRON E

M. Sato, H. Zushi, O. Motojima, H. Kaneko, K. Itoh, S. Sudo,
T. Mizuuchi, K. Kondo, S. Besshou, M. Iima, S. Kobayoshi,
A. Iiyoshi, K. UO
Plasma Physics Laboratory, Kyoto University, Gokasho, Uji, Japan.

1. Introduction

The currentless plasma, produced only by electron cyclotron resonance heating, has been developing in Heliotron E device[1),(2)]. The steady state plasmas can be obtained up to the average electron density of $3 \times 10^{19} m^{-3}$, which is close to the ordinary mode cutoff density for the fundamental resonance of 53.2 GHz, by increasing the microwave output power up to 500 kW level. The electron temperatures are 1.2 to 0.7 keV depending on the electron densities. The microwave absorption efficiencies are 50 to 70 % in average. The energy confinement properties are now under study.

2. Experimental results

The microwave are injected into Heliotron E vacuum chamber with TE_{02} mode. The magnetic field is 1.9T at the plasma center. The rf power is varied from 160 kW to 500 kW by changing the numbers of gyrotrons. Fig. 1 shows a typical example of temporal developments of line average electron density and electron and ion temperatures.

These parameters are kept constant during rf pulses. The bolometric and soft X ray signal intensities are also constant at the flat top values. As the flat top times are much longer than the decay times of electron and ion temperatures, we might expect that steady state plasma can be maintained only by electron cyclotron resonance heating in the helical

systems such as heliotrons and stellarators without any increase of impurities.

The radial profiles of the electron densities, electron and ion temperatures are measured by FIR and 2 mm microwave interferometers, ECE and Thomson scattering and neutral particle analyzer respectively. The electron density ($N_e(r)$) is flat for the average density of 2.5 x $10^{19}m^{-3}$. At the lower density it becomes to the hollow profiles. Fig. 2 a and b shows Te(r), Ti(r) and Ne(r) for the higher (Ne = 2.5 x $10^{19}m^{-3}$) and the lower (Ne =0.6 x $10^{19}m^{-3}$) density cases. The internal energy of the electron and ion components are calculated by the integration ($We,i \propto \int_0^r N_e T_{e,i} \gamma dr$). The rf energy deposition profiles are estimated from the electron energy decay time ($\tau_{Ee\ decay}$), if we assume that it does not change between rf pulse and just after the pulses. The total rf absorption efficiencies are almost in 50 to 70 %, depending on electron temperature and average density. Less than one third of the absorbed rf power is deposited inside a half radius of the plasma. The profile is flatter than that of expected by the single pass ray tracing calculation for TE_{02} mode injection.

§3. Energy confinement

The central electron temperatures (Te(0)) are plotted to the density normalized input power (P_r/Ne) in Fig. 3. The heating rate becomes small as P_{rf}/Ne increases. The electron components are in the plateau region at near the plasma center ($r/a < 0.2$). The dotted line in the figure illustrates the values $Te(0) \propto (P_{rf}/Ne)^{\frac{2}{5}}$. On the other hand, both electrons and ions are in trapped particle region in the radius $0.2 < r/a < 0.8$. The more detailed energy confinement property is now under study from the view point of neoclassical theories.

References

(1) K. Uo et. al., 10th European Conf. on Cont. Fusion and Plasma Phy., Moscow (1981), E-1

(2) A. Iiyoshi, et. al., Phy. Rev. Lett. (1982), Vol. 48, 11, 745.

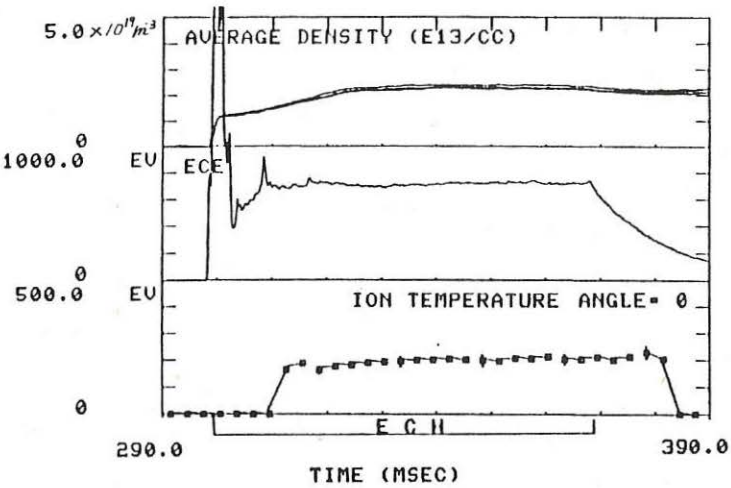

Fig. 1 Tempolal behaviors of $\bar{N}e$, Te(0) and Ti(0)
B_o = 1.9T, $P_{rf} \simeq$ 500 kW D_2 gas

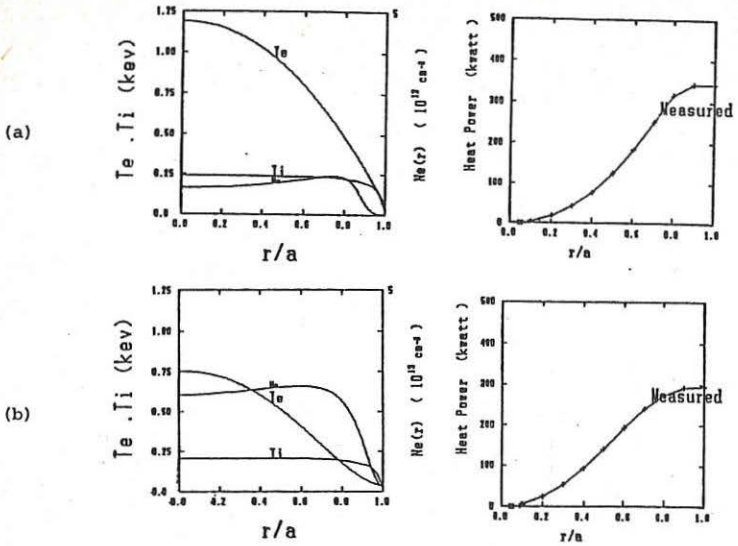

Fig. 2 Radial profiles of Ne(r), Te(r) and Ti(r) and absorbed power.

(a) $\bar{N}e = 0.6 \times 10^{19}\bar{m}^3$ (b) $\bar{N}e = 2.5 \times 10^{19}\bar{m}^3$

$B_o = 1.9T$, $P_{rf} \simeq 500$ kW D_2 gas

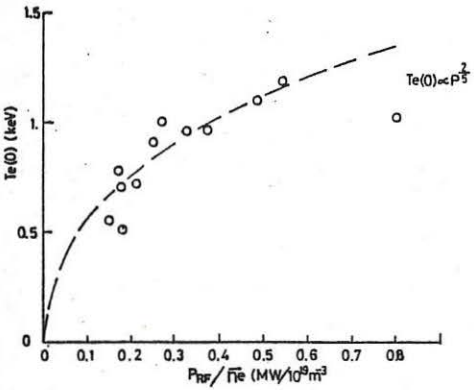

Fig. 3

Te(0) U.S. $P_{rf} / \bar{N}e$

$B_o = 1.9T$

$P_{rf} = 150 \sim 500$ kW

$\bar{N}e = 1.0 \sim 2.5 \times 10^{13}\bar{m}^3$

Alternative Confinement Schemes

STATIONARY FIELD PROFILES AND PLASMA CONFINEMENT IN RFP CONFIGURATIONS

V. Antoni, M. Giubbilei, P. Martin, D. Merlin,
S. Ortolani, R. Paccagnella, M. Valisa

Istituto Gas Ionizzati del C.N.R. - Associazione Euratom-CNR
Via Gradenigo, 6/a - 35131 Padova (Italy)

In the $q < 1$ Reversed Field Pinch (RFP) configuration both the poloidal and the toroidal magnetic field components vary across the plasma minor radius forming a high shear distribution with q ranging from typically $\approx 2a/3R$ on the axis to $\approx -a/4R$ at the plasma edge. The configuration is sligthly affected by the pressure since $(J_\perp/J_\parallel) \approx \beta \approx 0.1$ and then the magnetic field distribution is essentially characterized by $\mu = \mu_o (J_\parallel/B)$. Theoretically [1] μ should be uniform but experimentally μ decreases with minor radius and is small or zero at the edge. This is because plasma confinement and wall interactions require a cold edge plasma where little current flows. It has been found that the experimental distributions [2] are well described by μ radial profiles of the form $\mu = \mu(o)\left[1 - (r/a)^\alpha\right]$. Therefore two useful quantities are introduced to parametrize the equilibrium configurations: the on axis q value which is related to $\mu(o)$ by $q(o) = 2/R\mu(o)$ and α which characterizes the width of the parallel current density distribution ranging between $2 < \alpha < 8$.

Varying these parameters, an ideal and resistive MHD stability analysis of these profiles with $\beta = 0$ has been carried out. A completely stable region for both ideal and resistive current driven modes has been found. The resulting stability boundaries are shown in fig. 1 in terms of q(o) and q(a). The stable region is delimited by internal modes (with resonant surfaces inside the $q = q(o)/2$ surface) and external modes (with the resonant surface in the $q < 0$ region). In the same figure are also reported the experimental values of q(o) and q(a) showing that RFP configurations lie typically in the stable region below the uniform μ theoretical limit and close to the resistive internal modes boundary. In this way it is found that the external modes are not very significant in that they arise in conditions which are seldom produced experimentally. On the other hand it can be seen that a lower limit exists on q(o) as $q(o) > 2a/3R$ associated to the appeareance of $m = 1$ internal resistive unstable modes. This limit on q(o) was previously suggested from experimental considerations [3] and can be interpreted as an upper limit on the on axis current density as $J_o \leq 3B_o/\mu_o a$. Although on average the experimental profiles are stable to current driven modes resistive diffusion tends to destabilize the configuration leading to lower q(o) by peaking the current distribution on axis. A particular example, often realized in experiments, is that of sustained discharges where both the plasma current and the toroidal magnetic flux are constant in time. With these boundary

conditions resistive diffusion would lead to a decrease in q(o) (due to the increase of the current density on the axis and the decrease of the magnetic field). When q(o) drops below a critical value, $q \gtrsim 2a/3R$, the internal modes are excited and these modes are probably responsible for the current redistribution which restores the initial tearing mode stable configuration and so forth in a cyclic fashion. In fig. 2 is reported the experimental behaviour of q(o) measured by magnetic probes inserted in a low current low temperature plasma. Similar large and periodical oscillations with frequencies in the range $5 < f < 10$ KHz are found in externally measured quantities, as shown in fig. 3 for SXR signals, for a higher temperature discharge. The amplitude of these oscillations were found [3] to increase as a function of the reversal of the toroidal field but it was suggested that, although with lower amplitude they are always present in the plasma.

On the other hand RFP discharges are always characterized by a persistent turbulent activity which in normal conditions, is comparable to the coherent activity occuring in the central region. This background for magnetic fluctuations has a relatively high intensity ($b/B \gtrsim 1\%$ at $I_\phi \gtrsim 100$ kA) and it does not show a clear time periodicity. On ETA-BETA II it has been found that these fluctuations have correlation lengths $\lambda_\perp \leq a/2$, $\lambda_\parallel > a$. They show essentially $m = 0$ and $m = 1$ poloidal components and the intensity is peaked around the reversal surface [4]. This turbulent background is commonly referred to the competition of many resistive modes allowed by the low q configuration [5] as suggested by the finite β MHD stability analysis.

The ultimate effect on the plasma of these modes have been studied by a field line tracing code. The experimental spectrum and amplitude of these magnetic fluctuations result in ETA-BETA II in a wide stochastic region in the plasma as shown in fig. 4. The related magnetic diffusion coefficient D_M has been computed and the estimate of the electron thermal diffusivity, $\chi^e = D_M v^e_{th}$, gives a typical value for ETA-BETA II of $\chi^e \gtrsim 50 \div 100$ m^2/sec corresponding to a confinement time $\tau_e \leq 100$ μsec in good agreement with the experimental value.

The stochastic region is due to the combination of many $m = 1$ and $m = 0$ modes and practically extends up to the wall. However in the region between the wall and the reversal surface the edge effects as field errors and impurity release are dominant. Then, in analogy with the tokamak [6], it can be distinguished a plasma wall interaction edge region which extends between $q(a) < q < 0$ and a confinement region defined by $0 < q \lesssim q(o)/2$. While the edge region depends on the different experiments and is essentially determined by their technological features, the intermediate region is related to the nature of the RFP confinement. It has been observed that also adding the internal modes which periodically occur in the central region, the thermal diffusivity in the confinement region is slightly affected.

The thermal diffusivity has been computed from the plasma power balance in stationary conditions using the experimental RFP profiles and assuming that the dominant energy loss is due to heat transport. The typical values

found in the confinement region are quite insensitive to the detail of the profiles and are typically at least an order of magnitude higher than the ion neoclassical value, in good agreement with the stochastic model.

CONCLUSIONS

The MHD stability analysis shows that q(o) is limited in RFP, as in tokamaks, by current driven modes resonant in the central region of the plasma which restore the current distributions when a critical value is exceeded.

On the other hand the persistent turbulence typical of a RFP turns out in a wide stochastic region in the outer part of the plasma and transport, in present experiments, is well described by stochastic processes. Thus, in analogy with the tokamak, 3 regions can be identified for the RFP as shown in fig. 5:

a) a central region, with $(q(o)/2) < q \lesssim q(o)$, where periodical oscillations dominate ultimately limiting the on axis current density and leading to a lower q(o) limit as $q(o) > 2a/3R$;
b) an intermediate region $0 < q \lesssim q(o)/2$ completely stochastic, almost insensitive to the other regions and more related to the turbulent nature of the RFP;
c) an outer region $q(a) < q < 0$ where plasma-wall interactions, atomic processes and edge phenomena are dominant.

REFERENCES

[1] J.B. TAYLOR, 5th International Conference on Plasma Physics and Controlled Nuclear Fusion Research, Tokyo (Japan) 1974, IAEA, Vienna (1975), Vol. 1, p. 161.

[2] S. ORTOLANI, in Twenty Years of Plasma Physics, World Scientific Publishing Philadelphia, USA (1985), p. 75.

[3] V. ANTONI, S. ORTOLANI, 12th European Conference on Controlled Fusion and Plasma Physics, Budapest 1985, p. 582.

[4] V. ANTONI, S. ORTOLANI, Plasma Physics, 25, (1983) 799.

[5] B.B. KADOMTSEV, 6th International Conference on Plasma Physics and Controlled Nuclear Fusion Research, Berchtesgarten (West Germany) 1976, IAEA, Vienna (1977), Vol. 1, p. 555.

[6] P.H. REBUT, M. BRUSATI, Plasma Physics, 28, (1986) 113.

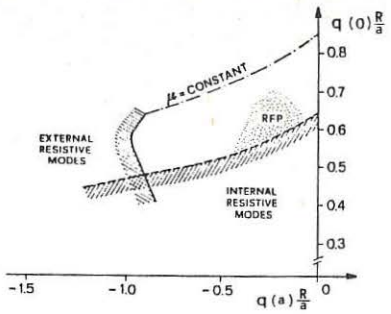

Fig.1

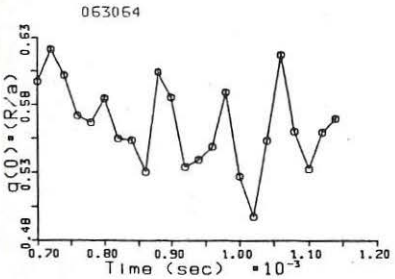

Fig.2

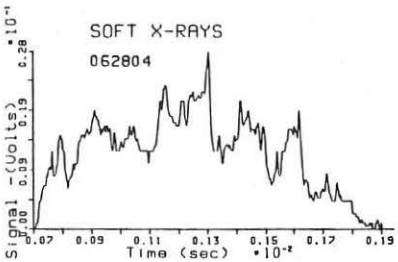

Fig.3

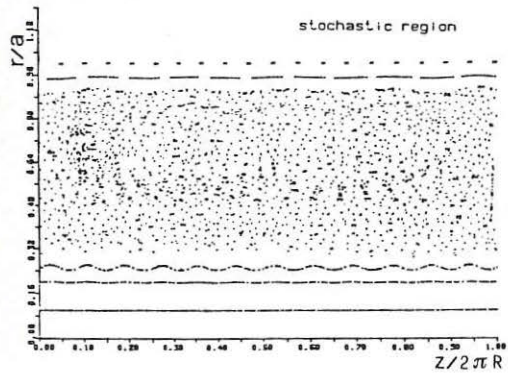

Fig.4

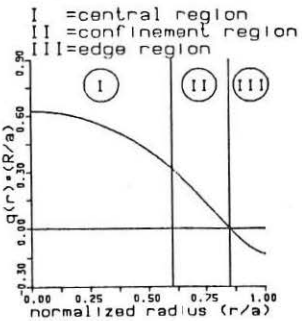

Fig.5

EQUILIBRIUM AND STABILITY OF A REVERSED FIELD PINCH WITH A RECTANGULAR CROSS-SECTION OF THE TORUS

J.W. Edenstrasser, University of Innsbruck, Austria

W. Schuurman, Association Euratom-FOM, FOM-Instituut voor Plasmafysica, Rijnhuizen, Nieuwegein, The Netherlands

Introduction

Present-day RFP-experiments usually have a circular cross-section. In the paper we set out to investigate whether elongated cross-sections might be favourable to stability.

The model consists of a plasma in the force-free Taylor state $\nabla\times\mathbf{B} = \mu\mathbf{B}$, surrounded by a perfectly conducting torus with a rectangular cross-section. Special solutions of the force-free equation have been known for some time. The case with no hole in the torus (cylindrical spheromak) has been considered e.g. in Ref. [1]. The toroidal spheromak (zero toroidal field at the boundary) was treated in Ref. [2]. We generalize the results of Ref. [2] to the case of a non-vanishing, possibly reversed, toroidal field at the rectangular boundary, in order to make them applicable to belt pinches and reversed-field (RFP) configurations. The general axisymmetric equilibrium solution (m=0) of the force-free equation with eigenvalue μ is constructed. The stability of this axisymmetric state is then determined by the statement that if a perturbed solution of $\nabla\times\mathbf{B} = \mu^*\mathbf{B}$ has an eigenvalue μ^* that is less than μ, the axisymmetric equilibrium is unstable. The F-θ-diagram and its dependence on aspect ratio and elongation of the torus is also discussed.

Solution of $\nabla\times\mathbf{B} = \mu\mathbf{B}$ for a torus with rectangular cross-section

The solution of $\nabla\times\mathbf{B} = \mu\mathbf{B}$ in cylindrical coordinates (r,θ,z) can be represented by

$$\mathbf{B} = \mathbf{e}_z \times \nabla\psi + \frac{1}{\mu}\nabla\times(\mathbf{e}_z\times\nabla\psi) \ , \tag{1}$$

where ψ is determined by the scalar Helmholtz equation

$$\Delta\psi + \mu^2\psi = 0 \ . \tag{2}$$

For the components of $\mathbf{B}$ we hence obtain

$$B_r = -\frac{1}{r}\frac{\partial\psi}{\partial\theta} - \frac{1}{\mu}\frac{\partial^2\psi}{\partial r\partial z} \ ; \ B_\theta = \frac{\partial\psi}{\partial r} - \frac{1}{\mu r}\frac{\partial^2\psi}{\partial\theta\partial z} \ ; \ B_z = -\frac{1}{\mu}\left(\frac{\partial^2\psi}{\partial z^2} + \mu^2\psi\right) \ . \tag{3}$$

We consider a force-free plasma enclosed by a perfectly conducting toroidal shell with rectangular cross-section of height b, width a, and major radius R. We choose the centre of coordinates such that the appropriate boundary conditions become

$$B_z(z=0,b) = 0 \quad \text{(Eq. (4.1))} \ ; \ B_r\left(r = R \pm \frac{a}{2}\right) = 0 \ . \quad \text{(Eq. (4.2))}$$

The axisymmetric solution of Eqs. (2),(3) with boundary conditions (4.1) is

$$B_r = -\frac{1}{\mu}\sum_n k_n k'_n Z'_o(k'_n r)\cos ny - \frac{c}{r}\cos \alpha y + \frac{d}{r}\sin \alpha y \ ;$$

$$B_\theta = \sum_n k'_n Z'_o(k'_n r)\sin ny + \frac{c}{r}\sin \alpha y + \frac{d}{r}\cos \alpha y \ ; \qquad (5)$$

$$B_z = \sum_n \frac{k_n^2 - \mu^2}{\mu} Z_o(k'_n r)\sin ny \ ,$$

where we have defined

$$k_n = \frac{n\pi}{b} \ [n=1,2,\ldots] \ ; \ k'_n = (|\mu^2 - k_n^2|)^{\frac{1}{2}} \ ; \ \alpha = \frac{\mu b}{\pi} \ ; \ y = \frac{\pi}{b} z \ [y\varepsilon(0,\pi)] \ . \qquad (6)$$

$Z_o(k'_n r)$ is a linear combination of the ordinary Bessel functions J_o, Y_o if $\mu^2 > k_n^2$ and of the modified ones if $\mu^2 < k_n^2$. Primes denote differentiation with respect to the argument.

Special axisymmetric (spheromak) solution

For $c = d = 0$ particular solutions exist satisfying boundary conditions (4.2) that lead to the eigenvalue equation

$$J_1(s)\,Y_1(\gamma s) - J_1(\gamma s)\,Y_1(s) = 0 \ , \qquad (7)$$

with $s = k'_n (R - \frac{a}{2})$; $\gamma = \frac{1+\varepsilon}{1-\varepsilon}$; $\varepsilon = \frac{a}{2R}$ (inverse aspect ratio) .

Thus, we obtain the discrete eigenvalue spectrum for μ

$$\bar{\mu}_{\nu n} = \mu_{\nu n}\frac{a}{2} = \varepsilon\left\{\left[\frac{s_\nu(\varepsilon)}{1-\varepsilon}\right]^2 + \left(\frac{n\pi}{2\varepsilon E}\right)^2\right\}^{\frac{1}{2}} , \qquad (8)$$

where $s_\nu(\varepsilon)$ is the ν-th zero of (7) and E is the elongation. In this solution the toroidal field at the boundary vanishes, it thus corresponds to a drum-shaped spheromak with a central hole.

General axisymmetric (RFP and belt pinch) solutions

If $c,d \neq 0$, we must expand $\cos \alpha y$ and $\sin \alpha y$ in a $\cos ny$ series in the interval $(0,\pi)$, before applying the boundary condition (4.2). This does not lead to an eigenvalue equation for μ but to a set of inhomogeneous equations for a_n, b_n in the linear combination $Z_o(k'_n r) = a_n J_o(k'_n r) + b_n Y_o(k'_n r)$. The result is

$$d = c\,\frac{\sin \alpha\pi}{1 - \cos \alpha\pi} \ ; \ a_{2n} = b_{2n} = 0 \ ; \qquad (9)$$

$$a_{2n-1} = Q_n\left\{\frac{Y'_o(d_n^-)}{1+\varepsilon} - \frac{Y'_o(d_n^+)}{1-\varepsilon}\right\} \quad b_{2n-1} = Q_n\left\{\frac{J'_o(d_n^+)}{1-\varepsilon} - \frac{J'_o(d_n^-)}{1+\varepsilon}\right\} ,$$

where we have defined

$$Q_n \equiv c\,\frac{4\alpha^2 \sin\alpha\pi}{1-\cos\alpha\pi}\;\frac{\{J_o'(d_n^+)\,Y_o'(d_n^-) - J_o'(d_n^-)\,Y_o'(d_n^+)\}^{-1}}{(2n-1)\,\{\alpha^2-(2n-1)^2\}\,d_n}\,, \tag{10}$$

$$\text{and}\quad d_n^{\pm} = d_n(1\pm\varepsilon)\;;\quad d_n = \frac{1}{\varepsilon}\left\{\bar\mu^2 - \left[\frac{(n-\tfrac12)\pi}{E}\right]^2\right\}^{\frac12}\;;\quad \alpha = \frac{2\bar\mu}{\pi E}\,. \tag{11}$$

This equilibrium state has a non-vanishing toroidal field at the boundary and a continuous spectrum of μ and may therefore be taken to describe belt pinches and RFP's with a rectangular (elliptical or race-track-like) cross-section. Since the coefficients strongly converge like $1/(2n-1)^4$, the main features of these equilibria are already determined by the first term $Z_o(k_1' r)$.

For the toroidal magnetic flux ϕ and the toroidal current I we obtain

$$\phi = \frac{a}{\pi}\left[2E\sum_{n=1}\{Z_o(d_n^+) - Z_o(d_n^-)\} + \frac{c\pi}{\bar\mu}\,\ell n\,\gamma(\varepsilon)\right]\;;\quad I = \mu\phi = 2(a+b)\,\langle B_{pol}\rangle_{surface}\,. \tag{12}$$

The pinch parameter θ becomes

$$\theta = \frac{\langle B_{pol}\rangle_{surface}}{\langle B_{tor}\rangle_{cross\text{-}section}} = \frac{\mu ab}{2(a+b)} = \frac{\bar\mu}{1+E}\,. \tag{13}$$

Finally, F in the familiar F-θ-diagram is found to be

$$F = \frac{2aE}{\phi(1+2E)}\left[\frac{2\varepsilon}{\pi E}\sum_n \frac{d_n}{2n-1}\{Z_o'(d_n^+) + Z_o'(d_n^-)\} + \frac{c\varepsilon}{\bar\mu(1-\varepsilon^2)} + \frac{c\,\sin\alpha\pi}{1-\cos\alpha\pi}\,\ell n\,\gamma(\varepsilon)\right]. \tag{14}$$

After replacing $\bar\mu$ by $\theta(1+E)$ we obtain $F = F(\theta;\varepsilon,E)$ and from stability requirements it follows $\bar\mu \le \mu_{max}(\varepsilon,E)$, limiting θ by

$$\theta_{max}(\varepsilon,E) \le \frac{\mu_{max}(\varepsilon,E)}{1+E}\,.$$

Explicit $F(\theta;\varepsilon,E)$-diagrams with the stability limit $\theta_{max}(\varepsilon,E)$ taken into account, will be discussed in a forthcoming paper.

Non-axisymmetric solution

In order to investigate the stability of the axisymmetric equilibrium, we need the non-axisymmetric solution $m \neq 0$. The particular solutions $\psi_m(r,\theta,z)$ from Eq. (2) satisfying the boundary conditions (4.1) are

$$\psi_m = F_m^s(r,z)\,\sin m\theta + F_m^c(r,z)\,\cos m\theta\,, \tag{15}$$

with

$$F_m^{s(c)} = \sum_{n=1} Z_m^{s(c)}(k_n' r)\,\sin ny + r^{\pm m}\{c_{s(c)}^{m\pm}\,\sin\mu z + d_{s(c)}^{m\pm}\,\cos\mu z\}\,. \tag{16}$$

With the aid of Eq. (3) we find from the boundary conditions (4.2)

$$\frac{m}{R_\pm} F_m^c(R_\pm,z) - \frac{1}{\mu}\frac{\partial^2 F_m^s(R_\pm,z)}{\partial r \partial z} = 0 \; ; \; \frac{m}{R_\pm} F_m^s(R_\pm,z) + \frac{1}{\mu}\frac{\partial^2 F_m^c(R_\pm,z)}{\partial r \partial z} = 0 \; . \qquad (17)$$

We now expand sin ny, sin αy, cos αy in $(0,\pi)$ in cosine series and find for each mode a set of 4 linear algebraic equations for the infinity of coefficients a_n, b_n, of the Bessel function pairs $Z_m(k'_n r)$. From the truncated coefficients matrix we obtain the eigenvalues needed in the stability analysis.

Stability

We apply the stability criterion derived in Ref. [3], necessary and sufficient for resistive modes and Taylor-relaxed states, and sufficient for ideal MHD modes. The eigenvalue μ must be smaller than μ_m, the smallest eigenvalue for which the solution satisfies the additional boundary condition $B_{tang} = \nabla X$ with X a single-valued function, leading to

$$\mu < \mu_m = \text{Min}\,\{\mu_{12},\, \mu_1(m=1)\} \; . \qquad (18)$$

Note that the special spheromak states with eigenvalues $\mu_{\nu 1}$ are not allowed conmparison states, i.e. there exist stable RFP's or belt pinches with $\mu > \mu_{11}$ or even $\mu > \mu_{\nu 1}$. In Fig. 1, μ_{11}, μ_{12} and $\mu(m=1)$ are plotted as functions of the elongation for $\varepsilon = 0.25$, showing the limitations in the pinch ratio θ.

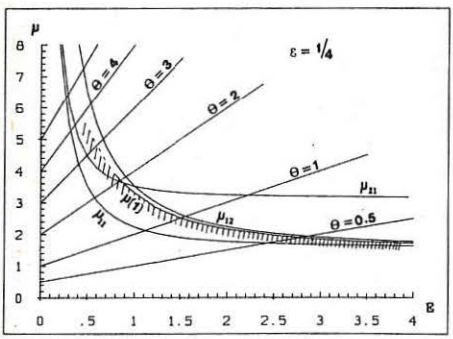

Fig.1

Stability diagram for ε=1/4 as function of the elongation E. The stability region is limited by the μ(m=1) curve. The special spheromak solution μ_{11} becomes unstable for E=6.3 .

Acknowledgement. The authors are indebted to M. Hauser for performing numerical calculations. This work was partly supported by the Austrian Research Funds Contracts P 5178 and 5179. This work was also partly performed under the Euratom-FOM association agreement with financial support from ZWO and Euratom.

References

[1] J.M. Finn et al., Phys. Fluids 24 (1981) 1336.
[2] M. Taguchi et al., Report IPPJ-716, February 1985.
[3] J.W. Edenstrasser and W. Schuurman, Proc. Int. Conf. on Plasma Phys., Lausanne 1984, Vol. I, p. 113.

RESISTIVITY OF REVERSED FIELD PINCH PLASMA

H Tsui*, A A Newton, M G Rusbridge*
Culham Laboratory, Abingdon, Oxon OX14 3DB
(UKAEA/Euratom Fusion Association)

*Department of Pure and Applied Physics, University of Manchester
Institute of Science and Technology, Manchester M60 1QD,
UK

Introduction

The magnetic field configuration of a Reversed field pinch (RFP) [1] has a near minimum magnetic energy with the toroidal field (B_ϕ) reversed in the outer region of the plasma improving the ideal MHD stability. The completely relaxed minimum energy state (MES) has $\mu_o \underline{j} = \mu \underline{B}$ [2, 3] with μ constant everywhere and in cylindrical geometry is described by the Bessel Function Model (BFM). In experiment, $\mu = \mu(r)$ is approximately uniform in the central 50-80% of the plasma radius and reduced in value in the outer regions [4, 5] with profiles described approximately by the Modified Bessel Function Model (MBFM) [6].

The relationship between the resistivity on axis ($\eta(0)$) and toroidal loop resistance (V_ϕ/I_ϕ) in RFP based on three distinct physics models are considered. When fluctuations are neglected, they become [7]:

1. $\eta^C(0)$ arising from the simplified Ohm's law applied to the axis,
2. $\eta^W(0)$ arising from the global magnetic energy balance,
3. $\eta^K(0)$ arising from the global magnetic helicity balance,

and give different estimates of $\eta(0)$.

Comparison of Resistivities: $\eta^C(0)$, $\eta^W(0)$ and $\eta^K(0)$

In the special case of the BFM, $\eta^W(0) = \eta^K(0)$ and $\eta^C(0) > \eta^W(0)$ as seen in figure 1, where $\eta^C(0)/\eta^W(0)$ is plotted vs the pinch ratio $\theta = B_\theta(a)/[B_\phi]$ where $[...]$ denotes the average over the plasma radius a. In general when $\mu(r)$ is decreasing towards the outside of the plasma we find that $\eta^W(0) > \eta^K(0)$ as seen in figure 2, where $\eta^W(0)/\eta^K(0)$ for the MBFM is plotted vs θ.

Contribution due to Fluctuations

In a steady state RFP, we find that the θ is related to the ratio of power input to the rate of helicity input by:

$$\theta = \frac{\mu_0 a}{2} \frac{\int \underline{E}.\underline{j}\ d^3x}{\int \underline{E}.\underline{B}\ d^3x} \qquad (1)$$

This expression reduces to an obvious identity in two limiting cases:
1. $\underline{E} = E_\phi$ is constant, ie the force free paramagnetic model; or
2. $\mu(r)$ is uniform (BFM). In all other cases, including those observed experimentally, there must be additional contributions to the integrals.

To investigate the contribution due to fluctuations, we define θ^* as the equivalent of θ neglecting fluctuations and expand the integrals in (1) by separating the variables into time averaged and fluctuating parts such as $\underline{B} = \underline{B}_0 + \tilde{\underline{B}}$

$$\theta = \theta^* \frac{1 + (\int \eta \langle \tilde{j}^2 \rangle - \langle \tilde{\underline{u}} \times \tilde{\underline{B}} \rangle . \underline{j}_0 - \langle \tilde{\underline{u}} \times \underline{B}_0 . \tilde{\underline{j}} \rangle\ d^3x) / \int \eta j_0^2\ d^3x}{1 + (\int \eta \langle \tilde{\underline{j}} . \tilde{\underline{B}} \rangle\ d^3x\ /\ \int \eta \underline{j}_0 . \underline{B}_0\ d^3x)}$$

where $\theta^* = \frac{\mu_0 a}{2} \frac{\int \eta j_0^2\ d^3x}{\int \eta \underline{j}_0 . \underline{B}_0\ d^3x}$ and $\langle \ldots \rangle$ denotes a time average.

In HBTX1A, the field profile can be described by the MRFM with $r_1/a = 0.7$ and $\eta(r)/\eta(0) = (1-(r/a)^{5.6})^{-3/2}$. In figure 3, we plot θ^* vs θ for the above profiles showing that $\theta^* < \theta$. The parameter $\varepsilon = \theta/\theta^* - 1$ represents the fraction of power coupled to the fluctuations (see later) and is about 0.2 at $\theta = 1.5$ for HBTX1A typically.

Based on the characteristics of the magnetic fluctuations estimated from experimental observations in HBTX1A [8], we find that the contribution to ε due to fluctuations in the helicity input integral (maximum $\sim 1 \times 10^{-3}$) is negligible compared to that in the power input integral (maximum ~ 6).

Calculation of Resistivity in a Steady State RFP

We introduce two factors f_1 and f_2 to take account of the helical current flow and the radial temperature distribution approximated by $T_e(r)/T_e(0) = 1 - (r/a)^\nu$. These factors for the MBFM and $\nu=6$ are plotted in figure 4. In experiment, the factors are selected according to the measured θ, $F = B_\phi(a)/[B_\phi]$ and the temperature index ν to give

$$\eta^k(0) = f_1\ f_2 \frac{V_\phi}{I_\phi} \frac{\pi a^2}{2\pi R} \qquad (2)$$

where πa^2 the cross-sectional area and $2\pi R$ the length of the plasma.

Conclusion

We find that the resistivities on axis based on three distinct physical models are different and in general $\eta^C(0) > \eta^W(0) > \eta^k(0)$ when $\mu(r)$ decreases towards the plasma edge; the differences can be attributed to turbulent fluctuations. Since the global helicity balance is insensitive to fluctuations, $\eta^k(0)$ is the most accurate electrical measurement of the plasma resistivity. The ratio $\eta^C(0)/\eta^k(0)$ is a measure of the additional electric field generated at the axis and $\eta^W(0)/\eta^k(0)$ a measure of both the power throughput coupled to the fluctuations and how close the magnetic field configuration approaches the relaxed minimum energy state.

References

[1] Bodin H A B and Newton A A, Nuclear Fusion 20 (1980) 1255
[2] Taylor J B, Phys. Rev. Lett, 33 (1974) 139
[3] Rusbridge M G, Nuclear Fusion 22 (1982) 1291
[4] Tamano et al, GA Technologies report GA-A17238 (1983)
[5] Brotherton-Ratcliffe D, et al, Culham Lab. Preprint CLM-P742 (1985)
[6] Johnston J W, Plasma Physics, 23 (1981) 187
[7] Schoenberg K F, Moses R W and Hagenson R L, Phys Fluid 27 (1984) 1671
[8] Hutchinson I H et al, Nuclear Fusion 24 (1984) 59.

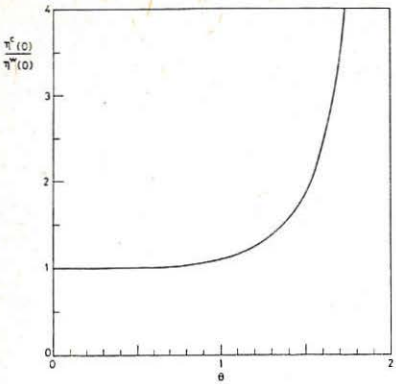

Fig 1 The ratio of the resistivities $\eta^C(0)/\eta^W(0)$ for the BFM and flat resistivity profile vs θ.

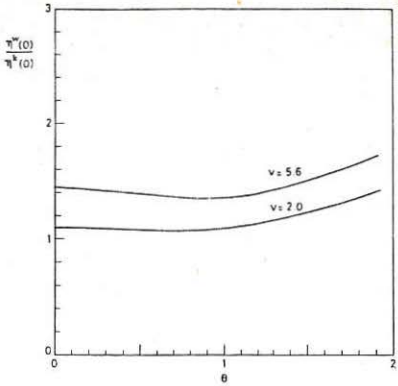

Fig 2 The ratio $\eta^W(0)/\eta^k(0)$ for the MBFM with r_1/a = 0.7 and ν = 2.0 and 5.6 vs θ.

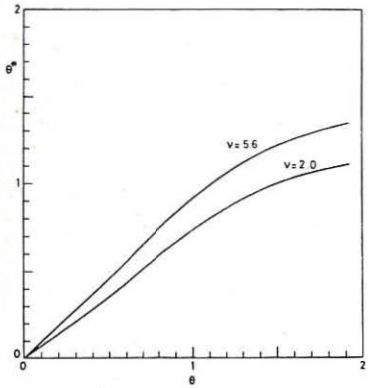

Fig 3 θ* which is the equivalent of θ neglecting fluctuations is plotted against θ for HBTX1A.

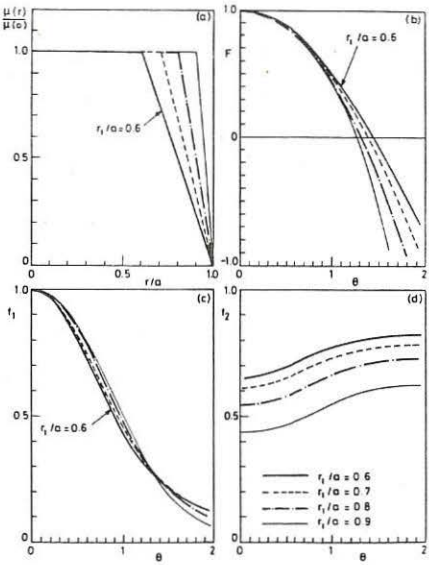

Fig 4 With f_1 and f_2, $\eta^k(0)$ can be calculated from the toroidal loop resistance as in equation (2).

OHMIC HEATING IN VARIOUS DENSITY REGIMES IN ETA-BETA II

A. Buffa, L. Carraro, S. Costa, F.Flora, L. Gabellieri, L. Giudicotti
P. Innocente, S. Martini, S. Ortolani, M.E. Puiatti, P. Scarin

Istituto Gas Ionizzati del C.N.R. - Padova (Italy)
(Associazione Euratom-CNR)

INTRODUCTION The ETA-BETA II (a=.125 m, R=.65 m) current flat-top phase has been studied over a set of ∿200 pulses at I= 150 kA. The relatively slow decrease of the density through the flat-top and its variation from shot-to-shot allows to study the β_θ and τ_E behaviour in different I/N regimes. The previously quoted [1,2] dependence of β_θ and $Z^*_{eff}(0)$ on I/N is confirmed and a negative dependence of τ_E on I/N is also found. A more thorough investigation of the impurities Z_{eff} time behaviour and a discussion of the various possible models for estimating plasma resistivity allow to make firmer ipoteses on the nature of the resistivity anomaly factor.

RESULTS Electron temperature and density profiles have been measured by a 5-point Thomson scattering system [3] at 8 different times and are shown in Figg.1a and 1b. The time evolution of the diameter-integrated electron density has been also measured by a 2-color interferometer and the comparison of the two density measurements shows good agreement. The β_θ negative dependence on I/N [1,2] is confirmed by this renewed and wider set of measurements. The energy confinement time computed according to the definition

$$\tau_E = \frac{3}{8}\,\mu_0 R \beta_\theta \,\frac{I}{\bar{V}_z}$$

also shows a clear tendency to decrease with I/N, as shown in fig.2 where each point corresponds to the time of the Thomson scattering measurement and to a different shot. This is due not only to the decrease of β_θ, but also to a strong increase of the resistivity anomaly factor. Indeed computing the resistivity anomaly factor on axis defined as

$$Z^*_{eff}(0) = \frac{\eta^*(0)}{\eta_{Spitzer}(0)}$$

leads to the values of $Z^*_{eff}(0)$ which are shown against time in fig.3 and against I/N in fig.4. Despite the large spread at late times and at high I/N, which is partly due also to uncertainties in the Thomson scattering measurements, $Z^*_{eff}(0)$ is found to rise from ∿1.5 to ∿10.

Measurements of the time evolution of the emission of iron and oxygen ions by a grazing incidence spectrometer ($\alpha=88^0$) and of the time and space behaviour of the oxygen ions by a 7-chord visible spectrometer have been made. From these data the following upper limits for the absolute densities of the dominant impurity ions have been derived: (OV $\lesssim 5\cdot10^{18}m^{-3}$, FeIX $\lesssim 10^{16}m^{-3}$, ClVIII $\lesssim 5\cdot10^{16}m^{-3}$, CV $\lesssim 5\cdot10^{16}m^{-3}$). In fig.5 the time behaviours of the higher ionization stage populations measured for oxygen are shown. A time resolved upper limit for the effective ion charge Z_{eff} can therefore be derived and is compared in fig.3 with $Z^*_{eff}(0)$. It is worth noting that the highest Z_{eff} would imply a $\sim$100% dilution of the plasma.

A possible explanation for the factor >2 between $Z^*_{eff}(0)$ and Z_{eff} may be given in terms of a dynamo contribution. Indeed the resistivity on axis, $\eta^*(0)$, has been computed for these data according to the Ohm's law as:

$$\eta^*(0) = \frac{V_z(0)}{2R}\,\frac{a^2}{I}\,f_j$$

where $V_z(0)$ is the on axis voltage and f_j is a form factor for the current density profile approximately equal to 1/4 [4]. Better estimates of the resistivity, i.e. in principle free from the dynamo contribution, are possible from a global power or helicity balance (η^W,η^k) [5], but these are crucially dependent on the assumed current density and temperature profile. For the case of a stationary distribution, by using the μ & p model [6] with $\mu/\mu(0)=1-(r/a)^{\alpha}$ for the field profiles and by assuming $T_e/T_e(0)=1-(r/a)^{\gamma}$ the following expressions for $\eta^W(0)$ and $\eta^k(0)$ can be obtained

$$\eta^W(0) = \frac{V_z I}{2\pi R\int_0^a [1-(r/a)^{\gamma}]^{-3/2} J^2(r)\, 2\pi r dr}$$

$$\eta^k(0) = \frac{\Phi(B_z)V_z}{2\pi R\int_0^a [1-(r/a)^{\gamma}]^{-3/2} \underline{J}(r)\cdot\underline{B}(r)\, 2\pi r dr}$$

The profile dependence is then highlighted in fig.5, where the $\eta^W(0)/\eta^*(0)$ and the $\eta^k(0)/\eta^*(0)$ ratios are shown for several α and γ values. For realistic current density and temperature profiles, e.g. $\alpha\sim4$, $\gamma\sim2$, a factor $\eta^W(0)/\eta^*(0)\sim1/2$ or $\eta^k(0)/\eta^*(0)\sim1/4$ may be obtained.

Therefore it seems that by assuming the maximum estimates for the impuritiy densities and by adding a dynamo contribution, even the highest $Z^{*}_{eff}(0)$ can be accounted for. On the other hand the radial profiles of the impurity ions which have been measured indicate that Z_{eff} should be close to unity on axis, which leaves the question still open.

REFERENCES [1] Alper,B.,et al., in Controlled Fusion and Plasma Physics (Proc. 12th Europ. Conf. Budapest, 1985), Vol.9F, Part I, European Physical Society (1985) 578
[2] Alper,B., Carolan,P.G., Martini,S., Ortolani,S., in Controlled Fusion and Plasma Physics (Proc. 12th Europ. Conf. Budapest, 1985), Vol.9F, Part I, European Physical Society (1985) 638
[3] Bassan,M., Buffa,A., Giudicotti,L., Rev.Sci.Instrum.56(1985)1027
[4] Antoni,V.,et al., RFP experiments at various plasma currents on the ETA-BETA II device, Ist.Gas Ionizzati Rep.,IGI/03 (May 1983)
[5] Shoenberg,K.F., et al., Phys. Fluids 27 (1984) 1671
[6] Ortolani,S., in Mirror-Based and Field-Reversed Appr. to Magnetic Fusion (Varenna 1983),Vol.II, Int.School of Plasma Phys.(1984) 513

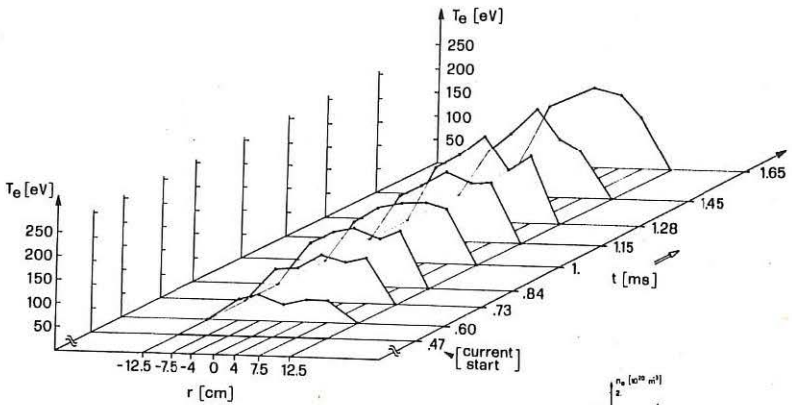

fig. 1a

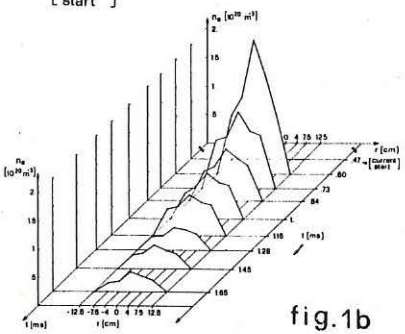

fig.1b

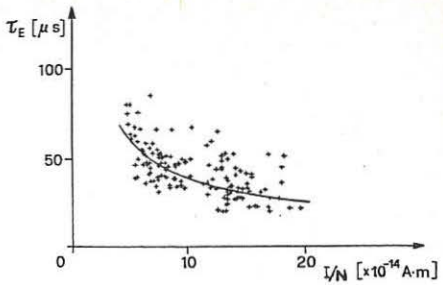

fig. 2

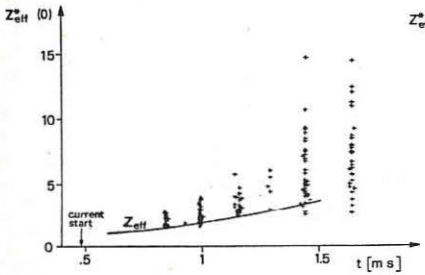

fig. 3

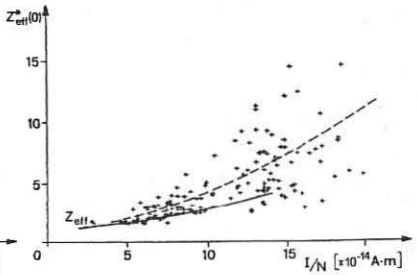

fig.4

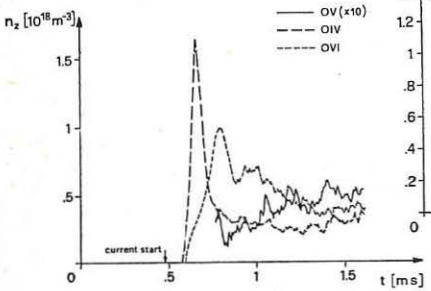

fig.5

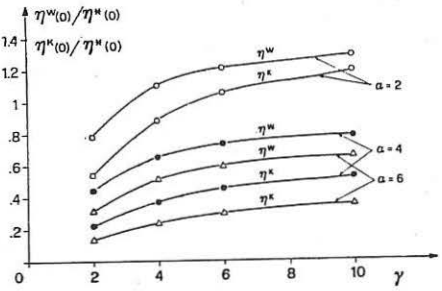

fig. 6

FULLY IMPLICIT SOLUTION OF MAXWELL'S EQUATIONS IN THREE DIMENSIONS BY PRECONDITIONED CONJUGATE METHODS WITH AN APPLICATION TO REVERSED FIELD CONFIGURATIONS*

D.V. Anderson, E.J. Horowitz, A.E. Koniges and D.E. Shumaker

National Magnetic Fusion Energy Computer Center
Lawrence Livermore National Laboratory
Livermore, California 94550, USA

MHD analysis of the reversed field theta pinch predicts a gross instability known as the tilt mode which should grow on an Alfvén transit period time scale. Experimental observations of such configurations show no such instability. Rather equilibria are seen which persist for comparatively long periods[1]. To analyse this stable behavior one must use a kinetic model from which one may learn what mechanism is responsible for the observed behavior. For this study, and others, we have built a full 3D non-linear plasma particle simulation code that uses particle ions but fluid electrons in the quasi-neutral approximation[2].

The need for this 3D simulation coincided with the availability of the first Cray-2 multiprocessor computer installation. Our code, QN3D, has been designed to make full use of the features of this computer including indirect vectorization, multitasking, and the large memory capability. As such it has been designed to employ algorithms that are fully parallelized. Presently, it is an explicit code and in particular uses an explicit field solver to evaluate the electromagnetic fields from a Darwin model.

We are planning, in the future, to modify the code to use particles to represent the electrons and to use the full electromagnetic field equations. Then explicit methodology will restrict time steps to the fastest phenomena occuring usually at the electron plasma or cyclotron frequency. To go beyond these short time scales we intend to adapt the direct implicit techniques to our code. Looking ahead to this goal we have formulated a fully implicit technique for solving the electromagnetic field equations. We report here on the progress in the development of this field solver and compare it to the explicit one presently in QN3D.

Over the past decade there has been rapid progress made in the techniques for solving sparse, linear matrix systems. While direct solvers based on Gaussian elimination are found superior for smaller matrix systems, semi-iterative methods are preferred for larger order matrices both for reasons of memory requirements and of computational speed. Preconditioned conjugate gradient (PCG) methods have been used to solve a wide range of the partial differential equations (PDE) of physics. Typically, a PDE operating on a 2D or 3D scalar field would be discretized by finite element or finite difference techniques and then solved by an appropriate PCG solver. For example, a 3D PDE that produces an asymmetric matrix could be solved by the ILUCG3 code[3]. This code allows a 27 point operator stencil which quite naturally arises in many applications. The global matrix, one obtains, is block tridiagonal with block elements that

*Work performed under the auspices of the U.S. Department of Energy by the Lawrence Livermore National Laboratory under contract No. W-7405-ENG-48.

are themselves block tridiagonal which in turn have sub-elements that are tridiagonal elementary matrices. Alternatively, the resulting global matrix can be described by its band structure. It has 27 non-zero diagonals arranged in clusters each of three elements width. By storing just these sub-diagonals the PCG codes economize on memory. Many of the preconditioning techniques rely on approximate factorizations that preserve the sparsity of the operator matrix.

For the solution of the Darwin form of Maxwell's equations we find a coupling between the three spatial components of $\underline{E}$ which can be expressed as,

$$\underline{w} \times (\nabla \times \nabla \times \underline{E}^n) + S(\nabla \times \nabla \times \underline{E}^n) + h\underline{E}^n = \underline{R} .$$

Here $\underline{w}$, s, h, and $\underline{R}$ represent physical quantities known from previous time levels. When discretized, this system again presents a block tridiagonal superstructure if the index of the spatial component is made the fastest turning one. But now the third level tridiagonal matrices possess dense 3x3 sub-matrices as elements--the smallest level matrices are no longer tridiagonal, but are penta-diagonal. A generalized operator has 3x3x3x5 = 135 stencil points. Sub-bands that were 3 points wide are now 5+1+5 = 11 points wide. Given that these 3D spatial operators always produce 9 such sub-bands we readily see that the matrix has 9x11 = 99 sub-diagonals.

We solve this matrix by the ILUCG method. First, incomplete factors L and U are obtained and used to transform the original matrix problem into a new one that has a very small spread of eigenvalues. Next, the transformed system is put into normal form by multiplication by the operator transpose. This widens the eigenvalue spread--enlarges the condition number by the square--but it yields a formally symmetric matrix problem for which the conjugate gradient (CG) algorithm may be applied. By applying the transformation and the conversion to normal form algebraically, one derives the ILUCG algorithm from the CG one.

The ILUCG algorithm can be viewed as a sequence of dot products of various sub-vectors. These sub-vectors are portions of the rows, columns, source vector, solution vector, and other temporary vectors of the algorithm. For the case reported in the ILUCG3 paper, these vectors are rather short and no attempt was made to vectorize the computer for them. Here we have generalized those methods by introducing innermost loops to perform all the dot products. Since we do not store the global matrices we must use an indirect indexing technique to relate the index of the innermost loop to the indices of our compressed storage arrangement. Given the Cray-2 ability to vectorize arrays with indirect indices, we obtain a code that is fully vectorized.

For the purpose of determining the convergence properties of this method we have set up matrices corresponding to different numbers of coupled PDE's. We use a random number generator to specify the elements of a preliminary matrix which is then forced to possess a given condition number and skewedness. The test problems are generalizations of the ones presented in Ref. 3 and used a 9x11x13 grid (with skew = 1.1, diagp = .01, frlapc = 0.0) and a relative error criterion of 10^{-10}. The Table gives results for runs done with up to five coupled PDE's. A figure of merit is

the ratio of solution time to the number of non-zero matrix elements which we dub "time per term." Note how it improves with more coupling.

To test the physical correctness of our new field solver, which we have named CPDES3[4] (coupled partial differential equation solver for 3D), we have used it in the particle code to propagate Alfvén waves. It is compared to our existing explicit field solver. The two field solvers and the analytical theory are all in good agreement. We realize that the implicit solver is intended for problems with longer time scales, so for the wave propagation are one would probably choose the explicit solver. It is not clear that even the tilting mode simulation will require the implicit solver over the explicit one, but we intend to use these simulations as a test bed for CPDES3 to improve it for later applications on the transport and equilibrium time scales where the explicit solver will be too expensive.

References

(1) W.T. Armstrong, R.K. Linford, J. Lipson, D.A. Platts, and E.G. Sherwood, Phys. Fluids 24 (1981), p. 2068.

(2) E.J. Horowitz, D.V. Anderson and D.E. Shumaker, Bull. Amer. Phys. Soc. 30 (1985), p. 1565; see also E.J. Horowitz, "Vectorizing the Interpolation Routines of Particle in Cell Codes," accepted for publication in J. Comput. Phys.

(3) D.V. Anderson, Comp. Phys. Commun. 30 (1983), p. 43-49.

(4) D.V. Anderson, E.J. Horowitz, A.E. Koniges and D.E. Shumaker, Bull. Amer. Phys. Soc. 30 (1985), p. 1565.

TIMINGS FOR CONVERGENT RESULTS

Num. of PDE's	Num. of Diagls.	Num. of Linear Eqns.	Dec. Time	Total Time	Time per Eqn.	Time per Term	CG Its.
1	27	1287	.462	3.78	2.93e-3	1.08e-4	63
2	63	2574	2.18	9.39	3.65e-3	5.79e-5	61
3	99	3861	5.11	17.23	4.46e-3	4.50e-5	58
4	135	5148	10.03	29.57	5.74e-3	4.25e-3	57
5	171	6435	16.03	41.85	6.50e-3	3.80e-3	57

MINIMUM MAGNETIC ENERGY PRINCIPLE FOR A WEAKLY RESISTIVE TOROIDAL, FINITE-β PLASMA

J.B.M.M. Eggen and W. Schuurman,
Association Euratom-FOM, FOM-Instituut voor Plasmafysica,
Rijnhuizen, Nieuwegein, The Netherlands

Abstract The cylindrical equilibrium profiles as predicted by a minimum magnetic energy principle for a relaxed weakly resistive, finite-β plasma are expressed in terms of measurable quantities. To these relations the first-order toroidal corrections are derived. In a comparison of the theoretical profiles with experimental data of the ETA-BETA-II experiment at Padua, good agreement is found. The F-θ-diagram is also given.

Introduction An extended version of Taylor's minimum energy principle minimizes the magnetic energy W_B of a relaxed weakly resistive, finite-β plasma enclosed by a perfectly conducting metal wall for fixed potential energy $E \equiv \int\{B^2/2\mu_0 + p/(\gamma-1)\}d\tau$ (closed system), magnetic helicity $K \equiv \int \mathbf{A}\cdot\mathbf{B}\ d\tau$ and longitudinal flux Ψ. The minimization is further constrained by the force-balance equation $\nabla p = \mathbf{j}\times\mathbf{B}$. This model is a special case of a general model introduced in a previous work [1].

In the present work the resulting equilibrium profiles in a cylindrical plasma are determined in terms of experimental quantities. The requirement of physically acceptable profiles puts limitations on the allowed values of the quantities. To improve the comparison with toroidal experiments, the first-order toroidal corrections to the cylindrical equilibrium profiles are derived together with a formula for the toroidal shift of the magnetic axis of the plasma. The resulting theoretical equilibrium profiles are compared with experimental data of the ETA-BETA-II experiment at Padua.

The model and resulting equilibria

The mathematical formulation of the variational principle reads:

$$\delta W \equiv \delta W_B - \alpha\delta E - \lambda/2\mu_0\ \delta K - \phi\delta\Psi - 1/(\gamma-1)\ \delta\int\mu(\mathbf{x})\cdot(\nabla p-\mathbf{j}\times\mathbf{B})d\tau = 0\ , \qquad (1)$$

where α, λ, ϕ are constant Lagrange multipliers and $\mu(\mathbf{x})$ a space-dependent one. For a cylindrical plasma of radius a with translational and rotational symmetry, all quantities depend only on the radial coordinate $\rho\varepsilon[0,a]$. The equilibrium profiles are found to be ([1], $B_\rho(\rho) = 0$)

$$B_z(\rho) = B_0 C_0(\nu\rho) \qquad (2) \qquad B_\theta(\rho) = B_0\left(\sigma\frac{1+\kappa\alpha}{1-\alpha}\right)^{1/2} C_1(\nu\rho) \qquad (3)$$

$$p(\rho) = \left[\frac{1}{\gamma-1}\frac{\alpha}{1-\alpha}\frac{1}{\beta_0}\{C_0^2(\nu\rho)-1\} + 1\right]p_0 \qquad (4) \qquad \mu(\rho) = \tfrac{1}{2}\alpha\rho\ , \qquad (5)$$

$$\text{where } \beta_0 \equiv 2\mu_0 p_0/B_0^2\ ; \quad \nu = \lambda\{\sigma(1+\kappa\alpha)(1-\alpha)\}^{-1/2}\ ; \quad \kappa = \frac{2-\gamma}{\gamma-1} \qquad (6)$$

and $C_n = J_n$, $\sigma = +1$ if $\kappa > 0$ and $(-1/\kappa) < \alpha < 1$,
or if $\kappa < 0$ and $\alpha < 1$ or $\alpha > -1/\kappa$,
$C_n = I_n$, $\sigma = -1$ otherwise

with J_n the ordinary, I_n the modified Bessel functions of the first kind. The solutions (2)-(5) depend on the Lagrange multipliers λ and α, and the normalization constants $B_o \equiv B_z(o)$ and $p_o \equiv p(o)$.
These equilibrium quantities yield the following related quantities:
poloidal current density: longitudinal current density:

$$j_\theta(\rho) = \nu \frac{B_o}{\mu_o} C_1(\nu\rho) \qquad (7) \qquad j_z(\rho) = \frac{B_o}{\mu_o} \frac{\lambda}{1-\alpha} C_o(\nu\rho) \qquad (8)$$

longitudinal current: longitudinal flux:

$$I_z = \frac{2\pi a B_o}{\mu_o} \left(\sigma \frac{1+\kappa\alpha}{1-\alpha}\right)^{\frac{1}{2}} C_1(\nu a) \qquad (9) \qquad \Psi = \frac{2B_o \pi a^2}{\nu a} C_1(\nu a) \; . \qquad (10)$$

The values of the parameters $\nu(\lambda)$, α, B_o and p_o distinguish different discharge regimes and in order to have a positive pressure, they must satisfy ([1], Fig. 1):

$$C_o^2(\nu\rho) - 1 + (\gamma-1)(1-\alpha)\beta_o/\alpha \geq [\leq]\ 0 \text{ if } \alpha/(1-\alpha) > [<]\ 0, \quad \rho\varepsilon[0,a] \; . \qquad (11)$$

The Eqs. (9) and (10) can be inverted to obtain the parameters α and νa (or λa) in terms of the longitudinal current and flux:

$$\frac{C_1(\nu a)}{\nu a} = \frac{\Psi}{2\pi a^2 B_o} \equiv \tilde{\Psi} \qquad (12) \qquad \alpha = \frac{\tilde{I}^2 - \sigma C_1^2(\nu a)}{\tilde{I}^2 + \kappa\sigma C_1^2(\nu a)} \; ; \; \tilde{I} \equiv \frac{\mu_o I_z}{2\pi a B_o} \; . \qquad (13)$$

[(12) is a transcendental equation to determine νa in terms of $\tilde{\Psi}$; it may have several roots $\nu_n a$. To each root corresponds an α_n. For given B_o and I_z the total magnetic energy is a function of $\nu_n a$ only; for given values $\{\nu_n a\}$ we choose the one that minimizes W_B].

Using the expressions for νa and α, Eqs. (12) and (13), we can express the equilibrium quantities, (2) - (5), in terms of the experimental quantitities I_z, Ψ, $B_z(o)$ and $p(o)$. As an example, the condition of positive pressure, Eq. (11), becomes (see Fig. 1):

$$\tilde{I} \leq \left\{ \frac{\sigma C_o^2(\nu a(\tilde{\Psi})) - 1 - \beta_o}{C_o^2(\nu a(\tilde{\Psi})) - 1} \right\}^{\frac{1}{2}} C_1(\nu a(\tilde{\Psi})) \; . \qquad (14)$$

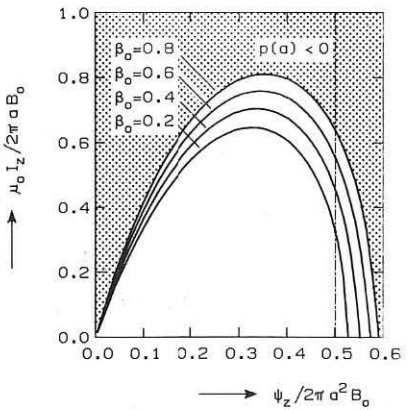

Fig. 1. Realistic pressure profiles as determined by Ψ, I_z, β_o.

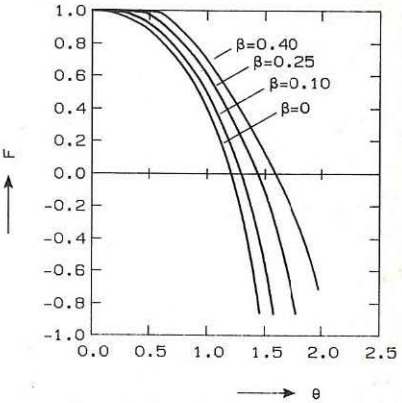

Fig. 2. F-θ-diagram.

F-θ-diagram: letting the pressure go to zero in the interval [0,a], we can use Eq. (4) to express β_o in terms of α and νa (or I_z and Ψ). This enables us to express both F and θ in terms of νa for given β_V, where

$$F \equiv \frac{B_z(a)}{\langle B_z \rangle} \qquad \theta \equiv \frac{B_\theta(a)}{\langle B_z \rangle} \qquad \beta_V \equiv \frac{\int p/(\gamma-1)\,d\tau}{\int (B^2/2\mu_o)\,d\tau} \quad . \tag{15}$$

This yields the F-θ-diagram as given in Fig. 2.

First-order toroidal corrections to the cylindrical equilibrium profiles

Using the familiar technique of an inverse aspect ratio ($\varepsilon \equiv a/R$) expansion of the Grad-Shafranov equation we determine the first-order toroidal correction to the cylindrical equilibrium state. In pseudo-toroidal coordinates (ρ, θ, φ), defined by:

$$x = R(1-\tfrac{\rho}{R}\cos\theta)\cos\phi, \quad y = R(1-\tfrac{\rho}{R}\cos\theta)\sin\phi, \quad z = \rho\sin\phi, \tag{16}$$

the corrections for a rotationally ($\frac{\partial}{\partial\phi} = 0$) symmetric plasma equilibrium of circular cross-section are:

$$B_\rho^{(1)}(\rho,\theta) = \varepsilon \frac{B_o \sin\theta}{2\rho\lambda a}\left[\frac{\alpha\nu}{\gamma-1}(\rho^2-a^2)C_1(\nu\rho)+(1+\kappa\alpha)\left\{\frac{aC_o(\nu a)}{C_1(\nu a)}C_1(\nu\rho)-C_o(\nu\rho)\right\}\right], \tag{17}$$

$$B_\theta^{(1)}(\rho,\theta) = -\varepsilon \frac{B_o\cos\theta}{2\lambda a}\left[\frac{\alpha\nu}{\gamma-1}\left\{\frac{\rho^2+a^2}{\rho}C_1(\nu\rho)+\nu(\rho^2-a^2)C_o(\nu\rho)\right\}+\right.$$

$$\left.+(1+\kappa\alpha)\left\{\frac{\nu aC_o(\nu a)-C_1(\nu a)}{C_1(\nu a)}C_o(\nu\rho)-\frac{aC_o(\nu a)+\nu\rho^2 C_1(\nu a)}{\rho C_1(\nu a)}C_1(\nu\rho)\right\}\right], \tag{18}$$

$$B_\phi^{(1)}(\rho,\theta) = \tfrac{1}{2}\varepsilon B_o\cos\theta\left[\frac{\rho}{a}C_o(\nu\rho)+\frac{\alpha\nu}{(\gamma-1)(1+\kappa\alpha)}(\rho^2-a^2)C_1(\nu\rho)+\frac{C_o(\nu a)}{C_1(\nu a)}C_1(\nu\rho)\right] \tag{19}$$

$$p^{(1)}(\rho,\theta) = \frac{\varepsilon\cos\theta}{\mu_o(\gamma-1)}C_o(\nu\rho)\,\frac{\alpha\nu^2 B_o^2}{2\lambda^2 a}\left[\frac{\alpha\nu}{\gamma-1}(\rho^2-a^2)C_1(\nu\rho)+\right.$$

$$\left.+(1+\kappa\alpha)\left\{\frac{\nu aC_o(\nu a)}{C_1(\nu a)}C_1(\nu\rho)-\rho C_o(\nu\rho)\right\}\right]. \tag{20}$$

The toroidal shift ρ_M of the magnetic axis is determined by
$B_\theta(\rho_M,\pi) = 0$.
Combining Eqs. (3) and (18) to obtain the total $B_\theta(\rho,\theta)$ and expanding this expression for small ρ, we find as an approximate expression for ρ_M:

$$\rho_M = \varepsilon\frac{1-\alpha}{\lambda^2 a}\left[\frac{\alpha(\nu a)^2}{2(\gamma-1)}-(1+\kappa\alpha)\left\{\frac{\nu aC_o(\nu a)}{2C_1(\nu a)}-1\right\}\right]. \tag{21}$$

Comparison with ETA-BETA-II

Using the following data [2] of the ETA-BETA-II experiment at Padua

$$B_o = 0.56\ \text{T} \quad I_z = 180\ \text{kA} \quad \Psi = 9\ \text{mWb} \quad (\varepsilon = 0.19) \tag{22}$$

(the pressure is only very roughly known), we find the parameter values:

$$\nu a = 2.70 \qquad \alpha = 0.19 \qquad p_o \geq \frac{B_o^2}{2\mu_o}\frac{1}{\gamma-1}\frac{\alpha}{1-\alpha} = 43\ \text{kN/m}^2 \tag{23}$$

and the corresponding profiles as predicted by the theory are given in Fig. 3. This figure also shows measured values of $B_\phi(\rho,\pi)$ and $B_\theta(\rho,\pi)$. The calculated $B_\phi(\rho,\pi)$-profile is in very good agreement with the experimental data; the calculated $B_\theta(\rho,\pi)$-profile has the correct shift of the magnetic axis, but there is a growing discrepancy for larger values of ρ/a between $B_\theta(\rho,\pi)$-experimental and $B_\theta(\rho,\pi)$-theoretical since we calculated α to obtain the measured current and according to the theory

$$I_z = 2\pi a\, B_\theta(a,\pi)/\mu_o \ . \qquad (24)$$

However, it should be noted that this discrepancy can be significantly reduced by allowing a deviation of the order of 10% in the current, yielding a lower α. This also affects p_o very much, Eq. (23): $p_o \gtrsim 12$ kN/m^2.

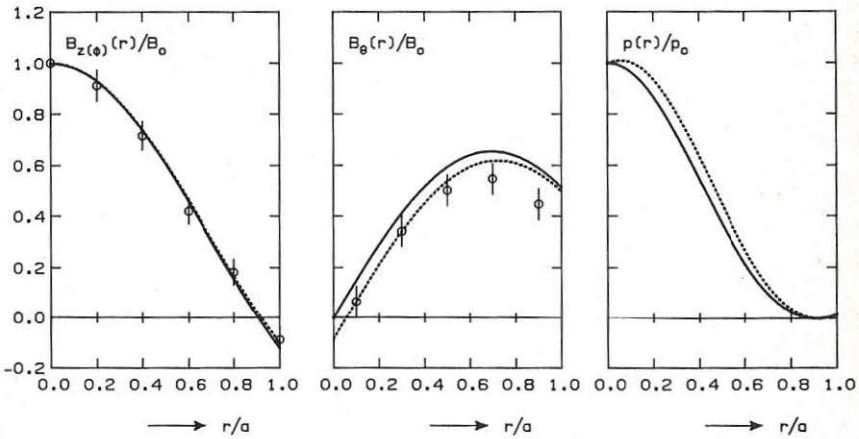

Fig. 3. Calculated equilibrium profiles with experimental data of ETA-BETA-II.
(_____ cylindrical solution; ..... toroidal solution).

Acknowledgement

This work was performed under the Euratom-FOM association agreement with financial support from ZWO and Euratom.

References

[1] J.B.M.M. Eggen and W. Schuurman, Proc. 12th Eur. Conf. on Contr. Fusion and Plasma Phys., Budapest, 2-6 September 1985, Vol. II, p. 370.
[2] J.W. Edenstrasser and G.F. Nalesso, Proc. 10th Eur. Conf. on Contr. Fusion and Plasma Phys., Moscow (1981), paper L16.

STABILITY OF TAYLOR STATES WITH RESPECT TO THE M = 1 MODE IN THE PRESENCE OF A VACUUM LAYER

W. Schuurman, FOM-Institute for Plasma Physics, Rijnhuizen, Nieuwegein, The Netherlands
and
M.P.H. Weenink, Eindhoven University of Technology, Eindhoven, The Netherlands.

Abstract

The minimum energy principle of Taylor is extended to the case where a vacuum layer is situated between the weakly resistive plasma and the perfectly conducting wall. The second variation is investigated for m = 1 perturbations and a necessary and sufficient criterion for stability is derived. The results are identical to those found by means of the resistive mode analysis.

Introduction

Taylor's variational principle [1] minimizes in the cylindrical approximation the magnetic energy of a toroidal plasma column enclosed by an infinitely conducting wall. The minimization is subjected to the constraints of constant longitudinal flux and magnetic helicity $K = \int \mathbf{A}\cdot\mathbf{B}\, d\tau$ (Lagrange multiplier $-\lambda/2$). The minimizing magnetic field satisfies the Euler equation $\nabla \times \mathbf{B} = \lambda \mathbf{B}$ and its Bessel solution has among others the merit of correctly demonstrating the reversal of the longitudinal field component, as observed in reversed field pinch experiments.

A minor shortcoming of this theory is its inability to describe plasma equilibria with a finite β, and equilibria with a current density that falls off rapidly towards the wall. In order to describe the latter type of equilibria we introduce a vacuum layer between the plasma and the wall and minimize the total magnetic energy subject to the plasma magnetic helicity and other constraints, necessary to let the occurring boundary terms in the principle vanish.

The first variation, yielding the equilibrium states has been dealt with in Ref. [2]. In our paper we investigate the stability of the equilibrium states with respect to m = 1 perturbations by means of minimization of the second variation derived previously [3]. As in the case without a vacuum layer the resulting stability criterion turns out to be identical to the one obtained with a resistive mode analysis.

Calculation

We consider a toroidal plasma column surrounded by a vacuum layer and a perfectly conducting wall with circular cross-section (radius b). In the variational principle, both the vector potentials and the position of the plasma edge are varied and acquire stationary values at minimum total magnetic energy of the configuration. Necessary constraints are the conservation of the toroidal fluxes in the plasma and in the vacuum region, the poloidal vacuum flux (the plasma-vacuum interface is ideally

conducting), the magnetic helicity of the plasma and the flux through the hole of the torus. The boundary conditions for this model are the continuity of the vector potential and of the magnetic pressure across the plasma boundary, and the magnetic field being tangential at the surfaces of the plasma and the metal wall. Minimization of the generalized energy $W = \int_P (B^2/2\mu_0 - \lambda/2\mu_0\, \mathbf{A}\cdot\mathbf{B})d\tau + \int_V B^2/2\mu_0\, d\tau$ for cylindrically symmetric equilibria with perturbations $\delta\mathbf{B}$ etc. $\propto e^{i(m\theta+kz)}$ and with the perturbation δa of the plasma radius $r = a$ chosen in the radial direction, leads to a first variation given in Ref. [2] and to the following second variation [3]:

$$\mu_0\delta^2W = \int_P\{\tfrac{1}{2}(\delta B_p)^2 - \frac{\lambda}{2}\,\delta A_p\cdot\delta B_p\}d\tau+\int_V\tfrac{1}{2}(\delta B_v)^2d\tau+\pi^2R\{B^2_{vz}(a)-B^2_{pz}(a)\}(\delta a)^2 \ . \quad (1)$$

We consider the case without zero-order plasma surface current, so that the last term in (1) vanishes.

The perturbation $\delta\mathbf{B}_v$ in the vacuum follows from $\nabla\times\delta\mathbf{B}_v = 0$, $\nabla\cdot\delta\mathbf{B}_v = 0$:

$$\delta B_{vr} = -i\{A_1I_m'(kr) + A_2K_m'(kr)\},$$

$$\delta B_{v\theta} = m/kr\ \delta B_{vz} = m/kr\ \{A_1I_m(kr) + A_2K_m(kr)\} \ , \quad (2)$$

where I_m, K_m denote the modified Bessel functions. $\delta\mathbf{A}$ then follows from $\delta\mathbf{B} = \nabla\times\delta\mathbf{A}$.

The variations in the plasma being free, we have to minimize δ^2W. If we define the Rayleigh ratio

$$R_A \equiv \frac{\int_P(\nabla\times\delta\mathbf{A})\cdot\delta\mathbf{A}d\tau}{\int_P(\nabla\times\delta\mathbf{A})^2d\tau+\int_V(\nabla\times\delta\mathbf{A})^2d\tau} = \frac{\int_P(\nabla\times\delta\mathbf{A})\cdot\delta\mathbf{A}d\tau}{c^2} \ , \quad (3)$$

we have $\delta^2W = \tfrac{1}{2}c^2(1-\lambda R_A)$ so that we have to find $\frac{1}{\alpha}$, the maximum of R_A, and the stability criterion becomes $\alpha \geq \lambda$. Putting $\delta R_A = 0$ we find the Euler equation in the plasma:

$$\nabla\times\nabla\times\delta\mathbf{A} - \alpha\nabla\times\delta\mathbf{A} = 0 \ , \quad (4)$$

and a surface condition on the plasma boundary

$$\int_{r=a}[\delta^2\mathbf{A}_p\times\delta\mathbf{A}_p-\frac{2}{\alpha}\,\delta^2\mathbf{A}_p\times\delta\mathbf{B}_p+\frac{2}{\alpha}\,\delta^2\mathbf{A}_v\times\delta\mathbf{B}_v]\cdot d\mathbf{S} = 0 \ . \quad (5)$$

It can be shown that (5) is satisfied because of the continuity at $r = a$ of the first order part of B^2.
The solution of (4) reads:

$$\delta B_r = \frac{im\alpha D}{(\alpha^2-k^2)r}J_m\{(\alpha^2-k^2)r\}^{\frac{1}{2}} + \frac{ikD}{(\alpha^2-k^2)^{\frac{1}{2}}}J_m'\{(\alpha^2-k^2)^{\frac{1}{2}}r\} \ ,$$

$$\delta B_\theta = -\frac{kmD}{w^2r}J_m(wr)-\frac{\alpha D}{w}J_m'(wr) \ ,$$

$$\delta B_z = DJ_m(wr) ,$$

$$\delta A_r = \frac{imD}{w^2 r} J_m(wr) + \frac{ikD}{\alpha w} J'_m(wr) + \chi'(r) ,$$

$$\delta A_\theta = -\frac{kmD}{\alpha w^2 r} J_m(wr) - \frac{D}{w} J'_m(wr) + \frac{im}{r} \chi(r) , \qquad (6)$$

$$\delta A_z = \frac{D}{\alpha} J_m(wr) + ik\chi(r) ,$$

where $\alpha^2 - k^2 \equiv w^2 > 0$ and $\chi(r)$ is a potential function to be determined from the boundary conditions. For $\alpha^2 - k^2 < 0$ an analogous solution is found with modified Bessel functions.

Application of the boundary conditions and the auxiliary condition $\delta\mathbf{A} = \delta a \times \mathbf{B}_o$, following from $\mathbf{E} + \mathbf{v} \times \mathbf{B} = 0$ as discussed in Ref. [2], leads to the expression for $\alpha(\lambda, m, k, \beta_m = \frac{b}{a})$:

$$\left[\left\{J_o(\lambda a) - \frac{mk}{aw^2} J_1(\lambda a)\right\} J_m(wa) - \frac{\alpha J_1(\lambda a)}{w} J'_m(wa)\right]\left\{I'_m(kb)K'_m(ka) - I'_m(ka)K'_m(kb)\right\} -$$

$$-\left\{\frac{\alpha m}{aw^2} J_m(wa) + \frac{k}{w} J'_m(wa)\right\}\left\{J_o(\lambda a) + \frac{m}{ka} J_1(\lambda a)\right\}\left\{I_m(ka)K'_m(kb) - I'_m(kb)K_m(ka)\right\} = 0. \qquad (7)$$

The marginal form of Eq. (7), where α is replaced by λ, is also found from a resistive mode analysis ("Δ'-method", see e.g. Ref. [4]). This stems from the fact that in the marginal state $\Delta' \to 0$ the boundary conditions to be applied are the continuity of δB_r and B^2 at the plasma edge and $\delta B_r = 0$ at the wall, conditions that are also fulfilled by the minimizing perturbations in the variational approach. Thus, it is satisfactory that the agreement between resistive mode analysis and Taylor's variational principle, already present without a vacuum layer, still exists in the presence of such a layer.

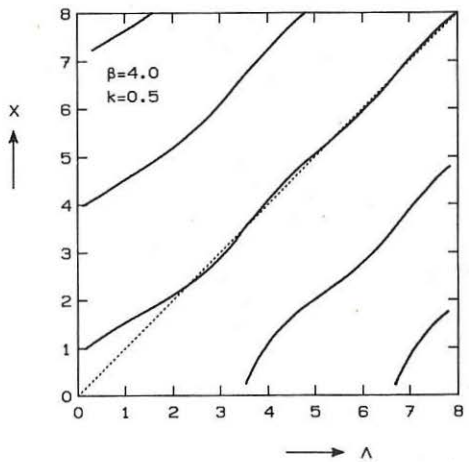

Fig. 1.

Numerical results

Equation (7) has been evaluated numerically for m = 1. At fixed values of k and $\beta_m = \frac{b}{a}$ the curves $\alpha(\lambda)$ are determined, exemplified in Fig. 1, where $\Lambda = \lambda a$ and $X = \alpha a$. In view of the stability criterion $\alpha \geq \lambda$, it is seen that the marginal value of λ is indicated by points where $\alpha(\lambda)$-branches intersect the line $\alpha = \lambda$. The value of λ, thus found as a function of ka at fixed β_m still shows a minimum as in the Taylor case ($\beta_m = 1$). For instance, for $\beta_m = 4.0$, Λ reaches a minimum of 2.39 at ka = 0.4. At growing β_m the minimum in the curve $\Lambda(k)$ shifts to lower k and to lower Λ, the latter effect expressing the destabilizing influence of the vacuum layer. Details of the numerical results of this stability analysis, also in comparison with the ideal MHD predictions, will be given in forthcoming papers.

Acknowledgement

The authors are indebted to I. Ongers for performing the numerical calculations.

This work was partly performed under the Euratom-FOM association agreement with financial support from ZWO and Euratom.

References

[1] J.B. Taylor, Phys. Rev. Lett. 33 (1974) 1139.

[2] P. Centen et al., Proc. 1984 Int. Conf. on Plasma Phys., June 27- July 3, 1984, Lausanne, Vol. I, p. 116.

[3] M.A. van Houten et al., Proc. 12th Eur. Conf. on Contr. Fusion and Plasma Phys. Budapest (1985), Vol. II, p. 382.

[4] R.D. Gibson and K.J. Whiteman, Plasma Phys. 10 (1968) 1101.

PLASMA CONFINEMENT PROPERTIES IN REB-RING SPHERATOR

S. Kubo, K. Narihara, Y. Tomita, M. Matsui, T. Tsuzuki and A. Mohri

Institute of Plasma Physics, Nagoya University, Japan

1. INTRODUCTION

In the experimental device SPAC VII, the field configuration like spherator is formed by injecting a relativistic electron beam (REB) where the internal solid conductor of spherator is replaced by a slender REB ring [1,2]. This configuration has a currentless region useable for plasma confinement outside the REB current channel,i.e., 'REB ring core'. Important features for plasma confinement: high magnetic shear and deep magnetic well are both present in this currentless region. This attractive magnetic configuration had been checked in spherator or levitron where the particle diffusion coefficient was worse by a factor 6 than that predicted from the classical theory in the temperature range $T_e < 100$ eV [3].

To confirm these good confinement properties in REB ring core spherator, a multi-channel HCN laser interferometer with fast time resolusion have been used to measure the temporal and spatial electron density evolution. Here, plasmas were additively supplied with a plasma gun to see details of particle diffusion for different parameters such as q-value and poloidal field.

2. EXPERIMENTAL ARRANGEMENT

The toroidal device SPAC-VII (Fig.1) has a vacuum chamber of the inner diameter of 166 cm and the maximum width of 42 cm. The toroidal magnetic field is generated by a current (500 kA maximum, 80 ms e-folding time) in a single center conductor. In order to proceed from REB-ring formation to major radius compression of REB-ring, the time-varying axial magnetic field is used. The REB injection is performed with the plasma anode method [1], by the use of a MARX generator: PHOEBUS-III (90 kJ, 2MV, 1.5 μs pulse width). To help the REB-ring formation [2], a resistive shell of 1 ms skin time is installed inside the vacuum chamber. The core minor radius of the REB-ring is inferred from the spatial distribution of X-ray emissivity measured with a nine-channel X-ray collimator system. The multi-channel HCN laser interferometer is composed of five sets of interferometric lay arrangements and two HCN lasers of slightly different wave lengths (Fig.2). The main laser beam is splitted into 5 beams. Then, after making each beam to pass doubly through the plasma , the beam is combined with another reference laser beam. These combined beams are rectified with Shottky Barrier diode mixers. The output beat signals are analized by TTL logic so that direct reading outputs can be obtained. Thus, fast time evolution of the density profile can be obtained easily with high reliability.

3. EXPERIMENTS

In Fig.3 are shown typical time dependences of ring current I_R and the line integrated electron density $n_e l$. At t=1.0 ms, a coaxial plasma gun was fired to satisfy the plasma anode condition in front of the cathode[1]. When an REB was injected at 2 ms, a toroidal REB ring of about 25 kA was formed within few microseconds and it continued for about 20 ms without further acceleration. Return current induced in the setup phase of ring produced a high density plasma which was immediately confined by the ring. Initially, the plasma density attained to about 2 x 10^{13} cm^{-3} at the central position and had a relatively broad spatial profile. This return current decayed fast and then the density profile settled to a certain one about 1 msec after the REB injection, while the plasma density decayed slowly with time. The REB core radius inferred from the spatial distribution of X-ray emission was about 6 cm at half maximum. This peaked current profile was held almost the same until the current terminated. Here, the REB ring core were formed and the currentless region for plasma confinement extends from 6 to 12 cm.

The REB itself hardly interacts with the neutral gas left unionized since the ionization cross section is so small in this REB energy range. The ionization time estimated with measured neutral density and beam parameter is a few tens of ms. The validity of this estimation was ascertained from the experiment that the electron density profile and its time evolution were hardly affected by adding neutral gas as much as that left unionized. On the other hand, the main electron loss mechanism except the diffusion may be the recombination, but its characteristic time is so long (of the order of sec) that this effect on the loss is negligible in this case. Therefore, the global electron confinement time can be roughly estimated from the observed density decay time. Typical confinement time is about 2 ms. This value is worse by a factor 4 to 5 than that estimated from the classical theory.

In such an experimental condition, both the source and the sink terms in the diffusion equation can be neglected. This simplifies the derivation of the diffusion coefficient. In cylindrical coordinates the diffusion equation can be experessed as

$$\frac{\partial n}{\partial t} - \frac{1}{r}\frac{\partial}{\partial r}\left(r D_\perp \frac{\partial n}{\partial r} \right) = S = 0 \quad ,$$

where, $D_\perp$ is the transverse diffusion coefficient. The diffusion coefficient can be expressed in terms of the quantities which are obtained from the observed density profile and its time evolution as

$$D_\perp = \frac{\int_0^r r' \frac{\partial n}{\partial t} dr'}{r \frac{\partial n}{\partial r}} \quad ,$$

assuming the axi-symmetry. Here, the raw data points on the radial density distribution at each time are smoothly connected with an appropriate fitting function and then it is Abel-inverted to get n(r,t). Examples of diffusion coefficients found in this manner are shown in Fig.4(a). The coefficient $D_\perp$ increases with radius. It is prominent that $D_\perp$ grows up outside the radius of nearly q=1. The diffusion coefficient estimated from the classical theory is in the order 10^3 $cm^2 sec^{-1}$.

It is important from the view point of confinement to see the diffusion in higher q region. However, the derivation of diffusion coefficient in such a region becomes difficult because of low S/N ratio. To avoid this

difficulty, a plasma gun set at the center conductor was fired 5 ms after REB injection (t=7 ms)(Fig.5(a)). The plasma density was built up at the plasma periphery and decayed in about 2 ms. On the other hand, the increment of the visible light intensity decreased in about 0.5 ms and became the same level as that before the gun plasma injection (Fig.5(b)). This indicates that, once the injected plasma was cooled down, it was no longer an origin of plasma source. Whence the diffusion coefficient can be derived in the same manner as before the additive plasma injection. This method enables the more accurate derivation of the diffusion coefficient in the high q peripheral region. In Fig.5(c) are shown the Abel-inverted density profiles. The diffusion coefficient at high q region becomes 10^4 to 10^5 $cm^2 s^{-1}$(Fig.4(b)). There is a clear tendency that the diffusion increases steeply as q passes over 1. This dependence of $D_\perp$ on q may be attributed to MHD-instabilities near the rational surface, micro-instabilities, or other diffusion mechanisms. The dependence study of the diffusion coefficient on T_e and field parameters are now on going.

4. CONCLUSION

The plasma confinement properties in the REB ring core spherator have been studied with the HCN laser interferometer system having fast time resolution power. The global particle confinement time is 2 ms which is worse by a factor 4 to 5 than that estimated from the classical theory. The diffusion coefficients derived from the measurement in both cases without and with the addtional plasma injection are of an order 10^3 cm^2 $s^{-1}$for $q < 1$ and 10^5 cm^2 $s^{-1}$for $q > 1$. This diffusion coefficient have a strong dependence on the safety factor q. The dependence is roughly as $D_\perp \propto q^2$.

REFERENCES

1. A. Mohri, K. Narihara, T. Tsuzuki, Y. Kubota, Y. Tomita, K. Ikuta, and M. Masuzaki: Proc. Int. Conf. on Plasma Phys. and Controlled Nucl. Fusion Research 1978 (IAEA,Vienna,1979) Vol. 3, p. 311.
2. A. Mohri, K. Narihara, Y. Tomita, M. Hasegawa, S. Kubo, T. Tsuzuki, T. Kobata, H. H. Fleischmann: Proc. Int. Conf. on Plasma Phys. and Controlled Nucl. Fusion Res. 1984 (IAEA,Vienna,1985) Vol. 3, p.395.
3. R. Freeman, M. Okabayashi, G. Pacher, B. Ripin, J. A. Schmidt, J. Sinnis and S. Yoshikawa: Proc. Int. Conf. on Plasma Phys. and Controlled Nucl. Fusion Res. 1970 (IAEA,Vienna,1971) Vol. 1, p.27.

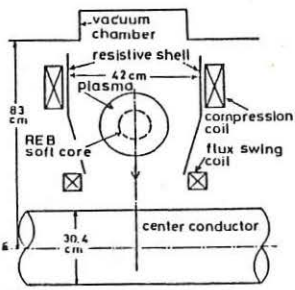

Fig. 1. Schematic drawing of toroidal device SPAC VII.

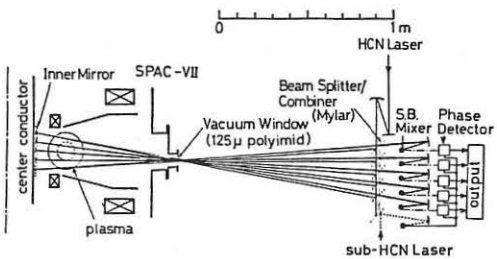

Fig. 2. Five channel HCN laser interferometer system.

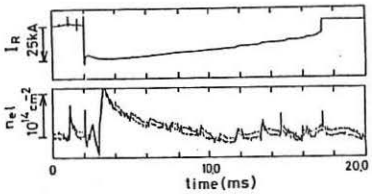

Fig. 3. Typical time evolutions of I_R, $n_e l$.

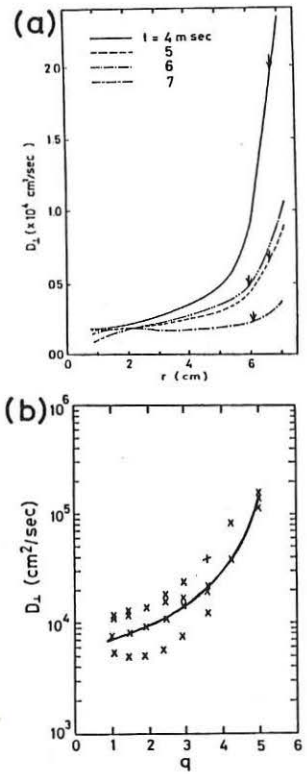

Fig. 4. (a) Radial profile of $D_\perp$, arrow indicates q = 1 position. (b) q dependence of $D_\perp$.

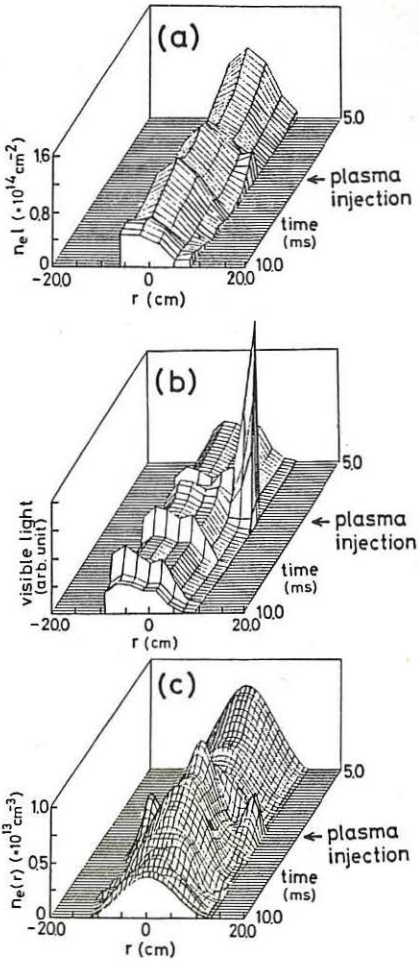

Fig. 5. Profile evolutions of (a) $n_e l$, (b) visible light, and (c) $n_e(r)$ in case of plasma injection.

CONFINEMENT OF MEV IONS IN A DENSE PINCH*

V. Nardi, C. M. Luo, C. Powell, J. Brzosko
Stevens Institute of Technology, Hoboken, NJ 07030, USA

A. Bortolotti, F. Mezzetti
Universita di Ferrara, FE 44100, Italy

Abstract Pinhole imaging from the ion emission of a deuterium plasma focus pinch shows a multiplicity of localized sources of $\gtrsim$3MeV ions ("hot spots"with linear dimensions not greater than the pinhole diameter 100 μm) which are embedded in a diffuse source (the pinch image) of $\sim$ 1 MeV ions. The ion energy distribution in the pinch image is obtained with a space resolution better than 50 μm. Data from Thomson spectrometers with a 2 ns time resolution indicate that low energy ions (E < 1 MeV) are ejected $\sim$ 100 ns earlier than the high energy ions (E > 1 MeV). The observed characteristics of the D-D neutron emission [(i) spread of neutron energy spectrum, (ii) neutron pulse duration, (iii) total neutron yield] are consistent with a novel mechanism of ion acceleration and ion confinement within localized regions of smaller dimension than those considered in earlier work[1]. A method for increasing the neutron yield by increasing the volume of the "hot spots" has been tested with a positive result: $\sim$ 4 x 10^9 D-D neutrons/shot with a 6 kJ, 16 kV, 6 Torr D_2 filling plasma focus discharge. This has been achieved with the insertion of suitable field-distortion elements in the interelectrode region.

1. Previous measurements[1] have shown that there is a strong correlation between the D-D neutron yield n in one shot of a plasma focus system (PF; 5-10 kJ capacitor bank at 14-18 kV) and the maximum value $E_{n,max}$ of the neutron energy E_n detected in the same shot. If we plot the observed n (measured by silver activation counter) in a series of 10^2-10^3 shots as a function of the corresponding $E_{n,max}$ we find that n is uniformly increasing with $E_{n,max}$ [$E_n = (D/\Delta\tau)^2$ m/2; $\Delta\tau$ is the neutron time of flight on the distance D = 1846 cm from the PF source to the NE-102 scintillation detector]. We have additionally found that the intensity of the ion emission from the PF pinch at 0, 45°, 90° is randomly changing from shot to shot without correlation with n. The energy spectrum of the D^+ emission in different directions is determined by (i) compact Thomson spectrometers[2] and by (ii) pinhole images of the PF pinch with differential filtering of the ion emission. The nonuniform distribution of etched ion tracks on CR-39 targets forms a sharp-boundary image of the pinch and the typical parabolic pattern from deflected ions in the Thomson spectrometer. The D^+ emission from the PF pinch in a high-yield shot with $n \lesssim 3\,\bar{n}$ can have such a low intensity that no pinhole image is formed, and no appreciable amount of tracks is formed on CR-39 targets of the spectrometer in any direction; the 0°, 45°, 90° directions are usually monitored in each shot; $\bar{n}$ is the mean value of n on a typical series of $\sim$ 100 shots in the same conditions of filling pressure p, and capacitor voltage V_o. On the other hand, also a shot with $n \lesssim 0.5\,\bar{n}$

*Work supported in part by AFOSR (Washington, DC), MPI (Roma, Italy), ONR (Arlington, VA).

can produce a sharp image of the pinch on CR-39 targets in any direction and a strong parabolic pattern in a Thomson spectrometer. It is generally true for shots with $n < \bar{n}$ - few exceptions - that if we compare two shots (a,b, say) which have about the same total emission $\int N(E_i)dE_i$ we find $N_a(E_i) > N_b(E_i)$ in the high-energy wing of the spectrum if $n_a > n_b$. This is no longer the case in shots with $n \gtrsim 3\text{-}4\ \bar{n}$ where $N(E_i)$ is essentially undetectable by spectrometers and imaging systems. The increase of n with $E_{n,max}$ and the decreasing ion emission N for increasing values of $n > 3\bar{n}$ indicate that the pinch self field and the related ion trapping is one of

Fig. 1. Neutron yield n as a function of $E_{n,max}$ (in MeV) from a series of 120 shots. Each data point is obtained by grouping together the n, $E_{n,max}$ (T_{nf}) values of all shots with the same $E_{n,max} \pm \Delta E_n$. The vertical coordinate is the mean value $\bar{n}$, and the vertical error bar is the standard deviation of each group of data. $E_{n,max}$ is obtained via the neutron time of flight T_{nf} from the PF source to the scintillation detector at a distance D=1486 cm. The scintillator/photomultiplier system was in saturation conditions for the neutron signal; $T_{nf} = T_{nl} + D/c$, $c = 3 \times 10^{10}$; T_{nl} is the time between the peak of the first x-ray pulse - photon energy > 1 MeV - and the time at which the neutron signal on the oscilloscope display reaches the conveniently chosen value of 1 Volt; the NE-102 detector is in a box with lead walls 6 cm thick (see Ref.3). The horizontal error bar is determined from the time of flight error ± 10 ns.

Fig. 2. (a) Time lag T_L in the emission of D^+ ions as a function of the ion energy E_i from a Thomson spectrometer with nanosec time resolution. The 1 MeV ions are emitted about 100 ns after the 70 keV ions in the same pulse. (b) Photograph of the CR-39 target (single shot) of the Thomson spectrometer from which we have derived T_L. The vertical coordinate gives the field induced displacement θ_B of the ions. The pinhole entrance of the spectrometer has a dia. of 50 μm (= diameter of the neutral particle spot in the low left corner of b). The period of the time dependent component of the electric field E - which is superposed to a constant component of about the same strength - is ∿ 17 nanosec.

Fig. 1

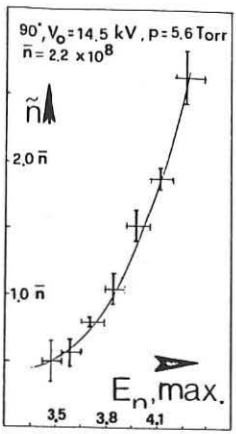

Fig. 2

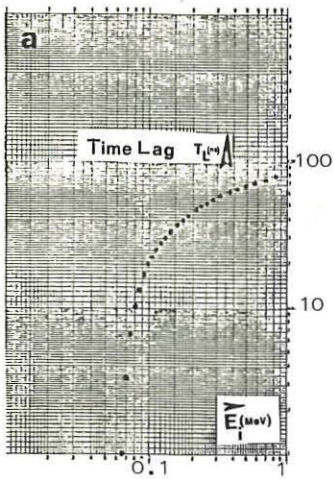

Fig. 2. (b) All data reported in this paper have been obtained with a hollow center electrode (anode).

Fig.3

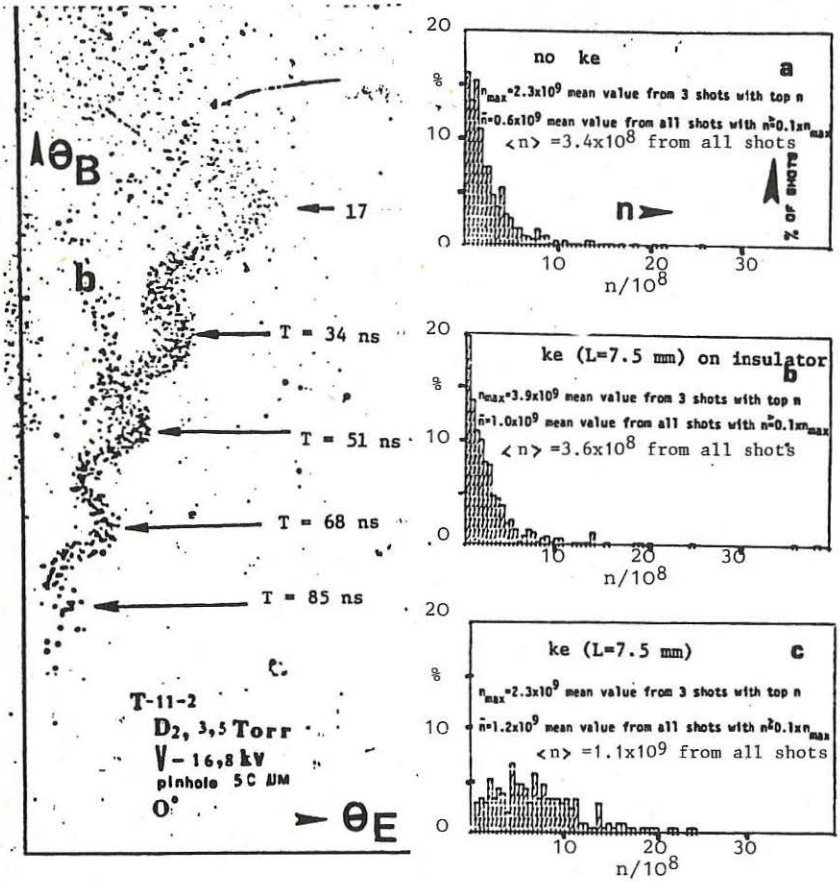

Fig. 3 Histograms with the percentage of shots with a neutron yield between n and n+Δn (Δn = 5×10^7) vs. n for three different initial configuration of the electric field in the interelectrode gap: (a) no ke; (b) ke touching the insulator surface; (c) ke with same length L = 7.5 mm but with a spacing between insulator surface and ke inner surface. The distribution of the data is substantially changed in (c) as compared to (a), (b) in that the misfiring are almost completely eliminated. Both (b) and (c) indicate a substantial increase of n and of $\bar{n}$ with a record yield of $n \sim 3.8 \times 10^9$/shot. All shots in the same conditions: p - 6 Torr, V_0 = 16.5 kV. The extension in space (inside the pinch image on CR-39 targets) of the hot spots (with a diameter smaller than 100 μm) and the quantity observed in each shot is increased by using the ke. Each hot spot is formed of ion tracks with $E_i \sim 3$ MeV; Nardi et al., in press).

the factors which control the magnitude of n. The other factor clearly controlling n is the rate of decay of the self-field which determines the ion-accelerating inductive fields and the observed $E_{n,max}$. The long ion confinement time inside the self-field-dominated plasma of the PF has been previously established also from (a) the production of 14 MeV neutrons via T-D secondary reactions in PF discharge with a pure D_2 filling, and (b) from the contact print - from 2.4 MeV D^+-ion tracks on a screened CR-39 target - of a plasmoid ejected from the PF pinch region[4]. We have used a Thomson spectrometer with $\sim$ 2 ns time resolution for determining the relative time of emission of 0.1-1 MeV D^+ ions. A periodic electric field $E_T \gtrsim$ 2 kV/cm, period $\sim$ 17 ns, has been applied to the pole pieces (8 kG) of the Thomson spectrometer described in Ref. 2. The relative time of the ion impact $T(E_i)$ on the CR-39 target is determined by the phase difference of the E_T field. The time of flight from the PF source at the distance d_o from the Thomson target (close to the pole pieces) is $T_f(E_i) = do/\sqrt{(2\ E_i/m)}$. The difference in the time of emission (time lag) for ions of energy E_1 and of energy E_2 $T_L(E_{i1},E_{i2}) = T(E_{i1}) - T_f(E_{i1}) - [T(E_{i2}) - T_f(E_{i2})]$ is reported in Fig. 2 as function of the ion energy [the time origin in here arbitrarily chosen at $T(E_{i2} = 65\ keV) = 0$]. The high-energy components of the D^+ ion beam at 3 Torr is detected from the nuclear activation of a Cu target at 0°, 2.5 cm dia., 11 cm from the anode end [$^{63}Cu(d,2n)^{63}Zn$, half life τ = 38 min, threshold $E_{i,th} \cong$ 8 MeV; $^{65}Cu(d,p)^{66}Cu$ τ = 5.1 min, $E_{i,th} \cong$ 5 MeV] in less than one shot every ten, with $N(E_i \gtrsim 5MeV) \gtrsim 10^8$. The corresponding fluence $d^2N/dEd\omega$ is only $\sim$ 10 times higher than the fluence measured with a high-resolution magnetic analyzer[2] with an acceptance angle $d\omega$ (=7.8x10^{-5}) 50 times smaller than the solid angle $d\omega$ = 4x10^{-3} sr intercepted by the Cu target.

2. The thickness of the current sheath in the interelectrode gap and the possibility that more than one current sheath may form in the PF breech region are dominant factors which control n. We affect these factors with the insertion of field distortion elements (e.g., a knife edge, ke) in the interelectrode gap. The best results have been obtained with a circular ke of length L = 7.5 mm inserted at the PF breech on the insulator sleeve (the outer electrode dia. is 10 cm, the center electrode dia. is 36 mm, the dia. of the pyrex insulator sleeve is 44 mm). The ke has been tested by using two locations: (a) In contact with the pyrex surface or (b) by increasing the ke diameter, at a distance d from the pyrex surface. The larger diameter ke reduces the emission of impurity ions from the pyrex surface. This improves the performance of the PF (the misfirings are eliminated, see fig. 3) because the current density is sharply peaked in a single sheath. The ke increases by a factor $\geq$ 2 the volume of the hot spots.

References

1. W. H. Bostick, V. Nardi, W. Prior: Proc. 7th Eur. Conf. Controlled Fusion (Lausanne 1975), p. 62, and Nuclear Fusion, Sup. V.3 497 (1977).
2. V. Nardi, C. Powell, W. Prior, W. H. Bostick, Proc. 11th Eur. Conf. Contr. Fus. (Aachen, 1983) Vol. 7D, p. 489, and AIP Proc., 111, 463 (1984).
3. W. H. Bostick, V. Nardi, W. Prior: Nuclear Fusion, Sup. V.3, p. 109 (1975).
4. W. H. Bostick, V. Nardi, W. Prior, J. Feugeas, A. Bortolotti, C. Cortese, F. Mezzetti, F. Pedrielli, Energy Storage Compression and Switching, Vol. 2, p. 267 (1983).

EXTRAP AS A DYNAMIC SYSTEM

M. Tendler

Royal Institute of Technology, Department of Plasma Physics and Fusion Research, S-10044 Stockholm, Sweden

1. QUALITATIVE DISCUSSION

The most obvious way to build a magnetic fusion reactor is to drive a strong current along a plasma column. The associated poloidal magnetic field induced by this current provides then for the plasma confinement, heating and compression. The configuration based on this idea is called Z-pinch, which was a main topic of fusion research during its early years in the fifties. Unfortunately, this scheme was found to be extremely unstable. The suggestion that bounding a Z-pinch by a purely transverse (without toroidal field at all), octupole magnetic field might strongly enhance the plasma stability of a Z-pinch was put forward by Lehnert in 1974 /1/. He suggested to call this configuration EXTRAP. His idea was confirmed by further experiments /2/. Stable discharges were attained in linear EXTRAP configurations for around 50 μsec, which corresponds to around 50 Alfvén transit times.

We turn over to the qualitative discussion of EXTRAP configuration as compared to the classical Z-pinches. Both configurations have the O-point in the magnetic field at the axis. Obviously the ideal MHD theory is incapable in treating it, because some assumptions invoked in this theory are not valid there. This fact, however, does not prevent the Z-pinch from being unstable. Besides, linear EXTRAP is non-circular at the periphery and has four well localized X-points, determining the form of the separatrix. The separatrix arises as a result of the pinch current combined with the opposite directed octupole field, generated by the parallel currents in the external conductors. As shown in /3/ the effect of the non-circularity seems to be rather weak and does not provide for stability. Kinetic effects might be important in the close vicinity of X-points, as discussed in /4/. However in the present study we retain the fluid approach and suggest that X-points affect the energy outflow in a certain way according to a plausible scaling, given below. This assumption is very likely to be fulfilled in EXTRAP, because of the high collisionality of EXTRAP plasma. The second important aspect, peculiar to the EXTRAP configuration, is the enhanced rigidity of this configuration, arising from current rods and the external magnetic field, generated by them. The excess of the total magnetic field (Z-pinch field plus the octupole field) over the plasma pressure might be the main reason for the enhanced stability. The external magnetic field, stored between the pinch plasma and rods prevent their direct contact. Finally, unlike the classical Z-pinch equilibrium arises where the magnetic field increases with distance from the boundary of the pinch. Here, we show how such equilibrium can be attained. The third important difference between linear EXTRAP and Z-pinch is how a discharge is initiated and ramped-up during the build-up phase. The formation of the discharge in EXTRAP starts at the O-point, where both the pinch field and the octupole field is zero, and builds up radially outwards. On the other hand in the classical Z-pinch the initial breakdown

occurs at the outer surfaces and then the discharge builds up radially inwards. This experimental observation proves the fact that the energy loss mechanism in EXTRAP is drastically different from this in the conventional Z-pinch. As shown by us before /5/ in EXTRAP the energy loss is small compared to ohmic heating in the initial phase of the discharge and in the steady state is determined by the scaling governed by the octupole field (see eqs. (6), (7)). Given the lack of experimental data on the peripheral plasma confinement, in the present study we suggest a scaling for the net energy loss with plasma density and temperature. It allows us, by using the self-similar methods to solve the strongly non-linear system of equations. We also briefly report some preliminary results on the stability of EXTRAP, considered as a strongly non-linear dynamic system and conclude with some speculations about the stability properties of it, emphasizing that the dynamic properties might be responsible for enhanced stability of EXTRAP. Finally some practical suggestions and implications of this theory for current and forthcoming experiments are described.

2. TIME-DEPENDENT EQUILIBRIUM IN A PINCH

We consider all parameters to be both time and spatial dependent. In this part of the study in order to simplify for the reader we list the Maxwell and transport equations. Besides, we employ cylindrical coordinates and assume the system to be cylindrically symmetric.

Considering transport equations, we get for the particle balance:

$$\partial n/\partial t + \partial(nrv)/r\partial r = 0 \qquad (1)$$

The momentum balance reads if viscous effects are neglected:

$$nmdv/dt = -\partial p/\partial r + j_z B/c \qquad (2)$$

In the present study we consider only fast processes with a typical time scale much shorter:

$$\tau \ll (\tau_{res}^{\alpha} \tau_{Alf}^{\beta})^{1/\gamma}; \quad \alpha + \beta = \gamma \qquad (3)$$

Here α, β and γ are numbers dependent on the type of the resistive instabilities, appearing in this configuration, their timescale, however, is of the same order of magnitude. In other words we consider the case of the large magnetic Reynolds number, so that:

$$\partial B/\partial t + \partial(vB)/\partial r = 0 \qquad (4)$$

Finally the energy balance in the cylindrical geometry reads:

$$3(n_e + n_i)dT/2dt + p\partial(rv)/r\partial r + \partial(rq)/\partial r = Q \qquad (5)$$

Integrating Eq. (5) over the plasma cross-section and assuming that the plasma temperature profile is almost flat we got the equation:

$$3NdT/dt + 4NTdR/Rdt = I^2/\pi R^2\sigma - L \qquad (6)$$

where R is the radius of the pinch and L is the energy loss of a pinch.

In EXTRAP L is very small during the build-up phase of the discharge, until the pinch radius R reaches the separatrix. The energy loss term L then drastically increases and the expansion of the discharge is terminated. In the classical Z-pinch just the opposite is valid. In the present study we consider Eq. (5), simplified as follows. The term Q scales as

$$Q = nT/\tau \qquad (7)$$

where τ is essentially the energy confinement time of the octupole field. It is assumed to be a constant. The energy is assumed to be transported primari-

ly by convection, owing to the X-points at the periphery.

We are looking for the self-similar solutions of Eqs. (1,2,4,5). The self similar variable is chosen as x=r/R. The pinch radius is also a function of time, even during the flat-top phase of the discharge. The velocity of convection is taken as v=rdR/Rdt. Then all physical parameters of the problem are functions of x and t and the factorization of Eqs. (1,2,4,5) becomes possible.

Solving Eqs. (,4) we obtain

$$n = N_0 R^{-2}(t) f_n(x); \quad B = B_0 R^{-1}(t) f_B(x) \tag{8}$$

Factorizing also the temperature $T=T(t)f_T(x)$ and requiring that:

$$\partial(f_n f_T)/\partial x = -A_1 x f_n(x) \tag{9}$$

$$f_B \partial(f_B x)/x\partial x = A_2 x f_n(x) \tag{10}$$

we get from the momentum balance:

$$d^2R/dt^2 = T_0(A_1 T/T_0 - B_0^2 A_2/4\pi T_0 N_0)/m_i R \tag{11}$$

where A_1 and A_2 are arbitrary constants. It is important to emphasize that the number of equations (9,10) is less than the number of profile functions, therefore one of them is arbitrary and may be chosen either from the experiment or from some other constraints, for example from the condition of the increasing magnetic field at the periphery and some other stability considerations. It is worth noting that to fulfill this constraint $f_n(x)$ has to be non-zero at the periphery of the discharge.

Considering now the energy balance we get:

$$T(t) = T_0 R_0^{4/3} R(t)^{-4/3} (\exp -t/\tau)^{2/3} \tag{12}$$

Substituting now Eq. (12) into Eq. (11) we get the equation describing strongly non-linear oscillations of the pinch boundary with damping:

$$d^2R/dt^2 = a\ bR^{-4/3}(\exp -t/\ )^{2/3} - c\ /R \tag{13}$$

Equation (13) was solved numerically and the result is shown in Fig. 1. If $\tau \gg t$, i.e. the confinement time of the octupole field is much longer than the pulse duration, these oscillations are almost unattenuated and the solution describes strongly non-linear adiabatic oscillations. They are extremely strong in amplitude and the maximum and the minimum plasma temperature at a given observation point can easily vary by factor 3-4. This conclusion seems consistent with the qualitative experimental observation made by Thomson scattering diagnostics, where such drastic variations of the plasma temperature were observed. If τ decreases the oscillations are damped more efficiently and the pinch collapses after a small number of the oscillation periods. However, the scaling of the energy losses will probably change as well and the whole problem has to be reconsidered with some other scaling. Finally we emphasize that most of the results obtained above are rather sensitive to the form of the scaling of the energy loss. The physical picture might change drastically if some other loss channels are inserted into the plasma.

3. STABILITY ANALYSIS

Here we report some preliminary results on the stability of EXTRAP configuration taking into account our previous results described in Sec. 2. First of all, axisymmetric rods and their magnetic field are "transparent" for perturbations, directed parallel to them, but they provide a strong stabilizing

influence on perturbations, perpendicular to the Z-axis. In order to use this effect most efficiently the magnetic field pressure outside the current rods has to exceed the plasma pressure in the pinch, so that the ß value is somewhat less than in the classical Z-pinch. On the other hand, the additional octupole magnetic field provides an enhanced stability.

Secondly, it is well known that the sausage instability can be stabilized in the Z-pinch if the pressure profile fulfills the condition that the Kadomtsev term rdp/pdr has to be small. However, in the Z-pinch with a sharp boundary this term goes to infinity at the boundary and the equilibrium becomes grossly unstable. J.R. Drake anticipated that in EXTRAP the situation should be different and the Kadomtsev term is small at the periphery. This assumption is consistent with our model, where, owing to the scaling chosen, density and temperature profiles turn out to fulfill this condition, In other words we point out the physical mechanism which might provide for the difference between EXTRAP and the classical Z-pinch. Furthermore we present the perturbation analysis of the self similar pinch in the stationary equilibrium, considering only the simplest example of the axially symmetric mode with m=0. The growth rate of the fastest growing eigenfunctions, in units of the Alfvén frequency, is plotted as a function of sausage wave number, normalized to the pinch radius in Fig. 2. At short wavelengths the growth rate saturates at $2\tau_{Alf}^{-1}$, unlike the growth calculated from simplified models of the classical Z-pinch. On the other hand, most dangerous global free boundary modes with long wavelengths get more stable with decreasing pinch radius. Owing to the extreme steepness of the curve in Fig. 2, the factor 40 or 50 may be easily obtained if the pinch radius is decreased by a factor 3-4.

Therefore, considering the pinch radius R as a parameter and having the strongly non-linear oscillations of it in mind, the enhanced stability of EXTRAP might result from these oscillations. This analysis must be extended to the kink instability and also higher-order modes. Finally it should be mentioned that the stability properties of the dynamic system might be drastically different from the static system. Therefore to answer the question of stability of the dynamic system the sophisticated stability analysis, according to Lyapunov criterium has to be performed.

4. PRACTICAL IMPLICATIONS

At first we suggest trying experimentally the new scheme. According to our calculations, this scheme will be favourable from the stability point of view and will also allow the new machine, EXTRAP T1, to run with longer pulses than is possible with the present transformer. The current in such a system can be induced by driving the primary current with a certain pulse form in the conducting vacuum vessel outside the rods.

The second conclusion from results described above, is that the physical processes taking place in EXTRAP are functions of the energy loss mechanism and its scaling with the main plasma parameters.

Attained results seem to indicate: the positioning metallic structures in the close vicinity of the pinch, such as vacuum vessel, sparkplugs for ignition and so on will either devastate the stability properties of EXTRAP or drastically increase the requirement on the external toroidal field. As it follows from the present study the decrease of the current rise time leads to the same effect without deteriorating the octupole field confinement. Increasing the energy losses at the periphery and destroying the confinement properties of the octupole field may lead to the degeneration of EXTRAP into the classical Z-pinch.

REFERENCES

/1/ B.Lehnert, Physica Scripta 10, 139 (1974); B.Lehnert, Physica Scripta 16, 147 (1977).
/2/ J.R.Drake, Plasma Physics and Controlled Fusion 26, 387 (1984).
/3/ J.R.Drake, TRITA-PFU-85-11 (1985).
/4/ B.Lehnert, Comments on Plasma Phys. and Controlled Fusion 8, 91 (1985).
/5/ M.Tendler, Europhys. Abstracts 7D, 347 (1983).

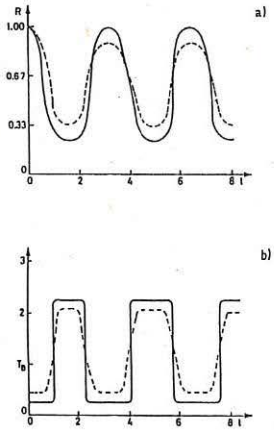

Fig.1

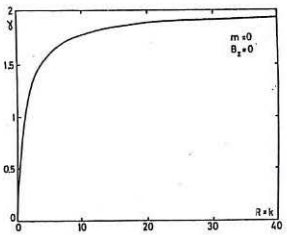

Fig.2

INITIAL EXPERIMENT IN A COMPACT TOROID FORMED BY MAGNETIZED T-TUBE (+)

A.SINMAN
Ankara Nuclear Research and Training Center, Nuclear Fusion Laboratory, Ankara - Turkey

S.SINMAN
Middle East Technical University, Electrical and Electronics Engineering Department, Plasma Engineering Laboratory, Ankara - Turkey

INTRODUCTION

In recent years, extensive investigations on the spheromak and the field reversed configuration have been carried out /1-3/. The spheromak configuration, in which a compact toroid plasma is confined by poloidal and internally generated toroidal magnetic fields, has attracted much interest because of its possible applicability to a fusion reactor /4/.

In our previous study, in order to produce a compact toroid by means of four magnetized T-tubes; a conceptual design and expected results had been presented /5/.

In this work, it has been demonstrated that a compact toroid may be formed by a single magnetized T-tube.

In the following paragraphs the explanation of the system and subsequently the results obtained will be submitted and interpreted.

SYSTEM DESCRIPTION

The system generally consists of the T-tube having a base-ball coil, the capacitor bank, the controlled spark-gap switch and the vacuum system.

The base-ball coil has two functions. Firstly, a belt shaped plasma current channel occured between vertical electrodes is pushed into the horizontal leg of the T-tube by the back-strap line. So it comes to existance of a mutual inductance between the part of the plasma current channel (time varying and non-linear properties) entered into horizontal leg and the base-ball coil itself. In this case, the base-ball coil terminated by a load resistor only generates a magnetic field perpendicular to plasma ring. Consequently, reconnecting the plasma current loop produced between the vertical electrodes, it transforms into a shape similar to the conchoid of Nicomedes $[(X-a)^2(X^2+y^2) = b^2X^2$ and $(r = b+a\sec\theta)]$ function.

Secondly, this ring formed is pushed into the flux conserver and then the compact toroid with a purely toroidal magnetic field is produced inside the flux conserver.

DIAGNOSTICS USED

In this study generally those known diagnostic techniques used in the high-beta systems are taken into consideration.

In this content, in order to investigate the electrical characteristics; the diagnostics such as the voltage divider,

the Rogowski coil and operational integrator are utilized. Besides pin-hole filter combined with the integrated photographic technique (with and without post fogging) is also applied. Only a base-ball coil is used as an external magnetic probe.

The Tektronix 454-A oscilloscope and HP-1744/A storage oscilloscope with its own polaroid camera are the recording systems for transient waveforms.

RESULTS OBTAINED

By means of the calibrated Rogowski coil and the fast integrator, the electrical characteristics have been investigated.

In Fig. 1, the plasma loop current of the T-tube versus time is shown. In this figure, the time scale is 1.0 μs/div and the vertical axis $I_{p\ell}(t)$ is 42.0 kA/div.

On the oscillograms taken from loaded base-ball coil (see Fig. 1) pushing the plasma loop from T-tube towards the horizontal leg can be observed. As a more detailed results in this figure; a comparison at the identical sweeping time, between the initial condition of the plasma loop current which is determined by the Rogowski coil and the signal taken from base-ball coil, have been illustrated.

According to this results, the drift velocity of the plasma loop is about 5×10^{6} cms^{-1}. When the base-ball coil is rotated 90^{0}; as it is also shown in Fig.1, there exist no signal on it. So it is understood that the plasma current loop belt has a definite position and it is possible to evaluate this MHD property by the angular rotation of the base-ball coil.

The plasma voltage on the T-tube have been measured by the voltage divider. In Fig.2, these results have been shown by the integrated signal and non-integrated plasma voltage waveforms.

By the help of these two oscillograms and the relation of

$$V_{p\ell}(t)=-d/dt\left[L_{p\ell}(t)I_{p\ell}(t)\right] \qquad (1)$$

it is possible to evaluate the changing of the plasma inductance in time.

On the other hand, calculating the logarithmic decrement found from the oscillogram, the approximate plasma electron temperatures have been determined. Combining the Spitzer's resistivity formula by the expression of the LCR circuit's logarithmic decrement, for the electron temperature

$$T_e=\left[(DT_pA)/(6.5\times10^{-5}C_B\ell_{p\ell})\right]^{-2/3}\ (\text{keV}) \qquad (2)$$

may be written; where T_p is the period, A is the cross section of the plasma current loop (pinched and pushed), C(B) is the capacitance of the storage bank, $\ell(p\ell)$ is the length of the plasma loop and the logarithmic decrement is given by $D=\text{Log}(e)\left[V1/V2\right]$.

According to the experimental results, the values of the electron temperature calculated by Eq. (2), have been found between 5.7 and 10.0 eV.

The electron densities may be calculated by the current parameters of the plasma loop. So the electron density $n_e(t)$ is given by

$$n_e(t)=\left[(1.05\times10^{11}I_{p\ell}(t)/AT_e^{1/2}\right] \qquad (3)$$

where $I_{p\ell}(t)$ is the plasma loop current and T_e is the electron temperature in eV. Using the integrated photographs taken from the plasma loop, the thickness of plasma channel transfered into horizontal leg may be found. Therefore the electron density may be approximately calculated from Eq. (3) since $I_{p\ell}(t)$ and T_e are known. From the experimental results electron densities of $6x10^{16}$ - $10^{17} cm^{-3}$ have been determined.

CONCLUSIONS

Without using any complex and programmable magnetic fields, by using only a base-ball coil, self controlled magnetic fields on the mode of magnetic flux feed-back by the plasma ring have been produced in the duration of 10.0 - 15.0 μs. Thus the plasma current loop pushed towards the horizontal leg of the T-tube have been transformed firstly the conchoid of Nicomedes function and then reconnecting into o closed elliptical current ring. This is the main current ring serving as the toroidal field of the compact toroid in oblate or prolate shapes with respect to plasma injecting mode to the flux conserver.

Although they change according to the experimental conditions; the plasma voltage, the plasma current, electron temperature, the electron density and the life time of the toroid are in the ranges of 5 - 8 kV, 100 - 150 kA, 5 - 10 eV, 10^{16} - $10^{17} cm^{-3}$ and 100 - 150 μs respectively. Experiments have been carried out using a back ground Argon filling gas in the pressure range of 50 - 550 mTorr.

(+) This work was performed under a cooperative agreement between Turkish Atomic Energy Authority and IAEA Vienna, the Division of Research and Laboratory, under Contract No.: 3823/RB.

REFERENCES

/1/ Yamada,M., et al., in Plasma Physics and Controlled Nuclear Fusion Research (Proc. 9th Int. Conf. Baltimore, 1982) Vol.2, IAEA Vienna (1983)265.
/2/ Watanabe,K., et al., ibid., p.311.
/3/ Siemon,R.E., et al., ibid., p.283.
/4/ Katsurai,M., et al., Nucl. Fusion 22(1982)1407.
/5/ in Controlled Fusion and Plasma Physics (Proc. 12th Eur. Conf. Budapest, 1985), Vol.9F, Part I (1985)642.

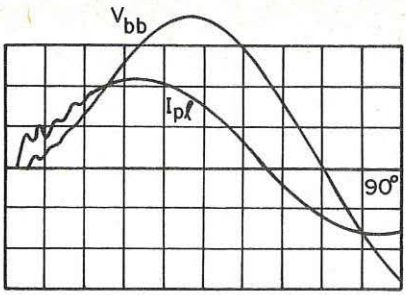

FIG.1. Comparison of the plasma loop current ($I_{p\ell}$) and voltage of loaded base-ball coil (V_{bb}) with time (1.0/us/div). Vertical scale: relative units.

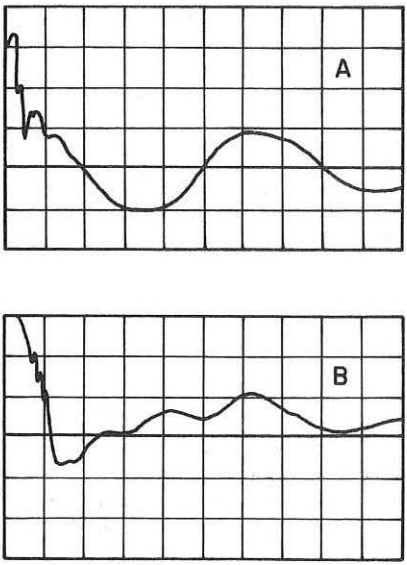

FIG.2. (A) Time evolution of the plasma voltage ($V_{p\ell}$ = 2.0 kV per division) with time (2.0/us/div). (B) Waveform of the integrated plasma voltage. Vertical scale: relative unit. Horizontal scale: 2.0/us/div.

AN ALTERNATIVE FORMATION SCHEME OF A COMPACT TOROID USING FOUR C-GUNS (+)

S.SINMAN
Middle East Technical University, Electrical and Electronics Engineering Department, Plasma Engineering Laboratory, Ankara - Turkey

A.SINMAN
Ankara Nuclear Research and Training Center, Nuclear Fusion Laboratory, Ankara - Turkey

ABSTRACT

A compact toroid formed by an alternative method and confined by its self generated toroidal magnetic field is submitted. Depending on the operating modes; an electron-plasma ring at high densities between 10^{15} and $5x10^{16}cm^{-3}$, the temperatures in the range of 25 - 90 eV and life times about 5 - 6 ms with disruptive instability have been determined. Nevertheless for the critical values of the gas pressure between 60 - 65 mTorr, a stable operating regime has been obtained and life time of the toroid at that condition is about 2.5 - 3.5 ms. In addition, at the gas pressures between 100 - 150 mTorr; it is possible to obtain an ion-plasma ring with the densities of 10^{15} - $10^{16}cm^{-3}$, the ion temperatures of 3 - 5 eV and life time of 2.5 ms. During the experiments, the back-ground filling gas of Helium has been used.

INTRODUCTION

In view of the recent rapid development of toroidal confinement systems towards a break-even plasma state, a serious question arises as to whether the present tokamak approach will indeed reach the final goal of a commercially feasible nuclear fusion reactor. In this sense, the compact toroid research /1/ is complemantary to tokamak research and will improve the understanding of plasma physics in toroidal devices, as the overall optimization of the toroidal experimental arrangements.

Compact toroid magnetic fusion concepts /2/ are those for which the confining magnetic field are determined by currents flowing within the plasma itself and for which no material structures are required to link the torus.

Concepts in this class, which includes spheromak /3-5/ and field reversed configuration /6-7/, offer reactor advantages that result from simplified geometries of the confinement chamber.

The field-reversed configuration is a prolate toroid formed with no toroidal field. The plasma within the separatrix is confined by closed poloidal field generated by internal toroidal plasma current.

The spheromak cofiguration has been successfully formed by three different type of production schemes of: i) the magnet-

ized co-axial injector; ii) the field reversed θ pinch with center column Z discharge and iii) electrodeless quasi-static scheme /3-5/.

In our previous study, in order to produce a compact toroid by means of four magnetized T-tubes; a conceptual design and expected results had been presented /8/.

In this work; modifying above mentioned system, four C-guns with 90^{o} aparts have been located inside the octagonal floating flux conserver of 40 litres, just like in the conventional T-tube by the influence of current in opposite direction on the back-strap which is settled down outside of the flux conserver, have been used to push the plasma rings towards the centre.

Since the profile of this structure looks like to the C letter, we will call it as C-gun.

By this purpose, the design and construction of a small scale system having a storage energy of 2 kJ per C-gun has been completed. In this experimental set-up generally those known diagnostic techniques used in conventional high-beta system are taken into consideration.

Preliminary experiments have been done using a back-ground filling gas of Helium with a pressure range of 40 - 150 mTorr in a single C-gun. In this content the main plasma parameters have been determined as follows: the electron densities between 10^{15} and $5x10^{16} cm^{-3}$; the electron temperature in the range of 25 - 90 eV depending on the gas pressure; the life time of dense toroid generated for 5 - 6 ms with the sawtooth perturbation but in the stable case in the range of 2.5 - 3.0 ms; the volume averaged total beta, 0.15 - 0.18; the form factor of elliptical shaped plasma b/a = 1.37; the safety factor q = 0.6; poloidal current density 200 - 300 A/cm^2 and lastly Troyon - Gruber constant of about 3.

If the results obtained are evaluated with respect to a MHD theory /9/ developed recently and other studies /10/, then this system realized takes place in the categories of 'High Beta Spherical Torus' or 'Spherical Pinch Tokamak'.

THE DEVICE

By the main points, the experimental arrangement has an octagonal 40 litres floating flux conserver which is the vacuum chamber at the same time. The back pressure in the flux conserver is $5x10^{-6}$ Torr. Four C-guns have been inserted around the flux conserver with 90^{o} aparts.

The system consists of 2 kJ capacitor bank for each C-gun, the spark-gap switches controlled by self generated UV ring and other needed diagnostic measuring equipments.

The main diagnostic techniques used are: the Langmuir electrical probes; the voltage dividers; the paramagnetic loop including a fast integrator; the magnetic probes; the Rogowski and base-ball coils; the L-R fast operational integrators; and visible light spectrum analyzer.

Besides, the fast storage oscilloscope of HP-1744/A and the other conventional fast oscilloscopes of HP-180/C and Tektronix 454/A have been used during data recording.

RESULTS

Preliminary experiments have been carried out by a single C-gun alone. Although it depends on gas pressure, the operating period of C-gun is about 50 - 60 μs. On the discharging circuit of the C-gun, the crowbaring technique has not been used. The current passing through the C-gun is 85 - 120 kA and damped sinusoidal in shape. During this period, a toroidal field in the form of damped sinusoidal again has been observed.

According to the oscillograms obtained from the high impedance, current limited Langmuir electrical probe or in other words the variation of the plasma space potential in time, between 40 - 60 mTorr gas pressure, just at the ending of C-gun operation, an electron ring has occured immediately and after 600 μs the microinstabilities due to the density fluctuations continuing 1.0 or 2.0 ms have came into ahead.

Following this phase, the density fluctuations have become more stable for 6.0 - 8.0 ms and in about 20 ms, the plasma space potential has approached to rest.

On the other hand, the signals taken by a single turn paramagnetic loop, have shown the toroidal field variations modulated by the sawtooth oscillations in the gas pressure range of 40 - 60 mTorr. Under this condition, the frequency of the sawtooth oscillations and the duration of toroidal field of electron ring were about 6.0 - 10.0 kHz and 5.0 - 6.0 ms respectively.

In order to find a correlation between the oscillograms belong to the different plasma parameters, the time base of recording oscilloscope has been synchronized by the light pulse of the photo transistor facing to the discharge.

According to the results obtained, from the visible light spectral analysis, using different optical filters, in the first 100 - 250 μs typically, the temperature of the electron ring has increased and evaluating the paramagnetic loop signals, it has understood that the electron temperature can rise up to 90 eV. Besides, the evaluations made parallelly by the plasma space potentials have indicated that the electron density can rise up to 5×10^{16} cm^{-3}.

At that time a fairly high toroidal magnetic fields of about 15 - 25 kG have been formed. The poloidal current densities of 200 - 250 A/cm^2, corresponding to 15 - 20 k-helical pitches encircling throughout the flux conserver have been calculated.

An ion ring has produced instead of the electron ring when the gas pressure approaches to 100 mTorr or higher values. The lifetime and the maximum temperature of this ion ring are 2.0-3.0 ms and 5.0 eV respectively. In the rather critical pressure limits of 65 - 75 mTorr, a stable and exponentially decreasing electron ring with a duration of 2.5 - 3.0 ms has been produced. The electron temperature of this ring is approximately 25 - 30 eV and the density varies between 10^{15} - 6×10^{15} cm^{-3}.

CONCLUDING REMARKS

The preliminary experimental findings obtained from a high beta spherical torus recently realized are being submitted. Although the C-gun resembles to the conventional T-tube, from the view point of operational principles, the device submitting in this study has an alternative arrangement.

By means of the C-guns inserted around the octagonal floating flux conserver and background filling gas, they have been possible to produce the long life (2.5 - 6.0 ms), dense (10^{15}- $5x10^{16}cm^{-3}$) and hot (25 - 90 eV) electron and warm ion rings.

The plasma rings have been confined by the influence its self generated toroidal magnetic field and electric field generated in the flux conserver itself.

The electron-plasma ring formation has determined the specifications of the aspect ratio and safety factor of the torus.

The flux conserver may also be used as a cavity with some additions on it. Thus high frequency heating method may become applied.

Besides, using some external poloidal field, it is possible to perform the ohmic heating mechanism.

According to the experimental results obtained, the strong paramagnetism has been observed and it has been understood that the turbulent heating has become dominate in the toroid at this situation. Furthermore the MHD instabilities at the compact toroid has shown a pecularity of the classical tokamak plasmas.

(+) Research is sponsored by IAEA Vienna, under contract No.: 3823/R1/RB with the Turkish Atomic Energy Authority.

REFERENCES

/1/ Proc. of the 7th CT Symposium, May 21-23, 1985 Santa Fe.
/2/ Katsurai,M., et al., Nucl. Fusion 22(1982)1407 and Finn, J.M. and Sudan,R.N., ibid., pp. 1443-1518.
/3/ Jarboe,T., et al., Phys. Rev. Lett. 45(1980)1264.
/4/ Goldenbaum,G., et al., Phys. Rev. Lett. 44(1980)393.
/5/ Yamada,M., et al., Phys. Rev. Lett. 46(1981)188.
/6/ Siemon,R.E., et al., in Plasma Physics and Controlled Nuclear Fusion Research (Proc. 9th Int. Conf. Baltimore, 1982) Vol.2, IAEA Vienna (1983)283.
/7/ Rej,D.J., et al., Ref. /1/.
/8/ in Controlled Fusion and Plasma Physics (Proc. 12th Eur. Conf. Budapest, 1985), Vol.9F, Part I (1985)642.
/9/ Coppi,B., et al., Nucl. Fusion 19(1979)715.
/10/ Peng,Y-K.M.,'Features of Spherical Torus Plasmas of Ultra Low Aspect Ratio and Large Elongation' and 'Small Tokamaks for Future Fusion Energy Research' by Gross,R.A., et al., oral presentation at the IAEA Technical Committee Meeting on Research Using Small Tokamaks, September 9-12, 1985 Budapest, Hungary; (to be published by IAEA, Vienna).

RFP PHYSICS AND EXPECTED PERFORMANCE IN RFX

V. Antoni, S. Martini, S. Ortolani

Istituto Gas Ionizzati del C.N.R. - Associazione Euratom-CNR
Via Gradenigo, 6/a - 35131 Padova (Italy)

The RFP plasma magnetic confinement system consists of a current distribution which is close to the theoretical force-free minimum energy state described by $\nabla \times B = \mu B$ with $\mu = \mu_o (J_{//}/B) = \text{const}$ [1], which characterizes many magnetic configurations found in nature [2]. In the laboratory since the confinement of plasma pressure is the goal and material walls are always in some contact with the plasma, the configurations depart somewhat from the theoretical ones, but a continuous process of relaxation acts to limit this deviation and to maintain the distribution against the resistive diffusion process. In this way a balance is achieved between diffusion and relaxation which, in present experiments, allows to confine plasmas with values of β of reactor interest obtained by ohmic heating only.

RFP characteristic parameters

The RFP operates in a region of parameters space which, similarly to a tokamak, is bounded in terms of plasma density and q values. Three parameters can be conveniently used to characterize the RFP [3]: I/N, $\Theta = \mu_o I/(2\pi a < B_\phi >)$ and $\Theta_o = \mu_o a J_o / 2B_o = a/Rq_o$. The ratio of plasma current to line density, I/N, is related to the tokamak Murakami parameter nR/B_T by the expression $nR/B_T = 10^7/(2\pi q \cdot I/N)$ and describes both a high density limit, which can be interpreted in terms of a balance between ohmic heating and impurity radiation losses, and a low density limit probably related to an excessive value of the streaming parameter. In general, although many pinches can easily operate at low density, it is clear that when operating close to the high density limit lower impurities, higher β and longer confinement times are obtained [4, 5].

The pinch parameter Θ is related to the parameter $I_N = I/aB$ (MA, m, T), often used to describe the tokamak β limit, by the relation $I_N = 5\Theta$; for a RFP Θ is theoretically bounded between 1.2 and 1.56 [1]. This upper limit would correspond to a total toroidal current limitation as $I < 3\pi a < B_\phi > /\mu_o$; this limit is not precisely found in experiments and the total current can exceed this value by 30-50%. However the central value of q, which is related to the parameter Θ_o as $q_o = a/(R\Theta_o)$, is limited experimentally and theoretically [6] by resistive MHD instabilities as shown in fig. 1 where the region of operation of a RFP and, for comparison, of a tokamak is represented. The limit on q_o can be interpreted in terms of a current density limit as $J_o \leq 3B_o/(\mu_o a)$ which is however less severe than in tokamaks. In fact the toroidal current density in the RFP can be typically $3R/(2a)$ times

larger than in a tokamak and, in addition, there is a poloidal current density comparable to the toroidal one.

In practice the boundary for stability to external m = 1 modes (i.e. modes resonant outside the toroidal field reversal surface) shown in fig. 1 is not very significant since it corresponds to configurations with deeper field reversal and lower q_a values than those generally measured. Although the q_o and q_a values for typical experimental mean field profiles lie in the stable region of fig. 1, resistive diffusion increases Θ_o by peaking the current distribution on the axis and tends to destabilize the configuration forcing it across the unstable internal modes boundary. These internal m = 1 modes (resonant inside the toroidal field reversal surface) are probably responsible for a current redistribution which restores the initial tearing mode stable configuration and so forth in a cyclic fashion. These periodical oscillations have been observed in experiments [6] and show a "sawtheet like" waveform similarly to tokamaks.

In summary the density limits and the range of possible q_a values can be used to represent the RFP operation on a Hugill plot similarly to a tokamak as shown in fig. 2. The RFP operating region extends up to values of $1/|q_a| \lesssim 50$.

β limits and confinement scaling

Although not yet as clearly characterized as for the tokamak, β limits are becoming apparent also for the RFP, both theroetically and experimentally.

According to MHD theory average $\beta \sim 30\%$ would be possible for ideal kink stability and $\beta \sim 20\%$ for tearing modes stability [7]. Resistive g-modes are probably the β limiting instabilities. These modes are characterized by high toroidal periodicity ($n > 10$) and their resonant surfaces accumulate near the reversal surface. Their ultimate effect is to generate a large volume in the plasma where the field lines are stochastic leading to enhanced electron transport. If relaxation is driven by resistive instabilities, both current driven (in the center) and pressure driven (in the outer region), the resulting β limit can be seen, more than as an MHD β limit, as the outcome of competing processes of relaxation and transport against ohmic heating. In present experiments this balance results in $\beta \sim 10\%$.

The data from present experiments covers about one order of magnitude for plasma current, density, I/N and confinement time. Though linear current scaling of T_e has often been quoted in the past, it is now clear both theoretically and experimentally that the β_θ or the T_e dependence on I and I/N is the most suitable description of RFP confinement behaviour. A negative dependence of β_θ on I/N is found on ETA-BETA II [4, 5]. Energy confinement time and consequently the Lawson parameter, $n\tau_E$, also display a negative dependence on I/N in ETA-BETA II, which is made stronger than that of β_θ by a more than linear increase of the resistive anomaly factor Z^*_{eff} with I/N [5]. However if one compares the best results of each experiment and moreover uses the same models and definitions, $\beta_\theta \cong$ const (~ 0.1) emerges quite

clearly as a likely RFP scaling as shown in fig. 3. At the same time, though complete control of the time behaviour of the density is still difficult on present experiments, it is proven that if Z_{eff} is kept reasonably low it is possible to operate with low I/N. This would allow to foresee a constant Z^*_{eff} and an energy confinement time scaling as $I^{3/2}$ or $n\tau_E \sim I^{5/2}$.

Assuming that stochastic magnetic fields created by resistive MHD turbulence determine the transport, two theoretical scalings have been suggested. For turbulence due to resistive g-modes the β is predicted to remain constant, i.e. the temperature scales as $T \sim (I/N)\, I$ [8]. This scaling corresponds to a variation of the fluctuation amplitude as $b/B \propto S^{-1/2}$ and is consistent with experimental results. On the other hand, assuming that tearing modes are responsible for stochasticity leads to a scaling for T and β as [9] : $\beta \sim a^{-1/6}\,(I/N)^{-1/3}\, I^{-1/3}$; $T \sim a^{-1/6}\,(I/N)^{2/3}\, I^{2/3}$. This scaling may not be ruled out on the basis of the present experimental data and the corresponding curve is also shown in fig. 3.

RFX

Although there are still uncertainties in the exact parameters dependence of the heating and confinement of a RFP it is clear that the plasma ohmic heating current must be increased substantially to discriminate between the various possible scalings. The main unresolved question in terms of physics is of course the nature of transport, whereas in terms of parameters it will be crucial whether or not β will remain constant as the current is increased. Various sets of plasma parameters expected in RFX are listed in table I according to the different scalings discussed above. The value of $\beta\tau_E$ which can be of the order of 1 ms in RFX is of particular interest. In fact the ignition condition and the Lawson criterion can be combined to give $n\tau_E T_o \geq 3 \cdot 10^{24}$ m^{-3} s eV which can be written as $\beta_o \tau_E B_o^2 \geq 2.4$ T^2 s. Assuming as technologically feasible a value of $B_o < 7$ T we find $\beta_o \tau_E \geq 5 \cdot 10^{-2}$ s. If however a limit on B_o/a (i.e. J) is set as $B_o/a < 10$ T/m it follows that $\beta_o \tau_E a^2 \geq 2.4 \cdot 10^{-2}$ $m^2 \cdot s$.

References

[1] J.B. TAYLOR, 5th Int. Conf. on Plasma Phys. and Contr. Nucl. Fus. Res., Tokyo (Japan) 1974, IAEA, Vienna (1975), Vol. 1, p. 161.

[2] L. WOLTJER, Proc. Nat. Acad. Sci., 44,(1958) 489.

[3] S. ORTOLANI, Nucl. Fus., 25, (1985) 1291.

[4] B. ALPER, et al., 12th Europ. Conf. on Contr. Fus. and Plasma Phys., Budapest 1985, Vol. 9F, Part I, 578.

[5] A. BUFFA, et al., this conference.

[6] V. ANTONI, et al., this conference.

[7] D.C. ROBINSON, Nucl. Fus., 18, (1978) 939.

[8] J.W. CONNOR, J.B. TAYLOR, Phys. Fluids, 27, (1984) 2676.

[9] Z.G. AN, et al., 10th Int. Conf. on Plasma Phys. and Contr. Nucl. Fus. Res., London (U.K.) 1984, IAEA, Vienna (1985), Vol. 2, 231.

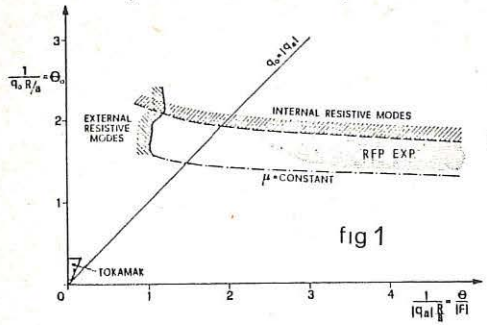

fig 1

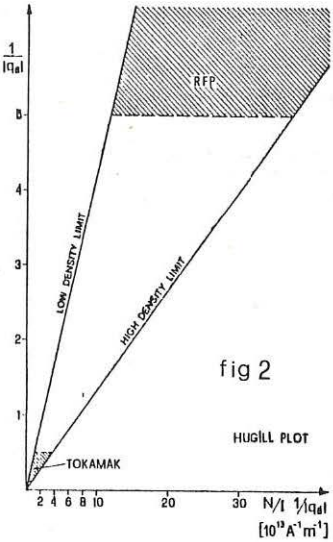

fig 2

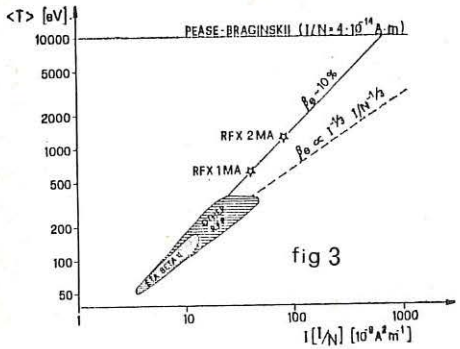

fig 3

TABLE I - RFX PARAMETERS

a) β = const scaling
b) $\beta \propto I^{-1/3}$ scaling
c) $\beta \propto I^{-1/3}\ a^{-1/6}$ scaling
† Temperature averaged over density profile

a (m)			0.5			
R (m)			2			
I/N (10^{-14} A·m)			4			
z^*_{eff}			4			
I (MA)		1			2	
$\langle n \rangle$ (10^{20} m^{-3})		0.3			0.6	
β_θ (%)	10	5.8	4.6	10	4.6	3.7
$\langle T \rangle^\dagger$ (KeV)	0.6	0.4	0.3	1.2	0.6	0.5
T(o) (KeV)	0.9	0.55	0.4	1.8	0.9	0.7
V_{Loop} (V)	6	12.5	18	4	12.5	18
τ_E (ms)	16	4.5	2.5	47	7	4
$\langle n \rangle \tau_E$ (10^{18} m^{-3} s)	0.5	0.15	0.1	3	0.5	0.25
$\beta_\theta \tau_E$ (ms)	1.6	0.25	0.12	4.7	0.3	0.15
ξ (%)	2.4	3.1	3.5	1.7	2.5	2.8
S (10^6)	2.5	1.1	0.8	10	4.6	1.5
		a)	b)	c)	a)	b)	c)

Plasma Edge Physics

EROSION AND REDEPOSITION OF METALS AND CARBON ON THE JET LIMITERS

J Ehrenberg*, G M McCracken+, R Behrisch*, P E Stott, J P Coad and L de Kock

JET Joint Undertaking, Abingdon, OX14 3EA, U.K.
* Max-Planck-Institut für Plasmaphysik, 8046 Garching bei München, FRG.
+ Culham Laboratory, Abingdon, OX14 3DB, U.K.

1. Introduction

It has been observed in JET and other tokamaks that the limiters become contaminated by material from the walls (1) (2) and in JET they are the main source of impurities in the plasma, although for current plasma discharges in JET the metals do not contribute significantly to the energy balance in the plasma centre. The analysis of the metal concentration on the limiter of JET gives indication on the erosion and redeposition processes for all impurities. These analyses have been carried out after the various periods of operation in 1983, 1984 and 1985 and have been described in detail elsewhere (3). The general features common to each period of operation are that the concentrations of metals have minima (~ 3×10^{20} atoms m^{-2}) near the centre and maxima (some 10^{21} atoms m^{-2}) near the edges. However the detailed distributions differ significantly for the three operating periods. In the present paper we discuss the possible mechanisms of contamination and some of the possible explanations for the observed spatial distributions.

2. Limiter Contamination and Cleaning Processes

The possible processes by which metals from the wall may be transferred to the limiter are: (a) Glow discharge cleaning (GDC). (b) Pulse discharge cleaning (PDC). (c) Disruptions or runaway electron interactions with the wall, leading to wall evaporation. (d) Arcing at the wall. (e) Charge exchange neutral sputtering of the wall. The contamination of the limiters by metals is clearly the integral effect of some or all of these processes. We have experimental evidence that all of these processes have occurred during the period of interest on JET.

Processes (a),(b) and (c) are expected to give a fairly uniform deposition flux onto the surface of the limiter. Process (c) may also result in discrete metal splashes and droplets on the limiter. Processes (d) and (e) would result in a deposition flux on the limiter peaked at the outside edge where material entering the scrape-off layer from the wall will be first ionized and swept along field lines onto the limiter.

However, the spatial distributions are modified by subsequent exposure of the limiter to tokamak discharges. Because of the limiter geometry in JET atoms sputtered from the limiter surface have a high probability of being ionized and entering the plasma. When these impurity ions subsequently diffuse out of the plasma they will be redeposited primarily on the limiter.

Direct experimental observations of impurity erosion from the limiter have been made spectroscopically. Early in the 1985 operating period one of the limiters was accidently contaminated by iron when a stainless steel probe was destroyed by a disruption. During the subsequent series of discharges the iron influx from this limiter was initially very high, but progressively fell to a negligable value after about 1 week. Similar results have been seen more recently when nickel and chromium deposited in discharges with r.f. heating have been removed in subsequent discharges without r.f.

3) Modelling of Erosion and Deposition Processes

In this section we examine in more detail the distribution of Ni on the limiter tiles from the 1983, 1984 and 1985 experimental period. Ni is chosen because it is the major wall (inconel 600) constituent. We first discuss empirical fits to the measured distributions and then propose a simple model which may explain some of the observed erosion and deposition phenomena.

Fig. 1 shows the Ni concentration per unit area of the limiter for the three limiter tiles of interest plotted as a function of the radial distance into the scrape-off layer X = r-a and divided by cos α to take into account the geometry of the limiter surface relative to the toroidal magnetic field lines. Where α is the angle between the surface normal and the toroidal magnetic field. We assume that the impurity distribution on the limiter is due to erosion and deposition and that this is composed of three terms:
(i) a uniform layer of metals C_o which represents the accumulated deposition due to glow and pulse discharge cleaning and to disruptions; (ii) an erosion fluence $C_e \exp(-x/\lambda_e) \cos\alpha$ which represents the removal of metals from the limiter during tokamak discharges (iii) a redeposition fluence $C_d \exp(-x/\lambda_d) \cos\alpha$ which represents the redeposition of metals from the plasma. Thus the resulting concentration on the limiter surface is

$$C(x) = C_o - C_e \exp(-x/\lambda_e) \cos\alpha + C_d \exp(-x/\lambda_d) \cos\alpha. \quad [1]$$

For simplication we will assume that $\lambda_e = \lambda_d$ and thus the difference $C_e - C_d$ represents the net erosion.
The date for the 1983 limiter is best fitted (figure 2) by $C_o = 2\ 10^{22}$ atoms m^{-2} and $C_e - C_d = 2.08\ 10^{22}$ atoms m^{-2}, ie. there is an initial uniform deposition consistent with the extensive glow clearing during this period of JET operations and a net erosion during subsequent tokamak discharges. It contrast the 1984 limiters is best fitted with a very small uniform deposit, Co = 0, and with net redeposition in tokamak discharges, $C_d - C_e = 1.07\ 10^{22}$ atoms m^{-2}. The difference between the 1983 and 1984 cases is not fully understood. There may have been a lower ratio of glow cleaning per tokamak discharge in 1984, particularly towards the end of the operating period resulting in the initial contamination being completely redeposited. It may also be significant that during this period of operation the limiter surface temperature was raised to around 1500°C compared to $\leq$ 700°C during earlier operation. A detailed surface analysis (4) suggests that diffusion of Ni into the bulk of the limiter to a depth of several μm took place due to the higher surface temperature. This would allow Ni to accumulate in the limiter at a depth where it would be protected against erosion but subsequently measured by the PIXE analysis technique which measures to a depth of several μm. Using the alternative technique of Rutherford backscattering with which a surface layer of about 10nm can be analysed, the concentrations on the actual surface have been found to have a distribution similar to that found on the 1983 limiter.

The 1985 data (figure 1) has a distribution similar to that for 1983 near to the centre, but increases sharply at x ~ 20nm and is much higher on the outer part of the limiter. The step coincides with the radius of the leading edge of the carbon shield surrounding the RF antenna which had been installed at the start of 1985. It seems resonable that the carbon shields which also act as limiters affect the scrape off layer and reduce the net erosion on the outer part of the limiter.

To examine these processes further we have developed a more detailed model of erosion and redposition in the scrape-off layer of a tokamak discharge.

The model is presented in more detail elsewhere (5) and we only give here a brief summary. We assume that the Ni distribution on the limiter is eroded by sputtering due to deuterons, light impurities (carbon) and self sputtering during plasma discharges. We also assume that the eroded flux of Ni enters the confined plasma and is then redeposited on the limiter by diffusion perpendicular to the magnetic flux surfaces. We assume further that the sputtering coefficients are energy dependent and therefore decrease with increasing radial distance from the leading edge of the limiter. By using measured data for the relative particle fluxes, the relative coverage of the limiter surface with metal (described by the factor f in figure 3) the scrape-off layer decay lengths and the plasma temperature at the limiter we get the erosion and deposition rates as indicated in fig. 3.

One result is that the limiter is split into an erosion and deposition zone the formation of which depends on the plasma boundary parameters. In our example this deposition zones is at $x \geq 15$mm for kT=100eV.

Another result is that erosion rates on the limiter surface are about 10^{20}atoms/m^2.s at $x \approx 10$mm. Thus an initial thin film surface coverage of 10^{21}atoms/m^2 would be eroded off in 10s. This is consistent with spectroscopic observation of the rate of which a limiter appears to clean up following contamination.

Erosion of droplets, however, which have been detected with diameter of up to 100 µm on the limiter will take much longer to erode. They may represent a more persistent source of Ni.

In view of this model we suggest that the surface concentration on the limiter does not reach steady state, as long as processes are present which contaminate the limiter in its erosion zone. This may occur in processes as mentioned under (a) - (c) in section (2).

4) Conclusions

A more detailed analysis of the metal distribution found on the JET limiters from three different operational periods indicates that the final distribution is largely affected by erosion and deposition processes caused by the plasma. Contamination of the limiter surface is probably due to tokamak operational processes as GDC and PDC as well as transfer of metal from the walls to the limiter in disruptive discharges. For a complete description the results suggest that the limiter surface conditions (temperature) and the positioning of the limiter in the torus relative to other structures (r.f. antenna) have to be taken into account. A theoretical model describing the 1983 limiter erosion and deposition processes gives results which are qualitatively in agreement with experimental observations during discharges.

References

(1) G M McCracken et al. J.Nucl.Mat. 111 & 112 (1982) 159.
(2) R Behrisch et al., J.Nucl.Mat. 128 & 129 (1984) 470.
(3) J Ehrenberg et al., 12th Europ.Conf.Fus.Plasma Phys. Budapest 2-6 September 1985.
(4) J Ehrenberg and P Borgesen, Proceed.7th Int.Conf. Ion Beam Analysis Berlin 7-12 July 1985.
(5) G M McCracken et al Proceed. 7th Int. Conf. Plasma Surface Interactions, Princeton N.J. USA 5-9 May 1986.

Fig. 1 Ni concentration distributions on JET carbon limiters from three experimental periods.

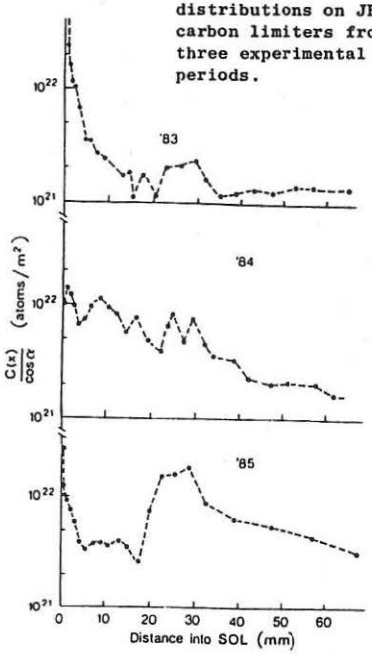

Fig. 2 Empirical fits to the Ni concentration distributions on JET limiters from two experimental periods

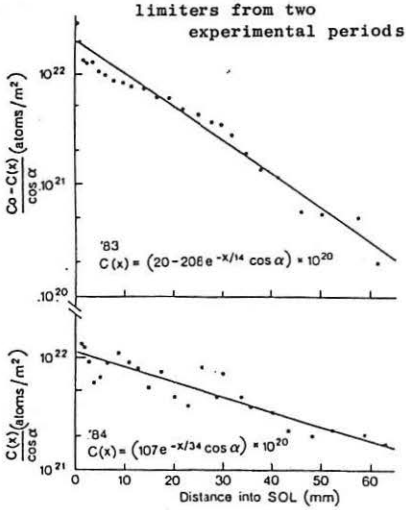

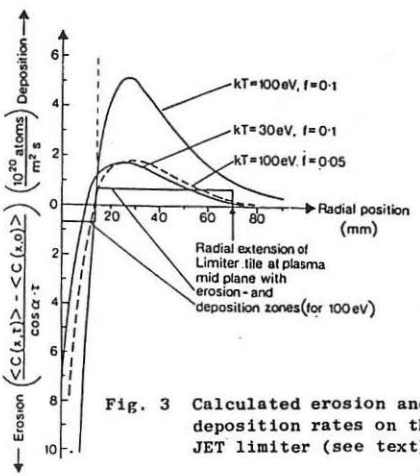

Fig. 3 Calculated erosion and deposition rates on the JET limiter (see text)

SPECTROSCOPIC STUDY OF HIGH DENSITY PHENOMENA IN DITE

N C Hawkes, J Allen, S J Fielding, J Hugill, P C Johnson,
G M McCracken and N J Peacock

Culham Laboratory Abingdon, Oxon, OX14 3DB, UK
(Euratom/UKAEA Fusion Association)

Introduction

As the high density limit is approached in DITE, there frequently appear a range of phenomena whose common feature is the formation of a cool extended region in the boundary of the plasma. These phenomena encompass: (1) strongly emitting, poloidally asymmetric regions positioned on the midplane, at the innermost major radius ('MARFE') and (2) the formation of a poloidally symmetric, weakly emitting layer sheathing a shrunken plasma column ('detached' plasma). Efforts have been made to produce these phenomena repeatably in order to study their properties. The TFTR scheme, in which the plasma current is reduced whilst simultaneously gas-puffing strongly, has been applied with some success, as has the simple application of a strong gas puff. Spectroscopic and bolometric studies were made of many of these discharges.

Instruments

The following instruments were used in the characterisation and measurement of detached plasmas and MARFES, figure 1 illustrates their position around the torus:

A visible/quartz-uv monochromator spatially scanned the plasma in the vertical direction every 8 mS, via a rotating mirror.

A radially viewing, non-scanning VUV, instrument covering the wavelength region 10-170 nm [1] was used at the same toroidal position as the visible instrument. This was later replaced by another instrument covering the range 30-170 nm [2]. Both instruments were equipped with multichannel diode array detectors.

A CCD camera equipped with interference filters with passbands corresponding to impurity lines in the visible had a line of sight tangential to the major radius, intersecting the inner poloidal limiter.

A Langmuir probe on a reciprocating drive made radial scans of the outer regions of the plasma once per discharge. It scanned vertically from above the plasma to 4 cm inside the limiter radius. A similar probe made measurements in the horizontal plane.

A 13 channel Bolometer camera gave a full spatial profile of total radiated power along a major radius.

MARFES

MARFEs are seen in DITE in high current, high density discharges, particularly in helium. They have been observed in deuterium but tend to be associated with detachment as mentioned below. MARFEs are seen clearly on the bolometer (figure 2a) and the CCD limiter viewing camera. They are characterised by the formation of a bright, radiating region centred on the median plane near the inner edge. The camera shows the poloidal extent of this region to be roughly ± 45°. Observations of the VUV emission along the major radius show an increase in radiation from low ion states (C II,III,O II,III,IV) when the MARFE appears. It is observed that different transitions of CIII increase by different amounts and from these increases we infer a lower limit temperature of 5 eV for the MARFE. The effect of the MARFE diminishes at higher ion states (above CIII and OIII) consistent with a upper limit temperature of 10 eV. The timescale for MARFE growth is of the order of 100 ms - many times the energy confinement time. There is no evidence of any effect on impurity concentration in the centre of the plasma. The scanning visible instrument and the bolometer show less or no effect of the MARFE at the outer major radius. There has been no attempt to quantify the toroidal symmetry of the MARFE, but its effect on diagnostics at greatly differing toroidal positions is qualitatively the same, suggesting that it is toroidally symmetric.

Detached Plasmas

Detached plasmas have been produced in low current (100 kA, $q \sim 8$) discharges near (above 70%) the density limit by strong gas puffing in both deuterium and helium. The bolometer (figure 2b) and the CCD camera show a layer 3 cm wide around the outside of the discharge with very low radiation losses. Probe measurements indicate a fall in edge electron temperature (from 10-12 to 6-8 eV) but only a small rise in density as detachment takes place. As the plasma density is increased over a range that includes both attached and detached plasmas a reduction in high Z (iron) and an increase in low Z (carbon) radiation is observed. There is no sudden change in radiation at the onset of detachment, but a smooth variation with density, implying that the detachment is not responsible for any change in plasma impurity content.

Detached MARFES

We have experimented with the technique used by the TFTR group [3] for producing detached plasmas in deuterium. This was found to produce a MARFE, which detached from the inner limiter. The plasma never recovers poloidal symmetry, the MARFE persisting to the disruption. This type of discharge was

studied with the spatially scanning visible spectrometer which recorded emission profiles from many different ion states of oxygen and carbon. A simple 1-D transport model was used to describe the outer region of the plasma. In this model it is assumed that neutral particles enter the plasma with thermal velocities, undergo ionisation and subsequent recombination and are transported by convection towards the plasma axis. Ionisation rates are given by Bell [4] and recombination rates by Summers [5]; diffusion is not included. The observed ion state radiation peaks are thus associated with different temperature regions in the plasma. The spatial profiles are then interpreted as shrinkage of the plasma temperature profile as shown in figure 3. Also shown on this figure are the largest possible radii for the q=2 and q=3 surfaces. As the density increases the temperature in the region outside the q=2 surface decreases continuously. This implies a corresponding contraction of the current density profile and a reduction in the current flowing in the outer region. The cold edge of the discharge approaches the q=2 surface as the density rises to the disruptive limit.

Conclusions

We have been able to produce detached discharges in DITE in deuterium and in helium. It has been found much easier to produce MARFES in helium than in deuterium. Both effects are features of high density plasmas (near the density limit).

Detached plasmas have a boundary temperature of 6-8 eV within 2 cm of the limiter as compared to 10-12 eV for an attached discharge. The density in this region in a detached discharge is only slightly (~20%) higher than in an attached discharge. A layer of cool plasma (less than 7-10 eV), which can be several centimetres thick and with very low radiation sheaths the main plasma column.

MARFES have a temperature of between 5 and 10 eV. They are poloidally asymmetric, usually appearing at the inner minor radius, near the midplane. MARFES and detachment seem to be independent phenomena, but both being high density phenomena have been observed in the same discharge.

There is no evidence of any effect of the MARFE or detachment on the central concentrations of either light or metallic impurities. There is an underlying trend of light impurity radiation to increase with density and of metals to fall.

References

[1] Fonck R J, Ramsey A T, and Yelle R V: Applied Optics Vol 21, No 12 (1982)

[2] Hawkes N C, Peacock N J: Proc 6th Topical Conf on High Temperature Plasma Diagnostics, Rev of Sci Inst (to be published)
[3] Strachan J D et al: Proc of 12th European Conf on Controlled Fusion and Plasma Physics, Eu Conf Abstr, Vol 9F, Part I, p339 (1985)
[4] Bell K L et al, Culham Laboratory Report CLM-R216
[5] Summers H P Appleton Report IM-367

Fig 1 Layout of diagnostics on DITE. Key: RLP - Reciprocating Langmuir Probe, BOL - Bolometer, CCD - Camera, VIS - Visible Spectrometer, VUV - VUV Spectrometer, L - Limiters.

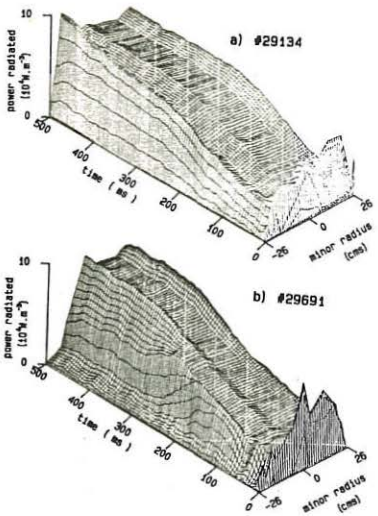

Fig 2 Bolometer signals showing (a) a MARFE and (b) detachment. Vertical axis is line of sight intensity.

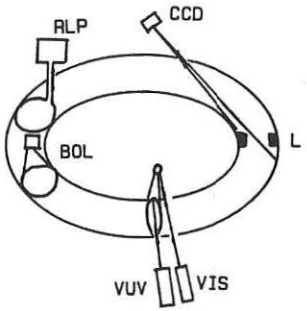

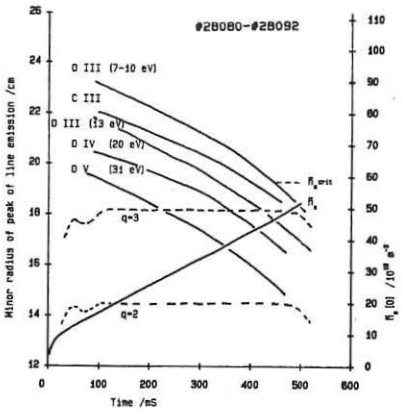

Fig 3 Time dependence of radiation maximum from various ion states during a MARFE. The poloidal extent of the bright region is small so inversion is not necessary. Ncrit is the density limit for this type of discharge.

Effects of ICRF-Heating on the Plasma Edge in TEXTOR

B. Schweer, H.L. Bay, W. Bieger*, P. Bogen, H. Hartwig, E. Hintz, K. Höthker, Y.T. Lie, A. Pospieszczyk, G. Ross**, D. Rusbüldt, U. Samm, R. Yamauchi***

Institut für Plasmaphysik, Kernforschungsanlage Jülich GmbH, Ass. EURATOM-KFA, P.O. Box 1913, D-5170 Jülich, FRG

R. Van Nieuwenhove, G. van Oost
Laboratoire de Physique des Plasmas - Laboratorium voor Plasmafysica
Association "Euratom-Etat belge"-Associatie "Euratom-Belgische Staat"
Ecole Royale Militaire - B-1040 Brussels - Koninklijke Militaire School

* Fachhochschule Jülich, D-5170 Jülich, FRG
** INRS-ENERGIE, Varennes, Québec, Canada
*** JAERI, Tokai, Japan

Introduction:
When ICRF power is applied to tokamak plasmas one observes in general not only the intended plasma heating but in addition several unintended and undesired changes in plasma properties /1, 2/. As one consequence of the rf-pulse a large amount of hydrogen gas is released from the walls or from the limiter and the plasma density is increased significantly. This is usually accompanied by an influx of light and heavy impurities, the type and magnitude of which depend on the experimental arrangements; frequently the plasma composition is changed considerably and current disruptions are triggered. It is suspected that the release of hydrogen and impurity fluxes is not only connected with the heating of the plasma core - as expected and predicted by theory /3/ - but also with a presently not fully understood transfer of rf-energy to particles in the plasma boundary and, may be, even directly to the wall.
By measuring the heat flux deposited at the limiter and the fluxes and densities of all important particle species at interesting parts of the wall and limiter system, we have tried to localize the particle sources, to determine their strengths in dependence on the rf-power, and to identify the underlying physical mechanisms, as far as possible.

Experimental arrangements:
Experiments have been performed in TEXTOR with carbonized walls and graphite limiters /4/ at I_p=480 kA, B_t=2T and a plasma radius of r=46 cm. The parameters of the ohmically heated target plasma have been varied in the range $1 \cdot 10^{13} cm^{-3} \leq \bar{n}_e \leq 4.5 \cdot 10^{13} cm^{-3}$ and 0.5 keV $\leq T_e(0) \leq$ 1 keV. The impurity concentration was typically 3 % C, 1.5 % O and 10^{-3} % metals. With the ICRH system on TEXTOR up to 2.25 MW of rf-power could be coupled into the plasma with two all-metal antennas at r = 48.5 cm which were also carbonized. The rf-heating experiments performed at 27 MHz, i.e. at the fundamental cyclotron resonance frequency of the minority ions (H) or $2\omega_{ci}$ (D) in a deuterium plasma with less than 1 % hydrogen /5/. With 2 MW of rf-power an increase of $\bar{n}_e(0)$ up to 50 % and of $T_e(0)$ up to 50 % was observed. For the investigation of the plasma edge effects the fluxes of the D-, O- and C-atoms from the main limiter and of the D-fluxes from the

antenna and from the wall have been measured by emission spectroscopy /6/. The fluxes from the main limiter and the antenna are measured in atoms per cm circumference /7/. The line averaged electron densities have been determined at r = 0 and at r = 40 cm using the HCN interferometer /8/. The radial profile of n_e has been obtained near the edge (46cm-50cm) from the emission of a thermal Li-beam /9/ and far in the limiter shadow ($\geq$50 cm) by a movable double probe /10, 11/.

Particle fluxes and densities during ICRH:
The temporal behaviour of n_e in the center and at r = 40 cm is shown in fig. 1. With the maximum rf-power of 1.8 MW coupled into the plasma an increase of $\bar{n}_e(0)$ by a factor of 1.3 and of $\bar{n}_e$ (40 cm) by 1.7 is observed. At r = 46 cm and far in the limiter shadow this factor increased up to 2.5-3.0, indicating a broadening of the density profile. A comparable increase is measured for the D-fluxes emitted from the main limiter (factor 2.0), from the antenna (3.0) and from the wall (2.6) taking the mean values during a sawtooth oscillation at 0.8 s and 1.2 s respectively (fig. 2). The fluxes of O and C, measured at the main limiter, increased by a factor of 2.3 and 1.8, respectively (fig. 3). The dependence of these fluxes on the rf-power is shown in fig. 4. Only a slightly different rise of O and C-fluxes was observed over the whole power range. The ratio of C-fluxes to D-fluxes from the main limiter as well as that of O-fluxes from the limiter to D-fluxes from the wall is approximately independent of rf-power suggesting that the limiter is the main C-source and the wall is the main O-source. For the investigated power range the D-and the light impurity fluxes did not show a saturation effect. In Fig. 5 the relative change of the $\bar{n}_e$ in the center and at 40 cm is plotted as a function of rf-power, showing that the profile broadens with increasing power. This broadening of the profile is demonstrated also by profiles (cf. fig. 6) derived from the Li-beam measurements. From the radial density profiles and from the D-fluxes a degradation of the particle confinement time can be deduced, which reaches nearly 50 % at 2 MW.

Discussion:
Since the deuterium flux from the limiter as well as the oxygen and carbon fluxes increases by about a factor of two, the plasma composition does not change significantly. The plasma had an all carbon surrounding and as a consequence the metal fluxes were only negligibly small. In order to investigate also the reaction to be expected from a metal wall, a stainless steel plate was installed at r = 52.5 cm with the surface almost parallel to the field lines. The iron flux from this plate was measured by laser induced fluorescence /12/. As shown in fig. 7 (see also fig. 4) the iron density in front of the plate increases by about a factor of ten. Since the signal disappears, when the target is withdrawn to r = 55 cm, it is obvious that bombardment by ions and not by neutrals is responsible for the sputtering. At kT_e = 5 eV, measured with probes near the wall, the sheath potential is below the threshold energy of 40 eV, and therefore the sputtering cannot be induced by a thermal plasma. At least a part of the ions must have supra-thermal energies. In order to explain a flux density of $2 \cdot 10^{13}$ Fe atoms/cm^{2}s, a flux of about $1 \cdot 10^{15}$ D-atoms/cm^{2}s with energies of about 500 eV is sufficient. This would be only 10 % of the measured flux of $1 \cdot 10^{16}$ D-atoms/cm^{2}s from the wall (cf. fig. 2).
As shown in fig. 8 the flux of D-atoms from the wall jumps to its final

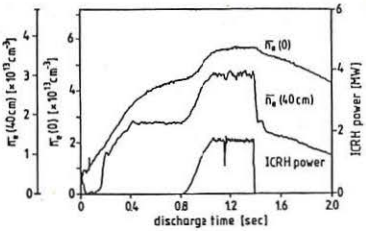

Fig. 1: Temporal development of the density in the center and at 40 cm in an ICRF heated plasma.

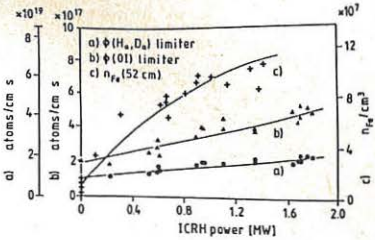

Fig. 4: ICRH-power dependence of the H/D and O-fluxes from the main limiter and of the FeI density in front of a SS-target.

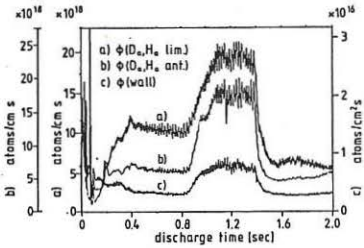

Fig. 2: Temporal development of the H/D fluxes from the main limiter, the antenna and the wall in an ICRF-heated plasma.

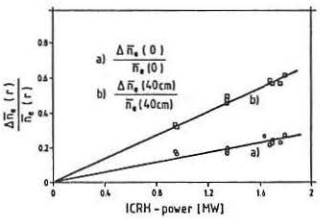

Fig. 5: ICRH-power dependence of the relative electron density increase in the center and at r = 40 cm.

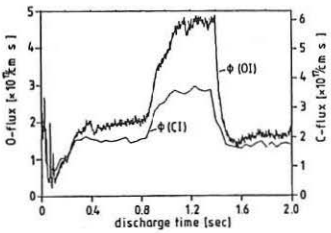

Fig. 3: Temporal development of the O- and C-fluxes from the main limiter in an ICRF-heated plasma.

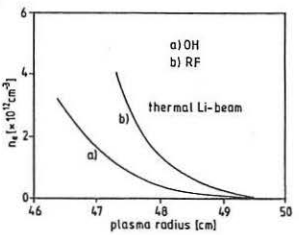

Fig. 6: Radial profile of the electron density in the ohmic and rf heated phase of the discharge.

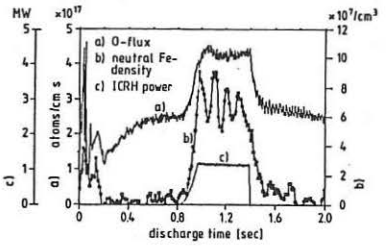

Fig. 7: Temporal development of the O-fluxes from the main limiter and the FeI density in front of a SS- target at 52.5cm in a rf-heated plasma.

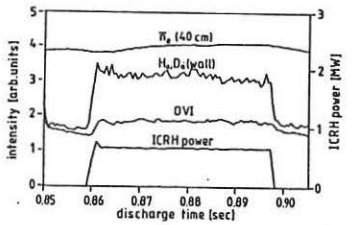

Fig. 8: Temporal response of the $\bar{n}_e$ (40 cm), the H/D wall fluxes and the O VI intensity in the core plasma on rapid changes in the ICRH-power.

value within 1 ms after switching on the rf-power, while the flux at the limiter (not shown in fig. 8) and $\bar{n}_e$ (40cm) increase on a much slower time scale (of the order τ_p). A possible explanation of these observations is that the D-flux as well as the Fe-fluxes are induced by fast ions. The short time constant, the bad screening of the wall by the limiter and the slow response of the limiter suggest that the fast ions are generated in the limiter shadow or that they have a high $v_\perp / v_{//}$ ratio. Particle fluxes and densities at the limiter radius increase both by a factor of about two. From this observation we conclude that the temperatures T_i and T_e at the edge are not significantly increased by the rf. Therefore the heat load at the limiter is expected to increase only by a factor of about two. This expectation is in contrast to the preliminary observation that the limiter load can increase by more than a factor of six (2 MW rf) compared to the ohmic phase with the scrape-off layer thickness remaining constant. One explanation for this discrepancy would be the occurrence of large $T_{i\perp}/T_{i//}$ ratios.

References:

/1/ P.L. Colestock et al., J. Vac. Technol. A3 (3), (1985), 1211
/2/ Messiaen et al., 12th Europ. Conf. Controlled Fusion Plasma Physics,Budapest, Sep. 1985 (EPS Geneva)
/3/ V.P. Bhatnagar et al., LPP-ERM/KMS Report 78, Brussels, (1981)
/4/ J. Winter, 7th Int. Conf. on Plasma-Surface-Interactions in controlled Fusion Devices, May 1986, invited paper Princeton
/5/ G.H. Wolf et al., invited paper, this conf.
/6/ A. Pospieszczyk et al., 12th Europ. Conf. Controlled Fusion Plasma Physics, Budapest, Sep. 1985 (EPS Geneva), Vol. II, 523
/7/ P. Bogen et al., J. Nucl. Mat. 128 & 129, (1984), 157
/8/ H. Soltwisch et al., Plasma Phys. and Contr. Fusion, 26, (1984), 23
/9/ Y.T. Lie et al., Proc. Int. Conf. on Plasma Physics, Lausanne/ Switzerland, June 1984, 320
/10/ K. Höthker, W. Bieger, Verhandl. DPG (VI) 21, P 38, (1986)
/11/ R. Van Nieuwenhove, G. Van Oost, Verhandl. DPG (VI) 21, P 37, (1986)
/12/ H.L. Bay, B. Schweer, J. Nucl. Mat. 128 & 129, (1984), 257

BEHAVIOUR OF THE PLASMA BOUNDARY DURING ICRH IN JET

H Brinkschulte, J A Tagle, M Bures, *S K Erents, P J Harbour, **T Huld, A S Kaye, ***C Lowry, *G M McCracken

JET Joint Undertaking, Abingdon, Oxon OX14 3EA, UK
* EUR-UKAEA Association, Culham Laboratory, Abingdon, Oxon OX14 3DB, UK
** Dept of Electro-Physics, Technical University of Denmark, Copenhagen
***Dept of Plasma Physics, Imperial College, London, UK

1. Introduction

A knowledge of the properties of the plasma boundary layer and their changes during the application of RF power is of general interest. Measurements of electron temperature and density are needed to understand the behaviour of impurities in the edge region. Radial profiles of electron density determine, in addition to other parameters, the coupling resistance of the ICRH antennae. The energy flux is needed for designing the limiters which are shaped to homogenize the radially dependent heat load. A very important parameter for the proper design of a limiter is the e-folding length for the energy flux. The total flux is also needed to understand the confinement of particles and energy during ICRH heating and from the density profile the diffusion coefficient $D_\perp$ in the boundary may be estimated.

2. Experimental

The JET scrape-off layer has been studied with 2 sets of single Langmuir probes mounted at two different poloidal and toroidal positions.

(i) A movable array of 4 probes (LPT in Fig. 1) introduced through a vertical port scans the boundary plasma near the top of the machine from the wall up to a minimum distance of 60 mm from the first closed flux surface defined by the limiters.

(ii) An additional set of two probes located in a side protection tile of an ICRH antenna (LP1 and LP2 in Fig. 1). These two probes monitor the plasma at distances of 15 mm and 27 mm, respectively, from the limiter separatrix (magnetic ripple taken into account).

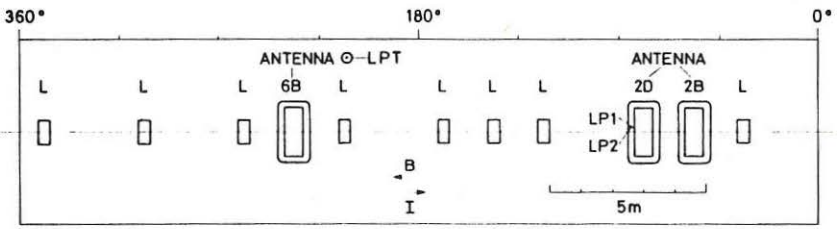

Fig. 1 Unfolded view of torus wall as seen from inside with 8 carbon limiters (L), 3 ICRH antennae (2B, 2D, 6B) and Langmuir probes (LP1, LP2, LPT).

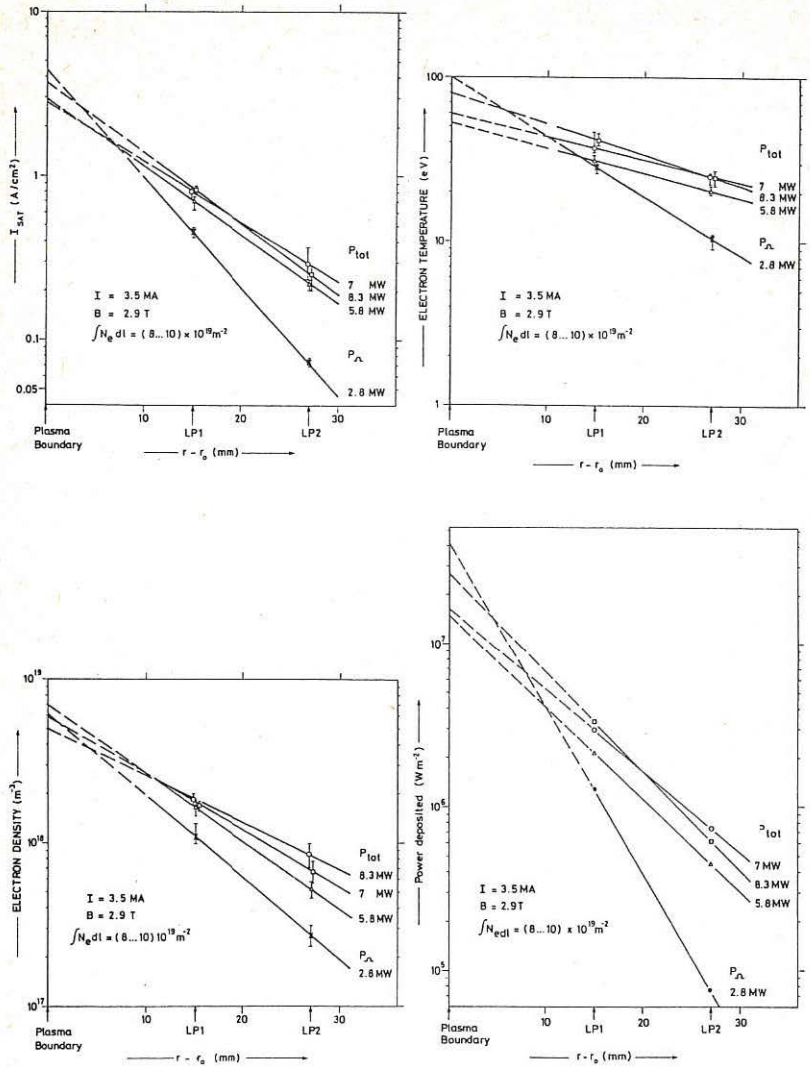

Fig. 2 Ion saturation current, electron density, electron temperature and power density versus distance from plasma boundary. Deuterium plasma with ^{3}He minority heating. JET pulses 6279...83.

Langmuir I-V characteristics ($-100\ V \leq V_p < +10\ V$) were taken at typically 0.5 second intervals during the plasma pulse, with a resolution of 50 ms for a single characteristic [1].

3. Results

Most of the results reported here have been obtained using the 2 antenna probes. The I-V scans have been arranged to determine the boundary properties before, during and after each 2 to 5 s long RF Heating pulse.

Fig. 2 shows the ion saturation current I_{sat}, the electron density n_e, the electron temperature T_e, the edge density n_e and the deposited power P_d versus radius for a typical discharge {$I_p = 3.5$ MA, $B_T = 2.9$ T, $\int n_e dl = (8..10) \times 10^{19}\ m^{-2}$} in which up to 6 MW ICRH power was added to the 3 MW ohmic plasma. The density as calculated from I_{sat} and T_e is obtained by assuming $T_e = T_i$ and the deposited power flux density is derived from $\gamma I_{sat} T_e$ with $\gamma = 10$.

As a general observation all the parameters increase at both probes as RF power is applied, with an exponential decay of the parameters toward the torus wall[3]. The particle flux rises rapidly, with a time constant between 0.25 and 3 ms. The rise time in the RF power is ≈ 0.25 ms. Rise times in H_α and CIII light have also been measured, and these are faster than the sampling rate, (< 5 ms). We find that the e-folding length for I_{sat} increases from $\lambda_{Isat} = 6.6$ mm (for $P_{tot} = P_\Omega = 2.8$ MW) to 10.2 mm at $P_{tot} = 8.3$ MW (Fig. 2).

The density behaves similarly: λ_{n_e} increases from 9 mm for the ohmic target plasma to 13.2 mm at $P_{tot} = 8.3$ MW. The temperature rises from an average of 30 eV in the ohmic discharge to 45 eV with RF heating, as recorded by probe LP1. The T_e radial profile also flattens. The heat flux at the first probe rises from 1.3×10^6 W m^{-2} for $P_\Omega = 2.8$ MW to 3.3×10^6 W m^{-2} at 8.3 MW total power.

These profiles for I_{sat}, n_e, T_e and P_d are consistent with those measured with the top Langmuir probe array at similar discharge conditions if one takes into account that the field lines are compressed by a factor of 3 (mid-plane compared to top) [1-3].

The observed increase of all the e-folding lengths is more pronounced for a 2 MA discharge than at higher plasma currents (as demonstrated for λ_{Isat} in Fig. 3). The curves appear to steepen as more RF power is added to the discharge.

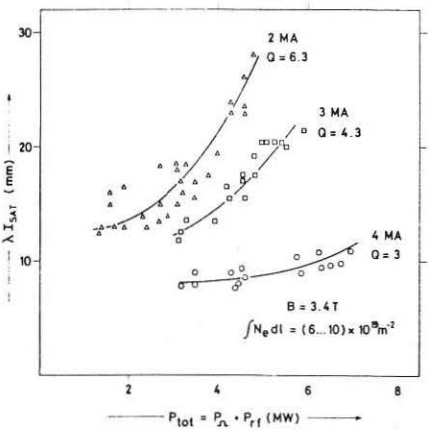

Fig. 3 e-folding length for ion saturation current versus total power for 3 different target plasmas (D with 5% ^{3}He).

4. Discussion and Conclusions

It was found that electron density, temperature and hence deposited power all increased during ICRH. The relative increase is higher towards the wall - leading to a broader

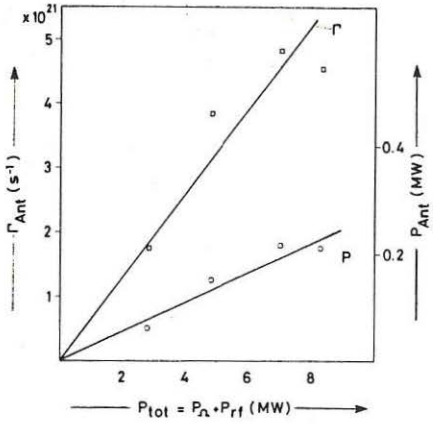

Fig. 4 Fluxes to the antenna limiters (at $r_s - r_o$ = 13 mm) versus P_{tot}.

boundary plasma during ICRH. (The absolute increases at the radii of LP1 and LP2 are similar.)

All parameters decay exponentially towards the torus wall. This is deduced from measurements taken between 15 mm and 60 mm from the separatrix. However one has to be cautious when extrapolating the measured data towards the plasma edge (dashed lines in Fig. 2).

The belt limiters for JET and the side protection tiles for the second generation ICRH antennae have been designed assuming a power flux e-folding length $\lambda_p \approx 10$ mm. The measured λ_p values are in that range. However, the increase in λ_p with power, taken in conjunction with the increases in I_{sat} and P_d, imply that the total particle flow and the total power flux to the limiters increase strongly with RF power. The calculated fluxes to the antenna limiters which are at $r - r_o$ = 13 mm are shown in Fig. 4. About 3% of P_{tot} is incident on the antenna limiters and up to 20% on the 8 carbon limiters. The increase of λ_p and P_d in the boundary with heating power is a matter of some concern.

The short timescale over which the boundary parameters increase (0.25-3 ms) is also observed for the CIII and H_α radiation. (The line averaged plasma density also increases during ICRH, but more slowly.) This implies that the plasma boundary is directly heated by the RF, the responsible mechanisms remain to be investigated.

The observed increase in e-folding lengths suggests an increase of perpendicular transport (and/or increased heating and/or ionisation in the S.O.L. [3]).

The rise in electron density with the associated flattening of the density profile should result in little change in antennae coupling resistance - which indeed has been observed.

References

1. S K Erents, J A Tagle, G M McCracken, P C Stangeby and L de Kock (Submitted to Nuclear Fusion).
2. P C Stangeby, S K Erents, J A Tagle, G M McCracken and L de Kock, 12th European Conference on Controlled Fusion and Plasma Physics (Budapest, Hungary, 2-6 September 1985), Vol. 9F,II,p 579
3. S K Erents, J A Tagle, P C Stangeby, G M McCracken, T Huld and L de Kock, to be presented at VIIth Int. Conf. on Plasma-Surface Interactions in Controlled Fusion Devices (Princeton, May 1986).

IMPURITY PRODUCTION DURING ICRF HEATING

G. Janeschitz, G. Fussmann, J.-M. Noterdaeme, K. Steinmetz, A. Izvozchikov[1], F. Ryter[2], G. Becker, H. S. Bosch, H. Brocken, A. Eberhagen, O. Gehre, J. Gernhardt, G.v.Gierke, E. Glock, O. Gruber, G. Haas, J. Hofmann, F. Karger, M. Keilhacker[3], O. Klüber, M. Kornherr, M. Lenoci, G. Lisitano, F. Mast, H. M. Mayer, K. McCormick, D. Meisel, V. Mertens, E. R. Müller[3], H. Murmann, H. Niedermeyer, W. Poschenrieder, H. Rapp, H. Röhr, F.Schneider, C. Setzensack, G. Siller, P. Smeulders[3], F.X. Söldner, E. Speth, K.-H. Steuer, S. Ugniewski, O. Vollmer, F. Wagner, F. Wesner, D. Zasche

Max-Planck-Institut für Plasmaphysik
EURATOM Association, D-8046 Garching

Abstract:
ICRF heating at $2\Omega_{CH}$ was investigated for a variety of different target plasmas and heating regimes. In all cases a significant increase of the radiated power, caused mainly by a higher iron concentration in the plasma, is observed. Neither the moderately improved particle confinement nor a reduction of impurity screening on account of changed plasma edge parameters is responsible for the high radiation losses, but enhanced wall erosion is required to explain the experimental data. The impurity production mechanisms are not yet fully understood. Impurity sputtering by oxygen and carbon, however, could be experimentally excluded as possible production processes. In all experiments a clear anticorrelation between wave absorption and impurity production was observed. Moreover, we find that suprathermal ions are produced in the plasma edge region by the non-absorbed ICRF power. It is assumed that these particles are responsible for the excessive impurity production.

General statements and features

ICRF heating at the second harmonic of hydrogen has been launched into different target plasmas (pure H, mixed H/D, and He; OH and NI preheated). The influence of wall carbonization has also been investigated /1/. As already outlined in /2/, in any case a significant increase of the impurity concentration (Fe, Ti - non-carbonized; C, Ti - carbonized) in the plasma and a concomitant enhancement of the radiation losses are found. In the non carbonized case the radiation profiles measured by a bolometer array are peaked in the plasma centre, whereas with carbonized walls the plasma radiates mainly in the edge region. Though the volume-integrated radiation losses are comparable in both cases (~45 % of input power), high-power ICRH (up to the maximum available level of 2.5 MW) can be launched into ohmic discharges only under carbonized conditions. Without carbonization the maximum ICRF power is limited to 1.5 MW owing to disruptions. In NI preheated discharges no power limit is oberved and the radiation losses are significantly reduced under both circumstances.
These observations underline the importance of impurity radiation in the case of high-power ICRF heating. An enhancement of the central impurity density can have various causes. We first checked the following possibilities:

- The impurity confinement in the core plasma is assessed from the decay of the TiXX line radiation after Ti injection by means of laser blow-off techniques into OH, ICRF, NI and combined NI/ICRF-heated plasmas. It is

[1]Academy of Sciences, Leningrad, USSR; [2]CEN Grenoble, France;
[3]Present address: JET Joint Undertaking, England;

found that the corresponding impurity confinement times (τ_I in the case of OH: 49 ms, NI: 19 ms, ICRH: 32 ms, NI + ICRH: 33 ms) are increased by a factor of ~1.5 when ICRH is added ($P_{NI} = P_{ICRH} = 0.8$ MW). This marginal improvement of central confinement cannot explain on its own the enhancement of the radiation losses.

- Larger changes of the plasma edge parameters, which could result in a deterioration of the screening efficiency could not be substantiated by edge diagnostics.

Consequently, enhanced wall erosion is required to explain our findings. The first hypothesis on impurity production mentioned in /3/ assumed that vertically drifting ions are accelerated in the resonance layer and release impurities at structural elements in the vicinity of the upper stagnation point. This hypothesis, however, had to be discarded on the basis of more extended investigations including spectroscopic Fe-flux measurements described below. In the following we present new experimental results with respect to the impurity production mechanisms.

Fe flux measurements

A double mirror system, specially developed for poloidal scanning, was used to measure spectroscopically the Fe fluxes originating in the vicinity of the upper and lower stagnation points, as well as from the inner wall (Fig. 1). The spectrometer used was a 1.5 m Cerny-Turner visible monochromator equipped with an OMA diode-array camera providing a high resolution (1000 channels, $\lambda/\Delta\lambda = 6000$). The evaluation of the spectra is rendered difficult by blending of the weak FeI lines with strong light impurity lines. For evaluation we used the 3719.9 Å and the 3734.9 Å FeI resonance lines. The system allows measurements during NI and combined NI + ICRF heating phases, but fails because of intensity problems during the OH phase. As seen from Fig. 1, no drastic increase of the FeI fluxes with the onset of ICRH occurs in contrast to the strong enhancement of the Fe concentration in the core plasma. Furthermore, in striking contradiction to the hypothesis mentioned in /3/ no up-down asymmetry in the fluxes is found (Fig. 1).

Sputtering by impurities

The possibility of sputtering by highly ionized light impurity ions, such as O^{+8} and C^{+6}, which compared with H^+ and D^+ have a much higher sputtering yield (~20 % instead of ~1 % for H^+), was checked by puffing oxygen and methane during the ICRH pulse. According to CX recombination/line intensity measurements of CVI and OVIII the concentrations of these light impurities were increased by a factor of 1.5. No change, however, of the Fe density (deduced from the FeXVI intensity) in the plasma could be seen. Self-sputtering of iron as a dominating mechanism can also be excluded, since under these circumstances the Fe signals should increase exponentially during the ICRF pulse, whereas generally a stationary behaviour is seen.

$2\Omega_{CH}$-heating in pure He plasmas

ICRH at $2\Omega_{CH}$ was applied to a pure helium plasma ($n_H{}^+/n_{He}{}^{++} \lesssim 3$ %). In this case no heating could be established and a low power limit at 200 kW exists. The FeXVI line intensity, the total radiation losses and the eletron density rise steadily during the whole ICRF pulse. In accordance with this behaviour we observe a reduction of the H_α divertor radiation, which is representative of the power flow into the divertor. Puffing hydrogen during the ICRF pulse, in order to increase the H^+ concentration to $n_H{}^+/n_{He}{}^{++} \sim 10$ %, results in a moderate heating of the plasma and the power limit is shifted up to 500 kW. The radiation losses and the FeXVI line intensity become stationary and are

reduced by factors of 2 and 4, respectively, at the end of the ICRH period. In this case the H_α divertor intensity does not change when ICRH (200 kW) is applied, indicating a power flow into the divertor during ICRH comparable to the OH phase. A similar type of discharge heated by 500 kW ICRF is presented in Fig. 2. In this case we stop hydrogen blowing 200 ms prior to the end of the ICRF pulse. As is clearly demonstrated in Fig. 2, all radiation signals (FeXVI, bolometer, soft X-ray) start to rise immediately after the end of H_2 puffing. A similar increase is found in the H^o CX-particle flux at 10 keV originating from the plasma edge (Fig. 2). These particles are produced by the wave and can be assumed to be representative of the behaviour of the non-confined high energy ions.
It is important to note that in contrast to the above-described relations no changes were observed when puffing deuterium instead of hydrogen into pure He discharges.

B_T-scans
In order to change the position of the resonance layer of the $2\Omega_{CH}$ ICRF in the plasma, the toroidal field B_T was varied in a sequence of discharges. In all these experiments a minimum of the radiation losses is found when the resonance layer is located in the vicinity of the plasma centre (Fig. 3). Furthermore, the H^o CX particle flux at 17 keV shows the same tendency. On the other hand, the heating efficiency (lower insert Fig. 3) is maximum for the optimum position of the resonance layer. These results also support the interpretation deduced from the He experiments that the variation of impurity density with the position of the resonance layer /3/ is caused by changes of the wave absorption.

Conclusions
ICRF heating in He discharges revealed a clear anticorrelation between wave absorption and impurity production. Consistently with these observations, we find strong indications that changes of the impurity density as a function of the resonance layer position can also be explained by a variation of the absorption conditions. Impurity sputtering as a possible process for enhanced wall erosion could be excluded by appropriate puffing experiments. Spectroscopic Fe-flux measurements did not yield strong poloidal asymmetries in the accessible range at the top and bottom divertor entrances and inner wall region. The observed Fe fluxes roughly correlate with the additional power input but no excessive increase is found in the case of ICRH. Therefore, it must be assumed that the excessive wall erosion takes place either at a closer distance to the antennae or at the outer wall regions which could not be observed. From CX-flux measurements we learned that - particularly in the case of bad ICRH absorption - high-energy ions ($\gtrsim$5 keV) are produced in the plasma boundary region. These particles are likely to move on purely confined banana orbits and may hit the outer torus wall at grazing incidence. Under these conditions enhanced sputtering is to be expected. This effect could possibly explain the discrepancy mentioned in /2/, where it was pointed out that with a maximum sputtering yield of 1 % (H^o - Fe) for normal incidence the necessary H^o/H^+ fluxes cannot be achieved under reasonable assumptions.

References:
/1/ K. Steinmetz, et al., this conference.
/2/ G. Fussmann, et al., Proc. 12th Int. Conf. on Controlled Fusion and Plasma Physics, Budapest (1985), Part I, A P Th 002.
/3/ K. Steinmetz, et al., Plasma Physics and Controlled Fusion, Vol. 28, No. 1A, pp. 235-238, 1986.

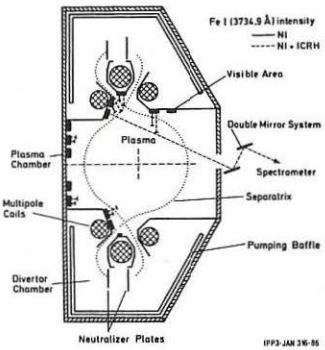

Fig. 1: Spectroscopic arrangement for Fe-flux measurements. The Fe I fluxes measured are proportional to the lengths of the bars perpendicular to the indicated areas.

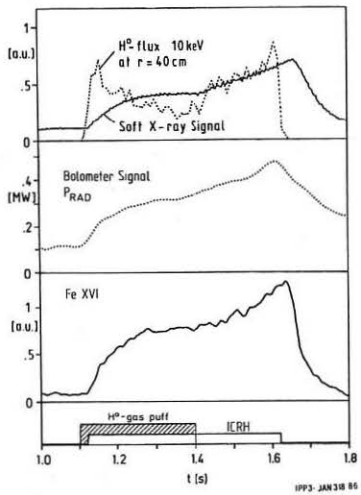

Fig. 2: Fe XVI line intensity, bolometer signal, soft X-ray signal, and the 10 keV H^0-CX flux, demonstrating the anticorrelation of impurity production and hydrogen concentration in a He discharge during ICRF heating (2 Ω_{CH}).

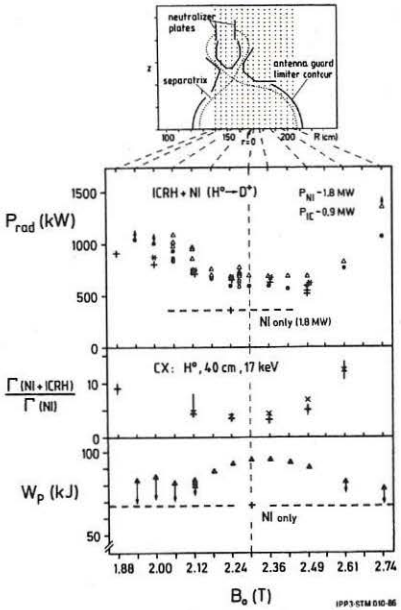

Fig. 3: Various plasma parameters during ICRH: total radiation losses (bolometer), relative fluxes of fast protons at the plasma edge and plasma energy content as a function of the position of the resonance layer (B_T-scan). Arrows in the W_p-plot indicate the increment of W_p due to increased ohmic input.

PLASMA FLOW IN A COLLISIONAL PRESHEATH REGION

R. Chodura

Max-Planck-Institut für Plasmaphysik, EURATOM Association,
D-8046 Garching, Fed. Rep. Germany.

ABSTRACT

Plasma flow from a source to an absorbing wall is studied in an 1-d kinetic particle model with Fokker-Planck collisions. The sheath forming in front of the wall in order to preserve ambipolar particle flow affects the heat flux in the upstream presheath region. Flow profiles and electron velocity distributions in the presheath are calculated for different collisionalities. Electron heat flux for different mean-free-path lengths is compared with values from classical Braginskii heat conductivity.

1. INTRODUCTION

In most fusion devices the plasma edge is in contact via magnetic field lines with a material wall, e.g. limiter or divertor plate. Plasma diffusing outward from the core into or generated within this scrape-off zone flows predominantly along field lines to the plate and is neutralized there. A schematic and simplified view of the scrape-off layer is a 1-d stationary flow between a plasma- and energy-creating source and an absorbing wall. The flow is determined by the properties of the source (which includes interactions with the background neutral gas), by the transport properties of the plasma and by the absorption properties of the wall. If the source generates equal amounts of positive and negative charges, the flow to the wall is ambipolar. Since ions and electrons have different mobilities, ambipolarity must be maintained by an electrostatic sheath in front of the wall which reflects all incoming electrons whith energies lower than the potential drop to the wall. Thus, the electron distribution in the sheath is truncated: reflected electrons with energies higher than the potential difference to the wall are lacking. In a region upstream of the sheath the untruncated electron distribution is restored by collisions. This region is called the presheath.

The sheath and presheath regions have characteristic dimensions which are respectively much smaller and comparable to the mean-free path length of plasma particles. It is, therefore, necessary to treat these regions by a kinetic model including collisions, i.e. by a Fokker-Planck model [1, 2].

2. MODEL

The numerical model consists of an 1-d electrostatic particle code including velocity changes by collisions. The coefficients of dynamical friction $\langle \Delta v_{\parallel} \rangle_{\alpha\beta}$ and diffusion $\langle (\Delta v_{\parallel})^2 \rangle_{\alpha\beta}$, $\langle (\Delta v_{\perp})^2 \rangle_{\alpha\beta}$ of a particle α are determined from the local moments of the distribution f_β of the collision partners β under the assumption of nearly Maxwellian f_β. The source is assumed to be well separated from the wall such that there is no particle and energy production within the presheath and sheath region. Electrons are generated with a finite temperature T_{e0}, ions as cold. Additionally, the plane of the symmetry $x = 0$ within the source is treated as heat bath: all electrons passing through this plane leave it with a Maxwellian distribution of temperature T_{e0}, thus simulating electron heat conduction from the core plasma. The wall at $x = L$ is assumed to be totally particle absorbing. No magnetic field is taken into account, i.e. the magnetic field is either absent or perpendicular to the wall.

Whereas the sheath has a thickness of only a few Debye lengths the presheath has an extension of the mean-free path of an electron with energy of about the sheath potential, which is for realistic cases by 3–4 orders of magnitude larger. In order to treat sheath and presheath with the same model, the latter had to be reduced to a comparable size by artificially enlarging the collision rate.

3. RESULTS

Figure 1 shows profiles of particle flux

$$\Gamma = \int f_{e,i} v_x d^3v,$$

ion flow velocity $V_i = \Gamma / n_i$, where n_i is the ion density, electron energy flux

$$Q_e = m_e/2 \int f_e v^2 v_x d^3v,$$

electron heat flux

$$q_e = m_e/2 \int f_e (\mathbf{v} - \mathbf{V}_e)^2 (v_x - V_{ex}) d^3v,$$

and potential ϕ. The space coordinate x is normalized to $\lambda_D = \lambda_D(n_0, T_{e0})$, the Debye length at n_0 and T_{e0} where T_{e0} is the temperature of electrons generated in the source and $n_0 = \Gamma_0 / v_{te0}$ with Γ_0 the total electron production per time of the source and $v_{te0} = (T_{e0}/m_e)^{1/2}$. C_0 is the ion sound speed at T_{e0}, $C_0 = (T_{e0}/m_i)^{1/2}$. The collisionality of the flow is indicated by the mean-free path length λ for 90° deflection of an electron with energy $3/2 T_{e0}$ by collisions with other electrons of density n_0 and the same temperature.

Electron flux Γ_0 crossing the sheath and being absorbed at the wall consumes more energy than that being transported convectively, i.e. $\delta T_{es} \Gamma_0, \delta = 2 + e(\phi_s - \phi_w)/T_{es}$ as compared to $5/2 T_{es} \Gamma_0$ (index s and w for sheath edge and wall respectively). The additional energy flux demand must be transported conductively from the source, i.e. by heat flux q_e. Far upstream from the wall q_e is maintained by a twist in the elctron distribution due to the temperature gradient (Fig. 2a). Less than a relaxation length in front of the wall the electron distribution

becomes a Maxwellian with a truncated upstream wing due to the lack of the wall-absorbed electrons (Fig. 2b). This relaxation length is determined by the diffusion length λ_{Diff} of reflected electrons into the truncated tail of its velocity distribution,

$$\lambda_{Diff} = v_c(\Delta v)^2/\langle(\Delta v_{\|})^2\rangle_{ee}$$

with Δv the diffusion interval, $v_c^2 = 2e(\phi_s - \phi_w)/m_e$, and $\langle(\Delta v_{\|})^2\rangle$ the coefficient of parallel diffusion at $v_e = v_c$. In case of Fig. 1,

$$\lambda_{Diff} = 1.9(\Delta v)^2/v_{te}^2\lambda$$

As shown in Fig. 3, the collisional heat flux q_e is nearly independent of x. Figure 4 shows the collisional heat flux for different ratios of mean-free-path length λ to system length L with n_0 fixed. For comparison the same relation is plotted for the classical Braginskii heat conductivity $\kappa = \kappa_0 T^{5/2}$, $\kappa_0 \propto \lambda$ [3]. Under the assumption of spatially constant q_e determined by the edge value $q_e = (\delta - 2.5)\Gamma_0 T_{es}$, $\delta = 4.4$, q_e is given by

$$[\frac{q_e}{(\delta - 2.5)\Gamma_0}]^{7/2} + \frac{7}{2}\frac{L}{\kappa_0}q_e = T_{e0}^{7/2}.$$

The Fokker-Planck curve is shifted toward lower q_e values indicating a heat flux limitation [4] at large mean-free-path lengths.

References

[1] S.A. Khan, T.D. Rognlien. Phys. Fluids **24** (1981), 1442

[2] R. Chodura. 12th European Conference on Controlled Fusion and Plasma Physics, Budapest, 1985, Europhysics Conference Abstracts **9F-II** (1985), 472.

[3] S.I. Braginskii. Reviews of Plasma Physics, (M.A. Leontovich ed.), Consultant Bureau New York (1965).

[4] J.F. Luciani, P. Mora, J. Virmont. Phys. Rev. Lett. **51** (1983), 1664

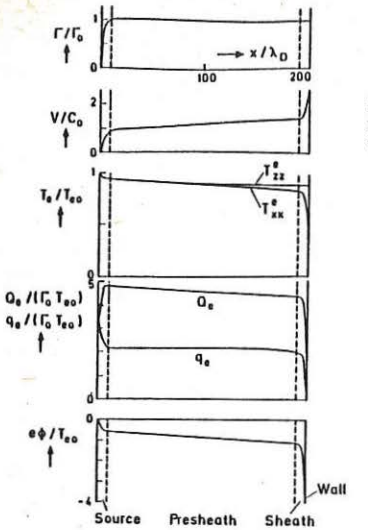

$\lambda / L = 0.62$
$m_i / m_e = 1836$
$T_{io} = 0$

Fig. 1 Profiles of particle flux Γ, ion flow velocity V_i, total energy and heat flux of electrons Q_e and q_e, and potential ϕ.

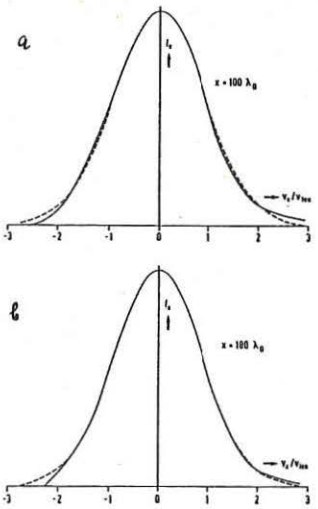

Fig. 2a,b Electron distribution functions in the collisional and non-collisional region.

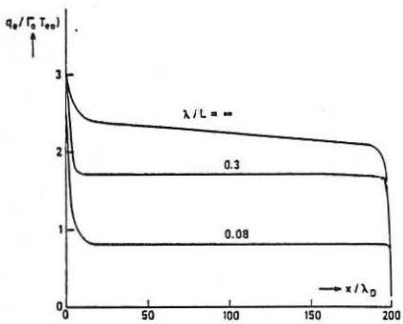

Fig. 3 Profiles of electron heat flux $q_e(x)$ for different mean-free-path lengths λ.

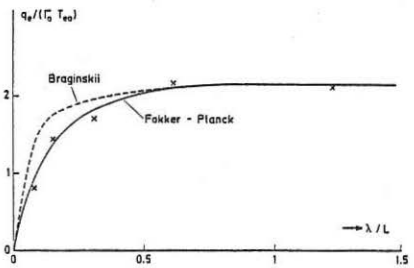

Fig. 4 Electron heat flux q_e for different ratios of mean-free-path length λ to system length L.

COHERENT PLASMA STRUCTURES IN THE UNSTABLE EDGE REGIONS OF A LINEAR QUADRUPOLE

R. Cherry and J.A. Elliott

UMIST, P O Box 88, Manchester M60 1QD, UK

The UMIST linear quadrupole (Phillips et al, 1978) operates as a steady state machine. The confining magnetic field is produced by two parallel conductors each of which carries the equivalent of 26000 amp-turns, creating a maximum field of some 2000 Gauss just above the conductors. The field null point lies on the separatrix, a figure of eight which encompasses both conductors and forms the division between the 'shared' and the 'private' flux (Fig.1).

Plasma from a duoplasmatron, is injected along the separatrix at one end of the device. The plasma expands, fills the 'shared' and 'private' flux regions and moves down to the end of the quadrupole whilst under the influence of various grad B and E/B drifts (Daly and Elliott, 1982). Plasma density and temperature vary with ψ/I (the radial flux coordinate which arises from the magnetic field geometry), the maximum density being 5×10^9 cm^{-1} with an electron temperature of up to 15ev (see Fig.2). In terms of ψ/I we calculated that the transition between the average stable magnetic field and the unfavourable curvature occurs at 0.34, the so called 'critical surface'. We define a second coordinate 'z' which represents longitudinal displacements in the quadrupole.

A number of fluctuations have been observed in the quadrupole, notably the 'shallow well flute mode' and the 'drift mode'. Both of these have received extensive theoretical (Hastie and Taylor, 1971) and practical (Carter et al, 1981) attention.

One type of fluctuation which is very interesting, but difficult to interpret occurs at the edge of the confinement region of the device. These fluctuations (see Fig.3) have a 'spike' like structure and represent a deviation from the local density of some 500%. The 'spikes' have been observed to take a number of forms. They can display either a leading or trailing skirt and seem to be able to travel either towards or away from the duoplasmatron with a speed of the order of 500 m/s. Their movement in ψ/I appears to be almost instantaneous, (i.e. $>10^5$ m/s) if indeed they are moving in ψ/I: they may be extended structures in $/I$. Of all their properties, perhaps the most peculiar is that of their dependence on residual gas levels. The ambient nitrogen partial pressure has been shown to be a critical factor in determining the form and appearance of the phenomenom.

As a consequence of their position in the MHD-unstable region, the 'spikes' were initially believed to be the non-linear limit of the interchange mode. This conclusion is attractive as it offers a

complete picture of plasma escaping across the magnetic field i.e. the drift mode would pass on plasma to the flute mode, which in turn would pass it on to the interchange (Rusbridge private communication.) However, cross-correlations (Bendat and Piersol, 1971) and bispectra (Kim and Powers, 1979) between the various modes suggests that only the flute and the drift are intimately related. Furthermore, even though the frequency of occurence of the 'spikes' is broadly similar to the 'flute' frequency, there seems to be no phase relationship between the two.

Models other than those which depend solely on the interchange instability concepts have been propounded (e.g. the 'vacuum cleaner model' (Williamson, 1985) and it was ideas such as these which suggested that an external source for the 'spikes' was increasingly likely.

Further investigation closer to the duoplasmatron reveals that the 'spikes' are in fact the result of the steepening of a relatively low frequency (300 Hz) oscillation. The purity of this oscillation immediately suggests that it is electromagnetic in origin, arising in the plasma source. The 'spikes' are then seen to be the result of a simple wave, the amplitude of which becomes large compared with the background plasma once it has moved into the more tenuous regions, the steepening effect being the essential non-linearity (c.f. long waves on a sloping beach). We note at this point that although the steepening effect is quite clear, the temporal progression is such that there is an apparent reversal to that usually predicted (e.g. Chen). The 'spikes' have exhibited leading steepened edges as well as the more common trailing edge, although the type of 'spike' observed does not appear to correlate with the apparent direction of the z-velocity. This may well have far reaching implications on the plasma flow in the outer regions. We believe intuitively that the steepened edge will be the leading edge in the plasma frame, and the apparent reversal may then be caused by convection of the plasma past the stationary probe.

Considering that the low frequency wave is propagating perpendicular to B, has the ion-acoustic velocity near the separatrix (a low field region) and seems able to steepen, one is tempted to identify it as a magnetosonic (or compressive Alfven) wave. However, this interpretation is inconsistent with that which is observed in the outer regions where the magnetic field is comparatively large and the plasma density small. Under these conditions the magnetoacoustic wave (which is a composite of the Alfven and acoustic wave) should assume the Alfven velocity (about 10^7 m/s) in 'z'. In fact, as mentioned, we observe a velocity of only some 500 m/s (which is the same order as the acoustic velocity with the same plasma conditions but in the absence of the magnetic field). Furthermore the frequency of an Alfven wave in the quadrupole is of the order of megaherz, many orders greater than that of the observed oscillation.

The velocity profile with ψ/I of the 'spikes' and the initial waveform is imprecise, even to the extent of ambiguous direction of the 'spikes' in 'z'. We know that the wave is subject to very variable conditions. We observe large velocity, magnetic field, temperature

and density gradients in the quadrupole not forgetting the all important turblence caused by the drift wave and the flute fluctuations. These conditions seem to combine, rendering the wavemotion complex even though the geometry of the system is comparatively simple.

In conclusion, we have discussed the properties of highly structured fluctuations found in the MHD unstable regions of a linear quadrupole. These were previously thought to represent some form of the interchange instability (Williamson, Hewitt, Daly et al, 1985), but have been shown to be an independently generated waveform, extending through the shared flux and finally reaching its nonlinear limit in the tenuous plasma in the edge of the device. These 'spikes' may be a contributory loss mechanism in these outer edge regions, but it has yet to be determined whether or not they are signifcant when compared to other loss mechanisms operating.

References

Bendat, J.S. and Piersol, A.G: Analysis and Measurement procedures, Wiley (1971)
Carter, P.S. et al: Plasma. Phys. 23 829, (1981)
Chen, F.F: Introduction to plasma physics, Plenum, New York, (1984)
Daly, E.J., Williamson,G.I., Rusbridge, M.G. and Jordan, A. Plas. Phys. 27, 761 (1985)
Daly, E.J. and Elliott, J.A: Plas. Phys. 24 923, (1982)
Hastie, R.J. and Taylor, J.B: Plas. Phys. 13, 265, (1971)
Kim, Y.C. and Powers, E.J: IEE Trans. Plas. Sci. Ps7,2, Jun 1979
Phillips, K. et al: Plas. Phys. 20, 653, (1978)
Williamson, G.I: PhD Thesis, UMIST (1985)

Fig.1 QUADRUPOLE MAGNETIC FIELD

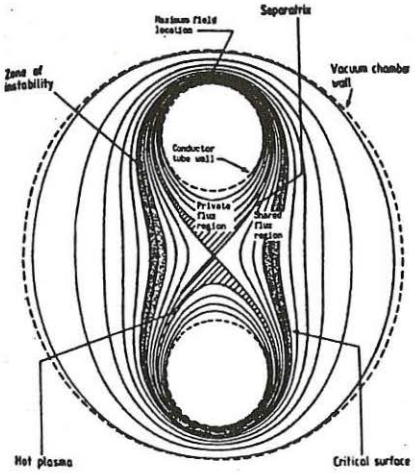

FIG.2 QUADRUPOLE PARAMETERS

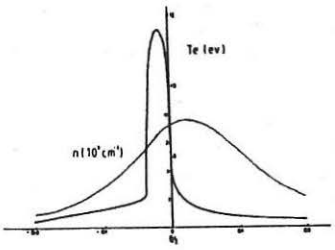

FIG. 3 FLUCTUATIONS IN ION SATURATION CURRENT

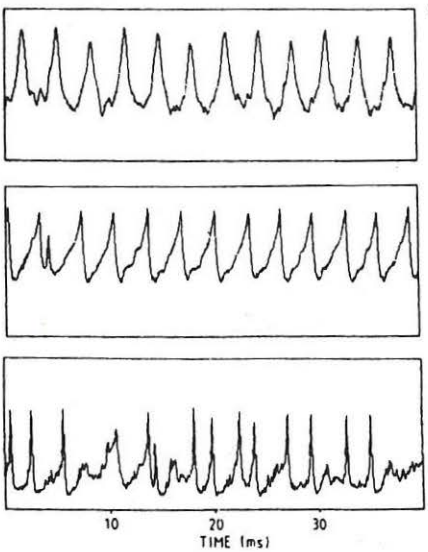

DENSITY PROFILE FROM MICROWAVE REFLECTOMETRY AND CONFINEMENT PROPERTIES OF A LOWER HYBRID CURRENT DRIVE SUSTAINED TOKAMAK DISCHARGE

G. ICHTCHENKO - H. BOTTOLLIER-CURTET - M. GONICHE
and the PETULA Group

Association EURATOM-CEA - Département de Recherches sur la Fusion Contrôlée
CENG-85X - 38041 Grenoble Cedex (France)

Two millimeter wave reflectometers using the extraordinary mode of propagation , have been installed on Petula in order to investigate their potentialities for application to larger tokamaks /1/.

By sweeping the frequency range 75-110 GHz, it was possible to measure the central part of the density profile. Both sides of this profile are accessible to the measurement if the density does not exceed a certain limit, which in our case is about $2.5\ 10^{13}$ cm^{-3} on the axis.(The exact condition applies on the density gradient and requires that :

$$\frac{d(\omega p^2)}{dR} < \omega\ \omega c/R \text{ everywhere)} \qquad (2)$$

The addition of a second reflectometer working in the range 60-90 GHz allowed the determination of the external part of the profile (R > 10 cm).

The detector output results from the beat between a reference wave and the wave reflected by a cut-off layer in the plasma. It exhibits a number of "fringes" which can be as large as 200 for each range of swept frequencies. The profile calculation is a step by step procedure using the frequency difference between two successive fringes. For a given frequency ω, the locus of the possible reflection points on a diagram $N_e(R)$ is determined by the cut-off condition :

$$\frac{\omega p^2}{\omega^2} = 1 - \frac{\omega c}{\omega} \qquad \text{(Fig. 1)}$$

To start the calculation, it is necessary to determine for the starting frequency the intersection of this locus with a density curve determined with another method. The particular case of a zero density can be also considered, but a threshold density certainly exists, under which the evanescence of the layer between the cut-off and the resonance is not large enough to ensure a proper reflection of the waves. It may be calculated by integrating the refractive index between cut-off and resonance. The result is in our case of the order of 10^{11} cm^{-2}.However, a movable multichannel grill interferometer gives us a profile of the scrape-off plasma which can be used in conjunction with the reflectometer measurements.

The resulting profile is presented on Fig. 1 with and without L.H. current drive application. The peaking which is observed at a low central density and for a moderate RF input power, is consistent with the observed increase of the internal inductance.

The effect of L.H. current drive application is particularly marked on the

scrape-off layer plasma, whose density can be decreased by more than an order of magnitude.

It is generally observed that in these conditions of moderate R.F. level, the scrape-off density has the same temporal and parametric dependence than the loop voltage, but when the input R.F. power is further increased, this effects saturates while the loop voltage continue to decrease (Fig. 2).

If one considers that the drop of the scrape-off layer density corresponds to a steepening of the profile near the limiter radius, and that this scrape-off plasma is due to the competition between the parallel particle diffusion and a transport of mass parallel to the magnetic field, such a steepening can be due either to an enhauced transport along the magnetic lines or to a reduced diffusion flux across the last closed magnetic surface just touching the limiter.

Both mechanisms do probably exist, since Langmuir probe measurements, made in comparable experimental conditions have shown that the electron temperature increased by about 20 % under RF application. Assuming that the particle drift towards the limiter has the sound velocity, the heating of the electrons can account only for 10 % in the steepening of the density gradient which then can be explained only by a reduction of about a factor of 2 of the particle flux escaping the central plasma.

Note that the total particle content of the plasma remains approximately constant or slightly increases like does the total energy content, while the total input power decreases under the short-circuiting of the induced voltage. Similar observations has been made also on Versator /4/ and the improvement of the particle confienement attributed to a stabilization of the anomalous Döppler instability. The reflectometry method provides also a mean for studying the turbulence with an enhauced sensitivity to a reflection zone.

For this purpose a sine-cosine arrangement has been added on the 75-110 GHz reflectometer in order to determine unambigously the phase of the reflected wave when working at a fixed incident frequency. A fast Fourier transform procedure can be applied in order to determine a fluctuation spectrum.

Fig. 3 represents the recorded phase versus time in a situation where a m = 2 mode is crossed by the probing millimeter wave beam, and Fig. 4 a typical drift wave turbulence spectrum obtained by averaging 4 spectra recorded during 4 comparable shots.

REFERENCES

/1/ F. Simonet, Rev. Sci. Instrum. 56 , 664 (1985)

/2/ H. Bottolier-Curtet, G. Ichtenchko, accepted for Review of Sci. Instrum. (1886)

/3/ G. Ichtchenko et al, Intern. Conf. on Plasma Physics, Lausanne p. 217 (1984)

/4/ S.C. Luckhardt et al, report PFC/JA, 84-42 MIT (1984)

/5/ M. Goniche et al, paper N° 213 (This Conference).

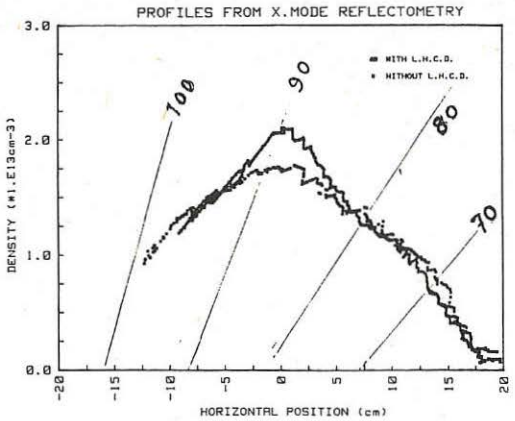

Fig.1: Density profiles with (——) and without (****) lower hybrid current drive application. Cut-off loci for different frequencies are also indicated.

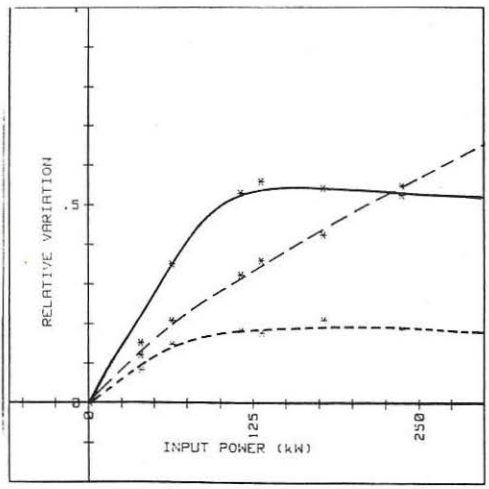

Fig.2: Relative variations of the loop voltage(- - - -),of the density at R = 15 cm(....) and at R = 17 cm (——).

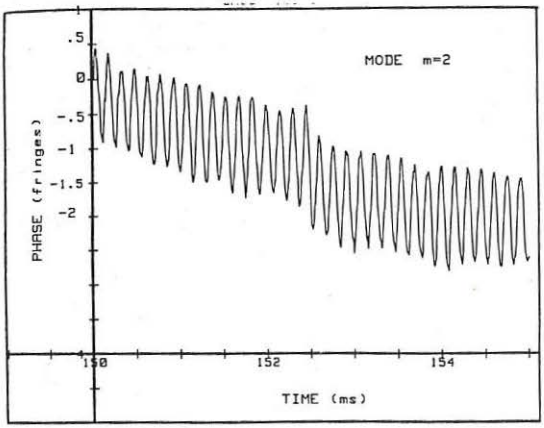

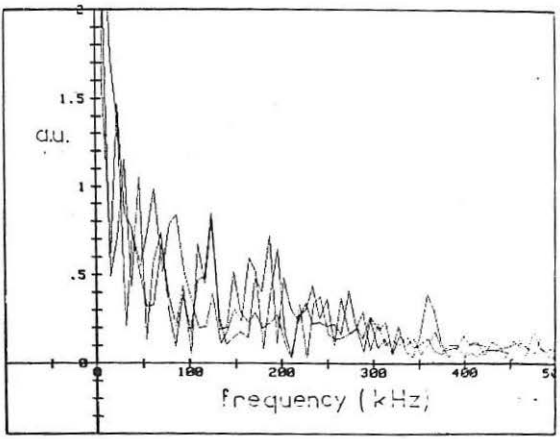

Fig.3: Observation by the reflectrometry of the m = 2 M.H.D. activity.

Fig.4: A spectrum of drift wave turbulence deduced from the reflectometry measurement.

DEUTERIUM AND IMPURITY FLUXES IN SCRAPE-OFF LAYER OF TOKAMAK STUDIED BY COLLECTING PROBES

S.A.GRASHIN, Yu.A.SOKOLOV
KURCHATOV INSTITUTE OF ATOMIC ENERGY, MOSCOW, USSR
V.H.ALIMOV, I.I.ARHIPOV, A.E.GORODETSKY, A.P.ZAKHAROV
INSTITUTE OF PHYSICAL CHEMISTRY, MOSCOW, USSR
G.A.TVARDAUSKAS
INSTITUTE OF SEMICONDUCTORS, VILNUS, USSR

Deuterium (hydrogen) and impurity fluxes in toroidal and poloidal directions and ions (D and H) energy in the scrape-off layer (SOL) of TM-4 and T-10 were defined by collecting probes method.

Monocrystalline Si-probes fixed to a special holder were exposed without time resolution at different radial positions for 1 shot on T-10 (Fig.1) or for many shots (from 5 to 500) on TM-4. Toroidal fluxes in e- and i-directions were defined. Transversal flux was defined as the flux on the poloidal side of the holder on T-10 (Fig.1.) and as the flux perpendicular to the chamber wall on TM-4. The main tokamak and plasma parameters are, TM-4: $R=53cm, r_w=10cm, r_L=8,5cm$, $H_z=15kOe$, $I=22-25kA$, $N_e=2-3\cdot10^{13}cm^{-3}$, $t_{pul}=0,03s$.

T-10: $R=150cm, r_w=39,5$ cm, $r_L=26,5cm$, $H_z=25kOe$, $I=200kA$, $N_e=4\times10^{13}cm^{-3}$, $t_{pul}=0,8s$.

TM-4 was operated with hydrogen, T-10 - with deuterium.

The surface study of exposed probes was fulfilled by the secondary ion mass-spectroscopy (SIMS) and by the reflected high energy electron difraction (RHEED). SIMS allows to obtain the depth distribution of implanted hydrogen, deuterium, and impurity atoms. The implantation depth is FWHM of the profiles. Calibration for the absolute measurements of deuterium was done. A SIMS-signal from the monolayer of deuterium absorbed on the surface of a reference probe under exposure to molecular deuterium at room temperature corresponds to $8\cdot10^{14}cm^{-2}$. The absolute calibration for impurities was not done. The depth distribution of D, Li, Cr-atoms in the probes exposed on T-10 for three radial positions are in Fig.2. The refrence signal is also given there. Implantation depth and trapping vs. fluence predicted by the code /2/ were used for definition of the ions energy. We also used data on ranges H and D in Si from /1/. Implantation depth varied from 4Å to 22Å in our experiment.

RHEED was used for the determination of atom displacement amount in the lattice of Si-probe under plasma bombardment. Changing the angle θ between the analysing electron beam and the surface of Si-probe we scanned the probe in depth. The angle θ at which the diffraction picture from the non-disturbed lattice was registered, gave us the number of amorphisied layers $n=n_0\theta$, where $n_0=400, 10^{-3}\leq\theta\leq10^{-1}$ /3/. The number of atom displace-

ments in the lattice $F_d = 1 \cdot 10^{15}$ n cm^{-2}. In our case, from 20 to 1 atomic layers were amorphisied. To produce an atom displacement in the lattice the implanted ion/atom must have the energy higher than the threshold energy E_{th}/4/. The threshold energy is different for different kinds of implanted ions: E^H_{th} = 150-200eV for hydrogen, E^D_{th} =80-100eV for deuterium, E^{Mo}_{th} = 25-30eV for impurity /Mo or Fe-like/. Having determined F_d, one can estimate the flux of the incident ions/atoms with the energy higher than the threshold one.

The data on the energyof deuterium, E, on the amount of trapped deuterium, F_D, and on the number of atom displacements, F_D, in the SOL of T-10 are given in Table.

N	r, cm	E, eV			F_D 10^{16} at/cm^2			F_d 10^{16} cm^{-2}		
		i-side,	e-	, p-	i-	,e-	,p-	i-,	e-,	,p-
I.	32,1	40-100	30-80	1-20	1,6	2,6	1,1	3,0	2,0	1,6
II.	34,0	10-40	10-50	1-10	1,6	1,5	0,6			
III.	36,4	10-20	10-20	1-10	1,6	1,2	0,25	1,5	0,6	0,3

The electron temperature T_e determined at the same radii with Langmuir probes is changed from 2eV (r=36,4cm) to 10 eV (r=32cm) Thus, the longitudinal energy of deuterium is a few times higher than T_e.

On TM-4 the energy of hydrogen ions, defined with the probes collected transversal flux at the wall radius, was E = =20-70 eV that is also a few times higher than T_e at the same radius. The transversal hydrogen flux on TM-4 was $\Phi = (1-2) \cdot 10^{16}$ cm^{-2}s^{-2}, that is in agreement with the flux obtained from the particle balance.

As the toroidal fluxes are much greater than the transversal ones and due to the long pulse duration on T-10 the probes have been saturated by deuterium even for 1 shot. In this case, the amount of trapped deuterium slightly depends on the fluence and one can only roughly estimate the toroidal flux value. These fluxes were independently defined with Langmuir probes: Φ = = 2 10^{19}cm^{-2}s^{-1} at r=32cm, $\Phi = 2 \cdot 10^{18}$cm^{-2}s^{-1} at r=34cm, Φ = = 3,5$\cdot 10^{17}$cm^{-2}s^{-1} at r=36cm.

The flux of ions with the energy higher than the threshold one is about 10^{-2} of the total flux incident on the probe. This ratio is true for both toroidal and transversal fluxes. In our case, the atom displacements in the Si-lattice can be provided by the fast ions/atoms with energy E$\simeq$150-200eV, related to the tail of ion distribution function. However, the same effect can be caused by the atoms of impurities (Fe-like, Mo) for which the E_{th} is noticeably lower. The transversal flux of the Cr ions on TM-4 estimated by their deposition on the probe, was about 2 10^{14}cm^{-2}s^{-1} that coincides with the high energy part of hydrogen flux. Thus, we can't point out the main reason of Si amorphisation and, therefore, the main reason of the sputtering.

An asymmetry in destruction of the lattice on i- and e-sides was clearly observed on T-10 and TM-4. The number of displacements on i-side (T-10) and on e-side (TM-4) exceeded a few times that one on the opposite sides at any radial position. It can be explained by the enhanced hydrogen flux, for example, due to the plasma rotation or by the enhanced flux of impurities from one side due to the local source of such impurity. An enhanced concentration of Cr on the i-side of the probe (T-10) is consistent with the second version.

Conclusions: 1. The ion energy is of the order of 10-100eV and some times higher than T_e at the same radii in the SOL of T-10 and TM-4.

2. The particle fluxes are $(1-2)\cdot 10^{16} cm^{-2}s^{-1}$ and $10^{17}-10^{19} cm^{-2}s^{-1}$ for transversal and toroidal directions correspondingly.

3. The study of the collecting probes by RHEED gave additional estimation of the flux with the energy higher than the threshold energy. This flux is about 10^{-2} of the total particle flux. Now we can't say which of the plasma component (high energy part of D/H distribution or heavy impurities) play the decisive role in the displacement emergence and, therefore, is the main source of the sputtering.

4. An assymetry in distruction of the lattice of Si-probe were observed. It could be both due to the plasma rotation and the presence of a local impurity source.

References.

1. A.F.Burenkov, M.A.Kumakhov et.al. IAE-3332/11, Moscow, 1980.
2. S.A.Cohen, G.M.McCracken. PPPL-1529, Princeton, 1979.
3. A.E.Gorodetsky. In a Book "Spectroscopy and diffraction of electrons in the surfaces studies in solids"(in Russian) Moscow, pp. 222-280.
4. Rhodes R.G. "Imperfections and active centres in semiconductors", Pergamon Press, Oxford, London, 1964.

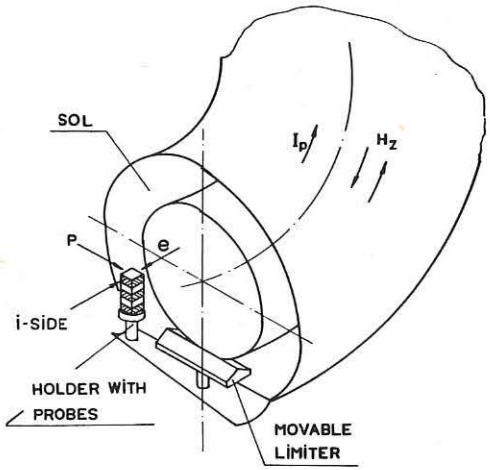
SOL
I_p
H_z
P
e
i-SIDE
HOLDER WITH
PROBES
MOVABLE
LIMITER

Fig.1.

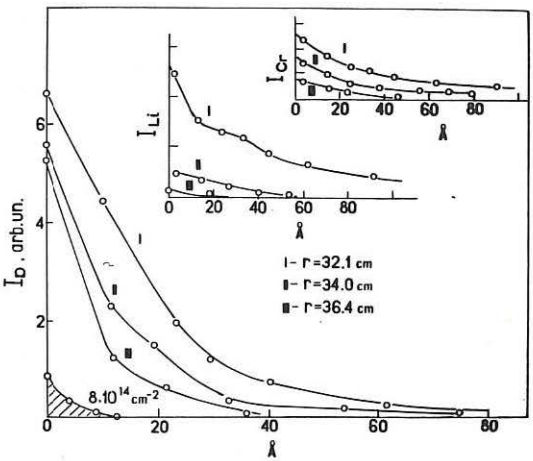
I_D, arb.un.
I_{Li}
I_{Cr}
Å
I- r=32.1 cm
II- r=34.0 cm
III- r=36.4 cm
8.10^{14} cm^{-2}

Fig.2.

ERGODIC MAGNETIC LIMITER ON TEXTOR

G.Fuchs, K.H.Dippel, B.Giesen, F.Schöngen, G.H.Wolf
and the TEXTOR Team
Institut für Plasmaphysik, Kernforschungsanlage Jülich GmbH,
Association EURATOM - KFA, P.O.B. 1913, D-517 Jülich, FRG

INTRODUCTION

"Ergodic magnetic limiters" have been proposed as an instrument to further reduce the particle confinement in the boundary, in particular to achieve some cooling effect, to enhance the fluxes into the pump limiter, and, perhaps, to obtain some impurity shielding. Generally speaking this method might help to approach the favorable regime of high recycling localized in the boundary under non-divertor conditions /1,2,3/. The proposed method is to destroy the containment by superimposing small radial magnetic fields (on the average a few 10^{-3} of the main field) which are resonant along those field lines where the containment is to be broken. The overlapping of magnetic islands resulting from such fields leads to a stochastic field line pattern; the appearance in a Poincaré plot is shown in fig.1. For some special cases Liapunov coefficients /4/ have been calculated to test the field for stochasticity. For experimental convenience the perturbation field coil system on TEXTOR is a compact and localized magnet, which excites a multitude of helical modes and thus allows to study both, effects in the plasma boundary and in the core.

PERTURBATION FIELD COILS

The perturbation field coil system mounted on TEXTOR (cf. fig.2) is a magnetic octupole, which is plugged into a rectangular porthole (80 cm x 65 cm) without breaking the vacuum. The four 16 turn coils are capable to carry 8 kA for 5 s. They are bolted together using distance slices to produce the desired gap width. The net force to the system is almost zero. The 250 kW power supply is controlled by a programmable function generator. The perturbation field and its Fourier coefficients have been calculated, the results have been published /5,6/.

EXPERIMENTAL RESULTS

Experiments have been performed for plasma densities $n=1...4x10^{13}cm^{-3}$ (line averaged), plasma currents I=200...480 kA and with a main field of 2 T. (for the machine parameters see /7/)

Plasma Boundary

The most obvious effect in the plasma boundary is the appearance of a luminescent pattern being more clearly pronounced in the thick luminous layer which is usually found in high density discharges (cf. fig.3). Although the interpretation of the pictures is impeded by the tangential viewing, the pattern strongly suggests the formation of magnetic islands. Similar patterns are also reported in /8/, where they are explained as being due to excitation of the backstreaming neutrals by plasma streaming along the island rims. The regions between the x-points of the islands and the wall appear dark, most likely because the field lines there are connected on both sides to the wall over short distances. The interior of islands cutting the wall or a limiter is supposed to appear dark for the same reason. When the plasma current is varied, we observe that islands move along the minor radius just as expected from field line tracing calculations. These "optical islands" persist even in those cases where strong perturbation fields have been applied and stochasticity is expected to exist. A structure in the boundary layer is also found from Langmuir probe measurements and from H_α and impurity (O^{5+},C^{4+}) luminescence. Depending on machine settings and plasma position, the above mentioned signals increase or de

crease under the application of the perturbation field. There is a general tendency for H_α luminescence to increase and for impurity luminescence to decrease.
Ergodization in the boundary layer has been used together with the pump limiter ALT-I. Again depending on specific discharge conditions, increases or decreases of the gas pressure in the pumping chamber have been observed. An example is given in fig.4, where an instantaneous rise of the gas flow into the pumping chamber is followed by a delayed but more pronounced increase; the latter can be attributed to a change of the density profiles and the particle confinement time.

Plasma Core

Not only for the boundary layer but also for the core plasma rather intriguing but yet no clear-cut results have been obtained at this early stage. Depending on discharge conditions in a rather subtle way both deterioration and improvement of core confinement have been found. Discharges with high plasma densities ($>3x10^{13}cm^{-3}$) are less sensitive to confinement deterioration at a given level of the perturbation field than those of the low density regime. The most pronounced effect observed in the plasma core is a turnover to new discharge conditions which are characterized by a flattening of the density profiles in such a way that the total number of particles is reduced (factor<2) whereas the density in the boundary is increased. (cf. fig.5) Whether or not this turnover occurs depends on the plasma parameters and on the perturbance field strength. The dependence on the strength of the disturbance field is very sensitive: a variation of only 2% can lead to a changeover from one case to the other. The drastic change of the plasma conditions is delayed up to 0.3 s with respect to the application of the perturbation field.
Occasionally, the plasma shows pronounced MHD-activity before the perturbation field is energized. In such cases the MHD oscillations are instantaneously stopped probably due to mode blocking; alternatively the onset of such modes has been observed during the ramp-down phase of the perturbation field (cf. fig.6 and /9/). During the turnover the density and current density profiles develop shoulders in the gradient region /10/. This observation coincides with a shifting of the helical m=2 n=1 mode signal derived from the Mirnov coils and indicates that a stationary m=2 n=1 mode is established. (Note that for a broken symmetry there is an uncertainty in the Abel inversion of the profiles.)
In a few experiments perturbation fields have been also applied together with ICR heating at power levels of up to 2 MW at I=480 kA. For the higher density regime investigated there, no negative effect of the perturbation field on global plasma confinement has been observed.

CONCLUSIONS

First "ergodic limiter" experiments on TEXTOR have shown, that the external perturbation fields effect both, the boundary region and the core. In particular, pronounced and stationary island structures in the boundary layer are observed. Internal MHD oscillations have been suppressed by rather low amplitudes of the magnetic perturbation field, an effect which may be desirable for extending the stability range of the plasma. In case that larger amplitudes of the perturbation field are applied, however, the global confinement is negatively affected. These negative side-effects can be reduced or suppressed by a more elaborate arrangement of the external magnetic field coils; in any case larger devices permit a better separation between the desired perturbation of the plasma boundary and the undesired large amplitude perturbation of the plasma core.
Both, boundary and core effects will be subject of further experiments on TEXTOR.

REFERENCES

/1/ W. Engelhardt and W. Feneberg, J. Nucl. Mat. **76&77**, 518, (1978)
/2/ W. Feneberg and G.H. Wolf, Nucl. Fusion, **21**, 669 (1981)

/3/ A. Samain, A. Grosman, T. Blenski, G.Fuchs and B. Steffen, J. Nucl. Mat. **128&129**, 395 (1984)
/4/ A.J. Lichtenberg and M.A. Liebermann, Regular and Stochastic Motion, Appl. Math. Sci. **38** Chap. 5, Springer (1983), see also literature referenced therein.
/5/ H. Belitz, K.H. Dippel, G. Fuchs and G.H. Wolf, EURATOM Programme Workshop, Schliersee 8-10 Nov (1982)
/6/ A. Nicolai, D. Reiter and F. Schöngen, Plasma Physics **27** 1479 (1985)
/7/ G. Fuchs and G. Waidmann, these proceedings
/8/ N. Ohyabu et al., Nucl. Fusion **25** 1684 (1985)
/9/ F. Karger et al., Nucl. Fusion Suppl. V I 267 Vienna (1976)
/10/ W. Stodiek, K.Bol, H. Eubank, S. von Goeler and D.J. Grove, Plasmaphy. and Contr. Nucl. Fusion V I 465 Vienna (1971)

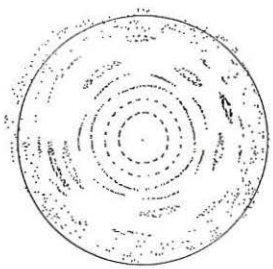

Fig. 1 Poincaré plot made for TEXTOR using the values R=1.75m, a=0.46m, I_p=360kA, B =2T, I_E=6.6kA and the ansatz $\iota=0.3[1-(1-f^2)^{3.3}]/f^2$, $f=r/a$. The machine axis is to the right.

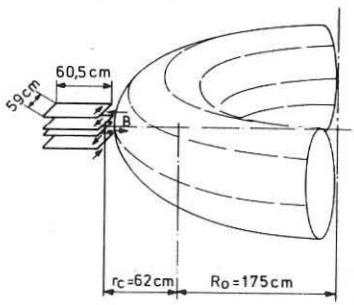

Fig. 2 Schematic of the perturbation field coils (total current up to 128 kA turns) on TEXTOR. The coils can be tilted by ±15° towards the horizontal plane.

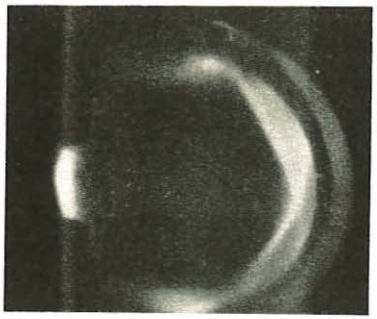

Fig. 3 Tangential view into TEXTOR with the perturbation field energized. The picture was taken before the onset of profile flattening. Discharge parameters as in fig.1.

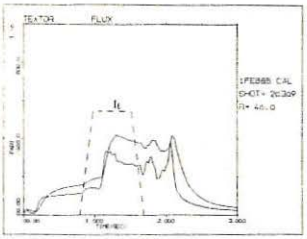

Fig. 4 Effect of the perturbation field on pump limiter performance. I_E is the perturbation coil current (90 kA at flat top). The upper solid line is the pressure in the pump limiter chamber, the lower solid line is the derived particle flux into the chamber.

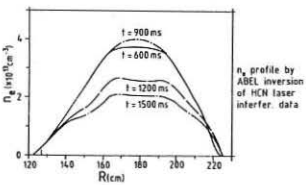

Fig. 5 Plasma density profiles derived from the HCN interferometer measurements for the same discharge as fig 4.

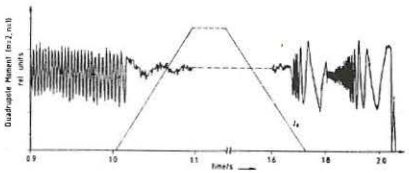

Fig. 6 Blocking and unblocking of MHD modes with m=2, n=1 (different discharge for the left and right hand side of the figure). The two growing MHD oscillations to the right are separated by a minor disruption; they coincide with the pressure rises seen after turnoff of the perturbation field in fig. 4.

EDGE PLASMA AND RADIAL ANTENNA CURRENT EFFECTS ON ALFVÉN WAVE HEATING

I. J. Donnelly†, B. E. Clancy† and M. H. Brennan‡

†Australian Atomic Energy Commission Research Establishment
Private Mail Bag, Sutherland, NSW 2232, Australia
‡School of Physics, University of Sydney, NSW 2006, Australia

1. INTRODUCTION

In Alfvén wave heating calculations the antenna is usually modelled by a helical current sheet situated in a vacuum region surrounding the plasma. Actual antennas have radial feeds, and many plasmas have a significant density in the scrape-off-layer around the antenna. We include both of these effects in a kinetic theory analysis using a cylindrical plasma model.

Fourier decomposition of a typical antenna current configuration results in a helical current sheet plus a radial volume current. For given toroidal and poloidal wavenumbers, the ratio of radial to toroidal antenna currents can be expressed as a function of a parameter λ. We evaluate the dependence on λ of the antenna resistance, and the energy deposition profile in the plasma, both with and without a low density plasma around the antenna.

2. PLASMA AND ANTENNA MODELS

The plasma parameters are typical of the TORTUS tokamak.

$r_\ell = 11$ cm, $r_a = 12$ cm, $r_w = 14$ cm, $R_o = 44$ cm

$J_\phi = 0$, $B_\phi = 0.7$ T, $\Omega_i = 6.7 \times 10^7$ rad s^{-1}

$n_{eo} = 2 \times 10^{19}$ m^{-3}, $T_{eo} = 2T_{io} = 400$ eV, H plasmas

The following density and temperature distributions are considered. They are parabolic for $r < r_\ell$, with an exponential tail.

(i) Vacuum around the antenna - the plasma ends at r_ℓ; $n_e(r_\ell)/n_{eo} = 0.05$.
(ii) Plasma around the antenna - the plasma extends to r_w.
(iii) Standard temperature profile - the temperature when $r > r_\ell$ is about 20 eV.
(iv) Anomalous temperature profile - the temperature in the region $r > r_\ell$ is very low (chosen so that $\nu_{ei} \cong \omega$). This is an attempt to simulate possible anomalous absorption of wave energy in the edge plasma.

Discrete antenna configurations can be Fourier decomposed into a sum of modes which have the form

$$\underset{\sim}{J}_{mn} = \left[\delta(r-r_a)\frac{(\hat{\theta}+\lambda\hat{z})}{(1+\lambda^2)^{\frac{1}{2}}} - \frac{i}{r}\frac{(m+\lambda k_n r_a)}{(1+\lambda^2)^{\frac{1}{2}}} H(r)\hat{r}\right] e^{i(m\theta+k_n z-\omega t)}$$

where $k_n = n/R_o$, $H(r) = 1$, $r_a \leq r \leq r_w$ (otherwise 0) and $\tan^{-1}\lambda$ is the pitch angle of the helical current in the discrete antenna. We consider cases with wavenumbers given by (m = -1, n = 2) and (m = -3, n = 2).

The wavefields in the plasma and vacuum, generated by the antenna current, are calculated using kinetic theory[1].

The antenna impedance is defined as

$$Z_{mn} = - \int E_{mn} \cdot J^*_{mn} \, rdr \quad .$$

3. DISCUSSION

In Figs. 1 and 2 the antenna resistance is plotted as a function of ω for various cases. The peaks in these diagrams correspond to eigenmodes of the surface electrostatic wave[1,2,3] (SEW).

The position-dependent power deposition P(r) is calculated from the divergence of the energy flux. In order to assess the edge heating it is appropriate to consider the radial profile of the power deposition/electron $\left(P^n(r) = P(r)/n_e(r)\right)$. Figs. 3 and 4 show P^n vs r; the top and bottom graphs are for $\omega = 2.5 \times 10^7$ and $\omega = 4.5 \times 10^7$ respectively.

We make the following observations:

(i) When the antenna is in vacuum then, for any specified wavemode (m,n), the amplitude (but not the shape) of the energy deposition profile depends on the orientation of the antenna (λ).

(ii) When the antenna is surrounded by plasma the energy deposition profile depends slightly on λ, especially when $r_o \gtrsim r_\ell$.

(iii) Incorporating an anomalously high resistivity in the edge plasma damps out the SEW eigenmodes, and leads to a large energy deposition in the edge plasma when $r_o \gtrsim r_\ell$.

(iv) The percentage energy deposition near the antenna increases with increasing $|m|$. Therefore, discrete antennas which have a small poloidal extent (and therefore have Fourier modes with large $|m|$ values) may give large edge heating, as suggested by Borg et al.[4]

4. REFERENCES

1. Donnelly, I. J. et al. [1986] - J. Plasma Phys. (in press).
2. Stix, T. H. [1980] - Proc. 2nd Joint Varenna-Grenoble Int. Symp. Heating in Toroidal Plasmas, Como, p. 631.
3. Ross, D. W. et al. [1985] - Uni. of Texas report FRCR/274.
4. Borg, G. G. et al. [1985] - Plasma Phys. Contr. Fusion 27, 1125.

PLASMA AND ANTENNA CONFIGURATIONS

Label	Antenna	λ	r_p(cm)	$T_e(r>r_\ell)$
-IN2.POL	Poloidal (J_z=0)	0	14	standard
-IN2.POL.ANOM	"	0	14	anomalous
-IN2.POL.VAC	"	0	11	-
-IN2.HEL	Helical (J_r=0)	$-m/(k_n r_a)$	14	standard
-IN2.HEL.ANOM	"	"	14	anomalous
-IN2.HEL.VAC	"	"	11	-

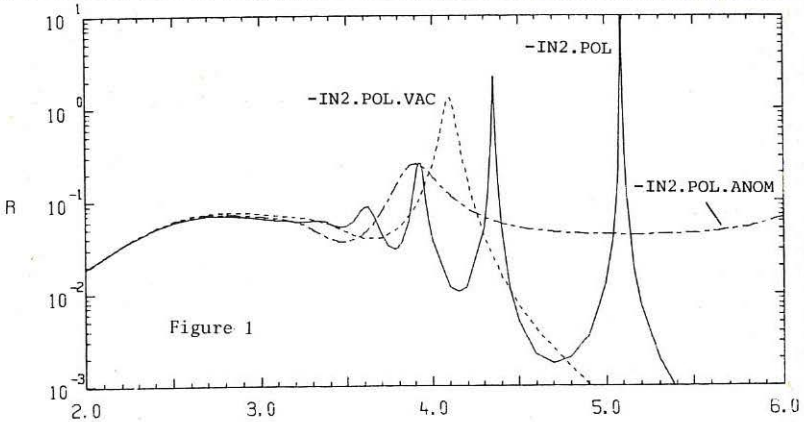

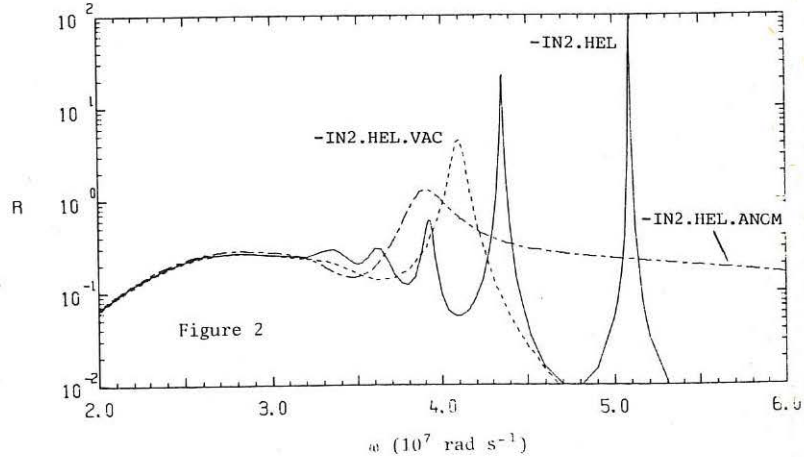

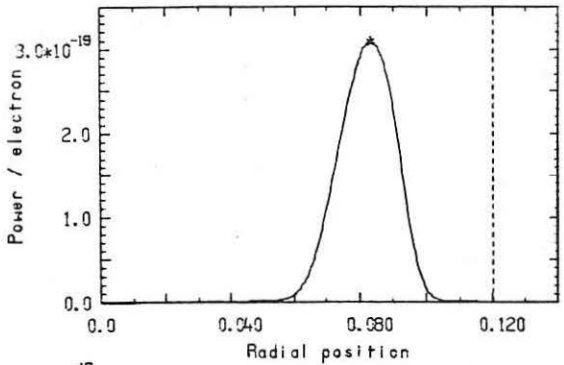

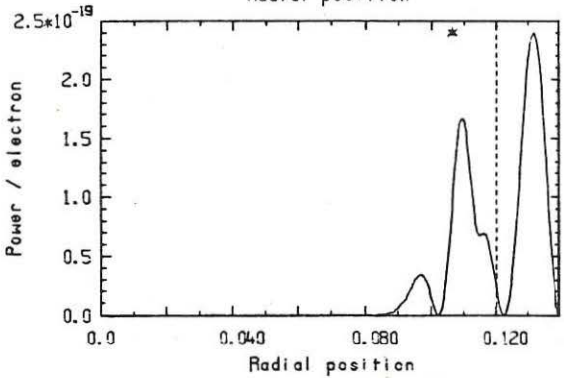

Figure 3 -IN2.POL

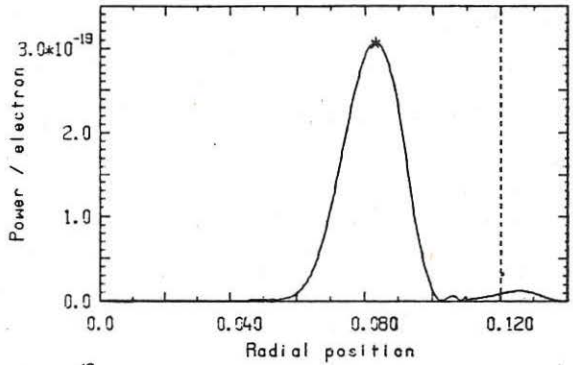

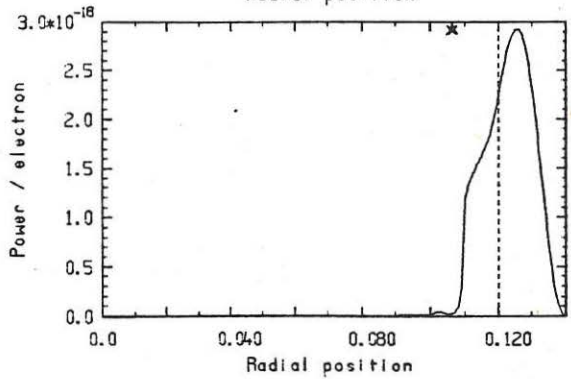

Figure 4 -IN2.POL.ANOM

The Alfvén resonance position (r_o) is denoted by *

Index